Holm Altenbach ·
Michael Beitelschmidt · Markus Kästner ·
Konstantin Naumenko ·
Thomas Wallmersperger *Editors*

Material Modeling and Structural Mechanics

Springer

Advanced Structured Materials

Volume 161

Series Editors

Andreas Öchsner, Faculty of Mechanical Engineering, Esslingen University of Applied Sciences, Esslingen, Germany

Lucas F. M. da Silva, Department of Mechanical Engineering, Faculty of Engineering, University of Porto, Porto, Portugal

Holm Altenbach , Faculty of Mechanical Engineering, Otto von Guericke University Magdeburg, Magdeburg, Germany

Common engineering materials reach in many applications their limits and new developments are required to fulfil increasing demands on engineering materials. The performance of materials can be increased by combining different materials to achieve better properties than a single constituent or by shaping the material or constituents in a specific structure. The interaction between material and structure may arise on different length scales, such as micro-, meso- or macroscale, and offers possible applications in quite diverse fields.

This book series addresses the fundamental relationship between materials and their structure on the overall properties (e.g. mechanical, thermal, chemical or magnetic etc.) and applications.

The topics of *Advanced Structured Materials* include but are not limited to

- classical fibre-reinforced composites (e.g. glass, carbon or Aramid reinforced plastics)
- metal matrix composites (MMCs)
- micro porous composites
- micro channel materials
- multilayered materials
- cellular materials (e.g., metallic or polymer foams, sponges, hollow sphere structures)
- porous materials
- truss structures
- nanocomposite materials
- biomaterials
- nanoporous metals
- concrete
- coated materials
- smart materials

Advanced Structured Materials is indexed in Google Scholar and Scopus.

More information about this series at https://link.springer.com/bookseries/8611

Holm Altenbach · Michael Beitelschmidt ·
Markus Kästner · Konstantin Naumenko ·
Thomas Wallmersperger
Editors

Material Modeling
and Structural Mechanics

 Springer

Editors
Holm Altenbach (ID)
Institute of Mechanics
Faculty of Mechanical Engineering
Otto-von-Guericke-Universität Magdeburg
Magdeburg, Germany

Markus Kästner
Institut of Solid Mechanics
Faculty of Mechanical Science
and Engineering
TU Dresden
Dresden, Germany

Thomas Wallmersperger
Institut of Solid Mechanics
Faculty of Mechanical Science
and Engineering
TU Dresden
Dresden, Germany

Michael Beitelschmidt
Institut of Solid Mechanics
Faculty of Mechanical Science
and Engineering
TU Dresden
Dresden, Germany

Konstantin Naumenko
Institute of Mechanics
Faculty of Mechanical Engineering
Otto-von-Guericke-Universität Magdeburg
Magdeburg, Germany

To Volker Ulbricht,

the great scientist
in the field of continuum mechanics
—

our colleague, collaborator, and friend.

Preface

Professor Volker Ulbricht (1949-2021)

Picture: Christian Hüller

This volume of the *Advanced Structured Materials* Series is dedicated to Professor Volker Ulbricht who sadly passed away on April 9, 2021.

Professor Ulbricht was a dedicated researcher and teacher in the field of Continuum and Engineering Mechanics. He was closely associated with Technische Universität Dresden, Germany, for more than 50 years – first as student, then as doctoral student, and since 1992 as professor. Volker Ulbricht has made contributions in many fields of mechanics, including theory of shells, micro-polar continua, constitutive models for inelastic material behavior, advanced discretization techniques and multiscale modelling techniques with applications to the simulation of sheet metal forming processes and the analysis of composite materials.

Volker Ulbricht was born on July 17, 1949. He grew up in Dresden where he passed the high school graduation exam in 1968. Simultaneously, he was awarded a craft certificate in mechanical engineering. Being luckily exempt from military service, Volker Ulbricht started his studies of Applied Mechanics at TUD in the same year. Volker Ulbricht completed the demanding course of study, which, according to Professor Göldner, study director at that time, meant a sixty-hour week and offered little free time, in four years. Without the otherwise obligatory diploma thesis, he was given direct access to doctoral studies in 1972. By the way, the fact of not being able to present a diploma certificate was to cause confusion during his appointment process later on.

With the start as research student, a period of intensive research on shell theory began, which led to the dissertation *"Berechnung von Rotationsschalen bei nichtlinearem Deformationsverhalten"* – English: "Calculation of rotation shells with non-linear deformation behavior" presented in 1975. From his doctoral supervisor and academic mentor Prof. Landgraf, Volker Ulbricht experienced a lasting imprint towards precisely formulated theories to solve challenging problems in mechanics without, however, losing sight of the relevance to applications. Equally important was the principle of intensive supervision of the doctoral students combined with continuous and personal support. Volker Ulbricht continued his successful research on shell theory as a scientific assistant at TU Dresden until 1981, combined with a stay abroad in Kharkov between 1977 and 1978, which had a formative influence both personally and professionally.

Cover page of Volker Ulbricht's doctoral thesis.

Between 1981 and 1987, Volker Ulbricht worked as development engineer at VEB Kombinat Robotron in Dresden. Even during his industrial activity, he never lost his interest in mechanics and continued his research on shell theory with great commitment in the scarce free time between work and family with two small children - an enormous challenge then as now. Volker Ulbricht was able to reap the fruits of his labor in 1986 with his habilitation *"Physikalisch und geometrisch nichtlineare Schalentheorie in konvektiver Metrik"* – English: "Physically and geometrically nonlinear shell theory in convective metric" in connection with the teaching

qualification "facultas docendi" in mechanics. He then returned to TU Dresden as a university lecturer.

In 1992 Volker Ulbricht was appointed Professor of Continuum Mechanics - since 2004 Professor of Nonlinear Solid Mechanics. In the following 24 years, Professor Ulbricht initiated and supervised 28 successful PhD projects. Together with the doctoral students, he set new accents in his field, in particular through the application of computational methods such as the finite element method in sophisticated multi-scale simulations. The available computing power enabled, for example, the modelling of complex material structures of textile fiber-reinforced plastics and the prediction of the effective elastic and inelastic deformation behavior.

A highlight of his scientific career was the initiation of the first DFG Research Training Group "Continuum Mechanics of Inelastic Solids" at TU Dresden together with Professor Kreißig from TU Chemnitz in 1994. The methods and material models developed there were later applied in numerous high-profile coordinated research projects initiated e.g. together with his colleagues Hufenbach and Offermann. With the DFG Priority Program 1123 "Textile Composite Structures and Manufacturing Technologies for Lightweight Structures in Mechanical and Automotive Engineering" (2001-2007), the DFG Collaborative Research Center 639 "Textile Reinforced Composite Components for Functionally Integrated Hybrid Structures in Complex Lightweight Applications" (2004-2015) as well as the European Centre for Emerging Materials and Processes Dresden (ECEMP, 2011-2015), long-standing, successful research collaborations could be established, which continue to have an impact today. In addition to research, teaching has always had a very special place in his academic work. With expert knowledge and humor, he was able to inspire students for mechanics. His didactic skills coupled with practical relevance have nourished his great popularity among students and thus served as a role model for many colleagues. His interaction with doctoral students, which was characterized by intensive supervision and personal contact, was exemplary. In both SFB 639 and ECEMP he acted as head of the integrated graduate college and graduate school, respectively.

Professor Ulbricht during a lecture (left), together with Professor Landgraf (middle) and with Professors Offermann and Hufenbach (right).

Prof. Ulbricht was a person involved in both science and academic life with great intellect. As Dean of the Faculty of Mechanical Science and Engineering, he shaped its future development and performed important mediation work with competence and enthusiasm. His recipe for success was being well prepared, having precise objectives and asserting them at the decisive moment. He was twice confirmed in the office between 2003 and 2009. Even after his active period at the helm of the faculty he remained an important advisor for his successors Beyer and Stelzer, partly as Vice Dean. In addition, he was a member of the Senate from 2003 to 2014 and actively participated in the Faculty Council from 1997 to 2014. Professor Ulbricht served as director of the Institute of Solid Mechanics for many years. In his work as a DFG review board member, he was highly regarded as a fair and mediating expert.

The Faculty of Mechanical Science and Engineering of TU Dresden, Holzhau, 2008.

Professor Ulbricht and his team in 2011 (left), walking tour in Moritzburg with colleagues of the Institute of Solid Mechanics (right).

Since 1996, Professor Ulbricht has been just as committed in actively contributing his expertise as a member of the Board of Directors to the "Association of Applied Mathematics and Mechanics" (GAMM), which he shaped as Secretary for many years between 1997 and 2008. During this time, Volker Ulbricht supported several presidents, ensured a smooth running of the board meetings, took care of the interests of GAMM with great experience, concentrated on the essentials and always

Volker Ulbricht together with Holm Altenbach and Konstantin Naumenko at GAMM 2003 in Abano-Padua (left); Volker Ulbricht and Reiner Kreißig at the colloquium on the occasion of Professor Ulbricht's 70th birthday 2019 in Dresden (right).

looking for balance, including the organization of the annual meeting in Dresden in 2004.

Professor Ulbricht not only impressed us with his technical expertise. It is in particular his charm – to all of us and most of his colleagues he was known as Ulbi – that we will miss in the future.

April 2022

Magdeburg,   *Holm Altenbach*
Dresden,   *Michael Beitelschmidt*
                                                                                 Markus Kästner
                                                                          Konstantin Naumenko
                                                                      Thomas Wallmersperger

Contents

12 Applications of Viscoplasticity and Damage Models, the Thermomechanical Consistency and the Prospect of a Microstructural Representation 311

Matthias Ziegenhorn, Rainer Adelung, Rainer Franke, Robert Roszak,
Ilja Sagradov, Daniela Schob, Holger Sparr, and Tomasz Kurzynowski

List of Contributors

Rainer Adelung
CAU Kiel, Kaiserstraße 2, 24143 Kiel, Germany
e-mail: ra@tf.uni-kiel.de

Holm Altenbach
Lehrstuhl für Technische Mechanik, Institut für Mechanik, Fakultät für
Maschinenbau, Otto-von-Guericke-Universität Magdeburg, Universitätsplatz 2,
39106 Magdeburg, Germany
e-mail: holm.altenbach@ovgu.de

Michael Beitelschmidt
Institute of Solid Mechanics, Technische Universität Dresden, Marschnerstraße 30,
01307 Dresden, Germany
e-mail: michael.beitelschmidt@tu-dresden.de

Sourav Chandra
Technical University Munich, Munich, Germany
e-mail: sourav.chandra@tum.de

Rainer Franke
BTU Cottbus-Senftenberg, Universitätsplatz 1, 01968 Senftenberg, Germany
e-mail: rainer.franke@b-tu.de

Ulrich Gabbert
Lehrstuhl für Numerische Mechanik, Institut für Mechanik, Fakultät für
Maschinenbau, Otto-von-Guericke-Universität Magdeburg, Universitätsplatz 2,
39106 Magdeburg, Germany
e-mail: ulrich.gabbert@ovgu.de

Sven Harzheim
Institute of Solid Mechanics, TU Dresden, George-Bähr-Straße 3c, 01069 Dresden,
Germany
e-mail: sven.harzheim@tu-dresden.de

Martin Hofmann
Institute of Solid Mechanics, TU Dresden, George-Bähr-Straße 3c, 01069 Dresden,
Germany
e-mail: martin.hofmann@tu-dresden.de

Markus Kästner
Institute of Solid Mechanics, TU Dresden, George-Bähr-Straße 3c, 01069 Dresden,
Germany
e-mail: Markus.Kaestner@tu-dresden.de

Michael Kaliske
Institute for Structural Analysis, TU Dresden, 01062 Dresden, Germany,
e-mail: michael.kaliske@tu-dresden.de

Valeriy L. Khavin
Department of Continuum Mechanics and Strength of Materials, National Technical
University "Kharkiv Polytechnic Institute", 2, Kyrpychova str., 61002, Kharkiv,
Ukraine
e-mail: vkhavin@kpi.kharkov.ua

Vladimir A. Kolupaev
Fraunhofer Institute for Structural Durability and System Reliability (LBF),
Schloßgartenstr. 6, 64289 Darmstadt, Germany
e-mail: Vladimir.Kolupaev@lbf.fraunhofer.de

Robert Kühne
Materials Characterization and Testing, Fraunhofer Institute for Material and Beam
Technology, Winterbergstraße 28, 01277, Dresden, Germany
e-mail: robert.kuehne@iws.fraunhofer.de

Tomasz Kurzynowski
Politechnika Wrocławska, Wydział Mechaniczny, ul. Ignacego Łukasiewicza 5,
50-371 Wrocław, Poland
e-mail: tomasz.kurzynowski@pwr.edu.pl

Claudius Lein
86899 Landsberg am Lech, Germany
e-mail: clein@gmx.de

Gennady Lvov
Department of Dynamics and Strength of Machines, National Technical University
"Kharkiv Polytechnic Institute", 2, Kyrpychova str., 61002, Kharkiv, Ukraine
e-mail: lvovdpm@ukr.net

Ivan Lvov
"HEJ Engineering UA" Limited Liability Company, 13-A Universitetska Str.,
03110 Kyiv, Ukraine
e-mail: ivlv@enabl.dk

Marcus Maeder
Technical University Munich, Munich, Germany
e-mail: Marcus.Maeder@tum.de

Steffen Marburg
Technical University Munich, Munich, Germany
e-mail: Steffen.Marburg@tum.de

Boris E. Melnikov
Peter the Great St. Petersburg Polytechnic University, Institute of Physics and
Mechanics, Polytechnicheskaya, 29, 195251 St. Petersburg, Russian Federation
e-mail: melnikovboris@mail.ru

Oleg Morachkovsky
Department of Computer Modelling of Processes and Systems, National Technical
University "Kharkiv Polytechnic Institute", 2, Kyrpychova str., 61002, Kharkiv,
Ukraine
e-mail: morachko@ukr.net

Konstantin Naumenko
Lehrstuhl für Technische Mechanik, Institut für Mechanik, Fakultät für
Maschinenbau, Otto-von-Guericke-Universität Magdeburg, Universitätsplatz 2,
39106 Magdeburg, Germany
e-mail: konstantin.naumenko@ovgu.de

Friedrich Pfeiffer
Lehrstuhl Angewandte Mechanik, TU München, 85747 Garching, Germany
e-mail: friedrich.pfeiffer@tum.de

Sergiy Yu. Pogorilov
Department of Continuum Mechanics and Strength of Materials, National Technical
University "Kharkiv Polytechnic Institute", 2, Kyrpychova str., 61002, Kharkiv,
Ukraine,
e-mail: ark95@ukr.net

Alexander Raßloff
Institute of Solid Mechanics, TU Dresden, George-Bähr-Straße 3c, 01069 Dresden,
Germany,
e-mail: Alexander.Rassloff@tu-dresden.de

Robert Roszak
BTU Cottbus-Senftenberg, Universitätsplatz 1, 01968 Senftenberg, Germany
e-mail: robert.roszak@b-tu.de

Ilja Sagradov
BTU Cottbus-Senftenberg, Universitätsplatz 1, 01968 Senftenberg, Germany
e-mail: ilja.sagradov@b-tu.de

Daniela Schob
BTU Cottbus-Senftenberg, Universitätsplatz 1, 01968 Senftenberg, Germany
e-mail: daniela.schob@b-tu.de

Benjamin Schmidt
Institute of Solid Mechanics, TU Dresden, George-Bähr-Straße 3c, 01069 Dresden,
Germany
e-mail: Benjamin.Schmidt@tu-dresden.de

Artem S. Semenov
Peter the Great St. Petersburg Polytechnic University, Institute of Physics and
Mechanics, Polytechnicheskaya, 29, 195251 St. Petersburg, Russian Federation &
TU Dresden, Institute of Solid Mechanics, George-Bähr-Str. 3c, 01069 Dresden,
Germany
e-mail: semenov_as@spbstu.ru,asemenov@tu-dresden.de

Yuhao Shi
Institute of Solid Mechanics, TU Dresden, George-Bähr-Straße 3c, 01069 Dresden,
Germany
e-mail: yuhao.shi@tu-dresden.de

Holger Sparr
BTU Cottbus-Senftenberg, Universitätsplatz 1, 01968 Senftenberg, Germany
e-mail: holger.sparr@b-tu.de

Johannes Storm
Institute for Structural Analysis, TU Dresden, 01062 Dresden, Germany
e-mail: johannes.storm@tu-dresden.de

Robert Tandler
BMW Group München, Germany
e-mail: robert.tandler@bmw.de

Thomas Wallmersperger
Institute of Solid Mechanics, TU Dresden, George-Bähr-Straße 3c, 01069 Dresden,
Germany
e-mail: thomas.wallmersperger@tu-dresden.de

Bo Yin
Institute for Structural Analysis, TU Dresden, 01062 Dresden, Germany
e-mail: bo.yin@tu-dresden.de

Matthias Ziegenhorn
BTU Cottbus-Senftenberg, Universitätsplatz 1, 01968 Senftenberg, Germany
e-mail: matthias.ziegenhorn@b-tu.de

Martina Zimmermann
Materials Characterization and Testing, Fraunhofer Institute for Material and Beam
Technology, Winterbergstraße 28, 01277, Dresden, Germany
e-mail: martina.zimmermann@iws.fraunhofer.de

Chapter 1
The Use of the Homogenization Method in the Analysis of Anisotropic Creep in Metal-matrix Composites

Holm Altenbach, Gennady Lvov, Ivan Lvov, and Oleg Morachkovsky

Abstract The primary purpose of this study is the development of a method for the numerical homogenization of the nonlinear creep properties of unidirectionally reinforced fiber composites. The constitutive relations for a homogeneous material, equivalent to composite, are based on the hypothesis of the existence of a potential for the strain rates of steady-state creep. The generalization of the power-law dependence of the strain rate on stresses for the case of a complex stress state is achieved by introduction of an equivalent stress using a 4th rank tensor. The structure of this tensor allows to take into account the required symmetry class for a particular form of fiber packing. The homogenization procedure is based on micromechanical analysis of a representative composite volume. A technique for the numerical simulation of physical experiments necessary for the identification of the material parameters of the theoretical model is proposed. A series of numerical calculations by the finite element method in the ANSYS software for a boron-aluminum composite has been carried out.

Holm Altenbach
Lehrstuhl für Technische Mechanik, Institut für Mechanik, Fakultät für Maschinenbau, Otto-von-Guericke-Universität Magdeburg, Universitätsplatz 2, 39106 Magdeburg, Germany,
e-mail: holm.altenbach@ovgu.de

Gennady Lvov
Department of Dynamics and Strength of Machines, National Technical University "Kharkiv Polytechnic Institute", 2, Kyrpychova str., 61002, Kharkiv, Ukraine,
e-mail: lvovdpm@ukr.net

Ivan Lvov
"HEJ Engineering UA" Limited Liability Company, 13-A Universitetska Str., 03110 Kyiv, Ukraine,
e-mail: ivlv@enabl.dk

Oleg Morachkovsky
Department of Computer Modelling of Processes and Systems, National Technical University "Kharkiv Polytechnic Institute", 2, Kyrpychova str., 61002, Kharkiv, Ukraine,
e-mail: morachko@ukr.net

1

Key words: Unidirectional composite, Nonlinear creep, Micromechanical modeling, Numerical homogenization

1.1 Introduction

Composite materials are increasingly used in various fields of modern technology due to the high ratio of strength and stiffness to weight, the possibility of creating materials with the required anisotropy of properties, and good manufacturability (Altenbach et al., 2003, 2018). In engineering applications, composite structures are often subjected to stresses for a long time, which can lead to the development of creep deformations. The temperature range at which creep appears is very wide, from room temperature for composites with a polymer matrix, up to 2000°C for carbon-carbon composites. Consideration of creep and stress relaxation in the design of structures is impossible without the development of rheological models (Reiner, 1969; Palmov, 1998) of composite materials. The relevance of such studies has led to a significant amount of recent publications devoted to various aspects of this problem.

Asyraf et al. (2020) presents a modern overview of the creep analysis of elements of structures made of composite materials and wood. The focus is on the work dedicated to the cantilever construction structures. Theoretical models, in which creep deformation velocities are determined by power law model dependencies on stress and time, are considered. Works are noted using various options for Norton's law. Temperature effect is taken into account by exponential dependencies like the Arrhenius law (Arrhenius, 1889). Publications, in which the creep is modeled by viscoelastic dependencies with various combinations of Kelvin-Voigt and Maxwell elements, are highlighted. The results of experimental work on bending and uniaxial stretching of rods were analyzed. The problems of the accuracy of the creep modeling and the formation of strength criteria for practical use are allocated.

Ornaghi Jr. et al. (2020a) describes the results of the analysis of the creep and relaxation of stresses of multilayer carbon fiber-reinforced polymer (CFRP) with different layered orientation of the fibers. Experiments were performed using a three-point bending clamp of plate samples. Samples were loaded at three stress levels. In each stress level, three different temperatures are applied: 50°C, 150°C and 210°C, which ensured the possibility of analysis of three aggregate states in the process of curing epoxy resin. Two variants of exponential dependence are used to approximate relaxation curves. Analytical predictions showed good agreement with experimental results, including temperature dependencies. The models presented in the work can be extended to other polymer composites.

Yang et al. (2021) analyzed the physical mechanisms and methods of mathematical modeling of metal matrix composites creep. A wide range of compositions is considered: from hardening by the nano-sized particles to composites reinforced by short and long fibers. In the second stage various variants of power laws of dependencies of the creep deformation rate were used for creep controlled by diffusion,

for migration models of vacancies, for creep polycrystalline alloys and for sliding mechanisms on grain boundaries. The features of the creep of metal matrix composites, reinforced by micro-sized particle and nano-sized particle, are considered in detail. The most widely used ceramic particles of silicon carbide and aluminum oxide due to high hardness and thermal stability at high temperatures. Based on the analysis performed, it was concluded that the addition of ceramic particles and fibers in metal matrix composites is an effective way to increase the creep resistance at elevated temperatures.

In Sala et al. (2021) the influence of the stress level and operating conditions on the creep characteristics of composites reinforced with flax and hemp fibers are experimentally analyzed. Flax unidirectional ribbon and hemp satin woven fabric were used for the preparation samples. Biosourced epoxy was used as a matrix. Creep and recovery experiments were carried out at various temperatures (23°C and 70°C) and relative humidity (50% and 70%C).

The model of an anisotropic viscoelastic body is used for the theoretical description of creep. The creep strain rates were set using the 4th rank compliance tensor, the structure of which corresponded to an orthotropic body. The flow law took into account the creep of the matrix and fibers.

The experimental results showed that the level of time-delayed deformation at the creep stage is higher than at the recovery stage. Dependencies of irreversible deformations on environmental conditions and stress levels have also been established.

Specific manifestations of rheological properties arise in structural elements created by 3D printing methods. In Chen et al. (2020), the thixotropy and creep of a cement composite based on calcium sulfoaluminate are experimentally analyzed. Empirically, a specific yield point has been established, which is the minimum value of the shear stress required to obtain flow. The second characteristic is plastic viscosity, which determines the ability to resist deformation when the yield point is exceeded. These two properties can be the main parameters for 3D printing of concrete structures.

Khatkar and Behera (2021) presented the results of an experimental analysis of the fatigue strength and creep of E-glass/epoxy-based composite leaf springs. Various types of reinforcement were used to make the samples: chopped fibers, unidirectional (UD), bidirectional plain woven (2D), and 3D woven solid structures. The leaf springs were tested for cyclic flexural strength using their own test rig. The leaf springs were subjected to pulsating flexural loading at a frequency of 1 Hz for up to 20000 cycles. Short-term analysis of flexural creep initially showed a rapid increase in compliance, and then the rate of its increase decreased for all composite leaf springs. It has been found that a leaf spring made of a three-dimensionally reinforced composite material has the highest cyclic bending strength. Unidirectional composites and fabric-reinforced materials showed poor creep resistance compared to 3D orthogonal composites. A 3D braided composite leaf spring with minimum binder has proven to be the best material for automotive leaf spring due to its high cyclic flexural strength and moderate creep.

The results of experimental research and theoretical modeling of the creep of multilayer fiberglass specimens are presented in Lv et al. (2020). Uniaxial tension and compression experiments were carried out on an INSTRON 8802 setup with a hydraulic loading system. The heating device kept the controlled temperature of the sample at 70°C during the tests. Samples were made using 12 prepreg layers with different stacking sequences. The stress-strain curves show significant non-linearity as well as differences in tension and compression.

For the theoretical generalization of the experimental results, a nonlinear viscoplastic model has been developed that reflects the asymmetry of tension and compression during creep. Putting the hydrostatic pressure into the constitutive relations made it possible to take into account the tension-compression asymmetry of anisotropic composites. The proposed model was implemented using finite element analysis in ABAQUS software through a custom subroutine UMAT. The model was tested against experimental creep curves for unidirectional and multilayer plastics in tension and compression.

In Karthik et al. (2020), the effect on the creep characteristics of a polymer composite with an epoxy base and various fillers was experimentally investigated. Samples for testing were made with organic fillers: agave, cornhusk, jute. Particles of basalt, carbon, glass and ash are used as inorganic fillers. Dissipative and elastic characteristics were determined by the dynamic method with flexural vibrations at frequencies of 1 Hz, 5 Hz and 10 Hz. Short-term creep tests were performed at 40°C. A static stress of 1.0 MPa was applied for 30 minutes after temperature stabilization, and creep strain was measured as a function of time. It was found that composites filled with inorganic particles have low creep strain due to the higher rigidity of inorganic fillers compared to organic fillers. Among organic materials, the greatest creep deformation was observed in composites filled with corn husk particles. The smallest creep strain was found in the case of ash particles due to their better adhesion to the epoxy resin.

The results of an experimental study of the creep of metal matrix composites $SiC_p/2024Al$ are presented in Gong et al. (2020). The experiments were carried out in an atmospheric environment using a CRIMS RDL100 setup. The choice of test modes for was carried out in such a way that the stresses did not exceed the yield point for a given temperature, but the rate of creep deformations was also sufficient for fixing by sensors in the section of steady creep. Tests were conducted at fixed temperatures of 250°C, 300°C and 350°C. The temperature maintenance error did not exceed $\pm$ 2°C. The samples were loaded with constant stresses in the range of 40 MPa -140 MPa so that at a given temperature three stages of creep appeared: primary creep, steady-state creep, and accelerated creep. The processing of the creep curves showed that the dependence of the creep strain rate at the second stage has a power-law form with an exponent $n = 8$. To set the temperature dependencies, the value of the activation energy was determined to be 227.7 kJ/mol.

The creep of a composite pipe has been investigated experimentally and theoretically in Rafiee and Ghorbanhosseini (2020) for the case of loading by compressive transverse forces. The investigated pipe is made by winding method. The composite consists of fiberglass and polyester resin. For the tests, a section of a pipe with a

diameter of 0.5 m, a length of 0.3, and a wall thickness of 0.012 m was used. The test setup provided the load of a constant force of 981 N distributed over two opposite sections parallel to the generatrix. The deflections of the pipe were recorded for 10000 h at a room temperature of $25\pm3°$C. Theoretical modeling was carried out at two levels. Micromechanical modeling of elastic and viscoelastic properties was carried out using the rule of mixtures. Modeling at the macro level was carried out by the finite element method using the ABAQUS software package and its own subroutine for setting material properties. Comparison of experimental and theoretical data showed good agreement.

Fliegener and Hohe (2020) developed and investigated viscoelastic models for unidirectionally and discontinuously long fiber reinforced composites. The modeling is based on the three term Kelvin–Voigt formulation. For composites reinforced with long fibers, the isotropic formulation is generalized to anisotropic form using scale functions for three spatial directions. Micromechanical composites analysis uses an isotropic viscoelastic matrix model and a transversely isotropic Hooke's law for fibers. To determine the parameters of the composite creep models, experimental studies of a pure thermoplastic polymer, as well as a thermoplastic material reinforced with discontinuously long and short fibers, have been carried out. As an example of the analysis of the creep of a structural element, a model (Fliegener et al., 2019) of a three-layer automobile structure under local loading is considered. The calculations were performed by the finite element method. Good agreement between the experimental and numerical results was noted. The discrepancy was observed only in cases where local damage develops in the experimental samples.

In Hao et al. (2020), the influence of the geometry and orientation of fibers on the properties of composites based on polyethylene reinforced with short fibers from natural materials was experimentally analyzed. The geometry of the fibers was investigated using a stereomicroscope followed by computer image analysis. Creep tests were performed at a constant temperature of $30°$. The test program provided for stretching the samples at a stress of 2 MPa for 30 min and measuring the deformation after removing the load for 30 min. The anisotropy of elastic properties, creep, and thermal expansion of specimens was systematically analyzed at various angles of fiber orientation relative to the direction of extrusion. It has been found that fillers with a high fiber length to diameter ratio can limit deformation of the polymer matrix. In addition to the experiments, the stress and strain distributions in the specimens were simulated by the finite element method.

Jafaripour and Taheri-Behrooz (2020) analyzed the creep of polymer composites using a nonlinear viscoelastic model of an anisotropic environment. Nonlinear parameters depending on temperature and stresses are added to integral relations of unsteady nonlinear viscoelasticity. The creep kernels are approximated using the Prony kernels. An iterative algorithm of successive approximations has been developed to solve nonlinear equations. An iterative process is used to minimize linearization errors. This made it possible to set the size of the time steps in a rational way.

This approach has been used to analyze the creep of isotropic matrix materials and for unidirectional composites reinforced with elastic fibers. Micromechanical

analysis of a representative volume was performed by the finite element method in the ABAQUS software package. The performed micromechanical studies make it possible to predict the creep parameters in polymer composites and obtain the required characteristics by varying the viscoelastic properties of the matrix and the elastic parameters of the fibers.

The results of experimental studies of the creep of composites made of bio-based epoxy resin, reinforced with flax fibers, are presented in Jia and Fiedler (2020). To prepare the reinforcement, the fibers were twisted into strands, sewn with textured polyester and formed into a non-corrugated fabric. The prepregs for the samples consisted of 4 layers of flax fabric, which was pre-dried at a temperature of $102°C$. The vacuum curing technology provided for two cycles: 8 hours at a temperature of $30°C$, then 16 h at a temperature of $60°C$. To determine the tensile strength and tensile modulus experiments were carried out on specimen tension on a Zwick 100 kN installation. Creep tests were carried out at five stress levels from 66 MPa to 240 MPa. The creep curves have two distinct sections. At the first stage, the creep strain increases rapidly with a decrease in the creep strain rate. In the second section, the dependence of deformation on time is almost linear. Pretreatment of linen fibers with furfuryl alcohol reduces the creep strain rate by up to 30% compared to the raw analogue.

Matrices of polymer composites demonstrate viscoelastic properties and sensitivity to ambient temperature and humidity. Nguyen et al. (2020) analyze the creep of multilayer composites taking into account the influence of a variable temperature field and humidity. The governing equations of viscoelasticity are based on the Boltzmann superposition principle. The integral relations for stresses include the parameters of thermal and hygroscopic expansion. Anisotropic relaxation moduli also include time, temperature and humidity dependencies. The relaxation kernels are approximated by a series of exponential Prony functions. The Laplace transform reduces the associated hygrothermo-mechanical problem for viscoelastic laminates to a linear one with respect to images. Numerical results for stresses and strains are obtained using inverse transformation methods. Tasks for a laminated plate with sinusoidal distribution over the upper and lower surfaces of pressures, temperatures and humidity parameters are considered as examples. The first stage of the analysis was to determine the temperature and humidity distributions over the plate thickness. Then the mechanical parameters were determined using the fast Fourier transform. The effectiveness of the proposed approach has been demonstrated for a number of particular problems of thermal conductivity, thermoelasticity, and creep.

The purpose of the experiments in Ornaghi Jr. et al. (2020b) was to study the creep of polymer composites reinforced with glass and carbon fibers. The influence of percentage ratios of filler types, alternation of layers, test temperature and porosity was studied. Prior to creep experiments, porosity was determined for each composite using optical microscopy. Elastic and dissipative characteristics at different temperatures in the range of $25\text{-}210°C$ were determined by a dynamic method. Creep experiments were carried out at the same temperatures with a constant stress of 2 MPa for 60 s. When processing the results, the creep curves were approximated by the power-law dependence of deformation on time. To predict long-term creep

based on short-term tests, a temperature-time analogy with the Arrhenius dependence was used. The analysis of numerous results allowed obtaining data for the rational choice of the structure of hybrid composites in relation to creep properties.

Samareh-Mousavi and Taheri-Behrooz (2020) present a new phenomenological model of decreasing the stiffness of composite materials with a polymer matrix during creep. The governing equations are formulated for a uniaxial stress state. These equations include non-linear relationships between stresses, strains, time, and number of loading cycles. The presented damage model consists of an elastic component that depends on the number of cycles. For creep deformations, nonlinear dependences on stresses and time are used, as well as a special parameter reflecting the effect of the number of loading cycles. The proposed model was tested on experimental data on the creep of short-fiber fiberglass with an epoxy matrix. It has been established that, on the basis of the proposed relations, it is possible to predict the form of isochronous curves for various numbers of loading cycles.

In Sun et al. (2020), a study was made of the effect of ambient humidity on the creep of polymer composites. Three-dimensional constitutive relations for the creep of an orthotropic body are given in a coordinate system that coincides with the symmetry planes of the material. Creep deformations are set by integral dependencies, which include swelling parameters reflecting the effect of moisture.

The basic orthotropic equation of a composite plate, taking into account the viscoelastic creep deformation and swelling deformation in the base material, the coordinates have the following form: obtained by introducing the moisture shear coefficient into the nonlinear Chapery equation. Hygrothermal-mechanical tests of adhesion for moisture absorption, as well as tests for static mechanical properties and short-term creep under tension. Recovery tests were performed with different moisture contents to obtain hygroscopic parameters and non-linear creep parameters depending on moisture and stress. A fully coupled numerical prediction model was developed in ABAQUS using a User Defined Materials Subroutine (UMAT) and a User Defined Field Variables (USDFLD) subroutine to simulate conjugate diffusion and nonlinear creep behavior. There is good agreement between the numerical and experimental results.

At present, before numerical simulations work with a three-dimensional orthotropic constitutive model of nonlinear creep, taking into account the effect of moisture, is derived by introducing the moisture shear coefficient into the nonlinear equation. Then, experimental studies of composite materials were carried out. laminates for obtaining hygroscopic parameters and non-linear creep parameters depending on moisture and stress. Based on the measured material data, a three-dimensional numerical model was then found to predict the fully coupled diffusion-nonlinear creep of composite laminates.

A feature of detachable joints of structural elements made of composite materials is the relaxation of contact stresses due to creep. Xie et al. (2020) is devoted to the application of the theory of viscoplasticity and the theory of fractal contact to study the processes of weakening of strength in bolted joints of structural elements made of carbon fiber reinforced plastics. The mathematical model of the material includes an associated flow law for plastic deformations, and the dependence of ef-

fective creep deformations on time includes the first section and the section of the steady-state stage. All constitutive relations are written for a transversely isotropic composite, taking into account the asymmetry of tension and compression. It is assumed that plastic deformations and creep do not develop in the direction of reinforcement.

To identify the parameters in the constitutive relations, experiments were carried out on samples made of carbon fiber. The samples were cut at different angles with respect to the direction of the fibers. Compression creep tests were carried out at $70°C$ at three stress levels for 50 h.

The proposed constitutive relations were implemented in the ABAQUS software package with the implementation of custom material models. Finite element analysis of a bolted joint was carried out on a model of two square sheets ($40 \times 40 \times 4$ mm) of carbon fiber compressed in the center by an M6 stainless steel bolt. Numerical modeling has made it possible to investigate the effect of plastic deformations on the distribution of contact pressures as a result of preliminary tightening of the bolt. The analysis of creep deformations made it possible to establish the features of the stress relaxation processes depending on the degree of roughness of the contact surfaces. Comparison of the numerical results with experimental data showed that the error of the FEM analysis decreases when the deformation of the microroughness of the contact surfaces is taken into account.

The given examples of publications indicate a wide variety of approaches to modeling the creep of composites. Structures of heterogeneous materials, in which reinforcement with nano- and macroparticles, various types of fiber reinforcement, and multilayer laminates are used, are of great importance. The rheological properties of polymer matrices are described by equations of viscoelastic environments, and nonlinear creep models are used for metal matrices. The methods of taking into account the influence of plastic deformations, temperatures, humidity, and other factors on creep are also varied. For the practical use of composites creep models in modern computational practice, a necessary stage is the homogenization procedure in the formation of constitutive relations with respect to the averaged characteristics of continuum mechanics. This article is devoted to the development of a method for homogenizing the creep properties of unidirectionally reinforced metal-matrix composite materials.

1.2 Homogenization Method for Determining the Properties of Composite Materials

It is known that on a micro- and meso-scale all materials are heterogeneous, but many of their properties can be determined within a continuous model involving the principle of efficient homogenization. According to this principle, the existence of representative volume is assumed, within which the properties of the heterogeneous material can be averaged. The scale of the representative volume of averaging should be much larger than the characteristic size of the inhomogeneity and small

compared to the characteristic size of the body. Under these conditions, the heterogeneous material can be idealized by considering it as equivalent to a homogeneous material with properties averaged over the representative volume. The problem of deformation of constructions made of composite material is solved using averaged properties.

We introduce the representative volume of a heterogeneous medium having a characteristic size equal to the averaging scale. Average stresses and strains are determined as follows:

$$\langle \sigma_{ij} \rangle = \int_V \sigma_{ij} dv, \tag{1.1}$$

$$\langle \varepsilon_{ij} \rangle = \int_V \varepsilon_{ij} dv, \tag{1.2}$$

where ε_{ij} is the tensor of small deformations, and σ_{ij} is the Cauchy stress tensor. The effective stiffness for elastic deformations, denoted by the tensor C_{ijkl}, is determined by the ratio:

$$\langle \sigma_{ij} \rangle = C_{ijkl} \langle \varepsilon_{kl} \rangle. \tag{1.3}$$

To solve the problem of the effective elastic properties, it is necessary to conduct a micro-mechanical analysis within the representative element and perform the averaging procedure defined by expressions (1.1) and (1.2). Details of the numerical method of calculating the components of the tensor C_{ijkl} for unidirectional reinforced composites are given in Darya Zadeh and L'vov (2015). The high scatter of test results complicates the problem of identifying creep parameters.

For homogeneous materials, the creep rates in samples cut from a single rod may differ by ten percent. In this case, it is difficult to determine that the difference in creep rate for samples cut from the same material in orthogonal directions is the result of anisotropy or data scatter. Creep anisotropy is more pronounced in heterogeneous materials. For example, in polymer composites reinforced with fibers, the experimental results show completely different creep rates in the fiber direction and orthogonal direction. Creep anisotropy also occurs in the weld metal (Naumenko and Altenbach, 2005) on samples cut in the welding directions and the transverse direction. For periodic heterogeneous structures, the theoretical method of averaging allows to determine the effective creep properties on the basis of known creep properties of the constituent components. Theoretical determination of the effective properties of periodic multiphase materials has many advantages over experimental research. Analytical or numerical methods of homogenization for periodic media allow finding effective creep properties for many variants of multiphase structures.

1.3 Creep Theory of Initially Orthotropic Materials

Consider a creep model of a unidirectional reinforced composite material with an orthogonal fiber packing scheme. Since the equivalent homogeneous material for a

unidirectional fibrous composite is an orthotropic material, it is possible to use the creep theory for orthotropic materials. Use the creep law of orthotropic heterogeneous materials described in Morachkovskii and Zolochevskii (1980); Naumenko and Gariboldi (2014); Naumenko and Altenbach (2016) in the matrix form using Voigt's notation:

$$\underline{\dot{c}} = \frac{\dot{c}_{eq}}{2\sigma_{eq}} [B] \underline{\sigma}, \tag{1.4}$$

where $\underline{\sigma} = (\sigma_{11}, \sigma_{22}, \sigma_{33}, 2\sigma_{12}, 2\sigma_{23}, 2\sigma_{31})^T, \underline{\dot{c}} = (\dot{c}_{11}, \dot{c}_{22}, \dot{c}_{33}, \dot{c}_{12}, \dot{c}_{23}, \dot{c}_{31})^T$ - vectors composed from components of stress and creep rates tensors; $\sigma_{eq}^2 = \frac{1}{2}\underline{\sigma}^T [B] \underline{\sigma}$ - equivalent stress.

Matrix of material constant creep properties, which are introduced to account for the initial orthotropy of homogeneous material, has the form:

$$[B] = \begin{vmatrix} b_{1111} & b_{1122} & b_{1133} & 0 & 0 & 0 \\ b_{1122} & b_{2222} & b_{2233} & 0 & 0 & 0 \\ b_{1133} & b_{2233} & b_{3333} & 0 & 0 & 0 \\ 0 & 0 & 0 & b_{1212} & 0 & 0 \\ 0 & 0 & 0 & 0 & b_{2323} & 0 \\ 0 & 0 & 0 & 0 & 0 & b_{3131} \end{vmatrix}. \tag{1.5}$$

From the condition of incompressibility due to creep deformations, the next restrictions follow:

$$\begin{aligned} b_{1111} + b_{1122} + b_{1133} &= 0, \\ b_{1122} + b_{2222} + b_{2233} &= 0, \\ b_{1133} + b_{2233} + b_{3333} &= 0. \end{aligned} \tag{1.6}$$

In the case of heterogeneous materials, this condition for averaged total deformations may not be met due to the compressibility of the fibers.

For steady-state creep the constitutive equations (1.4) for orthotropic creep can be transformed into a form:

$$\underline{\dot{c}} = \sigma_{eq}^{n-1} [B] \underline{\sigma}. \tag{1.7}$$

The component-by-component form of writing these equations takes the form:

$$\begin{aligned} \dot{c}_{11} &= \sigma_{eq}^{n-1} [b_{1111}\sigma_{11} + b_{1122}\sigma_{22} + b_{1133}\sigma_{33}], \\ \dot{c}_{22} &= \sigma_{eq}^{n-1} [b_{1122}\sigma_{11} + b_{2222}\sigma_{22} + b_{2233}\sigma_{33}], \\ \dot{c}_{33} &= \sigma_{eq}^{n-1} [b_{1133}\sigma_{11} + b_{2233}\sigma_{22} + b_{3333}\sigma_{33}], \\ \dot{c}_{12} &= 2\sigma_{eq}^{n-1}b_{1212}\sigma_{12}, \\ \dot{c}_{23} &= 2\sigma_{eq}^{n-1}b_{2323}\sigma_{23}, \\ \dot{c}_{31} &= 2\sigma_{eq}^{n-1}b_{3131}\sigma_{31}. \end{aligned} \tag{1.8}$$

1.4 Method for Determining the Average Creep Properties of Fiber Composites

The natural way to determine the material parameters of the theoretical model of the material is to carry out the required number of basic experiments. An alternative possibility is to numerically simulate basic experiments using the known creep properties of the matrix and fibers. The constitutive equation (1.4) for averaged stresses and creep strains take the following form:

$$\langle \dot{\underline{c}} \rangle = \langle \hat{\sigma} \rangle_{eq}^{n-1} [B] \langle \underline{\sigma} \rangle, \tag{1.9}$$

where

$$\langle \underline{\sigma} \rangle = \frac{1}{V} \int_V \underline{\sigma} dv, \qquad \langle \dot{\underline{c}} \rangle = \frac{1}{V} \int_V \dot{\underline{c}} dv. \tag{1.10}$$

Consider uniaxial uniform (on average) tension of the selected composite volume in the directions of the axes x_i, at constant stresses. Then the average rates of creep deformations in the direction of tension are determined by the relations:

$$\langle \dot{c}_{11} \rangle = b_{1111} \langle \sigma_{11}^n \rangle,$$
$$\langle \dot{c}_{22} \rangle = b_{2222} \langle \sigma_{22}^n \rangle, \tag{1.11}$$
$$\langle \dot{c}_{33} \rangle = b_{3333} \langle \sigma_{33}^n \rangle.$$

Considering the net shift of the selected volume of the composite in the coordinate planes at constant values of tangential stresses, we obtain for the average rates of shear deformation:

$$\langle \dot{c}_{12} \rangle = b_{1212} \langle \sigma_{12}^n \rangle,$$
$$\langle \dot{c}_{23} \rangle = b_{2323} \langle \sigma_{23}^n \rangle, \tag{1.12}$$
$$\langle \dot{c}_{31} \rangle = b_{3131} \langle \sigma_{31}^n \rangle.$$

Note that the dependencies (1.11)-(1.12) correspond to the curves of the steady creep of the composite material when tension in the coordinate directions $x_i, (i = 1, 2, 3)$ and shear in the coordinate planes $x_i x_j (ij = 12, 23, 31)$. If you calculate the rate of steady creep, for example, in the direction $1 - \langle \dot{c}_{11}^1 \rangle, \langle \dot{c}_{11}^2 \rangle$, corresponding to the steady creep of the representative volume of the composite when it is stretched by two different levels of stresses $\langle \sigma_{11}^1 \rangle, \langle \sigma_{11}^2 \rangle$ respectively, to determine the constants n and b_{1111} it is possible to use equations:

$$\lg \langle \dot{c}_{11}^1 \rangle = \lg b_{1111} + n \lg \langle \sigma_{11}^1 \rangle, \quad \lg \langle \dot{c}_{11}^2 \rangle = \lg b_{1111} + n \lg \langle \sigma_{11}^2 \rangle. \tag{1.13}$$

From Eqs. (1.13) the creep parameters can be obtained:

$$n = \frac{\lg \frac{\langle \dot{c}_{11}^1 \rangle}{\langle \dot{c}_{11}^2 \rangle}}{\lg \frac{\langle \sigma_{11}^1 \rangle}{\langle \sigma_{11}^2 \rangle}}, \quad b_{1111} = \left(\frac{\langle \dot{c}_{11}^1 \rangle}{\langle \sigma_{11}^1 \rangle^n} \right). \tag{1.14}$$

Similarly, by calculating the rate of steady creep for the other two directions can be found:

$$b_{2222} = \left(\frac{\langle \dot{c}_{22}^1 \rangle}{\langle \sigma_{22}^1 \rangle^n} \right), \qquad b_{3333} = \left(\frac{\langle \dot{c}_{33}^1 \rangle}{\langle \sigma_{22}^1 \rangle^n} \right). \tag{1.15}$$

Moreover, according to the calculated data of the rates of steady creep in the shift in the coordinate planes $x_i x_j$, determine:

$$b_{1212} = \left(\frac{\langle \dot{\gamma}_{12}^1 \rangle}{\langle \sigma^1{}_{12} \rangle^n} \right), \quad b_{2323} = \left(\frac{\langle \dot{\gamma}_{23}^1 \rangle}{\langle \sigma_{23}^1 \rangle^n} \right), \quad b_{3131} = \left(\frac{\langle \dot{\gamma}_{31}^1 \rangle}{\langle \sigma_{31}^1 \rangle^n} \right). \tag{1.16}$$

Described algorithm allows to determine all average creep properties of composite. The parameters of the constitutive relations can be found as a result of physical experiments or on the basis of micromechanical analysis.

1.5 Micromechanical Creep Analysis of Unidirectional Composite

By way of illustration, the calculation of the creep parameters is performed for an unrestricted orthogonally reinforced fiber composite material (**Fig. 1.1**). It consists of an aluminum matrix and boron cylinder inclusions.

Fiber and matrix materials are considered isotropic. Hooke's law describes the elastic properties of materials, creep deformations in the fibers do not develop, and Norton's law describes the creep properties of the matrix:

$$\dot{c} = A\sigma^n. \tag{1.17}$$

The parameters of the fiber and matrix materials are presented in **Table 1.1**.

Heterogeneous material in the sizes of those, which considerably exceed the size of the elements, which are periodically repeated, is accepted as homogeneous. The averaging procedure is allocated a representative volume that is repeated periodically. However, numerical experiments are performed on a composite model consisting of several minimal representative volumes (**Fig. 1.2**a). This is done to avoid problems with the boundary effects that can occur due to the setting of a constant
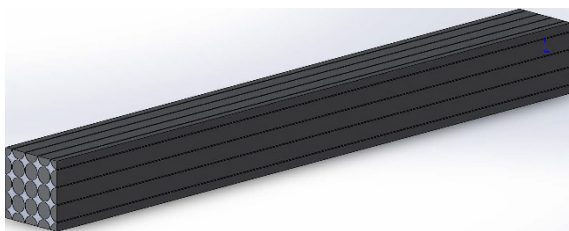
Fig. 1.1 Three-dimensional model of the composite.

Fig. 1.2 Selection of the minimum representative volume (a - composite model, b - minimum representative volume).

a)   b)
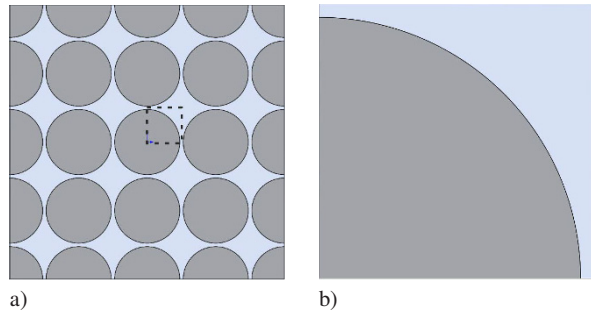
stresses on the boundaries of the model. When processing the data from the numerical experiment, the procedure for obtaining the averaged deformations was performed at the minimum representative volume, which is released near the middle of the composite model (**Fig. 1.2**b), where the influence of the boundary effects is negligible.

For such a heterogeneous material, the equivalent homogeneous material is orthotropic. Due to the similarity of the properties of the composite in the directions x_1 and x_2, the components of the tensor (1.9) must satisfy the following conditions:

$$b_{1111} = b_{2222},$$
$$b_{1133} = b_{2233}, \qquad (1.18)$$
$$b_{2323} = b_{3131}.$$

To identify the material constants in (1.9), numerical calculations were performed using the finite element method for cases of loading in the transverse plane.

Consider a numerical experiment performed on the minimum representative volume of uniaxial stretching in the direction x_1. The average creep rate in the case of uniaxial stretching is related to the average stress by expression (1.11). The averaging over the volume of stresses and strains can be reduced to averaging over the cross-sectional area of the representative volume. To reduce the computational costs when calculating the average deformation, you can use the Green's equation:

Table 1.1: Properties of composite materials.

Material parameter	Matrix	Fiber
Modulus of elasticity, Pa	$7.1 \cdot 10^{10}$	$4.2 \cdot 10^{12}$
Poisson's ratio	0.33	0.3
Parameter A of Norton's law, Pa^{-n}/s	$1.8 \cdot 10^{-33}$	-
Exponent n	3.4	-

$$\langle \dot{\varepsilon}_{11} \rangle = \frac{1}{S} \int_S \dot{\varepsilon}_{11} ds = \frac{1}{S} \int_S \frac{\partial \dot{u}}{\partial x} ds = \frac{1}{S} \oint_L \dot{u} dy = \frac{1}{ab} \int_0^b \dot{u} dy, \qquad (1.19)$$

where S is the cross-sectional area of the representative volume; L is the area contour, x and y are the coordinates in the coordinate system, which coincides with x_1 and x_2 directions, a and b are the dimensions of the cross-sectional area. Similar simplifications can be made to obtain stresses

$$\langle \sigma_{11} \rangle = \frac{1}{S} \int_S \sigma_{11} ds = \frac{1}{ab} \int_0^a dx \int_0^b \sigma_{11} dy = \frac{1}{b} \int_0^b \sigma_{11} dy. \qquad (1.20)$$

First, the time required to achieve a constant rate of creep deformation was determined. A series of creep analyzes on the composite model was performed under a constant uniform load in direction x_1 for different stress levels. Similar numerical experiments were carried out for the analysis of the steady-state creep during shear in the plane $x_1 x_2$. **Figure 1.3**a shows the picture of stress distribution in the tensile experiment, and **Fig. 1.3**b shows the shear stresses σ_{12} in the experiment for shear. These pictures correspond to the state of steady-state creep. These results indicate that the influence of edge effects is insignificant within the minimum representative volume marked by the dotted line in **Fig. 1.2**a. The distribution of stresses in this volume corresponds to a periodically repeating state of an infinite composite massif.

To obtain the degree in the law of creep, using (1.14), a set of numerical experiments at different stress levels $\langle \sigma_{11}^i \rangle$, $(i = 1, \ldots, M)$. The result of this series of M experiments is a set steady state creep strain rates $\langle \dot{\varepsilon}_{11}^i \rangle$ for different stress values. Statistical processing of the results was performed by the method of least squares. The value $n = 3.21$ was obtained as a result of a numerical experiment on tension along the x_1 axis. The values of the parameters of tensor $\mathbf{B}$, found from experiments on loading in the transverse plane, are given in **Table 1.2**.

Table 1.2: Parameters of the tensor $\mathbf{B}$, Pa^{-n}/s.

Parameters	Values
b_{1111}	$1.42 \cdot 10^{-34}$
b_{1122}	$6.14 \cdot 10^{-36}$
b_{1212}	$3.68 \cdot 10^{-33}$
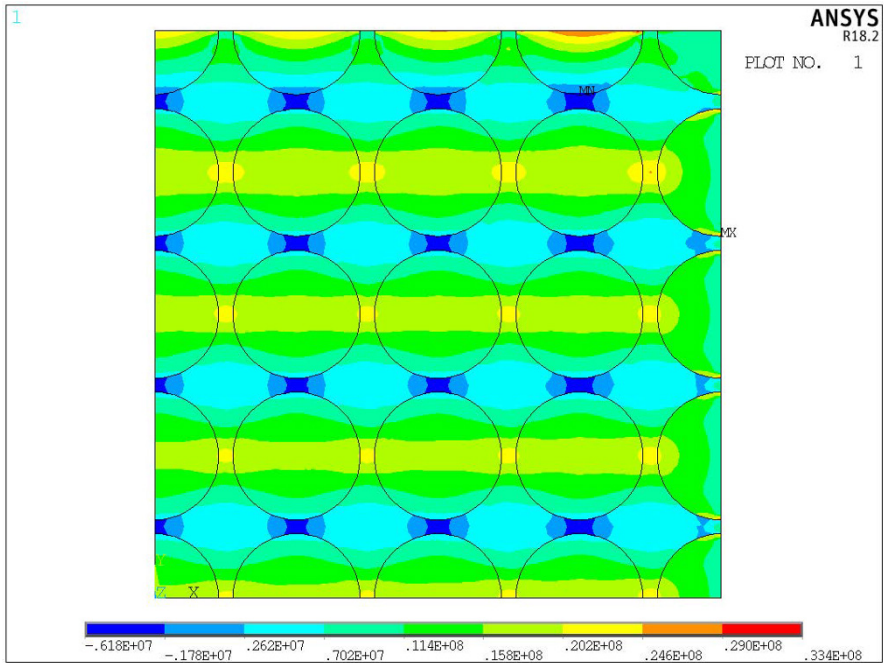
a)
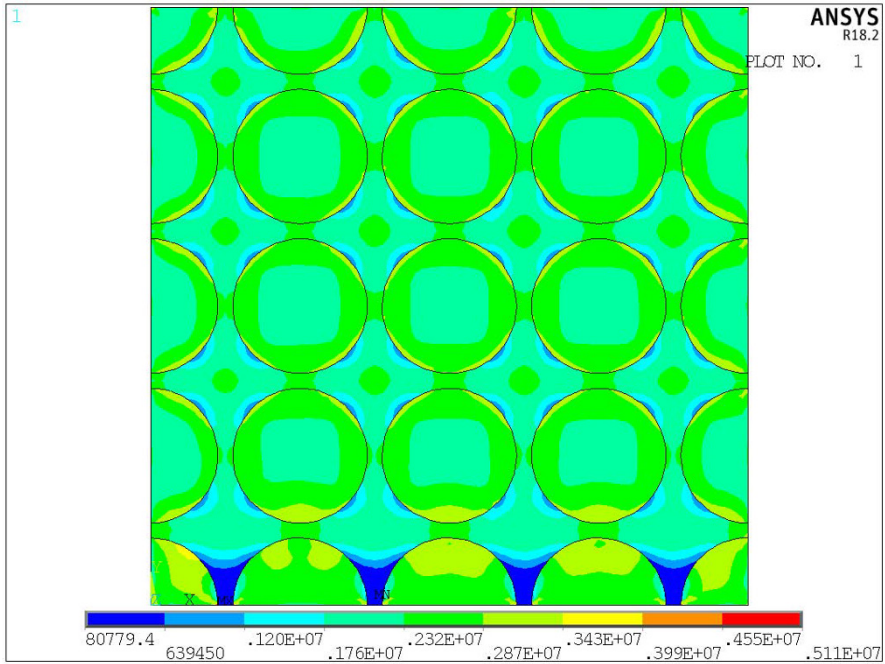
b)

Fig. 1.3: Stress distribution σ_{11} (a) and σ_{12} (b) Pa.

1.6 Conclusions

New technique has been developed for the numerical homogenization of the creep properties of unidirectionally reinforced fiber composites. The initial information for micromechanical analysis is the structure of the composite, the characteristics of the steady-state creep of the matrix and the elastic properties of the fibers. The theoretical model of the steady-state creep of the composite assumes the replacement of its properties with the properties of an equivalent orthotropic body. The constitutive equations for the creep rate tensor are based on the assumption of the quadratiform of the creep potential with respect to the stress tensor. The invariant form for the equivalent stress is introduced using the fourth rank tensor with orthotropic symmetry class.

To carry out micromechanical analysis, a geometric model was built and loading conditions were set, which ensure full compliance of the distribution of micro stresses within the minimum representative volume to the state that occurs during homogeneous macro deformation of the composite. As an example of the application of the developed technique, calculations were carried out for a boron-aluminum composite. A series of numerical calculations was performed by the finite element method in the ANSYS software package, simulating tension and shear in a plane perpendicular to the direction of reinforcement. Processing the results of micromechanical analysis made it possible to predict the parameters of the constitutive relations for the steady-state creep of this metal-matrix composite.

References

Altenbach H, Naumenko K, L'vov G, Pilipenko S (2003) Numerical estimation of the elastic properties of thin-walled structures manufactured from short-fiber-reinforced thermoplastics. Mechanics of Composite Materials 39(3):221–234, DOI 10.1023/A:1024566026411

Altenbach H, Altenbach J, Kissing W (2018) Mechanics of Composite Structural Elements, 2nd edn. Springer, Singapore, DOI 10.1007/978-981-10-8935-0

Arrhenius S (1889) Über die Reaktionsgeschwindigkeit bei der Inversion von Rohrzucker durch Säuren. Zeitschrift für Physikalische Chemie 4U(1):226–248, DOI 10.1515/zpch-1889-0416

Asyraf MRM, Ishak MR, Sapuan SM, Yidris N, Ilyas RA (2020) Woods and composites cantilever beam: A comprehensive review of experimental and numerical creep methodologies. Journal of Materials Research and Technology 9(3):6759–6776, DOI 10.1016/j.jmrt.2020.01.013

Chen M, Liu B, Li L, Cao L, Huang Y, Wang S, Zhao P, Lu L, Cheng X (2020) Rheological parameters, thixotropy and creep of 3D-printed calcium sulfoaluminate cement composites modified by bentonite. Composites Part B: Engineering 186:107,821, DOI 10.1016/j.compositesb.2020.107821

Darya Zadeh S, L'vov GI (2015) Numerical procedure of determining the effective mechanical characteristics of an aligned fiber composite. Strength of Materials 47(4):536–543, DOI 10.1007/s11223-015-9687-2

Fliegener S, Hohe J (2020) An anisotropic creep model for continuously and discontinuously fiber reinforced thermoplastics. Composites Science and Technology 194:108,168, DOI 10.1016/j.compscitech.2020.108168

Fliegener S, Rausch J, Hohe J (2019) Loading points for industrial scale sandwich structures – a numerical and experimental design study. Composite Structures 226:111,278, DOI 10.1016/j.compstruct.2019.111278

Gong D, Jiang L, Guan J, Liu K, Yu Z, Wu G (2020) Stable second phase: The key to high-temperature creep performance of particle reinforced aluminum matrix composite. Materials Science and Engineering: A 770:138,551, DOI 10.1016/j.msea.2019.138551

Hao X, Zhou H, Mu B, Chen L, Guo Q, Yi X, Sun L, Wang Q, Ou R (2020) Effects of fiber geometry and orientation distribution on the anisotropy of mechanical properties, creep behavior, and thermal expansion of natural fiber/hdpe composites. Composites Part B: Engineering 185:107,778, DOI 10.1016/j.compositesb.2020.107778

Jafaripour M, Taheri-Behrooz F (2020) Creep behavior modeling of polymeric composites using schapery model based on micro-macromechanical approaches. European Journal of Mechanics - A/Solids 81:103,963, DOI 10.1016/j.euromechsol.2020.103963

Jia Y, Fiedler B (2020) Tensile creep behaviour of unidirectional flax fibre reinforced bio-based epoxy composites. Composites Communications 18:5–12, DOI 10.1016/j.coco.2019.12.010

Karthik D, Baheti V, Novotná J, Samková A, Pulíček R, Venkataraman M, Srb P, Voleská K, Wang Y, Militký J (2020) Effect of particulate fillers on creep behaviour of epoxy composites. Materials Today: Proceedings 31:S217–S220, DOI 10.1016/j.matpr.2019.11.064, 4th International Conference on Natural Fibers – Smart Sustainable Materials, ICNF 2019

Khatkar V, Behera BK (2021) Experimental investigation of textile structure reinforced composite leaf spring for their cyclic flexural and creep behaviour. Composite Structures 258:113,439, DOI 10.1016/j.compstruct.2020.113439

Lv J, Xiao Y, Zhou Y, Xie Y (2020) Characterization and modeling of the creep behavior of fiber composites with tension and compression asymmetry. International Journal of Mechanical Sciences 170:105,340, DOI 10.1016/j.ijmecsci.2019.105340

Morachkovskii OK, Zolochevskii AA (1980) Effect of initial orthotropy of a material on the creep of structures made of shells. Soviet Applied Mechanics 16(6):487–482, DOI 10.1007/BF00883895

Naumenko K, Altenbach H (2005) A phenomenological model for anisotropic creep in a multipass weld metal. Archive of Applied Mechanics 74(11):808–819, DOI 10.1007/s00419-005-0409-2

Naumenko K, Altenbach H (2016) Modeling High Temperature Materials Behavior for Structural Analysis, Advanced Structured Materials, vol 28. Springer, Cham, DOI 10.1007/978-3-319-31629-1

Naumenko K, Gariboldi E (2014) A phase mixture model for anisotropic creep of forged Al–Cu–Mg–Si alloy. Materials Science and Engineering: A 618:368–376, DOI 10.1016/j.msea.2014.09.012

Nguyen SN, Lee J, Han JW, Cho M (2020) A coupled hygrothermo-mechanical viscoelastic analysis of multilayered composite plates for long-term creep behaviors. Composite Structures 242:112,030, DOI 10.1016/j.compstruct.2020.112030

Ornaghi Jr HL, Almeida JHS, Monticeli FM, Neves RM (2020a) Stress relaxation, creep, and recovery of carbon fiber non-crimp fabric composites. Composites Part C: Open Access 3:100,051, DOI 10.1016/j.jcomc.2020.100051

Ornaghi Jr HL, Monticeli FM, Neves RM, Zattera AJ, Cioffi MOH, Voorwald HJC (2020b) Effect of stacking sequence and porosity on creep behavior of glass/epoxy and carbon/epoxy hybrid laminate composites. Composites Communications 19:210–219, DOI 10.1016/j.coco.2020.04.006

Palmov V (1998) Vibrations of Elasto-Plastic Bodies, 2nd edn. Foundations of Engineering Mechanics, Springer, Berlin, Heidelberg, DOI 10.1007/978-3-540-69636-0

Rafiee R, Ghorbanhosseini A (2020) Developing a micro-macromechanical approach for evaluating long-term creep in composite cylinders. Thin-Walled Structures 151:106,714, DOI 10.1016/j.tws.2020.106714

Reiner M (1969) Deformation, Strain and Flow: an Elementary Introduction to Rheology, 3rd edn. H. K. Lewis, London

Sala B, Gabrion X, Trivaudey F, Guicheret-Retel V, Placet V (2021) Influence of the stress level and hygrothermal conditions on the creep/recovery behaviour of high-grade flax and hemp fibre reinforced greenpoxy matrix composites. Composites Part A: Applied Science and Manufacturing 141:106,204, DOI doi.org/10.1016/j.compositesa.2020.106204

Samareh-Mousavi SS, Taheri-Behrooz F (2020) A novel creep-fatigue stiffness degradation model for composite materials. Composite Structures 237:111,955, DOI 10.1016/j.compstruct.2020.111955

Sun T, Yu C, Yang W, Zhong J, Xu Q (2020) Experimental and numerical research on the nonlinear creep response of polymeric composites under humid environments. Composite Structures 251:112,673, DOI 10.1016/j.compstruct.2020.112673

Xie Y, Xiao Y, Lv J, Zhang Z, Zhou Y, Xue Y (2020) Influence of creep on preload relaxation of bolted composite joints: Modeling and numerical simulation. Composite Structures 245:112,332, DOI 10.1016/j.compstruct.2020.112332

Yang H, Gavras S, Dieringa H (2021) Creep characteristics of metal matrix composites. In: Brabazon D (ed) Encyclopedia of Materials: Composites, Elsevier, Oxford, pp 375–388, DOI 10.1016/B978-0-12-803581-8.11822-3

Chapter 2
General Forms of Limit Surface: Application for Isotropic Materials

Holm Altenbach and Vladimir A. Kolupaev

Abstract Limit surfaces are a tool used in theory of plasticity and failure analysis for dividing the safe from the unsafe regions. Their mathematical formulations are given by yield and strength criteria. The number of suggested criteria is unmanageable. By lack of the sufficient conditions only plausibility assumptions can limit this variety.

Typically, the TRESCA, VON MISES, and SCHMIDT-ISHLINSKY criteria are employed for the modeling of yielding. The effect of pressure-sensitivity is accounted for with the criteria of RANKINE and BURZYŃSKI-YAGN. Generalizations are obtained with linear combinations of these and further criteria. However, methods for the selection of efficient criteria for a particular application are still missing.

In this work, a nomenclature for isotropic yield criteria is introduced. Proposed systematization restricts the number of appropriate yield criteria. Global convexity limits for the yield criteria of trigonal and hexagonal symmetry are defined.

The basic idea is to find a general form of isotropic yield surface that satisfies the plausibility assumptions. This surface should contain possible yield surfaces lying between the lower and the upper bounds of the convexity restrictions. Any known or new criteria can then be considered as a special cases of the general criterion. The discussed yield criteria are extended for pressure-sensitive materials. The selection of the effective criterion for a particular application is simplified.

Key words: Equivalent stress, Deviatoric plane, Isogonal and isotoxal hexagon, Multi-axial loading

Holm Altenbach

Lehrstuhl für Technische Mechanik, Institut für Mechanik, Fakultät für Maschinenbau, Otto-von-Guericke-Universität Magdeburg, Universitätsplatz 2, 39106 Magdeburg, Germany,
e-mail: holm.altenbach@ovgu.de

Vladimir A. Kolupaev

Fraunhofer Institute for Structural Durability and System Reliability (LBF), Schloßgartenstr. 6, 64289 Darmstadt, Germany,
e-mail: Vladimir.Kolupaev@lbf.fraunhofer.de

2.1 Introduction

Engineering methods relate to macroeffects captured empirically. With the help of phenomenological criteria one can describe the beginning of yielding, damage or brittle failure of a certain material in a simplified way. The critical state of the sound material is represented only by the stresses, strains, and energetic or power considerations, at which the appropriate limit of a material is reached. Their gradients are not taken into account (Paul, 1968a,b).

In the case of stresses, a limit surface can be suggested in the principal stress space. A corresponding criterion is the mathematical expression taking into account of all points on the limit surface (Feodosjev, 1975; Franklin, 1971; Pisarenko and Lebedev, 1969; Skrzypek, 1993).

In order to formulate such criteria, the equivalent stress concept is typically used (Timoshenko, 1953). Within the concept, arbitrary stress states can be expressed as scalar quantities and compared to uniaxial tensile stress (Fromm, 1931) . Information about stress components and loading path is neglected (Paul, 1968a,b; Wu and Scheublein, 1974).

Uniaxial tensile properties can be readily measured in experiments. These data for different materials are compared in manuals, technical reports, and manufacturer's specifications. Solely, the proper criterion should be selected for design. Because of its simplicity and clarity, the equivalent stress concept found use in engineering applications.

Several criteria have been proposed over the last 150 years. They are summarized in numerous textbooks, see Altenbach et al. (1995); Bertram (2012); Pisarenko and Lebedev (1976); Potapova and Yarzev (2005); Skrzypek (1993); Yagn (1933); Yu (2004); Życzkowski (1981) among others. The amount of introduced criteria is remarkable. Until now, methods for comparison and selection of the most suitable criterion for a particular application are missing, see, for example, Lebedev (2010).

Further, choosing an appropriate criterion remains challenging because of generally incomplete data sets and their inevitable scattering. Trying to fit different criteria is intricate and the optimal evaluation cannot be guaranteed. In order to eliminate the necessity of a specific criterion selection, a general criterion is needed (Rosendahl et al., 2019b), cf. Voigt (1901).

In the present work, the geometric properties of isotropic yield criteria are examined. Global convexity limits of the yield criteria are defined and plausibility assumptions are listed. A general isotropic yield surface should be able to describe possible yield surfaces lying between the lower and the upper bounds of the convexity restrictions. Any known or new criteria can then be viewed as a special case of the general criterion and are, thus, secondary. The use of the general criterion with reasonable restrictions (Kolupaev et al., 2016; Kolupaev, 2018) prevents the risk of inappropriate extrapolations, cf. Życzkowski (1981).

In our work, a nomenclature of criteria based on their geometric properties is introduced. A general schematic for expressing pressure-insensitive yield criteria is provided. Known and new yield criteria are assigned to these schematic. This facilitates the selection of criteria for various applications. Critical gaps in the for-

mulation of criteria are closed. The best known criteria are generalized considering the plausibility assumptions (Appendix 2.7.8). The parameters of the criteria are restricted based on the convexity condition in the π-plane (deviatoric plane).

A universally applicable yield criteria, which describe a single, convex, and C^0- or C^1-continuously surface are proposed. These contain extreme yield figures as the convexity restrictions. Using a I_1-substitution as a function of the trace of the stress tensor, the introduced criteria are applicable to pressure-sensitive materials. They incorporate various conditions to obtain special "theories". The versatility of the introduced criteria is sufficiently high, which may help to stop the growth of the amount of proposed criteria, cf. Habraken (2004).

The present work is organized as follows. Section 2.2 presents methods, requirements, and restrictions in the formulation of yield and strength criteria. In Sect. 2.3, the nomenclature of yield and strength criteria is introduced, which allows their descriptive comparison. In Sect. 2.4, the best known criteria in the authors' opinion are discussed and new criteria proposed. Strength criteria with the shape variation in π-plane are discussed in Sect. 2.5. The most important points of our work are summarized in Sect. 2.6.

2.2 Geometric Properties of Criteria

This section presents methods, requirements, and restrictions in the formulation of yield and strength criteria for isotropic materials. The geometric properties of the surfaces are analyzed and systematized, see also Pisarenko and Lebedev (1969, 1976); Lebedev (2010). Linear, quadratic, and cubic I_1-substitutions are introduced in order to obtain the pressure-sensitive generalization of the yield criteria.

2.2.1 Requirements for Yield and Strength Criteria

Yield surfaces for pressure-insensitive isotropic materials are described by a cylinder or a prism centred around the hydrostatic axis in principal stress space (Paul, 1968a,b)

$$\sigma_I = \sigma_{II} = \sigma_{III}, \tag{2.1}$$

where σ_I, σ_{II}, and σ_{III} denote the principal stresses (Appendix 2.7.1). Such surfaces do not involve any restriction of hydrostatic stresses (**Fig. 2.1**).

Cross sections orthogonal to the hydrostatic axis are called deviatoric planes or π-planes (de Araújo, 1962; Życzkowski, 1981). Owing to isotropy, the cross sections in the π-plane must be of trigonal, hexagonal or rotational symmetry (**Fig. 2.2**).

Further, based on the DRUCKER postulate (Altenbach, 2018; Betten, 2001; Drucker, 1957, 1959), we require convex yield surfaces. Thus, basic cross sections may be described by a circle or regular polygons of trigonal or hexagonal symmetry
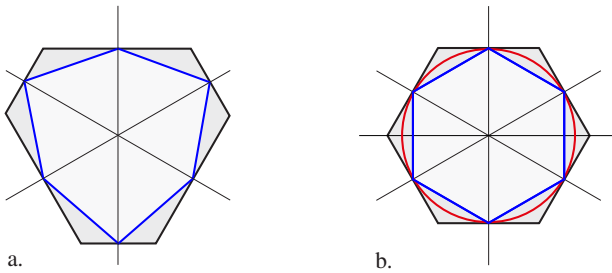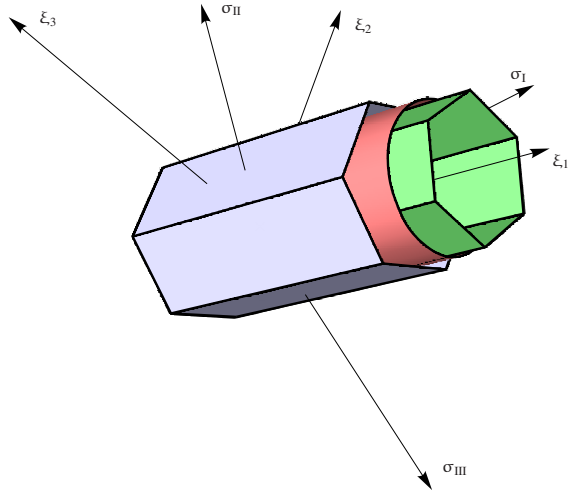
Fig. 2.2: Yield criteria in the π-plane normalized with respect to the appropriate uniaxial tensile limit loading σ_0^T: a. Isogonal (black) and isotoxal (blue) hexagons of trigonal symmetry, b. Regular hexagons of the SCHMIDT-ISHLINSKY (black) and TRESCA (blue) criteria of hexagonal symmetry and the circle of the VON MISES criterion (red) of rotational symmetry (Rosendahl et al., 2019b).

in the π-plane (Rosendahl et al., 2019b, see also Pisarenko and Lebedev (1976); Lebedev (2010)): e.g. triangles, hexagons, enneagons (nine-sided polygons), dodecagons (twelve-sided polygons), among others. Each surface described by a regular polygon in the π-plane has a counterpart, which is obtained by its rotation by π/n in the π-plane about the hydrostatic axis, where n is the number of corners (**Fig. 2.3**).

All materials fail under sufficiently large hydrostatic tensile loading (Gol'denblat and Kopnov, 1971b; Kolupaev, 2018). In this case, the hydrostatic component of loading should be introduced in the yield criterion. Hence, the strength criteria restrict the hydrostatic tensile stress. With the convexity requirement on the meridian of the limit surface it follows

$$3\,\sigma^{TTT} > \sigma_0^T.$$

The surface can be open

$$\sigma^{CCC} \to -\infty$$
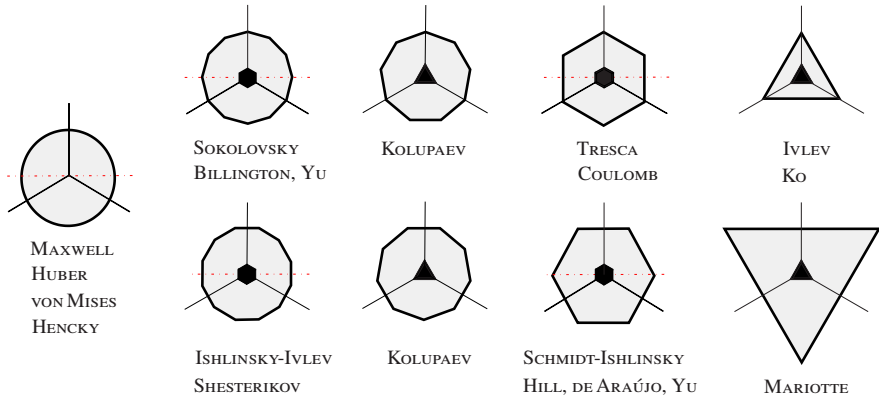
Fig. 2.3: Basic yield figures described by a circle and regular polygons of trigonal or hexagonal symmetry in the π-plane. The symbols of symmetry follow according to Nye (1985).

or closed

$$\sigma^{\mathrm{CCC}} = \mathrm{const.} < 0$$

in the direction $I_1 < 0$, where I_1 is the first invariant of the stress tensor (2.107). The superscripts T and C denote uniaxial tensile and compressive limit loading respectively. Accordingly, TTT denotes equitriaxial (hydrostatic) tensile limit loading and CCC - equitriaxial (hydrostatic) compressive limit loading (**Table 2.7**). The subscript 0 in σ_0^{T} refers to the stress angle $\theta = 0$ (2.112), see **Table 2.7**. Note that, the stress angle at the TTT and CCC loadings is indeterminate.

Criteria discussed in the present work are purely phenomenological. No sufficient conditions for their formulation can be given (Kolupaev, 2018). They are invented and, as a rule, not verified by multiaxial stress states (Wu and Scheublein, 1974). However, the quality of a certain yield or strength criterion may be assessed considering the plausibility assumptions (Appendix 2.7.8). These assumptions are not mandatory, but they allow to select user-friendly criteria for a wide range of applications.

2.2.2 Formulation of Yield and Strength Criteria

Yield and strength criteria for isotropic materials are invariant with respect to an arbitrary rotation of the coordinate system (Mālmeisters et al., 1977; Życzkowski, 1981). Therefore, such criteria are formulated using invariants of the stress tensor discussed in Appendix 2.7.1.

Functions of invariants are also invariants (Appendices 2.7.2-2.7.3). For the formulation of criteria Φ we may also use:

- the principal stresses (principal invariants) σ_I, σ_{II}, and σ_{III} (Altenbach et al., 1995; Haigh, 1920; Westergaard, 1920; Życzkowski, 1981)

$$\Phi\left(\sigma_I, \sigma_{II}, \sigma_{III}, \sigma_{eq}\right) = 0, \tag{2.2}$$

- the trace I_1 of the stress tensor and the invariants I_2', I_3' of the stress deviator (2.107)–(2.109) (Backhaus, 1983; Burzyński, 1928; Ottosen and Ristinmaa, 2005; Reuss, 1933; Sawczuk, 1982; Skrzypek, 1993; Yagn, 1931)

$$\Phi\left(I_1, I_2', I_3', \sigma_{eq}\right) = 0, \tag{2.3}$$

- the cylindrical invariants ξ, ρ, θ (2.110)–(2.112) (Lebedev, 2010; Murzewski, 1957, 1960; Novozhilov, 1951a,b; Ottosen and Ristinmaa, 2005)

$$\Phi\left(\xi, \rho, \theta, \sigma_{eq}\right) = 0, \tag{2.4}$$

and

- the spherical invariants ξ, ψ, and θ (2.110), (2.112), (2.113) (Altenbach and Kolupaev, 2014; Kolupaev, 2018; Lagzdin' and Tamuzh, 1971; Lebedev, 2010)

$$\Phi\left(\xi, \psi, \theta, \sigma_{eq}\right) = 0. \tag{2.5}$$

In the formulations (2.4)–(2.5), the invariant ξ (2.110) is the scaled invariant I_1 and describes the coordinate of the loading on the hydrostatic axis, the radius ρ in the π-plane (2.111) is the scaled root of the second invariant I_2', and θ (2.112) is the corresponding stress angle in the π-plane. The radius ρ may be replaced by the stress triaxiality factor ψ (2.113) or (2.114), which yields a description of the surface in terms of the spherical invariants.

In addition, a big family of criteria include positive first principal stress

$$\sigma_{maxt} = \frac{1}{2}\left(|\sigma_I| + \sigma_I\right), \tag{2.6}$$

the hydrostatic stress I_1, and the second invariant of stress deviator I_2' to capture mixed mode (brittle and ductile) fracture. Examples are presented in Sdobyrev (1959); Trunin (1965); Hayhurst (1972); Altenbach and Naumenko (1997, 2002) among others. The (non-linear) functions of the maximum tensile stress, the hydrostatic stress and the VON MISES equivalent stress is frequently used in damage evolution equations for the creep and creep-fatigue analysis. Examples are presented in Kowalewski et al. (1994); Othman et al. (1994); Dyson and McLean (2001); Altenbach et al. (2000); Naumenko et al. (2011).

All these formulations (2.2)–(2.5) are, from a mathematical point of view, equivalent. Formulation (2.2) has a historical origin and is primarily mentioned in textbooks of strength of materials and theory of plasticity in the discussion of the classical criteria. The YU strength theory (YST) as a generalization of these classical criteria was firstly expressed in the principal stresses (Yu, 2004) and, later, in the axiatoric-deviatoric invariants (2.3) for visualizations of the meridional cross sec-

tions (cross section of the limit surface containing the hydrostatic axis) together with the line of the plane stress state (Kolupaev, 2018). Formulations according to (2.3) were intensively elaborated until the beginning of XXI century. Although such criteria are being developed, they are, as a rule, not user-friendly (Appendix 2.7.8, violated assumptions PP1, PP3, and PM1).

Equations (2.4)–(2.5) allow to manipulate the geometric properties of the surface Φ. Formulation (2.4) seems to be very effective in regard of the applicability and satisfaction of the plausibility assumptions (Appendix 2.7.8). Equation (2.5) has hardly found any practical application and is included for the sake of completeness: it is omitted from our discussions. One or the other of the Eqs. (2.2)–(2.5) may be preferred depending on the didactic targets, modeling concept, consideration the plausibility assumptions or desired application.

When pressure-insensitivity is assumed, the first invariant I_1 does not influence failure / yielding (Mālmeisters et al., 1977; Życzkowski, 1981). For this property, the Eqs. (2.3)–(2.4) can be reduced to

$$\Phi(I_2', I_3', \sigma_{eq}) = 0 \qquad \text{or} \qquad \Phi(\rho, \theta, \sigma_{eq}) = 0. \tag{2.7}$$

Polynomial formulations of $\Phi(I_2', I_3', \sigma_{eq})$ in terms of series of the deviatoric invariants I_2' and I_3' are well elaborated (Kolupaev, 2018) but cannot be recommended for application because of additional outer contours around the physically meaningful surface in the π-plane. As a rule, the equivalent stress σ_{eq} occurs implicitly in such equations.

In order to satisfy the assumption PM1 (Appendix 2.7.8), the equivalent stress σ_{eq} can be specified explicitly:

$$\sigma_{eq} = \Phi(\rho, \theta). \tag{2.8}$$

Such formulations are advantageous for iterative computations, e.g. in FEM codes. We may further postulate a multiplicative split of yield criteria into a function of radius $\Psi(\rho)$ and a function of the stress angle $\Omega(\theta)$ (Życzkowski, 1981)

$$\sigma_{eq} = \Psi(\rho)\,\Omega(\theta). \tag{2.9}$$

To highlight deviations of the shape of the surface in the π-plane from the circle of the VON MISES criterion (**Figs. 2.2** b, red circle, and **2.3**)

$$\sigma_{eq} = \sqrt{3I_2'} \qquad \text{with} \qquad \Omega(\theta) = 1, \tag{2.10}$$

the function of $\Psi(\rho)$ is often replaced by $\sqrt{3I_2'}$ (Giraldo-Londoño and Paulino, 2020; Kolupaev, 2017; Kolupaev et al., 2018; Lebedev, 2010), which yields

$$\sigma_{eq} = \sqrt{3I_2'}\,\Omega(\theta). \tag{2.11}$$

Normalizing criteria with respect to the appropriate uniaxial tensile limit loading, e.g., the tensile yield or strength σ_0^T (**Table 2.7**), leads to the final formulation

$$\sigma_{eq} = \sqrt{3 I_2'} \, \frac{\Omega(\theta)}{\Omega(0)}, \tag{2.12}$$

which incorporates several well-known yield criteria and is beneficial for the application.

2.2.3 Pressure-sensitive Extension of Yield Criteria

Reintroducing the first invariant of the stress tensor I_1 in (2.12) using the substitution (Kolupaev, 2018)

$$\sigma_{eq} \to \left[\frac{\sigma_{eq} - \gamma_1 I_1}{1 - \gamma_1} \frac{\sigma_{eq} - \gamma_2 I_1}{1 - \gamma_2} \right]^{1/2} \qquad \text{with} \qquad \gamma_1 \in [0, 1[\tag{2.13}$$

does not violate the assumption PM1 (Appendix 2.7.8). The reciprocal values of the parameters γ_1 and γ_2 describe the intersection of the limit surface with the I_1-axis (scaled space diagonal in the principal stress space). These points are called the hydrostatic nodes TTT and CCC (**Table 2.7**). The parameters γ_1 and γ_2 do not interact with other parameters of the criterion (2.12), and thus do not influence the shape of cross sections in the π-plane.

Therefore, the general equation of a second-order surface of revolution about the hydrostatic axis in the principal stress space can be formulated as a function of the coordinates of the hydrostatic nodes TTT and CCC (Altenbach, 2018; Altenbach and Kolupaev, 2014; Kolupaev, 2018)

$$3 I_2' = \frac{\sigma_{eq} - \gamma_1 I_1}{1 - \gamma_1} \frac{\sigma_{eq} - \gamma_2 I_1}{1 - \gamma_2}. \tag{2.14}$$

A possibility of an explicit solution of (2.14) with respect to σ_{eq} was a widespread application of this criterion, which is known as the BURZYŃSKI-YAGN criterion.

The meridional cross sections of the rotationally symmetric criteria are shown in **Fig. 2.4**. The surfaces result with rotation of the corresponding line around the I_1-axis. The visualization of the criteria (2.14) in the $(I_1, \sqrt{3 I_2'})$–plane (BURZYŃSKI-plane) is then obvious and allows a straightforward comparison with the VON MISES criterion (2.10) (**Fig. 2.4**, red line).

For materials, which do not fail under hydrostatic compression (brass, lead, steel, etc.), the surface Φ has a single hydrostatic node TTT. Based on (2.13) three substitutions are possible:

- linear substitution with $\gamma_1 = \gamma_2$, at which the hydrostatic nodes at the point TTT coincide,

$$\sigma_{eq} \to \frac{\sigma_{eq} - \gamma_1 I_1}{1 - \gamma_1} \qquad \text{with} \qquad \gamma_1 \in [0, 1[\tag{2.15}$$

provides straight meridian in the BURZYŃSKI-plane,
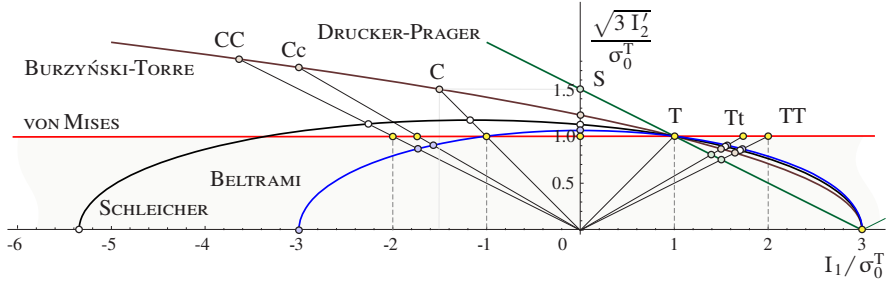
Fig. 2.4: Rotationally symmetric criteria with the setting $\gamma_1 = 1/3$ (point TTT) based on the normal stress hypothesis: cone of DRUCKER-PRAGER with $\gamma_2 = 1/3$, paraboloid of BURZYŃSKI-TORRE with $\gamma_2 = 0$, ellipsoid of SCHLEICHER with $\gamma_2 = (3 - \sqrt{17})/6$, and ellipsoid of BELTRAMI with $\gamma_2 = -1/3$ in the BURZYŃSKI-plane $(I_1, \sqrt{3I_2'})$. The VON MISES criterion $(\gamma_1 = \gamma_2 = 0$, red line) is shown for comparison.

- the parabolic meridians follow with $\gamma_2 = 0$

$$\sigma_{\text{eq}} \rightarrow \left[\frac{\sigma_{\text{eq}} - \gamma_1 I_1}{1 - \gamma_1} \sigma_{\text{eq}} \right]^{1/2} \qquad \text{with} \qquad \gamma_1 \in [0, 1[, \qquad (2.16)$$

- and the hyperbolic meridians follow with $\gamma_2 \in]0, \gamma_1[$. The second node with the position $1/\gamma_2$ on the hydrostatic axis does not belong to the physically meaningful region of the surface Φ, which is most closed the coordinate origin, cf. Wu (1973); Yagn (1931). Due to this fact, the hyperbolic surfaces are not recommended for applications, cf. Balandin (1937).

For materials, which fail under hydrostatic compression (aerated concrete and ceramics, hard foams, sintered and granular materials, sandstone, etc.) the second hydrostatic node CCC is significant. The parameters in (2.14) are then bounded as follows

$$\gamma_1 \in]0, 1[\qquad \text{and} \qquad \gamma_2 < 0. \qquad (2.17)$$

For the yield criteria (2.12), a pressure-sensitive extension (2.13) provides

$$\sqrt{3I_2'} \frac{\Omega(\theta)}{\Omega(0)} = \left[\frac{\sigma_{\text{eq}} - \gamma_1 I_1}{1 - \gamma_1} \frac{\sigma_{\text{eq}} - \gamma_2 I_1}{1 - \gamma_2} \right]^{1/2}. \qquad (2.18)$$

Suitable approximations are often obtained with the linear I_1-substitution Eq. (2.15)

$$\sqrt{3I_2'} \frac{\Omega(\theta)}{\Omega(0)} = \frac{\sigma_{\text{eq}} - \gamma_1 I_1}{1 - \gamma_1}, \qquad (2.19)$$

which leads to conical and pyramidal surfaces in the principal stress space (Lebedev et al., 1979; Lebedev, 2010; Kolupaev et al., 2018; Paul, 1968a,b; Pisarenko and Lebedev, 1976; Rosendahl et al., 2019b; Wronski and Pick, 1977). It is to note, that the linear substitution produces an additional surface beyond of the hydrostatics

node TTT (**Fig. 2.4**, Drucker-Prager cone)

$$\frac{I_1}{\sigma_0^{\mathrm{T}}} \geqslant \frac{1}{\gamma_1}$$

without physical meaning and the apex at the hydrostatic tensile limit loading is C^0-continuously, what contradicts our perceptions and aggravates the computation of gradient of the surface Φ, see Appendix 2.7.8, assumptions PP3 and PG10. This quirk can be fixed by the parabolic I_1-substitution (2.16) or by "rounding off" with the C^1-transition as multisurface criterion (Kolupaev, 2018).

The cubic I_1-substitution in the yield criterion (2.12)

$$\sigma_{\mathrm{eq}} \rightarrow \sqrt[j+l+m]{\left(\frac{\sigma_{\mathrm{eq}}-\gamma_1\,I_1}{1-\gamma_1}\right)^{j}\left(\frac{\sigma_{\mathrm{eq}}-\gamma_2\,I_1}{1-\gamma_2}\right)^{l}\sigma_{\mathrm{eq}}^{m}} \qquad (2.20)$$

with integer and positive powers j, l, and m

$$j+l+m = 3, \qquad j > 0, \qquad l \geqslant 0, \quad \text{and} \quad m \geqslant 0, \qquad (2.21)$$

which control the curvature of the meridian, leads to additional fitting possibilities (Kolupaev, 2018). The equation of the criterion can be still resolved analytically with respect to σ_{eq}. As example, the rotationally symmetric criterion

$$\left(3I_2'\right)^{(3/2)} = \left(\frac{\sigma_{\mathrm{eq}}-\gamma_1\,I_1}{1-\gamma_1}\right)^{j}\left(\frac{\sigma_{\mathrm{eq}}-\gamma_2\,I_1}{1-\gamma_2}\right)^{l}\sigma_{\mathrm{eq}}^{m} \quad \text{with} \quad \gamma_1 \in [0,1[\quad (2.22)$$

can be introduced. The meridian with $l = m = 0$ is a straight line and with $l = 0$ is a parabola. For materials, that fail at hydrostatic compression, it follows $l > 0$ with $\gamma_2 < 0$.

Further I_1-substitutions, e.g. with integer and positive powers

$$j+l+m = 6 \qquad (2.23)$$

are conceivable but, in general, can only be treated numerically. If the powers of the I_1-substitution (2.20) are chosen real for refined settings (Fahlbusch, 2015; Fahlbusch et al., 2016), the I_1-substitution with absolute values of the terms

$$\sigma_{\mathrm{eq}} \rightarrow \sqrt[j+l+m]{\left|\frac{\sigma_{\mathrm{eq}}-\gamma_1\,I_1}{1-\gamma_1}\right|^{j}\left|\frac{\sigma_{\mathrm{eq}}-\gamma_2\,I_1}{1-\gamma_2}\right|^{l}\sigma_{\mathrm{eq}}^{m}} \qquad (2.24)$$

for numerical stability is recommended. Such substitutions are excluded from our consideration.

2.3 Designation and Comparison of Yield Criteria

A clear designation of the yield and strength criteria is proposed, what provides overview and simplifies their selection for application. The criteria are systematized in tables and diagrams. A method for comparing of yield criteria is presented, which allows to identify missing criteria.

2.3.1 Nomenclature of Yield Criteria

The mathematical expressions for the yield and strength criteria can be very different (Subsect. 2.2.2), which makes their comparison for the best adjustment not directly possible, cf. Matsuoka and Nakai (1985); Yu (2002); Kolupaev et al. (2009); Zhang et al. (2011); Lagioia and Panteghini (2016); Giraldo-Londoño and Paulino (2020); Xu et al. (2021) among others. A unique nomenclature and consequent designation of the criteria can be performed based on their geometric shapes in the π-plane and meridional cross sections.

Possible shapes of the yield criteria in the π-plane are constrained by the requirement of convexity (Subsect. 2.2.1). The upper and lower convexity limits are referred to as extreme yield figures (Sayir and Ziegler, 1969; Lebedev et al., 1979; Marti, 1980; Bigoni and Piccolroaz, 2004; Lebedev, 2010; Rosendahl et al., 2019b). Extreme yield figures may take the shape of isogonal and isotoxal polygons of trigonal or hexagonal symmetry. Regular polygons are limit cases of the extreme yield figures.

Isogonal polygons are equiangular. An isotoxal polygon is equilateral, that is, all sides are of the same length (Koca and Koca, 2011; Tóth, 1964). In general, isogonal and isotoxal hexagons are of trigonal symmetry (**Fig. 2.2**a). The regular hexagons of the Tresca and Schmidt-Ishlinsky criteria have an additional symmetry axis and are of hexagonal symmetry (**Figs. 2.2**b and **2.3**, **Table 2.1**). Isogonal and isotoxal dodecagons (twelve-sided polygons) are of hexagonal symmetry, too.

In this work, the basic (regular) yield figures are labeled according to their shapes in the π-plane (**Table 2.1**), cf. Rosendahl et al. (2019b):

- the designation ◯ reflects the von Mises criterion,
- regular triangles are denoted with 3,
- regular hexagons with 6,
- regular enneagons with 9,
- regular dodecagons with 12,
- regular octadecagon with 18,
- regular icositetragons with 24,
- regular triacontahexagon (Modarres-Motlagh, 1997) with 36, etc.

Further regular polygons with the number of corners divisible by three

- pentadecagons denoted with 15,

- icosihenagons with 21
- icosiheptagons with 27,
- triacontagons with 30,
- triacontatrigons with 33, etc.

are also accepted as yield criteria for isotropic materials, but they has low practical significance. References of them were not found in the literature. These shapes are only mentioned for sake of completeness.

Circumflex ˆ and macron ¯ refer to an upward pointing tip or upward facing flat base of the criterion in the π-plane, respectively (**Fig. 2.3**). The designation of the discussed regular polygons is shown in **Table 2.1**. Further references of the criteria are given in Kolupaev (2018). The aim of the designation is a visual representation of the basic yield figures included in the discussed criteria (**Tables 2.2–2.5**).

Limit surfaces for isotropic materials can be characterized by the regular polygons and the circle in the π-plane they include. For example, the MOHR-COULOMB criterion contains the regular triangle of the RANKINE and regular hexagon of the TRESCA criteria in border cases (**Table 2.4**). The criteria involving less than three of the regular geometries can be considered as special cases of the general formulation and are excluded from our discussion. The limitation to three regular geometries is motivated in Subsect. 2.3.3.

Generalized yield criteria involving three or more basic geometries are significant for application. The number of their parameters should not exceed two. The remained criteria are easily manageable (**Tables 2.2** and **2.5**). However, the assumption, that the criteria should be a single surface in principal stress space, is fulfilled only for criteria marked as equations in **Table 2.2**. Such criteria are functions of the stress angle θ (2.12).

The ordinary pressure-sensitive generalizations of yield criteria, what are of invariable shape in the π-plane, are listed in **Table 2.3**. They are quite simple for real materials. Typical criteria with brittle-ductile transition, obtained as linear combinations of the non-parametric yield criteria of rotational or hexagonal symmetry with the maximum normal stress hypothesis (RANKINE criterion, NSH), are listed in **Table 2.4**, see also Lüpfert (1994). Although such criteria are particular, they are often used because of the lack of measured data. Their approximation with the DRUCKER-PRAGER cone (**Fig. 2.4**) given in some textbooks, is secondary.

In our consideration, further criteria are not effective for application. For example, the LEMAITRE-CHABOCHE yield criterion "intermediary between those of VON MISES and TRESCA" as function of I_2' and I_3' invariants with one parameter additionally to σ_{eq} (Lemaitre and Chaboche, 1985, 1990), see also Altenbach et al. (1995); Altenbach (2018); Jirásek and Bažant (2002); Koval'chuk (1981); Kroon and Faleskog (2013); Takeda et al. (1986) describing the transition

$$\hat{6} - \bigcirc$$

can be replaced with the SZWED criterion with also one parameter (**Table 2.2**)

$$\hat{6} - \bigcirc - \bar{6}.$$

The C^0-yield criterion of ALTENBACH-ZOLOCHEVSKY with two parameters (Altenbach et al., 1995; Altenbach, 2001; Altenbach and Kolupaev, 2014)

$$\hat{3} - \hat{6} | \bigcirc - \bar{3}$$

can be replaced with the modified ALTENBACH-ZOLOCHEVSKY C^0-yield criterion with the same number of parameters (Kolupaev, 2017, 2018; Kolupaev et al., 2018; Rosendahl et al., 2019b)

$$\hat{3} - \hat{6} | \hat{1}\hat{2} | \bar{6} - \bar{3}.$$

The symbol | is explained in **Table 2.2**. Here, only one C^1-criterion of VON MISES is replaced with the regular dodecagon $\hat{1}\hat{2}$. The definition range of the modified formulation is significantly larger.

The LECKIE-HAYHURST strength criterion (Hayhurst, 1972; Leckie and Hayhurst, 1977) with two parameters

$$\bigcirc + \text{NSH} + I_1 \quad \text{or, equivalently,} \quad \bigcirc - \bar{3} \rightarrow I_1,$$

where symbol $\rightarrow$ denotes the linear I_1-substitution (2.15) and symbol $+$ denotes convex combination, can be substituted with the SAYIR pyramid (Kolupaev, 2018) with also two parameters

$$\hat{3} - \bigcirc - \bar{3} \rightarrow I_1$$

but with the larger definition range. However, the PODGÓRSKI pyramid with three parameters and significantly larger definition range (**Table 2.5**)

$$\hat{3} - \hat{6} | \bigcirc - \bar{3} \rightarrow I_1$$

is clearly preferable. Further most important strength criteria are summarized in **Table 2.5**.

The strength criteria with the shape variation in π-plane are discussed in Sect. 2.5. They are not part of the designation and systematization.

2.3.2 Comparison of Yield Criteria

Measured data are normalized by the appropriate tensile limit loading
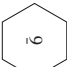
$$\left(\frac{\sigma_{\mathrm{I}}}{\sigma_0^{\mathrm{T}}}, \frac{\sigma_{\mathrm{II}}}{\sigma_0^{\mathrm{T}}}, \frac{\sigma_{\mathrm{III}}}{\sigma_0^{\mathrm{T}}} \right),$$

so that mechanical properties become unitless. The surfaces Φ for different isotropic materials can be now compared in the same diagrams.

We distinguish pressure-insensitive yield criteria (2.7), which are comprehensively described in the π-plane and pressure-sensitive strength criteria (2.3)–(2.4). Certain types of loading for pressure-insensitive materials coinside in the π-plane

Table 2.1: Basic criteria in the π-plane (Subsect. 2.3.1).

π-plane		IVLEV $\hat{3}$	MARIOTTE $\bar{3}$	TRESCA $\hat{6}$	SCHMIDT-ISHLINSKY $\bar{6}$
Geometry	r_{15}	$\sqrt{2}/2$	$\sqrt{2}\left(\sqrt{3}-1\right)$	$\sqrt{3}/2\left(\sqrt{3}-1\right)$	$\sqrt{2}\left(\sqrt{3}-1\right)$
	r_{30}	$1/\sqrt{3}$	$2/\sqrt{3}$	$\sqrt{3}/2$	$2/\sqrt{3}$
	r_{60}	$1/2$	2	1	1
Pdg	β_3	$\{0,1\}$	$\{1,0\}$	$1/2$	–
	η_3	$\{-1,1\}$	$\{-1,1\}$	$\{-1,1\}$	–
Rsn	β_6	–	–	$\{1,0\}$	$\{0,1\}$
	η_6	–	–	$\{1,-1\}$	$\{1,-1\}$
mAZ3	β_3	1	0	$1/2$	$[0,1]$
	α	1	1	1	0
mAZ6	β_6	–	–	1	0
	α	–	–	1	1
References		Ivlev (1959)	Mariotte (1718)	Coulomb (1776)	Burzyński (1928)
		Cicala (1961)	Shanley (1957)	Tresca (1868)	Schmidt (1932)
		Ko (1963)	Ivlev (1959)	Reuss (1933)	Ishlinsky (1940)
		Bishop (1966)	Finnie and Heller (1959)	Yagn (1933)	Hill (1950); Yu (1961)
		Kolupaev (2018)	Sayir and Ziegler (1969)	Prager and Hodge (1954)	Haythornthwaite (1961a)
		Rosendahl et al. (2019b)	Benvenuto (1991)	Życzkowski (1981)	de Araújo (1962)

Abbreviation: Pdg – PODGÓRSKI and Rsn – ROSENDAHL criteria, see **Table 2.2**

Table 2.1: Continuation.

π-plane		SOKOLOVSKY $\widehat{12}$	ISHLINSKY-IVLEV $\widehat{12}$	ROSENDAHL $\widehat{24}$	ROSENDAHL $\widehat{24}$	VON MISES ○
Geometry	r_{15}	$\frac{1}{2}\sqrt{2+\sqrt{3}}$	$\sqrt{2}\left(\sqrt{3}-1\right)$	1	1	1
	r_{30}	1	1	1	1	1
	r_{60}	1	1	1	1	1
Pdg	β_3	–	–	–	–	[0,1]
	η_3	–	–	–	–	0
Rsn	β_6	1/2	–	–	–	[0,1]
	η_6	$\{1,-1\}$	–	–	–	0
mAZ3	β_3	1/2	–	–	–	–
	α	$2\sqrt{3}-3$	–	–	–	–
mAZ6	β_6	1/2	[0,1]	1/2	–	–
	α	1	0	0.4913	–	–
References		Prager (1956) Yu (1961) Pisarenko and Lebedev (1976) Haythornthwaite (1983) Billington (1986) Owen and Hinton (1986)	Ivlev (1960) Shesterikov (1960) Lequeu et al. (1987) Yu (1999) Ishlinsky and Ivlev (2003) Altenbach (2018)	Kolupaev (2018) Rosendahl et al. (2019b)	Rosendahl et al. (2019b) Rosendahl (2020)	Huber (1904) von Mises (1913) Föppl and Föppl (1920) Hencky (1924) Yagn (1933) Skrzypek (1993)

Table 2.2: Designation of the most important yield criteria according Kolupaev (2018); Rosendahl et al. (2019b).

Name	Abbreviation	Designation	Eq.	Parameters	References
CAPURSO (IVLEV)	-	$\hat{3}-\hat{6}-\overline{3}$	-	1	Capurso (1967); Ivlev (1959); Sayir (1970)
SAYIR cubic criterion	CC	$\hat{3}-\bigcirc-\overline{3}$	(2.47)	1	Betten (1976); Sayir (1970); Sayir and Ziegler (1969)
HAYTHORNTHWAITE	-	$\hat{3}-\hat{6}-\overline{3}$	-	1	Candland (1975); Haythornthwaite (1961b, 1962)
YU yield criterion	YYC	$\hat{6}-1\hat{2}-\overline{6}$	-	1	Yu (2002, 2004, 2017); Yu and Yu (2019)
mod. YU yield criterion	mYu	$\hat{6}-1\hat{2}-\overline{6}$	(2.50)	1	Kolupaev (2017, 2018); Rosendahl et al. (2019b)
SZWED bicubic criterion*	BCC	$\hat{6}-\bigcirc-\overline{6}$	(2.53)	1	Szwed (2000, 2010, 2013)
Multiplicative ansatz criterion	MAC	$\hat{6}-1\hat{2}-\overline{6}$	-	1	Kolupaev (2018); Kolupaev and Altenbach (2010); Kolupaev et al. (2013a)
PODGÓRSKI**	Pdg	$\hat{3}-\hat{6}|\bigcirc-\overline{3}$	(2.45)	2	Podgórski (1983, 1984); Podgórski (1985, 1986)
ROSENDAHL	Rsn	$\hat{6}-1\hat{2}|\bigcirc-\overline{6}$	(2.50)	2	Rosendahl (2020); Rosendahl et al. (2019b)
C^0-criterion of trig. sym.	C^0-CTS	$\hat{3}-\hat{6}|1\hat{2}|\hat{6}-\overline{3}$	(2.65)	2	Kolupaev (2017, 2018); Rosendahl et al. (2019b)
CAPURSO+HAYTHORNTHWAITE	C^1-CTS	$\hat{3}-\hat{6}|\bigcirc|\hat{6}-\overline{3}$	-	2	Altenbach et al. (2014); Bolchoun et al. (2011); Kolupaev (2018)
C^0-criterion of hex. sym.	C^0-CHS	$\hat{6}-1\hat{2}|2\hat{4}|1\hat{2}-\overline{6}$	(2.74)	2	Rosendahl (2020); Rosendahl et al. (2019b)
C^1-CHS YYC+MAC	C^1-CHS	$\hat{6}-1\hat{2}|\bigcirc|1\hat{2}-\overline{6}$	-	2	Kolupaev (2018); Kolupaev et al. (2013c)

Comments: * - supplementary sources Barlat et al. (1991); Habraken (2004); Hershey (1954); Hosford (1972, 1979); Karafillis and Boyce (1993); Lagzdiņš (1997); Lagzdiņš and Zilaucs (1996); Paul (1968b); Tan (1990) and our references Kolupaev (2018); Kolupaev and Altenbach (2010); ** - supplementary sources Bigoni and Piccolroaz (2003, 2004); Lagioia and Panteghini (2016); Lagioia et al. (2016); Szwed (2000, 2010, 2013) and our investigations Kolupaev (2017, 2018); Rosendahl (2020); Rosendahl et al. (2019b). The symbol | refers the vertical line in the diagrams **Figs. 2.8 and 2.9.**

Table 2.3: Designation of the strength criteria of invariable shape in the π-plane.

Name	Abbreviation	Designation	Eq.	Parameters	References
DRUCKER-PRAGER (MIROLYUBOV)	DP	$\bigcirc \to I_1$	-	1	Botkin (1940a,b); Drucker and Prager (1952); Mirolyubov (1953)
BURZYŃSKI-YAGN	-	$\bigcirc \to I_1^2$	(2.14)	2	Burzyński (2008); Yagn (1931); Stassi-D'Alia (1967)
RANKINE	NSH	$\hat{3} \to I_1$	(2.135)	1	Ismar and Mahrenholtz (1982); Rankine (1876); de Saint-Venant (1871)
MARIOTTE-ST. VENANT	SC	$\overline{3} \to I_1$	-	1	Benvenuto (1991); Mariotte (1718); Shanley (1957)
KO (IVLEV) pyramid	-	$\hat{3} \to I_1$	-	1	Ko (1963); Ivlev (1959); Tschoegl (1971)
SCHMIDT-ISHLINSKY pyramid	-	$\overline{6} \to I_1$	-	1	Kolupaev (2006, 2018)
SANDEL (DRUCKER) pyramid	-	$\hat{6} \to I_1$	-	1	Drucker (1953); Sandel (1919, 1925)
ISHLINSKY-IVLEV pyramid	-	$1\overline{2} \to I_1$	-	1	-
SOKOLOVSKY pyramid	-	$1\hat{2} \to I_1$	-	1	-

Comments: strain criterion (SC) contains the maximum normal stress hypothesis (NSH) with the setting $\gamma_1 = 1/3$ or, equally, the POISSON's ratio $\nu_+^{in} = 0$ (Appendix 2.7.6); The symbol $\to$ denotes the substitutions: I_1 - linear substitution (2.15) and I_1^2 - quadratic substitution (2.13).

Table 2.4: Designation of the strength criteria with the classical properties $r_{60}^{TT} = 1$ and $r_{60}^C = r_0^{CC}$ (2.39) obtained with the linear combination based on the criterion of hexagonal or rotational symmetry with the NSH and describing brittle-ductile transition.

Name	Abbreviation	Designation	Eq.	Parameters	References
MOHR-COULOMB (single shear theory)	MC	$\hat{6}$+NSH	-	1	Mohr (1900a,b, 1914); Yu (2002, 2004, 2017)
PISARENKO-LEBEDEV (SDOBYREV)	PL	$\bigcirc$+NSH	-	1	Lebedev (1965); Pisarenko and Lebedev (1976); Sdobyrev (1959)
YU octahedral-shear theory	OST	$\hat{12}$+NSH	-	1	Yu (2002, 2004, 2017, 2018)
YU twin shear theory	TST	$\bar{6}$+NSH	-	1	-"-
-	-	$\hat{12}$+NSH	-	1	-

Comments: symbol + refers linear combination of the respective yield criterion with the NSH (Subsect. 2.3.1).

Table 2.5: Designation of the most important strength criteria. The number of parameters is given additionally to the equivalent stress $\sigma_{eq} = \sigma_0^T$.

Name	Abbreviation	Designation	Eq.	Parameters	References
PODGÓRSKI pyramid	-	$\hat{3} - \hat{6}\mid \bigcirc -\bar{3} \to I_1$	(2.48)	3	Kolupaev (2017, 2018); Rosendahl et al. (2019b)
ROSENDAHL pyramid	-	$\hat{6} - \hat{12}\mid \bigcirc -\bar{6} \to I_1$	(2.54)	3	Sect. 2.4.2.2
YU strength theory	YST	$\hat{6} - \hat{12} - \bar{6} + \text{NSH}$	-	2	Yu (2002, 2004, 2017, 2018)
ROSENDAHL+NSH	-	$\hat{6} - \hat{12}\mid \bigcirc -\bar{6} + \text{NSH}$	(2.89)	3	Sect. 2.4.4.1
-	C^0-CTS $\to I_1$	$\hat{3} - \hat{6}\mid \hat{12}\mid \bar{6} - \bar{3} \to I_1$	(2.73)	3	Rosendahl et al. (2019b)
-	C^1-CTS $\to I_1$	$\hat{3} - \hat{6}\mid \bigcirc \mid \bar{6} - \bar{3} \to I_1$	-	3	Kolupaev (2018)
-	C^0-CHS $\to I_1$	$\hat{6} - \hat{12}\mid \hat{24}\mid \hat{12} - \bar{6} \to I_1$	(2.82)	3	Sect. 2.4.3.5
-	C^1-CHS $\to I_1$	$\hat{6} - \hat{12}\mid \bigcirc \mid \hat{12} - \bar{6} \to I_1$	-	3	Sect. 2.4.3.2
extended C^0-YST	C^0-CHS+NSH	$\hat{6} - \hat{12}\mid \hat{24}\mid \hat{12} - \bar{6} + \text{NSH}$	-	3	Sect. 2.4.4.1
extended C^0-YST	C^0-CHS+NSH	$\hat{6} - \hat{12}\mid \bigcirc \mid \hat{12} - \bar{6} + \text{NSH}$	-	3	Sect. 2.4.4.1
extended C^1-YST	CHS+C^1-NSH	$\hat{6} - \hat{12}\mid \bigcirc -\bar{6} + C^1\text{-NSH}$	(2.97)	4	Sect. 2.4.4.2

Comments: symbol | refers the vertical line in the diagrams **Figs. 2.8** and **2.9**; I_1 – linear substitution (2.15), CTS – criterion of trigonal symmetry, CHS – criterion of hexagonal symmetry (**Table 2.2.**)

(**Fig. 2.5**): equal stress angle θ share the same radius ρ (2.111) and collapse onto one point. Introducing the corresponding nomenclature (**Table 2.7**) these are:

- $\theta = 0$: T (uniaxial tension) and CC (equibiaxial compression),
- $\theta = \pi/6$: S (shear), Tt (biaxial tension with $I_3' = 0$), and Cc (biaxial compression with $I_3' = 0$), and
- $\theta = \pi/3$: TT (equibiaxial tension) and C (uniaxial compression).

The values of radii ρ at these stress angles θ are characteristic properties of the yield surface (**Figs. 2.6** and **2.7**).

Pressure-sensitive strength criteria have additional characteristic values because of their I_1-dependence (Subsect. 2.2.3). In order to visualize pressure-sensitive criteria,

- certain cross sections $I_1 = \text{const.}$, e.g. through the particular points T, TT, C, CC, S, Tt, and Cc of the plane stress states (**Table 2.7**) and
- the $(I_1, \sqrt{3I_2'})$-plane (**Fig. 2.4**)

Fig. 2.5 Isogonal (black) and isotoxal (blue) hexagons in the π-plane normalized by the appropriate limit tensile loading σ_0^{T} (**Fig. 2.2**a): Enlarged detail with the VON MISES criterion (red) and the stress states (T, CC on the 0-meridian, S, Tt, Cc on the $\pi/6$-meridian, and C, TT on the $\pi/3$-meridian) for comparison (Rosendahl et al., 2019b).

a. $r_{30} = r_{60} = 1$ b. $r_{60} \in \{1/2, 2\}$ c. $r_{60} = 1$
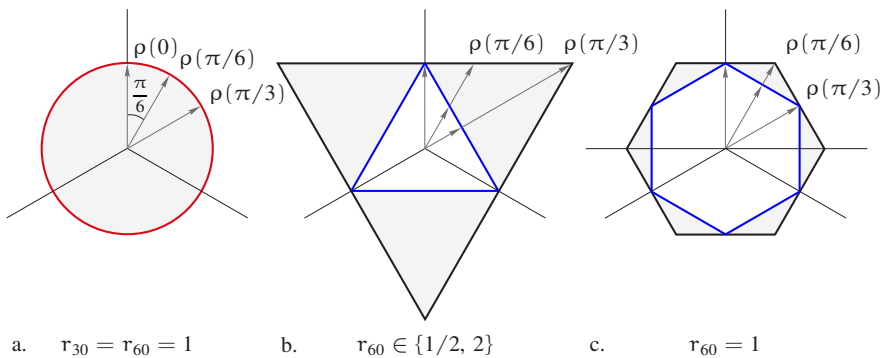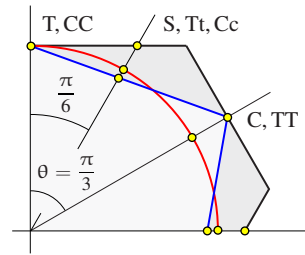
Fig. 2.6: Basic surfaces with the same radius $\rho(0)$ in the π-plane: a. Rotationally symmetric VON MISES criterion (2.10), b. Regular triangles $\hat{3}$ and $\check{3}$, and c. Regular hexagons $\hat{6}$ and $\check{6}$. The values r_{30} and r_{60} (2.26) are given for comparison (Rosendahl et al., 2019b).
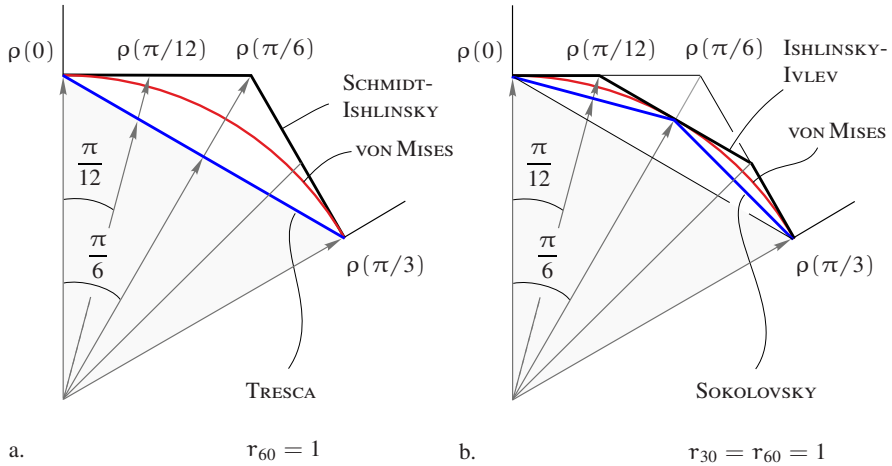
Fig. 2.7: Basic surfaces of hexagonal symmetry in the π-plane: a. Regular hexagons $\hat{6}$ and $\bar{6}$ and b. Regular dodecagons $\hat{12}$ and $\bar{12}$ with the VON MISES criterion (2.10). Because of hexagonal symmetry a cut-out of the angle $\theta \in [0, \pi/3]$ is representative (Kolupaev, 2018; Rosendahl et al., 2019b).

with the projection of the meridians $\theta = $ const. and the lines of the plane stress state are needed. Some examples of visualization are given in Altenbach et al. (2014); Kolupaev (2006, 2017, 2018); Kolupaev and Altenbach (2010); Kolupaev et al. (2013b, 2016, 2018); Rosendahl et al. (2019b).

The plane stress $\sigma_I - \sigma_{II}$ diagram with $\sigma_{III} = 0$ is not representative for 3D-modeling of the limit surface. However, measured data gained with conventional experimental technique are traditionally shown in this diagram. The meridians $\theta = 0$, $\pi/6$, and $\pi/3$ of the surface Φ can be projected in this diagram. It helps conditionally to check approximations by the fitting to the measured data and to visualize the points of the hydrostatic limit loading by different extrapolations (Kolupaev, 2018). The comparison of approximations in the $\sigma_{11} - \tau_{12}$ diagram is not recommended. Here, numerous effects are invisible.

2.3.3 Shapes of Yield Criteria in the π-plane

Cross sections of pressure-insensitive criteria (2.7) may be described in the π-plane as functions $\rho(\theta)$. Let us introduce geometric properties as relations of radii at the angles

$$\theta = \frac{\pi}{24}, \frac{\pi}{12}, \frac{\pi}{8}, \frac{\pi}{6}, \frac{\pi}{4}, \quad \text{and} \quad \frac{\pi}{3} \tag{2.25}$$

to the radius $\rho(0)$ as

$$r_{7.5} = \frac{\rho(\pi/24)}{\rho(0)}, \ r_{15} = \frac{\rho(\pi/12)}{\rho(0)}, \ r_{22.5} = \frac{\rho(\pi/8)}{\rho(0)},$$

$$r_{30} = \frac{\rho(\pi/6)}{\rho(0)}, \quad r_{45} = \frac{\rho(\pi/4)}{\rho(0)}, \quad r_{60} = \frac{\rho(\pi/3)}{\rho(0)}. \tag{2.26}$$

The subscript of r

$$7.5, \quad 15, \quad 22.5, \quad 30, \quad 45, \quad \text{or} \quad 60$$

corresponds to the stress angle θ of the respective radius in degree. With these values (2.26), different yield criteria can be easily compared in appropriate diagrams. The chosen angles θ are some fractions of the angle $\pi/3$ between the symmetry axes in the π-plane (**Figs. 2.6** and **2.7**).

Convexity of the polynomial formulated criteria

$$\Phi(I'_2, I'_3, \sigma_{eq}) = 0,$$

e.g. CC and BCC (**Table 2.2**), is most critical at these angles and needs to be checked firstly for parameter restriction, see (Betten, 1979, 2001; Bolchoun et al., 2011; Troost and Betten, 1974). In fact, it is impossible to say, at which other angles the convexity should be checked (Bolchoun et al., 2011). It can be numerically analyzed with small steps, e.g. with $\Delta\theta \leqslant \pi/360$.

All radii of the VON MISES criterion (2.10) are equal (**Fig. 2.6**a)

$$r_{7.5} = r_{15} = r_{22.5} = r_{30} = r_{45} = r_{60} = 1. \tag{2.27}$$

For direct comparison of the yield criteria of trigonal symmetry (**Fig. 2.6**b), the fractions r_{30} and r_{60} are significant. The fractions r_{15} and r_{45} can be used in refined analysis (Rosendahl et al., 2019b).

For the criteria of hexagonal symmetry (**Fig. 2.7**), the radii at the angles $\theta = 0$ and $\pi/3$ are equal $\rho(0) = \rho(\pi/3)$, which yields

$$r_{60} = 1, \tag{2.28}$$

and because $\rho(\pi/12) = \rho(\pi/4)$, we obtain

$$r_{15} = r_{45}. \tag{2.29}$$

In this case, the fractions $r_{7.5}$ and $r_{22.5}$ are sometimes required for the refined comparison of the shapes and, due to hexagonal symmetry, the fractions at the angles $5\pi/24$ and $7\pi/24$ are excluded from consideration.

Figures 2.8 and **2.9** show convexity restrictions for yield criteria of trigonal symmetry in the $r_{60} - r_{30}$ diagram and for yield criteria of hexagonal symmetry in the $r_{15} - r_{30}$ diagram, respectively. These diagrams allow a comparison of all yield criteria for isotropic materials. The yield figures

$$\bigcirc, \quad \hat{1}\bar{2}, \quad \bar{1}\bar{2}, \quad \hat{2}\bar{4}, \quad \text{and} \quad \bar{2}\bar{4}$$
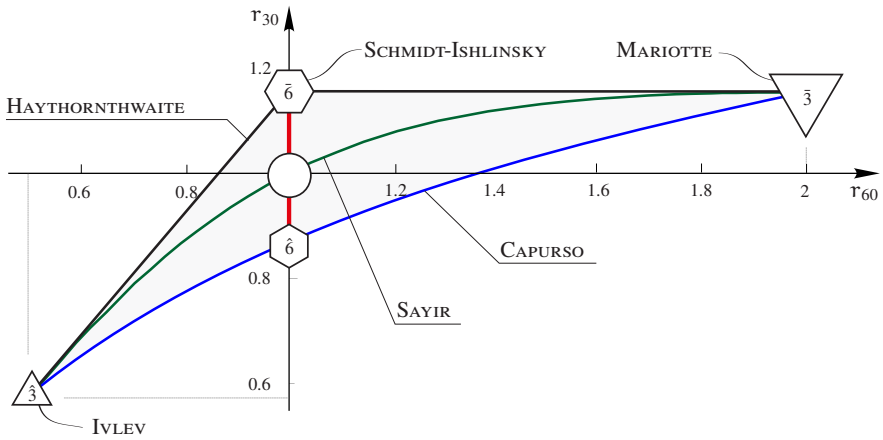
Fig. 2.8: Diagram $r_{60} - r_{30}$ for convex yield criteria of trigonal symmetry compared to the VON MISES criterion with $r_{30} = r_{60} = 1$ (Kolupaev, 2018). Denotation of criteria follows according to **Tables 2.1** and **2.2**.
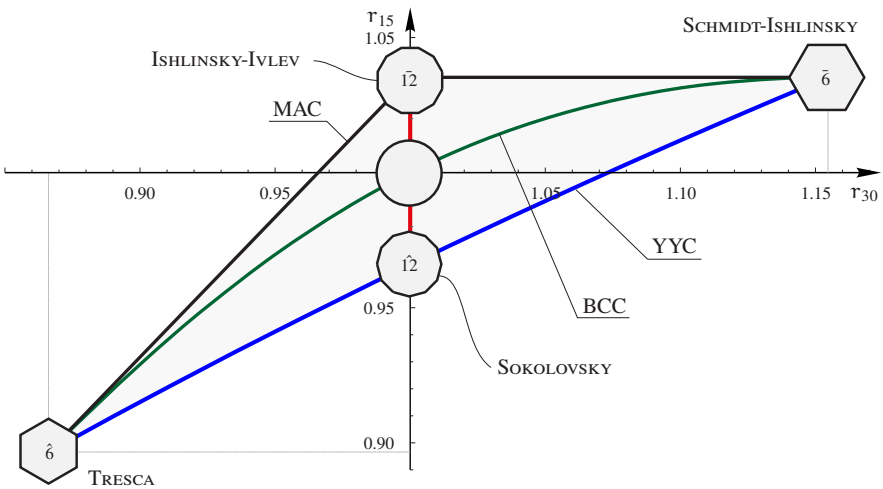
Fig. 2.9: Diagram $r_{30} - r_{15}$ for convex yield criteria of hexagonal symmetry ($r_{60} = 1$) compared to the VON MISES criterion with $r_{15} = r_{30} = 1$ (Rosendahl et al., 2019b). Denotation of criteria follows according to **Tables 2.1** and **2.2**.

coincide in the $r_{60} - r_{30}$ diagram (**Fig. 2.8**), while the yield figures

$$\bigcirc, \quad \hat{2}4, \quad \text{and} \quad \bar{2}4$$

coincide in the $r_{15} - r_{30}$ diagram (**Fig. 2.9**). The diagram $r_{7.5} - r_{15}$ for the criteria of hexagonal symmetry with $r_{60} = r_{30} = 1$ is conceivable, but not relevant for engineering application.

Setting

$$I_1 = \text{const.} \qquad (2.30)$$

in a particular cross section, the fractions (2.26) can be computed for pressure-sensitive criteria, as well. It is required for the criteria with variable cross sections in the π-plane as function of I_1 (Sect. 2.5). Details on the calculation of the discussed fractions (2.26) for any criterion are given in Appendices 2.7.4 and 2.7.5.

2.3.4 Extreme Yield Figures

Lower and upper bounds of convexity for isotropic criteria in the $r_{60} - r_{30}$ diagram (**Fig. 2.8**) are obtained with extreme yield figures of isotoxal and isogonal hexagons (**Figs. 2.10** and **2.11**). The polynomial formulations (2.7) of these hexagons are known (**Table 2.2**)

- the CAPURSO criterion $\hat{3} - \hat{6} - \bar{3}$ and
- the HAYTHORNTHWAITE criterion $\hat{3} - \bar{6} - \bar{3}$.

However, their polynomial forms feature plane intersections surrounding the physically reasonable shape of the surface Φ, which makes the application involved.
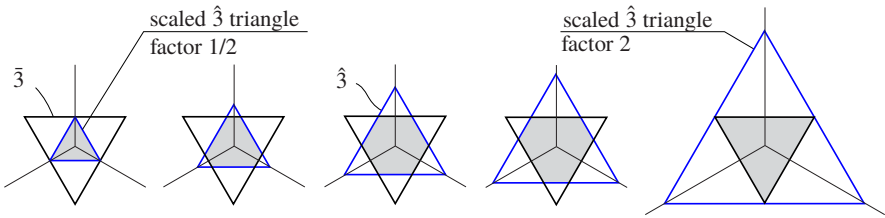
Fig. 2.10: Isogonal (equiangular) hexagons (upper convexity limit, **Fig. 2.8**) formed by the intersection of two triangles in the π-plane: the scaled $\hat{3}$ triangle (blue) and the $\bar{3}$ triangle (black) (Rosendahl et al., 2019b).
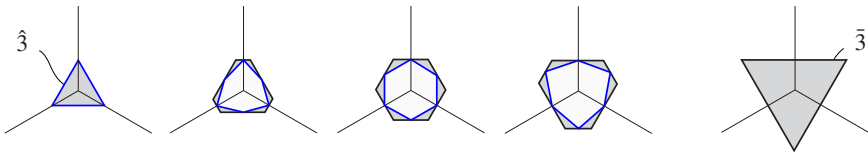
Fig. 2.11: Isotoxal (equilateral, lower convexity limit, blue) and isogonal hexagons (equiangular, upper convexity limit, black) in the π-plane with the $\hat{3}$ (blue) and $\bar{3}$ (black) triangle as limit cases (**Fig. 2.8**) (Rosendahl et al., 2019b).

Isotoxal hexagons (**Fig. 2.8**, lower bound $\hat{3} - \hat{6} - \bar{3}$) as function of stress angle (2.12) can be formulated using the PODGÓRSKI criterion (**Table 2.1** and **2.2**), which describes the geometry of the CAPURSO criterion as a single surface among others. A criterion for isogonal hexagons (**Fig. 2.8**, upper bound $\hat{3} - \bar{6} - \bar{3}$) as function of stress angle without case discrimination is missing (Kolupaev, 2018; Rosendahl et al., 2019b).

Isotoxal and isogonal hexagons degenerate to the same regular triangles $\hat{3}$ and $\bar{3}$ in limit cases (**Figs. 2.6**b and **2.11**) with

$$r_{60} \in \left[\frac{1}{2}, 2 \right].$$

These hexagons $\hat{3} - \hat{6} - \bar{3}$ and $\hat{3} - \bar{6} - \bar{3}$ in the π-plane extended with the linear I_1-substitution (2.15) represent pyramids in principal stress space (Subsect. 2.2.3), which are important strength criteria for practical applications. The transition from the hexagon $\hat{6}$ to $\bar{6}$ via $\bigcirc$ is designated with the vertical line

$$\hat{6} | \bigcirc | \bar{6}$$

according to **Fig. 2.8** and can be describe with the modified YU criterion using the ROSENDAHL criterion (**Table 2.2**, mYU).

The lower and upper bounds of the convexity restriction for the yield criteria of hexagonal symmetry in the $r_{30} - r_{15}$ diagram (**Fig. 2.9**) are obtained with extreme yield figures of isotoxal and isogonal dodecagons. Isotoxal dodecagons (lower bound $\hat{6} - \hat{12} - \bar{6}$) as function of the stress angle can be described with the modified YU criterion (**Table 2.2**, mYU). Only a polynomial formulation for isogonal dodecagons (upper bound $\hat{6} - \bar{12} - \bar{6}$) is known (**Fig. 2.9**, MAC, and **Table 2.2**).

Isotoxal and isogonal dodecagons degenerate to the same regular hexagons $\hat{6}$ and $\bar{6}$ in limit cases (**Figs. 2.6**c and **2.7**a) with

$$r_{30} \in \left[\frac{\sqrt{3}}{2}, \frac{2}{\sqrt{3}} \right].$$

Although the I_1-substitution (2.15) is possible here (**Table 2.3**), dodecagons are typically used as pressure-insensitive criteria. The differences between the regular dodecagons $\hat{12}$ and $\bar{12}$ (**Figs. 2.7**b) with $r_{30} = r_{60} = 1$ (**Table 2.1**) are

$$r_{15} \in \left[\frac{1}{2} \sqrt{2 + \sqrt{3}}, \sqrt{2} \left(\sqrt{3} - 1 \right) \right].$$

The deviation between the MAC and YYC including all criteria of hexagonal symmetry (**Fig. 2.9**) is relevant for comparison of the yield criteria.

The differences between the regular icositetragons $\hat{24}$ and $\bar{24}$ are negligible (see **Table 2.1**). These icositetragons are obtained as a result of the generalization of the yield criteria of hexagonal symmetry (**Table 2.1**).

2.3.5 Geometric Properties and Basic Experiments

For comparison of the limit surfaces, test results, approximations, and extrapolations, let us introduce the following limit loading values normalized with respect to the appropriate uniaxial tensile limit loading σ_0^T:

$$r_{60}^C = \frac{\sigma_{60}^C}{\sigma_0^T} \qquad \text{and} \qquad r_{60}^{TT} = \frac{\sigma_{60}^{TT}}{\sigma_0^T}, \tag{2.31}$$

where σ_{60}^C is the uniaxial compressive limit and σ_{60}^{TT} is the limit under equibiaxial tensile loading,

$$r_{30}^S = \sqrt{3}\,\frac{\sigma_{30}^S}{\sigma_0^T}, \qquad r_{30}^{Cc} = \frac{\sqrt{3}}{2}\frac{\sigma_{30}^{Cc}}{\sigma_0^T}, \qquad \text{and} \qquad r_{30}^{Tt} = \frac{\sqrt{3}}{2}\frac{\sigma_{30}^{Tt}}{\sigma_0^T}, \tag{2.32}$$

where σ_{30}^S is the shear limit, σ_{30}^{Tt} and σ_{30}^{Cc} are the limit loadings of thin-walled tube specimens with closed ends under inner (Tt) and outer pressure (Cc), respectively, and

$$r_0^{CC} = \frac{\sigma_0^{CC}}{\sigma_0^T}, \tag{2.33}$$

where σ_0^{CC} is the limit loading under equibiaxial compression (**Table 2.7**). The subscripts of r refer to the stress angles in degree $\theta = 0$, 30, and 60° (2.112). For the VON MISES criterion (2.10), it follows

$$r_{60}^C = r_{60}^{TT} = r_{30}^S = r_{30}^{Cc} = r_{30}^{Tt} = r_0^{CC} = 1, \tag{2.34}$$

exactly the same as (2.27). It means, all meridians of the cylindrical surface coincide in the BURZYŃSKI-plane and this straight line is parallel to the I_1-axis (**Fig. 2.4**, red line).

While a hydrostatic tensile and compressive test

$$\sigma_I = \sigma_{II} = \sigma_{III} > 0$$

and

$$\sigma_I = \sigma_{II} = \sigma_{III} < 0$$

until failure can be realized in special cases only (Balandin, 1937; Drass, 2020; Feodosjev, 1975; Kolupaev et al., 2014; Kolupaev, 2018; Paul, 1968a,b; Torre, 1950b), the corresponding properties are important for comparison of extrapolations. We may introduce

$$r^{TTT} = \frac{\sigma^{TTT}}{\sigma_0^T} = \frac{1}{3\gamma_1} \qquad \text{and} \qquad r^{CCC} = -\frac{\sigma^{CCC}}{\sigma_0^T} = -\frac{1}{3\gamma_2}. \tag{2.35}$$

where σ^{TTT} and σ^{CCC} are the limit loading under hydrostatic tension and compression, respectively. Except for porous and granular media, hydrostatic compressive failure does typically not occur for relevant loadings and

$$r^{CCC} \to \infty$$

can be assumed (Subsect. 2.2.3). Based on the NSH (Appendix 2.7.6), a reference value as coordinate TTT on the I_1-axis (**Fig. 2.4**)

$$\frac{1}{\gamma_1} = 3$$

is important for comparison. For porous and granular materials, a reference value as coordinate CCC on the I_1-axis (**Fig. 2.4**)

$$\frac{1}{\gamma_2} = -3\, r_{60}^C$$

can be used (Kolupaev, 2018).

Now, the values r_0, r_{30}, and r_{60} describe the π-plane shape at a chosen cross section (2.30) and

$$r_{60}^C, \quad r_{60}^{TT}, \quad r_{30}^S, \quad r_{30}^{Cc}, \quad r_{30}^{Tt}, \quad r_0^{CC}, \quad r^{CCC}, \quad \text{and} \quad r^{TTT}$$

describe corresponding material properties. When $\gamma_1 = \gamma_2 = 0$, pressure-sensitive criteria degenerate to pressure-insensitive criteria: the meridians are parallel to the hydrostatic axis. The values on the same meridians (characterized by the angle θ) coincide:

$$r_{60} = r_{60}^C = r_{60}^{TT}, \qquad r_{30} = r_{30}^S = r_{30}^{Cc} = r_{30}^{Tt}, \qquad \text{and} \qquad r_0^{CC} = 1. \qquad (2.36)$$

Pressure-insensitive criteria of hexagonal symmetry do not distinguish between tensile and compressive properties

$$r_{60} = r_{60}^C = r_{60}^{TT} = r_0^{CC} = 1. \qquad (2.37)$$

The meridians $\theta = 0$ and $\pi/3$ coincide in the BURZYŃSKI-plane and together with other meridians are parallel to the I_1-axis.

Classical yield and strength criteria such as VON MISES, TRESCA, SCHMIDT-ISHLINSKY (**Table 2.1**), and the normal stress hypothesis (**Table 2.3**) describe the material behaviour with the property

$$r_{60}^{TT} = 1 \qquad (2.38)$$

and the linear combinations (**Table 2.4**), e.g. the criteria of MOHR-COULOMB and PISARENKO-LEBEDEV describe the material behaviour with the properties

$$r_{60}^{TT} = 1 \qquad \text{and} \qquad r_{60}^C = r_0^{CC} \geqslant 1, \qquad (2.39)$$

which can be used for the comparison of approximations or for the formulation of fitting restrictions. In the case of missing measured data, it can be assumed, that

$$r_{60}^{TT} \in \left] \frac{1}{2}, 1 \right[.$$

The low bound follows with the convexity requirement on the meridian $\theta = \pi/3$ and the top bound yields as a conservative restriction of the idealized behavior (2.38).

Special attantion is focused to the value (Birger, 1977; Kolupaev, 2018; Sdobyrev, 1959; Yu, 2004)

$$r_{60}^{C} = 2$$

for the criteria in **Table 2.4** and YST (**Table 2.5**), which results as the middle of the restriction $1/r_{60}^{C} \in]0, 1]$. We note, if only the value

$$r_{60}^{C} \in \left[\frac{1}{2}, 2 \right]$$

is known, it is impossible to distinguish between pressure-insensitive and pressure-sensitive material behavior, see the statement in Burzyński (1928) and **Fig. 2.8**. Further measured data is mandatory for any statement. Details on fitting procedures and the parameter identification for pressure-sensitive materials are discussed in Kolupaev et al. (2016); Kolupaev (2017, 2018); Kolupaev et al. (2018); Rosendahl et al. (2019b).

2.4 Yield and Strength Criteria

The phenomenological nature of yield and strength criteria has caused an unmanageable number of possible formulations. Selecting a criterion for a particular application is usually not based on objective arguments. Having to choose an appropriate criterion under basically lack of information can leave engineers confused, see also Lebedev (2010).

Consideration of the plausibility assumptions (Appendix 2.7.8) reduce significantly the number of the criteria suitable for application and minimise risk of inappropriate computation. The aim of this work is the selection of the most effective criteria and their rationale (**Table 2.5**).

2.4.1 Recommended Yield and Strength Criteria

Desired are the C^1-continuous differential criteria (**Table 2.2**)

$$\hat{3} - \hat{6}| \bigcirc |\bar{6} - \bar{3}$$

and

$$\hat{6} - \hat{12} | \bigcirc | \bar{1}\bar{2} - \bar{6}$$

which fulfil the plausibility assumptions. These criteria should be formulated in the form (2.8) as a functions of two parameters (**Figs. 2.8** and **2.9**). Such criteria are not known so far. Some steps in this direction are proposed below.

In the authors' opinion, the PODGÓRSKI and the ROSENDAHL yield criteria (**Table 2.2**) meet the plausibility assumptions in the best way known and are recommended for application. Unfortunately,

- the PODGÓRSKI criterion does not include isogonal hexagons (**Figs. 2.8** and **2.10**) and
- the ROSENDAHL criterion – isogonal dodecagons (**Fig. 2.9**).

These two criteria are generalized for reliable application (Subsect. 2.4.3). Different ways are examined in order to satisfy the plausibility assumptions.

The C^0-CTS (**Table 2.2**, criterion of trigonal symmetry)

$$\hat{3} - \hat{6} | \hat{12} | \bar{6} - \bar{3}$$

and the C^0-CHS (**Table 2.2**, criterion of hexagonal symmetry)

$$\hat{6} - \hat{12} | \hat{24} | \bar{1}\bar{2} - \bar{6}$$

as functions of two parameters are derived on the basis of the modified ALTENBACH-ZOLOCHEVSKY criterion (Kolupaev, 2017, 2018; Rosendahl et al., 2019b). Together with the pyramid of PODGÓRSKI (**Table 2.5**)

$$\hat{3} - \hat{6} | \bigcirc - \bar{3} \rightarrow I_1$$

the pressure-sensitive generalization C^0-CTS $\rightarrow I_1$

$$\hat{3} - \hat{6} | \hat{12} | \bar{6} - \bar{3} \rightarrow I_1$$

is a powerful tool for fitting of the measured data. The linear I_1-substitution (2.15) is used here. The quadratic substitution with the parabolic meridians (2.16) can be tried alternatively for approximation. If necessary, these I_1-substitutions can be used for the C^0-CHS

$$\hat{6} - \hat{12} | \hat{24} | \bar{1}\bar{2} - \bar{6} \rightarrow I_1.$$

The YU strength theory (**Table 2.5**, YST)

$$\hat{6} - \hat{12} - \bar{6} + \text{NSH}$$

will be reformulated as function of the stress angle θ without plane intersections and then generalized as the ROSENDAHL + NSH criterion (**Table 2.5**)

$$\hat{6} - \hat{12} | \bigcirc - \bar{6} + \text{NSH}$$

for simple applicability. Based on the "rounded off" NSH (Appendix 2.7.6), the modified YST with the properties of real construction materials

$$r_0^{CC} \geqslant r_{60}^C \geqslant 1$$

is suggested (Subsect. 2.4.4.2).

The fundamentally different concept of the criteria with variable cross section approach is discussed in Sect. 2.5. These criteria have trigonal symmetry in standard loading region and hexagonal symmetry at high hydrostatic compressive loading, e.g.

$$\hat{6} - \bigcirc - \bar{6} \qquad \text{if} \qquad I_1 \to -\infty.$$

Because of their flexibility, such criteria provide good approximations of experimental data. A general expression is proposed.

With the selected criteria (**Tables 2.2** and **2.5**), it can be checked, whether an optimal approximation of the measured data with the convex shape in the π-plane and the convex meridian is possible. The criteria (**Tables 2.3** and **2.4**) have rather historical and, especially, didactic significance, see also Brandt et al. (1986). Further criteria will be only needed if they fulfil more of the plausibility assumptions compared with the selected criteria.

2.4.2 PODGÓRSKI-*type Shape Functions*

The systematization of the most effective yield criteria (Rosendahl et al., 2019b; Rosendahl, 2020) leads to the shape function

$$\Omega_{3k} = \cos\left[\frac{1}{3\,k}\left(\pi\,\beta_{3k} - \arccos\left[\eta_0 + \eta_{3k}\cos(3k\,\theta)\right]\right)\right], \quad k \in \mathbb{N} \qquad (2.40)$$

which contains with (**Table 2.2**)

- $k = 1$ – the $\hat{3} - \hat{6}\,|\,\bigcirc - \bar{3}$ criterion of trigonal symmetry,
- $k = 2$ – the $\hat{6} - \hat{12}\,|\,\bigcirc - \bar{6}$ criterion of hexagonal symmetry,
- $k = 3$ – the $\hat{9} - \hat{18}\,|\,\bigcirc - \bar{9}$ criterion of trigonal symmetry,
- $k = 4$ – the $\hat{12} - \hat{24}\,|\,\bigcirc - \bar{12}$ criterion of hexagonal symmetry.

The parameter η_0 in (2.40) introduced in Bouvet et al. (2002, 2004); Lexcellent (2018); Lexcellent et al. (2006), see also the series of the invariants (Appendix 2.7.7), is redundant and will be discarded

$$\eta_0 = 0.$$

The setting with $k = 1$ in (2.40) is of crucial importance in the formulation of the yield and strength criteria. The setting with $k = 2$ includes many well-known yield criteria of plasticity theory without tension / compression differences (2.28)

$$r_{60} = r_{60}^C = 1.$$

The setting with $k = 3$ is the consequence of generalization and only of theoretical significance (Kolupaev, 2006, 2018; Rosendahl et al., 2019b). The setting with $k = 4$ will be used to obtain the $\bar{1}2$ criterion for a C^0-generalization (Sect. 2.4.3.5). Further settings with $n \geqslant 5$ are possible, but have not found any application.

Note that, in order to avoid numerical issues, the real part function $\Re$ can be introduced to the shape function Ω_{3k} (2.40)

$$\Omega_{3k} = \Re \left[\cos \left[\frac{1}{3k} \left(\pi \beta_{3k} - \arccos \left[\eta_{3k} \cos(3k\theta) \right] \right) \right] \right]. \tag{2.41}$$

Replacing the parameter η_{3k} by

$$\eta_{3k} = \sin \left[\kappa_{3k} \frac{\pi}{2} \right] \tag{2.42}$$

yields improved parameter sensitivity and numerical stability. According to Szwed (2000), the parameter β_{3k} can be replaced with

$$\beta_{3k} = \arccos(\chi_{3k}). \tag{2.43}$$

This notion (2.43) will not be pursued here.

2.4.2.1 C^1-criterion $\hat{3} - \hat{6} | \bigcirc - \bar{3}$

Normalized with respect to the appropriate uniaxial tensile limit loading $\sigma_{eq} = \sigma_0^T$, the PODGÓRSKI criterion (**Table 2.2**) reads

$$\sigma_{eq} = \sqrt{3 I_2'} \frac{\Omega_3(\theta, \beta_3, \eta_3)}{\Omega_3(0, \beta_3, \eta_3)} \tag{2.44}$$

with the shape function of trigonal symmetry, see (2.40) with $k = 1$

$$\Omega_3(\theta, \beta, \eta) = \cos \left[\frac{1}{3} \left(\pi \beta_3 - \arccos[\eta_3 \cos 3\theta] \right) \right] \tag{2.45}$$

and the parameter restrictions

$$\beta_3 \in [0, 1], \quad \eta_3 \in [-1, 1]. \tag{2.46}$$

It contains the criteria (**Fig. 2.12**, **Tables 2.1** and **2.2**)

- the SAYIR cubic criterion $\hat{3} - \bigcirc - \bar{3}$ with $\beta_3 = \{0, 1\}$,
- the CAPURSO isotoxal hexagons $\hat{3} - \hat{6} - \bar{3}$ with $\eta_3 = \{-1, 1\}$, and
- the TRESCA-VON MISES transition $\hat{6} - \bigcirc$ with $\beta_3 = 1/2$, $\eta_3 \in [0, 1]$.

The criterion (2.44)–(2.45) results from the solution of the cubic equation in σ_{eq}
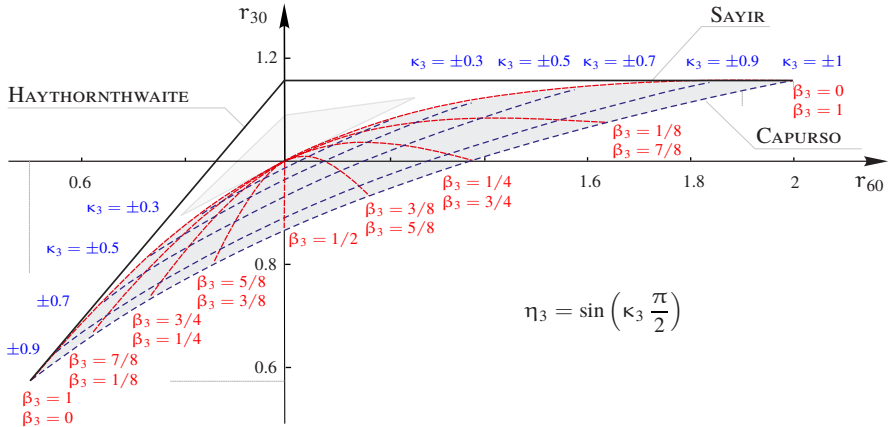
Fig. 2.12: PODGÓRSKI criterion (2.44) in the $r_{60} - r_{30}$ diagram (**Fig. 2.8**). The lines $\beta_3 = \text{const.}$, $\kappa_3 \in [-1, 1]$ (solid red) and $\kappa_3 = \text{const.}$, $\beta_3 \in [0, 1]$ (dashed blue) are shown (Rosendahl et al., 2019b), cf. Podgórski (1984); Podgórski (1985), adapted from Kolupaev (2017, 2018).

$$S'_3 + S'_2\,\sigma_{eq} + S'_1\,\sigma_{eq}^2 = \sigma_{eq}^3 \qquad (2.47)$$

for the rational deviatoric series (Appendix 2.7.7, Eq. (2.147)) with the trigonometric identity (Bronstein and Semendjajew, 2007). The number of the basic geometries included in the criterion is sufficient for many applications. The scheme of this C^1-criterion $\hat{3}-\hat{6}|\bigcirc-\bar{3}$ is shown in **Fig. 2.13**. The PODGÓRSKI criterion (2.44)–(2.45) has received great recognition from professional community (**Table 2.2**, comments).

The parameter restriction (2.46) is convenient for the practice. The parameters of the criterion β_3 and η_3 can be determined numerically by known values r_{60} and r_{30}.

The isogonal hexagons of the HAYTHORNTHWAITE criterion $\hat{3}-\bar{6}-\bar{3}$ containing the regular hexagon $\bar{6}$ (SCHMIDT-ISHLINSKY criterion) cannot be described with the PODGÓRSKI criterion limiting the application of the criterion in the general case. Although a confined field between the criteria $\hat{3}-\bar{6}-\bar{3}$ and $\hat{3}-\bigcirc-\bar{3}$ can be

Fig. 2.13 Scheme of the PODGÓRSKI criterion of trigonal symmetry (2.44)–(2.45). CC - cubic criterion (**Table 2.2**). Color meaning: black - criteria without any parameters, red – criteria with one parameter, and blue - the criterion with two parameters additionally to σ_{eq}.
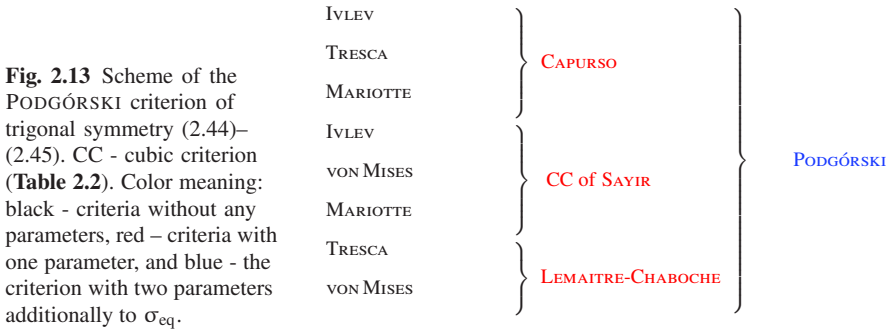
mapped with complex parameters β_3 and η_3 (Kolupaev, 2017, 2018), such approach is not user-friendly.

The PODGÓRSKI pyramid follows with the linear I_1-substitution (2.15) in (2.44) as

$$\frac{\sigma_{eq} - \gamma_1 I_1}{1 - \gamma_1} = \sqrt{3 I_2'} \frac{\Omega_3(\theta, \beta_3, \eta_3)}{\Omega_3(0, \beta_3, \eta_3)} \tag{2.48}$$

and is recommended for use (**Table 2.5**).

2.4.2.2 C^1-criterion $\hat{6} - \hat{12} | \bigcirc - \bar{6}$

Normalized with respect to the appropriate uniaxial tensile limit loading $\sigma_{eq} = \sigma_0^T$, the ROSENDAHL criterion (**Table 2.2**) reads

$$\sigma_{eq} = \sqrt{3 I_2'} \frac{\Omega_6(\theta, \beta_6, \eta_6)}{\Omega_6(0, \beta_6, \eta_6)} \tag{2.49}$$

with the shape function of hexagonal symmetry

$$\Omega_6(\theta, \beta_6, \eta_6) = \cos\left[\frac{1}{6}\left(\pi\beta_6 - \arccos[\eta_6 \cos 6\theta]\right)\right], \tag{2.50}$$

see (2.40) with $k = 2$, or, equivalently, with (2.118)

$$\Omega_6(\theta, \beta_6, \eta_6) = \cos\left[\frac{1}{6}\left(\pi\beta_6 - \arccos\left[\eta_6\left(2\cos^2 3\theta - 1\right)\right]\right)\right], \tag{2.51}$$

which may be preferred. The parameter restrictions are

$$\beta_6 \in [0, 1], \quad \eta_6 \in [-1, 1] \tag{2.52}$$

It contains the criteria (**Fig. 2.14**, **Tables 2.1** and **2.2**)

- the SZWED bicubic criterion $\hat{6} - \bigcirc - \bar{6}$ with $\beta_6 = \{0, 1\}$,
- the isotoxal dodecagons $\hat{6} - \hat{12} - \bar{6}$ of the YU yield criterion with $\eta_6 = \{1, -1\}$,
- the SOKOLOVSKY-VON MISES transition $\hat{12} - \bigcirc$ with $\beta_3 = 1/2$, $\eta_6 \in [0, 1]$.

The criterion (2.49)–(2.50) results from the solution of the bicubic equation

$$S_6' + S_4' \sigma_{eq}^2 + S_2' \sigma_{eq}^4 = \sigma_{eq}^6 \tag{2.53}$$

for the rational deviatoric series (Appendix 2.7.7, Eq. (2.147)) with the trigonometric identity, cf. PODGÓRSKI criterion (2.44)–(2.45).

The number of basic geometries included in the criterion is sufficient for many applications. The parameter restriction (2.52) is convenient for the practice, cf. (2.46). This criterion (2.49)–(2.50) is relatively new but suitable for the solutions of several problems in plasticity theory. The scheme of the criterion $\hat{6} - \hat{12} | \bigcirc - \bar{6}$
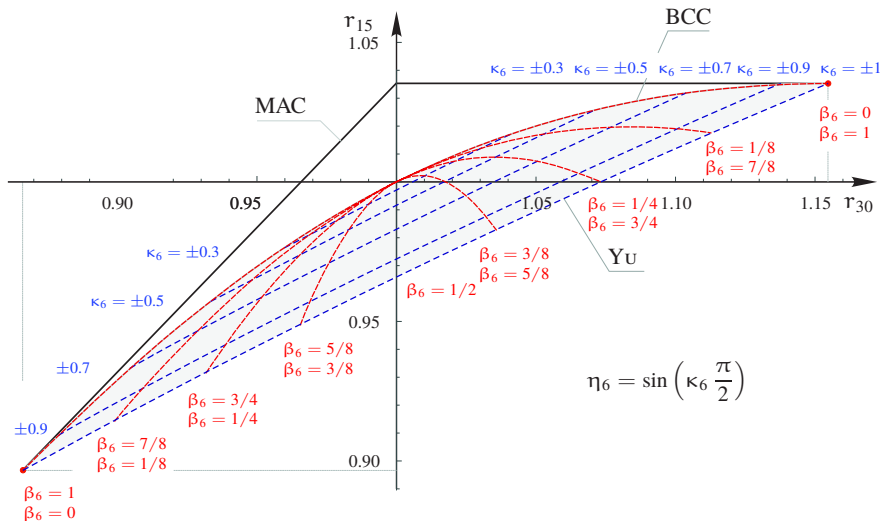
Fig. 2.14: ROSENDAHL criterion (2.50) with $\eta_0 = 0$ in the $r_{30} - r_{15}$ diagram (**Fig. 2.9**). The lines $\beta_6 = $ const., $\kappa_6 \in [-1, 1]$ (solid red) and $\kappa_6 = $ const., $\beta_6 \in [0, 1]$ (dashed blue) are shown, cf. **Fig. 2.12**. BCC – bicubic criterion of SZWED, MAC – multiplicative ansatz criterion (**Table 2.2**).

is shown in **Fig. 2.15**. The parameters of the criterion β_6 and η_6 can be determined numerically by known values r_{30} and r_{15}.

The isogonal dodecagons of the multiplicative ansatz criterion of hexagonal symmetry $\hat{6} - \bar{12} - \bar{6}$ containing the ISHLINSKY-IVLEV criterion (regular dodecagon $\bar{12}$) cannot be described by the ROSENDAHL criterion limiting the application of the criterion in the general case. Although a confined field between the criteria $\hat{6} - \bar{12} - \bar{6}$ and $\hat{6} - \bigcirc - \bar{6}$ can be mapped with complex parameters β_6 and η_6, this approach is not easy-to-use.

The ROSENDAHL pyramid follows with the linear I_1-substitution (2.15) in (2.49) as

$$\frac{\sigma_{\text{eq}} - \gamma_1 \, I_1}{1 - \gamma_1} = \sqrt{3 \, I_2'} \, \frac{\Omega_6(\theta, \beta_6, \eta_6)}{\Omega_6(0, \beta_6, \eta_6)} \tag{2.54}$$

and can be recommended for some applications (**Table 2.5**).

2.4.3 Inductive Derivation of Criteria

The deductive derived approaches Φ are seldom possible, see Gurson (1977). An attempt is made to provide a criterion inductively in order to approximate the general forms. This path is not clear. Several ansätze are conceivable, which are fuzzily restricted by the plausibility assumptions (Appendix 2.7.8).

In our opinion, the C^1-criteria containing the transitions

Fig. 2.15 Scheme of the ROSENDAHL criterion of hexagonal symmetry (2.50): YYC - YU yield criterion, BCC - bicubic criterion (**Table 2.2**). The SOKOLOVSKY-VON MISES criterion was not specified until now. Color meaning: black - criteria without any parameters, red – criteria with one parameter, and blue - the criterion with two parameters additionally to σ_{eq}.
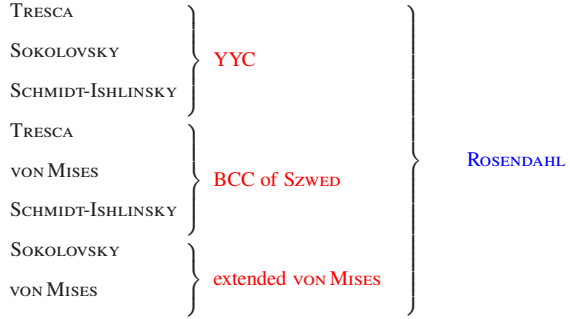
$$\hat{3} - \hat{6}| \bigcirc |\bar{6} - \bar{3}$$

and

$$\hat{6} - \hat{1}\hat{2}| \bigcirc |\bar{1}\bar{2} - \bar{6}$$

should be searched considering the plausibility assumptions. Though these criteria are provided in polynomial form as functions of two parameters (**Table 2.2**), their application is not straightforward.

The major problem in the formulation is that the criteria

- the HAYTHORNTHWAITE $\hat{3} - \bar{6} - \bar{3}$ criterion and
- the multiplicative ansatz criterion (MAC) $\hat{6} - \hat{1}\hat{2} - \bar{6}$

as a function of the stress angle θ without case discrimination are unknown. But these criteria can be sufficiently good approximated (Rosendahl et al., 2019b). Two methods are available:

- convex combination of the known criteria (Subsubsect. 2.4.3.1-2.4.3.5) and
- series developments (Subsubsect. 2.4.3.6).

2.4.3.1 Linear Combination of Yield Criteria

The criteria of PODGÓRSKI (Sect. 2.4.2.1) and ROSENDAHL (Sect. 2.4.2.2) have a similar structure. The generalized criterion of trigonal symmetry follows with the linear combination as

$$\sigma_{eq} = \sqrt{3I_2'} \left[\alpha \frac{\Omega_3(\theta, \beta_3, \eta_3)}{\Omega_3(0, \beta_3, \eta_3)} + (1 - \alpha) \frac{\Omega_6(\theta, \beta_6, \eta_6)}{\Omega_6(0, \beta_6, \eta_6)} \right], \qquad \alpha \in [0, 1]. \quad (2.55)$$

For a criterion of hexagonal symmetry we obtain in a analog path

$$\sigma_{eq} = \sqrt{3I_2'} \left[\alpha \frac{\Omega_6(\theta, \beta_6, \eta_6)}{\Omega_6(0, \beta_6, \eta_6)} + (1 - \alpha) \frac{\Omega_{12}(\theta, \beta_{12}, \eta_{12})}{\Omega_{12}(0, \beta_{12}, \eta_{12})} \right], \quad \alpha \in [0, 1]. \quad (2.56)$$

The advantage of the criteria (2.55) and (2.56) is that the parameter restrictions are known. The disadvantage is, the criteria with five parameters are difficult to manage. The shapes $\hat{6} - \bigcirc$ in (2.55) and $\hat{12} - \bigcirc$ in (2.56) can be describe with each of both terms, what is detrimental by parameter fitting.

The amount of the parameter can be reduced to four:

$$\sigma_{eq} = \sqrt{3I_2'} \left[\alpha \frac{\Omega_3(\theta, 0, \eta_3)}{\Omega_3(0, 0, \eta_3)} + (1 - \alpha) \frac{\Omega_6(\theta, \beta_6, \eta_6)}{\Omega_6(0, \beta_6, \eta_6)} \right], \qquad \alpha \in [0, 1]. \quad (2.57)$$

and

$$\sigma_{eq} = \sqrt{3I_2'} \left[\alpha \frac{\Omega_6(\theta, 0, \eta_6)}{\Omega_6(0, 0, \eta_6)} + (1 - \alpha) \frac{\Omega_{12}(\theta, \beta_{12}, \eta_{12})}{\Omega_{12}(0, \beta_{12}, \eta_{12})} \right], \qquad \alpha \in [0, 1] \quad (2.58)$$

but both terms in (2.57) and (2.58) contain the same $\bigcirc$-shape. Such formulations seem intricate and can not be recommended. The number of parameters should be further reduced.

2.4.3.2 C^1-continuous Differential Yield Criteria

The linear combination SAYIR + SZWED of trigonal symmetry (**Table 2.2**)

$$\hat{3} - \bigcirc - \bar{3} + \hat{6} - \bigcirc - \bar{6}$$

and the linear combination of hexagonal symmetry (C^1-LC-Hex)

$$\hat{6} - \bigcirc - \bar{6} + \hat{12} - \bigcirc - \bar{12}$$

are the functions of three parameters. The SAYIR + SZWED yield criterion follows with the shape functions (2.45) and (2.50) and with the setting $\beta_3 = \beta_6 = 0$ as

$$\sigma_{eq} = \sqrt{3I_2'} \left[\alpha \frac{\Omega_3(\theta, 0, \eta_3)}{\Omega_3(0, 0, \eta_3)} + (1 - \alpha) \frac{\Omega_6(\theta, 0, \eta_6)}{\Omega_6(0, 0, \eta_6)} \right], \qquad \alpha \in [0, 1]. \quad (2.59)$$

The SAYIR + SZWED pyramid is obtained with the linear I_1-substitution (2.15) as

$$\frac{\sigma_{eq} - \gamma_1 I_1}{1 - \gamma_1} = \sqrt{3I_2'} \left[\alpha \frac{\Omega_3(\theta, 0, \eta_3)}{\Omega_3(0, 0, \eta_3)} + (1 - \alpha) \frac{\Omega_6(\theta, 0, \eta_6)}{\Omega_6(0, 0, \eta_6)} \right]. \quad (2.60)$$

The C^1-LC-Hex yield criterion follows with the SZWED shape functions (2.50) and the PODGÓRSKI-type shape functions (2.40) with $k = 4$. The setting $\beta_6 = \beta_{12} = 0$ yields

$$\sigma_{eq} = \sqrt{3I_2'} \left[\alpha \frac{\Omega_6(\theta, 0, \eta_6)}{\Omega_6(0, 0, \eta_6)} + (1 - \alpha) \frac{\Omega_{12}(\theta, 0, \eta_{12})}{\Omega_{12}(0, 0, \eta_{12})} \right], \qquad \alpha \in [0, 1]. \quad (2.61)$$

The C^1-LS-Hex $\rightarrow I_1$ pyramid follows with the linear I_1-substitution (2.15) as

$$\frac{\sigma_{eq} - \gamma_1 I_1}{1 - \gamma_1} = \sqrt{3I_2'}\left[\alpha\frac{\Omega_6(\theta,0,\eta_6)}{\Omega_6(0,0,\eta_6)} + (1-\alpha)\frac{\Omega_{12}(\theta,0,\eta_{12})}{\Omega_{12}(0,0,\eta_{12})}\right]. \qquad (2.62)$$

Both criteria (2.59) and (2.61) can be thought of first as replacement for the missing criteria CAPURSO + HAYTHORNTHWAITE (**Table 2.2**)

$$\hat{3} - \hat{6}| \bigcirc |\bar{6} - \bar{3}$$

and YYC+MAC (**Table 2.2**)

$$\hat{6} - \hat{12}| \bigcirc |\bar{12} - \bar{6}.$$

Disadvantage is that both terms in (2.59) and (2.61) can describe the $\bigcirc$-shape. Due to an additional parameter, the shapes between the extreme yield criteria are not uniquely defined.

2.4.3.3 C^0-linear Combinations with Three Parameters

Possible modifications (Subsubsect. 2.4.3.1) as the C^0-linear combination of SAYIR and YYC of trigonal symmetry (**Table 2.2**)

$$\hat{3} - \bigcirc - \bar{3} + \hat{6} - \hat{12} - \bar{6}$$

or

$$\sigma_{eq} = \sqrt{3I_2'}\left[\alpha\frac{\Omega_3(\theta,0,\eta_3)}{\Omega_3(0,0,\eta_3)} + (1-\alpha)\frac{\Omega_6(\theta,\beta_6,1)}{\Omega_6(0,\beta_6,1)}\right], \qquad \alpha \in [0,1] \quad (2.63)$$

and the linear combination of hexagonal symmetry (C^0-LC-Hex)

$$\hat{6} - \bigcirc - \bar{6} + \hat{12} - \hat{24} - \bar{12}$$

or

$$\sigma_{eq} = \sqrt{3I_2'}\left[\alpha\frac{\Omega_6(\theta,0,\eta_6)}{\Omega_6(0,0,\eta_6)} + (1-\alpha)\frac{\Omega_{12}(\theta,\beta_{12},1)}{\Omega_{12}(0,\beta_{12},1)}\right], \qquad \alpha \in [0,1] \quad (2.64)$$

are also the functions of three parameters. They can not be recommended for application as over-refined for a C^0-criterion.

These criteria are C^1-criteria with the setting $\eta_6 \approx 0.9999$, $\beta_6 \in [0,1]$ in (2.63) and $\eta_{12} \approx 0.9999$, $\beta_{12} \in [0,1]$ in (2.64), but it contradicts our aspiration to consider a maximal number of extreme yield figures.

2.4.3.4 C^0-linear Combination $\hat{3} - \hat{6} - \bar{3} + \bar{6}$

A linear combination $\hat{3} - \hat{6} - \bar{3} + \bar{6}$

$$\Phi_3 = \sqrt{3 I_2'} \left[\alpha \frac{\cos\left[\frac{1}{3}\left(\pi\beta_3 - \arccos\left[\cos 3\theta\right]\right)\right]}{\cos\left[\frac{1}{3}\pi\beta_3\right]} + \right.$$

$$\left. (1-\alpha)\cos\left[\frac{1}{6}\arccos\left[\cos 6\theta\right]\right] \right] - \sigma_{eq} \tag{2.65}$$

with the parameter restriction

$$\alpha \in [0, 1] \qquad \text{and} \qquad \beta_3 \in [0, 1] \tag{2.66}$$

provides the C^0-criterion $\hat{3} - \hat{6} \,|\, \hat{12} \,|\, \bar{6} - \bar{3}$ of trigonal symmetry. The values are

$$r_{60} = \frac{2}{2 - \alpha + \alpha\sqrt{3}\tan\left[\dfrac{\pi\beta_3}{3}\right]}, \tag{2.67}$$

$$r_{30} = \frac{2}{\sqrt{3} + \alpha\tan\left[\dfrac{\pi\beta_3}{3}\right]}, \tag{2.68}$$

and

$$r_{15} = \frac{2\sqrt{2}}{1 + \sqrt{3} - \alpha(1-\sqrt{3})\tan\left[\dfrac{\pi\beta_3}{3}\right]}. \tag{2.69}$$

We obtain the parameters α and β_3 with known values r_{60} and r_{30} as

$$\alpha = \frac{2\sqrt{3}}{r_{30}} - 1 - \frac{2}{r_{60}}, \tag{2.70}$$

$$\beta_3 = \frac{3}{\pi}\arctan\left[\frac{r_{60}(\sqrt{3}\,r_{30} - 2)}{(2 + r_{60})\,r_{30} - 2\sqrt{3}\,r_{60}}\right]. \tag{2.71}$$

The dodecagon $\hat{12}$ with the values $r_{60} = r_{30} = 1$ (**Fig. 2.7** b) follows with

$$\alpha = 2\sqrt{3} - 3 \approx 0.4641 \qquad \text{and} \qquad \beta_3 = \frac{1}{2}. \tag{2.72}$$

The criterion Φ_3 (2.65) describes all points in the $r_{60} - r_{30}$ diagram (**Fig. 2.8**). The parameter setting for the basic geometries are given in **Table 2.1**. It is comparable to with the modified ALTENBACH-ZOLOCHEVSKY criterion of trigonal symmetry (Kolupaev, 2017, 2018; Rosendahl et al., 2019b) and is designated as mAZ3.

The equations and restrictions are easy, so this criterion is advocated for the practical application. The function $\cos 6\theta$ can be replaced with (2.118) for uniform presentation of the criterion as function of $\cos 3\theta$. A disadvantage is, that the geometry of the HAYTHORNTHWAITE criterion (**Table 2.2**) cannot be exactly described with

the settings

$$\beta_3 = 1 \quad \text{for} \quad \hat{3} - \bar{6}$$

and

$$\beta_3 = 0 \quad \text{for} \quad \bar{6} - \bar{3}$$

of mAZ3, although both criteria coincide in the $r_{60} - r_{30}$ diagram. It is also detrimental that the criterion (2.65) does not include the $\bigcirc$-criterion.

The C^0-CTS$\rightarrow I_1$ pyramid follows with the linear I_1-substitution (2.15) in (2.65) as

$$\frac{\sigma_{eq} - \gamma_1 I_1}{1 - \gamma_1} = \sqrt{3I_2'} \left[\alpha \frac{\cos\left[\frac{1}{3}\left(\pi\beta_3 - \arccos\left[\cos 3\theta\right]\right)\right]}{\cos\left[\frac{1}{3}\pi\beta_3\right]} + \right.$$

$$\left. (1 - \alpha)\cos\left[\frac{1}{6}\arccos\left[\cos 6\theta\right]\right] \right] - \sigma_{eq} \tag{2.73}$$

and is also recommended for application (**Table 2.5**).

2.4.3.5 C^0-linear Combination $\hat{6} - \hat{12} - \bar{6} + \bar{12}$

In analogy to mAZ3 (Sect. 2.4.3.4), a linear combination $\hat{6} - \hat{12} - \bar{6} + \bar{12}$

$$\Phi_6 = \sqrt{3I_2'} \left[\alpha \frac{\cos\left[\frac{1}{6}\left(\pi\beta_6 - \arccos\left[\cos 6\theta\right]\right)\right]}{\cos\left[\frac{1}{6}\pi\beta_6\right]} + \right.$$

$$\left. (1 - \alpha)\cos\left[\frac{1}{12}\arccos\left[\cos 12\theta\right]\right] \right] - \sigma_{eq} \tag{2.74}$$

with the parameter restriction

$$\alpha \in [0, 1] \quad \text{and} \quad \beta_6 \in [0, 1] \tag{2.75}$$

provides the C^0-criterion $\hat{6} - \hat{12}|\hat{24}|\bar{12} - \bar{6}$ of hexagonal symmetry. The values are

$$r_{60} = 1, \tag{2.76}$$

$$r_{30} = \frac{2}{2 + \alpha\left(\sqrt{3} - 2 + \tan\left[\frac{\pi\beta_6}{6}\right]\right)}, \tag{2.77}$$

and

$$r_{15} = \frac{2\sqrt{2}}{\sqrt{3}+1+\alpha\left(\sqrt{3}-1\right)\tan\left[\dfrac{\pi\beta_6}{6}\right]}. \tag{2.78}$$

We obtain the parameters α and β_6 with known values r_{30} and r_{15} as

$$\alpha = \frac{2+\sqrt{3}}{r_{15}\,r_{30}}\left(2\sqrt{2+\sqrt{3}}\,r_{30}-2\,r_{15}-\sqrt{3}\,r_{15}\,r_{30}\right), \tag{2.79}$$

$$\beta_6 = \frac{6}{\pi}\arctan\left[\frac{r_{30}\left(\sqrt{2}-\sqrt{6}+r_{15}\right)}{-2\sqrt{2+\sqrt{3}}\,r_{30}+2\,r_{15}+\sqrt{3}\,r_{15}\,r_{30}}\right]. \tag{2.80}$$

The icositetragon $\hat{2}4$ with the values $r_{15}=r_{30}=1$ follows with

$$\alpha = 5\sqrt{2}-4\sqrt{3}+3\sqrt{6}-7\approx 0.4913 \qquad \text{and} \qquad \beta_6 = \frac{1}{2}. \tag{2.81}$$

The criterion Φ_6 (2.74) describes all points in the $r_{30}-r_{15}$ diagram (**Fig. 2.9**). The parameter settings of this modified ALTENBACH-ZOLOCHEVSKY criterion of hexagonal symmetry (mAZ6) for the basic geometries are given in **Table 2.1**.

The equations are easy, so this criterion is recommended for the practical application. The function $\cos 12\theta$ can be replaced with (2.118) for uniform presentation of the criterion as function of $\cos 3\theta$ or $\cos 6\theta$. The disadvantage is, that the geometry of the MAC (**Table 2.2**) cannot be exactly described with the settings

$$\beta_6 = 1 \quad \text{for} \quad \hat{6}-\bar{1}\bar{2}$$

and

$$\beta_6 = 0 \quad \text{for} \quad \bar{1}\bar{2}-\bar{6}$$

of the mAZ6, although both criteria coincide in the $r_{30}-r_{15}$ diagram. The criterion (2.74) does not include the $\bigcirc$-criterion and is C^0-continuous, which is detrimental to the yield criteria.

The C^0-CHS$\rightarrow$I$_1$ pyramid follows with the linear I_1-substitution (2.15) in (2.74) as

$$\frac{\sigma_{eq}-\gamma_1\,I_1}{1-\gamma_1} = \sqrt{3I_2'}\left[\alpha\,\frac{\cos\left[\dfrac{1}{6}\left(\pi\beta_6-\arccos\left[\cos 6\theta\right]\right)\right]}{\cos\left[\dfrac{1}{6}\pi\beta_6\right]}+\right.$$
$$\left.(1-\alpha)\cos\left[\frac{1}{12}\arccos\left[\cos 12\theta\right]\right]\right]-\sigma_{eq} \tag{2.82}$$

and is recommended for application (**Table 2.5**).

2.4.3.6 Series Development

In the next step of the inductive derivations, the series development as sum of cosine is introduced (Bulla and Kolupaev, 2021)

$$\Omega_m = \cos\left[\frac{1}{3\lambda_m}\left(\pi\beta_m - \arccos\left[\eta_0 + \eta_3\cos(3\theta) + \eta_6\cos(6\theta) + \ldots\right]\right)\right] \quad (2.83)$$

with

- $m = 3$ for criteria of trigonal symmetry containing at least one odd term, e.g. η_3 and the even terms with η_6, η_{12}, etc. and
- $m = 6$ for criteria of hexagonal symmetry containing only even terms η_6, η_{12}, etc.

The idea originates with the compete series (2.145) or reduced series (2.146) of the invariants (Appendix 2.7.7).

The problem in (2.83) is the number of parameters which should be reduced for practical application. The associated issue is the necessary restriction of parameters. The functions $\cos 6\theta$, $\cos 12\theta$, etc. can be replaced with (2.118)–(2.119) for uniform presentation. Because of the number of the parameters and related convexity constraints, this shape function (2.83) is not user-friendly.

The next possibility to try it out is a sum of arccosine

$$\Omega_m = \cos\left[\pi\beta_m - \frac{1}{3}\arccos[\eta_3\cos 3\theta] - \frac{1}{6}\arccos[\eta_6\cos 6\theta] + \ldots\right]. \quad (2.84)$$

This formulation also requires further study with the convexity analysis. It can not be directly recommended.

A formally performed linear combination with two parameters

$$\Omega_3 = \cos\left[\alpha\frac{1}{3}\left(\pi\beta_3 - \arccos[\cos 3\theta]\right) - (1-\alpha)\frac{1}{6}\arccos[\cos 6\theta]\right], \quad (2.85)$$

containing $\hat{3} - \hat{6}|\bar{6} - \bar{3}$ with

$$\alpha \in [0, 1] \qquad \text{and} \qquad \beta_3 \in [0, 1] \qquad (2.86)$$

yields non-convex geometries for some setting of the parameters (2.86) and can also not be recommended.

We are of the opinion, that these series developments are not effective for practical use because of the number of parameters and the intricate convexity constraints. Maybe further investigations can show the usefulness of this approach.

2.4.4 Modified YU Strength Theory

The YU strength theory (YST) was introduced 2002 and has gained recognition from the community (**Table** 1.5). The word "theory" in relation to the criteria is a tribute to tradition. We adopt this denomination in relation to the YST. The YST can be interpreted as a linear combination of the TRESCA and SCHMIDT-ISHLINSKY criteria containing the SOKOLOVSKY criterion with the normal stress hypothesis (**Fig. 2.16**):

$$\hat{6} - \hat{12} - \bar{6} \quad + \quad \text{NSH}$$

or a convex combination of the equivalent stresses σ_{Tresca}, σ_{SI}, and σ_{I} of these criteria (TRESCA, SCHMIDT-ISHLINSKY, and the maximum normal stress hypothesis) with two parameters (ξ, ζ):

$$\xi \, \sigma_{\text{Tresca}} + \zeta \, \sigma_{\text{SI}} + (1 - \xi - \zeta) \, \sigma_{\text{I}} = \sigma_{\text{eq}} \qquad (2.87)$$

and with parameter restrictions to ensure convexity

$$\xi \in [0, 1], \qquad \zeta \in [0, 1], \qquad \text{and} \qquad \xi + \zeta \leqslant 1. \qquad (2.88)$$

The parameters in the formulation (2.87) have no direct physical meaning. This combination (2.87) can be realized in the different ways (Kolupaev, 2017, 2018; Kolupaev et al., 2018; Rosendahl et al., 2019b).

2.4.4.1 C^0-continuous Strength Criterion

Based on the normal stress hypothesis (Appendix 2.7.6) and the ROSENDAHL criterion (2.49), we introduce the linear combination, cf. Kolupaev (2017, 2018); Rosendahl et al. (2019b)

$$\hat{6} - \hat{12} | \bigcirc - \bar{6} \quad + \quad \text{NSH}$$

Fig. 2.16 Scheme of the YU strength theory (YST): TST – twin shear theory of YU, NSH – normal stress hypothesis, the SOKOLOVSKY criterion is a C^0-approximation of the VON MISES criterion with a regular dodecagon $\hat{12}$. Color meaning: black - criteria without any parameters, red – criteria with one parameter, and blue - the criterion with two parameters additionally to the equivalent stress σ_{eq}.
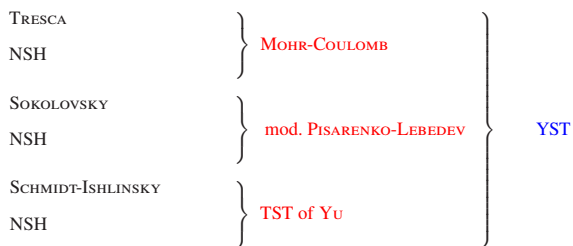
or

$$\sigma_{eq} = \frac{1}{r_{60}^C} \, \sigma_{Rsn} + \left(1 - \frac{1}{r_{60}^C}\right) \sigma_{NSH} \tag{2.89}$$

with the parameter restrictions

$$\frac{1}{r_{60}^C} \in]0, 1], \qquad \beta_6 \in [0, 1], \qquad \eta_6 \in [-1, 1]. \tag{2.90}$$

This results in a final equation of the modified YU strength criterion (mYU)

$$\sigma_{eq} = \frac{1}{r_{60}^C} \sqrt{3 I_2'} \frac{\cos\left[\frac{1}{6}\left(\pi\beta_6 - \arccos[\gamma_6 \cos 6\theta]\right)\right]}{\cos\left[\frac{1}{6}\left(\pi\beta_6 - \arccos[\gamma_6]\right)\right]}$$
$$+ \frac{1}{3}\left(1 - \frac{1}{r_{60}^C}\right)\left(I_1 + 2\sqrt{3 I_2'}\cos\theta\right), \tag{2.91}$$

which contains the criteria shown in **Fig. 2.17**. The modified YU criterion (2.91) describes the limit surface without plane intersections. The value r_{30}^S of the mYU is

$$r_{30}^S = 3\, r_{60}^C \times \left[\sqrt{3}\left(r_{60}^C - 1\right)\right.$$
$$\left. + 3\cos\left[\frac{1}{6}\left(\pi\beta_6 - \arccos[-\gamma_6]\right)\right] \sec\left[\frac{1}{6}\left(\pi\beta_6 - \arccos[\gamma_6]\right)\right]\right]^{-1}. \tag{2.92}$$

The value r^{TTT} for the hydrostatic tensile limit loading results to

Fig. 2.17 Scheme of the mYU criterion: UCC – unified classical criterion, YYT – YU yield theory, mYU-I and mYU-II – modified YU criteria, mPL – modified PISARENKO-LEBEDEV criterion, BCC – bicubic criterion of SZWED. Color meaning: black - criteria without any parameters, red – criteria with one, blue - with two, and bold black - with three parameters additionally to the equivalent stress σ_{eq}.
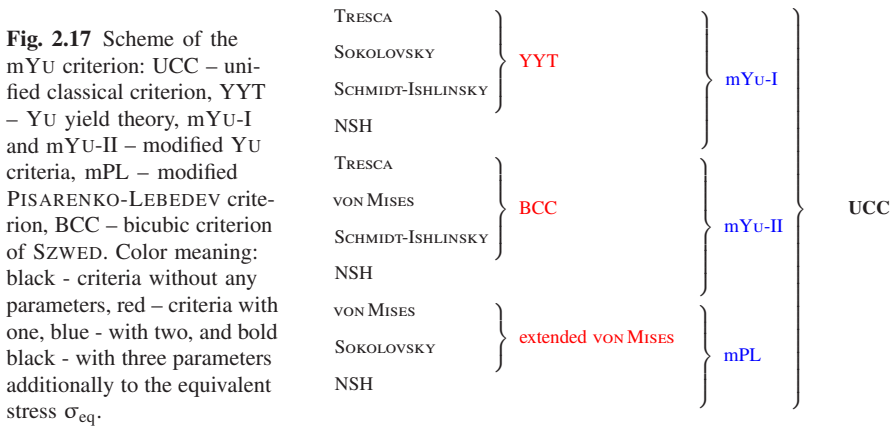
$$r^{\text{TTT}} = \frac{1}{1 - \dfrac{1}{r_{60}^{\text{C}}}} = \frac{1}{1 - 2\,v_+^{\text{in}}}. \tag{2.93}$$

The surface Φ of the mYU (2.91) is open in the hydrostatic compression direction $(I_1 < 0)$:

$$r^{\text{CCC}} \to \infty. \tag{2.94}$$

The inelastic POISSON's ratios at tension and compression are (Kolupaev, 2018)

$$v_+^{\text{in}} = \frac{1}{2\,r_{60}^{\text{C}}} \qquad \text{and} \qquad v_-^{\text{in}} = \frac{r_{60}^{\text{C}}}{2}, \tag{2.95}$$

as for the MOHR-COULOMB and further criteria in **Table 2.4**.

The TST (**Table 2.4**) cannot be reproduced exactly by this method (2.89). The deviation between $\hat{6} - \bigcirc - \bar{6}$ of the BCC and $\hat{6} - \hat{1}2 - \bar{6}$ of the YYC is relevant for "very ductile materials" (Christensen, 2019; Kolupaev, 2018; Lemaitre and Chaboche, 1990; von Mises, 1928; Theocaris, 1995)

$$v_+^{\text{in}} \to \frac{1}{2}. \tag{2.96}$$

The introduced criterion (2.89) is C^0-continuously in the π-plane. The criterion contains a singular peak at the hydrostatic node TTT for pressure-sensitive materials with $r_{60}^{\text{C}} > 1$, which should be treated separately (**Table 2.11**, PG10). Like the YST, the mYU criterion can be considered as unified classical criterion (UCC) with the properties (2.39).

The modified YU strength criterion (2.89) meet the plausibility assumptions in the best way and is recommended for application as a yield and strength criterion (**Figs. 2.18**, **2.19**, **2.20**, and **2.21** with $\eta_3 = \eta_6 = 1$). Various material properties can be described using this criterion. The implementation in the FEM code is simple due to solely surface in the principal stress space.

Generalization of (2.89) based on the C^0-linear combinations (2.74)

$$\hat{6} - \hat{1}2 \,|\, \hat{2}4 \,|\, \bar{1}2 - \bar{6}$$

or C^1-linear combinations (Sect. 2.4.3.2)

$$\hat{6} - \hat{1}2 \,|\, \bigcirc \,|\, \bar{1}2 - \bar{6}$$

and the NSH can be suggested (**Table 2.5**)

$$\hat{6} - \hat{1}2 \,|\, \hat{2}4 \,|\, \bar{1}2 - \bar{6} \qquad + \qquad \text{NSH}$$

or

$$\hat{6} - \hat{1}2 \,|\, \bigcirc \,|\, \bar{1}2 - \bar{6} \qquad + \qquad \text{NSH}.$$
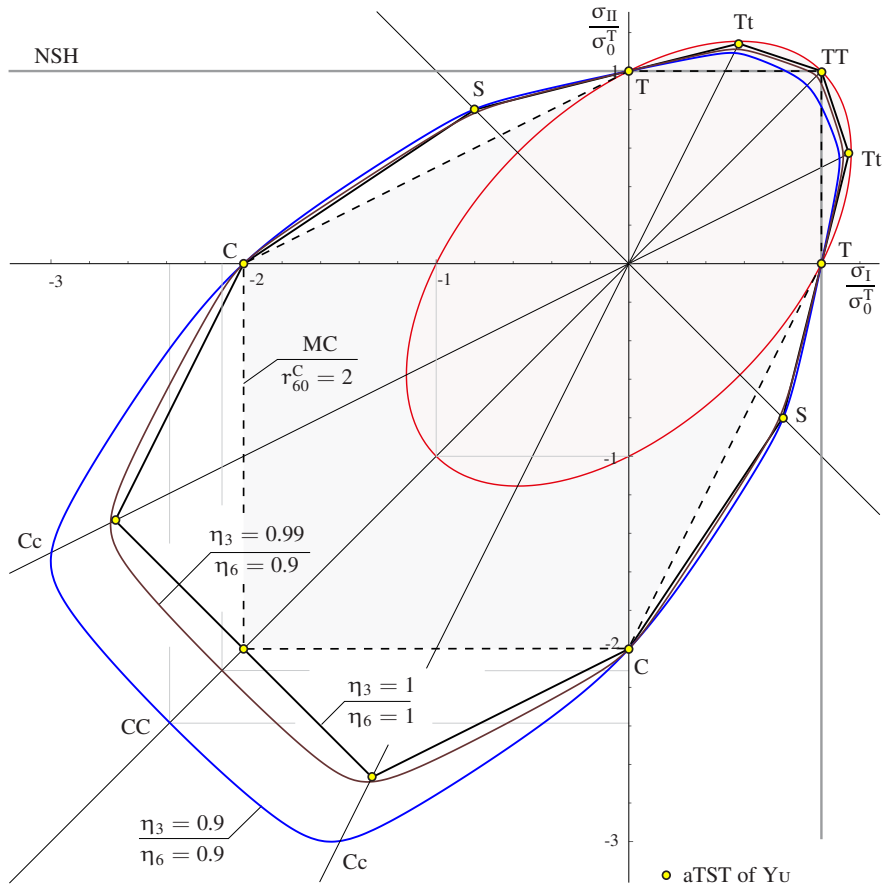
Fig. 2.18: Modified YST (2.98) as function of the parameters η_3 and η_6 with the setting $r_{60}^C = 2$ and $\beta_6 = 0$ in the normalized $\sigma_I - \sigma_{II}$ diagram. The points of the approximated TST (aTST) with $\eta_3 = \eta_6 = 1$ are highlighted. The ellipse of the VON MISES criterion (red) and the MOHR-COULOMB criterion (MC) (dashed line) are shown for comparison.

Such criteria are far from the practical relevance. The additional fitting possibilities with the transition $\hat{24}|\bar{12}$-NSH or $\bigcirc|\bar{12}$-NSH can be only relevant for very ductile material with $r_{60}^C \to 1$ or, equivalently, with (2.96).

2.4.4.2 C^1-continuous Strength Criterion

Linear combination (Sect. 2.4.4.1)

$$\hat{6} - \bigcirc - \bar{6} \quad + \quad \text{NSH}$$

Fig. 2.19 Modified YST (2.98) as function of the parameters η_3 and η_6 with the setting $r_{60}^C = 2$ and $\beta_6 = 0$ in the normalized $\sigma_I - \sigma_{II}$ diagram. The ellipse of the VON MISES criterion (red) is shown for comparison. The first quadrant is enlarged for better visualization.
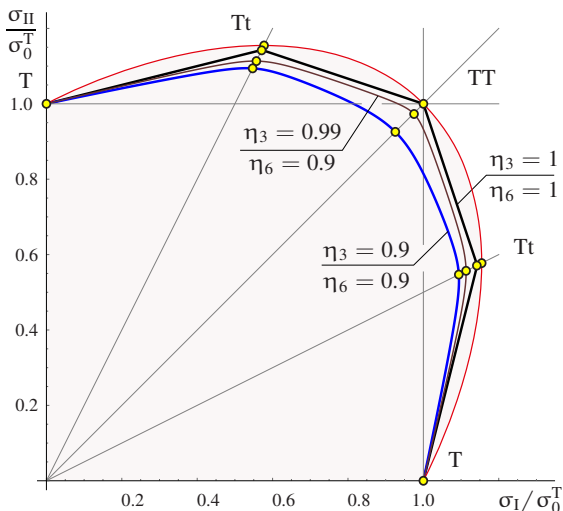
can be reformulated as linear combination with the linear I_1-substitution (2.15)

$$\hat{6} - \bigcirc - \bar{6} \quad + \quad \left(\hat{3} \to I_1\right), \qquad \gamma_1 = \frac{1}{3}$$

as function of two parameters. The method searched for is a formulation of the C^1-criterion of the above schema in accordance with the YST (**Table 2.5**).

With the equivalent stress σ_{C1} of the C^1-NSH (Appendix 2.7.6) and the ROSEN-DAHL criterion (2.49) we can write, cf. (2.89)

$$\sigma_{eq} = \frac{1}{r_{60}^C}\,\sigma_{Rsn} + \left(1 - \frac{1}{r_{60}^C}\right)\sigma_{C1} \tag{2.97}$$

or inserted

$$\sigma_{eq} = \frac{1}{r_{60}^C}\,\sqrt{3\,I_2'}\,\frac{\cos\left[\frac{1}{6}\left(\pi\beta_6 - \arccos[\eta_6\cos 6\theta]\right)\right]}{\cos\left[\frac{1}{6}\left(\pi\beta_6 - \arccos[\eta_6]\right)\right]} +$$

$$\left(1 - \frac{1}{r_{60}^C}\right)\left(\sqrt{3\,I_2'}\,\frac{\cos\left[-\frac{1}{3}\arccos[\eta_3\cos 3\theta]\right]}{\cos\left[-\frac{1}{3}\arccos[\eta_3]\right]}\,(1-\gamma_1) + \gamma_1\,I_1\right) \tag{2.98}$$

with the substitution (2.138)
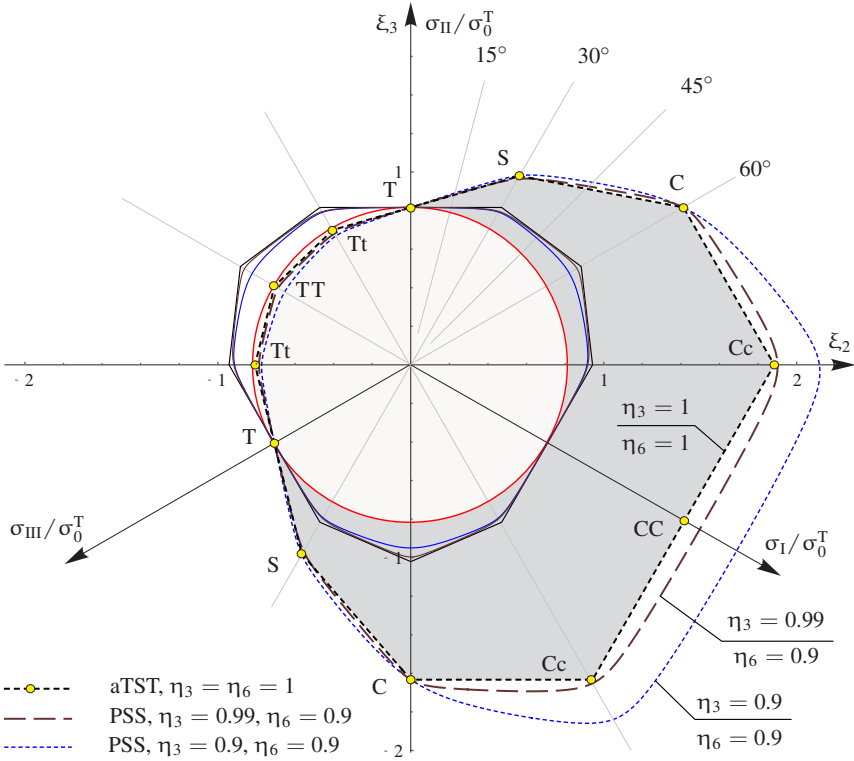
Fig. 2.20: Modified YST (2.98) as function of the parameters η_3 and η_6 with the setting $r_{60}^C = 2$ and $\beta_6 = 0$ in the normalized π-plane. The cross sections orthogonal to the hydrostatic axis at $I_1 = \sigma_0^T/\sqrt{3}$ and the lines of the plane stress state (PSS, dashed lines) are shown. The points of the C^0-approximated TST (aTST) with $\eta_3 = \eta_6 = 1$ are highlighted. The circle of the VON MISES criterion is shown for comparison.

$$\gamma_1(\eta_3) = 1 \left/ \left\{ 1 + \cos\left[\frac{1}{3}\arccos[\eta_3]\right] \sec\left[\frac{1}{3}\arccos[-\eta_3]\right]\right\}\right. \qquad (2.99)$$

as function of four parameters (**Figs. 2.18** and **2.19**)

$$\frac{1}{r_{60}^C} \in [0, 1], \qquad \beta_6 \in [0, 1], \qquad \eta_6 \in [-1, 1], \qquad \eta_3 \in [-1, 1].$$

The fourth parameter can first be set $\eta_3 \in [0.99, 1[$ for the "rounding off" NSH (**Table 2.8**). We obtain with $\eta_6 \in]-1, 1[$ the C^1-continuous strength criterion. The values are

$$\nu_+^{in} = \frac{1}{2} - \frac{3}{2}\frac{r_{60}^C - 1}{r_{60}^C}\gamma_1, \qquad (2.100)$$
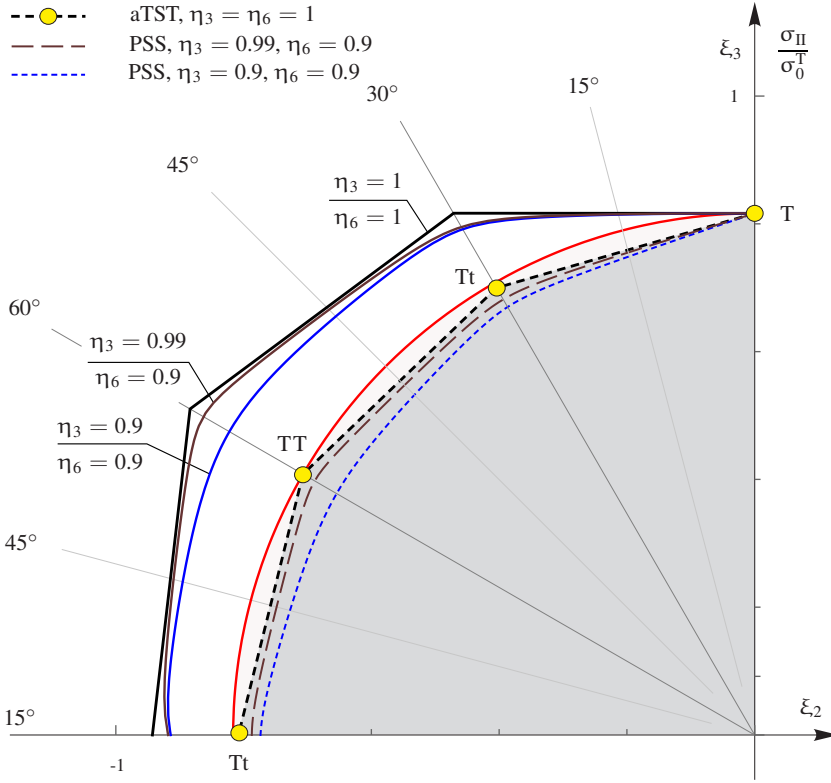
Fig. 2.21: Enlarged cut of the π-plane (**Fig. 2.20**): modified YST (2.98) as function of the parameters η_3 and η_6 with the setting $r_{60}^C = 2$ and $\beta_6 = 0$ in the normalized π-plane. The circle of the VON MISES criterion (red) is shown for comparison.

$$r^{TTT} = \frac{1}{3} \frac{r_{60}^C}{\left(r_{60}^C - 1\right) \gamma_1}, \tag{2.101}$$

and

$$r_0^{CC} = \frac{r_{60}^C}{r_{60}^C + 3\gamma_1 - 3 r_{60}^C \gamma_1}. \tag{2.102}$$

Further values are too large and therefore omitted.

Based on the value r_0^{CC} (2.102), the deviation of the real material properties from the classical assumption with $r_0^{CC} = r_{60}^C$ (2.39) can be introduced

$$\delta_{Yu} = \frac{r_0^{CC} - r_{60}^C}{r_{60}^C}. \tag{2.103}$$

And vice versa, the parameter η_3 dependent on the deviation δ_{Yu} of the value r_0^{CC} from the value r_{60}^C (2.102) can be set (**Table 2.6**).

Table 2.6: Setting of the parameter η_3 dependent on the default deviation $\delta_{Yu} = 1$ or 2% of the value r_0^{CC} from r_{60}^C.

r_{60}^C	η_3 at $\delta_{Yu} = 1\%$	η_3 at $\delta_{Yu} = 2\%$
1.1	0.963797	0.848176
1.2	0.991328	0.964532
1.5	0.998651	0.994610
2	0.999666	0.998677
5	0.999979	0.999919
10	0.999996	0.999984
12	0.999997	0.999990

This criterion (2.98) can be applied as the yield and strength criterion and is recommended for use. Problems with the derivation become obsolete, but the properties of the classical criteria (2.39) are lost.

The number of parameters seems excessive at first, but can be easily reduced based on the modeling concept:

- Setting $\beta_6 = 0$, $\eta_6 \in [-1, 1]$ for the C^1-transition $\hat{6} - \bigcirc - \bar{6}$ or
- Setting $\beta_6 \in [0, 1]$, $\eta_6 = \{-1, 1\}$ for the C^0-transition $\hat{6} - \hat{12} - \bar{6}$ of the YYC,

with formal or computed setting η_3 (**Table 2.6**). The setting $\eta_3 = 1$ provides the extended C^0-criterion according to YU with the classical properties (Sect. 2.4.4.1). Now, only two parameters remain for definition: (r_{60}^C, η_6) or (r_{60}^C, β_6).

If the amount of measured data is sufficiently large, the parameter $\eta_3 \in [-1, 1]$ in (2.134) can be used as an extra parameter. The physical background behind the YST is then lost, but fitting quality increases.

2.5 Criterion with Shape Variation in π-plane

Instead of generalizing possible shapes in the π-plane, Pisarenko and Lebedev (1969); Ottosen (1975, 1977, 1980); Ottosen and Ristinmaa (2005); Xiaoping et al. (1989) allowed for shape variation in the π-plane along the hydrostatic axis. Using the PODGÓRSKI shape function Ω_3 (2.45) and the POSENDAHL shape function Ω_6 (2.50), the OTTOSEN idea can be extended as (Rosendahl et al., 2019b)

$$3(1-\chi)\, I_2' \left(\frac{\Omega_6(\theta, \beta_6, \eta_6)}{\Omega_6(0, \beta_6, \eta_6)} \right)^2 + \chi\, \sigma_{eq} \left[(1-\xi)\sqrt{3\, I_2'}\, \frac{\Omega_3(\theta, \beta_3, \eta_3)}{\Omega_3(0, \beta_3, \eta_3)} + \xi\, I_1 \right] = \sigma_{eq}^2 \tag{2.104}$$

with the parameters of the convex combinations

$$\chi \in [0, 1] \quad \text{and} \quad \xi \in [0, 1]. \tag{2.105}$$

With $\xi \in]0, 1[$, we obtain a surface with cross sections of hexagonal symmetry in the π-plane for $I_1 \to -\infty$. Compared with (2.48), this effect is controlled with an

additional parameter χ. Some approximations are obtained for data measured by
KUPFER for three types of concrete with $\chi \in [0.9845, 1]$ and $\xi \in [0.3037, 0.3523]$
(Rosendahl et al., 2019b).

The criterion (2.104) can be considered as a generalization of

- the PODGÓRSKI pyramid (2.48) or its corresponding CTS-formulation (2.55)
  with $\chi = 1$,
- the ROSENDAHL criterion (2.49)–(2.50), which can be replaced with one of the
  CHS-formulations (2.56) with $\chi = 0$,
- the formulation in accordance with OTTOSEN if $\beta_3 = \beta_6 = \eta_6 = 0$, $\eta_3 \in [-1, 1]$,
- the strain criterion (**Table 2.3**) with $\chi = 1$ and the regular triangle $\bar{3}$ with $\beta_3 = \{0, 1\}$ and $\eta_3 = \{1, -1\}$. The NSH follows then with the setting $\xi = 1/3$,
- an alternative formulation of the PISARENKO-LEBEDEV criterion (**Table 2.4**)
  with $\chi \in]0, 1[$, $\beta_3 = \beta_6 = \eta_3 = \eta_6 = 0$, and $\xi = 1/3$,
- the DRUCKER-PRAGER criterion (**Table 2.3**, rotationally symmetric cone) with
  $\chi = 1$ and $\beta_3 = \beta_6 = \eta_6 = 0$, and
- the BURZYŃSKI-TORRE criterion (rotationally symmetric paraboloid) (Balandin,
  1937; Burzyński, 1928; Torre, 1947; Yagn, 1931) with $\beta_3 = \beta_6 = \eta_3 = \eta_6 = 0$,
  $\chi \in]0, 1[$ and $\xi = 1$.

The criterion (2.104) fulfils some plausibility assumptions (Appendix 2.7.8) quite
well and can be recommended for application. The variable cross section approach
according OTTOSEN is different from the fixed cross section approach. Because of
the greater flexibility, the criterion (2.104) provides very good approximations of
experimental data but such criteria require increased numerical effort in the appli-
cation.

Some measurements regarding the change of the cross section as function of
I_1 are given in Launay et al. (1970); Launay and Gachon (1971, 1972). Appro-
ximations are shown in Gol'dman (1994); Fahlbusch (2015); Kolupaev (2018);
Rosendahl et al. (2019b), among others.

2.6 Summary

In this work, a nomenclature of the yield criteria Φ is introduced. The regular poly-
gons of trigonal and hexagonal symmetry in the π-plane are represented schemat-
ically based on the number of their edges and the orientation in the π-plane. The
rotationally symmetric VON MISES criterion is denoted as a circle (Subsect. 2.3.1).

Known plausibility assumptions of the yield and strength criteria are summarized
(Appendix 2.7.8). They limit the variety of the criteria on the basis of applicability.
The relevant assumptions in the authors' opinion are highlighted, which are used for
selection of the recommended criteria (**Table 2.2** and **2.5**, criteria with the equation
number). It is posited, that only the yield criteria involving three or more regular
(basic) geometries (**Table 2.1**) are significant for application. This viewing reduces

the number of the suitable criteria. Further criteria are particular and can be easily approximated with these specified criteria.

The earlier strength criteria are presented in **Tables 2.3** and **2.4**. Some missing criteria are introduced according to the pattern. These criteria are too simple for design with current requirements but the introduced schematics can be primary used as support in didactic.

Nowadays the most effective yield criteria are the criteria of PODGÓRSKI-type with k = 1 and 2 (Subsect. 2.4.2). They meet the plausibility assumptions in the best way known. However, they do not include all relevant yield criteria at once. Thus, their application is associated with restrictions. Two ways for the formulation of the generalized yield criteria are discussed (Subsect. 2.4.3):

- convex combination of the known criteria (Subsects. 2.4.3.1–2.4.3.5) and
- series development as "arccosine of the sum" and "sum of arccosines" (Subsect. 2.4.3.6).

The first schema has proven for practical use. The second way is still being investigated.

Several ways can be envisaged for the linear combinations (Subsect. 2.4.3.1) with the PODGÓRSKI-type shape functions (2.40). The disadvantage of the proposed formulations is that the number of the parameters increases. Both terms in the linear combinations (Subsect. 2.4.3.1) can describe the same geometries: TRESCA and VON MISES criteria in (2.55) and SOKOLOVSKY and VON MISES criteria in (2.56). These criteria are modified according to ALTENBACH-ZOLOCHEVSKY in order to reduce the number of parameters (Subsects. 2.4.3.4 and 2.4.3.5). The resulting C^0-criteria extended with I_1-substitution can be easily applied for fitting of measured data.

Open question remains the formulation of the HAYTHORNTHWAITE and MAC criteria as a function of the stress angles without case discrimination (**Table 2.2**). If such criteria will be derived, the formulations (Subsect. 2.4.3) are no longer required.

The YU strength theory (Subsect. 2.4.4) is of crucial importance for practice. The C^0-generalization without plane intersections (Subsect. 2.4.4.1) provides decisive advantages compared to the original YU's formulation. The C^1-generalization (Subsect. 2.4.4.2) is a powerful tool that includes the YST and is recommended for use.

The yield and strength criteria can be easily compared based on the introduced relations (Subsects. 2.3.2 and 2.3.5). Different approximations can be visualized in the diagrams $r_{60} - r_{30}$ (**Fig. 2.8**) or $r_{30} - r_{15}$ (**Fig. 2.9**), π-plane, and the BURZYŃSKI-plane. Additional requirements can be set for the parameters to reduce their number, e.g. the classical properties (2.39) or, based on the NSH, the position of the node TTT with $\gamma_1 = 1/3$ in order to obtain the special "theories".

The study of the yield and strength criteria remains in focus of professional community (Altenbach, 2010). Further development of the equivalent stress concept can be seen in consideration of the adjusted plausibility assumptions, which should be

accompanied with restriction of the parameters. The number of parameters should be kept to a minimum.

2.7 Appendix

2.7.1 Invariants of Stress Tensor

Stress based criteria Φ for isotropic materials should be invariant with respect to the symmetric second-rank stress tensor $\boldsymbol{\sigma}$ (Życzkowski, 1981). Therefore, the criteria are built up using the invariants of this tensor. As a result of the eigenvalue problem, the principal values (principal stresses) are obtained and denoted by σ_I, σ_{II}, and σ_{III} (Altenbach et al., 1995; Altenbach and Kolupaev, 2014). The following order is assumed

$$\sigma_I \geqslant \sigma_{II} \geqslant \sigma_{III}. \tag{2.106}$$

The invariants of the stress tensor play an important role in the formulation of the equivalent stress expressions (Sect. 2.2). Three stress invariants: the trace (axiator) I_1 of the stress tensor and the invariants I_2', I_3' of the stress deviator as functions of the principal stresses (Życzkowski, 1981; Altenbach et al., 1995; Altenbach and Kolupaev, 2014)

$$I_1 = \sigma_I + \sigma_{II} + \sigma_{III}, \tag{2.107}$$

and

$$
\begin{aligned}
I_2' &= \frac{1}{6}\left[(\sigma_I - \sigma_{II})^2 + (\sigma_{II} - \sigma_{III})^2 + (\sigma_{III} - \sigma_I)^2\right] = \\
&= \frac{1}{2}\left[\left(\sigma_I - \frac{1}{3}I_1\right)^2 + \left(\sigma_{II} - \frac{1}{3}I_1\right)^2 + \left(\sigma_{III} - \frac{1}{3}I_1\right)^2\right],
\end{aligned}
\tag{2.108}
$$

$$
\begin{aligned}
I_3' &= \left(\sigma_I - \frac{1}{3}I_1\right)\left(\sigma_{II} - \frac{1}{3}I_1\right)\left(\sigma_{III} - \frac{1}{3}I_1\right) = \\
&= \frac{1}{3}\left[\left(\sigma_I - \frac{1}{3}I_1\right)^3 + \left(\sigma_{II} - \frac{1}{3}I_1\right)^3 + \left(\sigma_{III} - \frac{1}{3}I_1\right)^3\right]
\end{aligned}
\tag{2.109}
$$

are often used in modeling, see (2.3).

2.7.2 Scalar Functions of Invariants

Scalar functions of the invariants (2.107) - (2.109) are also invariants (Mālmeisters et al., 1977), e. g.

- the scaled axiator I_1 of the stress tensor (De Boer, 2000; Kolupaev, 2018)

$$\xi_1 = I_1/\sqrt{3} \tag{2.110}$$

  describes the coordinate of loading on the hydrostatic axis (**Fig. 2.1**, axis ξ_3),
- the root of the scaled second invariant of the stress deviator

$$\rho_{HW} = \sqrt{2\,I_2'} \tag{2.111}$$

  as radius in the HAIGH-WESTERGAARD coordinates (De Boer, 2000; Kolupaev, 2018),
- the stress angle θ in the π-plane (plane with the cross section $I_1 = \text{const.}$) (Novozhilov, 1951b; Życzkowski, 1981; Chen and Zhang, 1991; Ottosen and Ristinmaa, 2005)

$$\cos 3\theta = \frac{3\sqrt{3}}{2} \frac{I_3'}{\left(I_2'\right)^{3/2}}, \qquad \theta \in \left[0, \frac{\pi}{3}\right], \tag{2.112}$$

  and
- the elevation ψ (Hencky, 1943; Życzkowski, 1981; Altenbach and Kolupaev, 2014)

$$\tan\psi = \frac{\sqrt{3\,I_2'}}{I_1}, \qquad \psi \in [0, \pi] \tag{2.113}$$

  or a stress triaxiality factor (Yagn and Vinogradov, 1954; Davis and Connelly, 1959; Lebedev et al., 1979; Kolupaev, 2006; Lebedev, 2010; Kolupaev, 2018)

$$\eta = \frac{1}{\tan\psi}. \tag{2.114}$$

These invariants (2.110) - (2.113) are sometimes preferred because of the geometric interpretation of the loading in the stress space. Other invariants are given in Altenbach et al. (1995); Altenbach and Kolupaev (2014); Yagn and Vinogradov (1954); Życzkowski (1981) for instance.

2.7.3 Modified Invariants

The radius (2.111) can be also introduced based on the VON MISES hypothesis (von Mises, 1913, 1928) as

$$\rho = \sqrt{3\,I_2'} \tag{2.115}$$

for normalization of the measured data with respect to the appropriate uniaxial tensile limit loading

$$\sigma_{\mathrm{I}} = \sigma_0^{\mathrm{T}}, \qquad \sigma_{\mathrm{II}} = \sigma_{\mathrm{III}} = 0 \tag{2.116}$$

and uniform visualization (Subsects. 2.3.2 and 2.3.5).

The deviatoric invariant I_3' (2.108) can be expressed as a function of ρ and $\cos 3\theta$ (Szwed, 2000, 2013)

$$I_3' = \frac{2}{3\sqrt{3}} \sqrt{\left(I_2'\right)^3} \cos 3\theta = \frac{2}{3^3} \rho^3 \cos 3\theta, \tag{2.117}$$

what is used in Appendix 2.7.7 for deployment of the series of invariants.

With a double-angle function (Bronstein and Semendjajew, 2007) we obtain further invariants (Jemioło and Szwed, 1999; Szwed, 2000, 2013), see also Życzkowski (1981)

$$\cos 6\theta = 2\cos^2 3\theta - 1 = 2\frac{3^3}{2^2}\frac{\left(I_3'\right)^2}{\left(I_2'\right)^3} - 1 \tag{2.118}$$

and

$$\cos 12\theta = 2\cos^2 6\theta - 1 = 2\left(2\cos^2 3\theta - 1\right)^2 - 1 = 2\left(2\frac{3^3}{2^2}\frac{\left(I_3'\right)^2}{\left(I_2'\right)^3} - 1\right)^2 - 1, \tag{2.119}$$

which are used as "building blocks" in the formulation of the phenomenological criteria $\Phi(\rho, \theta)$ (Appendix 2.7.7).

2.7.4 Particular Points on Limit Surface

Particular points on the limit surface Φ can be obtained with the setting of the corresponding elevation ψ (2.113) and the stress angle θ (2.112)

$$\frac{\sqrt{3\,I_2'}}{I_1} = \tan\psi \qquad \text{and} \qquad \frac{3\sqrt{3}}{2}\frac{I_3'}{\left(I_2'\right)^{3/2}} = \cos 3\theta \tag{2.120}$$

normalized with

$$\sqrt{3\,I_2'} = 1.$$

Typical settings follows, among others, with

$$\tan\psi = \infty, \pm\sqrt{3} \pm 1, \pm\frac{1}{\sqrt{3}}, \pm\frac{1}{2}, \pm\left(2 - \sqrt{3}\right), \pm\left(\sqrt{6} - \sqrt{3} + \sqrt{2} - 2\right), \dots$$

for the angle

$$\psi = \frac{\pi}{2}, \pm\frac{\pi}{3}, \pm\frac{\pi}{4}, \pm\frac{\pi}{6}, \pm0.4636, \pm\frac{\pi}{12}, \pm\frac{\pi}{24}, \dots$$

and the meridians (Subsect. 2.3.3), e.g.

$$\theta = 0, \frac{\pi}{12}, \frac{\pi}{6}, \frac{\pi}{4}, \frac{\pi}{3}.$$

For example, we obtain with $I_1 = 0$ and

$$\text{meridian} \quad \theta = 0: \quad \sigma_I = \frac{2}{3} r_0^{Tcc} \sigma_0^T, \quad \sigma_{II} = \sigma_{III} = -\frac{1}{2}\sigma_I,$$

$$\text{meridian} \quad \theta = \frac{\pi}{6}: \quad \sigma_I = -\sigma_{II} = \frac{1}{\sqrt{3}} r_{30}^S \sigma_0^T, \quad \sigma_{III} = 0,$$

$$\text{meridian} \quad \theta = \frac{\pi}{3}: \quad \sigma_I = -\frac{2}{3} r_{60}^{ttC} \sigma_0^T, \quad \sigma_{II} = \sigma_{III} = -\frac{1}{2}\sigma_I.$$

The meridians of VON MISES criterion coincide in the BURZYŃSKI-plane and it follows

$$r_0^{Tcc} = r_{30}^S = r_{60}^{ttC} = 1.$$

The seven points of the plane stress states and the points of the hydrostatic loading are chosen for the analysis and comparison of the limit surfaces (**Table 2.7**). These loading cases have established definition and can be considered as the basic tests (Bulla and Kolupaev, 2021; Kolupaev, 2006, 2018).

2.7.5 Values for Comparison

In the following, details on the stress computation for comparison of geometric properties of the yield criteria Φ are given (Subsects. 2.3.2 and 2.3.5). These normalized stresses of the plane stress state are obtained with the setting

$$3 I_2' = 1 \qquad \text{and} \qquad \sigma_{III} = 0. \tag{2.121}$$

The value r_{15} is obtained setting

$$\cos\left[3\frac{\pi}{12}\right] = \frac{\sqrt{2}}{2}$$

with

$$\sigma_I = \sqrt{\frac{2}{3}}, \qquad \sigma_{II} = -\frac{1}{\sqrt{2}} + \frac{1}{\sqrt{6}}, \tag{2.122}$$

Table 2.7: Basic stress states with the corresponding stress angle θ and the dimensionless invariants η, $\cos 3\theta$, $\cos 6\theta$, $\cos 9\theta$, and $\cos 12\theta$ (Kolupaev, 2018).

Label	CCC	CC	Cc	C	S	T	Tt	TT	TTT
$\dfrac{\sigma_{\mathrm{I}}}{\sigma_0^{\mathrm{T}}}$	$-r^{\mathrm{CCC}}$	$-r_0^{\mathrm{CC}}$	$-\dfrac{2}{\sqrt{3}}r_{30}^{\mathrm{Cc}}$	$-r_{60}^{\mathrm{C}}$	$\dfrac{1}{\sqrt{3}}r_{30}^{\mathrm{S}}$	1	$\dfrac{2}{\sqrt{3}}r_{30}^{\mathrm{Tt}}$	r_{60}^{TT}	r^{TTT}
$\dfrac{\sigma_{\mathrm{II}}}{\sigma_0^{\mathrm{T}}}$	$-r^{\mathrm{CCC}}$	$-r_0^{\mathrm{CC}}$	$-\dfrac{1}{\sqrt{3}}r_{30}^{\mathrm{Cc}}$	0	$-\dfrac{1}{\sqrt{3}}r_{30}^{\mathrm{S}}$	0	$\dfrac{1}{\sqrt{3}}r_{30}^{\mathrm{Tt}}$	r_{60}^{TT}	r^{TTT}
$\dfrac{\sigma_{\mathrm{III}}}{\sigma_0^{\mathrm{T}}}$	$-r^{\mathrm{CCC}}$	0	0	0	0	0	0	0	r^{TTT}
θ	-	0	$\dfrac{\pi}{6}$	$\dfrac{\pi}{3}$	$\dfrac{\pi}{6}$	0	$\dfrac{\pi}{6}$	$\dfrac{\pi}{3}$	-
η	$-\infty$	-2	$-\sqrt{3}$	-1	0	1	$\sqrt{3}$	2	∞
$\cos 3\theta$	-	1	0	-1	0	1	0	-1	-
$\cos 6\theta$	-	1	-1	1	-1	1	-1	1	-
$\cos 9\theta$	-	1	0	-1	0	1	0	-1	-
$\cos 12\theta$	-	1	1	1	1	1	1	1	-

Comments: C - uniaxial compression, Cc - biaxial compression in the stress relation 1:2, CC - equibiaxial compression, CCC - hydrostatic compression, S or TC - shear, T - uniaxial tension, Tt - biaxial tension in the stress relation 1:2, TT - equibiaxial tension, TTT - hydrostatic tension.

$$\sigma_{\mathrm{I}} = -\sqrt{\frac{2}{3}}, \qquad \sigma_{\mathrm{II}} = -\sqrt{\frac{2}{3}+\frac{1}{\sqrt{3}}} \tag{2.123}$$

or

$$\sigma_{\mathrm{I}} = \sqrt{\frac{2}{3}+\frac{1}{\sqrt{3}}}, \qquad \sigma_{\mathrm{II}} = \sqrt{\frac{2}{3}-\frac{1}{\sqrt{3}}}. \tag{2.124}$$

The value r_{30} is obtained setting

$$\cos\left[3\,\frac{\pi}{6}\right] = 0 \qquad \text{and} \qquad \sigma_{\mathrm{I}} = -\sigma_{\mathrm{II}}$$

with

$$\sigma_{\mathrm{I}} = \frac{1}{\sqrt{3}}. \tag{2.125}$$

The value r_{45} is obtained setting

$$\cos\left[3\,\frac{\pi}{4}\right] = -\frac{\sqrt{2}}{2}$$

with

$$\sigma_{\mathrm{I}} = \sqrt{\frac{2}{3}}, \qquad \sigma_{\mathrm{II}} = \frac{1}{\sqrt{2}}+\frac{1}{\sqrt{6}} \tag{2.126}$$

or

$$\sigma_I = \pm\sqrt{\frac{2}{3}}, \qquad \sigma_{II} = \sqrt{\frac{2}{3} \pm \frac{1}{\sqrt{3}}}. \qquad (2.127)$$

The value r_{60} is obtained setting

$$\cos\left[3\frac{\pi}{3}\right] = -1 \qquad \text{and} \qquad \sigma_{II} = 0$$

with

$$\sigma_I = -1. \qquad (2.128)$$

The value $r_{7.5}$ is obtained setting (Weisstein, 2021)

$$\cos\left[3\frac{\pi}{24}\right] = \frac{1}{2}\sqrt{2+\sqrt{2}}$$

with

$$\sigma_I = \pm\sqrt{\frac{1}{3}\left(2+\sqrt{2}\right)}, \qquad \sigma_{II} = \pm\sqrt{\frac{1}{3}\left(2\mp\sqrt{2\pm\sqrt{3}}\right)} \qquad (2.129)$$

or

$$\sigma_I = -\sqrt{\frac{1}{3}\left(2-\sqrt{2+\sqrt{3}}\right)}, \qquad \sigma_{II} = \sqrt{\frac{1}{3}\left(2+\sqrt{2-\sqrt{3}}\right)}. \qquad (2.130)$$

And the value $r_{22.5}$ is obtained setting (Weisstein, 2021)

$$\cos\left[3\frac{\pi}{8}\right] = \frac{1}{2}\sqrt{2-\sqrt{2}}$$

with

$$\sigma_I = \pm\sqrt{\frac{1}{3}\left(2-\sqrt{2}\right)}, \qquad \sigma_{II} = \sqrt{\frac{1}{3}\left(2\pm\sqrt{2\pm\sqrt{3}}\right)} \qquad (2.131)$$

or

$$\sigma_I = -\sqrt{\frac{1}{3}\left(2+\sqrt{2+\sqrt{3}}\right)}, \qquad \sigma_{II} = -\sqrt{\frac{1}{3}\left(2-\sqrt{2-\sqrt{3}}\right)}. \qquad (2.132)$$

Further values of the plane stress state (Sect. 2.3.5)

$$r_{30}^S, \quad r_{30}^{Tt}, \quad r_{60}^{TT}, \quad r_{60}^C, \quad r_{30}^{Cc}, \quad \text{and} \quad r_0^{CC}$$

for pressure-sensitive criteria are given in Rosendahl et al. (2019b). The values for hydrostatic tensile limit loading (Subsect. 2.3.5) is

$$r^{TTT} = \frac{\sigma^{TTT}}{\sigma_0^T} = \frac{1}{3\gamma_1}$$

and hydrostatic compressive limit loading is

$$r^{CCC} = \frac{\sigma^{CCC}}{\sigma_0^T} = -\frac{1}{3\gamma_2},$$

which follow with $3I_2' = 0$. Accordingly, $\cos 3\theta$ (2.112) is indeterminate in these two points.

2.7.6 Modified Normal Stress Hypothesis

Based on the PODGORSKI criterion (2.44) with (2.45), we obtain a conical (pyramidal at the border of the parameter η_3) criterion with the linear I_1-substitution (2.15)

$$\sqrt{3I_2'} \frac{\Omega_3(\theta, 0, \eta_3)}{\Omega_3(0, 0, \eta_3)} = \frac{\sigma_{eq} - \gamma_1 I_1}{1 - \gamma_1} \qquad \text{with} \qquad \gamma_1 \in [0, 1[, \qquad \eta_3 \in [-1, 1]$$

(2.133)

or resolved with respect of the equivalent stress σ_{eq}

$$\sigma_{eq} = \sqrt{3I_2'} \frac{\cos\left[-\frac{1}{3}\arccos[\eta_3 \cos 3\theta]\right]}{\cos\left[-\frac{1}{3}\arccos[\eta_3]\right]} (1 - \gamma_1) + \gamma_1 I_1.$$

(2.134)

This criterion is named the SAYIR cone $\hat{3} - \bigcirc - \bar{3} \to I_1$ (Kolupaev, 2018). The maximum normal stress hypothesis (NSH) follows with the setting

$$\gamma_1 = \frac{1}{3} \qquad \text{and} \qquad \eta_3 = 1$$

or after substitution (Chen and Zhang, 1991; Kolupaev, 2018; Rosendahl et al., 2019b)

$$\sigma_{NSH} = \frac{1}{3}\left(I_1 + 2\sqrt{3I_2'}\cos\theta\right)$$

(2.135)

which results in the most important properties of the NSH (**Fig. 2.22**, **Table 2.8**)

$$r_{60}^C \to \infty, \qquad v_+^{in} = 0, \qquad r_{30}^S = \sqrt{3}, \qquad r_{60}^{TT} = r^{TTT} = 1.$$

Restrictive is that the derivation at the corners of the surface Φ is discontinuous (Lagioia and Panteghini, 2016). These corners in the π-plane can be "rounded off" with the parameter $\eta_3 \in [0.99, 1[$ depending on the required computation accuracy (**Fig. 2.22**, **Table 2.8**).
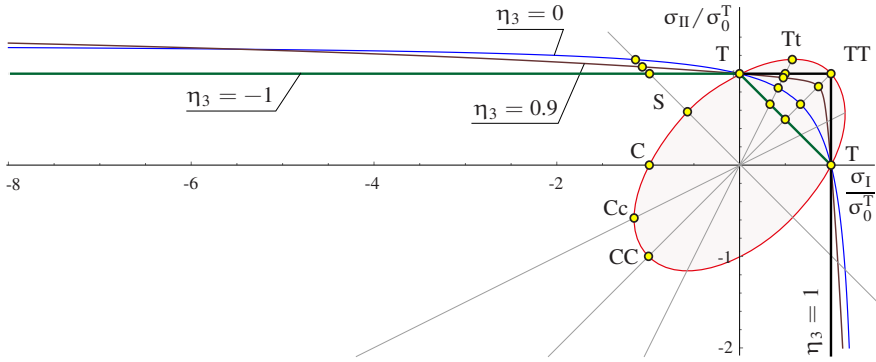
Fig. 2.22: Modified normal stress hypothesis (2.134) as function of the parameter η_3 (2.138) in the normalized $\sigma_I - \sigma_{II}$ diagram. The ellipse of the VON MISES criterion (red line) and the NSH (thick black line) are shown for comparison.

Table 2.8: Settings of the parameter $\eta_3 \in [-1, 1]$ and corresponding values for the modified normal stress hypothesis (2.134) with the property $r_{60}^C \to \infty$ (2.138).

η_3	γ_1	v_+^{in}	r_{30}^S	r_{30}^{Tt}	r_{60}^{TT}	r^{TTT}	π-plane
1	1/3	0	$\sqrt{3}$	$\sqrt{3}/2$	1	1	$\bar{3}$
0.999999	0.3335	-0.0003	1.7325	0.8659	0.9995	0.9995	-
0.99999	0.3339	-0.0009	1.7335	0.8657	0.9982	0.9982	-
0.9999	0.3351	-0.0027	1.7368	0.8648	0.9946	0.9946	-
0.999	0.3390	-0.0085	1.7468	0.8623	0.9832	0.9832	-
0.99	0.3510	-0.0265	1.7773	0.8542	0.9496	0.9496	-
0.9	0.3870	-0.0804	1.8623	0.8284	0.8614	0.8614	-
0	1/2	-1/4	2	$\sqrt{3}-1$	2/3	2/3	○
-1	2/3	-1/2	$\sqrt{3}$	$1/\sqrt{3}$	1/2	1/2	$\hat{3}$

The value r_{60}^C for the criterion (2.134) can be computed as

$$r_{60}^C = 1 \left/ \left[(1-\gamma_1) \cos\left[\frac{1}{3}\arccos[-\eta_3]\right] \sec\left[\frac{1}{3}\arccos[\eta_3]\right] - \gamma_1 \right] \right. \qquad (2.136)$$

and the property $r_{60}^C \to \infty$ follows with the denominator

$$(1-\gamma_1) \cos\left[\frac{1}{3}\arccos[-\eta_3]\right] \sec\left[\frac{1}{3}\arccos[\eta_3]\right] - \gamma_1 = 0. \qquad (2.137)$$

The parameter $\gamma_1(\eta_3)$ results in

$$\gamma_1(\eta_3) = 1 \Big/ \left[1 + \cos\left[\frac{1}{3}\arccos[\eta_3]\right] \sec\left[\frac{1}{3}\arccos[-\eta_3]\right] \right]. \qquad (2.138)$$

This means that the $\pi/3$-meridian is parallel to the straight line $I_1 = -\sqrt{3\,I_2'}$ in the BURZYŃSKI-plane (Kolupaev, 2018). Inserted Eq. (2.138) in Eq. (2.134) results in the values of the modified normal stress hypothesis (C^1-NSH):

$$r_{30}^S = \frac{2}{\sqrt{3}\,(1-\gamma_1)} \cos\left[\frac{1}{3}\arccos[\eta_3]\right] \qquad (2.139)$$

or

$$r_{30}^S = \frac{2}{\sqrt{3}} \left[\cos\left[\frac{1}{3}\arccos[-\eta_3]\right] + \cos\left[\frac{1}{3}\arccos[\eta_3]\right] \right], \qquad (2.140)$$

$$r_{30}^{Tt} = \frac{2}{\sqrt{3}\left[2\gamma_1 + (1-\gamma_1)\sec\left[\frac{1}{3}\arccos[\eta_3]\right] \right]} \qquad (2.141)$$

or

$$r_{30}^{Tt} = 2\sqrt{3}\,\frac{\cos\left[\frac{1}{3}\arccos[-\eta_3]\right] + \cos\left[\frac{1}{3}\arccos[\eta_3]\right]}{3 + 6\cos\left[\frac{1}{3}\arccos[-\eta_3]\right]}, \qquad (2.142)$$

$$r_{60}^{TT} = \frac{1}{3\gamma_1}, \qquad (2.143)$$

and the inelastic POISSON's ratio at tension follows with

$$\nu_+^{in} = \frac{1}{2}\,(1 - 3\gamma_1). \qquad (2.144)$$

This formulation (2.134) with (2.138) is used to derive a C^1-continuous strength criterion according to YST (Subsect. 2.4.4).

The C^1-continuous normal stress hypothesis (C^1-NSH) can be applied in the whole range of the parameter $\eta_3 \in [-1, 1]$ for better approximation of measured data (**Table 2.8**). Although the property $r_{60}^C \to \infty$ is retained (**Fig. 2.22**), physical background of the normal stress hypothesis is then lost.

2.7.7 Series of Invariants

The general structure of the yield criterion Φ is unknown and can not be deduce based on theoretical considerations (Subsect. 2.4.3). It is known that the criteria Φ are functions of the stress invariants (Subsect. 2.2.2), which can be grouped into the number of series. One of possibilities is to construct the deviatoric series of the same powers of the radius ρ (2.115) and increasing powers of $\cos 3\theta$.

The complete deviatoric series S_n'

$$S_n' = \rho^n \left(b_n + c_{n1} \cos 3\theta + c_{n2} \cos^2 3\theta + \ldots \right), \qquad n \in \mathbb{N} \tag{2.145}$$

contains several parameters b_n and c_{ni}, which should be restricted based on the theoretical considerations and later fitted to the test data. The terms with fractional exponents (Chen and Han, 1993)

$$(I_3')^{1/3}, \qquad (I_3')^{2/3}, \qquad (I_3')^{4/3}, \qquad \text{etc.}$$

or, what is the same,

$$\rho \, (\cos 3\theta)^{1/3}, \qquad \rho^2 \, (\cos 3\theta)^{2/3}, \qquad \rho^4 \, (\cos 3\theta)^{4/3}, \qquad \text{etc.}$$

are excluded from these series because they lead to non-convex surfaces, see Altenbach et al. (1995); Gol'denblat and Kopnov (1968, 1971b); Spitzig et al. (1975); Spitzig and Richmond (1979) and cf. Desai (1980); Desai and Faruque (1984b,a); Jemioło (1992); Wojewódzki et al. (1995).

The applicability of the complete series (2.145) in a criterion is controversial because of the large number of parameters. The method is sought for restriction of this number in order to formulate the effective criteria according to the plausibility assumptions (Appendix 2.7.8).

We obtain the reduced deviatoric series if only the invariants ρ (2.115), I_3' in the form $\rho^3 \cos 3\theta$ (2.117), and their products of the same power n of ρ are taken:

$$S_1' = b_1 \rho,$$

$$S_2' = b_2 \rho^2,$$

$$S_3' = (b_3 + c_3 \cos 3\theta) \, \rho^3,$$

$$S_4' = (b_4 + d_{13} \cos 3\theta) \, \rho^4,$$

$$S_5' = (b_5 + d_{23} \cos 3\theta) \, \rho^5,$$

$$S_6' = (b_6 + d_{33} \cos 3\theta + c_6 \cos^2 3\theta) \, \rho^6,$$

$$S_7' = (b_7 + d_{43} \cos 3\theta + d_{16} \cos^2 3\theta) \, \rho^7, \tag{2.146}$$

$$S_8' = (b_8 + d_{53} \cos 3\theta + d_{26} \cos^2 3\theta) \, \rho^8,$$

$$S_9' = (b_9 + d_{63} \cos 3\theta + d_{36} \cos^2 3\theta + c_9 \cos^3 3\theta) \, \rho^9,$$

$$S_{10}' = (b_{10} + d_{91} \cos 3\theta + d_{46} \cos^2 3\theta + d_{19} \cos^3 3\theta) \, \rho^{10},$$

$$S_{11}' = (b_{11} + d_{83} \cos 3\theta + d_{56} \cos^2 3\theta + d_{29} \cos^3 3\theta) \, \rho^{11},$$

$$S_{12}' = (b_{12} + d_{93} \cos 3\theta + d_{66} \cos^2 3\theta + d_{39} \cos^3 3\theta + c_{12} \cos^4 3\theta) \, \rho^{12},$$

$$\ldots$$

The parameters b_n weight the invariant ρ and the parameters c_n weight the invariant $\rho^3 \cos 3\theta$ of the appropriate powers n. The parameter d_{kl} weights the product of the invariants $(\rho)^k$ and $(\rho^3 \cos 3\theta)^l$ of the powers $n = k + l$.

The terms $b_n \rho^n$ with odd powers and the terms with the parameters d_{kl} for odd k are often neglected in the modeling. The reason for this lies in the structure of the polynomial criteria formulated as the intersection of three, six, nine, or twelve planes in the principal stress space. Such formulations contain only terms with ρ^2, $\rho^3 \cos 3\theta$ or, what the same, positive integer powers of the invariants I_2' and I_3' (2.117) and their products (Kolupaev, 2018). The rational deviatoric series follows with

$$S_2' = b_2 \rho^2,$$

$$S_3' = c_3 \cos 3\theta \, \rho^3,$$

$$S_4' = b_4 \rho^4,$$

$$S_5' = d_{23} \cos 3\theta \, \rho^5,$$

$$S_6' = (b_6 + c_6 \cos^2 3\theta) \, \rho^6,$$

$$S_7' = d_{43} \cos 3\theta \, \rho^7,$$

$$S_8' = (b_8 + d_{26} \cos^2 3\theta) \, \rho^8,$$

$$S_9' = d_{63} \cos 3\theta + c_9 \cos^3 3\theta) \, \rho^9,$$

$$S_{10}' = (b_{10} + d_{46} \cos^2 3\theta) \, \rho^{10},$$

$$S_{11}' = (d_{83} \cos 3\theta + d_{29} \cos^3 3\theta) \, \rho^{11},$$

$$S_{12}' = (b_{12} + d_{66} \cos^2 3\theta + c_{12} \cos^4 3\theta) \, \rho^{12},$$

$$\dots$$

(2.147)

The highest art in the formulation of the phenomenological yield criteria Φ is to select the appropriate terms S_i', which are relevant for the considered material behavior. As this is hardly possible, various formulations are tried out and tested for the fulfillment of the plausibility assumptions (Appendix 2.7.8). The relevant formulations are obtained with:

- cosine ansatz criterion (Altenbach and Kolupaev, 2009; Kolupaev, 2018; Kolupaev and Altenbach, 2010)
- quadratic, bi-, tri-, and sextaquadratic equations (Kolupaev, 2018), and
- cubic (2.47), bicubic (2.53), tri- and quadracubic equations (Sect. 2.4.2),

which are the explicit functions of σ_{eq} (2.12). Further formulation possibilities are shown in Subsect. 2.4.3.6.

2.7.8 Plausibility Assumptions

Several requirements on the yield and strength criteria Φ (Sect. 2.2) were pronounced in the past, which can be interpreted as plausibility assumptions. These requirements are not mandatory but the quality of the criteria may be assessed considering the plausibility assumptions, which are formally separated in physical, mathematical, geometric, and "subjective" assumptions (Tables **2.9**-**2.12**). Their relevance is shown in the authors' opinion.

Two assumptions PM14 and PS1 are in contradiction with the known statements. PM14 is immediately justified when an elasticity theory of higher order is considered and the number of parameters increases. Contradiction to PS1 comes from the past as lack of tools was vindicated by lack of necessity.

The desires PS14 and PS15 disagree with the idea of the phenomenology. In engineering methods the microstricture is homogenized. There are no physical principles, e.g. balance equations in Continuum Mechanics (Altenbach, 2018), underlying such a formulation. The criteria should only not contradict the physical principles.

PS18 is problematic because the term "failure mode of isotropic material" is in progress, see (Cuntze and Freund, 2004; Cuntze, 2006, 2013, 2021). If the polynomial criteria Φ (2.3) of power three or greater in the stress are considered, different failure modes can be set in the "global fitting" and the additional parameters can be interpreted as "interaction parameters". Furthermore, the mastery of convexity in the criteria of the failure mode concept is not clear.

Table 2.9: Physical plausibility assumptions.

Label	Content	References	Relevance
PP1	possess only one root for any given radial load path	Bower and Koedam (1997); Torre (1947); Wu (1973)	✓
PP2	nonintersecting of limit surfaces in dependence of the parameters	Brandt et al. (1986); Gol'denblat and Kopnov (1968), Gol'denblat and Kopnov (1971a)	✓
PP3	single surface in principal stress space without any additional outer contours and plane intersections	Lagioia et al. (2016); Rosendahl (2020); Rosendahl et al. (2019b); Wu (1973); Wu and Scheublein (1974)	✓
PP4	restriction of hydrostatic tensile stress	Balandin (1937); Filonenko-Boroditsch (1961) Gol'denblat and Kopnov (1971a); Kolupaev (2018); Skrzypek (1993)	✓
PP5	limit condition in any stress states	Brandt et al. (1986)	
PP6	time and temperature should be explicitly taken into account	Brandt et al. (1986); Gol'denblat and Kopnov (1968), Lüpfert (1994); Pisarenko and Lebedev (1976)	
PP7	consideration of stress gradients	Gol'denblat and Kopnov (1968); Pisarenko and Lebedev (1976)	
PP8	criteria for isotropic materials should be the consequence of the criteria for anisotropic materials	Banabic et al. (2000); Bazhanov et al. (1970); Christensen (2013) Cuntze and Freund (2004); Cuntze (2013); Habraken (2004) Labossière and Neale (1987); Mittelstedt and Becker (2016) Mittelstedt (2021); Wilczynski (1992); Wu (1973)	
PP9	formulation in the stress and strain space	Wilczynski (1992); Rosendahl et al. (2019a); Wu (1973)	

Table 2.10: Mathematical plausibility assumptions.

Label	Content	References	Relevance
PM1	explicit solvability of the criterion w.r.t. the equivalent stress σ_{eq}	Kolupaev (2018); Rosendahl et al. (2019b)	✓
PM3	homogeneous function of stresses	Kolupaev (2018)	
PM4	dependence of the criterion on all three invariants	Altenbach and Kolupaev (2014); Gol'denblat and Kopnov (1971a) Lagioia et al. (2016); Lebedev (2010); Kolupaev (2018)	
PM5	maximum power of the stress n in the equation with the polynomial formulations not higher than 12	Altenbach and Kolupaev (2014); Kolupaev (2018)	
PM6	separate definition of the meridional and deviatoric sections	Lagioia et al. (2016)	
PM7	invariants I_1 and I_3' in odd and even powers	Brandt et al. (1986); Gol'denblat and Kopnov (1968), Gol'denblat and Kopnov (1971a); Kolupaev (2018)	
PM8	reality of the limit state of stress (reality of the root of Φ)	Gol'denblat and Kopnov (1971a)	✓
PM9	no case discrimination	Rosendahl et al. (2019b)	
PM10	unique assignment of the limit surface to parameters of the criterion	Rosendahl et al. (2019b)	
PM11	restrictions imposed on the inelastic POISSON's ratio at tension ν_+^{in} and compression ν_-^{in} even for the strength criteria	Altenbach et al. (2014); Kolupaev (2018)	
PM12	provision of an explicit expression for the equivalent stress σ_{eq}	Rosendahl (2020)	
PM13	parameter restrictions as $[0, 1]$ or $[-1, 1]$	-	
PM14	no analogies with the linear elasticity theory regards the amount of parameters	Christensen (2013); Cuntze (1999); Cuntze and Freund (2004) Cuntze (2013)	
PM15	statistical nature of the modeled process	Lebedev (2010); Pisarenko and Lebedev (1969, 1976), Lebedev et al. (1979)	
PM16	numerically robust in the application	Mittelstedt and Becker (2016)	

Table 2.11: Geometric plausibility assumptions.

Label	Content	References	Relevance
PG1	clear geometric background	Balandin (1937); Lebedev et al. (1979); Kolupaev (2018); Pisarenko and Lebedev (1969, 1976)	
PG2	smooth surface	Gol'denblat and Kopnov (1971a); Lebedev (2010); Labossière and Neale (1987); Wu (1973)	
PG3	convexity, convexity restrictions for yield and strength criteria	Brandt et al. (1986); Franklin (1971); Wu (1973); Murzewski and Mendera (1963); Torre (1950a)	
PG3.1	C^1-continuous differential criteria	Balandin (1937); Murzewski and Mendera (1963); Puck (1996); Rosendahl (2020); Torre (1947)	
PG3.2	C^2-continuous differential criteria	Lagioia et al. (2016); Torre (1949); Zhang et al. (2021)	
PG4	convexity in the meridional plane	Kolupaev (2018)	
PG5	C^1 continuous differentiability of the criterion in the π-plane except at the border of the convexity limits	Altenbach and Kolupaev (2014); Abbo and Sloan (1995); Rosendahl et al. (2019b)	
PG6	convex restrictions in the parameter space	Kolupaev (2018)	
PG7	continuous differentiable change of the cross section of the surface in the π-plane as function of the invariant I_1	Altenbach and Kolupaev (2014); Kolupaev (2018)	
PG8	wide range of possible convex shapes in the π-plane	Altenbach and Kolupaev (2014); Rosendahl et al. (2019b)	
PG9	wide range of possible convex shapes in the meridian cross section	Rosendahl et al. (2019b)	
PG10	no singularity at the apex	Altenbach and Kolupaev (2014); Abbo and Sloan (1995), Franklin (1971); Kolupaev (2018); Lagioia et al. (2016), Theocaris (1995); Zhang et al. (2021)	
PG11	classical strength hypotheses, reduction to known criteria in limit cases	Altenbach and Kolupaev (2014); Brandt et al. (1986) Gol'denblat and Kopnov (1968); Kolupaev (2018) Rosendahl (2020); Wilczynski (1992)	✓
PG12	the surface cannot contain the zero point of the origin	Torre (1950a)	

Table 2.12: Subjective plausibility assumptions (application requirements).

Label	Content	References	Relevance
PS1	maximum generality	Brandt et al. (1986); Ponomarev et al. (1957); Rosendahl (2020)	
PS2	reliability and trustworthiness of predictions	Balandin (1937); Burzyński (2008); Pisarenko and Lebedev (1969)	
PS3	simple and confident application	Burzyński (2008); Pisarenko and Lebedev (1969); Sendeckyj (1972)	
PS5	easy to understand for mechanical engineers	Habraken (2004); Mittelstedt and Becker (2016); Ponomarev et al. (1957)	
PS6	easy to implement in FE-code	Banabic et al. (2000); Barlat et al. (1991); Habraken (2004)	
PS7	minimum number of parameters	Boehler and Delafin (1982); Burzyński (2008); Murzewski and Mendera (1963)	
PS8	independence and uniqueness of the parameters	Rosendahl et al. (2019b); Rosendahl (2020)	
PS9	dimensionless parameters	Asteris (2013); Altenbach and Kolupaev (2014); Kolupaev (2018)	
PS10	easy parameter identification	Habraken (2004); Balandin (1937); Collins (1993); Hashin (1980)	
PS11	elegance in the formulation	Christensen (2013); Cohen et al. (2009); Puck (1996); Yoshimine et al. (2004)	
PS12	geometrical meaning of the parameters	Kolupaev (2018)	
PS13	derivation (origin) of the formula	Christensen (2013)	
PS14	reference to the microstructure	Pisarenko and Lebedev (1976)	
PS15	physical background	Lebedev et al. (1979); Ponomarev et al. (1957); Puck (1996)	✓
PS16	clear advantages in the application	–	
PS17	clear parameter restriction	–	
PS18	reference to the failure mode	Christensen (2013); Cuntze et al. (1997); Cuntze (1999, 2021)	
PS19	parameters as material properties	Christensen (2013)	
PS20	mechanical sense of the single terms	Burzyński (2008)	
PS21	meaning of behavior resulting from approximation	Kirkpatrick (1954)	

References

Abbo AJ, Sloan SW (1995) A smooth hyperbolic approximation to the Mohr-Coulomb yield criterion. Computers & Structures 54(3):427–441

Altenbach H (2001) A generalized limit criterion with application to strength, yielding, and damage of isotropic materials. In: Lemaitre J (ed) Handbook of Materials Behaviour Models. Academic Press, San Diego, pp 175–186

Altenbach H (2010) Strength hypotheses - a never ending story. Czasopismo Techniczne Mechanika (Technical Transactions Mechanics) Wydawnictwo Politechniki Krakowskiej 107(20):5–15

Altenbach H (2018) Continuum Mechanics: Introduction to Material-independend and Material-dependend Equations (in German: Kontinuumsmechanik: Einführung in die material-unabhängigen und materialabhängigen Gleichungen), 4th edn. Springer, Vieweg, Berlin, Heidelberg

Altenbach H, Kolupaev VA (2009) Fundamental forms of strength hypotheses. In: Indeitcev DA, Krivtsov AM (eds) Proc. of XXXVI Summer School Advanced Problems in Mechanics, Institute for Problems in Mechanical Engineering RAS, St. Petersburg, pp 32–45

Altenbach H, Kolupaev VA (2014) Classical and non-classical failure criteria. In: Altenbach H, Sadowski T (eds) Failure and Damage Analysis of Advanced Materials, Springer, Wien, Heidelberg, Int. Centre for Mechanical Sciences CISM, Courses and Lectures Vol. 560, pp 1–66

Altenbach H, Naumenko K (1997) Creep bending of thin-walled shells and plates by consideration of finite deflections. Computational Mechanics 19(6):490–495

Altenbach H, Naumenko K (2002) Shear correction factors in creep-damage analysis of beams, plates and shells. JSME Int J Series A Solid Mechanics and Material Engineering, The Japan Society of Mechanical Engineers 45(1):77–83

Altenbach H, Altenbach J, Zolochevsky A (1995) Advanced Deformation Models and Failure Criteria in Material Mechanics (in German: Erweiterte Deformationsmodelle und Versagens-kriterien der Werkstoffmechanik). Deutscher Verlag für Grundstoffindustrie, Stuttgart

Altenbach H, Kolarow G, Morachkovsky O, Naumenko K (2000) On the accuracy of creep-damage predictions in thinwalled structures using the finite element method. Computational Mechanics 25(1):87–98

Altenbach H, Bolchoun A, Kolupaev VA (2014) Phenomenological yield and failure criteria. In: Altenbach H, Öchsner A (eds) Plasticity of Pressure-Sensitive Materials, Springer, Berlin Heidelberg, Engineering Materials, pp 49–152

de Araújo FC (1962) Elasticidade e Plasticidade. Imprensa Portuguesa, Porto

Asteris PG (2013) Unified yield surface for the nonlinear analysis of brittle anisotropic materials. Science Letters A Mathematics, Physics and Mechanics 4(2):46–56

Backhaus G (1983) Deformationsgesetze. Akademie-Verlag, Berlin

Balandin PP (1937) On the strength hypotheses (in Russ.: K voprosu o gipotezakh prochnosti). Vestnik inzhenerov i tekhnikov 1:19–24

Banabic D, Bunge HJ, Pöhlandt K, Tekkaya AE (2000) Formability of Metallic Materials: Plastic Anisotropy, Formability Testing, Forming Limits. Springer, Berlin

Barlat F, Lege DJ, Brem JC (1991) A six-component yield function for anisotropic materials. Int J of Plasticity 7(7):693–712

Bazhanov VL, Gol'denblat II, Kopnov VA, Pospelov AD, Sinjukov AM (1970) Plates and Shells Made of Fiberglass Plastics (In Russ. Plastinki o obolochki iz stekloplastikov). Visshaja Shkola, Moscow

Benvenuto E (1991) An Introduction to the History of Structural Mechanics. Springer, New York

Bertram A (2012) Elasticity and Plasticity of Large Deformations. Springer, Berlin

Betten J (1976) Plastische Anisotropie und Bauschinger-Effekt; allgemeine Formulierung und Vergleich mit experimentell ermittelten Fließortkurven. Acta Mechanica 25(1-2):79–94

Betten J (1979) Über die Konvexität von Fließkörpern isotroper und anisotroper Stoffe. Acta Mech 32:233–247

Betten J (2001) Kontinuumsmechanik. Springer, Berlin

Bigoni D, Piccolroaz A (2003) A new yield function for geomaterials. In: Viggiani C (ed) Constitutive Modeling and Analysis of Boundary Value Problems in Geotechnical Engineering, Hevelius Edizioni, Benevento, Italy, pp 266–281

Bigoni D, Piccolroaz A (2004) Yield criteria for quasibrittle and frictional materials. Int J of Solids and Structures 41(11):2855–2878

Billington EW (1986) Introduction to the Mechanics and Physics of Solids. Adam Hilger Ltd., Bristol

Birger IA (1977) On a criterion for fracture and plasticity (in Russ.: Ob odnom kriterii razrushenija i plastichnosti). Mekhanika tverdogo tela, Izvestija Akademii Nauk SSSR 9(4):143–150

Bishop AW (1966) The strength of soils as engineering materials. Geotechnique 16(2):91–130

Boehler JP, Delafin M (1982) Failure criteria for unidirectional fiber-reinforced composites under confining pressure. In: Boehler JP (ed) Mechanical Behavior of Anisotropic Solids / Nr. 295 – Comportment Méchanique des Solides Anisotropes, Proceedings of the Euromech Colloquium 115, Villard-de-Lans, June 19–22, 1979, Springer, pp 449–470

Bolchoun A, Kolupaev VA, Altenbach H (2011) Convex and non-convex flow surfaces (in German: Konvexe und nichtkonvexe Fließflächen). Forschung im Ingenieurwesen 75(2):73–92

Botkin AI (1940a) Equilibrium of granular and brittle materials (in Russ.: O ravnovesii sypuchikh i khrupkikh materialov). Transactions of the Scientific Research Institute of Hydrotechnics, Izvestija NIIG, Leningrad 28:189–211

Botkin AI (1940b) Theories of elastic failure of gramelar and of brittle materials (in Russ.: O prochnosti sypuchikh i khrupkikh materialov). Transactions of the Scientific Research Institute of Hydrotechnics, Izvestija NIIG, Leningrad 26:205–236

Bouvet C, Calloch S, Lexcellent C (2002) Mechanical behavior of a Cu-Al-Be shape memory alloy under multiaxial proportional and nonproportional loadings. J Engng Materials and Technology 124(2):112–124

Bouvet C, Calloch S, Lexcellent C (2004) A phenomenological model for pseudoelasticity of shape memory alloys under multiaxial proportional and nonproportional loadings. European J of Mechanics-A/Solids 23(1):37–61

Bower MV, Koedam DH (1997) Tensor polynomial failure criterion: Coefficient limits based on convexity requirements. J of Reinforced Plastics and Composites 16(5):435–477

Brandt AM, Dzieniszewski W, Jendo S, Marks W, Owczarek S, Wasiutyński Z (1986) Criteria and Methods of Structural Optimization. Martinus Nijhoff Publishers, PWN - Polish Scientific Publishers, Dordrecht, Warszawa

Bronstein IN, Semendjajew KA (2007) Handbook of Mathematics. Springer, Berlin

Bulla M, Kolupaev VA (2021) Stress analysis in design with plastics: Accessible method with huge impact. Kautschuk, Gummi Kunststoffe KGK, Hüthig GmbH 74(6):60–67

Burzyński W (1928) Study on Material Effort Hypotheses, (in Polish: Studjum nad Hipotezami Wytężenia). Akademia Nauk Technicznych, Lwów

Burzyński W (2008) Theoretical foundations of the hypotheses of material effort, Wlodzimierz Burzyński (1900-1970), Czasopismo Techniczne (1929) 47, 1–41, Lwów, (in Polish: Teoretyczne podstawy hipotez wytężenia). Engineering Transactions, Polish Academy of Sciences 56 (Special Issue):9–45

Candland CT (1975) Implications of macroscopic failure criteria which are independent of hydrostatic stress. Int J of Fracture 11(3):540–543

Capurso M (1967) Yield conditions for incompressible isotropic and orthotropic materials with different yield stress in tension and compression. Meccanica 2(2):118–125

Chen WF, Han DJ (1993) Failure criteria for concrete materials. In: Boehler JP (ed) Failure Criteria of Structured Media, Balkema, Rotterdam, pp 375–384

Chen WF, Zhang H (1991) Structural Plasticity - Theory, Problems, and CAE Software. Springer, New York

Christensen R (2019) Failure criteria for fiber composite materials, the astonishing sixty year search, definitive usable results. Composites Science and Technology 182:107,718

Christensen RM (2013) The Theory of Materials Failure. University Press, Oxford

Cicala P (1961) Presentazione geometrica delle relazioni fondamentali d'elastoplasticità. Giornale del Genio Civile 99:125–137

Cohen T, Masri R, Durban D (2009) Analysis of circular hole expansion with generalized yield criteria. Int J of Solids and Structures 46(20):3643–3650

Collins JA (1993) Failure of Materials in Mechanical Design: Analysis, Prediction, Prevention. Wiley, New York

Coulomb CA (1776) Essai sur une application des regles des maximis et minimis a quelques problemes de statique relatifs, a la architecture. Mem Acad Roy Div Sav 7:343–387

Cuntze R, Deska R, Szelinski B, Jeltsch-Fricker R, Meckbach S, Huybrechts D, Kopp J, Kroll L, Gollwitzer S, Rackwitz R (1997) Neue Bruchkriterien und Festigkeitsnachweise für unidirektionalen Faserkunststoffverbund unter mehrachsiger Beanspruchung: Modellbildung und Experimente, BMBF-Förderkennzeichen: 03N8002, Abschlussbericht Nr. 506. 5: Grund- und Werkstoffe, VDI-Verlag, Düsseldorf

Cuntze RG (1999) The Failure Mode Concept - A new comprehensive 3D-strength analysis concept for any brittle and ductile behaving material. In: Europ. Conf. on Spacecraft Structures, Materials and Mechan. Testing, ESTEC, Noordwijk, no. ESA SP-428 in ESA-CNES-DLR-DGLR, pp 269–287

Cuntze RG (2006) Failure conditions for isotropic materials, unidirectional composites, woven fabrics-their visualization and links. In: Busse G, Kröplin B (eds) Conf. on Damage in Composite Materials CDCM, 18th-19th of September 2006, Stuttgart

Cuntze RG (2013) Strength failure conditions of isotropic materials. Industrieausschuss Strukturberechnungsunterlagen (IASB), HSB Handbuch Struktur Berechnung 51101-01-730C, Augsburg

Cuntze RG (2021) Failure Mode Concept (FMC) and Strength Mechanics Building: A Physical and Theoretical Material Symmetry. Manuscript, Augsburg

Cuntze RG, Freund A (2004) The predictive capability of failure mode concept-based strength criteria for multidirectional laminates. Composites Science and Technology 64(3):343–377

Davis EA, Connelly FM (1959) Stress distribution and plastic deformation in rotating cylinders of strainhardening material. Transactions of the ASME, J of Applied Mechanics 26:25–30

De Boer R (2000) Theory of Porous Media: Highlights in Historical Development and Current State. Springer, Berlin

Desai CS (1980) A general basis for yield, failure and potential functions in plasticity. Int J for Numerical and Analytical Methods in Geomechanics 4(4):361–375

Desai CS, Faruque MO (1984a) A generalized basis for modelling plastic behavior of materials. In: Desai CS, Gallagher RH (eds) Mechanics of Engineering Materials, Wiley, Chichester, pp 211–230

Desai CS, Faruque O (1984b) Constitutive model for (geological) materials. J of Engineering Mechanics 110(9):1391–1408

Drass M (2020) Constitutive Modelling and Failure Prediction for Silicone Adhesives in Façade Design, Diss., FB 13 Bauingenieurwesen, Technical University of Darmstadt, Mechanik, Werkstoffe und Konstruktion im Bauwesen, vol 55. Springer Vieweg, Wiesbaden

Drucker DC (1953) Limit analysis of two and three dimensional soil mechanics problems. J of the Mechanics and Physics of Solids 1(4):217–226

Drucker DC (1957) A definition of stable inelastic material. Techn. Report No. 2 AD143756, Nonr-562(20)/2, Division of Engineering, Brown University, Providence, Rhode Island

Drucker DC (1959) A definition of stable inelastic material. J of Applied Mechanics, Transactions of the ASME 26(1):101–106

Drucker DC, Prager W (1952) Soil mechanics and plastic analysis or limit design. Quarterly of Appl Mathematics 10:157–165

Dyson BF, McLean M (2001) Micromechanism-quantification for creep constitutive equations. In: Murakami S, Ohno N (eds) IUTAM Symposium on Creep in Structures, Kluwer, Dordrecht, pp 3–16

Fahlbusch NC (2015) Entwicklung und Analyse mikromechanischer Modelle zur Beschreibung des Effektivverhaltens von geschlossenzelligen Polymerschäumen. Diss., Fachbereich Maschinenbau der Technischen Universität Darmstadt

Fahlbusch NC, Kolupaev VA, Becker W (2016) Generalized limit surfaces – with an example of hard foams. In: Naumenko K, Aßmus M (eds) Advanced Methods of Continuum Mechanics for Materials and Structures, Springer Science + Business Media, Singapore, Advanced Structured Materials, vol 60, pp 337–365

Feodosjev VI (1975) Ten Lecture-conversations on Strength of Materials (in Russ.: Desjat' lekzij-besed po soprotivleniju materialov). Nauka, Moscow

Filonenko-Boroditsch MM (1961) Mechanical Theories of Strength (in Russ.: Mechanicheskie teorii prochnosti). Izdatel'stvo Moskovskogo Universiteta MGU, Moscow

Finnie I, Heller WR (1959) Creep of Engineering Materials. McGraw-Hill, New York

Föppl A, Föppl L (1920) Drang und Zwang: Eine höhere Festigkeitslehre für Ingenieure. R. Oldenbourg, München

Franklin JA (1971) Triaxial strength of rock materials. Rock Mechanics 3(2):86–98

Fromm H (1931) Grenzen des elastischen Verhaltens beanspruchter Stoffe. In: Auerbach F, Hort W (eds) Statik und Dynamik elastischer Körper nebst Anwendungsgebieten. II. Teil. Zum Gebrauch für Ingenieure, Physiker und Mathematiker, vol 4, Barth-Verlag, Leipzig, pp 359–435

Giraldo-Londoño O, Paulino GH (2020) A unified approach for topology optimization with local stress constraints considering various failure criteria: von Mises, Drucker-Prager, Tresca, Mohr-Coulomb, Bresler-Pister and Willam-Warnke. Proceedings of the Royal Society A 476(2238):20190,861

Gol'denblat II, Kopnov VA (1968) Yield and Strength Criteria for Structural Materials (in Russ.: Kriterii prochnosti i plastichnosti konstrukzionnych materialov). Mashinostroenie, Moscow

Gol'denblat II, Kopnov VA (1971a) General criteria of the strength of isotropic media. Polymer Mechanics 7(2):251–261

Gol'denblat II, Kopnov VA (1971b) General theory of criteria of strength for isotropic and anisotropic materials. Strength of Materials 3(2):184–188

Gol'dman AY (1994) Prediction of the Deformation Properties of Polymeric and Composite Materials. ACS Professional Reference Book, American Chemical Society, Washington

Gurson AL (1977) Continuum theory of ductile rupture by void nucleation and growth: Part I - yield criteria and flow rules for porous ductile media. J of Engineering Materials and Technology 99(1):2–15

Habraken AM (2004) Modelling the plastic anisotropy of metals. Archives of Computational Methods in Engineering 11(1):3–96

Haigh BP (1920) The strain-energy function and the elastic limit. Engineering 109:158–160

Hashin Z (1980) Failure criteria for unidirectional fiber composites. J of Applied Mechanics pp 329–334

Hayhurst DR (1972) Creep rupture under multi-axial states of stress. J of the Mechanics and Physics of Solids 20(6):381–390

Haythornthwaite RM (1961a) The range of the yield condition in stable, ideally plastic solids. Technical report, ORA Project 04403, University of Michigan, College of Engineering, Department of Engineering Mechanics, Detroit

Haythornthwaite RM (1961b) Range of yield condition in ideal plasticity. Proc ASCE J Eng Mech Division EM6 87:117–133

Haythornthwaite RM (1962) Range of yield condition in ideal plasticity. Transactions ASCE 127(1):1252–1269

Haythornthwaite RM (1983) Piecewise linear yield criteria in invariant form. J of Engineering Mechanics 109(4):1016–1022

Hencky H (1924) Zur Theorie plastischer Deformationen und der hierdurch im Material hervorgerufenen Nachspannungen. ZAMM 4(4):323–334

Hencky H (1943) Ermüdung, Bruch, Plastizität. Stahlbau 16(23/24):95–97

Hershey AV (1954) The plasticity of an isotropic aggregate of anisotropic face-centered cubic crystals. J of Applied Mechanics 21(3):241–249

Hill R (1950) LXVI. On the inhomogeneous deformation of a plastic lamina in a compression test. The London, Edinburgh, and Dublin Philosophical Magazine and J of Science, Series 7 41(319):733–744

Hosford WF (1972) A generalized isotropic yield criterion. Transactions of the ASME, J of Applied Mechanics 39(June):607–609

Hosford WF (1979) On yield loci of anisotropic cubic metals. In: 7th North American Metalworking Research, SME, Proc. NAMRC, Dearborn, 7, pp 191–196

Huber MT (1904) Specific strain work as a measure of material effort (in Polish: Właściwa praca odkształcenia jako miara wytężenia materyału). Czasopismo Techniczne, Lwów, Organ Towarzystwa Politechnicznego we Lwowie 22:34–40, 49–50, 61–62, 80–81

Ishlinsky AY (1940) Hypothesis of strength of shape change (in Russ.: Gipoteza prochnosti formoizmeneniya). Uchebnye Zapiski Moskovskogo Universiteta, Mekhanika 46:104–114

Ishlinsky AY, Ivlev DD (2003) Mathematical Theory of Plasticity (in Russ.: Matematicheskaya teoriya plastichnosti). Fizmatlit, Moscow

Ismar H, Mahrenholtz O (1982) Über Beanspruchungshypothesen für metallische Werkstoffe. Konstruktion 34:305–310

Ivlev DD (1959) The theory of fracture of solids (in Russ.: K teorii razrushenija tverdykh tel). J of Applied Mathematics and Mechanics 23(3):884–895

Ivlev DD (1960) On extremum properties of plasticity conditions (in Russ.: Ob ekstremal'nykh svojstvakh uslovij plastichnosti). J of Applied Mathematics and Mechanics 24(5):1439–1446

Jemioło S (1992) Rational formulation of yield conditions for isotropic materials, (in Polish: O racjonalnym formułowaniu warunków plastyczności dla materiału izotropowego). Prace Naukowe Politechniki Warszawskiej, Budownictwo 120:51–62

Jemioło S, Szwed A (1999) Application of convex isotropic functions in failure theory for isotropic materials: Yield criteria for metals, (in Polish: O zastosowaniu funkcji wypukłych w teorii wytężenia materiałów izotropowych: Propozycja warunków plastyczności metali). Prace Naukowe Politechniki Warszawskiej, Budownictwo 133:5–52

Jirásek M, Bažant ZP (2002) Inelastic Analysis of Structures. Wiley, London and New York

Karafillis AP, Boyce MC (1993) A general anisotropic yield criterion using bounds and a transformation weighting tensor. J of the Mechanics and Physics of Solids 41(12):1859–1886

Kirkpatrick WM (1954) The behaviour of sands under three dimensional stress systems. PhD thesis, Department of Civil and Mechanical Engineering at the Royal Technical College, University of Glasgow

Ko WL (1963) Application of the finite elastic theory to the behavior of rubber-like materials. PhD thesis, California Institute of Technology, Pasadena

Koca M, Koca NO (2011) Quasi regular polygons and their duals with Coxeter symmetries D_n represented by complex numbers. In: J. of Physics: Conference Series, Group 28: Physical and Mathematical Aspects of Symmetry, IOP Publishing, vol 284, pp 1–10

Kolupaev VA (2006) 3D-Creep Behaviour of Parts Made of Non-Reinforced Thermoplastics (in German: Dreidimensionales Kriechverhalten von Bauteilen aus unverstärkten Thermoplasten). Diss., Martin-Luther-Universität Halle-Wittenberg, Halle-Saale

Kolupaev VA (2017) Generalized strength criteria as functions of the stress angle. J of Eng Mechanics 143(9):04.017.095

Kolupaev VA (2018) Equivalent Stress Concept for Limit State Analysis. Springer, Cham

Kolupaev VA, Altenbach H (2010) Considerations on the Unified Strength Theory due to Mao-Hong Yu (in German: Einige Überlegungen zur Unified Strength Theory von Mao-Hong Yu). Forschung im Ingenieurwesen 74(3):135–166

Kolupaev VA, Bolchoun A, Altenbach H (2009) Unified representation and evaluation of the strength hypotheses. In: Elboujdaini M, Tyson B, Patnaik P (eds) 12th Int. Conference on Fracture ICF 12, 10 p., National Research Council Canada, Ottawa

Kolupaev VA, Bolchoun A, Altenbach H (2013a) Yield criteria for incompressible materials in the shear stress space. In: Öchsner A, Altenbach H (eds) Experimental and Numerical Investigation of Advanced Materials and Structures, Springer, pp 107–119

Kolupaev VA, Yu MH, Altenbach H (2013b) Visualisation of the Unified Strength Theory. Archive of Applied Mechanics 83(7):1061–1085

Kolupaev VA, Yu MH, Altenbach H (2013c) Yield criteria of hexagonal symmetry in the π-plane. Acta Mechanica 224(7):1527–1540

Kolupaev VA, Becker W, Massow H, Dierkes D (2014) Design of test specimens from hard foams for the investigation of biaxial tensile strength (in German: Auslegung von Probekörpern aus Hartschaum zur Ermittlung der biaxialen Zugfestigkeit). Forschung im Ingenieurwesen 78(3-4):69–86

Kolupaev VA, Yu MH, Altenbach H (2016) Fitting of the strength hypotheses. Acta Mechanica 227(6):1533–1556

Kolupaev VA, Yu MH, Altenbach H, Bolchoun A (2018) Comparison of strength criteria based on the measurements on concrete. J of Eng Mechanics (ASCE) 144(6)

Koval'chuk BI (1981) Criterion for the limiting state of some hull steels under combined strain at room and elevated temperatures. Strength of Materials 13(5):548–554

Kowalewski ZL, Hayhurst DR, Dyson BF (1994) Mechanisms-based creep constitutive equations for an aluminium alloy. J of Strain Analysis for Engineering Design 29(4):309–316

Kroon M, Faleskog J (2013) Numerical implementation of a J_2- and J_3-dependent plasticity model based on a spectral decomposition of the stress deviator. Computational Mechanics 52(5):1059–1070

Labossière P, Neale KW (1987) Macroscopic failure criteria for fiber-reinforced composite materials. Solid Mechanics Archives, 439–450 12(2):65–95

Lagioia R, Panteghini A (2016) On the existence of a unique class of yield and failure criteria comprising Tresca, von Mises, Drucker-Prager, Mohr-Coulomb, Galileo-Rankine, Matsuoka-Nakai and Lade-Duncan. Proceedings of the Royal Society of London, Series A 472:20150713(2185):1–21

Lagioia R, Panteghini A, Puzrin AM (2016) The I_3 generalization of the Galileo-Rankine tension criterion. Proceedings of the Royal Society A: Mathematical, Physical and Engineering Sciences 470:20140568(2172):1–23

Lagzdin' A (1997) Smooth convex limit surfaces in the space of symmetric second-rank tensors. Mechanics of Composite Materials 33(2):119–127

Lagzdin' AZ, Tamuzh VP (1971) Construction of a phenomenological theory of the fracture of an anisotropic medium (in Russ.: K postroeniju fenomenologicheskoj teorii razrushenija anizotropnoj sredy). Mekhanika Polimerov 7(4):563–571

Lagzdinš A, Zilaucs A (1996) Constructing convex limit surfaces in material mechanics. Mechanics of Composite Materials 32(3):233–241

Launay P, Gachon H (1971) Strain and ultimate strength of concrete under triaxial stress. In: Proceedings of the First Int. Conference on Structural Mechanics in Reactor Technology, Berlin, September 20-24, 1971. Commission of the European Communities, Brussels (EUR-4820), Vol. 3, paper Hl/3, pp 23–40

Launay P, Gachon H (1972) Strain and ultimate strength of concrete under triaxial stress, Paper SP 34-13. In: Kesler CE (ed) Concrete for Nuclear Reactors, Bundesanstalt für Materialprüfung in Berlin, Oct. 5-9, 1970, ACI Publication SP-34, American Concrete Institute, Detroit, pp 269–282

Launay P, Gachon H, Poitevin P (1970) Déformation et résistance ultime du béton sous étreinte triaxiale. Annales de l'institut Technique du Batiment et de Travaux Publics, Série: Essais et Mesures (123) 269(5):21–48

Lebedev AA (1965) Generalized criterion for the fatigue strength (in Russ.: Obobshhennyj kriterij dlitel'noj prochnosti). In: Thermal Strength of Materials and Structure Elements (in Russ.: Termoprochnost' materialov i konstrukcionnykh elementov), vol 3, Naukova Dumka, Kiev, pp 69–76

Lebedev AA (2010) Development of the theories of strength in the mechanics of materials. Strength of Materials 42(5):578–592

Lebedev AA, Koval'chuk BI, Lamashevsky VP, Giginjak FF (1979) Computation of Complex Stress State: Determining of Equivalent Stresses. Akademija Nauk Ukrainskoj SSR, Institut Problem Prochnosti, Kiew

Leckie FA, Hayhurst DR (1977) Constitutive equations for creep rupture. Acta Metallurgica 25(9):1059–1070

Lemaitre J, Chaboche JL (1985) Mécanique des Matériaux Solides. Dunod, Paris

Lemaitre J, Chaboche JL (1990) Mechanics of Solid Materials. Cambridge University Press, Cambridge

Lequeu PH, Gilormini P, Montheillet F, Bacroix B, Jonas JJ (1987) Yield surfaces for textured polycrystals. Acta Metall 35(2):439–451, 1159–1174

Lexcellent C (2018) Linear and Non-linear Mechanical Behavior of Solid Materials. Springer, Cham

Lexcellent C, Boubakar ML, Bouvet C, Calloch S (2006) About modelling the shape memory alloy behaviour based on the phase transformation surface identification under proportional loading and anisothermal conditions. Int J of Solids and Structures 43(3-4):613–626

Lüpfert HP (1994) Beurteilung der statischen Festigkeit und Dauerfestigkeit metallischer Werkstoffe bei mehrachsiger Beanspruchung. Dt. Verl. für Grundstoffindustrie, Leipzig

Mālmeisters A, Tamužs V, Teters G (1977) Mechanik der Polymerwerkstoffe. Akademie-Verlag, Berlin

Mariotte E (1718) Traité du Mouvement des Eaux et des Autres Corps Fluides. J. Jambert, Paris

Marti P (1980) Zur plastischen Berechnung von Stahlbeton, Institut für Baustatik und Konstruktion, vol 104. Birkhäuser, Basel, Diss. ETH Zürich

Matsuoka H, Nakai T (1985) Relationship among Tresca, Mises, Mohr-Coulomb and Matsuoka-Nakai failure criteria. Soils and Foundations 25(4):123–128

Mirolyubov IN (1953) On the generalization of the strengt theory based on the octaedral stresses in the case of brittle materials (in Russ.: K voprosu ob obobshhenii teorii prochnosti oktaedricheskikh kasatelnykh naprjazhenij na khrupkie materialy). Trudy Leningradskogo Technologicheskogo Instituta pp 42–52

von Mises R (1913) Mechanik des festen Körpers im plastischen deformablen Zustand. Nachrichten der Königlichen Gesellschaft der Wissenschaften Göttingen, Mathematisch-physikalische Klasse pp 582–592

von Mises R (1928) Mechanik der plastischen Formänderung von Kristallen. J of Applied Mathematics and Mechanics, ZAMM 8:161–185

Mittelstedt C (2021) Structural Mechanics in Lightweight Engineering. Springer, Cham

Mittelstedt C, Becker W (2016) Strukturmechanik ebener Laminate. Studienbereich Mechanik, Technische Universität Datmstadt, Lasertype GmbH, Darmstadt

Modarres-Motlagh A (1997) Lower bound to collapse load for structures. PhD thesis, School of Mechanical and Manufacturing Engineering, Faculty of Engineering, University of New South Wales UNSW

Mohr O (1900a) Welche Umstände bedingen die Elastizitätsgrenze und den Bruch eines Materials. Zeitschrift des VDI 45:1524–1530

Mohr O (1900b) Welche Umstände bedingen die Elastizitätsgrenze und den Bruch eines Materials. Zeitschrift des VDI 46:1572–1577

Mohr O (1914) Abhandlungen aus dem Gebiete der technischen Mechanik. Wilhelm & Sohn, Berlin

Murzewski J (1957) Une theorie statistique du corps fragile quasihomogene. In: IXe Congrès International de Mécanique Appliquée, ICAM-1956, Université de Bruxelles, vol 5, pp 313–320

Murzewski J (1960) A probabilistic theory of plastic and brittle behaviour of quasi-homogeneous materials. Archiwum Mechaniki Stosowanej 3(12):203–227

Murzewski J, Mendera Z (1963) Yield surface of steel determined by semi-empirical method. Bulletin de L'Academie Polonaise des Sciences, Serie des Sciences Techniques XI(7):35–42

Naumenko K, Altenbach H, Kutschke A (2011) A combined model for hardening, softening, and damage processes in advanced heat resistant steels at elevated temperature. Int J of Damage Mechanics 20(4):578–597

Novozhilov VV (1951a) On the connection between stresses and strains in a nonlinear-elastic continuum (in Russ.: O svjazi mezhdu naprjazhenijami i deformazijami v nelinejno-uprugoj srede). Prikladnaja Matematika i Mekhanika XV(2):183–194

Novozhilov VV (1951b) On the principles of the statical analysis of the experimental results for isotropic materials (in Russ.: O prinzipakh obrabotki rezultatov staticheskikh ispytanij izotropnykh materialov). Prikladnaja Matematika i Mekhanika XV(6):709–722

Nye JF (1985) Physical Properties of Cristals: Their Representation by Tensors and Matrices. Oxford University Press, Oxford

Othman AM, Dyson BF, Hayhurst DR, Lin J (1994) Continuum damage mechanics modelling of circumferentially notched tension bars undergoing tertiary creep with physically-based constitutive equations. Acta Metallurgica et Materialia 42(3):597 – 611

Ottosen NS (1975) Failure and elasticity of concrete. Report Risø-M-1801, Danish Atomic Energy Commission, Research Establishment Risö, Engineering Department, Roskilde

Ottosen NS (1977) A failure criterion for concrete. J of the Engineering Mechanics Division 103(4):527–535

Ottosen NS (1980) Nonlinear finite element analysis of concrete structures. Tech. rep., Forskningscenter Risoe. Risoe-R, No. 411, Roskilde: Risø National Laboratory

Ottosen NS, Ristinmaa M (2005) The Mechanics of Constitutive Modeling. Elsevier Science, London

Owen DRJ, Hinton E (1986) Finite Elements in Plasticity, Theory and Practice. Pineridge Press Limited, Swansea

Paul B (1968a) Generalized pyramidal fracture and yield criteria. Int J of Solids and Structures 4(2):175–196

Paul B (1968b) Macroscopic plastic flow and brittle fracture. In: Liebowitz H (ed) Fracture: An Advanced Treatise, vol II, Academic Press, New York, pp 313–496

Pisarenko GS, Lebedev AA (1969) Deformation and Fracture of Materials under Combined Stress (in Russ.: Soprotivlenie materialov deformirovaniju i razrusheniju pri slozhnom naprjazhennom sostojanii). Naukowa Dumka, Kiev

Pisarenko GS, Lebedev AA (1976) Deformation and Strength of Materials under Complex Stress State (in Russ.: Deformirovanie i prochnost' materialov pri slozhnom naprjazhennom sostojanii). Naukowa Dumka, Kiev

Podgórski J (1983) Ogólny warunek stanu granicznego dla materiałów izotropowych. Prace IPPT PAN, IFTR Reports, Instytut Podstawowych Problemów Techniki Polskiej Akademii Nauk 17:4–21

Podgórski J (1984) Limit state condition and the dissipation function for isotropic materials. Archives of Mechanics 36(3):323–342

Podgórski J (1985) General failure criterion for isotropic media. J of Engineering Mechanics 111(2):188–201

Podgórski J (1986) Critical states in bodies with internal friction, (in Polish: Stany krytyczne w ciałach z tarciem wewnętrznym). Praca doktorska, Prace IPPT, IFTR Reports, Instytut Podstawowych Problemów Techniki Polskiej Akademii Nauk, 25, Warszawa

Ponomarev SD, Biderman VL, Likharev KK, Makushin VM, Malinin NN, Feodosjev VI (1957) Strength Analysis in Mechanical Engineering (in Russ.: Raschety na prochnost' v mashinostroenii), vol 1. Gosudarstvennoe nauchno-technicheskoe izdatel'stvo mashinostroitel'noj literatury, Moskow

Potapova LB, Yarzev VP (2005) Mechanics of Materials under Complex Stress State. How Predict the Limit Stresses? (in Russ.: Mekhanika materialov pri slozhnom naprjazhennom sostojanii. Kak prognozirujut predel'nye naprjazhenija?). Mashinostroenie-1, Moscow

Prager W (1956) A new methods of analyzing stresses and strains in work hardening plastic solids. J of Applied Mechanics (ASME) 23:493–496

Prager W, Hodge P (1954) Theorie ideal plastischer Körper. Springer, Wien

Puck A (1996) Festigkeitsanalyse von Faser-Matrix-Laminaten: Modelle für die Praxis. Hanser, München

Rankine WJM (1876) Manual of Applied Mechanics. Griffin, London

Reuss A (1933) Vereinfachte Beschreibung der plastischen Formänderungsgeschwindigkeiten bei Voraussetzung der Schubspannungsfließbedingung. ZAMM 13(5):356–360

Rosendahl PL (2020) From bulk to structural failure: Fracture of hyperelastic materials. Diss., Fachgebiet Strukturmechanik, Technische Universität Darmstadt

Rosendahl PL, Drass M, Felger J, Schneider J, Becker W (2019a) Equivalent strain failure criterion for multiaxially loaded incompressible hyperelastic elastomers. Int J of Solids and Structures 166:32–46

Rosendahl PL, Kolupaev VA, Altenbach H (2019b) Extreme yield figures for universal strength criteria. In: Altenbach H, Öchsner A (eds) State of the Art and Future Trends in Material Modeling, Advanced Structured Materials, Springer Nature, Cham, 100, pp 259–324

de Saint-Venant AJCB (1871) Theorie du mouvement non permanent des eaux, avec application aux crues des rivieres et a l'introduction de marees dans leurs lits. Comptes Rendus des Séances de L'Académie des Sciences 73:237–240

Sandel GD (1919) Ueber die Festigkeitsbedingungen: Ein Beitrag zur Lösung der Frage der zulässigen Anstrengung der Konstruktionsmaterialen. Diss., Technische Hochschule zu Stuttgart

Sandel GD (1925) Über die Festigkeitsbedingungen: Ein Beitrag zur Lösung der Frage der zulässigen Anstrengung der Konstruktionsmaterialen. Jänecke, Leipzig

Sawczuk A (1982) Introduction to Mechanics of Plastic Structures (in Polish: Wprowadzenie do mechaniki konstrukcji plastycznych). Panstwowe Wydawnictwo Naukowe PWN, Warszawa

Sayir M (1970) Zur Fließbedingung der Plastizitätstheorie. Ingenieur-Archiv 39(6):414–432

Sayir M, Ziegler H (1969) Der Verträglichkeitssatz der Plastizitätstheorie und seine Anwendung auf räumlich unstetige Felder. Zeitschrift für angewandte Mathematik und Physik ZAMP 20(1):78–93

Schmidt R (1932) Über den Zusammenhang von Spannungen und Formänderungen im Verfestigungsgebiet. Ingenieur-Archiv 3(3):215–235

Sdobyrev VP (1959) Criterion for the long term strength of some heat-resistant alloys at a multiaxial loading (in Russ.: Kriterij dlitelnoj prochnosti dlja nekotorykh zharoprochnykh splavov pri slozhnom naprjazhennom sostojanii). Izvestija Akademii Nauk SSSR, Otdelenie Tekhnicheskikh Nauk, Mekhanika i Mashinostroenie 1(6):93–99

Sendeckyj GP (1972) A brief survey of empirical multiaxial strength criteria for composites. In: Corten HT (ed) Composite Materials: Testing and Design (Second Conference), ASTM STP 497, ASTM International, Philadelphia, pp 41–51

Shanley FR (1957) Strength of Materials. McGraw-Hill, New York

Shesterikov SA (1960) On the theory of ideal plastic solid (in Russ.: K postroeniju teorii ideal'no plastichnogo tela). Prikladnaja Matematika i Mekhanika, Otdelenie Tekhnicheskikh Nauk Akademii Nauk Sojusa SSR, Russian Academy of Science 24(3):412–415

Skrzypek JJ (1993) Plasticity and Creep: Theory, Examples and Problems. CRC Press, Boca Raton

Spitzig W, Sober R, Richmond O (1975) Pressure dependence of yielding and associated volume expansion in tempered martensite. Acta Metallurgica 23(7):885–893

Spitzig WA, Richmond O (1979) Effect of hydrostatic pressure on the deformation behavior of polyethylene and polycarbonate in tension and in compression. Polymer Engineering & Science 19(16):1129–1139

Stassi-D'Alia F (1967) Flow and fracture of materials according to a new limiting condition of yelding. Meccanica 2(3):178–195

Szwed A (2000) Strength hypotheses and constitutive relations of materials including degradation effects, (in Polish: Hipotezy wytężeniowe i relacje konstytutywne materiałów z uwzględnieniem efektów degradacji). Praca doctorska, Wydział Inżynierii Lądowej Politechniki Warszawskiej, Warszawa

Szwed A (2010) General strength criterion for incompressible materials. In: Szcześniak WE, Zbiciak A (eds) Theoretical Foundations of Civil Engineering : Polish-Ukraïnian-Lithuanian Transactions, Oficyna Wydawnicza Politechniki Warszawskiej, Warsaw, 18, pp 313–318

Szwed A (2013) Construction of the deviatoric shape function for the cross-sections of the limit surfaces, (in Polish: Konstrukcja funkcji kształtu przekrojów dewiatorowych powierzchni

granicznych). In: Jemioło S, Szwed A (eds) Seria Monografie Zakładu Wytrzymałości Materiałów, Teorii Sprężystości i Plastyczności ZWMTSiP, Deformacje i Wytrzymałość Materiałów i Elementów Konstrukcji, Wydział Inżynierii Lądowej Politechniki Warszawskiej, Warszawa, 3, pp 51–66

Takeda T, Kikuchi S, Nasu Y (1986) Experimental evaluation of yield condition containing third invariant of deviatoric stresses. In: Proceedings of the Thirtieth Japan Congress on Materials Research, Society of Materials Science, Japan, Kyoto, pp 13–18

Tan JJ (1990) Unified form of yield criteria for metallic materials. Chinese Science Bulletin 35(7):555–557

Theocaris PS (1995) Failure criteria for isotropic bodies revisited. Eng Fracture Mechanics 51(2):239–264

Timoshenko SP (1953) History of Strength of Materials: With a Brief Account of the History of Theory of Elasticity and Theory of Structure. McGraw-Hill, New York

Torre C (1947) Einfluß der mittleren Hauptnormalspannung auf die Fließ- und Bruchgrenze. Österreichisches Ingenieur-Archiv I(4/5):316–342

Torre C (1949) Die Grenzzustände statisch beanspruchter Stoffe. Schweizer Archiv für angewandte Wissenschaft und Technik pp 116–121, 145–158

Torre C (1950a) Die Mechanik der Grenzbeanspruchungen. Österreichisches Ingenieur-Archiv IV(1):93–108

Torre C (1950b) Grenzbedingung für spröden Bruch und plastisches Verhalten bildsamer Metalle. Österreichisches Ingenieur-Archiv IV(2):174–189

Tóth LF (1964) Regular Figures. Pergamon Press, Oxford

Tresca H (1868) Mémoire sur l'ecoulement des corps solides. Mémoires Pres par Div Savants 18:733–799

Troost A, Betten J (1974) Zur Frage der Konvexität von Fließbedingungen bei plastischer Inkompressibilität und Kompressibilität. Mechanics Research Communications 1:73–78

Trunin II (1965) Failure criteria under creep conditions in multiaxial stress state (in Russ.: Kriterii prochnosti v usloviyakh polzuchesti pri slozhnom napryazhennom sostoyanii). Prikl Mekhanika 1(7):77–83

Tschoegl NW (1971) Failure surfaces in principial stress space. J of Polymer Science, Part C - Polymer Symposium 32:239–267

Voigt W (1901) Zur Festigkeitslehre. Annalen der Physik, Leipzig 309(3):567–591

Weisstein EW (2021) Trigonometry Angles – Pi/8. https://mathworld.wolfram.com/ TrigonometryAnglesPi8.html

Westergaard HM (1920) On the resitance of ductile materials to combined stress in two or three directions perpendicular to one another. J of the Franklin Institute 189:627–640

Wilczynski AP (1992) Some relationships and limitations of tensorial polynomials strength theories. Composites Science and Technology 44(3):209–213

Wojewódzki W, Jemioło S, Lewiński P, Szwed A (1995) On constitutive relationships modelling the mechanical properties of concrete (in Polish: O relacjach konstytutywnych modelujących własności mechaniczne betonu). Prace Naukowe Politechniki Warszawskiej, Budownictwo 128:1–150

Wronski AS, Pick M (1977) Pyramidal yield criteria for epoxides. J of Materials Science 12(1):28–34

Wu EM (1973) Phenomenological anisotropic failure criterion. In: Broutman LJ, Krock RH, Sendeckyi GP (eds) Treatise on Composite Materials, Academic Press, New York, vol 2, pp 353–431

Wu EM, Scheublein JK (1974) Laminate strength - a direct characterization procedure. In: Berg CA, McGarry FJ, Elliott SY (eds) Composite Materials: Testing and Design (Third Conference), ASTM International, Special Technical Publication 546, Philadelphia

Xiaoping V, Ottosen NS, Thelandersson S, Nielsen MP (1989) Review of constructive models for concrete, EUR 12394 EN. Final Report Ispra, Reactor Safety Programme 1985-1987, Commission of the European Communities, Nuclear Science and Technology, Contract No. 3301-87-12 ELISPDK, Luxembourg

Xu P, Sun Z, Shao S, Fang L (2021) Comparative analysis of common strength criteria of soil materials. Materials 14(15):4302

Yagn YI (1931) New methods of strength prediction (in Russ.: Novye metody pascheta na prochnost'). Vestnik inzhenerov i tekhnikov 6:237–244

Yagn YI (1933) Strength of Materials: Theory and Problems (in Russ.: Soprotivlenie materialov: teorja i zadachnik). Kubuch, Leningrad

Yagn YI, Vinogradov IN (1954) Influence of the shape of the stress deviator upon the strength of metals at plastic deformations (in Russ.: Vlijanie vida deviatora naprjazhenij na soprotivlenie metallov plasticheskomy deformierovaniju). Doklady Akademii Nauk SSSR (Moskva) 96(3):515–517

Yoshimine M, Yu MH, He LN, Iwatate T (2004) The beauty of strength criteria. In: Kleibner M, Legocki A (eds) Int. Symposium on Developments in Plasticity and Fracture, Centenary of M. T. Huber Criterion, August 12–14, 2004, Cracow, Poland, p 1

Yu MH (1961) General behaviour of isotropic yield function (in Chinese). Scientific and Technological Research Paper of Xi'an Jiaotong University pp 1–11

Yu MH (1999) Engineering Strength Theory (in Chinese). Higher Education Press, Beijing

Yu MH (2002) Advances in strength theories for materials under complex stress state in the 20th century. Applied Mechanics Reviews 55(5):169–218

Yu MH (2004) Unified Strength Theory and its Applications. Springer, Berlin

Yu MH (2017) Unified strength theory (UST). In: Feng XT (ed) Rock Mechanics and Engineering, Volume 1: Principles, CRC Press, Balkema, Leiden, pp 425–452

Yu MH (2018) Unified Strength Theory and its Applications. Springer, Singapore

Yu MH, Yu SQ (2019) Introduction to Unified Strength Theory. CRC Press/Balkema, London

Zhang J, Zhang ZX, Huang CP (2011) Representation based classification of strength theories of concrete. In: Advanced Materials Research, vol 168, pp 74–77

Zhang N, Li X, Wang D (2021) Smoothed classic yield function for C2 continuities in tensile cutoff, compressive cap, and deviatoric sections. Int J of Geomechanics 21(3):04021,005

Życzkowski M (1981) Combined Loadings in the Theory of Plasticity. PWN-Polish Scientific Publ., Warszawa

Chapter 3
Model Order Reduction: The Bridge Between Structural Mechanics and System Simulation

Michael Beitelschmidt and Claudius Lein

Abstract System simulation using the multibody systems method is a standard procedure for the design of machines, plants and vehicles. It can be used to investigate large movements including the behavior of drives and control. Often, individual bodies have to be modeled elastically because relevant elastic deformations already occurs in the frequency range under investigation. The state of the art is the "Floating Frame of Reference" method, in which the motion of a body is divided into a rigid-body motion and small, superimposed, linear-elastic deformations. Elastic bodies are usually discretized using the finite element method, sometimes producing very large models. For the integration of such models into the MBS, a model order reduction must be performed beforehand. This typically consists of a sequence of steps: After a model preparation the actual reduction follows. Several different methods therefore have been developed in the last years. Subsequently, the quality of the reduced model can be estimated by correlation methods. Finally, the data is converted for import into the MBS tool. For this purpose, the software tool MOR-PACK was developed at the Chair of Dynamics and Mechanism Design at the TU Dresden. MORPACK can perform all steps of the model order reduction and outputs models that can be directly imported into MBS tools. In addition to numerous MOR algorithms, various correlation methods are also stored in the software, ensuring the greatest possible automation and standardization for the EMBS user.

Key words: Multi-body system simulation, Elastic bodies, Model order reduction

Michael Beitelschmidt
Institute of Solid Mechanics, Technische Universität Dresden, Marschnerstraße 30, 01307 Dresden, Germany,
e-mail: michael.beitelschmidt@tu-dresden.de

Claudius Lein
86899 Landsberg am Lech, Germany,
e-mail: clein@gmx.de

3.1 Introduction

Simulation has become an indispensable part of modern product development. Predicting the dynamic behavior of components, assemblies or entire systems before building prototypes can save considerable costs in development and significantly accelerate development processes.

Especially in mechanical and vehicle engineering, multi-body simulation (MBS) has established itself as a proven tool for predicting motions and associated forces and torques. The kinematics of a processing machine, the wheel suspension of a vehicle or the flap mechanism in an aircraft wing are characterized by large movements of individual bodies connected by ideal joints. The resulting equations of motion are nonlinear due to the kinematics of large rotations and possible gyroscopic effects. Thus, only an approximate solution by means of numerical time step integration is possible here (Shabana, 2005; Wittenburg, 2008; Rill and Schaeffer, 2014; Wörnle, 2011). On the one hand, this solution method offers the opportunity to take into account the effects of drives or control inputs and to expand the calculation to a system simulation. On the other hand, the level of detail of the simulation is limited. Due to the poor parallelizability of time-step integrations, the number of state variables, usually corresponding to the number of mechanical degrees of freedom, is limited.

The finite element method (FEM) has become the standard method for calculating the stresses in components and the elastic deformation of complex-shaped bodies under load. For this purpose, the elastic body under consideration is divided into a large number of small elements, the elastic field equations are set up and assembled into a large system of equations. This system can be used to determine the stresses and deformations at any location on the body as a result of external loads. In the case of linear material laws and small distortions, the system of equations is linear and can be solved in one step, using parallelization if necessary (Zienkiewicz and Taylor, 2000; Bathe, 2002; Wissmann and Sarnes, 2006). Thus, even relatively large systems resulting from a very fine discretization of the bodies can be handled.

A major challenge arises when MBS calculations have to include elastic bodies, which is then called elastic multibody simulation (EMBS) (Schwertassek and Wallrapp, 1999; Shabana, 2005; Bremer and Pfeiffer, 1992). Then the two worlds "time step simulation with a limited number of degrees of freedom" and "many degrees of freedom of elastic bodies" collide. For this reason, it makes sense to use elastic bodies in an MBS only when it is unavoidable. The criterion for this is that dynamic elastic deformations actually influence the system motion or resulting joint loads in the frequency range of interest. If this is not the case and if, on the other hand, only the internal stresses in the elastic bodies as a result of the movement are affected, these can also be calculated in a post-processing based on the load boundary conditions that are the result of the MBS.

Therefore, to be able to perform a system simulation with MBS including elastic bodies, the number of degrees of freedom of the elastic bodies, which are typically modeled with the FEM, must be reasonably limited. For this purpose, numerous methods for model order reduction (MOR) have been developed in the past.

3.2 Multi-body Simulation Including Elastic Bodies

A typical MBS model is composed of three essential elements:

- bodies, rigid or elastic
- joints
- force elements

The joints link the bodies together. On the one hand they restrict the bodies' mobility against each other, on the other hand they enable movements in specific spatial directions. The design of a mechanism or machine with many degrees of freedom is essentially characterized by the selection of the right joints at the right place. In the design of an MBS, ideal joints are used in which resistance-free directions of movement and ideally rigid constrained directions are always orthogonal to each other and thus no mechanical work is performed in the joints.

All load effects on the system are summarized as force elements. On the one hand, these can be forces between bodies such as springs or dampers. Gravity, external drives and friction in joints can also be modeled by using force elements.

Two competing modeling approaches exist for setting up the equation of motion for MBS, which lead to different types of equations. In the descriptor form, the Newton-Euler equations are set up for each body and the constraints by the joints are built-in using Lagrange multipliers. The result is the equation system (simplified).

$$\mathbf{M}\ddot{\mathbf{z}} + \mathbf{h} = \mathbf{F} + \left(\frac{\partial \mathbf{\Phi}}{\partial \mathbf{z}}\right)^{\mathrm{T}} \cdot \boldsymbol{\lambda},$$

$$\mathbf{\Phi}(\mathbf{z}) = \mathbf{0}. \tag{3.1}$$

The vector $\mathbf{z}$ contains the deflection coordinates of all bodies in the unbound state. The mass matrix $\mathbf{M}$ contains the mass matrices of the involved bodies, the vector $\mathbf{h}$ all gyroscopic forces. In $\mathbf{F}$ all external loads are summarized. The equation $\mathbf{\Phi}(\mathbf{z}) = \mathbf{0}$ describes all constraints in implicit form, which are introduced into the system by joints. For simplicity only holonomic and rheonomic constraints will be considered here. The vector $\boldsymbol{\lambda}$ contains the Lagrange multipliers, which can be directly interpreted as constraint forces or constraint torques in the joints if the constraints $\mathbf{\Phi}(\mathbf{z})$ are suitably formulated. The system of equations (3.1) is comparatively simple to set up, but it is a differential-algebraic (DAE) system of equations. Moreover, the system is very large because the dimension of $\mathbf{z}$, even for strongly bound systems, is always 6 times the number of bodies. Such systems are much more difficult to treat numerically, but special solution methods have been established, especially for MBS.

Another formulation variant for MBS starts from the so-called minimal coordinates. These coordinates describe the possible motions of the system under compliance with all constraints. Especially for tree-structured systems these coordinates are easy to find: The admissible joint deflections can be used as coordinates. Thus, the equation of motion of a MBS can be written in the form

$$\mathbf{M\ddot{q}} + \mathbf{h} = \mathbf{F} \tag{3.2}$$

where $\mathbf{q}$ describes the deflection of the minimal coordinates. The matrices and vectors $\mathbf{M}$, $\mathbf{h}$ and $\mathbf{F}$ are not identical to those in Eq. (3.1) since they are reduced to the minimal coordinates. Equation (3.2) is a system of ordinary differential equations (ODE), which is much more complicated to formulate, but can be solved using simple numerical integration techniques. In addition, it is much smaller, since $\mathbf{q}$ has only the dimension of the degrees of freedom actually present in the system.

For the inclusion of elastic bodies in a MBS, usually the "Floating Frame of Reference Formulation" (Schwertassek and Wallrapp, 1999) method is used. This is based on the idea that the motion of the elastic body can be divided into a "large" rigid-body part, viewed via the body-fixed coordinate system K, and superimposed, "small", linear-elastic deformations $\mathbf{u}$. Thus, the equation of motion derived from FEM can be used for the elastic part of the motion. The position vector $\mathbf{r}_{OP}$ to the body point P can be divided into two partial vectors $\mathbf{r}_{OR}$ and $\mathbf{d}_{RP}$, the latter being composed of a constant part $\mathbf{r}_{RP}$ and the linear-elastic deformation $\mathbf{u}_P$ (Fig. 3.1):

$$\mathbf{r}_{OP} = \mathbf{r}_{OR} + \mathbf{A} \cdot \mathbf{d}_{RP} = \mathbf{r}_{OR} + \mathbf{A} \cdot (\mathbf{r}_{RP} + \mathbf{u}_P). \tag{3.3}$$

The rotation matrix $\mathbf{A}$ describes the transformation of a vector from the body-fixed reference frame K into the inertial frame I. The linear-elastic deformation $\mathbf{u}_P$ of all points of the body is described by a global RITZ-approach, where usually the global natural modes of vibration of the structure serve as shape functions $\boldsymbol{\varphi}_P$. The shape functions must not contain any rigid body components, since these are already taken into account by the reference motion. The position vector follows with the help of additional modal coordinates $\mathbf{q}_e$ for the elastic body:

$$\mathbf{r}_{OP} = \mathbf{r}_{OR} + \mathbf{A} \cdot (\mathbf{r}_{RP} + \boldsymbol{\varphi}_P \cdot \mathbf{q}_e). \tag{3.4}$$
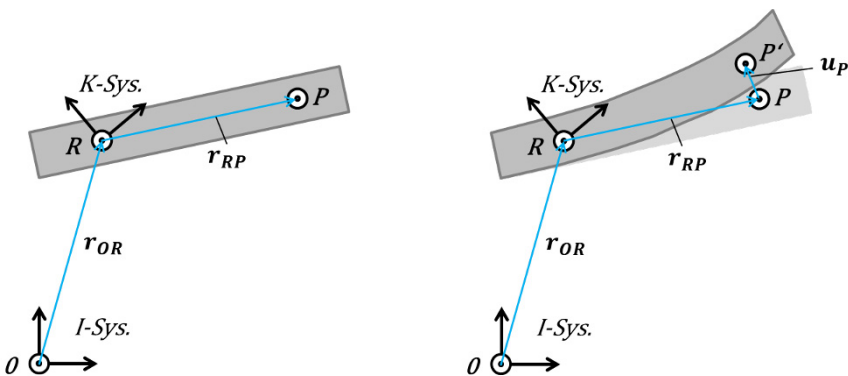
Fig. 3.1: Floating-Frame of Reference Formulation, elastic body undeformed (left) and deformed (right)

Thus, in Eq. (3.2), the minimal coordinate set of the rigid multi-body system $\mathbf{q}_r$ can be extended by an elastic part $\mathbf{q}_e$ and represented in matrix form. For an elastic single body holds:

$$\begin{bmatrix} \mathbf{M}_r & \mathbf{M}_{re} \\ \mathbf{M}_{er} & \mathbf{M}_e \end{bmatrix} \begin{bmatrix} \ddot{\mathbf{q}}_r \\ \ddot{\mathbf{q}}_e \end{bmatrix} + \begin{bmatrix} \mathbf{h}_r \\ \mathbf{h}_e \end{bmatrix} + \begin{bmatrix} \mathbf{0} \\ \mathbf{D}_e\dot{\mathbf{q}}_e + \mathbf{K}_e\mathbf{q}_e \end{bmatrix} = \begin{bmatrix} \mathbf{F}_r \\ \mathbf{F}_e \end{bmatrix}. \tag{3.5}$$

The first line contains the rigid component, line two the elastic component. The components of the elastic body $\mathbf{M}_e$, $\mathbf{D}_e$, $\mathbf{K}_e$ represent the mass matrix, damping matrix and stiffness matrix according to Eq. (3.6). The coupling matrices $\mathbf{M}_{re}$ and $\mathbf{M}_{er}$ describe the occurring interaction between flexible and rigid body due to inertia effects caused by large deflections. Model order reduction (MOR) methods can be used for the dimensional reduction of the elastic part.

3.3 Methods of Model Order Reduction

The linear elastic behavior of an elastic body at small distortions is given by the equation of motion derived from the FEM

$$\mathbf{M}\ddot{\mathbf{x}} + \mathbf{D}\dot{\mathbf{x}} + \mathbf{K}\mathbf{x} = \mathbf{F}. \tag{3.6}$$

In it, $\mathbf{x}$ contains the nodal displacements in the FE grid. $\mathbf{M}$, $\mathbf{D}$ and $\mathbf{K}$ are the mass, damping and stiffness matrices, respectively. The vector $\mathbf{F}$ represents the external loads applied to nodes. This can be formulated in the form $\mathbf{F} = \mathbf{B}\mathbf{u}$ with the input matrix $\mathbf{B}$ and arbitrary external control inputs $\mathbf{u}$.

If a FE grid is connected to other bodies at specified coupling nodes, the measuring equation

$$\mathbf{y} = \mathbf{C}\mathbf{x} \tag{3.7}$$

is important, which uses the often sparse output matrix $\mathbf{C}$ to filter out the relevant deflections from the entire deformation field. For the correct behavior of the elastic body in the environment of a MBS, the connection between the system inputs $\mathbf{u}$ and the outputs $\mathbf{y}$ is ultimately responsible. The intermediate system model (3.6) can be simplified for this purpose if the mentioned relation is preserved as unaltered as possible. This opens the door to model order reduction (Qu, 2004; Antoulas, 2005).

In linear MOR, a new, much smaller set of coordinates $\bar{\mathbf{x}}$ is introduced with a transformation

$$\mathbf{x} = \mathbf{V}\bar{\mathbf{x}} + \boldsymbol{\epsilon} \approx \mathbf{V}\bar{\mathbf{x}} \tag{3.8}$$

that expresses its relation to the full set of coordinates. In case of vector $\mathbf{x}$ being of length N representing the original system and vector $\bar{\mathbf{x}}$ being of length n representing the reduced system with $n \ll N$, the projection matrix $\mathbf{V}$ consists of a dimension

$N \times n$. Using an orthogonal projection, the Eqs. (3.6) and (3.7) can now be put into the form

$$\mathbf{V}^T \mathbf{M} \mathbf{V} \ddot{\bar{\mathbf{x}}} + \mathbf{V}^T \mathbf{D} \mathbf{V} \dot{\bar{\mathbf{x}}} + \mathbf{V}^T \mathbf{K} \mathbf{V} \bar{\mathbf{x}} = \mathbf{V}^T \mathbf{B} \mathbf{u},$$
$$\mathbf{y} = \mathbf{C} \mathbf{V} \bar{\mathbf{x}} \tag{3.9}$$

where the matrices

$$\bar{\mathbf{M}} = \mathbf{V}^T \mathbf{M} \mathbf{V}, \quad \bar{\mathbf{D}} = \mathbf{V}^T \mathbf{D} \mathbf{V}, \quad \bar{\mathbf{K}} = \mathbf{V}^T \mathbf{K} \mathbf{V} \tag{3.10}$$

have only the dimension $n \times n$ and thus allow a much smaller system description with a significantly lower degree of freedom.

The art of model order reduction is to find a suitable projection matrix $\mathbf{V}$. For this purpose, after many years of research, a large variety of MOR methods now exists. In parallel, numerous procedures for the quality assurance of a MOR have also been developed (Sect. 3.4). These allow to estimate the admissibility of the reduction for the respective application.

The MOR methods, can be roughly divided into three families according to the nature of the reduced coordinates (Beitelschmidt and Lein, 2012):

1. The reduced coordinates are still nodal displacements in the cartesian space. Only a partitioning into preserved master nodes and omitted slave nodes takes place.
2. The coordinates describe the abstract deflections of vibration modes of the body or more general deflection modes.
3. Hybrid methods use a mixture of coordinates in the cartesian space and abstract coordinates.

In the following, two methods will be presented in more detail: The Craig-Bampton method (Craig and Bampton, 1968; Craig, 2000; Wijker, 2005) and the Krylov subspace method (Antoulas et al., 2004; Bai, 2002).

The Craig-Bampton method is a hybrid method that combines the static reduction to coupling nodes with the use of modal coordinates. On the one hand, this ensures the connection of the reduced model to the coupling nodes (**Fig. 3.2**). On the other hand, a physically based reduction can be achieved by using modal coordinates and truncating accordingly at a frequency boundary. The Craig-Bampton method has meanwhile been overtaken by more modern methods, but it is still used as a quasi-industry standard, which is available in all commercial calculation programs, since a further utilization is easy due to the node displacements being in the cartesian space.

In the independent static reduction part, also known as method of Guyan reduction (Guyan, 1965), the coordinates are divided into master and slave coordinates $\mathbf{x}^T = [\mathbf{x}_m^T \quad \mathbf{x}_s^T]$. The criterion for this is that there are no inputs or outputs, i.e. couplings, at slave coordinates or the associated slave nodes. The corresponding rows in $\mathbf{B}$ or columns in $\mathbf{C}$ are zero. The matrices in equation (3.6) can be partitioned, neglecting damping, as
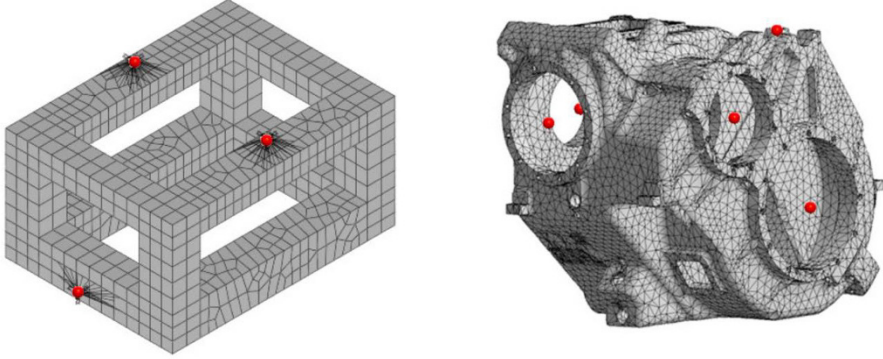
Fig. 3.2: FE-model of a frame structure (left) and a gearbox housing (right) with master nodes connected to the FE-structure, which are used for coupling in the MBS model.

$$\begin{bmatrix} \mathbf{M}_{mm} & \mathbf{M}_{ms} \\ \mathbf{M}_{sm} & \mathbf{M}_{ss} \end{bmatrix} \begin{bmatrix} \ddot{\mathbf{x}}_m \\ \ddot{\mathbf{x}}_s \end{bmatrix} + \begin{bmatrix} \mathbf{K}_{mm} & \mathbf{K}_{ms} \\ \mathbf{K}_{sm} & \mathbf{K}_{ss} \end{bmatrix} \begin{bmatrix} \mathbf{x}_m \\ \mathbf{x}_s \end{bmatrix} = \begin{bmatrix} \mathbf{B}_m \\ \mathbf{0} \end{bmatrix} \mathbf{u}. \tag{3.11}$$

In static reduction, the inertia is neglected and the second line of Eq. (3.11) can be resolved to

$$\mathbf{x}_s = -\mathbf{K}_{ss}^{-1} \mathbf{K}_{sm} \mathbf{x}_m. \tag{3.12}$$

This solution describes the quasi-static deformation of the body at the slave nodes caused by displacements of the master nodes. For a pure static reduction, $\bar{\mathbf{x}} = \mathbf{x}_m$ can be set and the projection matrix holds:

$$\mathbf{V} = \begin{bmatrix} \mathbf{E} \\ -\mathbf{K}_{ss}^{-1} \mathbf{K}_{sm} \end{bmatrix}. \tag{3.13}$$

Here $\mathbf{E}$ is a unit matrix whose dimension corresponds to the number of master degrees of freedom. However, this reduction is insufficient for motions and resulting inertial loads on the bodies and gives poor results.

For this reason the oscillation modes of the system with blocked master nodes are calculated. This results in the modal matrix $\boldsymbol{\Phi}$ with the corresponding eigenvalues or natural frequencies ω_i^2. The motions of the slave nodes can now be calculated using the modal coordinates $\mathbf{x}_\phi$ in the form $\mathbf{x}_s = \boldsymbol{\Phi} \mathbf{x}_\phi - \mathbf{K}_{ss}^{-1} \mathbf{K}_{sm} \mathbf{x}_m$ as the sum of the dynamic and static components, where the dimension of $\mathbf{x}_\phi$ is initially still exactly the same as that of $\mathbf{x}_s$. As a reduction step, all modes with a natural frequency above a suitable frequency limit can now be neglected or "truncated". This also eliminates their modal coordinates, leaving a reduced set $\bar{\mathbf{x}}_\phi$ with associated reduced modal matrix $\bar{\boldsymbol{\Phi}}$. The master deflections $\mathbf{x}_m$ and the reduced modal deflections $\bar{\mathbf{x}}_\phi$ are used as the reduced coordinate set. The projection matrix is then

$$V = \begin{bmatrix} E & 0 \\ -K_{ss}^{-1}K_{sm} & \bar{\Phi} \end{bmatrix}. \tag{3.14}$$

Estimates are available for determining the frequency limit during truncation. In addition, the frequency limit can be determined iteratively with the methods described in the Sect. 3.4. It should be noted, however, that due to the coupling of the elastic body in the overall system by coupled masses, natural frequencies may decrease sharply and initially neglected modes may become significant later.

As a method that has recently gained importance for MOR, the Krylov subspace method (KSM) will be presented here. This method approximates the transfer function matrix H, which is obtained from the equation of motion (3.6) associated with the input matrix B and the output matrix C according to Eq. (3.7)

$$H(s) = C \left(s^2 M + s D + K\right)^{-1} B. \tag{3.15}$$

The most original form of the KSM formulation is based on Krylov (1931) and is set up for first order systems, further developed by Grimme (1997) and Gallivan et al. (2004), among others. Therefore, Eq. (3.15) can be written in a first-order form with the descriptor matrix E and the system matrix A:

$$H(s) = \check{C} \left(s E - A\right)^{-1} \check{B}. \tag{3.16}$$

With the help of a power series formulation at expansion point σ one obtains according to Lehner and Eberhard (2006):

$$\begin{aligned} H(s) &= \sum_{j=1}^{\infty} \check{C} \left[(\sigma E - A)^{-1} \cdot E\right]^j \cdot (\sigma E - A)^{-1} \cdot \check{B} \cdot (\sigma - s)^j \\ &= \sum_{j=1}^{\infty} T_j^{\sigma} \cdot (\sigma - s)^j. \end{aligned} \tag{3.17}$$

The coefficients T_j^{σ} are called moments. By a so-called moment matching the moments between original and reduced model are brought into agreement. Similar to a Taylor polynomial, the transfer function matrix is approximated accordingly.

For the determination of the Krylov subspace two basic methods are available: The Arnoldi algorithm according to Arnoldi (1951) is preferred over the Lanczos algorithm after Lanczos (1950) because of its simple implementability. Furthermore, the choice of the development points σ determines the success of the approximation: The case $\sigma = 0$ is henceforth called original KSM. If $\sigma \neq 0$ is valid for one or more development points, we speak of rational KSM (RKSM). In case of an iterative choice of the expansion point e.g. Fehr et al. (2013) one speaks then of iterative rational KSM.

In mechanics, second-order multi-input-multi-output (MIMO) systems are usually present according to (3.6). For these, it is useful to remain in a second order formulation (3.15) and not to revert to a first order formulation (3.16). This is ac-

complished by means of a second order Arnoldi (SOAR) algorithm Salimbahrami (2005); Lehner (2007) and Koutsovasilis (2009). The Krylov subspace $\mathbf{V}_K$ is composed of the basis vectors in $\mathbf{V}_{K,j}$ and reads for an undamped system for $\sigma = 0$ with moment j:

$$\mathbf{V}_{K,j} = \mathrm{span}\left((\mathbf{K}^{-1}\mathbf{M})^{j-1}\mathbf{K}^{-1}\mathbf{b} \right). \tag{3.18}$$

The Boolean starting vector $\mathbf{b}$ contains only values 1 at the places where inputs or outputs are present, which is accomplished interpolatively using the input and output matrices of the system Bunse-Gerstner et al. (2007). The dimension of the reduced model depends on the number of columns in $\mathbf{V}_K$ and results from the number of expansion points σ multiplied by the order of series j. In contrast to the Craig-Bampton approach (3.14), the number of master nodes does neither play a role for the approximation quality nor for the dimension of the reduced model.

Preferably, an RKSM approach with a SOAR algorithm is used for an arbitrary number and distribution of expansion points σ. The choice of σ and j is essential and significantly determines the reduction success and the reduced model dimension. The original KSM is rather conservative and usually yields passable results, but numerical stability is not always given. For details see Koutsovasilis (2009) and Lein and Beitelschmidt (2015), the latter work dealing with an optimal choice of expansion points for a minimal model dimension.

3.4 Quality Assurance of the Model Order Reduction

A reduced system no longer has the full information content of the original system, cf. eq. (3.8). Whether an information is important or unimportant can be determined for mechanical systems mostly by the covered frequency range. Below a frequency limit, which is different for each system, the reduced system should behave as much as possible like the original system. Above this frequency limit, considerable deviations can occur, but these are deliberately neglected.

To check the agreement between the original system and the reduced system in the desired frequency range, several procedures for quality assurance of reduced systems exist. These can be roughly divided into four types (Lein and Beitelschmidt, 2014):

- consideration of the eigenvalues (eigenfrequencies) of both systems.
- comparison of the eigenvectors (mode shapes) of both systems
- comparison of the transfer behavior of both systems
- comparison of properties of the system matrices

Both the information content and the computational effort increase from top to bottom. In addition, there is the possibility to compare mass properties or the static behavior, which will not be discussed in detail.

Comparison of eigenfrequencies is a quick but crude procedure with limited significance. Even seemingly matching eigenfrequencies can belong to strongly different eigenmodes or to eigenmodes that are reversed in order. Therefore, mode pairing is absolutely necessary in advance. For the comparison of the eigenfrequencies of p mode pairs without rigid body modes, the Normalized Relative Frequency Difference (NRFD) is suitable (**Fig. 3.3**), which provides the percentage error of the eigenfrequencies between reduced system $f_{r,i}$ and original system $f_{v,i}$

$$\text{NRFD}_i = \left| 1 - \frac{f_{r,i}}{f_{v,i}} \right|, \qquad i = 1, 2, \ldots, p. \tag{3.19}$$

Since a pure comparison of eigenfrequencies is not sufficient in many cases, a numerical comparison of mode shapes is often considered. However, the eigenvectors of the reduced model $\boldsymbol{\Phi}_r$ and the original model $\boldsymbol{\Phi}_v$ have different dimensions n and N, which requires an adjustment of the eigenvectors. Different methods are used for the dimension adjustment (Lein and Beitelschmidt, 2014):

- expansion of the reduced system to dimension N
- contraction of the original system to dimension n
- selection of common representative coordinates from both systems
- comparison based on a common intermediate dimension based on expansion of the reduced and contraction of the original system

The various approaches differ significantly in numerical effort and expressiveness. Very common but also numerically costly is the comparison based on the expanded reduced model $\boldsymbol{\Psi}_r$ using the projection matrix $\mathbf{V}$ from Sect. 3.3:

$$\boldsymbol{\Psi}_r = \mathbf{V}\boldsymbol{\Phi}_r. \tag{3.20}$$

The choice of available correlation methods based on the dimension-adjusted eigenvectors is manifold, the best known representative being the Modal Assurance Criterion (MAC), of which numerous variations exist (Allemang, 2003). For the comparison of two eigenvectors of the reduced system $\boldsymbol{\psi}_{r,i}$ and the original system $\boldsymbol{\phi}_{v,i}$, the MAC yields values between 0 and 1 (Allemang, 1980):

$$\text{MAC}_{i,j} = \frac{\left(\boldsymbol{\psi}_{r,i}^H \cdot \boldsymbol{\phi}_{v,j} \right)^2}{\left(\boldsymbol{\psi}_{r,i}^H \cdot \boldsymbol{\psi}_{r,i} \right) \left(\boldsymbol{\phi}_{v,j}^H \cdot \boldsymbol{\phi}_{v,j} \right)}, \qquad i,j = 1, 2, \ldots, p. \tag{3.21}$$

The individual terms can be combined to form the MAC matrix. The terms on the main diagonal of the matrix express the agreement of reduced and original mode shape. Values above 0.9 indicate a good correlation. The off-diagonal elements should not exceed 0.1 (**Fig. 3.4**).

Both methods NRFD and MAC depend on an identification and assignment of the mode shapes, which can lead to problems in models with high mode density or component symmetries. Furthermore, both methods only compare the maximum peaks, but not the anti-resonances of the transfer behavior.
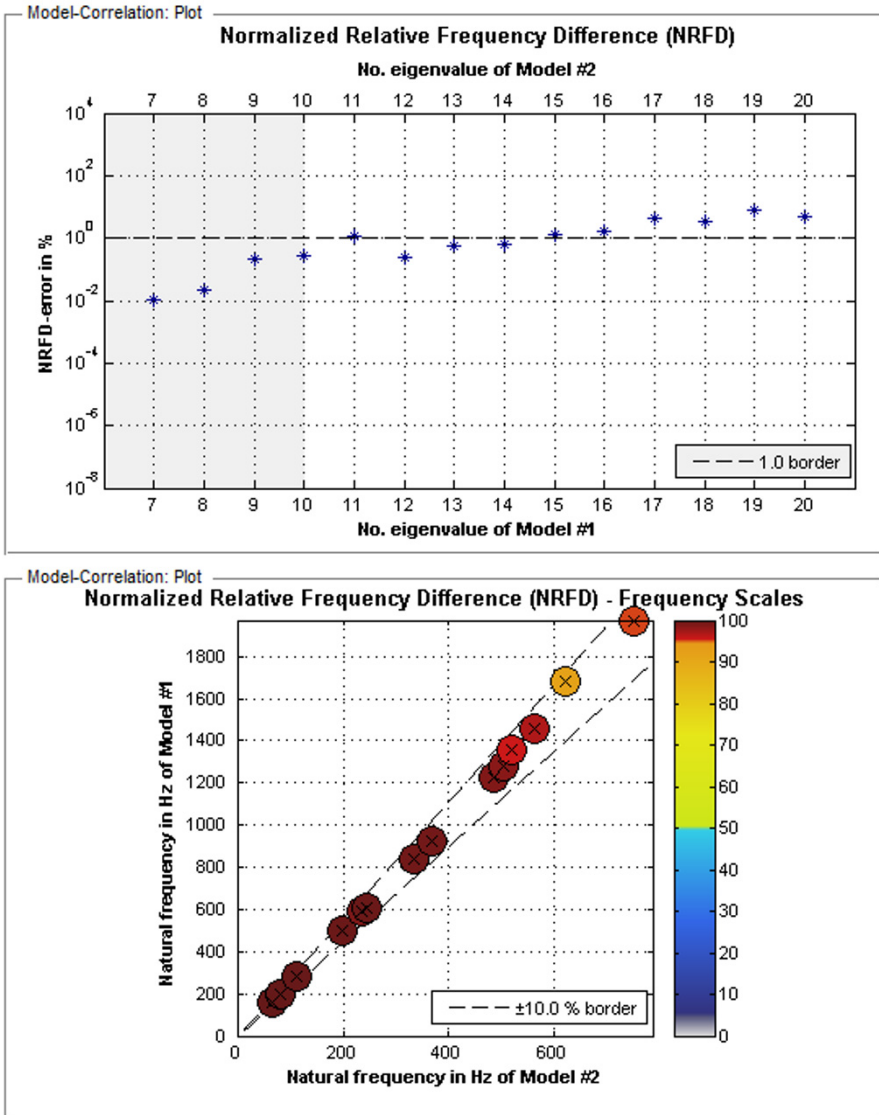
Fig. 3.3: Natural frequency based correlation methods between original and reduced model, NRFD error (top), NRDF error shown as frequency scaling (bottom).

The correlation based on the transfer behavior is the state of the art in automation technology, even if the calculation of the transfer behavior according to (3.15) for discrete frequency points Ω is numerically complex. Therefore, a modal formulation $\tilde{\mathbf{H}}$ based on the modal matrix $\mathbf{\Phi}$ is suitable as a starting point:
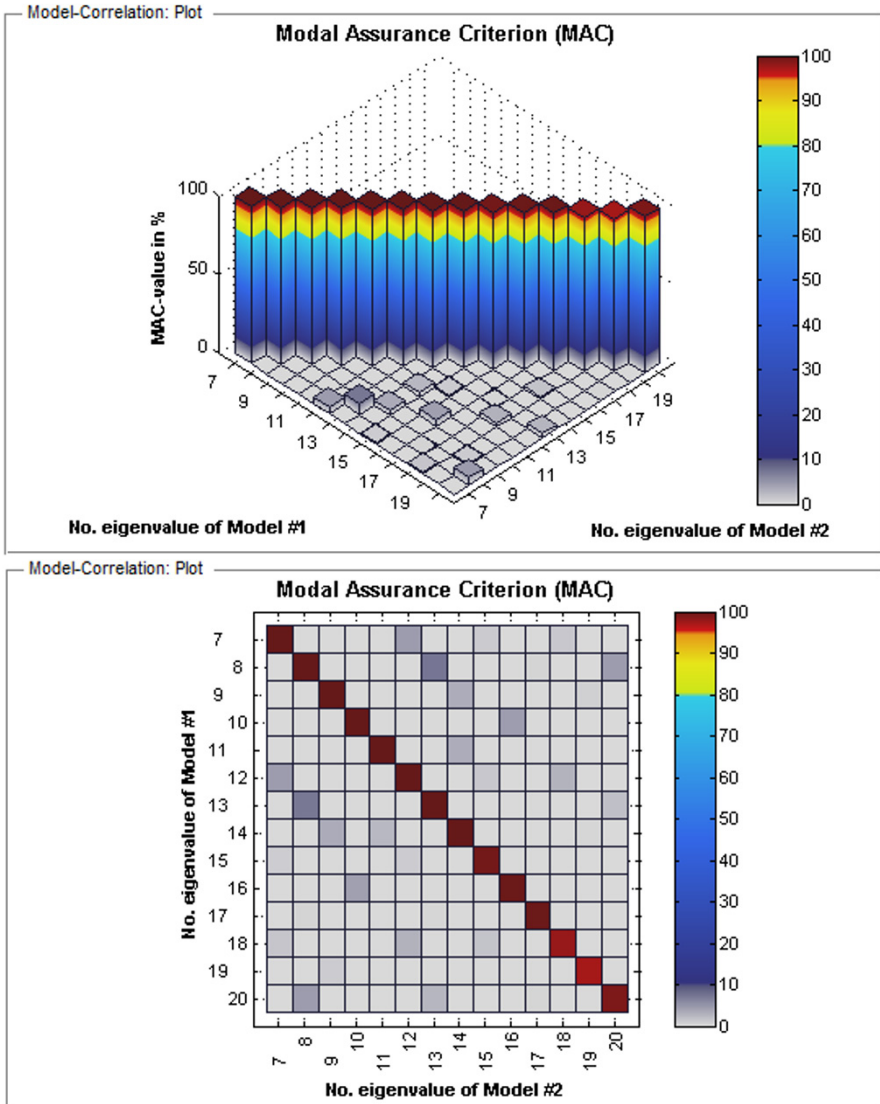
Fig. 3.4: Eigenvector-based correlation methods between original and reduced model, MAC isometric (top), MAC top view (bottom).

$$\tilde{\mathbf{H}}(\Omega) = \mathbf{\Phi}(-\Omega^2\mathbf{M} + j\Omega\mathbf{D} + \mathbf{K})^{-1}\mathbf{\Phi}^{\mathrm{T}}. \tag{3.22}$$

Since the transfer function matrix $\tilde{\mathbf{H}}$ consists of dimension $N \times N$, it is convenient to calculate Eq. (3.22) only for selected $i = o = a$ inputs/outputs. The modal transfer function matrix $\tilde{\mathbf{H}}^{\mathrm{IO}}$ of dimension $i \times i$ follows with the help of input matrix $\mathbf{B}$ and

output matrix $\mathbf{C}$ (Eqs. (3.6) and (3.7)):

$$\tilde{\mathbf{H}}^{\mathrm{IO}}(\Omega) = \mathbf{C}\mathbf{\Phi}(-\Omega^2\mathbf{M}+j\Omega\mathbf{D}+\mathbf{K})^{-1}\mathbf{\Phi}^{\mathrm{T}}\mathbf{B}. \qquad (3.23)$$

Analogously to the MAC in Eq. (3.21), the Frequency Domain Assurance Criterion (FDAC) can be derived using the principal diagonal terms of the transfer function matrix of the reduced model $\mathbf{h}_{\mathrm{r}}(\Omega)$ and the original model $\mathbf{h}_{\mathrm{v}}(\Omega)$ for a frequency point (Pascual et al., 1997):

$$\mathrm{FDAC}(\Omega) = \frac{\left(\mathbf{h}_{\mathrm{r}}^{\mathrm{H}}(\Omega)\cdot\mathbf{h}_{\mathrm{v}}(\Omega)\right)^2}{\left(\mathbf{h}_{\mathrm{r}}^{\mathrm{H}}(\Omega)\cdot\mathbf{h}_{\mathrm{r}}(\Omega)\right)\left(\mathbf{h}_{\mathrm{v}}^{\mathrm{H}}(\Omega)\cdot\mathbf{h}_{\mathrm{v}}(\Omega)\right)}. \qquad (3.24)$$

The FDAC provides a better evaluation of the anti-resonances, which is relevant for example for the analysis of a minimal sound radiation (Woller et al., 2016). The frequency points can be equidistant or adaptively distributed. The comparison of system matrices is also usually based on modal approaches, but will not be discussed further.

Another approach, often used in control engineering (Antoulas, 2005), is to apply the infinity matrix norm to the transfer function matrices $\tilde{\mathbf{H}}$. By relative value formation, the frequency-dependent $\mathcal{H}_\infty$-error-norm $e^{\mathcal{H}\infty}$ follows:

$$e^{\mathcal{H}\infty}(\Omega) = \frac{\left\|\mathbf{H}_{\mathrm{r}}^{\mathrm{H}}(\Omega)-\mathbf{H}_{\mathrm{v}}^{\mathrm{H}}(\Omega)\right\|_\infty}{\left\|\mathbf{H}_{\mathrm{r}}^{\mathrm{H}}(\Omega)\right\|_\infty}. \qquad (3.25)$$

The $\mathcal{H}_\infty$-error-norm is a measure of the maximum error in the input-output gain due to a harmonic excitation. However, in FDAC, the evaluation of the maximum valid frequency range is greatly facilitated for the user by the percentage representation (see **Fig. 3.5**).

3.5 Example for Model Order Reduction

At the Chair of Dynamics and Mechanism Design of the TU Dresden a program for MOR is under development since 2008 (Koutsovasilis, 2009; Beitelschmidt and Lein, 2012; Lein et al., 2015; Lein and Beitelschmidt, 2015; Lein et al., 2017). The MORPACK program will be briefly introduced in this section and explained with an example.

The MORPACK software can be used to automatically create and validate reduced body models based on FE-models for use in elastic multi-body systems (EMBS) or FE-programs. Since the providing of elastic bodies has not been very systematized so far and is associated with a large number of sub-steps in different programs, MORPACK combines the entire process in one software, starting with
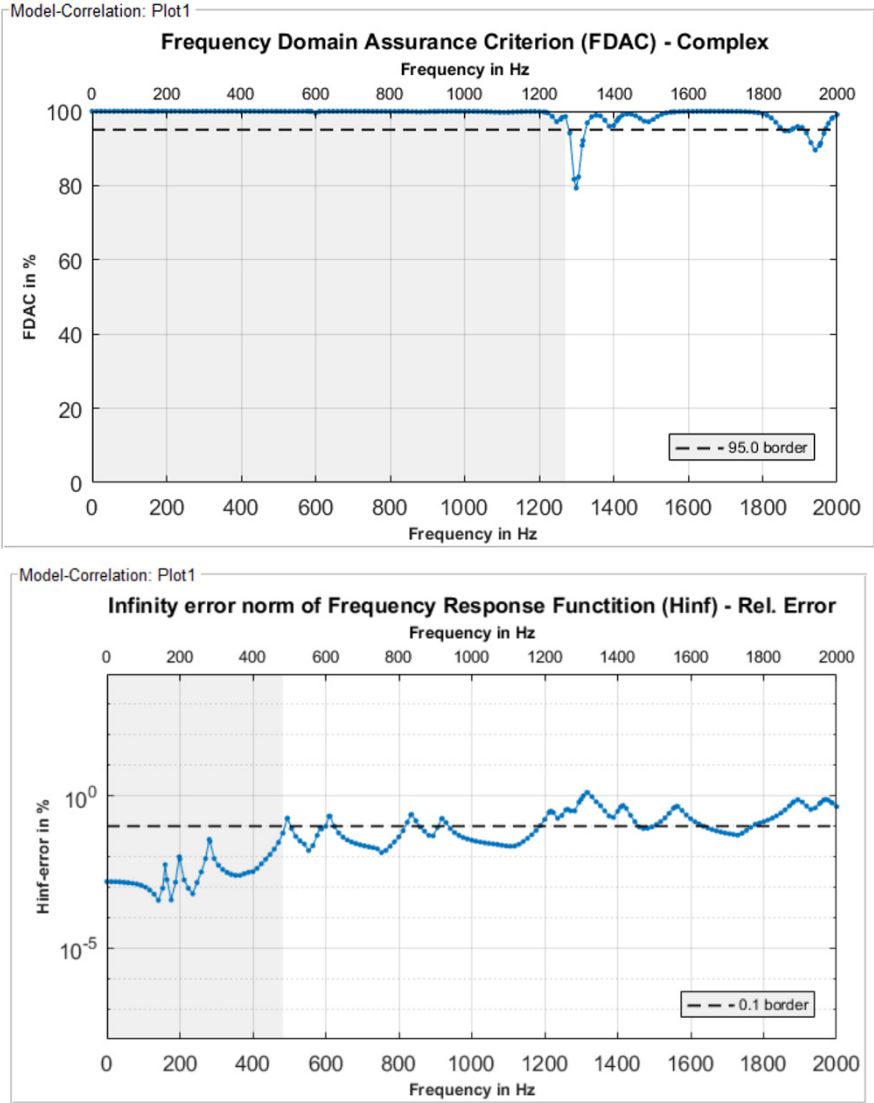
Fig. 3.5: Transfer function based correlation methods between original and reduced model, FDAC (top), H_∞ (bottom).

model preparation, through model reduction with quality assurance, up to the export of the reduced, elastic body (**Fig. 3.6**). All substeps in MORPACK are systematized and preset depending on the model, so that the greatest possible automation and standardization as well as reproducibility are ensured.
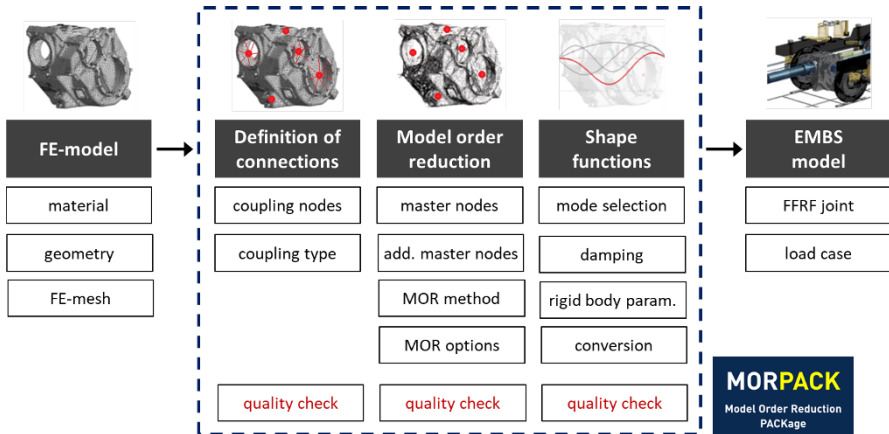
Fig. 3.6: Modified sequence of the FEM-MKS coupling process using MORPACK software

MORPACK is a MATLAB®-based tool and tailored to the specific EMBS user requirements. By means of a comfortable user interface all settings can be adjusted model-specific. MORPACK acts as an interface between the FE-program and the MKS software.

The automated process is modular and includes the following steps:

1. data import (FE-program or measurement via EMA).
2. model preparation (definition of connections and coupling nodes, as well as additional master nodes)
3. model order reduction (automated minimal models)
4. quality assurance (automated correlation)
5. data export (FE or MBS program)
6. EMBS program (spatial EMBS algorithm)

In the following, the reduction process is presented using a gearbox housing of a locomotive. Large, thin-walled housing structures may well exhibit elastic deformations in frequency ranges relevant to propulsion simulations. At the latest, if the structure-borne noise, as it arises e.g. in the gear meshes, is to be investigated, an elastic modeling of such large-surface structures is inevitable.

Figure 3.7 shows the imported FE-model. The import of detailed FE-elements is omitted, since this limits the flexibility of the import process considerably. Instead, a coarse surrogate mesh based on nodal coordinates is automatically created for visualization. In this step, the coupling nodes with which the elastic body is later connected to other components must also be defined. Additional master nodes are defined automatically, which are relevant for the unique description of the mode shapes, among other things.

In **Table 3.1** the selection list of model order reduction methods is presented. In addition to the methods presented in 3.3, Craig-Bampton and Krylov, numerous other methods are implemented for experimental reasons.
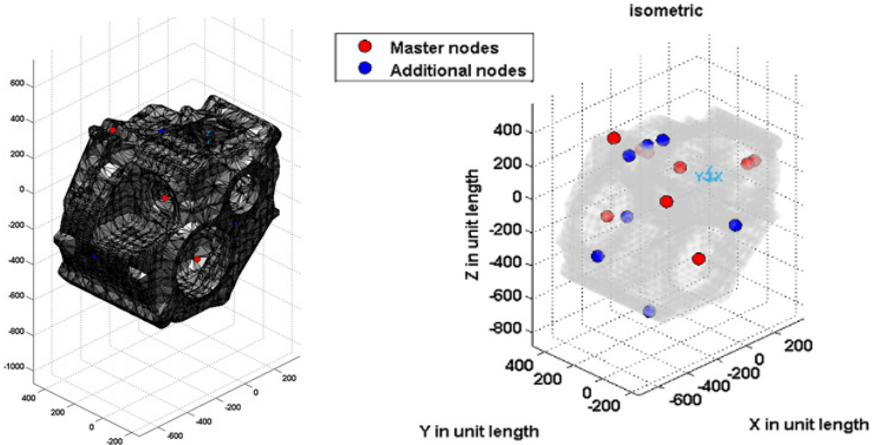
Fig. 3.7: MORPACK modules FE-model (left) and master node selection (right)

Table 3.1: MORPACK module model order reduction, overview of available reduction methods

Basic methods	Cartesian space	hybride space	general space	ANSYS®	MORPACK
Static Reduction **Guyan**	X			X	X
Dynamic Reduction **Dynamic**	X				X
Standard Improved Reduction System Method **IRS**	X				X
System Equivalent Reduction Expansion Process **SEREP**		X			X
Component Mode Synthesis **CMS / Craig-Bampton Method**		X		X	X
Combinations based on IRS / CMS / KSM **ICMS / KCMS / IKCMS**		X			X
Krylov Subspace Method **KSM / Rational KSM / Block-KSM**			X		X
Second Order Balanced Truncation **SOBT / frequency-weighting**			X		X

Figure 3.8 shows screenshots of the model correlation. It can be seen that the reduced model is well correlated to the original model up to a frequency of 996 Hz (NRFD) or to 3183 Hz (MAC), meaning the mode shapes correlate better than the natural frequencies. This is important for the selection of the modal shape functions in the MBS program, because modes above 3200 Hz must not be considered.
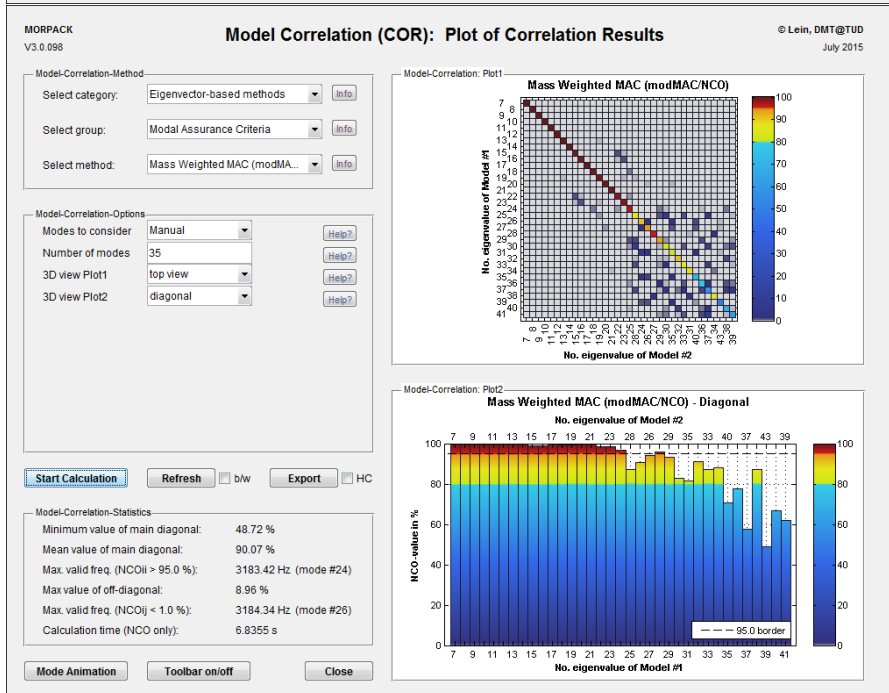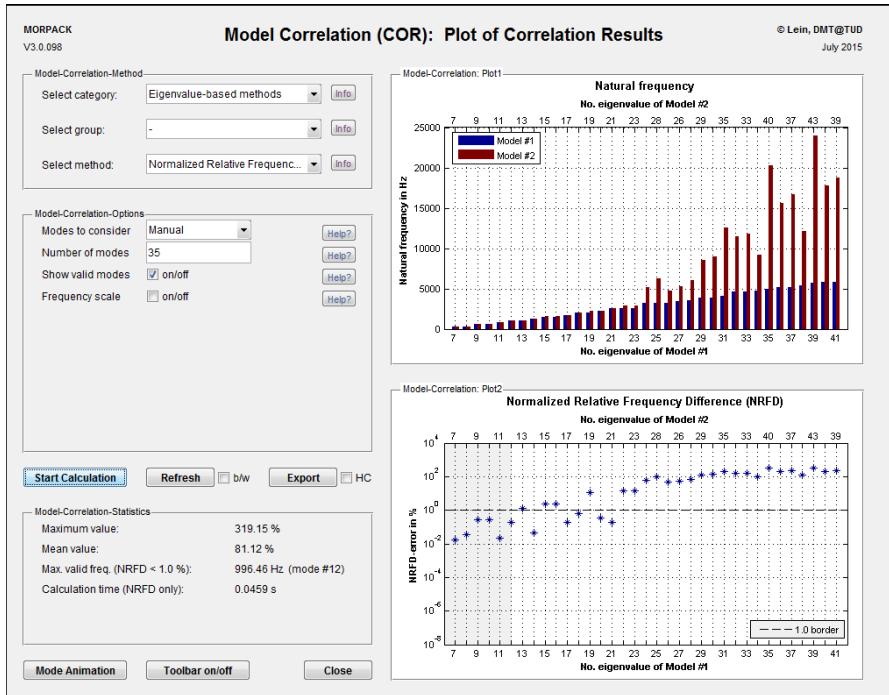
Fig. 3.8: MORPACK module correlation, based on eigenfrequencies (top) and based on eigenvectors (bottom)
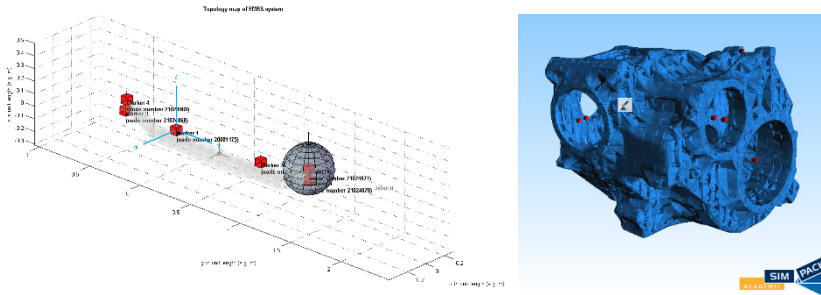
Fig. 3.9: MORPACK EMBS module (left) and an exported model from MORPACK to SIMPACK (right)

Finally, the final reduced model can be exported to MBS programs. **Figure 3.9** (top) shows the implemented EMBS algorithm in MATLAB$^{®}$, which can be used for a preliminary analysis to optimize the selection of modal shape functions depending on specific load cases. **Figure 3.9** (bottom) shows the model imported to SIMPACK$^{®}$, which is based on the equivalent mesh created at the beginning. However, the elastic properties are determined solely by the selection of the modal shape functions and not by the visualized geometry.

3.6 Summary

System simulation using the multibody systems method is a standard procedure for the design of machines, plants and vehicles. It can be used to investigate large movements including the behavior of drives and control. Often, individual bodies have to be modeled elastically because relevant elastic deformations already occur in the frequency range under investigation. The state of the art is the "Floating Frame of Reference" method, in which the motion of a body is divided into a rigid-body motion and small, superimposed, linear-elastic deformations.

It is obvious that a model order reduction (MOR) is necessary to reduce the often huge number of dregrees of freedom of the models of elastic bodes produced by FEA for a fast simulation. For this purpose, the software tool MORPACK was developed at the Chair of Dynamics and Mechanism Design at the TU Dresden. MORPACK can perform all steps of the model order reduction process chain. A focus in the development of MORPACK was to implement established MOR algorithms as well as experimental new methods. Furthermore, the quality assurance algorithms of MORPACK basing on model correlation were introduced in this article.

Although model order reduction has already reached a high level of maturity, it is still a research topic. Among other things, the goals of development are to efficiently reduce even larger systems and to generate models that are as small as possible.

Link MORPACK:

https://tu-dresden.de/ing/maschinenwesen/ifkm/dmt/forschung/projekte/morpack

References

Allemang RJ (1980) Investigation of some multiple input/output frequency response function experimental modal analysis techniques. Phd thesis, University of Cincinnati, Department of Mechanical Engineering, Ohio, USA

Allemang RJ (2003) The modal assurance criterion – twenty years of use and abuse. Journal of Sound and Vibration 37(8):14–23

Antoulas A, Sorensen D, Gallivan KA, van Dooren P, Grama A, Hoffmann C, Sameh A (2004) Model Reduction of Large-Scale Dynamical Systems, vol 3038, Springer, Berlin, Heidelberg

Antoulas AC (2005) Approximation of Large-Scale Dynamical Systems, vol 6. SIAM (Society for Industrial and Applied Mathematics), Philadelphia, Pennsylvania, USA

Arnoldi WE (1951) The principle of minimized iterations in the solution of the matrix eigenvalue problem. Quarterly of Applied Mathematics 9(1):17–29

Bai Z (2002) Krylov subspace techniques for reduced-order-modeling of large-scale dynamical systems. Applied Numerical Mathematics 43(1):9–44

Bathe KJ (2002) Finite-Elemente-Methoden. Springer, Berlin, Heidelberg, New York

Beitelschmidt M, Lein C (2012) MORPACK-Schnittstelle zum Import von FE-Strukturen nach SIMPACK. at (Automatisierungstechnik) 60(9):547–560

Bremer H, Pfeiffer F (1992) Elastische Mehrkörpersysteme. Teubner Verlag, Stuttgart

Bunse-Gerstner A, Kubalinska D, Vossen G, Wilczek D (2007) h_2-norm optimal model reduction for large-scale discrete dynamical MIMO systems. Journal of Computational and Applied Mathematics 233(2010):1202–1216

Craig RR (2000) Coupling of substructures for dynamic analysis – an overview. In: Proceedings AIAA (American Institute of Aeronautics and Astronautics) Dynamics Specialists Conference, Atlanta, Georgia, USA, Paper No. 2000-1573, pp 1–12

Craig RR, Bampton MC (1968) Coupling of substructures for dynamic analysis. AIAA Journal 6(7):1313–1319

Fehr J, Fischer M, Haasdonk B, Eberhard P (2013) Greedy-based approximation of frequency-weighted Gramian matrices for model reduction in multibody dynamics. Journal of Applied Mathematics and Mechanics 93(8):501–519

Gallivan K, Vandendorpe A, Van Dooren P (2004) Model reduction of MIMO systems via tangential interpolation. Journal on Matrix Analysis and Applications 26(4):328–349

Grimme EJ (1997) Krylov projection methods for model reduction. Phd thesis, Department of Electrical and Computer Engineering, University of Illinois at Urbana Champaign, Urbana, Illinois, USA

Guyan RJ (1965) Reduction of mass and stiffness matrices. AIAA Journal 3(2):380

Koutsovasilis P (2009) Model order reduction in structural mechanics – coupling the rigid and elastic multi body dynamics. URL https://nbn-resolving.org/urn:nbn:de:bsz:14-qucosa-24551, abgerufen am 21.10.2021 von Qucosa

Krylov AN (1931) On the numerical solution of the equation by which in technical questions frequencies of small oscillations of material systems are determined. Izvestija AN SSSR 7(4):491–539

Lanczos C (1950) An iteration method for the solution of the eigenvalue problem of linear differential and integral operators. Journal of Research of the National Bureau of Standards 45(4):255–282

Lehner M (2007) Modellreduktion in elastischen Mehrkörpersystemen. Disertation, Institut für Technische und Numerische Mechanik, Universität Stuttgart, Germany

Lehner M, Eberhard P (2006) Modellreduktion in elastischen Mehrkörpersystemen. at (Automatisierungstechnik) 54(4):170–177

Lein C, Beitelschmidt M (2014) Comparative study of model correlation methods with application to model order reduction. In: Proceedings 26th ISMA (International Conference on Noise and Vibration Engineering), Leuven, Belgium, pp 2683–2700

Lein C, Beitelschmidt M (2015) Back-transformation into physical configuration space after model order reduction onto a general subspace. In: PAMM (Proceedings in Applied Mathematics and Mechanics), Wiley Verlag, vol 15, pp 61–62

Lein C, Beitelschmidt M, Bernstein D (2015) Improvement of Krylov-subspace-reduced models by iterative mode-truncation. In: 8th Vienna International Conferenceon Mathematical Modelling (MATHMOD), IFAC-PapersOnLine, vol 48(1), pp 178–183

Lein C, Woller J, Hopf H, Beitelschmidt M (2017) Approach for modeling flexible bodies based on experimental data with utilization in elastic multibody simulation. In: ECCOMAS (European Community on Computational Methods in Applied Sciences), Multibody Dynamics, Prag, pp 189–198

Pascual R, Golinval JC, Razeto M (1997) A frequency domain correlation technique for model correlation and updating. In: 15th IMAC (International Modal Analysis Conference), Orlando, Florida, USA, pp 587–593

Qu ZQ (2004) Model order reduction techniques with applications in finite elemente Analysis. Springer, London Berlin Heidelberg

Rill G, Schaeffer T (2014) Grundlagen und Methodik der Mehrkörpersimulation. Springer-Vieweg, Wiesbaden

Salimbahrami B (2005) Structure preserving order reduction of large scale second order models. Phd thesis, Lehrstuhl für Regelungstechnik, Technische Universität München, Germany

Schwertassek R, Wallrapp O (1999) Dynamik flexibler Mehrkörpersysteme. Vieweg, Braunschweig, Wiesbaden

Shabana AA (2005) Dynamics of Multibody Systems. Cambridge University Press, Cambridge

Wijker JJ (2005) Approximation of large-scale dynamical systems. Advances in Design and Control 6

Wissmann J, Sarnes KD (2006) Finite Elemente in der Strukturmechanik. Springer, Berlin, Heidelberg, New York

Wittenburg J (2008) Dynamics of multibody systems. Springer, Berlin, Heidelberg, New York

Woller J, Lein C, Zeidler R, Beitelschmidt M (2016) A numerical study of the structure-borne sound transmission of a bogie. In: The Third International Conference on Railway Technology, Cagliari

Wörnle C (2011) Mehrkörpersysteme – Eine Einführung in die Kinematik und Dynamik von Systemen starrer Körper. Springer, Heidelberg

Zienkiewicz OC, Taylor RL (2000) The Finite Element Method 1. Butterworth-Heinemann, Oxford UK

Chapter 4
Identification of Temperature Dependent Material Properties in Composite Plates Utilizing Experimental Vibration Data

Marcus Maeder, Sourav Chandra, and Steffen Marburg

Abstract In recent three decades, composite materials have received an increasing interest among engineers and scientists. These materials are characterized by a higher stiffness with reduced weight, compared to commonly used materials such as aluminum or steel. It is not surprising that a wide range of applications emerged within the aerospace and transportation sector for example for aircraft and high-speed train hulls. However, these composite materials are generally made out of fiber and matrix material. This material behavior strongly depends on the environmental conditions such as temperature. This results in a complex macroscopic material behavior and the precise knowledge of the corresponding properties is a key factor for computer aided engineering and virtual prototyping. Especially when composite structures are subjected to dynamic loading and changing temperatures, resonances can occur and ultimately lead to fatal dynamic behavior in the absence of sufficient damping. Therefore, the experimental investigation of the material behavior under dynamic loading for different temperatures together with a proceeding parameter identification scheme is necessary to precisely capture the material properties of the underlying model, which is the essence of the work at hand. Utilizing the presented approach, the parameter identification is easy to implement and reliable.

Key words: Composites, Parameter identification, Temperature dependent elastic material parameters, Experimental investigation, Optimization

4.1 Introduction

In the past several decades, the application of composite plates in transportation industries, for example aircrafts, high-speed trains, sports-cars etc., is increasing

Marcus Maeder · Sourav Chandra · Steffen Marburg
Technical University Munich, Munich, Germany,
e-mail: Marcus.Maeder@tum.de, sourav.chandra@tum.de, Steffen.Marburg@tum.de

rapidly. The light-weight, high-strength, and higher fatigue strength inspired re-searchers and engineers to consider composite materials as a principal structural material to design light-weight vehicles without compromising safety and comfort of passengers. In new commercial aircrafts like the Boeing 787 or the Airbus 380, composite materials comprise 50% of the total net mass (Gay, 2014). Furthermore, to accomplish aerodynamically contoured nose designs of high-speed trains, the us-age of composite materials shows better performance. Due to the high-speed move-ment of these vehicles, the ambient temperature increases which may modify the elastic properties of the composite materials. In general, these composite materials consist of fibers and matrix material which both posse viscoelastic properties that are frequency and temperature dependent. Generally, carbon-epoxy, graphite-epoxy, and IM7-PEEK composites are extensively used as a high-strength composite ma-terial in the field of aircraft or high-speed train production. These materials are ca-pable to withstand prolong vibration and aerodynamic heating. However, altering material properties due to changes in temperature can lead to unwanted vibrations or even a loss in structural integrity. Therefore, the precise knowledge of tempera-ture dependent elastic properties of these composite materials is essential for a safe and reliable design of composite structures.

Primarily, determining the elastic properties of composite plates is carried out using two methods – namely the direct method on the one hand and the inverse method on the other hand. Different static test procedures can be used to evaluate elastic properties of composite lamina (D3039/D3039M, 2017; D4255/D4255M, 2020; Adams and Bacon, 1973). However, the accuracy of these methods highly depends on boundary conditions and the overall geometry of the lamina. Various micro-mechanical theories have been implemented by scientists and engineers to calculate the elastic and damping properties of a lamina by knowing the material properties of the single fibers and the matrix material (Ni and Adams, 1984). Sara-vanos and Chamis (1989) have proposed a micro-mechanic theory to evaluate elas-tic properties of composite lamina by including hygrothermal effects. Based on this theory, calculations of the temperature-dependent elastic properties of the lamina provide only unsatisfactory results due to the lack of accurate knowledge of tem-perature, fiber volume fraction, and fiber-matrix interaction (Brantseva et al., 1999). Despite these circumstances, Lecompte et al. (2007) and Mi et al. (2020) have im-plemented extensive static test procedures to identify the elastic properties of com-posite plates. However, these static procedures fail to provide in-situ methods when the composite laminates are subjected to dynamic loading with special consideration of a varying thermal environment.

For this scenario, the determination of elastic properties of lamina based on dy-namic test results together with an identification scheme offers several advantages. The fundamental idea of the inverse technique is to minimize the error between in-situ response measurements and simulated responses by numerically optimizing the elastic properties of the material. This way, composite plates subjected to dynamic loading should be evaluated using elastic properties that are obtained from dynamic test. Zhou et al. (2017) have shown a variation of the identified elastic properties for a wooden plate based on static and dynamic tests. Their study indicates that static

tests underestimate E_x and E_y, and overestimate G_{xy} of the underlying orthotropic material model. Furthermore, the elastic properties obtained from the dynamic test results are sufficiently influenced by the applied boundary conditions. Therefore, the material property identification based on the dynamic test data is receiving much attention by the scientific community. Mota Soares et al. (1993) and Rikards et al. (1999) proposed conducting an experimental modal analysis of laminated composite plates and subsequently evaluate the elastic properties by considering an inverse approach. The finite element (FE) technique is utilized to develop numerical models of such plates using a first order shear deformation theory (FSDT). To investigate the effect of various shear deformation theories, Frederiksen (1997b,a) have identified the elastic properties of a laminated composite plate utilizing FSDT and different higher order shear deformation theories (HSDTs). Overall, the determination of elastic properties based on the experimental modal analysis imparts more realistic values for laminated composite plate being subjected to dynamic loading.

To determine the temperature dependent elastic and damping properties, a suitable experimental procedure and instrumental setup needs to be implemented. Commonly, a dynamic mechanical analysis (DMA) is used for this purpose. However, the DMA is conducted using only a small sample of laminate within a certain frequency range. Typically, this frequency range is limited as $0 < f \leqslant 100$ Hz. Melo and Radford (2005) used a DMA to identify the temperature and frequency dependent material properties of a IM7-PEEK lamina. Recognizing the importance of conducting an experimental modal analysis of a laminated composite plate to identify the temperature dependent elastic properties, Frederiksen (1992); Sefrani and Berthelot (2006) have conducted such experiments within a thermal environment and suitable minimization techniques, which have been implemented during the identification process. Recently, Li et al. (2019, 2020) have presented a mixed experimental-numerical strategy to identify the temperature dependent material properties of such composites. In their work, the authors fixed the composite plate at one end inside the thermal chamber which may impart extra rigidity to the plate and thus to the identified material properties.

An extensive survey of available literature indicates the importance of the discussed identification strategies based on the experimental data. Moreover, the experimental-modal-analysis-based identification technique is receiving greater attention within the scientific community due to its simplicity and reliability. However, several challenges have been encountered while conducting experimental modal analysis within a thermal chamber, which need to be addressed. Furthermore, studies in this field are very limited. To extent the horizon of the identification of temperature dependent elastic properties of a laminated composite plate, a mixed numerical-experimental procedure has been investigated. Therefore, the work at hand proposes an efficient experimental strategy to investigate laminated composite plate within a thermal chamber and evaluate the temperature dependent elastic properties by utilizing modal data such as modal frequencies. This modal data is evaluated based on measurements. In addition, an exhaustive search optimization technique is implemented to solve this inverse problem, which avoids the numerical complexity of the optimization procedure and evidently achieves the global minimum.

4.2 Theory

To identify the temperature dependent elastic parameters, a mixed experimental-simulation based procedure has been adopted utilizing an inverse approach and experimental modal data at different temperatures. The minimization of the error between simulated and experimental modal data is the core idea of the identification procedure. In this section, the theoretical formulation of the laminated composite plate is discussed.

4.2.1 Plate Theory

An equivalent single layer theory (ESLT) based on the FSDT is used to numerically evaluate eigenfrequencies of a thin laminated composite plate. The dimension of the plate is defined by the length, a, the width, b, and the overall thickness, h. This laminate consists of n numbers of lamina of equal thickness (**Fig. 4.1**). Here, a Cartesian coordinate system (x, y, z) at the mid-plane of the laminate is used to describe the laminate dimensions and the system dynamics. The fiber orientation of an individual lamina is defined by the local lamina coordinate system $(1, 2, 3)$ (**Fig. 4.1**) and the corresponding fiber angle is measured between the local and the global coordinate system, i.e. the angle between 1-axis and x-axis for each lamina, respectively.

According to the FSDT, the mid-plane displacement of a laminate is described as $\mathbf{d} = \{u_0 \quad v_0 \quad w_0 \quad \theta_x \quad \theta_y\}^T$, where u_0 and v_0 are in-plane translations of a com-
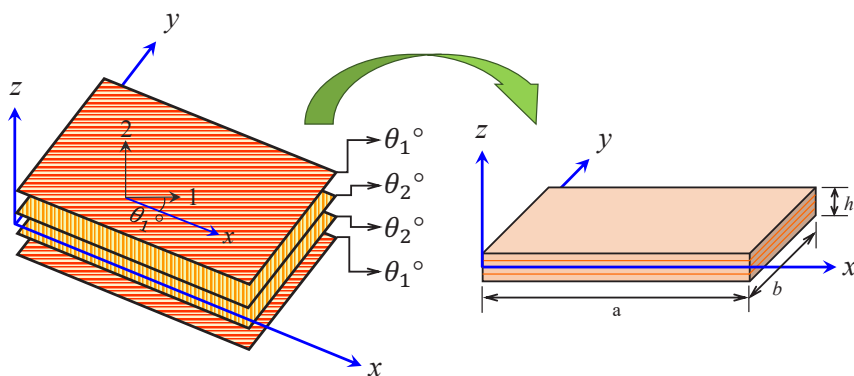
Fig. 4.1: A typical stacking sequence of lamina to form a symmetric angle-ply laminate, $\theta_1^\circ/\theta_2^\circ/\theta_2^\circ/\theta_1^\circ$, with reference to the global coordinate system (x, y, z).

posite plate in the directions of x and y, respectively. The out-of-plane displacement is denoted by w_0 and rotations about x and y axes are presented by θ_x and θ_y. The generalized displacement field of the composite plate at an arbitrary distance z is calculated using the following expressions.

$$
\begin{aligned}
u &= u_0 + z\theta_y, & v &= v_0 - z\theta_x, & w &= w_0, \\
\theta_x &= w_{,y} - \varphi_y, & \theta_y &= -w_{,x} + \varphi_x,
\end{aligned}
\tag{4.1}
$$

where φ_y and φ_x indicate share rotations in the $x - z$ and $y - z$ planes, respectively. In FSDT, a shear correction factor of $\kappa = 5/6$ is used to account for the general nonlinear distribution of shear strains.

With a uniform increment of temperature change, ΔT, above the reference temperature (room temperature), the stress-strain relation for the kth lamina is written as

$$
\sigma_k = \mathbf{Q}_k \{\varepsilon_k - \varepsilon_T\} =
\begin{bmatrix}
Q_{11} & Q_{12} & Q_{16} & 0 & 0 \\
Q_{12} & Q_{22} & Q_{26} & 0 & 0 \\
Q_{16} & Q_{26} & Q_{66} & 0 & 0 \\
0 & 0 & 0 & Q_{44} & Q_{45} \\
0 & 0 & 0 & Q_{45} & Q_{55}
\end{bmatrix}
\{\varepsilon_k - \alpha_k \Delta T\},
\tag{4.2}
$$

where, ε_k and $\varepsilon_T = \alpha_k \Delta T$ are the mechanical strain and the thermal strain vectors, respectively for the kth lamina. Furthermore, the transformed reduced stiffness matrix of the lamina is presented as $\mathbf{Q}_k$ and the corresponding stress vector is indicated as $\sigma_k = \{\sigma_x \ \ \sigma_y \ \ \tau_{xy} \ \ \tau_{xz} \ \ \tau_{yz}\}_k^T$ (Niyogi et al., 1999). Here, the matrix $\mathbf{Q}_k$ is developed based on the elastic parameters of the lamina, i.e., E_{11}, E_{22}, G_{12}, G_{13}, G_{23}, ν_{12} and ν_{21}. Due to the transversely isotropic property of the lamina, the relationship between elastic properties of G_{12}, G_{13}, G_{23}, G_{12}, ν_{21} and ν_{12} can be set based on theoretical concepts or suitable measurements (Reddy, 2001; Daniel and Ishai, 1994; Tsai and Daniel, 1990; Knight, 1982; Altenbach et al., 2018; Frederiksen, 1997b). Thereby, E_{11}, E_{22}, G_{12}, and ν_{12} appear as principle elastic parameters of the orthotropic lamina. In addition, the coefficient of thermal expansion, α_k, is expressed in laminate coordinate system (x, y, z) as

$$
\alpha_k = \{\alpha_x \ \ \alpha_y \ \ \alpha_{xy} \ \ 0 \ \ 0\}_k^T,
\tag{4.3}
$$

and the stress-resultant vector, $\mathbf{F}_r = \{N_x \ N_y \ N_{xy} \ M_x \ M_y \ M_{xy} \ Q_x \ Q_y\}^T$, of the composite is obtained by integrating the lamina stress over the thickness and takes the compact form as

$$
\mathbf{F}_r = \mathbf{D}\{\varepsilon^* - e^*\} =
\begin{bmatrix}
\mathbf{A} & \mathbf{B} & \mathbf{0} \\
\mathbf{B} & \mathbf{D} & \mathbf{0} \\
\mathbf{0} & \mathbf{0} & \bar{\mathbf{A}}
\end{bmatrix}
\varepsilon^* -
\begin{Bmatrix}
\mathbf{N_T} \\
\mathbf{M_T} \\
\mathbf{Q_T}
\end{Bmatrix}.
\tag{4.4}
$$

Here, ε^* and e^* represent the mid-plane strain vector and the mid-plane thermal strain vector of the composite laminate. The components of the stress-resultant and the mid-plane strain vector relationship matrix, $\mathbf{D}$, are expressed as

$$(\underline{\mathbf{A}}, \underline{\mathbf{B}}, \underline{\mathbf{D}}) = \int_{-h/2}^{h/2} Q_{ij}(1, z, z^2)dz, \quad i, j = 1, 2, 6,$$

$$\bar{\mathbf{A}} = \kappa \int_{-h/2}^{h/2} Q_{ij}dz, \quad i, j = 4, 5; \quad \kappa = 5/6. \tag{4.5}$$

For a general case, the solution of the well-known conservation equations of continuum mechanics together with the above discussed constitutive relations must fulfill boundary and initial conditions, which hardly exists in a closed form. Therefore, state-of-the-art numerical methods have been utilized that are briefly discussed in the subsequent section. At this point, it must be mentioned that the influence of the resultant thermal stress vector, $\{\mathbf{N_T} \quad \mathbf{M_T} \quad \mathbf{Q_T}\}^{\mathrm{T}}$ in Eq. (4.4) can be neglected when conducting a numerical analysis with free-free boundary conditions, which is the case for the work at hand.

4.2.2 Numerical Methods

The plate domain is divided into a number of finite elements, which is the basic idea of the finite element method (FEM) in order to compute the dynamics of the laminated composite. A 2-dimensional eight-node element with five degrees of freedom (DOFs), i.e. u_0, v_0, w_0, θ_x, and θ_y, at each node is used for the FE analysis. Here, the ESLT, as explained before, is used and implemented for the FE analysis to investigate the plates modal properties.

The governing equations for small deformation problems in an elastic continuum are derived by the minimization of the total potential and kinetic energies. Accordingly, these equations for the free vibration under a thermal environment are stated as

$$\left([\mathbf{K} + \mathbf{K_G}] - \omega_{\text{num}}^2 \mathbf{M}\right)d = 0, \tag{4.6}$$

which reassembles a system of equations. Here, the stiffness matrix, $\mathbf{K}$, of the plate that provides the interaction of n_e elements is expressed as

$$\mathbf{K} = \sum_{i=1}^{n_e} \int_{A_e} \mathbf{B}^{\mathrm{T}}\mathbf{D}\mathbf{B}dA_e, \tag{4.7}$$

where A_e indicates the surface area of the corresponding element and $\mathbf{B}$ is the strain-displacement matrix Niyogi et al. (1999); Das and Niyogi (2020). The geometric stiffness matrix, $\mathbf{K_G}$, is given as

$$\mathbf{K}_G = \sum_{i=1}^{n_e} \int\limits_{A_e} \mathbf{G}^T \mathbf{S}_r \mathbf{G} dA_e, \tag{4.8}$$

where $\mathbf{S}_r$ denotes the initial stress-stiffness matrix due the thermal pre-stressing effect and $\mathbf{G}$ is the corresponding shape function matrix (Chandra et al., 2019; Das and Niyogi, 2020). The mass matrix, $\mathbf{M}$, is written as

$$\mathbf{M} = \sum_{i=1}^{n_e} \int\limits_{A_e} \mathbf{N}^T \bar{\mathbf{M}} \mathbf{N} dA_e, \tag{4.9}$$

where, $\mathbf{N}$ is the shape function matrix which relates $\mathbf{d}$ and the elemental mid-plane displacement vector, $\mathbf{d}_e$, as $\mathbf{d} = \mathbf{N}\mathbf{d}_e$, and $\bar{\mathbf{M}}$ is the inertia matrix (Chandra et al., 2019). The eigenvalue solution of Eq. (4.6) imparts the numerically evaluated modal frequencies, $\omega_{num,m}$, of the laminated composite plates within the thermal environment.

The widely known commercially available FE software, ANSYS, is utilized to calculate the modal frequencies in the thermal environment. A user defined FE code is written in ANSYS parametric design language (APDL) applying the eight-node shell element 'SHELL281' of the ANSYS element library. In a first step, a static analysis is conducted to consider the thermal effect in the laminated composite plate which is included as a pre-stressing force. These forces are then included in a second step in which the modal analysis is considered to compute the eigenvalues and associated mode shapes.

4.2.3 Operational Modal Analysis

Since the 1990's, the operational modal analysis (OMA) has constantly gained increasing interest among engineers for experimentally investigating the structural dynamics of complex and large systems (Zhang and Brincker, 2005). Originally, it was intended to analyzing large structures such as building, bridges, off-shore platforms, and towers, where natural conditions serve as excitation mechanisms. In contrast to the wider known experimental modal analysis (EMA), where both the excitation as well as the system responses are measured (Ewins, 2000), the OMA procedure only requires the knowledge of system responses only. This way, a number of advantages can be stated with respect to the EMA method (Zhang and Brincker, 2005):

- OMA is cheap and fast to conduct.
- It is possible to investigate complex structures.
- Systems under operational conditions can be analyzed.

In addition to the advantages when conducting measurements under operational conditions, the OMA can be utilized within laboratory conditions, where the ex-

citation with its special requirements can be synthesized. This way, it is possible to construct various operational conditions under which the structure is investigated.

In this work, a white noise excitation serves as a suitable load, whereas a number of DOFs are measured sequentially. For this reason, each DOF measurement possesses a unique references signal which can be handled by the utilized OMA algorithm. The algorithm is constructed as a stochastic subspace identification (SSI) procedure, where the parametric model is directly fitted to the raw time data of each DOF measurement. This identification method can be written in a generalized form as:

$$\hat{x}_{t+1} = A\hat{x}_t + Ke_t, \tag{4.10}$$
$$y_t = C\hat{x}_t + e_t, \tag{4.11}$$

where the matrix, A, contains the physical information, the matrix, C, extracts the information from the system response, and the K-matrix contains statistical information. In addition, the vector, e_t, represents measurement noise and $\hat{x}_t$ reassembles the discrete state vector. Finally, y_t denotes the sampled output vector, i.e. the measurements (Peeters and De Roeck, 2001; Au, 2017). As the theory is well known and state of the art, the authors refer to Au (2017); Brincker and Ventura (2015); Zhang and Brincker (2005); Peeters and De Roeck (2001) for deeper insight. For analyzing the measured date, the software OMA Pulse 22 distributed by Brüel & Kjær is utilized, which provides the SSI algorithm.

The obtained results consist of modal parameters such as the eigenfrequencies, the mode shapes, and modal damping values. In this work, the authors utilize the eigenfrequencies, $f_{m,exp}$, as part of an optimization procedure which is discussed in the following section.

4.2.4 Optimization Strategy

To calculate the temperature dependent elastic moduli of the laminated composite plates, a suitable optimization strategy is implemented. The core idea of the optimization strategy is to minimize the error between experimentally evaluated modal responses and numerically simulated modal responses by adjusting the elastic parameters at different temperature, and thus identify the temperature dependent elastic moduli. The numerically predicted modal responses are expressed in terms of the modal frequencies, $f_{m,num}$, i.e. $\omega_{m,num}/2\pi$. Similarly, the experimental modal frequencies, $f_{m,exp}$, are obtained from the operational modal analysis.

Assuming $\bar{r}$ as the identified parameters, the optimization problem is defined as

$$\begin{aligned} &\text{Minimize}: \ \mathcal{C}(\bar{r}) \\ &\text{subjected to}: \ \bar{r}_{min} < \bar{r} < \bar{r}_{max}, \end{aligned} \tag{4.12}$$

where

$$\mathcal{C}(\mathbf{\bar{r}}) = \sum_{m=1}^{N_m} \left(\frac{f_{m,exp} - f_{m,num}}{f_{m,exp}} \right)^2. \tag{4.13}$$

Here, the number of modal frequencies considered to develop the cost function, $\mathcal{C}(\mathbf{\bar{r}})$, is represented by N_m. In this study, three principle elastic parameters, i.e., E_{11}, E_{22}, and G_{12} are identified. To follow the physical relationship between the elastic parameters of laminated composite plates, the identified parameters are expressed by $\mathbf{\bar{r}} = \{E_{11} \quad E_{11}/E_{22} \quad E_{22}/G_{12}\}$. The sensitivity of the Poisson's ratio, ν_{12}, is negligible and therefore excluded in the identification process. The density, ρ, of the composite plate has been determine experimentally by knowing the plate geometry and mass of the plate with a satisfactory precision.

A brute-force search or exhaustive search optimization technique is implemented for the elastic property identification. Considering a suitable step size, a sufficiently large number of $\mathbf{\bar{r}}$ values are generated within a physically valid domain, $\mathbb{R}^d$, such that $(\mathbf{\bar{r}}_{min}, \mathbf{\bar{r}}_{max}) \in \mathbb{R}^d$, and combined them to develop a set of parameters as $[\mathbf{\bar{r}_1} \quad \mathbf{\bar{r}_2} \quad ... \quad \mathbf{\bar{r}_n}]^\top$. Subsequently, based on the parameter set cost functions, $\mathcal{C}(\mathbf{\bar{r}})$, the parameter configuration, $\mathbf{\bar{r}}$, which minimizes the cost function is considered as the sought material parameter set. The main advantage of implementing an exhaustive search optimization technique in this problem is that it achieves the global minimum. Henceforth, the temperature dependent elastic moduli of the composite plate are calculated after suitable manipulation on the identified parameters. The exhaustive search optimization is carried out using a MATLAB routine, linked with APDL as a solver. The analysis framework is understood best by viewing it in a flowchart (**Fig. 4.2**), which presents the link between the MATLAB script and the ANSYS solver. As an example, a typical MATLAB script to link the solver is given below:

```
1  %% MATLAB script to execute APDL script.
2  % APDL script as a slover: inputAPDL.txt
3  % Output file: FreqOupout.txt
4  % Location of ANSYS executable file: "C:\Program Files\ ... "
5
6  system('set ANS_CONSEC=YES & set ANSYS_LOCK=OFF & SET
       KMP_STACKSIZE = 4096k & "C:\Program Files\ANSYS Inc\v193\
       ansys\bin\winx64\ansys2019R1.exe" -b -p ANSYS -i inputAPDL.
       txt -o FreqOupout.txt -smp -np2');
```

4.3 Measurements and Simulations

An experimental modal analysis of a laminated composite plate has been conducted to evaluate the experimental modal frequencies within a thermal chamber at different temperatures, which is explained in more detail in the subsequent outlines.
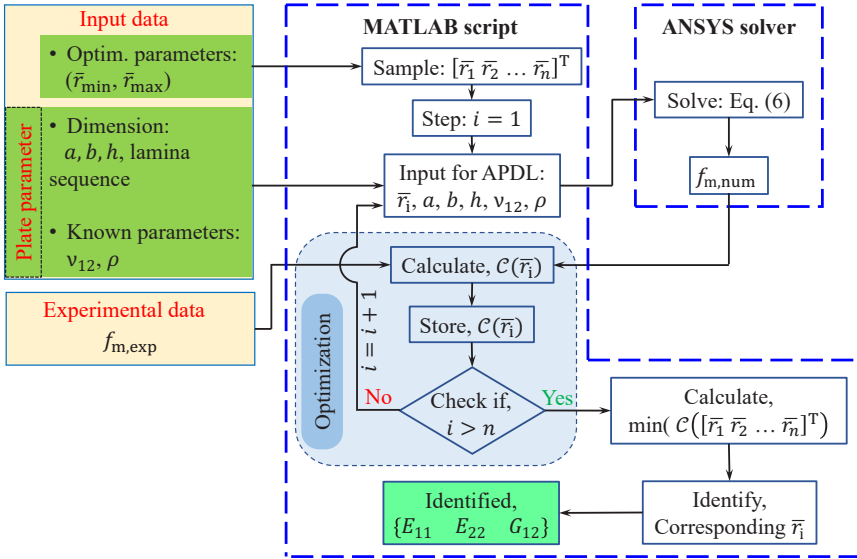
Fig. 4.2: Analysis framework showing interface between MATLAB and ANSYS solver.

4.3.1 Measurement Setup

The measurement setup consists of a thermal chamber, in which a carbon-epoxy laminated composite plate has suspended through elastic strings. Note that the elastic strings where mounted in the nodal lines of the first principle deflection shape of the plate. This way, it was possible to realize a free-free boundary condition. The plate has been exited with a white-noise sound signal generated from a loudspeaker which has been placed at the corner of the thermal chamber. Two laser doppler vibrometers (LDVs) are used to measure the vibration of the composite plate through windows, covered with glass plates, at the two opposite walls of the thermal chamber. One LDV scanned the vibrating of the plate (i.e., scanning LDV), and the other LDV measurement position remained fixed, which served as a phase reference (i.e., reference LDV). During the experiment, controlling the input, i.e., white noise, and collecting measured data have been done through a data acquisition (DAQ) system. A sufficient large time responses at each measurement point was collected. A schematic diagram (**Fig. 4.3**) of the measurement setup provides an overview of the overall setup. The internal temperature of the thermal chamber has been set to a constant value during the measurement operation. Therefore, a sequential measurement procedure was possible.
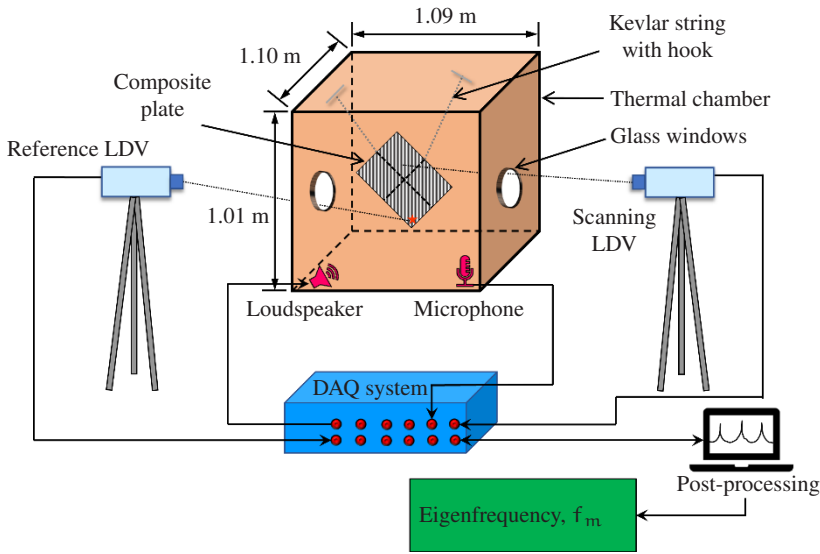
Fig. 4.3: Measurement setup with Laser Doppler Vibrometer (LDV); PDV100 as reference LDV, PSV500 as scanning LDV (Polytec GmbH, Waldbronn, Germany).

4.3.2 Test Sample

A 14-layered symmetric cross ply laminated composite plate, $(45°/-45°)_{7s}$, made out of unidirectional T700 carbon fiber-epoxy is used as the sample structure. To idealized a free-free boundary condition, the composite plate is suspended diagonally through Kevlar wires, as shown in **Fig. 4.3**. Moreover, the dimension of the plate has been selected wisely, so that the acoustic cavity together with its corresponding acoustic resonances could be considered as a high frequency regime. This way, the required uncorrelated excitation to conduct the OMA was satisfied. In contrast, the size of the structure was relatively small. Therefore, the lowest structural vibration resonances where excited by the acoustic excitation. The dimensions of the plate are $(150 \times 110 \times 4.018)$ mm. The Measurements on the vibrating plate are carried out over a temperature range that varied between $0°$C and $125°$C with temperature increments of $25°$C. Moreover, a 0% humidity level has been maintained during the experimental study. The density, ρ, of the laminated composite plate is considered as 1603.7 kg/m^3. Poisson's ratio, ν_{12}, is assumed as temperature independent with a value of 0.32.

4.3.3 Numerical Model

The carbon-epoxy composite plate which is used as a sample structure during experimental study is numerically model by 2-dimensional FEM. The commercially available FE software ANSYS is used for this purpose in which the eight-node shell element 'SHELL281' of the ANSYS element library was utilized. Within this eigenvalue analysis, the modal data in terms of eigenfrequencies and corresponding mode shapes have been computed. The theoretical background of the FEM for analyzing a laminated composite plate is described in Sects. 4.2.1 and 4.2.2. The geometry and known parameters of the plate are stated in previous subsection.

For the underlying FE model, the plate is discretized with a 8×7 element mesh for which a free-free boundary condition was assumed. Consequently, the numerically obtained first six rigid modes are neglected while accounting the first six deformation mode shapes in the optimization algorithm.

4.4 Results

The experimentally obtained modal frequencies at prescribed temperatures are presented here. Further, these modal frequencies are used to identify the temperature dependent elastic properties of the experimented carbon-epoxy composite plate.

4.4.1 Experimental Results and Analysis

A T700-carbon fiber-epoxy laminated composite plate was excited by a white noise sound signal inside the thermal chamber at different temperatures, and a scanning LDV measured the structural vibration of the plate. The experimental setup inside the thermal environment is shown in **Fig. 4.3**, where the plate is suspended through the elastic string which simulate the free-free boundary condition. Measurements have been conducted at every DOF on the plate for a duration of 50 s and the corresponding time responses were stored using the DAQ system. The post-processing of the raw time data had been carried out with the use of the Brüel & Kjær Software OMA Pulse 22 to conduct the operational modal analysis and to evaluate the modal results such as eigenfrequencies and mode shapes of the composite plate.

In order to analyze the temperature dependent material behavior, a set of six different temperature conditions, namely at $0°C$, $25°C$, $50°C$, $75°C$, $100°C$, and $125°C$ have been realized within the climate chamber. Before initiating the measurement, the temperature and humidity inside the thermal chamber was controlled through an automatic controller, where a delay time of 10 min has been set to achieve equilibrium condition.

The experimentally obtained modal frequencies at each temperature for the symmetric angle-ply laminated composite plate are plotted in **Fig. 4.4**a. To understand

(a)   (b)
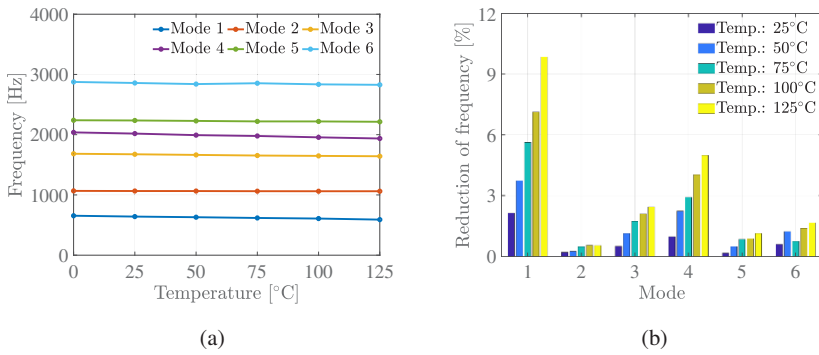
Fig. 4.4: (a) Experimental modal frequencies at different temperature; (b) percentage of reduction of modal frequencies, $\Delta_{exp,m}^{(j)}$, at different temperature with respect to the modal frequencies at $0°C$ for symmetric angle-ply laminate $(45°/-45°)_{7s}$ at different temperatures.

the trend of the variation of the modal frequencies with increasing temperature, a comparative bar chart is shown in **Fig. 4.4**b. The percentage of the reduction of the modal frequencies at 25°C, 50°C, 75°C, 100°C, and 125°C temperatures are depicted. Here, the obtained eigenfrequencies at 0°C have been used as the reference and the relative estimate of the eigenfrequency reduction has been calculated as

$$\Delta_{exp,m}^{(j)} = \frac{f_{exp,m}^{(j)} - f_{exp,m}^{(0)}}{f_{exp,m}^{(0)}}, \quad \text{where} \quad j = 25°, 50°, 75°, 100°, \text{ and } 125°C. \quad (4.14)$$

The first five modes clearly show a decreasing trend of the modal frequency with increasing temperature. Furthermore, the rate of reduction of the first modal frequency is significantly large as compared to the other modes. The modes 2 and 3 exhibit some exception of the trend at the temperature between 100°C and 125°C, and 50°C and 75°C, respectively.

The associated mode shapes obtained by the operational modal analysis at 0°C are shown in **Fig. 4.6** in the Appendix. At this point, it is not clear, why mode 1, 3, and 4 show a significant higher dependency on the temperature changes than the remaining modes. The investigation of this behavior is subject of future research.

4.4.2 Identified Elastic Properties

The modal frequencies which are evaluated based on experimental data and shown in **Fig. 4.4** are used in a process for material parameter identification. This process includes two different mode set combinations. Here, the modal frequencies with combinations of (a) 1 to 3 and (b) 1 to 6 are considered to evaluate the cost function

within the optimization strategy. The results of this parameter identification for each set of mode combination are shown in **Table 4.1**. It can be seen that the variation of E_{11} with increasing temperature is rather insignificant. With increasing temperature, E_{22} obtained from modes 1 to 3 shown an overall deteriorating tendency except a small peak at $100°C$. In the second set where the modes $1 - 6$ are taken into account, the authors believe that an over-determined system exists, which results in an un-physical behavior of the material properties with respect to temperature. For this reason, sudden changes in the material parameters can be noticed at $75°C$ and $125°C$ for E_{22}. Here, a less strictly decreasing behavior was expected. In contrast, the identified temperature dependent shear modulus, G_{12}, has shown a decreasing trend with the increasing temperature for both types of modal contributions.

It is of interest to evaluate the accuracy of the identification. This verification of the results is performed by calculating the relative error in percent between the experimental modal frequencies and simulated modal frequencies based on the identified elastic parameters (**Table 4.1**). The calculated errors of discrepancy at all temperatures are shown in **Fig. 4.5**. It can be seen that the differences between experimental and numerical frequencies are very small and overall remain below 1%. This level of accuracy is maintained for the modes which are not participate for the identification, i.e., for the first set of identification results using modes 1 to 3. This indicates the accuracy of identified elastic parameters and adopted optimization techniques. By adopting the identified elastic properties of the composite plates (modes 1 to 3) at $0°C$, it was possible to compute the mode shapes numerically using ANSYS, which are shown in **Fig. 4.7** in the Appendix. It is evident that the numerically simulated mode shapes are similar with those obtained from OMA (see, **Fig. 4.6**). Both facts, i.e. low errors between numerical and experimental calculated

Table 4.1: Identified temperature dependent elastic moduli of T700carbon-epoxy lamina considering the modal frequencies (experimental and simulated) ranges between 1 to 3 and 1 to 6 for the symmetric angle-ply laminate $(45° / - 45°)_{7s}$.

Contributing modes	Temp. [°C]	Identified elastic moduli [GPa]		
		E_{11}	E_{22}	G_{12}
1 to 3	0	129.26	9.65	5.85
	25	129.80	9.41	5.53
	50	130.68	8.27	5.33
	75	130.88	7.88	5.09
	100	130.80	8.07	4.89
	125	131.96	7.76	4.57
1 to 6	0	128.58	10.20	5.83
	25	129.12	9.93	5.52
	50	129.68	8.76	5.31
	75	129.08	10.08	5.04
	100	131.02	7.80	4.87
	125	130.96	8.85	4.54
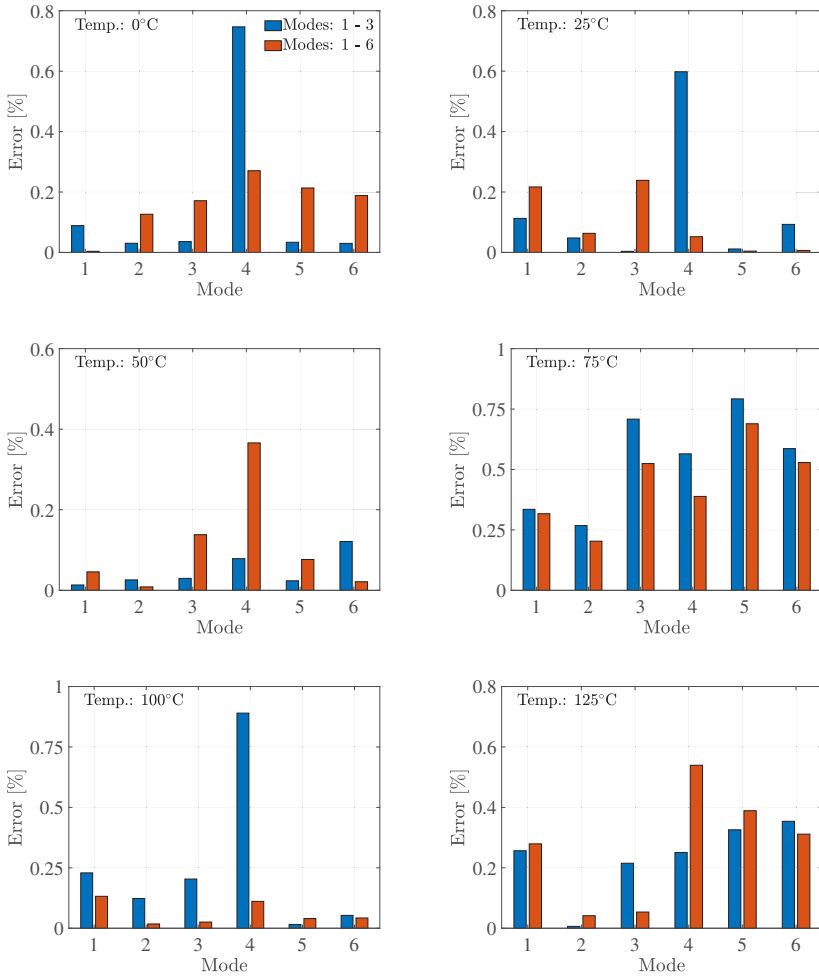
Fig. 4.5: Percentage of error between experimental and simulated eigenfrequencies at different temperature.

eigenfrequencies as well as matching of mode shapes proves the accuracy of the identified elastic properties of the carbon-epoxy laminated composite plate.

4.5 Conclusion

The identification of the temperature dependent elastic properties of carbon-epoxy laminated composite plate is presented here. The identification is carried out using an inverse process based on the experimental modal frequencies. The experiment has been conducted within a thermal chamber at different temperature conditions ranging from $0°C$ to $125°C$ with an $25°C$ interval. An exhaustive search optimization technique is implemented to identify the elastic properties. The minimization of the error between experimental and numerical modal frequencies are the key idea of the identification process. Furthermore, using the exhaustive search optimization method leads to the global minimum which is confirmed by the accuracy of the elastic properties; though it is computationally expensive. Two sets of modal contributions, i.e., 1 to 3 and 1 to 6 are accounted during the optimization process. It has been found that the experimental modal frequencies are temperature dependent, and the first modal frequencies are shown higher sensitivity with the variation of the temperature. Furthermore, the identified elastic properties of the carbon-epoxy lamina vary with temperature. However, this variation is insignificant for the E_{11} parameter. The temperature dependent shear modulus, G_{12} have shown an inverse variation with the increasing temperature.

In summary, utilizing a contact free excitation and measurement procedure within a climate chamber together with an OMA of the raw time data gives reliable modal estimates that serve as a basis for an inverse material parameter identification. In this identification an exhaustive optimization has been carried out with the use of adequate FE simulations. This way, it was possible to achieve high accuracies of the identified material parameters under dynamic loading of the underlying composite plate. The presented method is easy to implement and has the potential for future improvements with respect to time and computational cost.

4.6 Appendix

4.6.1 Mode Shapes of OMA

(a) Mode 1

(b) Mode 2

(c) Mode 3

(d) Mode 4

(e) Mode 5
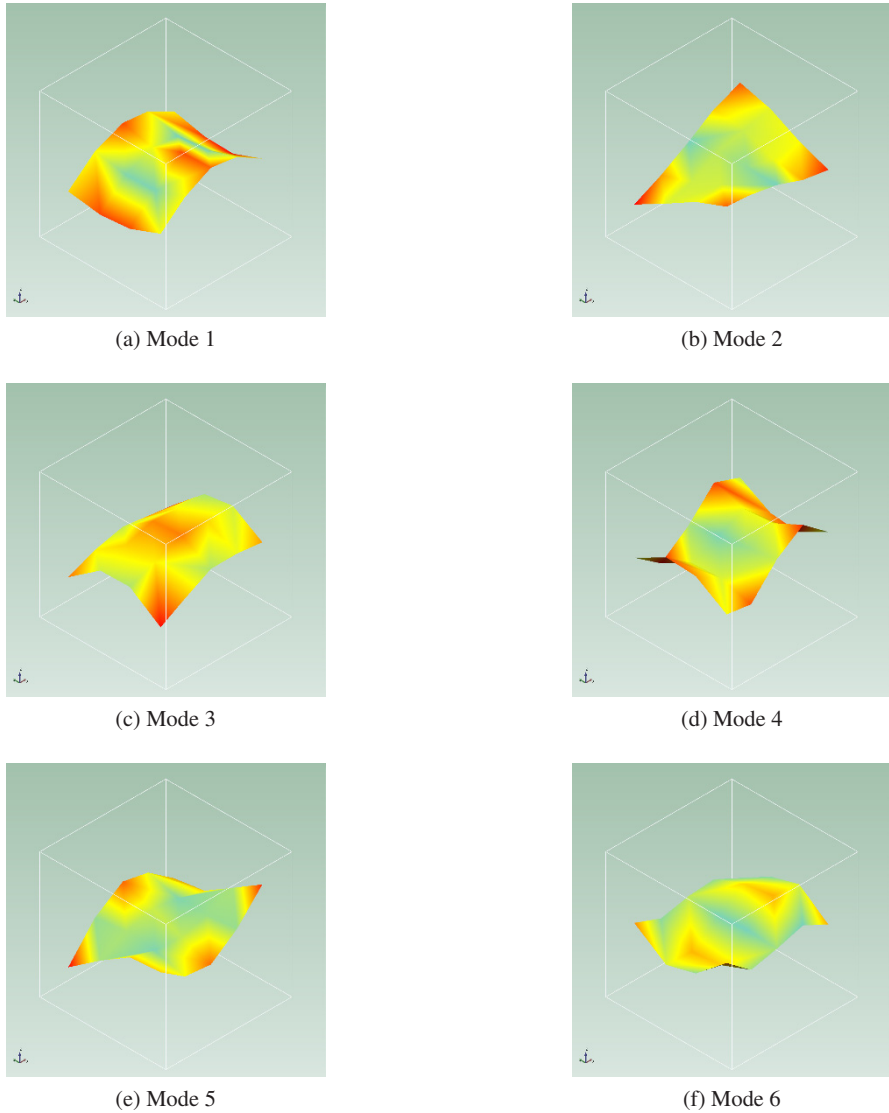
(f) Mode 6

Fig. 4.6: Mode shapes of OMA with (a) Mode 1 to (f) Mode 6 at $0°C$; All off diagonals in MAC-Matrix less than 0.01.

4.6.2 ANSYS *Simulated Mode Shapes*

(a) Mode 1

(b) Mode 2

(c) Mode 3

(d) Mode 4

(e) Mode 5
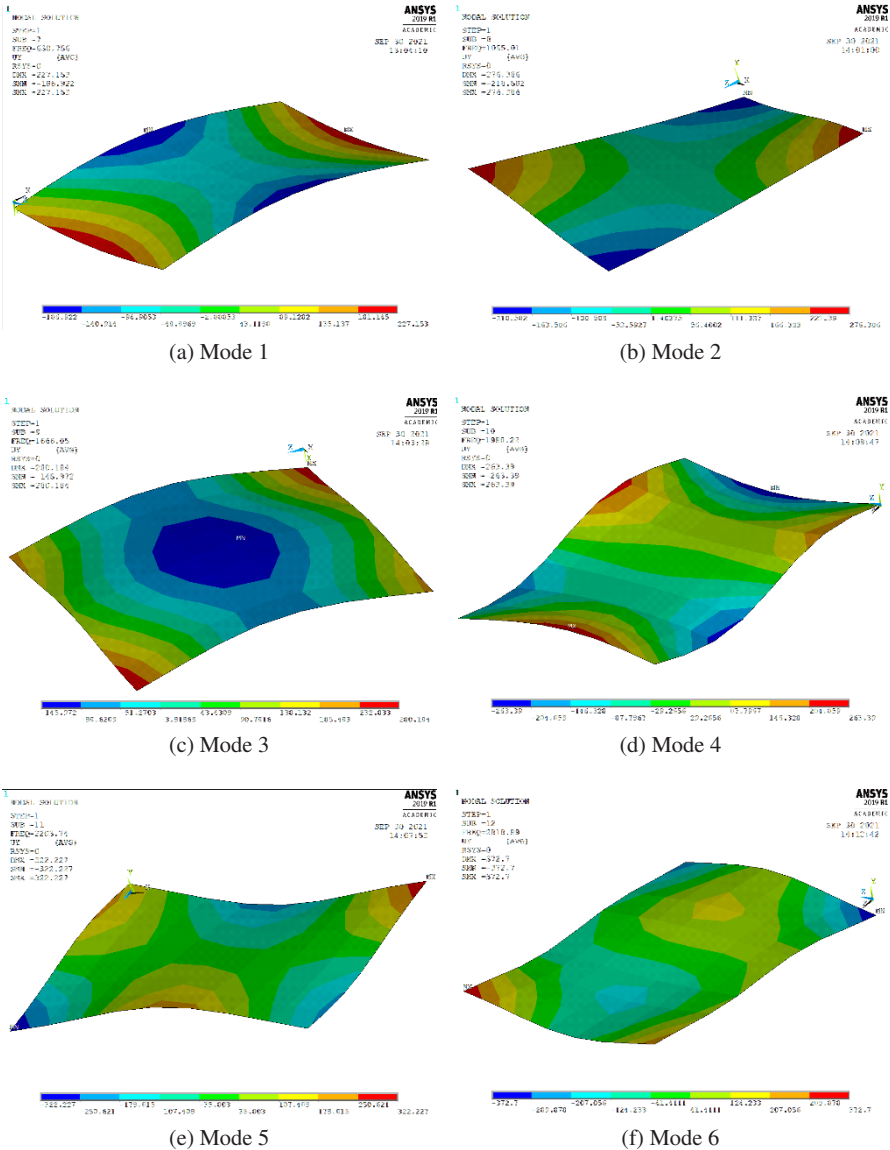
(f) Mode 6

Fig. 4.7: Mode shapes obtained from ANSYS simulation from (a) Mode 1 to (f) Mode 6 at 0°C.

References

Adams RD, Bacon DGC (1973) Effect of fibre orientation and laminate geometry on the dynamic properties of CFRP. Journal of Composite Materials 7(4):402–428

Altenbach H, Altenbach J, Kissing W (2018) Mechanics of Composite Structural Elements. Springer, Singapore

Au SK (2017) Operational Modal Analysis. Springer Singapore, Singapore, DOI 10.1007/978-981-10-4118-1

Brantseva TV, Antonov AV, Gorbatkina YA, Kerber ML (1999) Behaviour of polymer - fiber interface under various loading rates. In: Proceedings of the ICCM-12, paper 426, pp 1–8

Brincker R, Ventura C (2015) Introduction to operational modal analysis. John Wiley & Sons

Chandra S, Sepahvand K, Matsagar VA, Marburg S (2019) Stochastic dynamic analysis of composite plate with random temperature increment. Composite Structures 226:111,159

D3039/D3039M (2017) Standard test method for tensile properties of polymer matrix composite materials. Tech. rep., ASTM International, West Conshohocken, PA 19428-2959, U.S.

D4255/D4255M (2020) Standard test method for in-plane shear properties of polymer matrix composite materials by the rail shear method. Tech. rep., ASTM International, West Conshohocken, PA 19428-2959, U.S.

Daniel IM, Ishai O (1994) Engineering Mechaincs of Composite Materials. Oxford University Press, New York

Das S, Niyogi AG (2020) Free-vibration analysis of epoxy-based cross-ply laminated composite folded plates subjected to hygro-thermal loading. Journal of The Institution of Engineers (India): Series C 101(3):541–557

Ewins DJ (2000) Modal Testing: Theory, Practice and Application, 2nd edn. Wiley

Frederiksen PS (1992) Identification of temperature dependence for orthotropic material moduli. Mechanics of Materials 13(1):79–90

Frederiksen PS (1997a) Application of an improved model for the identification of material parameters. Mechanics of Composite Materials and Structures 4(4):297–316

Frederiksen PS (1997b) Experimental procedure and results for the identification of elastic constants of thick orthotropic plates. Journal of Composite Materials 31(4):360–382, DOI 10.1177/002199839703100403

Gay D (2014) Composite Materials: Design and Applications, Third Edition. CRC Press, New York

Knight M (1982) Three-dimensional elastic moduli of graphite/epoxy composites. Journal of Composite Materials 16(2):153–159

Lecompte D, Smits A, Sol H, Vantomme J, Van Hemelrijck D (2007) Mixed numerical-experimental technique for orthotropic parameter identification using biaxial tensile tests on cruciform specimens. International Journal of Solids and Structures 44(5):1643–1656

Li H, Wu H, Zhang T, Wen B, Guan Z (2019) A nonlinear dynamic model of fiber-reinforced composite thin plate with temperature dependence in thermal environment. Composites Part B: Engineering 162:206–218

Li H, Wu T, Gao Z, Wang X, Ma H, Han Q, Qin Z (2020) An iterative method for identification of temperature and amplitude dependent material parameters of fiber-reinforced polymer composites. International Journal of Mechanical Sciences 184:105,818

Melo JDD, Radford DW (2005) Time and temperature dependence of the viscoelastic properties of CFRP by dynamic mechanical analysis. Composite Structures 70(2):240–253

Mi Y, Zhu C, Li X, Wu D (2020) Acoustic emission study of effect of fiber weaving on properties of fiber-resin composite materials. Composite Structures 237:111,906

Mota Soares CM, de Freitas MM, Araújo AL, Pedersen P (1993) Identification of material properties of composite plate specimens. Composite Structures 25(1):277–285

Ni RG, Adams RD (1984) The damping and dynamic moduli of symmetric laminated composite beams - theoretical and experimental results. Journal of Composite Materials 18(2):104–121

Niyogi AG, Laha MK, Sinha PK (1999) Finite element vibration analysis of laminated composite folded plate structures. Shock and Vibration 6(5-6):273–283

Peeters B, De Roeck G (2001) Stochastic System Identification for Operational Modal Analysis: A Review. Journal of Dynamic Systems, Measurement, and Control 123(4):659–667, DOI 10.1115/1.1410370

Reddy JN (2001) Mechanics of Laminated Composite Plates and Shells: Theory and Analysis, 2nd edn. CRC Press, London, UK

Rikards R, Chate A, Steinchen W, Kessler A, Bledzki AK (1999) Method for identification of elastic properties of laminates based on experiment design. Composites Part B: Engineering 30(3):279–289

Saravanos DA, Chamis CC (1989) Unified micromechanics of damping for unidirectional fiber reinforced composites. Tech. rep., NASA

Sefrani Y, Berthelot JM (2006) Temperature effect on the damping properties of unidirectional glass fibre composites. Composites Part B: Engineering 37(4):346–355

Tsai CL, Daniel IM (1990) Determination of in-plane and out-of-plane shear moduli of composite materials. Experimental mechanics 30(3):295–299

Zhang L, Brincker R (2005) An overview of operational modal analysis: major development and issues. In: Proceedings of the 1st International Operational Modal Analysis Conference, April 26-27, 2005, Copenhagen, Denmark, Aalborg Universitet, pp 179–190

Zhou J, Chui YH, Gong M, Hu L (2017) Comparative study on measurement of elastic constants of wood-based panels using modal testing: choice of boundary conditions and calculation methods. Journal of Wood Science 63(5):523–538

Chapter 5
Unilateral Constraints and Multibody Dynamics

Friedrich Pfeiffer

Abstract Constraints are the most important design elements of all moving mechanical systems. They decide about the structure of the system allowing its components only certain directions of free motion. Most applications deal with smooth constraints and thus with no interruption of the smooth flow of motion. Mechanical systems with contacts, being able to be open or closed, do not possess this property. Motion might be interrupted, be it as a wanted design element, be it as suddenly appearing constraints, or be it as a consequence of unavoidable tolerance effects in all machine interconnections. Chapter will give some review about the dynamics of such systems, theoretically and practically.

5.1 Introduction

Multibody systems are interconnected rigid or elastic bodies with bilateral or unilateral interconnections, being defined by kinematic constraints. Very often underestimated, the constraints decide about the structure of a machine or a mechanism much more than the bodies. They tell mechanical systems, where to go thus enabling free motion where it is wanted and where it is needed. **Figure 5.1** depicts the possibilities.

Graph (a) illustrates a constraint surface where motion has to take place, a classical concept characterized by tangential manifolds of the constraints themselves and Riemann space properties. Graph (b) shows an interconnection by force laws, a case we shall not discuss here, but which is of some importance in practical descriptions of machines. Finally, graph (c) depicts the situation of a unilateral constraint in the form of a contact, which is open showing relative distance and no constraint force. This case and friction problems will be matter of the following chapter.

Friedrich Pfeiffer
Lehrstuhl Angewandte Mechanik, TU München, 85747 Garching, Germany,
e-mail: friedrich.pfeiffer@tum.de

(a) *constraint surface - bilateral case*

(b) *multibody interconnection by force law*

(c) *contact features - unilateral case*
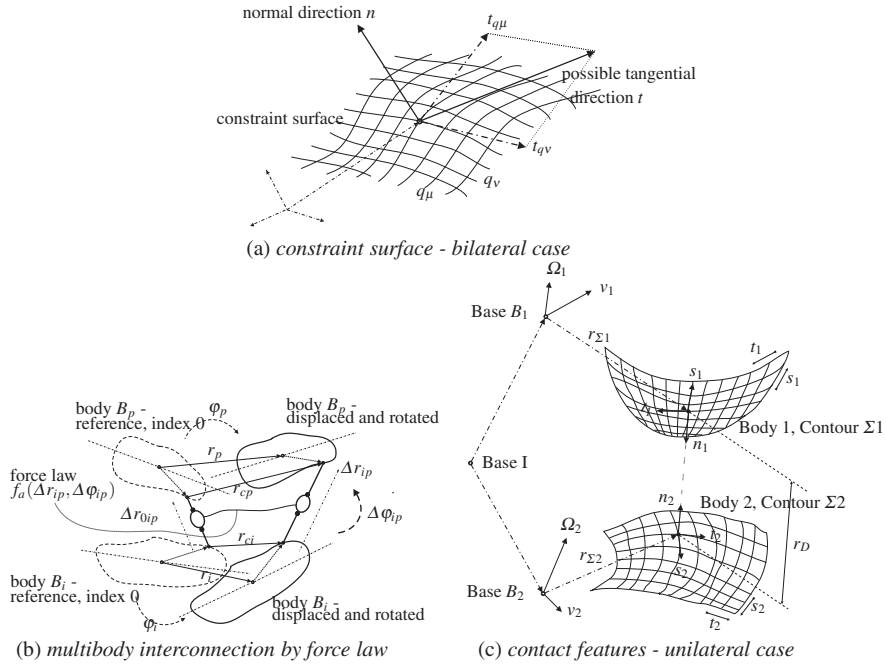
Fig. 5.1: Constraints and interconnections form the structure of mechanical systems.

Classical multibody system theory is well established, kinematics and dynamics are smooth, see, for example, Shabana (2013); Bremer (2008); Pfeiffer (2008); Woernle (2016). Very fundamental and general aspects are given in Papastavridis (2002), and an excellent kinematical basis is presented by Wittenburg (2016).

Unilateral constraints appear with contacts between rigid or elastic bodies. Contacts may be closed, and the contact partners may detach again. Within a closed contact we might have sliding or sticking, both connected with local friction. If two bodies come into contact, they usually penetrate into each other leading to local deformations. If contacts are accompanied by tangential forces and by tangential relative velocities within the contact plane, we get in addition to normal also tangential deformations. Depending on the dynamical (or statical) environment contacts may change their state, from closure to detachment, from sliding to sticking, and vice versa. We call a contact active, if it is closed or if we have stiction, otherwise we call a contact passive.

The birth of non-smooth mechanics mainly took place in France, Italy and Greece, in the second half of the last century. Fathers of this development are Moreau in Montpellier (Moreau, 1988) and Panagiotopoulos in Thessaloniki (Panagiotopoulos, 1993). The crucial step to a set-theoretical formulation was done by Alart and Curnier (1991). Their theory reduced computer time drastically for the price of diminishing mechanical transparency. An excellent presentation of the

whole field is given by Brogliato (1999), and very good introduction to the set-theoretical background of non-smooth dynamics give the books of Glocker (2001); Leine and Nijmeijer (2004).

At the author's Institute and pushed by practical problems non-smooth theories were applied for large multibody systems with many contact connections (Pfeiffer and Glocker, 1996; Pfeiffer, 2008). Glocker (2001) introduced the concept of "set-valued" forces, which is adequate for non-smooth problems due to the friction cone properties. Large multibody systems with unilateral constraints automatically generate large numerical problems, which were successfully treated by Foerg et al. (2006); Foerg (2007) giving an efficient solution of the constraint prox-formulation. Currently this seems to be the best solution concept for large non-smooth multibody systems.

5.2 Concepts of Dynamics

5.2.1 Bilateral Dynamics

Classical theory for multibody dynamics starts with the equations of motion for interconnected masses and with the appropriate constraints. For putting that in a suitable form, usually the principles of d'Alembert or Jourdain are applied (Pfeiffer and Schindler, 2015). Using Jourdain's principle of lost power and assuming rigid bodies results in

$$
\sum_{i=1}^{n} \delta \underbrace{\begin{pmatrix} \mathbf{v}_{O'} \\ \boldsymbol{\omega} \end{pmatrix}^{\mathsf{T}}}_{\dot{\mathbf{z}}^{\mathsf{T}}} \left\{ \frac{\mathrm{d}}{\mathrm{d}t} \left[\underbrace{\begin{pmatrix} m\mathbf{I} & m\tilde{\mathbf{r}}_{O'S}^{\mathsf{T}} \\ m\tilde{\mathbf{r}}_{O'S} & \boldsymbol{\Theta}_{O'} \end{pmatrix}}_{\mathbf{M}} \underbrace{\begin{pmatrix} \mathbf{v}_{O'} \\ \boldsymbol{\omega} \end{pmatrix}}_{\dot{\mathbf{z}}} \right] + \underbrace{\begin{pmatrix} m\tilde{\boldsymbol{\omega}}\tilde{\boldsymbol{\omega}}\mathbf{r}_{O'S} \\ \tilde{\boldsymbol{\omega}}\boldsymbol{\Theta}_{O'}\boldsymbol{\omega} \end{pmatrix}}_{\mathbf{f}^g} - \right.
$$
$$
\left. - \underbrace{\begin{pmatrix} \mathbf{F}^e + \mathbf{F}^a + \mathbf{F}^p \\ \mathbf{M}_{O'}^e + \mathbf{M}_{O'}^a + \mathbf{M}_{O'}^p \end{pmatrix}}_{\mathbf{f}^e + \mathbf{f}^a + \mathbf{f}^p} - \underbrace{\begin{pmatrix} \mathbf{F}^c \\ \mathbf{M}_{O'}^c \end{pmatrix}}_{\mathbf{f}^c} \right\}_i = 0, \quad (5.1)
$$

written in body-fixed coordinates ($\mathbf{v}_{O'}, \boldsymbol{\omega}$ translational and rotational velocities, $m, \mathbf{I}, \boldsymbol{\Theta}_{O'}$ masses and mass moments of inertia, O', S reference point and center of gravity, $\mathbf{f}^g, \mathbf{f}^e, \mathbf{f}^a, \mathbf{f}^p, \mathbf{f}^c$ gyroscopic, applied, driving, process and constraint forces and torques). Systems with time-dependent masses are included.

The virtual velocities $\delta\dot{\mathbf{z}}$, as presented in Eq. (5.1), cannot be chosen arbitrarily, but they must satisfy side-conditions in form of bilateral constraints with well-known classification (Pfeiffer, 2008). Taking this into consideration and following the ideas of Jacobi (1866), usually addressed to as Lagrange I, in the form given in Bremer (2008), we come out with the typical example

$$\mathbf{M}\ddot{\mathbf{z}}+\dot{\mathbf{M}}\dot{\mathbf{z}}+\mathbf{f}-\mathbf{f}^c=\mathbf{0}, \ \in \mathbb{R}^n \qquad (\mathbf{f}=\mathbf{f}^g-\mathbf{f}^e-\mathbf{f}^a-\mathbf{f}^p)$$

$$\dot{\boldsymbol{\Phi}}=\mathbf{W}^{\mathsf{T}}\dot{\mathbf{z}}+\bar{\mathbf{w}}, \ \in \mathbb{R}^m$$

$$\ddot{\boldsymbol{\Phi}}=\mathbf{W}^{\mathsf{T}}\ddot{\mathbf{z}}+\left[\left(\frac{\mathrm{d}\mathbf{W}^{\mathsf{T}}}{\mathrm{dt}}\right)\dot{\mathbf{z}}+\left(\frac{\mathrm{d}\bar{\mathbf{w}}}{\mathrm{dt}}\right)\right]=\mathbf{W}^{\mathsf{T}}\ddot{\mathbf{z}}+\hat{\mathbf{w}},$$

$$\mathbf{f}^c=-\mathbf{W}(\mathbf{z},t)\boldsymbol{\lambda}. \tag{5.2}$$

The mass matrix is positive definite and symmetric. The constraints $\dot{\boldsymbol{\Phi}}$ include all multibody constraints $\boldsymbol{\Phi}$. The $\mathbf{W}$-matrices are Jacobians defining the tangential constraint surfaces. The constraint forces are perpendicular to these manifolds. All constraints are assumed to be bilateral and independent from each other. Jacobi (1866) has been aware of the fact already that the differentiated form of the constraints is needed to solve the complete set of equations of motion and constraints, see third equation of Eqs. (5.2). It is

$$\ddot{\mathbf{z}}=-\mathbf{M}^{-1}\left[(\dot{\mathbf{M}}\dot{\mathbf{z}}+\mathbf{f})+\mathbf{W}(\mathbf{W}^{\mathsf{T}}\mathbf{M}^{-1}\mathbf{W})^{-1}\mathbf{W}^{\mathsf{T}}\mathbf{M}^{-1}[(\dot{\mathbf{M}}\dot{\mathbf{z}}+\mathbf{f})-\hat{\mathbf{w}}]\right],$$

$$\boldsymbol{\lambda}=-(\mathbf{W}^{\mathsf{T}}\mathbf{M}^{-1}\mathbf{W})^{-1}\left[\mathbf{W}^{\mathsf{T}}\mathbf{M}^{-1}(\dot{\mathbf{M}}\dot{\mathbf{z}}+\mathbf{f})-\hat{\mathbf{w}}\right]. \tag{5.3}$$

If the coordinate $\mathbf{z}$ depends on some other coordinates $\mathbf{q}$, where $\mathbf{z}$ might be non-minimal and $\mathbf{q}$ might be minimal, then we get from Bremer (2008)

$$\dot{\boldsymbol{\Phi}}=\mathbf{W}^{\mathsf{T}}\dot{\mathbf{z}}+\bar{\mathbf{w}}=\mathbf{W}^{\mathsf{T}}\left(\frac{\partial \mathbf{z}}{\partial \mathbf{q}}\right)\dot{\mathbf{q}}+\bar{\mathbf{w}}=\mathbf{0}, \qquad \frac{\partial \dot{\boldsymbol{\Phi}}}{\partial \dot{\mathbf{q}}}=\mathbf{W}^{\mathsf{T}}\left(\frac{\partial \mathbf{z}}{\partial \mathbf{q}}\right)=\left(\frac{\partial \mathbf{z}}{\partial \mathbf{q}}\right)^{\mathsf{T}}\mathbf{W}=\mathbf{0},$$
$$\tag{5.4}$$

which is very helpful for projection needs.

5.2.2 Unilateral Dynamics

5.2.2.1 Classical Approach

Two problems have to be solved for multibody systems with many unilateral contacts: the problem of non-smooth solution trajectories and the combinatorial problem. We start with the last one. For this purpose we define all contact sets, which can be found in a multibody system:

$$\begin{aligned}
I_A(t) &= \{1,2,\ldots,n_A\} && \text{with } n_A \text{ elements} \\
I_C(t) &= \{i \in I_A : g_{Ni}=0\} && \text{with } n_C \text{ elements} \\
I_N(t) &= \{i \in I_C : \dot{g}_{Ni}=0\} && \text{with } n_N \text{ elements} \\
I_T(t) &= \{i \in I_N : |\dot{g}_{Ti}|=0\} && \text{with } n_T \text{ elements}
\end{aligned} \tag{5.5}$$

These sets describe the kinematic state of each contact point. The set I_A consists of the n_A indices of all contact points. The set combination $I_A \setminus \{I_C, I_N, I_T\}$ includes

all contacts. The elements of set I_C are the n_C indices of the unilateral constraints with vanishing normal distance $g_{Ni} = 0$, but arbitrary relative velocity in the normal direction. In the index set I_N are the n_N indices of the potentially active normal constraints, which fulfill the necessary conditions for continuous contact (vanishing normal distance $g_{Ni} = 0$ and no relative velocity $\dot g_{Ni}$ in the normal direction). The index set I_N includes for example all contact states with slipping. The n_T elements of the set I_T are the indices of the potentially active tangential constraints. The corresponding normal constraints are closed and the relative velocities $\dot g_{Ti}$ in the tangential direction are zero. The numbers of elements of the index sets I_C, I_N and I_T are not constant, but depend on time, because there are variable states of constraints due to separation and stick-slip phenomena.

As a next step we must organize all transitions from contact to detachment and from stick to slip and the corresponding reversed transitions. In **normal direction** of a contact we find the following situation (Pfeiffer and Glocker, 1996):

- Passive contact i
  $g_{Ni}(g,t) \geqslant 0,\ \lambda_{Ni} = 0,\ $ indicator g_{Ni},
- Transition to contact
  $g_{Ni}(g,t) = 0,\ \lambda_{Ni} \geqslant 0,$
- Active contact i
  $g_{Ni}(g,t) = 0,\ \lambda_{Ni} > 0,$ indicator λ_{Ni},
- Transition to detachment
  $g_{Ni}(q,t) \geqslant 0,\ \lambda_{Ni} = 0.$

The kinematical magnitudes $g_{Ni}, \dot g_{Ni}, \ddot g_{Ni}$ are determined from contact kinematics (Sect. 5.4). The constraint forces λ_{Ni} must be compressive forces. If they change sign, we get separation. The properties above establish a complementarity behavior, which might be expressed by n_N (set I_N) complementarity conditions (put on an acceleration level)

$$\ddot{\mathbf g}_N \geqslant \mathbf 0 \ ;\ \boldsymbol\lambda_N \geqslant \mathbf 0 \ ;\ \ddot{\mathbf g}_N^{\mathsf T}\boldsymbol\lambda_N = 0\ , \tag{5.6}$$

The complementarity problem defined in Eq. (5.6) might be interpreted as a corner law, which requires for each contact $\ddot g_{Ni} \geqslant 0,\ \lambda_{Ni} \geqslant 0,\ \ddot g_{Ni}\lambda_{Ni} = 0.$ **Figure 5.2** illustrates this property.

With respect to the **tangential direction** of a contact we shall confine our considerations to the application of Coulomb's friction law, which in no way means a loss of generality. The complementary behavior is a characteristic feature of all contact phenomena independent of the specific physical law of contact. Furthermore we assume that within the infinitesimal small time step for a transition from stick to slip and vice versa the coefficients of static and sliding friction are the same. For $\dot g_{Ti} \neq 0$ any friction law may be applied. With this property Coulomb's friction law distinguishes between the two cases

$$\begin{aligned} &\text{Stiction: } |\lambda_{Ti}| < \mu_{0i}\lambda_{Ni} \Rightarrow |\dot g_{Ti}| = 0 \quad (\text{Set } I_T) \\ &\text{Sliding: } |\lambda_{Ti}| = \mu_{0i}\lambda_{Ni} \Rightarrow |\dot g_{Ti}| > 0 \quad (\text{Set} I_N \setminus I_T). \end{aligned} \tag{5.7}$$
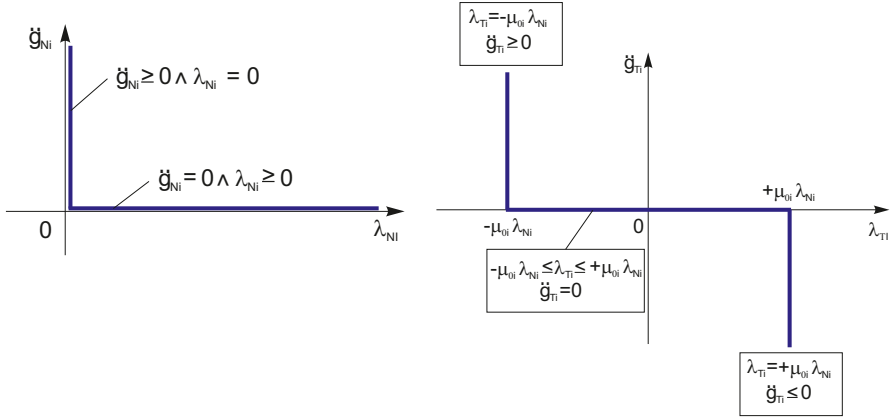
Fig. 5.2: Corner laws for normal and tangential contact behavior.

Equation (5.7) formulates the mechanical property that we are within the friction cone if the relative tangential velocity is zero and the tangential constraint force $|\lambda_{Ti}|$ is smaller than the maximum static friction force $(\mu_{0i}\lambda_{Ni})$. Then we have stiction. We are on the friction cone if we slide with $|\dot{g}_{Ti}| > 0$. At a transition point the friction force is then $(\mu_{0i}\lambda_{Ni})$ (see (5.7)). In addition we must regard the fact that in the tangential contact plane we might get one or two directions according to a plane or a spatial contact. From this we summarize in the following way keeping in mind that these are conditions not equations:

- Passive contact i (Sliding, Set $I_N \setminus I_T$)
  $|\dot{g}_{Ti}| \geqslant 0$, $|\mu_{0i}\lambda_{Ni}| - |\lambda_{Ti}| = 0$, indicator $|\dot{g}_{Ti}|$,
- Transition Slip to Stick
  $|\dot{g}_{Ti}| = 0$, $|\mu_{0i}\lambda_{Ni}| - |\lambda_{Ti}| \geqslant 0$,
- Active contact i (Sticking, Set I_T)
  $|\dot{g}_{Ti}| = 0$, $|\mu_{0i}\lambda_{Ni}| - |\lambda_{Ti}| > 0$, indicator $|\mu_{0i}\lambda_{Ni}| - |\lambda_{Ti}|$,
- Transition Stick to Slip
  $|\dot{g}_{Ti}| \geqslant 0$, $|\mu_{0i}\lambda_{Ni}| - |\lambda_{Ti}| = 0$.

From a classical numerical point of view we have to check the indicator for a change of sign, which then requires a subsequent interpolation. For a transition from stick to slip one must examine the possible development of a non-zero relative tangential acceleration as a start for sliding.

Equation (5.7) put on an acceleration level can then be written in a more detailed form

$$\begin{aligned}
|\lambda_{Ti}| &< \mu_{0i}\lambda_{Ni} \wedge \ddot{g}_{Ti} = 0 \quad (i \in I_T \ \text{sticking}) \\
\lambda_{Ti} &= +\mu_{0i}\lambda_{Ni} \wedge \ddot{g}_{Ti} \leqslant 0 \ (i \in I_N \setminus I_T \ \text{negative sliding}) \\
\lambda_{Ti} &= -\mu_{0i}\lambda_{Ni} \wedge \ddot{g}_{Ti} \geqslant 0 \ (i \in I_N \setminus I_T \ \text{positive sliding})
\end{aligned} \tag{5.8}$$

This contact law may be represented by a double corner law as indicated in **Fig. 5.2**. A complementarity formulation for the tangential direction might be evaluated as follows.

For stiction we are within a friction cone, either a plane or a spatial one. Let us consider a plane one, see **Fig. 5.2**, right side. Being within a friction cone, the relative tangential velocities and accelerations ($\dot{g}_T = 0$, $\ddot{g}_T = 0$) are zero within the range $(-\mu_0\lambda_N \leqslant +\mu_0\lambda_N)$. Suppose, the tangential force in contact i comes out after some time step with λ_{Ti}, then the following complementarity can be formulated

$$\ddot{g}_{Ti} \geqslant 0, \quad (\mu_0\lambda_{Ni} - \lambda_{Ti}) \geqslant 0, \quad \ddot{g}_{Ti}(|\mu_0\lambda_{Ni}| - \lambda_{Ti}) = 0. \tag{5.9}$$

We call the term $(\mu_0\lambda_{Ni} - \lambda_{Ti})$ friction reserve, because it defines the distance of the tangential friction force λ_{Ti} from the maximum possible static friction force $\mu_0\lambda_{Ni}$.

All classical concepts are characterized by the necessity to determine such kinematic indicators describing a change of the contact situation for each of the contacts. This makes the numerical evaluation lengthy and sometimes cumbersome. Modern approaches avoid these problems.

5.2.2.2 Modern Approaches

Considering non-smooth systems simply means replacing bilateral by unilateral constraints, which writes (Pfeiffer, 2008)

$$\mathbf{M}(\mathbf{q},t)\ddot{\mathbf{q}}(t) + \mathbf{h}(\mathbf{q},\dot{\mathbf{q}}t) - [(\mathbf{W}_N + \mathbf{W}_R) \quad \mathbf{W}_T]\begin{pmatrix} \boldsymbol{\lambda}_N(t) \\ \boldsymbol{\lambda}_T(t) \end{pmatrix} = \mathbf{0}, \quad \in \mathbb{R}^f,$$

$$\ddot{\mathbf{g}}_N = \mathbf{W}_N^T\ddot{\mathbf{q}} + \bar{\mathbf{w}}_N, \quad \in \mathbb{R}^{n_N},$$

$$\ddot{\mathbf{g}}_T = \mathbf{W}_T^T\ddot{\mathbf{q}} + \bar{\mathbf{w}}_T, \quad \in \mathbb{R}^{2n_T},$$

$$\ddot{\mathbf{g}}_N \geqslant \mathbf{0}, \quad \boldsymbol{\lambda}_N \geqslant \mathbf{0}, \quad \ddot{\mathbf{g}}_N^T\boldsymbol{\lambda}_N = 0,$$

$$|\lambda_{Ti}| < \mu_{0i}\lambda_{Ni} \wedge \ddot{g}_{Ti} = 0 \qquad (i \in I_T \text{ sticking}),$$
$$\lambda_{Ti} = +\mu_{0i}\lambda_{Ni} \wedge \ddot{g}_{Ti} \leqslant 0 \qquad (i \in I_N\backslash I_T \text{ negative sliding}),$$
$$\lambda_{Ti} = -\mu_{0i}\lambda_{Ni} \wedge \ddot{g}_{Ti} \leqslant 0 \qquad (i \in I_N\backslash I_T \text{ positive sliding}). \tag{5.10}$$

Contacts are assumed to be plane. The unilateral possibilities are described by the last four inequalities. Active or passive contacts require a complementarity of the normal relative distance $\mathbf{g}_N$ and the force $\boldsymbol{\lambda}_N$. In tangential direction we are either within the local friction cone for sticking, or on the friction cone surface for positive or negative sliding (Glocker, 2001; Leine and Nijmeijer, 2004; Pfeiffer, 2008). To evaluate this set requires the computation of contact kinematics in terms of relative distances, velocities and accelerations ($\mathbf{g}, \dot{\mathbf{g}}, \ddot{\mathbf{g}}$). Modern theories of non-smooth systems use another form by introducing Moreau's measure differential equations together with a representation of unilateral constraints by prox-functions from convex

analysis (Moreau, 1988; Alart and Curnier, 1991; Brogliato, 1999). This combination is called Augmented Lagrange method (Leine and Nijmeijer, 2004). It can be shown that the prox-formulation for the unilateral contacts is perfectly equivalent to the complementarity relations as applied above (Schindler et al., 2011). A proximal point to a convex set C is defined by

$$\text{prox}_C(z) = \arg\min_{x^* \in C} |z - x^*|, \quad z \in \mathbb{R}^n \tag{5.11}$$

and returns the closest point in C to its argument, which is illustrated in **Fig. 5.3** (Leine and Nijmeijer, 2004). If we look at this convex set as the cut of a friction cone with different friction coefficients in the two contact directions, then every solution of the system falling outside the convex set has to be brought back to the hull of the set, which defines numerically an iteration procedure. In the case of a complementarity in normal direction (contact/detachment-case) the set is just the half space with non-negative constraint forces λ_N, **Fig. 5.2**. Therefore we get the relation

$$\boldsymbol{\lambda}_N = \text{prox}_{C_N}(\boldsymbol{\lambda}_N - r\ddot{\boldsymbol{g}}_N), \qquad C_N(\boldsymbol{\lambda}_N) = \{\boldsymbol{\lambda}_N | \boldsymbol{\lambda}_N \geqslant 0\}. \tag{5.12}$$

In the same manner we can put Coulomb's friction law of the tangential direction into the form

$$\boldsymbol{\lambda}_T = \text{prox}_{C_T(\lambda_N)}(\boldsymbol{\lambda}_T - r\ddot{\boldsymbol{g}}_T), \qquad C_T(\boldsymbol{\lambda}_N) = \{\boldsymbol{\lambda}_T | \ |\lambda_{Ti}| \leqslant \mu_i \lambda_{Ni}\}. \tag{5.13}$$
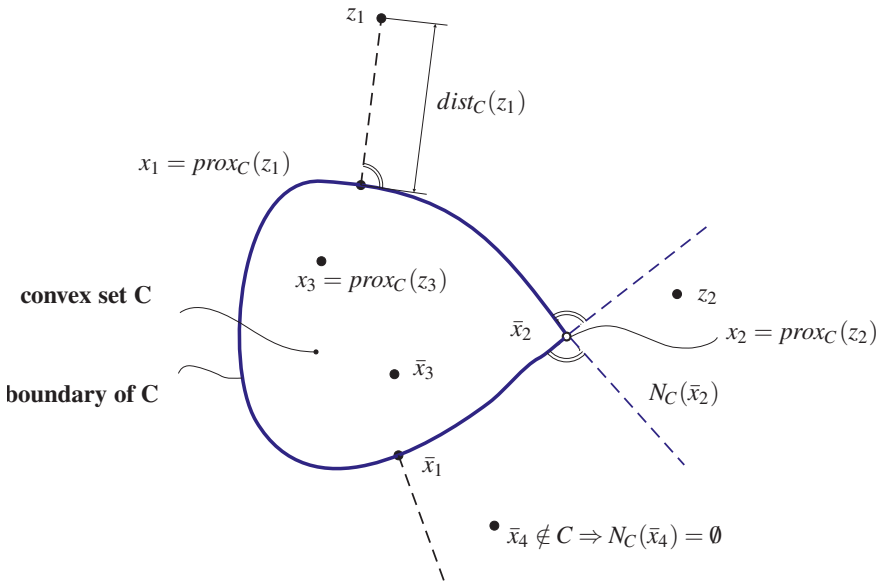
Fig. 5.3: Normal cone, proximal point and distance function (Leine and Nijmeijer, 2004).

The arbitrary auxiliary parameter $r > 0$ represents the slope of the regularizing function. More details may be found in Leine and Nijmeijer (2004); Foerg et al. (2006); Foerg (2007).

Keeping that in mind, Moreau's measure differential equation writes

$$\mathbf{M}\mathrm{d}\mathbf{u} + \mathbf{h}\mathrm{d}t - [(\mathbf{W}_\mathrm{N} + \mathbf{W}_\mathrm{R}) \quad \mathbf{W}_\mathrm{T}] \begin{pmatrix} \mathrm{d}\boldsymbol{\Lambda}_\mathrm{N}(t) \\ \mathrm{d}\boldsymbol{\Lambda}_\mathrm{T}(t) \end{pmatrix} = \mathbf{0},$$

$$\mathrm{d}\dot{\mathbf{g}}_\mathrm{N} = \mathbf{W}_\mathrm{N}^\mathrm{T}\mathrm{d}\mathbf{u} + \bar{\mathbf{w}}_\mathrm{N}\mathrm{d}t,$$

$$\mathrm{d}\dot{\mathbf{g}}_\mathrm{T} = \mathbf{W}_\mathrm{T}^\mathrm{T}\mathrm{d}\mathbf{u} + \bar{\mathbf{w}}_\mathrm{T}\mathrm{d}t,$$

$$\boldsymbol{\lambda}_\mathrm{N} = \mathrm{prox}_{C_\mathrm{N}}(\boldsymbol{\lambda}_\mathrm{N} - r\mathbf{g}_\mathrm{N}), \qquad \boldsymbol{\Lambda}_\mathrm{N} = \mathrm{prox}_{C_\mathrm{N}}(\boldsymbol{\Lambda}_\mathrm{N} - r\mathbf{g}_\mathrm{N}),$$

$$\boldsymbol{\lambda}_\mathrm{T} = \mathrm{prox}_{C_\mathrm{T}}(\boldsymbol{\lambda}_\mathrm{T} - r\dot{\mathbf{g}}_\mathrm{T}), \qquad \boldsymbol{\Lambda}_\mathrm{T} = \mathrm{prox}_{C_\mathrm{T}}(\boldsymbol{\Lambda}_\mathrm{T} - r\dot{\mathbf{g}}_\mathrm{T}), \qquad (5.14)$$

which includes also impacts with or without friction. Glocker (2001) introduces a decomposition of the velocity $\mathbf{u}$ into parts, an absolute continuous part $\mathrm{d}\mathbf{u}_\mathrm{L} = \dot{\mathbf{u}}\mathrm{d}t$ with the Lebesgue measure $\mathrm{d}t$ and a discontinuous part $\mathrm{d}\mathbf{u}_\mathrm{A} = (\mathbf{u}^+ - \mathbf{u}^-)\mathrm{d}\eta$ in the form of a step function with the atomic measure $\mathrm{d}\eta = \sum_i \mathrm{d}\delta_i$. In a similar way we may split up the forces in a continuous and thus Lebesgue-measurable part $\boldsymbol{\lambda}\mathrm{d}t$ and in an atomic part $\boldsymbol{\Lambda}\mathrm{d}\eta$ with $\mathrm{d}\boldsymbol{\Lambda} = \boldsymbol{\lambda}\mathrm{d}t + \boldsymbol{\Lambda}\mathrm{d}\eta$. The part $\boldsymbol{\lambda}\mathrm{d}t$ contains all contact reactions due to non-impulsive contacts and the part $\boldsymbol{\Lambda}\mathrm{d}\eta$ all impulsive contact reactions.

5.3 Impacts with Friction

5.3.1 General Theory

Impacts with and without friction play an important role in many machines and mechanisms. They were a research topic at the author's former institute since many years starting with impacts without friction (Pfeiffer, 2008) and finally proceeding to a theory, which describes impacts with friction in a rather general way (Glocker, 2001, 2013, 2014). This new theory has convincingly been verified by a large variety of experiments performed by Beitelschmidt (1999). In the following we shall give a short survey. As a matter of fact there have been quite a number of remarkable and significant contributions to this topic, for example Moreau (1988); Frémond (2002, 2007); Brogliato (1999).

We assume as usual that an impact takes place in an infinitesimal short time and without any change of position, orientation and of all non-impulsive forces. Nevertheless and virtually we zoom the impact time, establish the equations for a compression and for an expansion phase and then apply these equations again for an infinitesimal short time interval. The evaluation has to be performed on a velocity level, which we realize by formal integration of the equations of motion (5.10), the constraints and the contact laws. Denoting the beginning of an impact, the end of

compression and the end of expansion by the indices A, C, E, respectively, we get for $\Delta t = t_E - t_A$

$$\mathbf{M}(\dot{\mathbf{q}}_C - \dot{\mathbf{q}}_A) - (\mathbf{W}_N \mathbf{W}_T) \begin{pmatrix} \mathbf{\Lambda}_{NC} \\ \mathbf{\Lambda}_{TC} \end{pmatrix} = \mathbf{0}, \quad \mathbf{M}(\dot{\mathbf{q}}_E - \dot{\mathbf{q}}_C) - (\mathbf{W}_N \mathbf{W}_T) \begin{pmatrix} \mathbf{\Lambda}_{NE} \\ \mathbf{\Lambda}_{TE} \end{pmatrix} = 0$$

$$\text{with } \mathbf{\Lambda}_i = \lim_{t_E \to t_A} \int_{t_A}^{t_E} \lambda_i dt, \qquad (5.15)$$

Here $\mathbf{\Lambda}_{NC}, \mathbf{\Lambda}_{TC}$ are the impulses in the normal and tangential direction, which are transferred during compression, and $\mathbf{\Lambda}_{NE}, \mathbf{\Lambda}_{TE}$ those of expansion. Defining $\dot{\mathbf{q}}_A = \dot{\mathbf{q}}(t_A); \dot{\mathbf{q}}_C = \dot{\mathbf{q}}(t_C); \dot{\mathbf{q}}_E = \dot{\mathbf{q}}(t_E)$ we express the relative velocities as

$$\begin{pmatrix} \dot{\mathbf{g}}_{NA} \\ \dot{\mathbf{g}}_{TA} \end{pmatrix} = \begin{pmatrix} \mathbf{W}_N^T \\ \mathbf{W}_T^T \end{pmatrix} \dot{\mathbf{q}}_A + \begin{pmatrix} \tilde{\mathbf{w}}_N \\ \tilde{\mathbf{w}}_T \end{pmatrix},$$

$$\begin{pmatrix} \dot{\mathbf{g}}_{NE} \\ \dot{\mathbf{g}}_{TE} \end{pmatrix} = \begin{pmatrix} \mathbf{W}_N^T \\ \mathbf{W}_T^T \end{pmatrix} \dot{\mathbf{q}}_E + \begin{pmatrix} \tilde{\mathbf{w}}_N \\ \tilde{\mathbf{w}}_T \end{pmatrix}, \qquad (5.16)$$

$$\begin{pmatrix} \dot{\mathbf{g}}_{NC} \\ \dot{\mathbf{g}}_{TC} \end{pmatrix} = \begin{pmatrix} \mathbf{W}_N^T \\ \mathbf{W}_T^T \end{pmatrix} \dot{\mathbf{q}}_C + \begin{pmatrix} \tilde{\mathbf{w}}_N \\ \tilde{\mathbf{w}}_T \end{pmatrix}.$$

Considering in a first step the **compression phase** and combining the Eqs. (5.15) and (5.16) we come out with

$$\begin{pmatrix} \dot{\mathbf{g}}_{NC} \\ \dot{\mathbf{g}}_{TC} \end{pmatrix} = \underbrace{\begin{pmatrix} \mathbf{W}_N^T \\ \mathbf{W}_T^T \end{pmatrix} \mathbf{M}^{-1} \begin{pmatrix} \mathbf{W}_N \\ \mathbf{W}_T \end{pmatrix}^T}_{\mathbf{G}} \cdot \begin{pmatrix} \mathbf{\Lambda}_{NC} \\ \mathbf{\Lambda}_{TC} \end{pmatrix} + \begin{pmatrix} \dot{\mathbf{g}}_{NA} \\ \dot{\mathbf{g}}_{TA} \end{pmatrix}, \qquad (5.17)$$

where $\mathbf{G}$ is the matrix of projected inertia. It consists of the four blocks ($\mathbf{G}_{NN}$, $\mathbf{G}_{NT}$, $\mathbf{G}_{TN}$, $\mathbf{G}_{TT}$). Equation (5.17) gives the relative velocities $\dot{\mathbf{g}}_{NC}$ and $\dot{\mathbf{g}}_{TC}$ at the end of compression phase, depending on the velocities at the beginning of the impact $\dot{\mathbf{g}}_{NA}$ and $\dot{\mathbf{g}}_{TA}$ under the influence of the contact impulses $\mathbf{\Lambda}_{NC}$ and $\mathbf{\Lambda}_{TC}$. To calculate these impulses two impact laws in normal and tangential direction are necessary.

As already indicated magnitudes of relative kinematics and constraint forces (here impulses) are complementary quantities. In normal direction these are $\dot{\mathbf{g}}_{NC}$ and $\mathbf{\Lambda}_{NC}$. In tangential direction we have the relative tangential velocity vector $\dot{\mathbf{g}}_{TC}$ and the friction saturation ($\mathbf{\Lambda}_{TC} - (\text{diag}\mu_i)\mathbf{\Lambda}_{NC}$). Decomposing the tangential behavior we obtain (see **Fig. 5.4**)

$$\begin{aligned} \mathbf{\Lambda}_{TCV,i} &= \mathbf{\Lambda}_{TC,i} + \mu_i \mathbf{\Lambda}_{TN,i}, \qquad & \dot{g}_{TC,i} &= \dot{g}^+_{TC,i} - \dot{g}^-_{TC,i}, \\ \mathbf{\Lambda}^{(+)}_{TCV,i} &= \mathbf{\Lambda}_{TCV,i}, \qquad & \mathbf{\Lambda}^{(-)}_{TCV,i} &= -\mathbf{\Lambda}_{TCV,i} + 2\mu_i \mathbf{\Lambda}_{NC,i}, \end{aligned} \qquad (5.18)$$

Fig. 5.4 Decomposition of tangential friction law (Beitelschmidt, 1999).
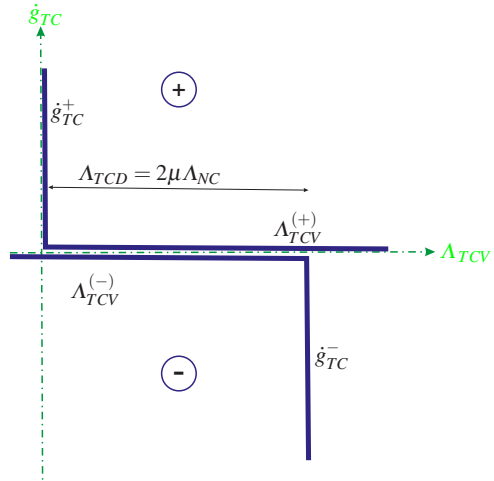
Together with equation (5.17) this results in a Linear Complementary Problem (LCP) in standard form $\mathbf{y} = \mathbf{A}\mathbf{x} + \mathbf{b}$ with $\mathbf{x} \geqslant 0, \mathbf{y} \geqslant 0$ and $\mathbf{x}^\mathsf{T}\mathbf{y} = 0$

$$
\underbrace{\begin{pmatrix} \dot{\mathbf{g}}_{NC} \\ \dot{\mathbf{g}}^+_{TC} \\ \boldsymbol{\Lambda}^{(-)}_{TCV} \end{pmatrix}}_{\mathbf{y}} = \underbrace{\begin{pmatrix} \mathbf{G}_{NN} - \mathbf{G}_{NT}\boldsymbol{\mu} & \mathbf{G}_{NT} & 0 \\ \mathbf{G}_{TN} - \mathbf{G}_{TT}\boldsymbol{\mu} & \mathbf{G}_{TT} & \mathbf{E} \\ 2\boldsymbol{\mu} & -\mathbf{E} & 0 \end{pmatrix}}_{\mathbf{A}} \cdot \underbrace{\begin{pmatrix} \boldsymbol{\Lambda}_{NC} \\ \boldsymbol{\Lambda}^{(+)}_{TCV} \\ \dot{\mathbf{g}}^-_{TC} \end{pmatrix}}_{\mathbf{x}} + \underbrace{\begin{pmatrix} \dot{\mathbf{g}}_{NA} \\ \dot{\mathbf{g}}_{TA} \\ 0 \end{pmatrix}}_{\mathbf{b}}, \quad (5.19)
$$

wherein $\boldsymbol{\mu}$ is a diagonal matrix, containing the friction coefficients of the contacts. The problem is solved numerically. The velocities $\dot{\mathbf{g}}_{NC}, \dot{\mathbf{g}}_{TC}$ and the impulsions $\boldsymbol{\Lambda}_{NC}, \boldsymbol{\Lambda}_{TC}$ are either part of the result or can be obtained by transformation (5.18) and by $\boldsymbol{\Lambda}_{TC} = \boldsymbol{\Lambda}^{(+)}_{TCV} - \boldsymbol{\mu}\boldsymbol{\Lambda}_{NC}$.

In the compression phase kinetic energy of the colliding bodies is stored as potential energy. During the **expansion phase** parts of this energy are regained. This process is governed by two coefficients of restitution in normal and tangential direction ε_N and ε_T respectively.

In the case of multiple impacts Poisson's hypothesis does not guarantee impenetrability of the bodies (Glocker, 2001). So the law is enhanced by an additional condition. The normal impulse during phase of restitution $\boldsymbol{\Lambda}_{NE}$ is in the minimum $\varepsilon_E \boldsymbol{\Lambda}_{NC}$ in each contact, but can be arbitrary high to avoid penetration. In this case the bodies remain in contact after the impact. This impact law with a complementary character is drawn in **Fig. 5.5**.

In tangential direction the impact law is influenced by three effects: At first a minimum impulse $[\varepsilon_N (\varepsilon_T \boldsymbol{\Lambda}_{TC})]$ must be transferred. It is the impulse stored during compression reduced by losses due to Poisson's law, but as all contact actions in tangential direction are always connected with constraints in normal direction we have to consider also a loss due to ε_N. In addition the impulse must not ex-

Fig. 5.5 Impact law for the
phase of expansion in normal
direction.
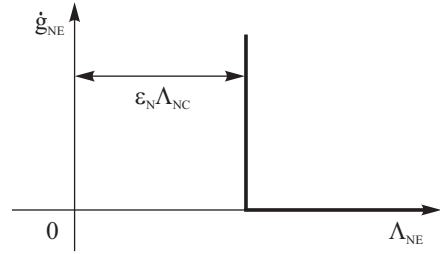
ceed the static friction limit. Usually it is assumed that between these two limits
the tangential velocity is zero. The measurements of Beitelschmidt (1999) however
indicate a small tangential velocity $\dot{g}_{TE0}$ in this area. It might be produced by the
local difference of the contact point and that point, where the tangential restoring
force due to tangential compression applies. The inclusion of this velocity gives a
slight improvement for the comparison theory/measurement. With

$$\dot{\mathbf{g}}_{TE0} = \mathbf{G}_{TN}\boldsymbol{\varepsilon}_N\boldsymbol{\Lambda}_{NC} + \mathbf{G}_{TT}\boldsymbol{\varepsilon}_N(\boldsymbol{\varepsilon}_T\boldsymbol{\Lambda}_{TC}) \tag{5.20}$$

one can calculate $\dot{g}_{TE0}$ for all contacts and the tangential impact law looks like
drawn in **Fig. 5.6**. $\boldsymbol{\varepsilon}_N$ and $\boldsymbol{\varepsilon}_T$ are diagonal matrices containing the different coef-
ficients for all contacts. To formulate the equation for the phase of restitution as a
LCP similar to the compression phase the two matrices

$$\begin{aligned}
\mathbf{S}^+ &= \mathrm{diag}\left(\frac{1}{2}\left(1+\mathrm{sign}(\Lambda_{TC,i})\right)\right) \ , \\
\mathbf{S}^- &= \mathrm{diag}\left(\frac{1}{2}\left(1-\mathrm{sign}(\Lambda_{TC,i})\right)\right)
\end{aligned} \tag{5.21}$$

are introduced. After some transformations similar to those of the compression
phase the LCP writes
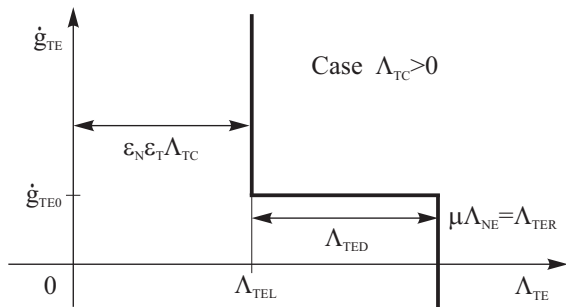
Fig. 5.6 Impact law for the
phase of restitution in tangen-
tial direction.

$$\begin{pmatrix} \dot{\mathbf{g}}_{NE} \\ \dot{\mathbf{g}}_{TEV}^{+} \\ \boldsymbol{\Lambda}_{TEV}^{(-)} \end{pmatrix} = \begin{pmatrix} \mathbf{G}_{NN} - \mathbf{G}_{NT}\mathbf{S}^{-}\boldsymbol{\mu} & \mathbf{G}_{NT} & 0 \\ \mathbf{G}_{TN} - \mathbf{G}_{TT}\mathbf{S}^{-}\boldsymbol{\mu} & \mathbf{G}_{TT} & \mathbf{E} \\ \boldsymbol{\mu} & & -\mathbf{E} & 0 \end{pmatrix} \cdot \begin{pmatrix} \boldsymbol{\Lambda}_{NP} \\ \boldsymbol{\Lambda}_{TEV}^{(+)} \\ \dot{\mathbf{g}}_{TEV}^{-} \end{pmatrix} + \begin{pmatrix} b_1 \\ b_2 \\ b_3 \end{pmatrix} \quad (5.22)$$

with

$$\begin{aligned}
b_1 &= \mathbf{G}_{NN}\varepsilon_N\boldsymbol{\Lambda}_{NC} + \mathbf{G}_{NT}\mathbf{S}^{+}\varepsilon_N\varepsilon_T\boldsymbol{\Lambda}_{TC} - \mathbf{G}_{NT}\mathbf{S}^{-}\boldsymbol{\mu}\varepsilon_N\boldsymbol{\Lambda}_{NC} + \dot{\mathbf{g}}_{NC}, \\
b_2 &= \mathbf{G}_{TT}(\mathbf{S}^{+} - \mathbf{E})\varepsilon_N\varepsilon_T\boldsymbol{\Lambda}_{TC} - \mathbf{G}_{TT}\mathbf{S}^{-}\boldsymbol{\mu}\varepsilon_N\boldsymbol{\Lambda}_{NC} + \dot{\mathbf{g}}_{TC}, \quad (5.23) \\
b_3 &= \boldsymbol{\mu}\varepsilon_N\boldsymbol{\Lambda}_{NC} - \varepsilon_N\varepsilon_T|\boldsymbol{\Lambda}_{TC}|,
\end{aligned}$$

After solution the velocities $\dot{\mathbf{g}}_{NC}, \dot{\mathbf{g}}_{TC}$ and the impulses $\boldsymbol{\Lambda}_{NC}, \boldsymbol{\Lambda}_{TC}$ are either part of the result or can be obtained by the transformations

$$\begin{aligned}
\dot{\mathbf{g}}_{TE} &= \dot{\mathbf{g}}_{TEV}^{+} - \dot{\mathbf{g}}_{TEV}^{-} + \dot{\mathbf{g}}_{TE0}, \\
\boldsymbol{\Lambda}_{NE} &= \boldsymbol{\Lambda}_{NP} + \varepsilon_N\boldsymbol{\Lambda}_{NC}, \\
\boldsymbol{\Lambda}_{TE} &= \boldsymbol{\Lambda}_{TEV}^{(+)} + \boldsymbol{\Lambda}_{TEL} = \boldsymbol{\Lambda}_{TEV}^{(+)} + \mathbf{S}^{+}\varepsilon_N\varepsilon_T\boldsymbol{\Lambda}_{TC} - \mathbf{S}^{-}\boldsymbol{\mu}\boldsymbol{\Lambda}_{NE},
\end{aligned}$$

If the impulses during the two phases of the impact are known, one can calculate the motion $\dot{\mathbf{q}}_E$ of the multibody system at the end of the impact,

$$\dot{\mathbf{q}}_E = \dot{\mathbf{q}}_A \mathbf{M}^{-1}(\mathbf{W}_N(\boldsymbol{\Lambda}_{NC} + \boldsymbol{\Lambda}_{NE}) + \mathbf{W}_T(\boldsymbol{\Lambda}_{TC} + \boldsymbol{\Lambda}_{TE})), \quad (5.24)$$

The above impact theory has been verified in Beitelschmidt (1999), utilizing an especially developed precision throwing machine. More than 600 throwing measurements have been performed. **Figure 5.7** depicts a typical result for a material pair PVC/PVC. The comparison with measurements is excellent, as in many other cases. In addition, such a precision machine can be conveniently used for measurement of the friction coefficients ϵ resulting in excellent accuracy; ϵ is the slope of the measured functions.
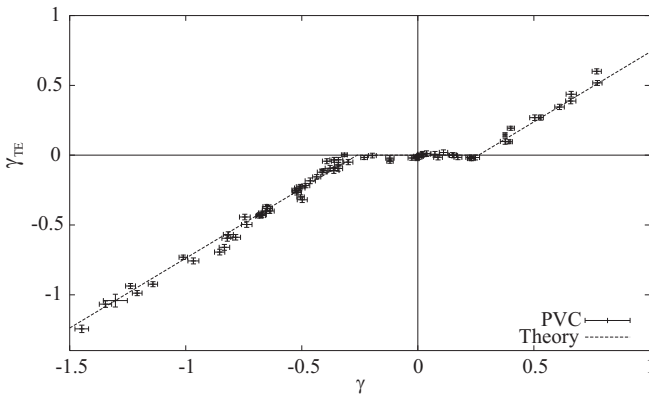
Fig. 5.7: Dimensionless tangential relative velocity after versus before the impact for a PVC-body $(\gamma = \dot{g}_{TA}/(-\dot{g}_{NA}), \quad \gamma_{TE} = \dot{g}_{TE}/(-\dot{g}_{NA}))$ (Beitelschmidt, 1999).

5.3.2 Energy Considerations

All contact processes are accompanied by losses due to the energy conversion mechanisms taking place within the contact zone. The loss of energy is the difference of the total system energy after an impact and before an impact (Pfeiffer, 2016). In terms of the generalized velocities $\dot{\mathbf{q}}$ we write

$$\Delta T = T_E - T_A \quad \leqslant \quad 0,$$
$$\Delta T = \frac{1}{2}\dot{\mathbf{q}}_E^T \mathbf{M} \dot{\mathbf{q}}_E - \frac{1}{2}\dot{\mathbf{q}}_A^T \mathbf{M} \dot{\mathbf{q}}_A = \frac{1}{2}(\dot{\mathbf{q}}_E + \dot{\mathbf{q}}_A)^T \mathbf{M}(\dot{\mathbf{q}}_E - \dot{\mathbf{q}}_A). \tag{5.25}$$

These are expressions considering scleronomic systems without an excitation by external kinematical sources and consequently do not take into account the $\mathbf{w}$-terms of the Eqs. (5.16), for example. Using the Eqs. (5.15) to (5.17) we can express the generalized velocities by the relative velocities $\dot{\mathbf{g}}$ in the contacts or by the contact impulses $\mathbf{\Lambda}$. We get

$$2\Delta T = +2\begin{pmatrix}\dot{\mathbf{g}}_{NE}\\\dot{\mathbf{g}}_{TE}\end{pmatrix}^T \mathbf{G}^{-1}\left[\begin{pmatrix}\dot{\mathbf{g}}_{NE}\\\dot{\mathbf{g}}_{TE}\end{pmatrix} - \begin{pmatrix}\dot{\mathbf{g}}_{NA}\\\dot{\mathbf{g}}_{TA}\end{pmatrix}\right] -$$
$$- \left[\begin{pmatrix}\dot{\mathbf{g}}_{NE}\\\dot{\mathbf{g}}_{TE}\end{pmatrix} - \begin{pmatrix}\dot{\mathbf{g}}_{NA}\\\dot{\mathbf{g}}_{TA}\end{pmatrix}\right]^T \cdot \mathbf{G}^{-1}\left[\begin{pmatrix}\dot{\mathbf{g}}_{NE}\\\dot{\mathbf{g}}_{TE}\end{pmatrix} - \begin{pmatrix}\dot{\mathbf{g}}_{NA}\\\dot{\mathbf{g}}_{TA}\end{pmatrix}\right],$$

$$2\Delta T = +2\begin{pmatrix}\dot{\mathbf{g}}_{NE}\\\dot{\mathbf{g}}_{TE}\end{pmatrix}^T \left[\begin{pmatrix}\mathbf{\Lambda}_{NC}\\\mathbf{\Lambda}_{TC}\end{pmatrix} + \begin{pmatrix}\mathbf{\Lambda}_{NE}\\\mathbf{\Lambda}_{TE}\end{pmatrix}\right] -$$
$$- \left[\begin{pmatrix}\mathbf{\Lambda}_{NC}\\\mathbf{\Lambda}_{TC}\end{pmatrix} + \begin{pmatrix}\mathbf{\Lambda}_{NE}\\\mathbf{\Lambda}_{TE}\end{pmatrix}\right]^T \cdot \mathbf{G}\left[\begin{pmatrix}\mathbf{\Lambda}_{NC}\\\mathbf{\Lambda}_{TC}\end{pmatrix} + \begin{pmatrix}\mathbf{\Lambda}_{NE}\\\mathbf{\Lambda}_{TE}\end{pmatrix}\right]. \tag{5.26}$$

The second term of these two energy equations is a quadratic form and for itself always positive or zero. The matrix $\mathbf{G}$ is at least positive semi-definite, which is also true for its inverse $\mathbf{G}^{-1}$. The energy loss has to be negative, which will be decided by the first term of the above relations. If this term is negative or at least zero, the condition $\Delta T \leqslant 0$ will hold. Therefore we shall concentrate on these first terms, which writes in more detail (see equation for the matrix $\mathbf{G}$ and the abbreviations $\mathbf{G}^{-1} = \bar{\mathbf{G}}$, $\Delta T = \Delta T_1 + \Delta T_2$ for the two energy terms in Eq. (5.26))

$$\Delta T_1 = +\begin{pmatrix}\dot{\mathbf{g}}_{NE}\\\dot{\mathbf{g}}_{TE}\end{pmatrix}^T \bar{\mathbf{G}}\left[\begin{pmatrix}\dot{\mathbf{g}}_{NE}\\\dot{\mathbf{g}}_{TE}\end{pmatrix} - \begin{pmatrix}\dot{\mathbf{g}}_{NA}\\\dot{\mathbf{g}}_{TA}\end{pmatrix}\right]$$
$$= \{\dot{\mathbf{g}}_{NE}^T[\bar{\mathbf{G}}_{NN}(\dot{\mathbf{g}}_{NE} - \dot{\mathbf{g}}_{NA}) + \bar{\mathbf{G}}_{NT}(\dot{\mathbf{g}}_{TE} - \dot{\mathbf{g}}_{TA})]$$
$$+ \dot{\mathbf{g}}_{TE}^T[\bar{\mathbf{G}}_{TN}(\dot{\mathbf{g}}_{NE} - \dot{\mathbf{g}}_{NA}) + \bar{\mathbf{G}}_{TT}(\dot{\mathbf{g}}_{TE} - \dot{\mathbf{g}}_{TA})]\},$$
$$\Delta T_2 = +\begin{pmatrix}\dot{\mathbf{g}}_{NE}\\\dot{\mathbf{g}}_{TE}\end{pmatrix}^T \left[\begin{pmatrix}\mathbf{\Lambda}_{NC}\\\mathbf{\Lambda}_{TC}\end{pmatrix} + \begin{pmatrix}\mathbf{\Lambda}_{NE}\\\mathbf{\Lambda}_{TE}\end{pmatrix}\right]$$
$$= \{\dot{\mathbf{g}}_{NE}^T(\mathbf{\Lambda}_{NC} + \mathbf{\Lambda}_{NE}) + \dot{\mathbf{g}}_{TE}^T(\mathbf{\Lambda}_{TC} + \mathbf{\Lambda}_{TE})\}. \tag{5.27}$$

To estimate the sign of these terms we need to look at the contact laws, for example the complementarities of the relations (5.10) and (5.14). For this consideration the second form of the energy losses is more convenient than the first form, we only have to find out the signs of the expression $\{\dot{\mathbf{g}}_{NE}^{T}(\mathbf{\Lambda}_{NC}+\mathbf{\Lambda}_{NE})+\dot{\mathbf{g}}_{TE}^{T}(\mathbf{\Lambda}_{TC}+\mathbf{\Lambda}_{TE})\}$. For this purpose we investigate the possible impact cases, namely compression and expansion either with sticking or sliding, which makes altogether four cases under the assumption that we have always contact and no detachment *during* the impact.

At this point we must discuss our model concept. We consider the beginning of an impact with index A, a compression phase with index C and an expansion phase with index E, all indices expressing the end of the corresponding phase. Therefore we get from our model and the evaluation of the preceding chapters the C-magnitudes at the end of compression and the E-magnitudes at the end of expansion, the last ones being the magnitudes after the impact. This is all clear, theoretically and experimentally often verified, and gives correct results. For the consideration of an impact we do not need the internal details of compression and expansion. But we need them for an energy consideration.

We need to know, for example, how and where a transition sticking/sliding or vice versa occurs within the structure of the impact. As we do not have some means to determine that, we say, transitions occur always at the end of the phases compression and expansion in an infinitesimal short instant of time not influencing the impact dynamics but only going from one branch of the corner laws of the **Figs. (5.5)**, **(5.6)** to another branch, which means, transitions take place in the corners of the contact laws. This model concept has influence on the energy evaluation.

So it can be shown that the first term $\dot{\mathbf{g}}_{NE}^{T}(\mathbf{\Lambda}_{NC}+\mathbf{\Lambda}_{NE})$ of the energy equation (5.27), last line, is not zero due to positive normal impulses $(\mathbf{\Lambda}_{NC}+\mathbf{\Lambda}_{NE})$ and due to a non-zero end velocity $\dot{\mathbf{g}}_{NE}$ after the impact, which is physically reasonable for a separation of the two contacting bodies. But on the other hand sliding during expansion requires a zero normal relative velocity $\dot{g}_{NE}=0$ in the contact, which makes the above mentioned term to zero. The solution can only consist in a model concept, where the change from contact to detachment takes place at the very last end of the expansion phase. The $(\mathbf{\Lambda}_{NE})$-value slips into the corner of **Fig. (5.5)** allowing the system to build up the necessary separation velocity.

As a result of the last condition of continual contact during the impact we get for compression and expansion $\mathbf{\Lambda}_{N}>0$ and $\dot{\mathbf{g}}_{N}=0$, which is also part of the complementarity eq. (5.10), and therefore simply

$$2\Delta T_{I}=2\dot{\mathbf{g}}_{TE}^{T}(\mathbf{\Lambda}_{TC}+\mathbf{\Lambda}_{TE}),\qquad(5.28)$$

the sign of which we have to investigate. Before doing so we consider the sliding cases. All sticking cases are governed by set-valued impulse laws, all sliding cases by a single-valued impulse law, the one by Coulomb. Accordingly, the sliding impulse is proportional to the normal constraint impulse and opposite to $(\dot{\mathbf{g}}_{Tk})$. Therefore it holds

$$\mathbf{\Lambda}_{Tk}=-\mathrm{diag}(\mu)\mathrm{sign}(\dot{\mathbf{g}}_{Tk})\mathbf{\Lambda}_{Nk},\qquad(k=C,E)\qquad(5.29)$$

and for sliding $(\dot{\mathbf{g}}_{Tk}) \neq \mathbf{0}$, always, and therefore we get for the second expression of the energy term ΔT_1 in Eq. (5.28) together with Eq. (5.29) the following result

$$\dot{\mathbf{g}}_{TE}^{\mathsf{T}}\mathbf{\Lambda}_{TE} = -\text{diag}(\mu)|\dot{\mathbf{g}}_{TE}|\mathbf{\Lambda}_{NE} \leqslant 0 \qquad (5.30)$$

due to the fact of continual contact and thus $\mathbf{\Lambda}_{NE} > 0$. With these results in mind we come to the four impact cases:

- **Sticking during compression, sticking during expansion**
  The tangential impulses have to be within the appropriate friction cones. The tangential velocities are zero, therefore we need not to consider the magnitudes of the impulses. For the definitions see also the **Figs. 5.5** and **5.6**.
  $-\text{diag}(\mu_0)\mathbf{\Lambda}_{NC} \leqslant \mathbf{\Lambda}_{TC} \leqslant +\text{diag}(\mu_0)\mathbf{\Lambda}_{NC}, \qquad \mathbf{\Lambda}_{TEL} \leqslant \mathbf{\Lambda}_{TE} \leqslant \mathbf{\Lambda}_{TER}$
  $\implies \quad \dot{\mathbf{g}}_{TE}^{\mathsf{T}}(\mathbf{\Lambda}_{TC} + \mathbf{\Lambda}_{TE}) = 0.$
- **Sliding during compression, sliding during expansion**
  Sliding means single-valued impulse laws according to equation (5.29). Some difficulties will appear for the cases with reversed sliding. That means, with a tangential relative velocity the sign of which is different during compression and during expansion. Therefore we have to consider the two cases without and with tangential reversibility. For the first case we do not have a change of sign of the relative tangential velocity, which gives $\text{sign}(\dot{\mathbf{g}}_{TC}) = \text{sign}(\dot{\mathbf{g}}_{TE})$. This comes out with the relations
  $\dot{\mathbf{g}}_{TE}^{\mathsf{T}}\mathbf{\Lambda}_{TC} = -\dot{\mathbf{g}}_{TE}^{\mathsf{T}}[\text{diag}(\mu)\text{sign}(\dot{\mathbf{g}}_{TE})\mathbf{\Lambda}_{NC}] = -\text{diag}(\mu)|\dot{\mathbf{g}}_{TE}|\mathbf{\Lambda}_{NC} \leqslant 0$
  $\implies \quad \dot{\mathbf{g}}_{TE}^{\mathsf{T}}(\mathbf{\Lambda}_{TC} + \mathbf{\Lambda}_{TE}) < 0.$
  The case with tangential reversibility is more complicated, because it includes a change of sign of the tangential relative velocity and thus at least an extremely short stiction phase, which we put exactly at the point (end of compression)/(beginning of expansion). The sliding velocity during compression decreases until it arrives at one of the corners of **Fig. 5.6**, then we get an extremely short shift from this corner to the other one, which allows the contact to build up a tangential velocity with an opposite sign, then valid for the expansion phase. Only by such a short stiction phase a reversal of tangential velocity is possible. On the other hand such a transition from stick to slip, as short as it might be, follows the same process as for the next case sticking/sliding. Therefore it is dissipative.
  $\implies \quad \dot{\mathbf{g}}_{TE}^{\mathsf{T}}(\mathbf{\Lambda}_{TC} + \mathbf{\Lambda}_{TE}) < 0.$
- **Sticking during compression, sliding during expansion**
  The transition from sticking in compression and sliding in expansion follows the mechanism (**Fig. 5.6**): If $\mathbf{\Lambda}_{TC} \gtrless \mathbf{0}$, then sliding is only possible for being at the very end of compression on the friction cone boundary with

$$\mathbf{\Lambda}_{TC} = \pm\text{diag}(\mu)\mathbf{\Lambda}_{NC}$$

and $\dot{\mathbf{g}}_{TC-at} \lessgtr \mathbf{0}$ (at = after transition stick-slip). This results always in a negative sign of the expression $(\dot{\mathbf{g}}_{TE}^{\mathsf{T}}\mathbf{\Lambda}_{TC})$. For the rest we assume a continuation of the signs after going from stick to slip [$\text{sign}(\dot{\mathbf{g}}_{TE}) = \text{sign}(\dot{\mathbf{g}}_{TC-at})$]. Then we arrive

at:
$$\implies \quad \dot{\mathbf{g}}_{TE}^{T}(\mathbf{\Lambda}_{TC} + \mathbf{\Lambda}_{TE}) < 0.$$

- **Sliding during compression, sticking during expansion**
  This case is again simpler, because we get sticking at the end with a zero relative tangential velocity. Therefore we need not to consider the impulses.
  $$\implies \quad \dot{\mathbf{g}}_{TE}^{T}(\mathbf{\Lambda}_{TC} + \mathbf{\Lambda}_{TE}) = 0.$$

- **Summarized result for all four cases**
  $$\implies \quad \dot{\mathbf{g}}_{TE}^{T}(\mathbf{\Lambda}_{TC} + \mathbf{\Lambda}_{TE}) \leqslant 0 \implies \Delta T_1 \leqslant 0,$$
  $$\implies \quad \Delta T \leqslant 0.$$

One may object that the above considerations assume in the case of multiple impacts the same impact structure for all simultaneously appearing impacts, which is usually not true. But even any combination of the above four cases for simultaneous impacts gives a loss of energy. Practical experience indicates in addition that the simultaneous appearance of impacts is extremely scarce, it is an event, which nearly does not happen.

As a final result we may state that the above evaluation confirms the physical argument, that any impact processes are accompanied by energy losses. This confirms also the well-known statement of Carnot, that *"in the absence of impressed impulses, the sudden introduction of stationary and persistent constraints that change some velocity reduces the kinetic energy. Hence, by the collision of inelastic bodies, some kinetic energy is always lost"* (Pars, 1979).

5.4 Contact Kinematics

Geometry and kinematics are the fundament for establishing models of dynamical systems. In the case of unilateral contacts this is especially important, because magnitudes of relative kinematics serve as indicators for passive contacts and as constraints for active contacts (see Sect. 5.1). As most of the applications require more or less arbitrary body contours it makes sense to derive the kinematical contact equations in a general form applying well-known rules of the differential geometry of surfaces (Glocker, 1995; Meitinger, 1998; Pfeiffer and Glocker, 1996).

In practice we find two types of contacts, two- and three-dimensional ones. For the two-dimensional case the contacting bodies lie in a plane thus defining a contact line with given direction. Only the sense of direction has to be determined. Problems of that kind are connected with linear complementarity.

For the three-dimensional case the contacting bodies have a spatial form, and the contact takes place in a plane allowing two tangential directions. The resulting direction for the contact process is not known beforehand and usually must be determined iteratively. Problems of that kind are connected with nonlinear complementarity.

5.4.1 Plane Contact Kinematics

Plane contact kinematics has been presented in Glocker (1995) and are then applied to many practical problems (see also Pfeiffer and Glocker, 1996). We start with the geometry of a single body as indicated in **Fig. 5.8**. We assume a convex contour and describe it by a parameter s. Connecting with s a moving trihedral $(\mathbf{t}, \mathbf{n}, \mathbf{b})$ and introducing a body-fixed frame B we write

$$
\begin{aligned}
&_B\mathbf{t} = {}_B\mathbf{r}'_{P\Sigma}; \quad \kappa_B\mathbf{n} = {}_B\mathbf{r}''_{P\Sigma}; \quad (\;\cdot\;)' = \frac{d}{ds} \; , \\
&_B\mathbf{n} = {}_B\mathbf{b} \times {}_B\mathbf{t}, \quad _B\mathbf{b} = {}_B\mathbf{t} \times {}_B\mathbf{n} \; , \\
&_B\mathbf{t} = {}_B\mathbf{n} \times {}_B\mathbf{b} \; , \\
&_B\mathbf{n}' = {}_B\mathbf{b} \times {}_B\mathbf{t}' = {}_B\mathbf{b} \times {}_B\mathbf{n}\kappa = -\kappa_B\mathbf{t}, \\
&_B\mathbf{t}' = \kappa_B\mathbf{n} \; .
\end{aligned}
\tag{5.31}
$$

For planar contours the binormal $_B\mathbf{b}$ is constant. Therefore

$$
_B\dot{\mathbf{n}} = {}_B\mathbf{n}'\dot{s} = -\kappa\dot{s}\,_B\mathbf{t} \; , \qquad _B\dot{\mathbf{t}} = {}_B\mathbf{t}'\dot{s} = +\kappa\dot{s}\,_B\mathbf{n} \; .
\tag{5.32}
$$

On the other hand, the absolute changes of $\mathbf{n}$ and $\mathbf{t}$ are given by the Coriolis equation

$$
_B(\dot{\mathbf{n}}) = {}_B\dot{\mathbf{n}} + {}_B\tilde{\boldsymbol{\Omega}}\,_B\mathbf{n} \; , \qquad _B(\dot{\mathbf{t}}) = {}_B\dot{\mathbf{t}} + {}_B\tilde{\boldsymbol{\Omega}}\,_B\mathbf{t} \; ,
\tag{5.33}
$$

where we must keep in mind that $_B\boldsymbol{\omega}_{IB} = {}_B\boldsymbol{\Omega}$ for body-fixed frames B. Putting (5.32) into (5.33) we get a coordinate-free representation of the overall changes $\dot{\mathbf{n}}, \dot{\mathbf{t}}$.

$$
\dot{\mathbf{n}} = \tilde{\boldsymbol{\Omega}}\mathbf{n} - \kappa\dot{s}\mathbf{t} \; , \qquad \dot{\mathbf{t}} = \tilde{\boldsymbol{\Omega}}\mathbf{t} + \kappa\dot{s}\mathbf{n} \; ,
\tag{5.34}
$$

which we can evaluate in any basis. The main advantage of (5.34) consists of the eliminated, frame-dependent differentiations $_B\dot{\mathbf{n}}$ and $_B\dot{\mathbf{t}}$.
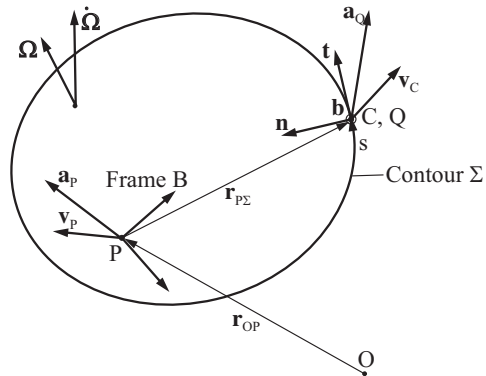
Fig. 5.8 Planar contour geometry.

In the same manner we proceed with the contour vector $\mathbf{r}_{P\Sigma}$. According to (5.32), (5.33) we write

$$_B\dot{\mathbf{r}}_{P\Sigma} =_B \mathbf{r}'_{P\Sigma}\,\dot{s} = \dot{s}\,_B\mathbf{t}, \qquad _B(\dot{\mathbf{r}}_{P\Sigma}) =_B \dot{\mathbf{r}}_{P\Sigma} +_B \tilde{\boldsymbol{\Omega}}\,_B\mathbf{r}_{P\Sigma} \ , \tag{5.35}$$

and eliminate $_B\dot{\mathbf{r}}_{P\Sigma}$. Then we get the absolute changes of $\mathbf{r}_{P\Sigma}$,

$$\dot{\mathbf{r}}_{P\Sigma} = \tilde{\boldsymbol{\Omega}}\mathbf{r}_{P\Sigma} + \dot{s}\,\mathbf{t} \ . \tag{5.36}$$

Due to $\mathbf{v}_\Sigma = \mathbf{v}_P + \dot{\mathbf{r}}_{P\Sigma}$, the absolute velocity of the moving contour point is given by

$$\mathbf{v}_\Sigma = \mathbf{v}_P + \tilde{\boldsymbol{\Omega}}\mathbf{r}_{P\Sigma} + \dot{s}\,\mathbf{t} \ , \tag{5.37}$$

where

$$\mathbf{v}_C := \mathbf{v}_P + \tilde{\boldsymbol{\Omega}}\,\mathbf{r}_{P\Sigma} \ . \tag{5.38}$$

The velocity $\mathbf{v}_C$ results from rigid body kinematics and corresponds to the velocity of a body-fixed point at the contour. From (5.37) and (5.38) we see that

$$\mathbf{v}_\Sigma = \mathbf{v}_C + \dot{s}\,\mathbf{t} \ . \tag{5.39}$$

Next, we want to derive the absolute acceleration of C by differentiating (5.38) with respect to time:

$$\dot{\mathbf{v}}_C = \dot{\mathbf{v}}_P + \dot{\tilde{\boldsymbol{\Omega}}}\mathbf{r}_{P\Sigma} + \tilde{\boldsymbol{\Omega}}\dot{\mathbf{r}}_{P\Sigma} \ . \tag{5.40}$$

With $\dot{\mathbf{v}}_C = \mathbf{a}_C, \dot{\mathbf{v}}_P = \mathbf{a}_P$ and $\dot{\mathbf{r}}_{P\Sigma}$ from Eq. (5.35) we get

$$\mathbf{a}_C = \mathbf{a}_P + \dot{\tilde{\boldsymbol{\Omega}}}\mathbf{r}_{P\Sigma} + \tilde{\boldsymbol{\Omega}}\tilde{\boldsymbol{\Omega}}\mathbf{r}_{P\Sigma} + \tilde{\boldsymbol{\Omega}}\mathbf{t}\,\dot{s}, \tag{5.41}$$

which is *not* the acceleration of a body-fixed point on the contour. Only the part

$$\mathbf{a}_Q := \mathbf{a}_P + \dot{\tilde{\boldsymbol{\Omega}}}\mathbf{r}_{P\Sigma} + \tilde{\boldsymbol{\Omega}}\tilde{\boldsymbol{\Omega}}\mathbf{r}_{P\Sigma} \tag{5.42}$$

corresponds to such an acceleration, so we can write

$$\mathbf{a}_C = \mathbf{a}_Q + \tilde{\boldsymbol{\Omega}}\mathbf{t}\,\dot{s} \ . \tag{5.43}$$

Later we have to determine the relative velocities of contact points in the normal and tangential directions and their time derivatives. For this purpose we introduce the scalars

$$v_n = \mathbf{n}^\mathsf{T}\mathbf{v}_C, \quad v_t = \mathbf{t}^\mathsf{T}\mathbf{v}_C \tag{5.44}$$

and state their derivatives as

$$\dot{v}_n = \dot{\mathbf{n}}^\mathsf{T}\mathbf{v}_C + \mathbf{n}^\mathsf{T}\dot{\mathbf{v}}_C \ , \qquad \dot{v}_t = \dot{\mathbf{t}}^\mathsf{T}\mathbf{v}_C + \mathbf{t}^\mathsf{T}\dot{\mathbf{v}}_C \ . \tag{5.45}$$

With $\dot{\mathbf{n}}, \dot{\mathbf{t}}$ from (5.34), $\dot{\mathbf{v}}_C = \mathbf{a}_C$ from (5.43), and noting $\mathbf{n}^\mathsf{T}\tilde{\boldsymbol{\Omega}}\mathbf{t} = \mathbf{b}^\mathsf{T}\boldsymbol{\Omega}, \mathbf{t}^\mathsf{T}\tilde{\boldsymbol{\Omega}}\mathbf{t} = 0$ we derive

$$\dot{v}_n = \mathbf{n}^\mathsf{T}\left(\mathbf{a}_Q - \tilde{\mathbf{\Omega}}\mathbf{v}_C\right) - \kappa\dot{s}\mathbf{t}^\mathsf{T}\mathbf{v}_C + \dot{s}\mathbf{b}^\mathsf{T}\mathbf{\Omega},$$
$$\dot{v}_t = \mathbf{t}^\mathsf{T}\left(\mathbf{a}_Q - \tilde{\mathbf{\Omega}}\mathbf{v}_C\right) + \kappa\dot{s}\mathbf{n}^\mathsf{T}\mathbf{v}_C \ . \tag{5.46}$$

With this basis we are able to derive the relative kinematics of two bodies such as relative distances, relative velocities and accelerations. Without going into details and referring especially to Pfeiffer and Glocker (1996) we summarize the relationships as depicted in **Fig. 5.9**:

Potential contact points can be characterized by

$$\mathbf{n}_1^\mathsf{T}(s_1)\cdot\mathbf{t}_2(s_2) = 0 \ \Leftrightarrow \ \mathbf{n}_2^\mathsf{T}(s_2)\cdot\mathbf{t}_1(s_1) = 0 \ , \tag{5.47}$$

$$\mathbf{r}_D^\mathsf{T}(s_1,s_2)\cdot\mathbf{t}_1(s_1) = 0, \qquad \mathbf{r}_D^\mathsf{T}(s_1,s_2)\cdot\mathbf{t}_2(s_2) = 0 \ . \tag{5.48}$$

From each set we need only one equation. The relative distance g_N is

$$g_N(\mathbf{q},t) = \mathbf{r}_D^\mathsf{T}\mathbf{n}_2 = -\mathbf{r}_D^\mathsf{T}\mathbf{n}_1. \tag{5.49}$$

Since the normal vectors always point inward, g_N is positive for separation and negative for overlapping. Therefore, a changing sign of g_N from positive to negative indicates a transition from initially separated bodies to contact.

With these equations and considering **Fig. 5.9** we derive the relative velocities in normal and tangential direction

$$\dot{g}_N = \mathbf{n}_1^\mathsf{T}\mathbf{v}_{C1} + \mathbf{n}_2^\mathsf{T}\mathbf{v}_{C2}, \qquad \dot{g}_T = \mathbf{t}_1^\mathsf{T}\mathbf{v}_{C1} + \mathbf{t}_2^\mathsf{T}\mathbf{v}_{C2}, \tag{5.50}$$

where $\mathbf{v}_{C1},\mathbf{v}_{C2}$ are the absolute velocities of the potential contact points C_1,C_2. These velocities might be expressed by the generalized velocities $\dot{\mathbf{q}}$ and some Jacobians $\mathbf{J}_{C1},\mathbf{J}_{C2}$ to give

$$\mathbf{v}_{C1} = \mathbf{J}_{C1}\dot{\mathbf{q}} + \tilde{\mathbf{j}}_{C1}, \qquad \mathbf{v}_{C2} = \mathbf{J}_{C2}\dot{\mathbf{q}} + \tilde{\mathbf{j}}_{C2}. \tag{5.51}$$

Putting (5.50) into (5.51) yields
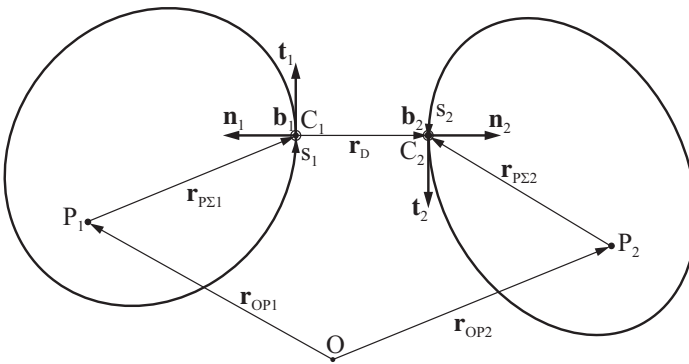
Fig. 5.9: General orientation of two bodies.

$$\dot{g}_N = \mathbf{w}_N^\mathsf{T}\dot{\mathbf{q}} + \tilde{w}_N; \qquad \dot{g}_T = \mathbf{w}_T^\mathsf{T}\dot{\mathbf{q}} + \tilde{w}_T \qquad (5.52)$$

with

$$\begin{aligned}
\mathbf{w}_N &= \mathbf{J}_{C1}^\mathsf{T}\mathbf{n}_1 + \mathbf{J}_{C2}^\mathsf{T}\mathbf{n}_2; & \mathbf{w}_T &= \mathbf{J}_{C1}^\mathsf{T}\mathbf{t}_1 + \mathbf{J}_{C2}^\mathsf{T}\mathbf{t}_2, \\
\tilde{w}_N &= \tilde{\mathbf{j}}_{C1}^\mathsf{T}\mathbf{n}_1 + \tilde{\mathbf{j}}_{C2}^\mathsf{T}\mathbf{n}_2; & \tilde{w}_T &= \tilde{\mathbf{j}}_{C1}^\mathsf{T}\mathbf{t}_1 + \tilde{\mathbf{j}}_{C2}^\mathsf{T}\mathbf{t}_2,
\end{aligned} \qquad (5.53)$$

which we use in the following as a representation of the relative velocities. It may be noticed here that a negative value of $\dot{g}_N$ corresponds to an approaching process of the bodies and coincides at vanishing distance $g_N = 0$ with the relative velocity in the normal direction before an impact. In the case of a continual contact ($g_N = \dot{g}_N = 0$) the term $\dot{g}_T$ shows the relative sliding velocity of the bodies, which we can use to determine the time points of transitions from sliding ($\dot{g}_T \neq 0$) to sticking or rolling ($\dot{g}_T = 0$).

The relevant accelerations follow from a further time differentiation.

$$\ddot{g}_N = \mathbf{w}_N^\mathsf{T}\ddot{\mathbf{q}} + \overline{w}_N, \quad \ddot{g}_T = \mathbf{w}_T^\mathsf{T}\ddot{\mathbf{q}} + \overline{w}_T, \qquad (5.54)$$

where $\mathbf{w}_N, \mathbf{w}_T$ are given by (5.53), and $\overline{w}_n, \overline{w}_T$ are

$$\begin{aligned}
\overline{w}_N &= \mathbf{n}_1^\mathsf{T}(\bar{\mathbf{j}}_{Q1} - \tilde{\mathbf{\Omega}}_1\mathbf{v}_{C1}) - \kappa_1\dot{s}_1\mathbf{t}_1^\mathsf{T}\mathbf{v}_{C1} + \dot{s}_1\mathbf{b}_{12}^\mathsf{T}\mathbf{\Omega}_1 \\
&\quad + \mathbf{n}_2^\mathsf{T}(\bar{\mathbf{j}}_{Q2} - \tilde{\mathbf{\Omega}}_2\mathbf{v}_{C2}) - \kappa_2\dot{s}_2\mathbf{t}_2^\mathsf{T}\mathbf{v}_{C2} + \dot{s}_2\mathbf{b}_{12}^\mathsf{T}\mathbf{\Omega}_2, \\
\overline{w}_T &= \mathbf{t}_1^\mathsf{T}(\bar{\mathbf{j}}_{Q1} - \tilde{\mathbf{\Omega}}_1\mathbf{v}_{C1}) + \kappa_1\dot{s}_1\mathbf{n}_1^\mathsf{T}\mathbf{v}_{C1} \\
&\quad + \mathbf{t}_2^\mathsf{T}(\bar{\mathbf{j}}_{Q2} - \tilde{\mathbf{\Omega}}_2\mathbf{v}_{C2}) + \kappa_2\dot{s}_2\mathbf{n}_2^\mathsf{T}\mathbf{v}_{C2},
\end{aligned} \qquad (5.55)$$

with

$$\dot{s}_1 = \frac{\kappa_2\mathbf{t}_1^\mathsf{T}(\mathbf{v}_{C2} - \mathbf{v}_{C1}) - \kappa_2 g_N\mathbf{b}_{12}^\mathsf{T}\mathbf{\Omega}_1 + \mathbf{b}_{12}^\mathsf{T}(\mathbf{\Omega}_2 - \mathbf{\Omega}_1)}{\kappa_1 + \kappa_2 + g_N\kappa_1\kappa_2},$$

$$\dot{s}_2 = \frac{\kappa_1\mathbf{t}_1^\mathsf{T}(\mathbf{v}_{C2} - \mathbf{v}_{C1}) - \kappa_1 g_N\mathbf{b}_{12}^\mathsf{T}\mathbf{\Omega}_2 - \mathbf{b}_{12}^\mathsf{T}(\mathbf{\Omega}_2 - \mathbf{\Omega}_1)}{\kappa_1 + \kappa_2 + g_N\kappa_1\kappa_2}$$

The angular velocities $\mathbf{\Omega}_1, \mathbf{\Omega}_2$ relate to the two contacting bodies (**Figs. 5.8** and **5.9**).

5.4.2 Spatial Contact Kinematics

Spatial contact kinematics has been presented in the dissertation (Meitinger, 1998) and since then applied to many practical problems. The situation in this case is of course more complex. We still assume that the two approaching bodies are convex (**Fig. 5.10**) at least in that area where contact points might occur. The two bodies are moving with $\mathbf{v}_i, \mathbf{\Omega}_i (i = 1, 2)$. For the description of a surface Σ we need two parameters s and $t : \mathbf{r}_\Sigma = \mathbf{r}_\Sigma(s, t)$. The tangents $\mathbf{s}$ and $\mathbf{t}$, which span the tangent plane at a point of the surface, are defined as

Fig. 5.10 Contact geometry of two surfaces.
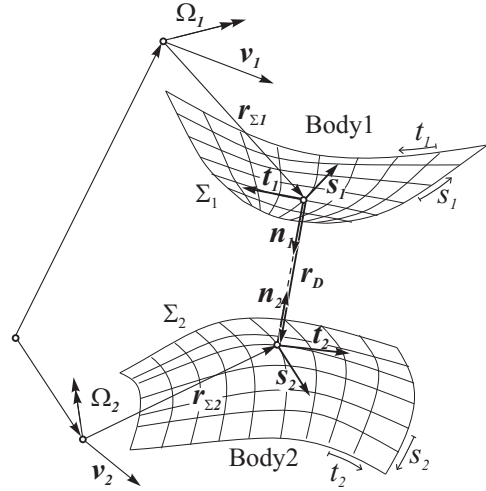
$$\mathbf{s} = \frac{\partial \mathbf{r}_\Sigma}{\partial s}, \quad \mathbf{t} = \frac{\partial \mathbf{r}_\Sigma}{\partial t}. \tag{5.56}$$

From these basic vectors the fundamental magnitudes of the first order are calculated

$$E = \mathbf{s}^\mathsf{T}\mathbf{s}, \quad F = \mathbf{s}^\mathsf{T}\mathbf{t}, \quad G = \mathbf{t}^\mathsf{T}\mathbf{t}. \tag{5.57}$$

The normalized normal vector $\mathbf{n}$ is perpendicular to the tangential plane pointing outwards

$$\mathbf{n} = \frac{\mathbf{s} \times \mathbf{t}}{\sqrt{EG - F^2}}. \tag{5.58}$$

We further need the fundamental magnitudes of the second order

$$L = \mathbf{n}^\mathsf{T}\frac{\partial^2 \mathbf{r}_\Sigma}{\partial s^2}, \quad M = \mathbf{n}^\mathsf{T}\frac{\partial^2 \mathbf{r}_\Sigma}{\partial s \partial t}, \quad N = \mathbf{n}^\mathsf{T}\frac{\partial^2 \mathbf{r}_\Sigma}{\partial t^2}. \tag{5.59}$$

For a contact point we require that the normal vector of body 1 ($\mathbf{n}_1$) and the distance vector $\mathbf{r}_D$ are perpendicular to the tangent vectors of body 2 ($\mathbf{s}_2$ and $\mathbf{t}_2$). Thus we obtain four nonlinear equations

$$\begin{aligned} \mathbf{n}_1^\mathsf{T}\mathbf{s}_2 &= 0, \quad \mathbf{r}_D^\mathsf{T}\mathbf{s}_2 = 0, \\ \mathbf{n}_1^\mathsf{T}\mathbf{t}_2 &= 0, \quad \mathbf{r}_D^\mathsf{T}\mathbf{t}_2 = 0. \end{aligned} \tag{5.60}$$

This nonlinear problem has to be solved at every time step of the numerical integration. After the solution is found the distance g_N between the possible contact points can be calculated as

$$g_N = \mathbf{n}_1^\mathsf{T}\mathbf{r}_D = -\mathbf{n}_2^\mathsf{T}\mathbf{r}_D. \tag{5.61}$$

g_N is used as an indicator for the contact state. Its value is positive for 'no contact' and negative for penetration. The constraints are again formulated on velocity level, where in the spatial case we have three of them, one in normal direction $\dot{g}_N$ and two in the tangential directions $\dot{g}_S, \dot{g}_T$

$$
\begin{aligned}
\dot{g}_N(\mathbf{q},\dot{\mathbf{q}},t) &= \mathbf{n}_1^{\mathsf{T}}(\mathbf{v}_{\Sigma 2} - \mathbf{v}_{\Sigma 1})\,, \\
\dot{g}_S(\mathbf{q},\dot{\mathbf{q}},t) &= \mathbf{s}_1^{\mathsf{T}}(\mathbf{v}_{\Sigma 2} - \mathbf{v}_{\Sigma 1})\,, \\
\dot{g}_T(\mathbf{q},\dot{\mathbf{q}},t) &= \mathbf{t}_1^{\mathsf{T}}(\mathbf{v}_{\Sigma 2} - \mathbf{v}_{\Sigma 1})\,,
\end{aligned}
\tag{5.62}
$$

with $\mathbf{v}_{\Sigma 1}$ and $\mathbf{v}_{\Sigma 2}$ being defined in an analoguous way as in (5.51). Differentiating these equations with respect to time leads to the constraints on acceleration level

$$
\begin{aligned}
\ddot{g}_N &= \mathbf{n}_1^{\mathsf{T}}(\dot{\mathbf{v}}_{\Sigma 2} - \dot{\mathbf{v}}_{\Sigma 1}) + \dot{\mathbf{n}}_1^{\mathsf{T}}(\mathbf{v}_{\Sigma 2} - \mathbf{v}_{\Sigma 1})\,, \\
\ddot{g}_S &= \mathbf{s}_1^{\mathsf{T}}(\dot{\mathbf{v}}_{\Sigma 2} - \dot{\mathbf{v}}_{\Sigma 1}) + \dot{\mathbf{s}}_1^{\mathsf{T}}(\mathbf{v}_{\Sigma 2} - \mathbf{v}_{\Sigma 1})\,, \\
\ddot{g}_T &= \mathbf{t}_1^{\mathsf{T}}(\dot{\mathbf{v}}_{\Sigma 2} - \dot{\mathbf{v}}_{\Sigma 1}) + \dot{\mathbf{t}}_1^{\mathsf{T}}(\mathbf{v}_{\Sigma 2} - \mathbf{v}_{\Sigma 1})\,.
\end{aligned}
\tag{5.63}
$$

The time derivatives of the contact point velocities $\mathbf{v}_{\Sigma 1}$ and $\mathbf{v}_{\Sigma 2}$ can be written in the form

$$
\begin{aligned}
\dot{\mathbf{v}}_{\Sigma 1} &= \mathbf{J}_{\Sigma 1}(\mathbf{q},t)\ddot{\mathbf{q}} + \bar{\mathbf{j}}_{\Sigma 1}(\dot{\mathbf{q}},\mathbf{q},t)\,, \\
\dot{\mathbf{v}}_{\Sigma 2} &= \mathbf{J}_{\Sigma 2}(\mathbf{q},t)\ddot{\mathbf{q}} + \bar{\mathbf{j}}_{\Sigma 2}(\dot{\mathbf{q}},\mathbf{q},t)\,.
\end{aligned}
\tag{5.64}
$$

The vectors $\dot{\mathbf{n}}_1, \dot{\mathbf{s}}_1$ and $\dot{\mathbf{t}}_1$ are determined by the formulas of Weingarten and Gauss Zeidler et al. (2003), which express the derivatives of the normal vector and of the tangent vectors in terms of the basic vectors:

$$
\dot{\mathbf{n}}_1 = \boldsymbol{\Omega}_1 \times \mathbf{n}_1 + \frac{\partial \mathbf{n}_1}{\partial s_1}\dot{s}_1 + \frac{\partial \mathbf{n}_1}{\partial t_1}\dot{t}_1\,,
$$

$$
\frac{\partial \mathbf{n}_1}{\partial s_1} = \underbrace{\frac{M_1 F_1 - L_1 G_1}{E_1 G_1 - F_1^2}}_{\alpha_1}\mathbf{s}_1 + \underbrace{\frac{L_1 F_1 - M_1 E_1}{E_1 G_1 - F_1^2}}_{\beta_1}\mathbf{t}_1\,,
$$

$$
\frac{\partial \mathbf{n}_1}{\partial t_1} = \underbrace{\frac{N_1 F_1 - M_1 G_1}{E_1 G_1 - F_1^2}}_{\alpha_1'}\mathbf{s}_1 + \underbrace{\frac{M_1 F_1 - N_1 E_1}{E_1 G_1 - F_1^2}}_{\beta_1'}\mathbf{t}_1\,,
\tag{5.65}
$$

$$
\dot{\mathbf{s}}_1 = \boldsymbol{\Omega}_1 \times \mathbf{s}_1 + \frac{\partial \mathbf{s}_1}{\partial s_1}\dot{s}_1 + \frac{\partial \mathbf{s}_1}{\partial t_1}\dot{t}_1\,,
$$

$$
\frac{\partial \mathbf{s}_1}{\partial s_1} = \Gamma_{11,1}^1 \mathbf{s}_1 + \Gamma_{11,1}^2 \mathbf{t}_1 + L_1 \mathbf{n}_1\,,
$$

$$
\frac{\partial \mathbf{s}_1}{\partial t_1} = \Gamma_{12,1}^1 \mathbf{s}_1 + \Gamma_{12,1}^2 \mathbf{t}_1 + M_1 \mathbf{n}_1\,,
\tag{5.66}
$$

$$\dot{\mathbf{t}}_1 = \mathbf{\Omega}_1 \times \mathbf{t}_1 + \frac{\partial \mathbf{t}_1}{\partial s_1}\dot{s}_1 + \frac{\partial \mathbf{t}_1}{\partial t_1}\dot{t}_1 \,,$$

$$\frac{\partial \mathbf{t}_1}{\partial s_1} = \Gamma^1_{12,1}\mathbf{s} + \Gamma^2_{12,1}\mathbf{t} + M_1\mathbf{n}_1 \,,$$

$$\frac{\partial \mathbf{t}_1}{\partial t_1} = \Gamma^1_{22,1}\mathbf{s} + \Gamma^2_{22,1}\mathbf{t} + N_1\mathbf{n}_1 \,. \tag{5.67}$$

The definition of the Christoffel symbols $\Gamma^{\sigma}_{\alpha\beta}$, $\alpha,\beta,\sigma = 1,2$ can be found in standard textbooks (Zeidler et al., 2003). Inserting Eqs. (5.66), (5.67) in (5.63) yields the constraint equations:

$$\ddot{g}_N = \mathbf{n}_1^{\mathsf{T}}(\mathbf{J}_{\Sigma 2}-\mathbf{J}_{\Sigma 1})\ddot{\mathbf{q}} + \mathbf{n}_1^{\mathsf{T}}\left(\bar{\mathbf{j}}_{\Sigma 2}-\bar{\mathbf{j}}_{\Sigma 1}\right) + (\mathbf{v}_{\Sigma 2}-\mathbf{v}_{\Sigma 1})^{\mathsf{T}}(\mathbf{\Omega}_1\times\mathbf{n}_1) + (\mathbf{v}_{\Sigma 2}-\mathbf{v}_{\Sigma 1})^{\mathsf{T}}\cdot$$
$$\left[(\alpha_1\mathbf{s}_1 + \beta_1\mathbf{t}_1)\dot{s}_1 + \left(\alpha'_1\mathbf{s}_1 + \beta'_1\mathbf{t}_1\right)\dot{t}_1\right] \,,$$

$$\ddot{g}_S = \mathbf{s}_1^{\mathsf{T}}(\mathbf{J}_{\Sigma 2}-\mathbf{J}_{\Sigma 1})\ddot{\mathbf{q}} + \mathbf{s}_1^{\mathsf{T}}\left(\bar{\mathbf{j}}_{\Sigma 2}-\bar{\mathbf{j}}_{\Sigma 1}\right) + (\mathbf{v}_{\Sigma 2}-\mathbf{v}_{\Sigma 1})^{\mathsf{T}}(\mathbf{\Omega}_1\times\mathbf{s}_1) + (\mathbf{v}_{\Sigma 2}-\mathbf{v}_{\Sigma 1})^{\mathsf{T}}\cdot$$
$$\left[(\Gamma^1_{11,1}\mathbf{s}_1 + \Gamma^2_{11,1}\mathbf{t}_1 + L_1\mathbf{n}_1)\dot{s}_1 + (\Gamma^1_{12,1}\mathbf{s}_1 + \Gamma^2_{12,1}\mathbf{t}_1 + M_1\mathbf{n}_1)\dot{t}_1\right] \,,$$

$$\ddot{g}_T = \mathbf{t}_1^{\mathsf{T}}(\mathbf{J}_{\Sigma 2}-\mathbf{J}_{\Sigma 1})\ddot{\mathbf{q}} + \mathbf{t}_1^{\mathsf{T}}\left(\bar{\mathbf{j}}_{\Sigma 2}-\bar{\mathbf{j}}_{\Sigma 1}\right) + (\mathbf{v}_{\Sigma 2}-\mathbf{v}_{\Sigma 1})^{\mathsf{T}}(\mathbf{\Omega}_1\times\mathbf{t}_1) + (\mathbf{v}_{\Sigma 2}-\mathbf{v}_{\Sigma 1})^{\mathsf{T}}\cdot$$
$$\left[(\Gamma^1_{12,1}\mathbf{s}_1 + \Gamma^2_{12,1}\mathbf{t}_1 + M_1\mathbf{n}_1)\dot{s}_1 + (\Gamma^1_{22,1}\mathbf{s}_1 + \Gamma^2_{22,1}\mathbf{t}_1 + N_1\mathbf{n}_1)\dot{t}_1\right] \,. \tag{5.68}$$

These equations depend on the Jacobians with respect to the contact points $\mathbf{J}_{\Sigma 1}$, $\mathbf{J}_{\Sigma 2}$, the basic vectors of the surfaces and the time derivatives of the contour parameters $\dot{s}_1, \dot{t}_1, \dot{s}_2, \dot{t}_2$. The Jacobians are known from the rigid body algorithm, the basic vectors from the surface description. The time derivatives of the contour parameters can be calculated by deriving (5.60) with respect to time:

$$(\mathbf{n}_1^{\mathsf{T}}\mathbf{s}_2)^{\cdot} = 0 \,, \qquad (\mathbf{r}_D^{\mathsf{T}}\mathbf{s}_2)^{\cdot} = 0 \,,$$
$$(\mathbf{n}_1^{\mathsf{T}}\mathbf{t}_2)^{\cdot} = 0 \,, \qquad (\mathbf{r}_D^{\mathsf{T}}\mathbf{t}_2)^{\cdot} = 0 \,, \tag{5.69}$$

which means, that the conditions for the contact point should not change while the two bodies are moving. Evaluating Eq. (5.69) we obtain a system of equations, which are linear in the derivatives of the contour parameters

$$\begin{pmatrix} \mathbf{s}_2^{\mathsf{T}}(\alpha_1\mathbf{s}_1+\beta_1\mathbf{t}_1) & \mathbf{s}_2^{\mathsf{T}}\left(\alpha'_1\mathbf{s}_1+\beta'_1\mathbf{t}_1\right) & L_2 & M_2 \\ \mathbf{t}_2^{\mathsf{T}}(\alpha_1\mathbf{s}_1+\beta_1\mathbf{t}_1) & \mathbf{t}_2^{\mathsf{T}}\left(\alpha'_1\mathbf{s}_1+\beta'_1\mathbf{t}_1\right) & M_2 & N_2 \\ -\mathbf{s}_1^{\mathsf{T}}\mathbf{s}_2 & -\mathbf{s}_1^{\mathsf{T}}\mathbf{s}_2 & \mathbf{s}_2^{\mathsf{T}}\mathbf{s}_2 & \mathbf{s}_2^{\mathsf{T}}\mathbf{t}_2 \\ -\mathbf{s}_1^{\mathsf{T}}\mathbf{t}_2 & -\mathbf{s}_1^{\mathsf{T}}\mathbf{t}_2 & \mathbf{s}_2^{\mathsf{T}}\mathbf{t}_2 & \mathbf{t}_2^{\mathsf{T}}\mathbf{t}_2 \end{pmatrix} \cdot \begin{pmatrix} \dot{s}_1 \\ \dot{t}_1 \\ \dot{s}_2 \\ \dot{t}_2 \end{pmatrix} = \begin{pmatrix} (\mathbf{s}_2\times\mathbf{n}_1)^{\mathsf{T}}(\mathbf{\Omega}_2-\mathbf{\Omega}_1) \\ (\mathbf{t}_2\times\mathbf{n}_1)^{\mathsf{T}}(\mathbf{\Omega}_2-\mathbf{\Omega}_1) \\ \mathbf{s}_2^{\mathsf{T}}(\mathbf{v}_{\Sigma 1}-\mathbf{v}_{\Sigma 2}) \\ \mathbf{t}_2^{\mathsf{T}}(\mathbf{v}_{\Sigma 1}-\mathbf{v}_{\sigma 2}) \end{pmatrix} \tag{5.70}$$

This linear problem has to be solved at every time step of numerical integration. Let us summarize the constraint equations in the well known form, by rewriting Eq. (5.68):

$$\ddot{g}_N = \mathbf{w}_N^\mathsf{T}\ddot{\mathbf{q}} + \overline{w}_N \;,$$

$$\ddot{g}_S = \mathbf{w}_S^\mathsf{T}\ddot{\mathbf{q}} + \overline{w}_S \;, \qquad\qquad (5.71)$$

$$\ddot{g}_T = \mathbf{w}_T^\mathsf{T}\ddot{\mathbf{q}} + \overline{w}_T \;.$$

The terms in (5.68), which are linearly dependent on $\ddot{\mathbf{q}}$, are collected in the constraint vectors $\mathbf{w}_N, \mathbf{w}_S$ and $\mathbf{w}_T$, all the rest is included in the scalars $\overline{w}_N, \overline{w}_S, \overline{w}_T$.

5.5 Numerical Aspects

A simple and common approach for integrating mechanical systems with frictional contacts in time is to regularize the set-valued force laws or to replace the unilateral constraints by some compliant models. However, this approach not only results in stiff differential equations with large integration times but also leads to inexact solutions with respect to the non-smooth model. In order to deal with the unilateral nature of the constraints two groups of numerical schemes can be distinguished, namely event-driven and time-stepping schemes (Pfeiffer et al., 2006).

Event-driven schemes detect changes of the constraints (events), for example stick-slip transitions, and resolve the exact transition times. Between these events the motion of the system is smooth and can be computed by a standard ODE/DAE-integrator with root-finding. If an event occurs the integration stops and the computation of the contact forces is performed by solving a (N)LCP or the non-smooth equations of the Augmented Lagrangian formulation (5.14). While this approach is very accurate, the event-detection can be time consuming, especially in case of frequent transitions. This approach is only recommended for systems with few contacts. Another drawback is the fact that the constraints are only fulfilled at the acceleration level, which results in a numerical drift effect. Therefore we shall consider in the following only time stepping algorithms.

Time-stepping schemes are based on a time-discretization of the system dynamics including the contact conditions in normal and tangential direction. The whole set of discretized equations and constraints is used to compute the next state of the motion. In contrast to event-driven schemes these methods need no event-detection. Moreover, time discretization can be formulated such that unilateral constraints are satisfied at the position and velocity level without any correction step. Excellent presentations of the dynamics of non-smooth systems are given in the books of Glocker (2001) and Leine and Nijmeijer (2004), the last one also with respect to numerical algorithms.

To present at least an idea of the solution techniques, the augmented Lagrange approach will be discussed shortly (Pfeiffer et al., 2006). It can be applied to Moreau's measure differential equations (5.14), which is written in a discretized form. The corresponding set writes

$$\Delta\mathbf{q} - (\mathbf{u} + \Delta\mathbf{u})\Delta t = 0,$$
$$\mathbf{M}\Delta\mathbf{u} - \mathbf{h}\Delta t - \mathbf{W}_N\mathbf{\Lambda}_N - \mathbf{W}_T\mathbf{\Lambda}_T = 0,$$
$$\mathbf{\Lambda}_N - \mathrm{prox}_{C_N}(\mathbf{\Lambda}_N - r_1\mathbf{g}_N) = 0,$$
$$\mathbf{\Lambda}_T - \mathrm{prox}_{C_T(\mathbf{\Lambda}_N)}(\mathbf{\Lambda}_T - r_2\dot{\mathbf{g}}_T) = 0. \tag{5.72}$$

In order to proceed to the next state during the time integration, the unknowns $\Delta\mathbf{q}$, $\Delta\mathbf{u}$, $\mathbf{\Lambda}_N$ and $\mathbf{\Lambda}_T$ have to be found by solving the above set of non-smooth equations, which might be accomplished by the generalized Newton method. Unfortunately, the discretization in (5.72) suffers from problems that are known from DAE systems of index 3. One way to overcome this problem is to consider the constraints in normal and tangential direction on the velocity level only. The formulation in terms of the Augmented Lagrangian method is then given by

$$\mathbf{M}\Delta\mathbf{u} - \mathbf{h}\Delta t - \mathbf{W}_N\mathbf{\Lambda}_N - \mathbf{W}_T\mathbf{\Lambda}_T = 0,$$
$$\mathbf{\Lambda}_N - \mathrm{prox}_{C_N}(\mathbf{\Lambda}_N - r_1\dot{\mathbf{g}}_N) = 0,$$
$$\mathbf{\Lambda}_T - \mathrm{prox}_{C_T(\mathbf{\Lambda}_N)}(\mathbf{\Lambda}_T) - r_2\dot{\mathbf{g}}_T) = 0, \tag{5.73}$$

with

$$\dot{\mathbf{g}}_N^e = \mathbf{W}_N^\top(\Delta\mathbf{u} + \mathbf{u}) + \tilde{\mathbf{w}}_N\Delta t, \tag{5.74}$$
$$\dot{\mathbf{g}}_T = \mathbf{W}_T^\top(\Delta\mathbf{u} + \mathbf{u}) + \tilde{\mathbf{w}}_T\Delta t. \tag{5.75}$$
$$\tag{5.76}$$

Now the dependence on the positions is not taken into account anymore and the unknowns that have to be evaluated in each integration step reduce to $\Delta\mathbf{u}$, $\mathbf{\Lambda}_N$ and $\mathbf{\Lambda}_T$ (Foerg et al., 2006; Foerg, 2007).

5.6 Applications

Keeping in mind that the real world of mechanics is as much bilateral as it is unilateral, we could expect from the very beginning a large field of applications waiting for being treated by the new methods. Contact systems of any form are widely spread everywhere, concerning machines, transportation, biological systems and much more. In the following we shall give only a few examples, which are typical for that kind of problems. At my former Institute we always tried to establish and to maintain a certain balance of theoretical and applied research allowing a transfer of newest theoretical findings into challenging and large industrial applications. **Figure 5.11** illustrates the evolution of theory and applications. From utilizing the classical methods of interconnections by force laws or bilateral constraints the first progress in modeling non-smooth systems came along with the formulation of complementarity constraints, which at the beginning has been not self-evident but a new finding. The next steps to set-valued considerations and to the prox-approach

traditional approach (force laws)	MBS with inequality constraints, (LCP, NCP)	time stepping on the basis MBS and mde	Augmented Lagrange and "prox" approach
•Gear rattling •Gear hammering •Gear synchronizers •power transmissions •Turbine blade dampers •Landing gear dynamics	•assembly processes •clutches •hydraulics •walking •CVT-chains •CVT-belts •grasping •harmonic drive gear	•Chimney damper •Roller coaster •CVT-chains •CVT-belts •roller chains •drive train systems	•CVT-belts •hydraulics •drive trains •cam shaft control •granular media

about 40 years evolution

Fig. 5.11: The evolution of large applications (LCP, NCP linear, nonlinear complementarity problem , MBS multibody system; mde measure differential equation).

was the result of international efforts culminating in contributions like that of Alart and Curnier (1991). So, in the course of the years, a new approach was established characterized by Augmented Lagrange Method and measure differential equations. The examples of **Fig. 5.11** reflect the theoretical progress by more and more complicated industrial applications. CVT-belts, for example, include some thousands of unilateral contacts. The same is true for granular media. In the following we shall present some typical examples.

5.6.1 Woodpecker, a Non-smooth Toy

The woodpecker toy has been from the very beginning an important motivation to look into non-smooth theories available at that time and to try to transfer these findings into multibody theory. The first investigation was published in 1984 (Pfeiffer, 1984) including a woodpecker analysis, where the impacts with friction were approximated by a semi-empirical algorithm. The next step was then done by Glocker (1995), who introduced a concise theoretical model of impacts with friction allowing a description without empirical approximations. The last step, at least at the time being, is a contribution of Zander et al. (2007), who analyzed the woodpecker going down an elastic bar based on a theory of elastic continua with non-smooth contacts. A woodpecker toy hammering down a pole is a typical system combining impacts, friction and jamming. It consists of a sleeve, a spring and the woodpecker. The hole of the sleeve is slightly larger than the diameter of the pole, thus allowing a kind of pitching motion interrupted by impacts with friction.

The motion of the woodpecker can be described by a limit cycle behavior as illustrated in **Fig. 5.12**. The gravitation represents an energy source, the energy of which is transmitted to the woodpecker mass by the y-motion. The woodpecker itself os-
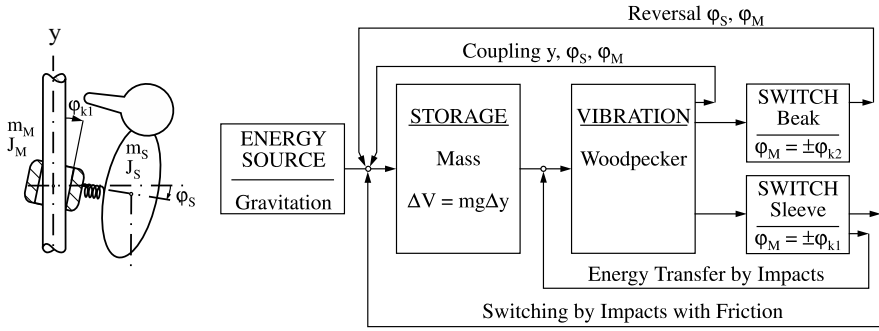
Fig. 5.12: Self-sustained vibration mechanism of a woodpecker toy (Pfeiffer and Glocker, 1996).

cillates and possesses a switching function by the beak for quick φ_S reversal and by the jammed sleeve, which transmits energy to the spring by jamming impacts.

A typical sequence of events is portrayed in **Fig. 5.13**. We start with jamming in a downward position, moving back again due to the deformation of the spring, and including a transition from one to three degrees of freedom between phases 1 and 2. Step 3 is jamming in an upward position (1 DOF) followed by a beak impact which supports a quick reversal of the φ-motion. Steps 5 to 7 are then equivalent to steps 3 to 1.

1. Jamming (1 DOF)
   $(\dot{y} = \dot{\varphi}_M = 0)$

2. Three DOF
   nearly no friction

3. Jamming (1 DOF)
   $(\dot{y} = \dot{\varphi}_M = 0)$

4. Beak impact

5. See 3.

6. See 2.

7. See 1.

Fig. 5.13 Sequence of events for a woodpecker toy.

The system possesses three degrees of freedom $\mathbf{q} = (y, \varphi_M, \varphi_S)^T$, where φ_S and φ_M are the absolute angles of rotation of the woodpecker and the sleeve, respectively, and y describes the vertical displacement of the sleeve (**Fig. 5.14**): Horizontal deviations are negligible. The diameter of the hole in the sleeve is slightly larger than the diameter of the pole. Due to the resulting clearance, the lower or upper inner edge of the sleeve may come into contact with the pole. This is modeled by the edge contact constraints 2 and 3, see **Fig. 5.14**. Further contact may occur when the beak of the woodpecker hits the pole, which is expressed by constraint 1. The special geometrical design of the toy enables us to assume only small deviations of the displacements. Thus a linearized evaluation of the system's kinematics is sufficient and leads to the dynamical terms and constraint magnitudes listed below. For the dynamics of the woodpecker we apply the theory above for impacts with friction, but we assume that no tange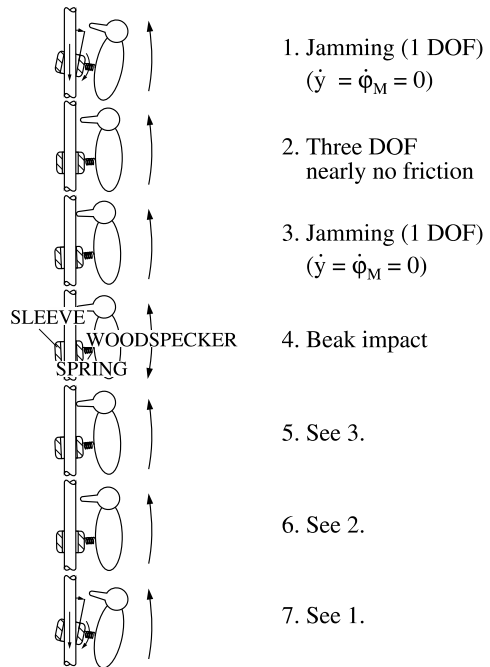ntial impulses are stored during the impulsive processes. The mass matrix $\mathbf{M}$, the force vector $\mathbf{h}$ and the constraint vectors $\mathbf{w}$ follow from **Fig. 5.14** in a straightforward manner. They are (see (5.10) and (5.15))

$$\mathbf{M} = \begin{pmatrix} (m_S + m_M) & m_S l_M & m_S l_G \\ m_S l_M & (J_M + m_S l_M^2) & m_S l_M l_G \\ m_S l_G & m_S l_M l_G & (J_S + m_S l_G^2) \end{pmatrix},$$

$$\mathbf{h} = \begin{pmatrix} -(m_S + m_M)g \\ -c_\varphi(\varphi_M - \varphi_S) - m_S g l_M \\ -c_\varphi(\varphi_S - \varphi_M) - m_S g l_G \end{pmatrix}, \quad \mathbf{q} = \begin{pmatrix} y \\ \varphi_M \\ \varphi_S \end{pmatrix},$$

$$\mathbf{w}_{N1} = \begin{pmatrix} 0 \\ 0 \\ -h_S \end{pmatrix}, \quad \mathbf{w}_{N2} = \begin{pmatrix} 0 \\ h_M \\ 0 \end{pmatrix}, \quad \mathbf{w}_{N3} = \begin{pmatrix} 0 \\ -h_M \\ 0 \end{pmatrix},$$

$$\mathbf{w}_{T1} = \begin{pmatrix} 1 \\ l_M \\ l_G - l_S \end{pmatrix}, \quad \mathbf{w}_{T2} = \begin{pmatrix} 1 \\ r_M \\ 0 \end{pmatrix}, \quad \mathbf{w}_{T3} = \begin{pmatrix} 1 \\ r_M \\ 0 \end{pmatrix}. \tag{5.77}$$
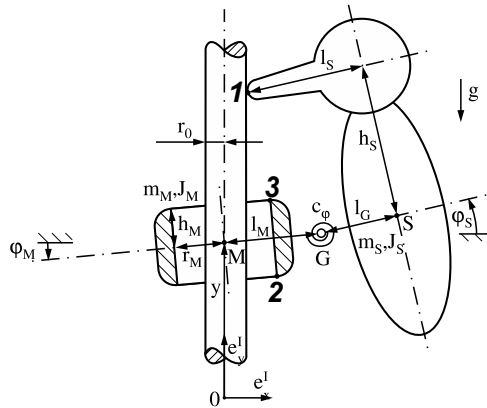
Fig. 5.14 Woodpecker model.

For a simulation we consider theoretically and experimentally a woodpecker toy with the following data set:

- Dynamics: $m_M = 0.0003$; $J_M = 5.0 \cdot 10^{-9}$; $m_S = 0.0045$; $J_S = 7.0 \cdot 10^{-7}$; $c_\varphi = 0.0056$; $g = 9.81$.
- Geometry: $r_0 = 0.0025$; $r_M = 0.0031$; $h_M = 0.0058$; $l_M = 0.010$; $l_G = 0.015$; $h_S = 0.02$; $l_S = 0.0201$.
- Contact: $\varepsilon_{N1} = 0.5$; $\varepsilon_{N2} = \varepsilon_{N3} = 0.0$; $\mu_1 = \mu_2 = \mu_3 = 0.3$; $\varepsilon_{T1} = \varepsilon_{T2} = \varepsilon_{T3} = \nu_1 = \nu_2 = \nu_3 = 0.0$.

Using these parameters, the contact angles of the sleeve and the woodpecker result in $|\varphi_M| = 0.1$ rad and $\varphi_S = 0.12$ rad, respectively. Before discussing the dynamical behavior obtained by a numerical simulation, some results from an analytical investigation of the system may be presented.

Firstly, we assume that constraint 2 is sticking. The coordinates φ_M and y are then given by certain constant values ($\varphi_M = -0.1$ rad), and the system has only one degree of freedom (φ_S) with an equilibrium position at $\varphi_{S0} = -0.218$ rad. Sticking at that position is only possible if $\mu_2 \geqslant 0.285$. Such values of μ_2 correspond at the same time to a jamming effect of the system in the sense that no vertical force, acting on the woodpecker's center of mass, could lead to a transition to sliding, however large it would be. Undamped oscillations around this equilibrium with a frequency of 9.10 Hz influence the contact forces and lead the system to change into another state if the amplitudes are large enough.

The second analytically investigated system state is the unconstrained motion with three degrees of freedom. Besides the fourfold zero eigenvalue, which describes the rotational and translational free-body motion, a complex pair of eigenvalues with a frequency of $f = 72.91$ Hz exists. The corresponding part of the eigenvector $\mathbf{q} = (y, \varphi_M, \varphi_S)^\mathsf{T}$ is given by $\mathbf{u} = (-0.086, 10.7, -1.0)^\mathsf{T}$ and shows the ratio of the amplitudes.

The limit cycle of the system, computed by a numerical simulation, is depicted in **Fig. 5.15**. We start our discussion at point (6) where the lower edge of the sleeve hits the pole. This completely inelastic frictional impact leads to continual contact of the sleeve with the pole. After a short episode of sliding (6)–(7) we observe a transition of the sleeve to sticking (7). The angle of the woodpecker is now large enough to ensure continual sticking of the sleeve by the self-locking mechanism. In that state the system has only one degree of freedom, and the 9.10 Hz oscillation can be observed where the woodpecker swings down and up until it reaches point (1).

At (1) the tangential constraint becomes passive and the sleeve slides up to point (2) where contact is lost. Note that the spring is not free of stresses in this situation; thus during the free-flight phase (2)–(3) the high-frequency oscillation ($f = 72.91$ Hz) of the unbound system occurs in the phase space plots. In this state the sleeve moves downward (y decreases), and the first part of the falling height Δy at one cycle is achieved.

At (3) the upper edge of the sleeve hits the pole with a frictional, completely inelastic impact. Contact, however, is not maintained due to the loaded spring. Point (4) corresponds to a partly elastic impact of the beak against the pole. After that
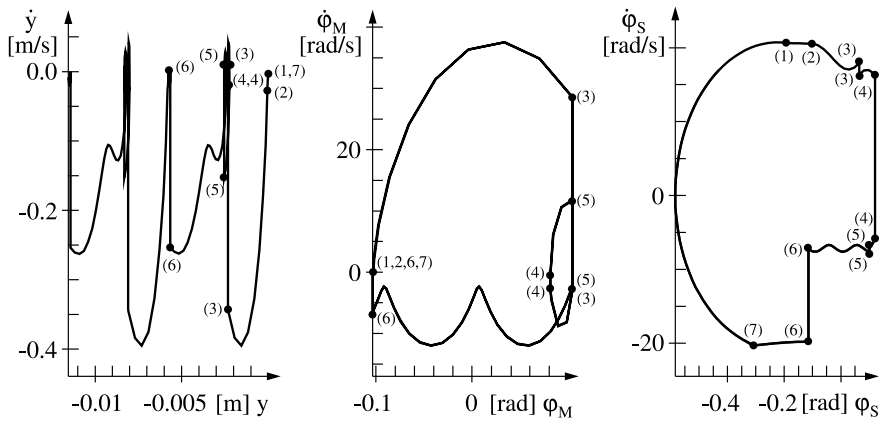
Fig. 5.15: Phase space portraits (Glocker and Stude, 2005).

collision the velocity $\dot{\varphi}_S$ is negative and the woodpecker starts to swing downward. At (5) the upper edge of the sleeve hits the pole a second time with immediate separation. Then the system is unbound and moving downward (5)–(6), where the second part of the falling height is achieved and the 72.91-Hz frequency can be observed once more.

Table 5.1 summarizes all of the state transitions during one cycle, and **Table 5.2** compares the amounts of dissipated energy. The main dissipation results from

Table 5.1: **Table** of the possible transitions.

Phase Plot Point	State Transitions	
(1) Constraint 2	Sticking → Sliding	
(2) Constraint 2	Sliding → Separation	
(3) Constraint 3	Separation → Separation	First upper sleeve impact
(4) Constraint 1	Separation → Separation	Beak impact
(5) Constraint 3	Separation → Separation	Second upper sleeve impact
(6) Constraint 2	Separation → Sliding	Lower sleeve impact
(7) Constraint 2	Sliding → Sticking	

the beak impact and lower sleeve impact, which contribute 88% of the dissipation. The remaining 12% are shared by the upper sleeve impacts and phases of sliding, which are nearly negligible. The frequency of the computed limit cycle in **Fig. 5.15** amounts to $f = 8.98$ Hz and is slightly different from the measured value of $f = 9.2$ Hz. The total falling height during one cycle can be seen in the left diagram of **Fig. 5.15**. The computed and measured values are $\Delta y = 5.7$ mm and $\Delta y = 5.3$ mm, respectively.

Table 5.2: Amounts of dissipated energy.

Change in Potential Energy	$\Delta V = 2.716 \cdot 10^{-4}$	100.00%
First upper sleeve impact	$\Delta T_{(3)} = -0.223 \cdot 10^{-4}$	8.21%
Second upper sleeve impact	$\Delta T_{(5)} = -0.046 \cdot 10^{-4}$	1.69%
Beak impact	$\Delta T_{(4)} = -1.370 \cdot 10^{-4}$	50.44%
Lower sleeve impact	$\Delta T_{(3)} = -1.032 \cdot 10^{-4}$	38.00%
Phases of sliding	$\Delta T_{(G)} = -0.045 \cdot 10^{-4}$	1.66%

5.6.2 Vibration Conveyor

Vibratory feeders are used in automatic assembly to feed small parts. They are capable to store, transport, orient and isolate the parts. An oscillating track with frequencies up to 100 Hz excites the transportation process, which is mainly based on impact and friction phenomena between the parts and the track. Vibratory feeders are applied for a wide variety of parts and for lots of different tasks. In the majority of cases, the parts are available as a sort of bulk material that is stored in a container. The transportation process, starting in this reservoir, is often combined with orienting devices that orient parts, or select only these parts having already the right orientation (**Fig. 5.16** shows an example of a vibratory bowl feeder with an orienting device). Each kind of parts, with its special geometry and mechanical properties, requires an individual adaption of the feeder. This individual tuning comprises the development of suitable track and orienting device geometries and the adjustment of the excitation parameters frequency and amplitude. Due to the complex mechanics of the feeding process this design is usually done by trial and error without any theoretical background. A complete dynamical model of the transportation process allows a theoretical investigation and consequently an improvement of the the feeder properties (Wolfsteiner, 1999; Wolfsteiner and Pfeiffer, 1999).
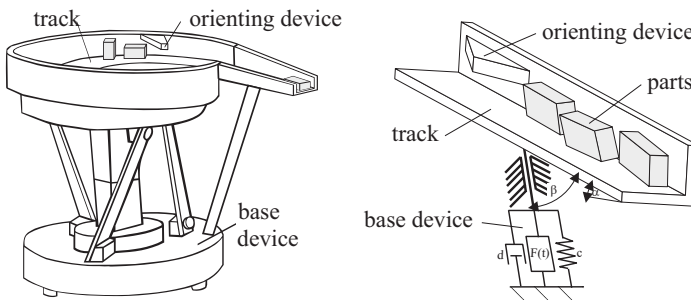
Fig. 5.16: Vibratory bowl feeder and mechanical model.

Friction and impact phenomena between the parts and the track are the most important mechanical properties of transportation processes. Consequently, the required dynamical model has to deal with unilateral constraints, dry friction and multiple impacts. The mechanical model of the vibratory feeder can be split in two parts: the transportation process and the base device. Wolfsteiner (1999) focuses on modeling and simulation of the transportation process. The modeling of the base device can be done with well known standard techniques of multibody systems.

For the verification of the developed model of the transportation process an experimental vibratory feeder was built, allowing different measurements concerning the impact model and the average transportation rates. **Figure 5.17** shows the principle of the device. The track, fixed on leaf springs is excited with an electromagnetic shaker with a frequency about 50 Hz. The eigenfrequency of the system is at 52 Hz. The resulting vibration amplitude reaches a maximum value of about 2 mm. The track has an inclination angle $\alpha = 3^{o}$, the angle between the track and the direction of the vibration is $\beta = 15^{o}$. For the accurate contact-free measurement of the motion of the transported part six laser distance sensors were applied. For the vibration measurement of the track an eddy current sensor is used.

For a comparison of the theory and the measurements the averaged transportation rate was used. **Figure 5.18** gives a result, which taking into account the complexity of the problem looks good. An interesting finding is the fact that the averaged transportation velocity does not depend very much on the number of parts and also not on the type of modeling, plane or spatial (Wolfsteiner, 1999). Therefore the design of vibration conveyors can be carried through considering one part only. For the layout of orienting devices we need of course a spatial theory.
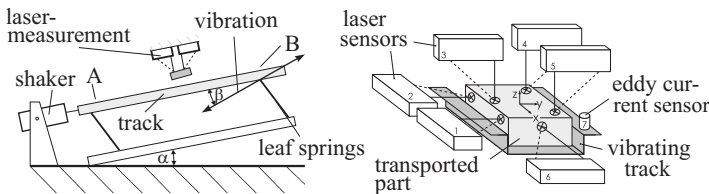
Fig. 5.17: Test setup and part measurement.
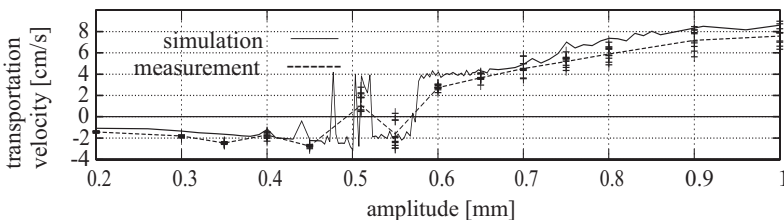
Fig. 5.18: Simulation and measurement of the average transportation rate.

5.6.3 Roller Coaster

One of the challenging practical examples concerning unilateral multibody theory are roller coasters (Stiegelmeyr and Pfeiffer, 1999; Stiegelmeyr, 2001). In Germany, we have amongst others a system called Wild Mouse. The trajectory configuration for this Wild Mouse is depicted in **Fig. 5.19** together with the vehicle system. The track generates frequent and abrupt changes of the vehicle's course resulting in a special thrill for the passengers. Thereby, and due to the slackness of the wheel rail contact, sequences of impacts with friction take place producing a significant amount of load and stress to the wheels and the undercarriage system. Each carriage possesses four packages each with six wheels coming out with altogether 24 wheel-track-contacts of a spatial character.

The six carriage wheels per wheel-package are necessary to keep the carriage safely on the track for all possible accelerations, which means two wheels on three sides of the track, top, bottom, side. The model includes the vehicle body and the two axes, front and transaxle, and the four wheel packages, all considered to be rigid bodies, body and axes with six degrees of freedom each. Between vehicle body and the axes we have force laws in the form of a spring-damper-arrangement. **Figure 5.20** illustrates the arrangement of the body-axes- and of the axis-wheel-configuration.

The wheels, manufactured from plastic materials, are modelled as sliding elements due to their very small masses in comparison with the mass of the axes. In addition we assume rolling without sliding, which is realistic for nearly all operation
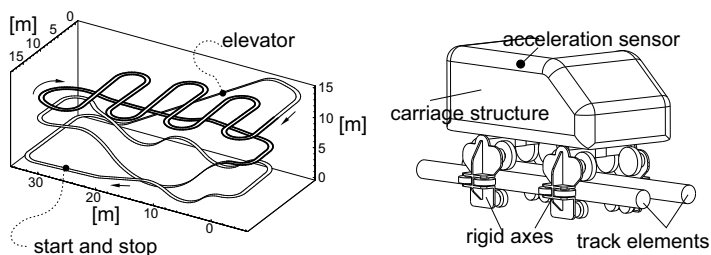
Fig. 5.19: "Wild Mouse" and roller coaster carriage.
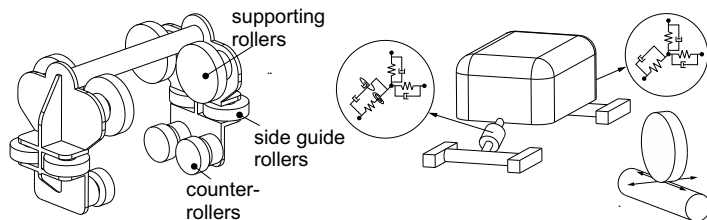
Fig. 5.20: Models of axes and wheels.

conditions. The wheel-track contact thus includes three contact possibilities, namely contact/detachment, stiction/sliding in lateral direction and rolling without sliding in trajectory direction (**Fig. 5.20**). For the first case impacts with friction are considered, for the second case the relevant complementarities, and for the third case we introduce rolling friction in the form of an empirical coefficient. The derivation of the equations of motion is straightforward by first modelling the bodies, connecting them either with smooth or set-valued force laws and by establishing the accompanying geometrical and kinematical algebraic equations.

A model has been established with 18 DOF and 24 potential contacts. Direct measurements of the roller contacts are either impossible or very difficult. Therefore the vehicle has been simply equipped with acceleration sensors for measuring the lateral motion. **Figure 5.19** depicts the location of the sensor, and **Fig. 5.21** compares these measurements with the simulation. The agreement is very good and validates the model of the overall dynamics. On the basis of the simulation model some improvements of the roller design could be performed.

5.6.4 Drop Tower Hydraulics

An interesting example is the hydraulic safety brake system of a fun ride, the free fall tower. **Figure 5.22** shows such a tower. Under normal operation conditions the passenger cabin is lifted by a cable winch to a height of about 60 m. Subsequently, the cabin is released and falls down nearly undamped. Before reaching the ground, the normal brake system stops the cabin softly via the cable winch. For safety reasons, a redundant brake system is necessary. In the case of a failure of the regular brakes or a cable rupture the safety brake system has to catch the cabin even under disadvantageous conditions.

The safety brake system is a hydraulic system, which moves brake-blocks via hydraulic cylinders. For this purpose steel blades are fixed to the cabin. The steel blades fall into a guide rail with the brake-blocks fixed to it. They are closed by very large spring forces and opened by hydraulic cylinders, which must operate very fast and synchronously. Under normal operation conditions, the brake-blocks are moved out of the guide rail shortly before the cabin reaches them. Only in case of
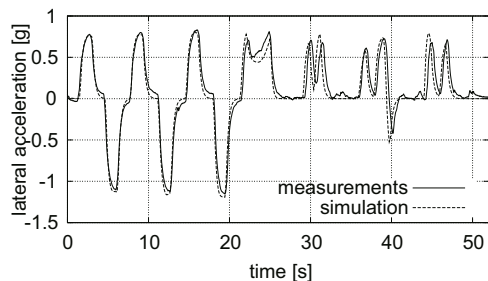
Fig. 5.21 Comparison with measurements for the lateral motion.

Fig. 5.22 Droptower.

some failure, the safety brakes remain closed and the cabin is stopped by the friction forces. Due to the very short opening time of the brake, the hydraulic cylinders move fast and reach the end stop with high velocities. In some cases, the resulting impact forces have caused damages to the cylinders.

The safety brakes are designed in modules, where each module contains the mechanical and the complete hydraulic part of the brake. According to the functionality of the passenger cabin, they must be arranged in a vertical sense, one on the top of the other. Depending on the height of the drop tower one needs usually about six to seven of these brake segments. The brakes are realized in such a way that they safely catch the passenger cabin even under very disadvantageous conditions like rope rupture at maximum height in combination with rain.

Hydraulic systems can conveniently be modeled as non-smooth systems leading to computing times up to three orders of magnitude smaller than the classical approach as often used in commercial codes. Therefore we establish a hydraulic model on the basis of non-smooth and smooth hydraulic components according to **Fig. 5.23**, see, for example, Borchsenius (2003). The underlying mathematical model for one segment including the oil supply component consists of 202 differential equations, for each further module not containing the oil supply we get 132 differential equations. For seven brake segments, we have thus altogether 994 differential equations, which correspond to the number of hydraulic degrees of freedom. Mechanics is involved only with a few degrees of freedom for the drop tower model.

The model has been verified by measurements. **Figure 5.24** shows the result. The opening of the cylinders starts at t = 0.1 s. After that point, the cylinders move, thus increasing the pressure due to the growing spring force in the cylinders. After having reached the end stop the oil pressure becomes stable at a level of 120 bar. This large pressure is kept constant, because the oil cannot flow back after the check valves have been closed in the feed lines. The agreement between the simulations and measurements is very good, confirming the theory. The simulations have been

Fig. 5.23 Hydraulic model of the drop tower safety brakes.
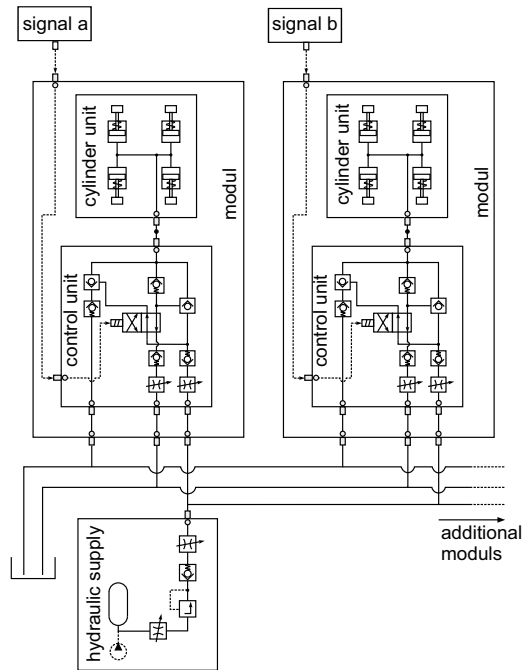
Fig. 5.24 Comparison measurements/simulations.
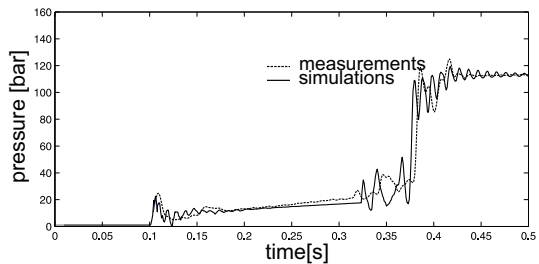
used to improve the time-behavior of the hydraulic modules in connection with the brakes.

5.6.5 CVT Power Transmission

For technological developments in the field of CVT-gears see the SAE-publication (Maten and Anderson, 2006). My former Institute started modeling CVT's in the early nineties considering in a first step CVT rocker pin chains and in a second step CVT push belts. Push belts are complicated including a very large amount of degrees of freedom and extraordinary many unilateral contacts (Schindler et al., 2007). In

the following we shall present this type of belts. **Table 5.3** gives a comparison of two types. Note the large frequencies, DOF's and number of contacts.

CVT-belts have a multiple contact structure (**Fig. 5.25**). We have a unilateral spatial contact between element and pulley, a plane unilateral contact between element and ring and five contacts between the elements themselves. The last ones are covered by an empirical nonlinear force law. All other contacts are unilateral contacts described by complementarities, then converted and solved by prox-functions (Geier et al., 2006). For an element this sums up to 17 contacts, see **Fig. 5.26**. For building a simulation the equations of motion and the relevant bilateral and unilateral constraints are established resulting in a large structure to be evaluated, see Schindler et al. (2007); Pfeiffer (2008). The whole set has the following form

- equations of motion

$$
\begin{pmatrix} \mathbf{M}_p & \mathbf{0} & \mathbf{0} \\ \mathbf{0} & \mathbf{M}_e & \mathbf{0} \\ \mathbf{0} & \mathbf{0} & \mathbf{M}_r \end{pmatrix} \begin{pmatrix} \dot{\mathbf{u}}_p \\ \dot{\mathbf{u}}_e \\ \dot{\mathbf{u}}_r \end{pmatrix} = \begin{pmatrix} \mathbf{h}_p \\ \mathbf{h}_e \\ \mathbf{h}_r \end{pmatrix} + \begin{pmatrix} \mathbf{W}_{B,er}\lambda_{B,er} + \mathbf{W}_{T,er}\lambda_{T,er} \\ \mathbf{W}_{U,pe}\lambda_{U,pe} + \mathbf{W}_{T,pe}\lambda_{T,pe} \\ \mathbf{W}_{U,ee}\lambda_{U,ee} \end{pmatrix} \quad (5.78)
$$

- constraints:

Table 5.3: Typical Data of CVT-chain and -belt.

	LUK	VDT
number of elements	63	382
element length (thickness)	9.85 mm	1.80 mm
element width	36 mm	29.6 mm
polygonal frequency	550 Hz	3000 Hz
elements/second (1000 rpm, i=1)	550	3000
lowest eigenfrequency	90 Hz	120 Hz
DOF, plane case	≈200	≈1300
contacts, plane case	≈150	>1000
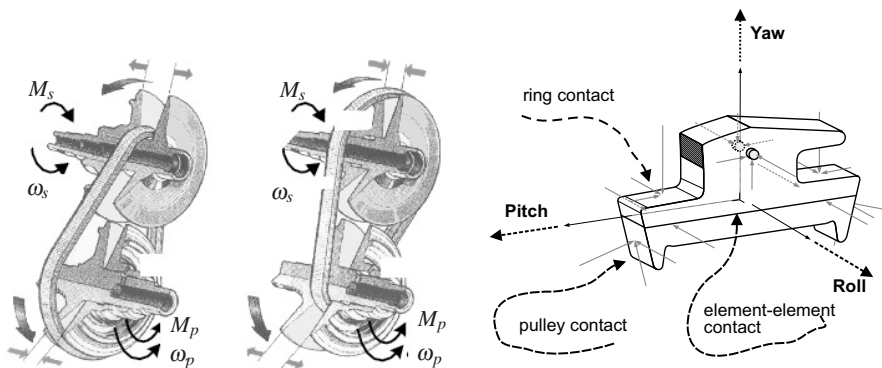
Fig. 5.25: Contact configurations of push belt elements (p = primary, s = secondary).
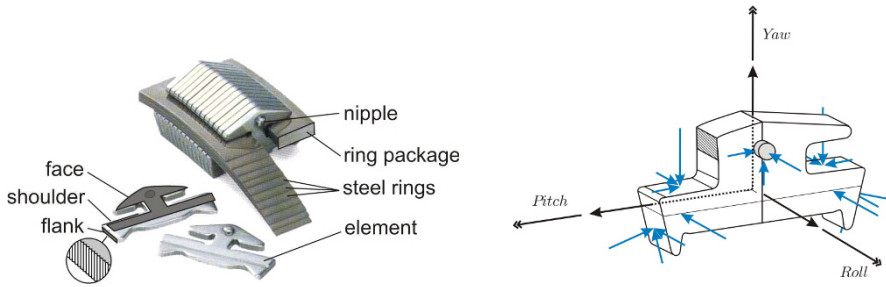
Fig. 5.26: Interactions of element/element, element/ring package, element/pulley, pulley/environment with 17 contacts per element.

$$\lambda_{B,er} = \text{prox}_{C_B}(\lambda_{B,er} - rg_{B,er}), \; \lambda_{U,pe} = \text{prox}_{C_U}(\lambda_{U,pe} - rg_{U,pe}),$$
$$\lambda_{U,ee} = \text{prox}_{C_U}(\lambda_{U,ee} - rg_{U,ee}), \; \lambda_{T,pe} = \text{prox}_{C_T(\lambda_{N,pe})}(\lambda_{T,pe} - r\dot{g}_{T,pe}),$$
$$\lambda_{T,er} = \text{prox}_{C_T(\lambda_{N,er})}(\lambda_{T,er} - r\dot{g}_{T,er}) \tag{5.79}$$

The indices (p,e,r) stand for pulley, element and ring, respectively. The indices (U, B, T) indicate unilateral, bilateral and tangential, respectively. The M are the mass matrices, W the constraint matrices, $u = \dot{q}$ are velocities, and λ are constraint forces. The magnitudes $g, \dot{g}$ indicate relative displacements and velocities in the contacts, r is an iteration variable, which has been discussed in connection with (5.13).

The system (5.78), (5.79) is solved numerically by a time stepping scheme including prox-algorithms. The modular configuration of the model comprising subsystems and constraints enables a refinement or even a substitution of models for single components and interactions in a convenient manner. By this, both bodies and contacts can be modeled rigidly or flexibly in a hybrid way.

We consider some results concerning push forces, see **Fig. 5.27**. The top row presents the measurements, the bottom row simulations. Agreement is very good
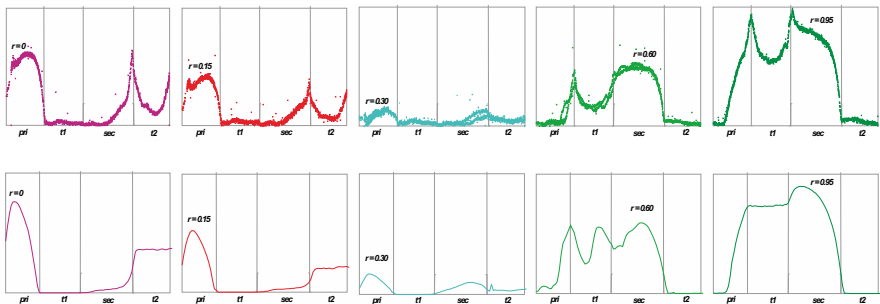
Fig. 5.27: Representation of measured (top row) and simulated (bottom row) push forces at increasing torque levels $r = 0, 0.15, 0.30, 0.60, 0.95$.

taking into account the complexity of the model. With increasing output torque ratio r the level of push forces is growing. The existing simulation software has been used to consider noise and wear problems.

5.7 Conclusion

Classical theory of rigid or elastic multibody systems dynamics may be characterized by d'Alembert's principle in the form of Lagrange and extended by Jourdain allowing to project the equations of motion of all interconnected bodies into their free directions according to their individual constraints. These constraints are bilateral in classical theory and do not include contact phenomena.

If we want to consider dynamical problems with unilateral contacts, especially multibody systems with multiple contacts, and if we further want to model such contacts by unilateral constraints, we must enlarge multibody theory by certain rules describing unilateral features. One fundamental property, sometimes addressed to as Signorini's law, consists in the fact that for each contact either quantities of relative kinematics are zero and the corresponding constraint forces are not zero, or vice versa. This establishes a linear or nonlinear complementarity problem for each of the contacts, which has to be added to the classical multibody formalism.

Direct numerical treatment of complementarity is cumbersome, so an approach from convex analysis has been developed using proximity functions. It offers many numerical advantages for the prize of largely diminished mechanical transparency. But these alternative algorithms allow to solve also non-smooth problems of very large dimensions.

Contribution gives an overview of the activities at the author's Institute during the last decades, indicating also the evolution of the methods concerning multibody dynamics with unilateral constraints. Theory of non-smooth multibody dynamics is presented, and some typical applications from industry are discussed.

References

Alart P, Curnier A (1991) A mixed formulation for frictional contact problems prone to Newton-like solution methods. Computer Methods in Applied Mechanics and Engineering 92(3):353–375

Beitelschmidt M (1999) Reibstösse in Mehrkörpersystemen. No. 275 in Fortschritt-Berichte VDI, Reihe 11, VDI-Verlag, Düsseldorf

Borchsenius F (2003) Simulation ölhydraulischer Systeme. No. 1005 in Fortschritt-Berichte VDI, Reihe 8, VDI-Verlag, Düsseldorf

Bremer H (2008) Elastic Multibody Dynamics. Springer Science + Business Media, B.V.

Brogliato B (1999) Nonsmooth Mechanics. Springer, London

Foerg M (2007) Mehrkörpersysteme mit mengenwertigen Kraftgesetzen - Theorie und Numerik. No. 411 in Fortschritt-Berichte VDI, Reihe 20, VDI-Verlag, Düsseldorf

Foerg M, Geier T, Neumann L, Ulbrich H (2006) r-factor strategies for the augmented Lagrangian approach in multi-body contact mechanics. In: Mota Soares CA, Martins JAC, Rodrigues HC, Ambrosio JAC, Pina CAB, Mota Soares CM, Pereira EBR, Folgado J (eds) III European Conference on Computational Mechanics - Solids, Structures and Coupled Problems in Engineering, Book of Abstracts, Springer, Dordrecht, p 316

Frémond M (2002) Nonsmooth Thermomechanics. Springer, Berlin, Heidelberg

Frémond M (2007) Collisions. Edizioni del Dipartimento di Ingegneria Civile, Universretà di Roma Tor Vergata, Rome

Geier T, Foerg M, Zander R, Ulbrich H, Pfeiffer F, Brandsma A, van der Velde A (2006) Simulation of a push belt CVT considering uni- and bilateral constraints. ZAMM - Journal of Applied Mathematics and Mechanics / Zeitschrift für Angewandte Mathematik und Mechanik 86(10):795–806

Glocker C (1995) Dynamik von Starrkörpersystemen mit Reibung und Stössen. No. 182 in Fortschritt-Berichte VDI, Reihe 18, VDI-Verlag, Düsseldorf

Glocker C (2001) Set-Valued Force Laws - Dynamics of Non-Smooth Systems. Springer, Berlin, Heidelberg, New York

Glocker C (2013) Energetic consistency conditions for standard impacts, Part I: Newton-type inequality impact laws and Kane's example. Multibody System Dynamics 29 (1) 29:77–117

Glocker C (2014) Energetic consistency conditions for standard impacts, Part II: Poisson-type inequality impact laws. Multibody System Dynamics 32(4):445–509

Glocker C, Stude C (2005) Formulation and preparation for numerical evaluation of linear complementarity systems in dynamics. Multibody System Dynamics 13(4):447–463

Jacobi CGJ (1866) Vorlesungen über Dynamik. Verlag Georg Reimer, Berlin

Leine R, Nijmeijer H (2004) Dynamics and Bifurcations of Non-Smooth Mechanical Systems. Springer Berlin Heidelberg, New York

Maten JR, Anderson BD (2006) Continuously variable transmission (CVT). Tech. Rep. PT-125, SAE International

Meitinger T (1998) Dynamik automatisierter Montageprozesse. No. 476 in Fortschrittberichte VDI, Reihe 2, VDI-Verlag, Düsseldorf

Moreau JJ (1988) Unilateral contact and dry friction in finite freedom dynamics. In: Moreau JJ, Panagiotopoulos PD (eds) Nonsmooth Mechanics and Applications, Springer, Wien, International Centre for Mechanical Sciences (Courses and Lectures), vol 302, pp 1–82

Panagiotopoulos PD (1993) Hemivariational Inequalities. Springer Verlag, Berlin, Heidelberg, New York

Papastavridis G (2002) Analytical Mechanics. Oxford University Press

Pars LA (1979) Analytical Dynamics. Ox Bow Press, Woodbridge, Connecticut 06525, first published 1965

Pfeiffer F (1984) Mechanische Systeme mit unstetigen Übergängen. Ingenieur-Archiv 54(3):232–240

Pfeiffer F (2008) Mechanical System Dynamics. Springer, Heidelberg

Pfeiffer F (2016) Impacts with friction - structures, energy, measurements. Springer, Berlin, Heidelberg, Archive of Applied Mechanics, 1-2/2016

Pfeiffer F, Glocker C (1996) Multibody Dynamics with Unilateral Contacts. Wiley Series of Nonlinear Science (ed. A Nayfeh), John Wiley & Sons, INC., New York

Pfeiffer F, Schindler T (2015) Introduction to Dynamics. Springer, Berlin, Heidelberg

Pfeiffer F, Foerg M, Ulbrich H (2006) Numerical aspects of non-smooth multibody dynamics. Computer Methods in Applied Mechanics and Engineering 195(50):6891–6908

Schindler T, Geier T, Ulbrich H, Pfeiffer F, van der Velde A, Brandsma A (2007) Dynamics of Pushbelt CVTs. In: VDI-Berichte, Nr. 1997: Umschlingungsgetrieb, VDI-Gesellschaft Entwicklung Konstruktion Vertrieb

Schindler T, Nguyen B, Trinkle J (2011) Understanding the difference between prox and complementarity formulations for simulation of systems with contact. In: 2011 IEEE/RSJ International Conference on Intelligent Robots and Systems, pp 1433–1438

Shabana A (2013) Dynamics of Multibody Systems, 4th edn. Cambridge University Press

Stiegelmeyr A (2001) Zur numerischen Berechnung strukturvarianter Mehrkörpersysteme. No. 271 in VDI Fortschrittberichte, Reihe 18, VDI Verlag, Düsseldorf

Stiegelmeyr A, Pfeiffer F (1999) A Time Stepping Algorithm for Mechanical Systems With Unilateral Contacts. In: Proceedings of the ASME 1999 Design Engineering Technical Conferences, ASME, vol 7B: 17th Biennial Conference on Mechanical Vibration and Noise, pp 2245–2253

Wittenburg J (2016) Kinematik - Theory and Applications. Springer Berlin Heidelberg 2016

Woernle C (2016) Mehrkörpersysteme, 2nd edn. Springer, Berlin, Heidelberg

Wolfsteiner P (1999) Dynamik von Vibrationsförderern. No. 511 in Fortschrittberichte VDI, Reihe 2, VDI-Verlag, Düsseldorf

Wolfsteiner P, Pfeiffer F (1999) The parts transportation in a vibratory feeder. In: Pfeiffer F, Glocker C (eds) IUTAM Symposium on Unilateral Multibody Contacts, Springer, Dordrecht, Solid Mechanics and its Applications, vol 72

Zander R, Schindler T, Friedrich M, Huber R, Förg M, Ulbrich H (2007) Non-smooth dynamics in academia and industry: recent work at TU München. Acta Mechanica 195(1):183–195

Zeidler E, Schwarz R, Hackbusch W (2003) Teubner-Taschenbuch der Mathematik. Teubner, Wiesbaden

Chapter 6
Influence of Thermal Stabilisation on the Thermal Regime in the Strapdown Inertial Navigation System

Sergiy Yu. Pogorilov, Valeriy L. Khavin, Konstantin Naumenko, and Holm Altenbach

Abstract This paper proposes an approach to modeling the temperature field of a strapdown inertial unit that is part of an inertial navigation system based on fiber-optic gyroscopes. Mathematical and finite element models for heat transfer analysis of the strapdown inertial unit has been developed. Results of numerical simulations including the effect of changes in external temperature on the temperature field in the device and temperature rates at specified points of the device are presented. It is found that the application of thermal stabilisation in the considered makes it possible to form a temperature field with a temperature difference of 2 K on the fibre optic gyroscopes platform, which provides a minimum level of thermal strains and reduces the fluctuations of external temperature to 0.2 K/min.

6.1 Introduction

Modern aerospace technology makes extensive use of strapdown inertial navigation systems (SINS) based on fibre optic gyroscopes (FOGs). Due to the high sensitivity of FOGs to temperature variations, ensuring stable thermal operation is an important problem. The key step in improving the accuracy of the system is to develop methods of thermal protection and thermal stabilisation of the FOG.

This paper is concerned with the modelling of the temperature field of a Strapless Inertial Unit (SIN), which is part of the SINS, in order to ensure a minimum temperature difference at the FOG platform under temperature stabilisation conditions.

Sergiy Yu. Pogorilov · Valeriy L. Khavin
Department of Continuum Mechanics and Strength of Materials, National Technical University "Kharkiv Polytechnic Institute", 61002, Kharkiv, Ukraine,
e-mail: ark95@ukr.net,vkhavin@kpi.kharkov.ua

Konstantin Naumenko · Holm Altenbach
Institut für Mechanik, Otto-von-Guericke-Universität Magdeburg, 39106 Magdeburg, Germany,
e-mail: konstantin.naumenko@ovgu.de,holm.altenbach@ovgu.de

Modern fibre optic gyroscopes have high performance requirements, the most important of which is to provide an inertial accuracy of less than 0.01 deg/h under conditions of significantly varying temperature range [−60°C ÷ +60°C] (Dzhashitov and Pankratov, 2014). As a consequence, there is a need to consider the quantitative impact of thermal effects on the performance of the FOG (Dzhashitov et al., 2014). It is important to take into account thermal influences, leading to so-called thermal drift (fictitious, thermally induced changes of instrument readings) and thermal deformations of SINS elements (Dzhashitov and Pankratov, 2014).

In order to ensure the necessary accuracy of the FOG, both passive methods of preventing the influence of the temperature field such as thermal compensation, special methods of winding the FOG coil fibre, thermal bypass, design improvements of the FOG coil, etc. (Shen and Chen, 2012; Wang and Ma, 2009; Zhang et al., 2012) and active methods consisting in creation of multiloop reversible thermal control systems for both individual FOG and the entire SINS are used in practice (Dzhashitov and Pankratov, 2014; Zhang et al., 2015).

The most commonly used approach to improve the accuracy of angular velocity measurements by fiber optic and laser gyroscopes is based on post-processing of angular velocity measurements according to an algorithmic model called the temperature model of measurement errors (Plaksiy et al., 2021). A widely used approach is to use the measurement error dependence (drifts) of a fibre optic gyroscope as a third order polynomial (Diesel and Dunn, 1996). When implementing this approach in angular velocity measurement devices, the problem of estimating the value of the temperature gradient arises.

The greatest influence on the FOG signal drift is exerted by the coil of the fibre loop. Although it has no inherent heat generation, it is very sensitive to changes in temperature. At the same time, the gradient and the rate of temperature change have a much greater influence on the drift of the useful signal than the temperature level (Dzhashitov et al., 2013).

In (Breslavsky et al., 2012; Pogorilov et al., 2020) it is proposed to determine the temperature gradient for the fiber-optic gyroscope OIS501 by calculating the difference between the temperature sensor readings at a given point and the temperature sensor located at another point of the same object. The same approach is used in this paper to numerically estimate the temperature field gradient of the original BIB system under temperature-stabilized conditions.

The aim of this study is to simulate the temperature field of the SIN measuring unit, and to determine the conditions that ensure a minimum of temperature variation on the FOG platform under temperature-stabilised conditions. In order to achieve the objective, the following problems are addressed

- develop a finite element model of the SIN device,
- analyse the effect of changes in external temperature on the temperature field of the SIN device, and
- compute the temperature gradients at given points of the device

6.2 Description of the Model and Physical Process

The idealized geometric model of the SIN is presented in **Figs. 6.1** and **6.2**. It includes the following components

1. heat sink base,
2. emulator of the electronics unit,
3. four insulating sleeves,
4. FOG platform,
5. four FOG emulators, each of which consists of a FOG base and a FOG cover, and
6. side heat receiving panels and the top cover of the FOG compartment (not shown in the figures)
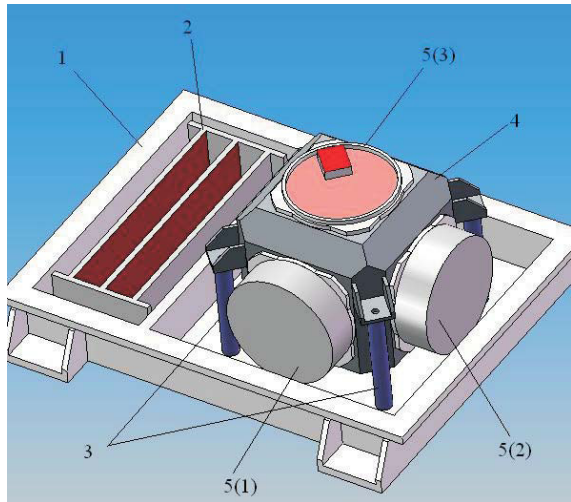
Fig. 6.1 Geometric model including retracted side panels, the upper FOG cover and the cover of the gyroscope number 3.
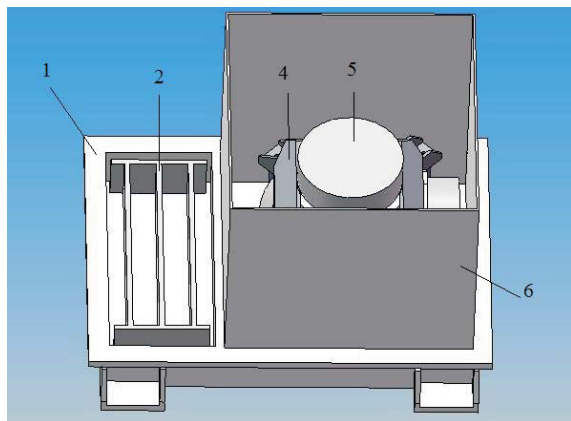
Fig. 6.2 Geometric model without top FOG compartment cover.

During the operation of SIN, the following heat sources can be considered (**Fig. 6.3**):

1. Three sources of the emulator of the electronics unit, which are three planes (each plane with a surface of heat generation of 85 cm^2). Every source generates heat with a power of 12 W;
2. Four sources of FOG (in each FOG there are two heat-generating surfaces), having the following heat generation characteristics:

    - the mounting surface (6.27 cm^2) of the emitting laser based on FOG with the power of 1.2 W
    - the rest of the inner surface of the base FOG (71.74 cm^2) with the power of 0.6 W

3. Four elements of the thermal stabilization system (heat-release surface area 27 cm^2) located on the FOG platform under the FOG installation sites. Each element has a power of 26 W.

The physical heat transfer process was modeled as follows:

1. Heat flow from the cells of the electronics unit to the heat sink base is modeled by conductive heat transfer
2. The heat sink from the FOG platform to the heat-receiving panels and the inner surface of the heat-removing base is considered due to radiation from the FOG platform to the heat-receiving panels and the inner surface of the heat-removing base
3. Heat transfer between the heat-receiving panels and the heat-dissipating base is assumed by conduction at the fixing points of the panels to the base
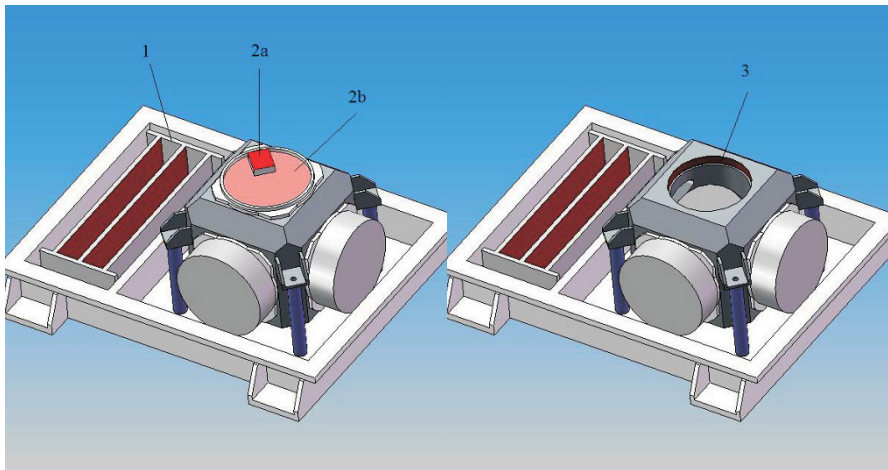
Fig. 6.3: Heat sources.

4. Heat transfer between all components of the FOG platform is modeled by conduction through the contact points of the components
5. Conductive heat transfer at the contact points of system elements is simulated by an ideal thermal contact
6. The heat exchange of the device with the environment is modeled by the function of the temperature variation of the bottom plane of the heat sink base over time (interaction with the object on which the SIN is installed).
7. Convective heat transfer is ignored because of the intended use of FOG in vacuum

6.3 Mathematical Framework and Solution Method

The analysis of the heat transfer process and the temperature field is carried out by solving a transient heat conduction problem in a three-dimensional formulation. All elements of the FOG geometric model (**Figs. 6.1** and **6.2**) were considered as bulk bodies occupying a volume V with boundary Γ. The body is exposed to heat flux $q(x,y,z,t)$, where x,y,z are Cartesian coordinates and t is the time. The density of internal heat sources which can also be present inside the body is specified $Q(x,y,z,t)$. The temperature distribution function inside the domain V is denoted by $T(x,y,z,t)$. To determine the unknown temperature distribution it is necessary to solve the following differential equation for the transient heat transfer (Nellis and Klein, 2009; Naumenko and Altenbach, 2016).

$$\frac{\partial}{\partial x}\left(k\frac{\partial T}{\partial x}\right) + \frac{\partial}{\partial y}\left(k\frac{\partial T}{\partial y}\right) + \frac{\partial}{\partial z}\left(k\frac{\partial T}{\partial z}\right) + Q - \rho c\frac{\partial T}{\partial t} = 0, \qquad (6.1)$$

where k is the coefficient of thermal conductivity, c is the specific heat capacity and ρ is the material density. For the uniqueness of the solution of the differential equation (6.1), the boundary and initial conditions should be supplemented. As initial conditions, the initial temperature distributions over the volume V are specified as follows

$$T(x,y,z,0) = \overline{T}(x,y,z) \qquad (6.2)$$

The boundary conditions are considered as follows:

1. Specified temperature values on the part of the surface of the body Γ_1 (condition of the 1st kind)

$$T(x,y,z,t)|_{\Gamma_1} = \overline{\overline{T}}(x,y,z,t) \qquad (6.3)$$

The function $\overline{\overline{T}}$ was set based on the experimental conditions. The surface Γ_1 in the model corresponds to the bottom surface of the heat sink base.

2. The specified values of the heat flux on the surface part of the body Γ_2 (condition of the 2nd kind)

$$-k\frac{\partial T(x,y,z,t)}{\partial n}\bigg|_{\Gamma_2} = \bar{q}_n, \qquad (6.4)$$

where n is the unit normal to the surface part Γ_2 and $\bar{q}_n$ is the given heat flux. The surface part Γ_2 corresponds to heat sources. The heat flux is determined by dividing the released thermal power to the areas of the respective surfaces.

3. Heat transfer by radiation. The following non-linear dependence of the heat flow rate on the temperature is applied

$$\dot{q} = \varepsilon_{eq} C_0 A_1 \left[\left(\frac{T_1}{100} \right)^4 - \left(\frac{T_2}{100} \right)^4 \right], \quad \varepsilon_{eq} = \frac{1}{\frac{1}{\varepsilon_1} + \frac{A_1}{A_2} \left(\frac{1}{\varepsilon_2} - 1 \right)}, \quad (6.5)$$

where ε_{eq} is the reduced emissivity coefficient, ε_1 the degree of blackness of the internal radiating surface, ε_2 the degree of blackness of the outer radiating surface, C_0 is the black body radiation coefficient, A_1 is the area of the internal radiating surface (elements of the FOG platform), A_2 is the area of the outer radiating surface (heat-receiving panels and the surface of the heat sink base bounded by them, as well as the compartment cover) T_1 is the temperature of the internal radiating surface, and T_2 is the temperature of the external radiating surface.

In the model, the radiation from the FOG platform to the heat-receiving panels as well as to the surface of the heat-dissipating base and the cover of the compartment limited by them is considered. To solve the heat transfer problem the finite element method and the ANSYS finite element code was applied. The finite element model of SIN consists of

- 362392 10-node tetrahedron elements for heat transfer analysis,
- 54533 auxiliary plane 4-node elements for collecting radiation parameters, and
- 45867 auxiliary plane 4-node elements for implementing thermal contact

The material properties of the components of SIN are presented in (Pogorilov et al., 2020). Heat radiation from external surfaces of the FOG platform and FOG covers with a blackness degree of 0.89 to the heat-receiving surfaces of the heat sink base, compartment covers and heat-receiving panels with a blackness degree of 0.90 is considered. Heat transfer through insulating sleeves was minimized by choosing the low thermal conductivity of the material. External thermal processes of the installation plane of the heat sink base are modeled by the function of temperature variation over time.

6.4 Results

The validation of the model by comparing results of simulation with experimental data is discussed in Pogorelov and Schastlivets (2005), where the temperature field of a similar device, namely a ring laser gyroscope (RLG), obtained by finite element analysis and a series of thermographic snapshots of working RLG was compared.

The comparison parameters of the computational model and the experimental thermograms were the qualitative coincidence of the temperature field in the resonator, as well as the coincidence of the temperature values at the selected points.

Based on modeling the thermal mode of the device using a cyclogram of a constant external temperature, the analysis of the temperature field parameters in the "self-heating" mode ("self-heating time", overheating, temporary and alternative gradients) for a constant external temperature was performed. Furthermore possible locations of external temperature sensors for the purpose of simultaneous measurement of the temperature gradient over time were determined.

The parameters for comparing the calculated model and the thermograms obtained from the experiment are the qualitative coincidence of the temperature field pattern of the resonator in all angles, as well as the coincidence of the model and thermogram temperature values at selected points. Based on the results of simulation of the thermal regime of the device with a thermal stabilisation system for accelerated heating using an external temperature cyclogram as a periodic function, the parameters of the temperature field (ramp-up time, superheat value, time gradients, power value of controlled heat sources) have been investigated.

The following heat sources were activated for this calculation experiment

1. two electronics unit emulator sources, far from the FOG platform compartment,
2. three sources of FOG: FOG1, FOG2, FOG3, and
3. three thermostatic stabilisation system elements located on the FOG platform in the recesses below the FOG, FOG2, FOG3 mounting locations, each of 23 W.

During the computational experiment, a non-stationary heat transfer problem with a duration of 17641 s (three change cycles of 98 min each) was solved in a constant step of 120 s. The computational experiment was carried out with initial conditions corresponding to the lower limit of the operating temperature range. The initial temperature of the SIN model was assumed to be 268 K (-5 °C).

The temperature of the heat sink base changed according to the following law

$$T(t) = T_A \sin\left(\frac{2\pi t}{t_{max}} + \varphi\right) + T_0, \tag{6.6}$$

where t, is the time variable within the interval [0, 17641s], $T_A = 20°C$ is the amplitude of temperature change, $t_{max} = 5880$ s, is the period of temperature change, $\varphi = 3\pi/4$ is the phase of the temperature change and $T_0 = 288$ K is the temperature offset. The model of the thermal stabilisation system is described by the following equation

$$\dot{Q}_{Stb}(T_{FOG}) = \begin{cases} 69, & T_{FOG} < T_{TAR}, \\ 0, & T_{FOG} \geqslant T_{TAR}. \end{cases} \tag{6.7}$$

where $\dot{Q}_{Stb}$ is the total power of the three active thermal stabilisation elements, T_{FOG} is the arithmetic mean of the temperatures of FOG1, FOG2 and FOG3. $T_{TAR} = 298$ K is the target value for the average FOG temperature, upon reaching which the appliance is considered warm. All the thermal stabilisation elements

are controlled simultaneously. The following results were obtained from the computational experiment. **Figure 6.4** illustrates the temperature graphs including the diagram of the outside temperature change (line 5) at the node corresponding to the point on the bottom surface of the heat sink base at the intersection of the diagonals between the attachment points of the thermal insulating bushings and the temperature of the FOG, and graphs of temperature changes at the bases of FOGs (lines 1-4). From these results, it can be seen that thermal stabilisation takes approx. 1800 seconds, compared to 3 cycles of external temperature change (17640 s) without the thermal stabilisation system (Pogorilov et al., 2020).

The rates of the external temperature and the base temperature are calculated using the time-differentiated method described in (Breslavsky et al., 2012). The rates of the outside temperature and the base temperature of FOG1-FOG4 are shown in **Fig. 6.5**. From the graphs it can be seen that the temperature rates of FOG1–FOG4 do not exceed 0.27K per minute after the accelerated warm-up period. **Figure 6.6**

Fig. 6.4 Temperature variations vs. time: 1 – FOG1, 2 – FOG2, 3 – FOG3, 4 – FOG4, 5 – external temperature.
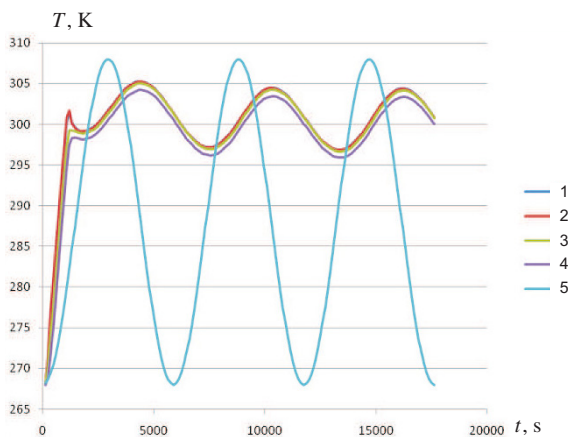
Fig. 6.5 Temperature rates in FOGs vs. time: 1 – FOG1, 2 – FOG2, 3 – FOG3, 4 – FOG4, 5 – external temperature.
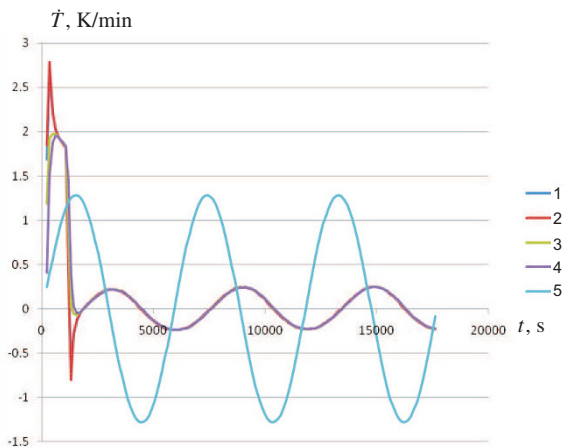
Fig. 6.6 Heat output of the thermal stabilisation system vs. time.
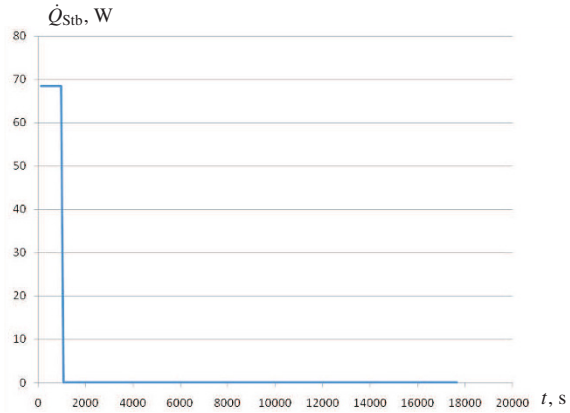
illustrates the change in power of the thermal stabilisation system over time $\dot{Q}_{FOG}$ over time.

Next, the temperature field parameters were investigated using thermal stabilisation to accelerate warm-up and reduce temperature gradients at the FOG sensors with a control law corresponding to changes in the base temperature. In the computational experiment, a non-stationary heat transfer problem with a duration of 17641 s (three change cycles of 98 min each) was solved in a constant step of 120 s. The analysis was carried out with initial conditions corresponding to the lower limit of the operating temperature range. The initial temperature of the SIN model is 268 K. The temperature of the heat sink base was changed according to Eq. (6.6).

For the thermal stabilisation system the following equation is applied

$$\dot{Q}_{Stb}(T_{FOG}) = \begin{cases} 69, & T_{FOG} < T_{TAR}, \\ \dot{Q}_A \sin(2\pi t/t_{max} + \varphi + \pi) + \dot{Q}_A, & T_{FOG} \geqslant T_{TAR}, \end{cases} \tag{6.8}$$

where $\dot{Q}_{Stb}$ is the total power of the three active thermal stabilisation elements, T_{FOG}, K is the arithmetic mean of the temperatures of FOG1, FOG2, FOG3, $T_{TAR} = 312$ K is the target value for average FOG temperature, upon reaching which the appliance is considered warmed up. $\dot{Q}_A = 8.0$ W is the amplitude of total thermal stabilisation power.

All the thermal stabilisation elements are controlled simultaneously. **Figure 6.7** illustrates temperature changes at the base of the FOGS. Furthermore the diagram of the external temperature change at the node corresponding to the point on the bottom surface of the heat sink base at the intersection of the diagonals between the attachment points of the thermal insulation sleeves is presented. From these results it can be seen that at a given level of the temperature T_{TAR} the steady-state heat build-up occurs within 2000 s.

The temperature rates are presented in **Fig. 6.8**. From the graphs it can be seen that the temperature rates in FOG1–FOG4 after the accelerated warm-up period are

Fig. 6.7 Temperature varia-
tions vs. time: 1 – FOG1,
2 – FOG2, 3 – FOG3,
4 – FOG4, 5 – external tem-
perature.
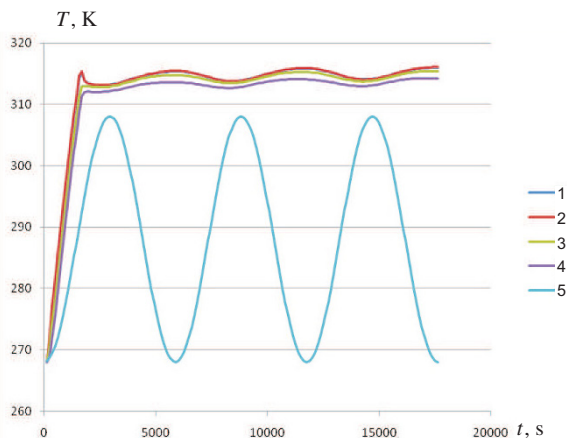
Fig. 6.8 Temperature rates in
FOGs vs. time: 1 – FOG1,
2 – FOG2, 3 – FOG3,
4 – FOG4, 5 – external tem-
perature.
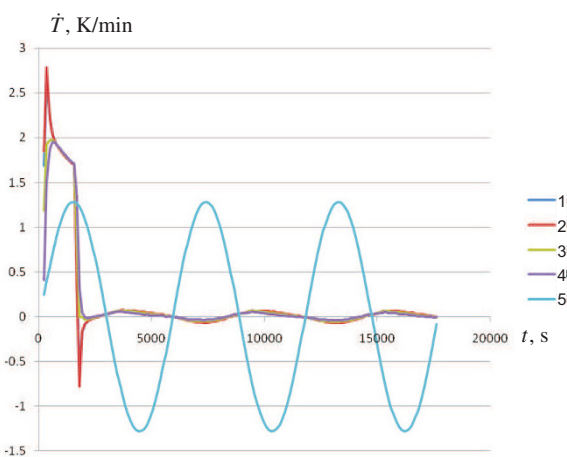
less than 0.1 K/min. The graphs of the change in power of the thermal stabilisation
system over time are presented in **Fig. 6.9**.

6.5 Conclusions

In this study a finite element model of the SIN device has been developed in order
to simulate the temperature field of the SIN. In particular, conditions that ensure a
minimum of temperature variation on the FOG platform under thermally stabilised
conditions have been determined. A computational thermal model of the device has
been developed and verified.

   Based on the results of numerical simulation, the parameters of the temperature
field of the device and characteristics of the thermal stabilisation system have been

Fig. 6.9 Heat output of the thermal stabilisation system vs. time.
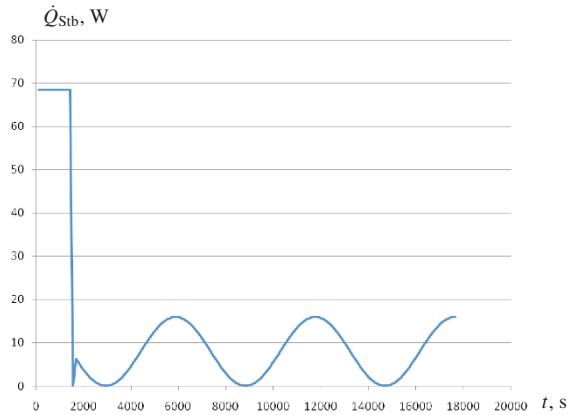
investigated. The temperature rates at the given points of the device have been numerically determined. It is found that the thermal stabilisation law must ensure the stability of the temperature field (small temperature rate). The temperature value of the FOG itself has no significant effect on the drift value.

It is found that the application of thermal stabilisation in the considered design of the SIN device with heat dissipation from the FOG platform by means of radiation makes it possible to form a temperature field with a temperature difference of 2 K on the FOG platform, which provides a minimum level of thermal strains in the FOG platform and reduces the fluctuations of external temperature at a rate of over 8K/min down to 0.2 K/min. When stabilised with a control law corresponding to the temperature change of the FOG platform, it is possible to reduce the temperature fluctuations of the FOG platform down to 0.1 K/min.

A temperature stabilisation system should only be used to bring the system to operating temperature for a maximum of 30min and should not be used during operation.

References

Breslavsky DV, Pogorelov SY, Schastlivets KY, Batyrev BI, Kuznetsov YA, Oleynik SV (2012) Development of method to determine temperatur gradients in fiber-optic gyroscope OIUS501 (in Russ.). Mechanika ta Mashinobuduvannya (1):90–101

Diesel JW, Dunn GP (1996) Method for in-field updating of the gyro thermal calibration of an intertial navigation system. US Patent 5,527,003

Dzhashitov VE, Pankratov VM (2014) Control of temperature fields of a strapdown inertial navigation system based on fiber optic gyroscopes. Journal of Computer and Systems Sciences International 53(4):565–575

Dzhashitov VE, Pankratov VM, Barulina MA (2013) Mathematical models of thermal stress-strain state and scale factor error of fiber optic gyro sensors. Journal of Machinery Manufacture and Reliability 42(2):124–131

Dzhashitov VE, Pankratov VM, Golikov AV (2014) Mathematical simulation of temperature field control of the strapdown inertial navigation system based on optical fiber sensors. Journal of Machinery Manufacture and Reliability 43(1):75–81

Naumenko K, Altenbach H (2016) Modeling High Temperature Materials Behavior for Structural Analysis: Part I: Continuum Mechanics Foundations and Constitutive Models, Advanced Structured Materials, vol 28. Springer

Nellis G, Klein S (2009) Heat Transfer. Cambridge University Press

Plaksiy Y, Breslavsky D, Homozkova I, Naumenko K (2021) Closed-form quaternion representations for rigid body rotation: application to error assessment in orientation algorithms of strapdown inertial navigation systems. Continuum Mechanics and Thermodynamics 33:1141–1160

Pogorelov SY, Schastlivets Ku (2005) Refinement of the computational model of a ring laser gyroscope based on experimental data (in Russ.). Vestnik NTU KhPI (47):153–158

Pogorilov SY, Khavin VL, Naumenko K, Schastlivets KY (2020) Heat transfer analysis in the strapdown inertial unit of the navigation system. In: Plasticity, Damage and Fracture in Advanced Materials, Springer, pp 119–133

Shen C, Chen X (2012) Analysis and modeling for fiber-optic gyroscope scale factor based on environment temperature. Applied Optics 51(14):2541–2547

Wang X, Ma S (2009) Nonlinearity of temperature and scale factor modeling and compensating of FOG. Journal of Beijing University of Aeronautics and Astronautics 25(1):28–31

Zhang Y, Guo Y, Li C, Wang Y, Wang Z (2015) A new open-loop fiber optic gyro error compensation method based on angular velocity error modeling. Sensors 15(3):4899–4912

Zhang Ys, Wang Y, Yang T, Yin R, Fang J (2012) Dynamic angular velocity modeling and error compensation of one-fiber fiber optic gyroscope (OFFOG) in the whole temperature range. Measurement Science and Technology 23(2):025,101

Chapter 7
Experimental-numerical Analysis of Microstructure-property Linkages for Additively Manufactured Materials

Benjamin Schmidt, Alexander Raßloff, Robert Kühne, Martina Zimmermann, and Markus Kästner

Abstract The innovation of new or improved products fabricated from additive manufacturing processes with desired properties depends on a multitude of trials as stated by the *Materials Genome Initiative for Global Competitiveness* of the US National Science and Technology Council. Therefore, a systematic approach is essential to accelerate materials development. This can be realised by developing systematic materials knowledge in the form of process-structure-property linkages. In this envisioned framework, the present work aims to derive the structure-property linkages of additively manufactured Ti-6Al-4V alloy.

One main focus is to investigate the influence of potential defects, in the form of pores, inherited from the fabrication process on the fatigue properties. For this purpose, the pore microstructure is obtained by x-ray computed tomography and a low-dimensional representation of the structure is derived by a statistical analysis. In a following numerical analysis, statistical volume elements (SVEs) with varying pore microstructures are reconstructed and microscale crystal plasticity simulations are performed in DAMASK to obtain the material properties such as yield strength and fatigue indicator parameters (FIPs). The influence of pore statistics on FIPs is obtained numerically and a comparison with Murakami's empirical square root area concept is made.

In a second part, the influence of the grain microstructure on mechanical properties is analysed. To this end, the grain microstructure is obtained by scanning electron microscopy (SEM) for specimens manufactured with different process configurations. Those structures are characterised through spatial three-point auto-

Benjamin Schmidt, Alexander Raßloff, Markus Kästner
Institute of Solid Mechanics, TU Dresden, George-Bähr-Straße 3c, 01069 Dresden, Germany,
e-mail: Benjamin.Schmidt@tu-dresden.de, Alexander.Rassloff@tu-dresden.de,
Markus.Kaestner@tu-dresden.de

Robert Kühne, Martina Zimmermann
Materials Characterization and Testing, Fraunhofer Institute for Material and Beam Technology,
Winterbergstraße 28, 01277, Dresden, Germany,
e-mail: robert.kuehne@iws.fraunhofer.de, martina.zimmermann@iws.fraunhofer.de

correlation functions. The main properties of this high-dimensional descriptor are transformed to a low-dimensional representation by employing principal component analysis (PCA). Using LASSO regression, a meta model is derived, which allows for linking the microstructure to experimentally obtained micro hardness. This makes predictions of the hardness for new, unknown microstructures possible.

Key words: Additive manufacturing, Structure-property linkages, Microstructure, Defects, Multiscale modelling, Fatigue

7.1 Introduction

Additive manufacturing (AM) paves the way to customised, lightweight and innovative materials. The process of qualifying new materials with desired properties and their reliable utilisation requires more than ten years according to the *Materials Genome Initiative for Global Competitiveness* of the US National Science and Technology Council. Understanding the relationships between process, structure and properties is essential for accelerating materials development. Deriving a large database of associated process-structure and structure-property pairs based on experiments and augmented by numerical simulations allows for an inverse materials design. However, a major challenge in transforming AM into the efficient and reliable commercial application can be seen in the lack of sufficient and systematic knowledge about process-structure-property (PSP) relationships. Hence, AM components often contain imperfections and inhomogeneities that cause premature failure especially under cyclic loading. Therefore, further development of methods for material qualification, structure and process simulation as well as component construction and quality control is necessary and addressed within the project *AMTwin*.

The goal of AMTwin is the data-driven prediction of PSP linkages for the widely used metal alloy Ti-6Al-4V manufactured by laser powder bed fusion (LPBF). A multitude of steps as illustrated in **Fig. 7.1** is necessary to achieve this goal by accumulating enough data through data fusion, i.e. the augmentation of few experimental data by numerical simulations. A digital process chain and workflows are established to create a digital twin of the AM process and material. Starting with a detailed analysis of the Ti-6Al-4V powder, all data and metadata are coherently stored. Many specimens are built by design of experiment through variation of the LPBF process parameters to capture a significant range of microstructures and associated properties, allowing for both establishing process-structure relationships and the derivation of a process model for data augmentation.

In this contribution, the microstructure-property relationship is analysed. The microstructure is characterised on the one hand by pores and defects in the microstructure, which is referred to as pore microstructure in the further course. On the other hand, the microstructure is characterised by the grain morphology and the phase distribution, which is referred to as grain microstructure in this contribution.
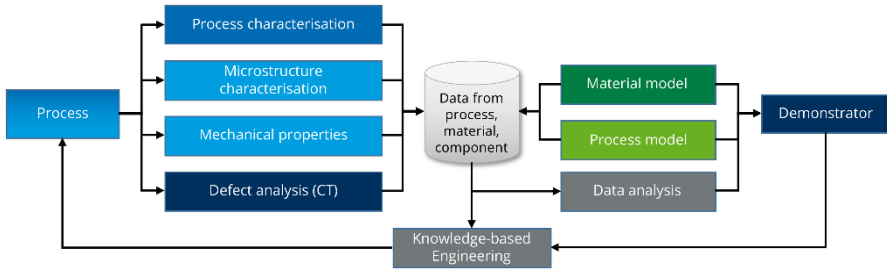
Fig. 7.1: Schematic overview over processes within AMTwin for the data-driven prediction of PSP relationships.

The grain microstructure is experimentally characterised by light microscopy (LM). In a first study, the resulting images are to be statistically analysed and serve as basis for the *in silico* reconstruction of grain microstructures. The material's mechanical properties are determined by static and cyclic tests. Capturing the pores by x-ray computed tomography (CT) is essential for a comprehensive pore microstructure analysis. Based on these experimental data, a process model is derived that simulates the LBPF process. Additionally, methods are developed to reconstruct microstructures based on statistical and translation-invariant descriptors, see Seibert et al. (2021a). A low-dimensional description in the form of few meaningful scalars that capture the crucial microstructural features is key for establishing the PSP relationships. The reconstructed SVEs – synthetic structures that are as a single one not representative for all possible instances of a microstructure associated with that statistic, but as a set – serve as simulation domains for the numerical crystal plasticity (CP) simulations. Mechanical properties such as fatigue indicator parameters (FIPs) or yield stress are determined by modelling the material behaviour. Processing these mechanical parameters yields the properties which are incorporated in the data base. Finally, the latter one can be used to establish the desired PSP relationships.

As a show case of this approach, the current article aims at presenting an experimental-numerical approach and an exemplary demonstration for the investigation of the influence of pores on the fatigue properties by numerical simulation as illustrated in **Fig. 7.2**. To that end, specimens of Ti-6Al-4V are manufactured and their microstructures statistically characterised on the basis of LM images and CT scans. SVEs are reconstructed and CP simulations are conducted to calculate FIPs. Analysing the simulation results by extreme value distribution yields the targeted data of pore structure and fatigue property pairs, enabling the ranking of microstructures. Additionally, a ranking based on the empirical $\sqrt{\text{area}}$ parameter as introduced by Murakami (1989) is comparatively considered.

In addition to porosity, a factor that significantly influences the mechanical properties of Ti-6Al-4V is the crystalline microstructure, which is analysed in the second part of this contribution. As thoroughly described in Kühne et al. (2021) and ter Haar and Becker (2021), the microstructure is composed of α- and β-phase. The grain mi-
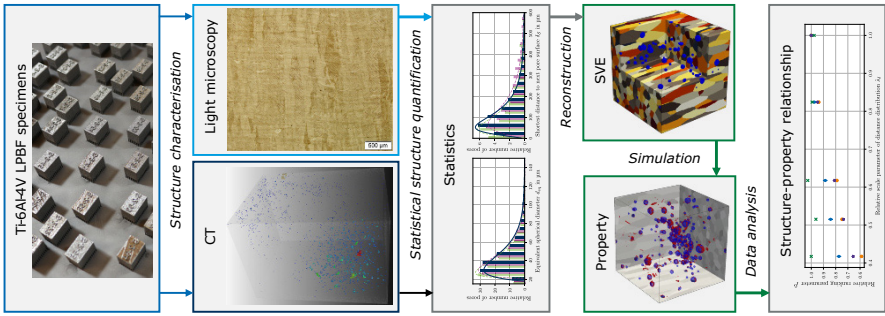
Fig. 7.2: Illustration of the approach to access pore microstructure-property relationships based on experimentally observation and numerical simulation: Specimens are printed, the material microstructure is observed by light microscopy and computed tomography, the structure is statistically quantified and SVEs are *in silico* reconstructed for simulating fatigue indicator parameters by crystal plasticity simulations to derive the relationships by data analysis.

crostructure and ratio of α- and β-phase is strongly influenced by the LPBF process parameters and thermal post-treatment. Hence, microstructures that were produced by different configurations are analysed and compared. From SEM images of the microstructure the distribution of α- and β-phase can directly be derived, as presented in **Fig. 7.3** for images from different batches. The phase distributions are described by spatial three-point correlations. They are a high-dimensional descriptor, which is disadvantageous for the further analyses. In order to create a low-dimensional descriptor, a PCA is performed.

In Kühne et al. (2021) it is demonstrated, that the microstructure and ratio of the two phases influence the micro hardness of the material, which was determined experimentally. As a demonstration, the linkage between low-dimensional microstruc-

(a) SEM batch (b) SEM batch (c) SEM batch (d) SEM batch (e) SEM batch (f) SEM batch
1.   3.   5.   6.   7.   8.

(g) Phases batch (h) Phases batch (i) Phases batch (j) Phases batch (k) Phases batch (l) Phases batch
1.   3.   5.   6.   7.   8.

20 µm
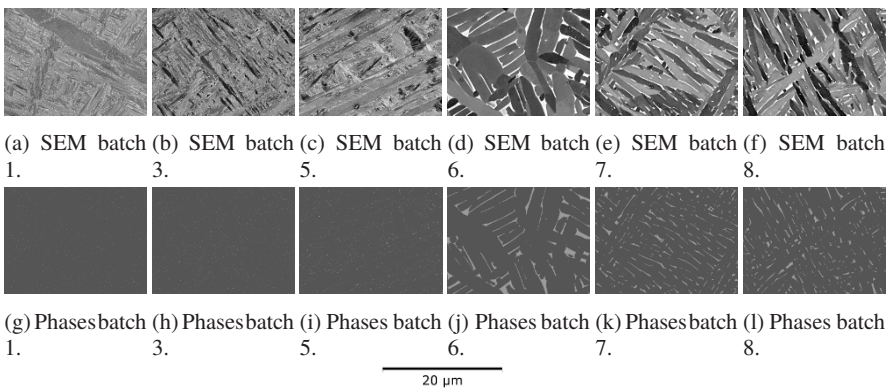
Fig. 7.3: SEM images (a)-(f) and derived phases (g)-(l) of the microstructures.

ture descriptors and micro hardness is analysed through meta models, which allow for a prediction of the micro hardness for new microstructures.

The experimental and numerical methods are briefly introduced in Sect. 7.2. In Sect. 7.3 the results of illustrative studies are presented and briefly discussed. A conclusion is given in Sect. 7.4.

7.2 Methods

7.2.1 Experimental Characterisation of Microstructure and Defect Population

For this study, Ti-6Al-4V powder of Grade 23, atomised by argon, is utilised. A LPBF is used to build rectangular specimens of size $10 \times 10 \times 15$ mm as shown in **Fig. 7.2**. LM images as in the same figure of sections parallel to the building direction are taken to measure the width of the visible prior β-grains, yielding an average width of $192\,\mu$m. These values constitute a simplified characterisation of the grain structure.

In order to characterise the pores, x-ray CT scans as illustrated in **Fig. 7.2** are conducted with a voxel resolution of $9\,\mu$m. The pores are detected and analysed using the software VGSTUDIO Max 3.4. For the porosity analysis, a workflow based on du Plessis et al. (2018) is utilised. To achieve a more sophisticated processing, the data is transferred to MATLAB, where additional quantities are calculated to serve as input for the microstructure characterisation as described in the subsequent section.

7.2.2 Numerical Characterisation of Microstructure and Defect Population, and Reconstruction

7.2.2.1 Microstructural Descriptors

An adequate and condensed description of the structure is mandatory for deriving PSP relationships and for reconstructing synthetic microstructures. For the present study, the spatial distribution and morphology of the pores need to be captured. For this purpose, each voxel cluster from the CT that was identified as a pore is approximated by an ellipsoid to allow for a simplified, analytical description of the pores, that the authors are well aware of the fact, that the failure-relevance of a defect significantly relies on the defect shape and here in particular the aspect ratio and its position relative to the loading direction. These pores are characterised by the distributions of two meaningful parameters, the equivalent spherical diameter (ESD) d_{eq} and the shortest distance between the surfaces to the nearest pore δ_S. As the pores

are to be reconstructed as spheres for this first demonstration, the ESD captures not only the crucial effect of pore size, but also the complete morphology. The latter parameter contributes to the significant effect of high plastification in dense areas. Describing the distribution of these quantities by probability density functions (PDFs) allows for characterising the structure in the desired low-dimensional manner by few parameters, i.e. the descriptors. **Figure 7.4** shows the distribution of d_{eq} and δ_S derived by CT for three real specimen. As can been seen, the ESD distribution can be well fitted to a gamma PDF

$$f\left(d_{eq}; a, l_\Gamma, s_\Gamma\right) = \left(\frac{d_{eq}}{s_\Gamma} - l_\Gamma\right)^{a-1} \exp\left(l_\Gamma - \frac{d_{eq}}{s_\Gamma}\right)\Gamma^{-1}(a), \quad d_{eq} \geqslant 0, a > 0. \quad (7.1)$$

The parameters s and l scale and shift the function, whereas a denotes the shaping parameter and $\Gamma(\cdot)$ denotes the gamma function[1]. A lognormal PDF

$$f(x; \sigma, l_{ln}, s_{ln}) = \left[(m)\,\sigma\sqrt{2\pi}\right]^{-1} \exp\left(-\frac{\log^2(m)}{2\sigma^2}\right),$$

$$\text{with} \quad x > 0,\ \sigma > 0,\ m = \frac{\delta_S}{s_{ln}} - l_{ln}, \quad (7.2)$$

is applied to fit the distribution of the shortest distance to the nearest pore surface. Here, the shape parameter is denoted by σ. The Python package SciPy is employed for identifying the parameters by maximising a log-likelihood function. The volume fraction of pores, i.e. the porosity ϕ, serves as another descriptor.
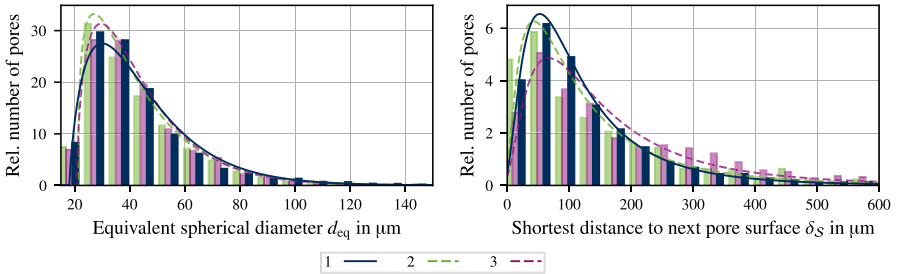
Fig. 7.4: **(Left)** ESD d_{eq} distribution and fitted gamma PDF for three exemplary CT scans; **(right)** distribution of the shortest distance to the next pore surface δ_S and fitted lognormal PDF.

---

[1] The gamma function is defined as

$$\Gamma(z) = \int_0^\infty t^{z-1}e^{-t}\,dt$$

for arguments z with a positive real part.

7.2.2.2 Reconstruction

The grain structure and pores are reconstructed separately. As the focus of the present work lies on the investigation of the influence of pores, *one* grain structure is reconstructed in which the pores are incorporated. DREAM.3D (Groeber and Jackson, 2014) is utilised for this task. The structure parameters for DREAM.3D are chosen so that the resultant grains represent lamellae colonies, i.e. regions of similar orientation within a prior β-grain. The mean grain ESD is set to 200 μm with a length/width-ratio of 4 to 5, based on the LM observation. The resultant SVE of size $(1200\,\mu m)^3$ is discretised in 200^3 elements and is visualised on the left in **Fig. 7.5**.

The pores are reconstructed following a procedure of sampling random variates from the distribution functions (7.1), (7.2) for given parameters. For the present study, they are chosen to resemble CT scan 1 from **Fig. 7.4**. A Python script is used to *(a)* compute the ESD and number of pores by sampling from the corresponding PDF, *(b)* distribute the spherical pores spatially by sampling from the distance PDF and *(c)* compare the resultant distribution to the input and either restart or finish procedure. Now, the pores are incorporated into the grain domain from DREAM.3D, yielding the final SVE for the CP simulation as described in the subsequent section. **Figure 7.5** shows an exemplary SVE.
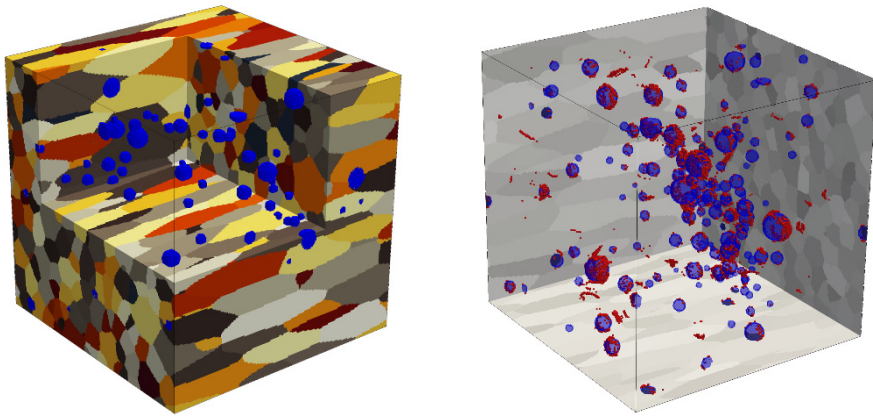
Fig. 7.5: **(Left)** Reconstructed polycrystalline simulation domain with spherical pores (blue); **(right)** spatial distribution of the highest Fatemi-Socie FIPs (red) in a SVE with 114 pores (blue).

7.2.3 Microstructure Properties and Ranking

7.2.3.1 Crystal Plasticity Simulations to Derive Fatigue Indicator Parameters

The Düsseldorf Advanced Material Simulation Kit (DAMASK) (Roters et al., 2019) is used to conduct the CP simulations. Taking the crystalline structure of the material into account enables a thorough investigation of the structure-property linkages. The material of the grains is modelled by a phenomenological powerlaw constitutive equation, see Roters et al. (2019) for detailed information, assuming a hexagonal lattice. The material parameters are chosen to depict the behaviour of Ti-6Al-4V lamellae colonies and are motivated from Bridier et al. (2009); Mayeur and Mc-Dowell (2007); Zambaldi et al. (2012). The mechanical behaviour of the pores is modelled by an elastic and plastically dilatational material model proposed by Maiti and Eisenlohr (2018).

For the derivation of fatigue related properties, FIPs are calculated from results of cyclic simulations. The processed quantities comprise the plastic shear strain tensor $\boldsymbol{\gamma}$, the first Piola-Kirchhoff stress tensor $\mathbf{P}$ and the plastic velocity gradient tensor $\mathbf{L}^{\mathrm{p}}$. Following the definition as introduced by, e.g. McDowell (2007), the local FIP fields are computed as

$$\Phi_{\mathrm{FS}} = \max_{\alpha} \left\{ \frac{\Delta\gamma_{\max}^{\alpha}}{2} \left(1 + \mathrm{k} \frac{\mathrm{P}_{\mathrm{n,max}}^{\alpha}}{\mathrm{P_y}} \right) \right\}$$

$$\Phi_{\mathrm{MPS}} = \max_{\alpha} \left\{ \frac{\Delta\gamma_{\max}^{\alpha}}{2} \right\}$$

$$\Phi_{\mathrm{APS}} = \int_{\mathrm{cyc}} \sqrt{\frac{2}{3} \mathbf{D}^{\mathrm{p}} : \mathbf{D}^{\mathrm{p}}} \, \mathrm{dt} \quad . \tag{7.3}$$

The Fatemi-Socie (FS) FIP Φ_{FS} is defined as a function of the maximum range of plastic shear strain of the last cycle $\Delta\gamma_{\max}$, the maximum stress normal to the slip plane $\mathrm{P}_{\mathrm{n,max}}$, the yield stress $\mathrm{P_y}$ and a mediating parameter k. Φ_{MPS} denotes the maximum plastic shear strain range (MPS) FIP and Φ_{APS} denotes the accumulated plastic shear strain (APS) FIP. For the latter FIP, the plastic rate of the deformation tensor

$$\mathbf{D}^{\mathrm{p}} = \frac{1}{2} \left(\mathbf{L} + \mathbf{L}^{\mathrm{T}} \right)$$

is used.

To extract a representative fatigue property for a specific microstructure characterised by a certain statistical description from simulations on non-representative SVEs, an adequate data analysis is conducted. Employing an extreme value distribution approach as by, e.g. Muth et al. (2021), all FIPs from a SVE set, i.e. a set of SVEs that share the same statistical descriptors, above a certain threshold are described by a distribution function. This method is illustrated in **Fig. 7.6** at the example of structures with varying porosity. For three porosities, the real distribution of the highest FS FIPs is plotted on the left alongside a dashed line, indicating
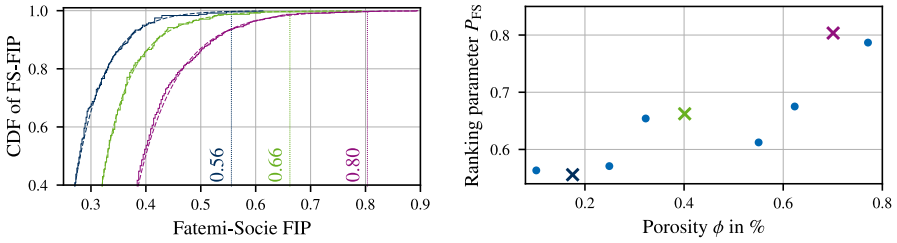
Fig. 7.6: **(Left)** Cumulative distribution of highest Fatemi-Socie FIPs and fitted distribution function (dashed line) for three exemplary SVE sets of differing porosity; **(right)** associated Fatemi-Socie ranking parameter based on extreme value distribution.

the cumulative distribution function F_{EVD} of the fitted generalised gamma PDF. The function is defined as

$$f(x; a, c, l, s) = |c| \left(\frac{\Phi_{FS}}{s} - l \right)^{ca-1} \exp \left\{ - \left(\frac{\Phi_{FS}}{s} - l \right)^{c} \right\} \Gamma^{-1}(a)$$
$$\Phi_{FS} \geqslant 0,\ a > 0,\ c \neq 0, \tag{7.4}$$

where l and s denote the shift and scale parameters, a and c the shape parameters and Γ is the already introduced gamma function. A ranking parameter P is now introduced to describe the fatigue proneness of the SVE set. It is defined as the FIP that will not be exceeded with a probability of 99.5%, i.e.

$$P = F_{EVD}^{-1}(0.995).$$

In **Fig. 7.6** this ranking parameter is shown. To allow for a better comparison, a relative ranking parameter

$$\tilde{P} = \frac{P_{ref}}{P}$$

is introduced.

7.2.3.2 Murakami's $\sqrt{area}$ Estimation

To serve as a comparative value, an empirical method for the estimation of the fatigue strength is additionally employed. The Kitagawa-Takahashi diagram established by Liu et al. (2020) is used here. It can be expressed as

$$\Delta\sigma_w = \Delta\sigma_{w0} \sqrt{\frac{a_0}{a + a_0}} = \Delta\sigma_{w0} \sqrt{\frac{\sqrt{area_{eff0}}}{\sqrt{area_{eff}} + \sqrt{area_{eff0}}}} \quad . \tag{7.5}$$

The fatigue limit $\Delta\sigma_w$ of the AM structure can be calculated based on the fatigue limit of the defect-free structure $\Delta\sigma_{w0}$ and two size parameters a and a_0. Liu et al. (2020) substituted the latter ones by the $\sqrt{area}$ parameter introduced in Murakami

(1989). Based on the work of Leuders et al. (2013), the specific value of

$$\Delta\sigma_{w0} = 420\,\text{MPa}$$

was chosen. For defects within the specimen,

$$\sqrt{\text{area}_{\text{eff0}}} = 102.6\,\mu\text{m}$$

was determined. Comparing this empirical determination of a fatigue property to the FIPs is facilitated by defining the ranking parameter as

$$\tilde{P}_{\sqrt{\text{area}}} = \frac{\Delta\sigma_w}{\Delta\sigma_{w,\text{ref}}},$$

analogously to the FIP-based one, so that higher values indicate a better fatigue performance.

7.2.4 Grain Structure Characterisation

7.2.4.1 Microstructural Descriptors

As presented in **Fig. 7.3**, from SEM images, a binary image with the phase distribution can directly be derived with colour value limits, where one colour represents the α-phase (light grey) and the other the β-phase (dark grey). Similar as described in Subsect. 7.2.2, for interpretation of these binary images and deriving PSP linkages it is necessary to find meaningful descriptions.

In this case, the spatial three-point auto-correlation is used for this purpose. A generalised definition and thorough discussion is given in Jiao et al. (2007), here, an implementation introduced by Seibert et al. (2021b) is utilised: for two vectors $\mathbf{r}_a$ and $\mathbf{r}_b$, the three-point auto-correlation of the β-phase

$$S_3^{\beta\to\beta}(\mathbf{r}_a,\mathbf{r}_b)$$

is defined as the probability of both vectors starting and ending in the β-phase, if their mutual starting point is placed randomly in the microstructure. The three-point auto-correlation captures generalized information about distribution of α- and β-phase, as exemplified in **Fig. 7.7**.

7.2.4.2 Dimensionality Reduction

Correlation fields contain a lot of information, however, with only few sample points this high-dimensional representation is disadvantageous for the following meta model fitting. The meta model would have much more parameters than sample
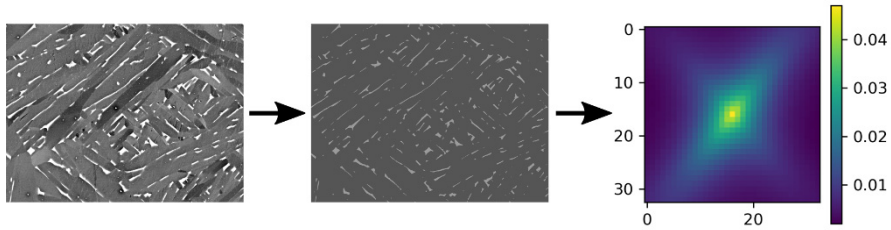
Fig. 7.7: SEM image, derived binary image representing α- and β-phase and corresponding two-point auto-correlation of the β-phase. The two-point autocorrelation is included in the three-point autocorrelation.

points to fit those parameters. One way to get around this problem is dimensionality reduction, the transformation of a high-dimensional descriptor to a low-dimensional representation, that still contains meaningful properties of the original data set. In this contribution, PCA, which is a linear method, is used for this purpose. The basic idea of this method is the construction of eigenvectors of the covariance matrix, so only few values contain a majority of the systems significant properties, so that

$$\text{PCA}: \mathbb{R}^n \rightarrow \mathbb{R}^m \tag{7.6}$$
$$\mathbf{S} \mapsto \mathbf{PC}$$

the n entries of the correlation are mapped to m principal components with $m \ll n$.

In the specific case of dimensionality reduction of auto-correlation fields, there is the problem, that many values are near zero with only few larger values, which dominate the PCA and mask weaker effects. Here an element-wise scaling of the entries of the three-point correlation $S_3^{\beta \rightarrow \beta}$ in the form of

$$S_{3,\text{norm}}^{\beta \rightarrow \beta} = \arctan(a\, S_3^{\beta \rightarrow \beta}) \tag{7.7}$$

with a factor $a > 1$ can mitigate this effect and reduce the error of the meta model. For this analysis the PCA function implemented in scikit-learn (Pedregosa et al., 2011) is used.

7.2.4.3 Meta Modelling

One aim of this study is the micro hardness prediction for new batches with adapted process parameters based on SEM images of those specimens. For this purpose a meta model was fitted to the SEM images and micro hardness values of the present data set. From a variety of different models, the linear LASSO regression implemented in scikit-learn (Pedregosa et al., 2011) showed the smallest error and the highest robustness. A detailed overview of the method is provided by Kim et al.

(2007). The objective of LASSO regression is the minimisation

$$\min_{w} \frac{1}{2n_{\text{samples}}} \|Xw - y\|_2^2 + \alpha \|w\|_1 \tag{7.8}$$

of the sum of least-square error and the product of a constant model factor α and the ℓ_1-norm of the coefficient vector. While the first summand minimises the error of the prediction Xw, the regularisation in the second summand prevents overfitting.

7.3 Results

The following section presents the results of studies that have been conducted to illustrate the presented approaches.

7.3.1 Pore Microstructure-property Linkage

Three pore structure descriptors are chosen and varied, namely *(a)* the scale parameter of the ESD s_{esd}, *(b)* the size of the largest pore $\sqrt{\text{area}}$ and *(c)* the porosity ϕ. **Figure 7.5** shows the local spatial distribution of the highest FS FIP. It can be seen that they locate at the pores as expected.

The results of the studies are shown in **Fig. 7.8** in terms of the ranking parameter. The scale parameters are presented as relative values to allow for a better evaluation. Per study only one parameter is varied and the others are set to constant values as given in the same figure.

The study on the ESD as shown in **Fig. 7.8**(a) indicates that the proneness to fatigue increases for higher scale parameters $\tilde{s}_{\text{esd}}$. As can be seen from the associated plot of the gamma PDF, a high value of $\tilde{s}_{\text{esd}}$ means that there are more larger pores compared to small values. This result seems plausible as larger pores tend to have a major impact on the fatigue performance. The empirical ranking parameter $\tilde{P}_{\sqrt{\text{area}}}$ remains fairly constant for $\tilde{s}_{\text{esd}} \geqslant 0.8$, indicating that the size of the largest pore does not change significantly. However, the FIP based parameters suggest a further decreasing trend, underlining the potential of high-resolution CP simulations, allowing for a more sophisticated investigation.

The data in **Fig. 7.8**(b) shows the defined trend of $\tilde{P}_{\sqrt{\text{area}}}$. The other parameters pose significant scatter. $\tilde{P}_{\text{FS}}$ and $\tilde{P}_{\text{APS}}$ even rise for pores below $\sqrt{\text{area}} = 100\,\mu\text{m}$. That could imply a less pronounced impact of the largest pore compared to other factors related to local phenomena. This relation seems to change as the ranking parameters decrease for higher $\sqrt{\text{area}}$.

The study on the influence of the porosity shows the expected outcome of worse fatigue performance for higher porosity. It can be seen from **Fig. 7.8**(c) that the
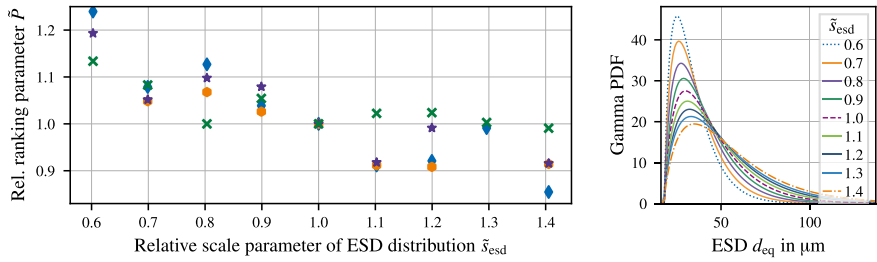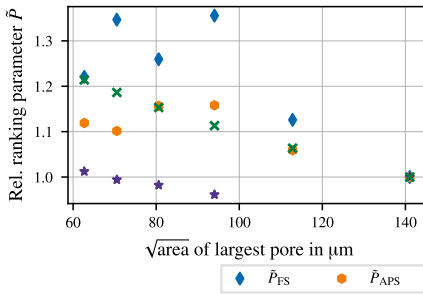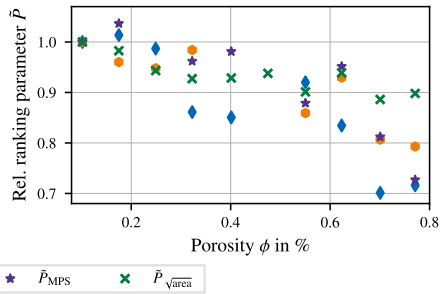
Fig. 7.8: Relative ranking parameters $\tilde{P}$ from simulations and empirical estimations.

empirically motivated parameter follows roughly the same trend. The cause could lie in the increased possibility of larger pores for higher volume fraction of pores.

7.3.2 Grain Microstructure-property Linkage

The presented approaches for the grain microstructure-property linkage are demonstrated on a data set of 31 SEM images and their derived binary images of α- and β-phase. The total of 31 samples were produced by six different process parameter configurations, one sample of each batch is presented in **Fig. 7.3**. For each of the six batches, the micro hardness was measured on an additional specimen. While all batches have different processing parameters, batch 1, 3 and 5 are all low temperature stress relieved (550°C, 3 h, Ar), batch number 6 was treated with Hot Isostatic Pressing (HIP, 920°C, 1000 bar, 2 h, Ar) and batches 7 and 8 were annealed at higher temperature (843°C, 4.5 h, Ar). The high temperature treatments of the batches 6, 7 and 8 significantly decrease the micro hardness. The PCA was performed with a scaling parameter α = 10^5 in Eq. (7.7). In **Fig. 7.9** the first three PCA parameters (PC1, PC 2 and PC 3) and the micro hardness are presented, the marker colour represents the value of PC 1. The first component shows two clusters, which differentiate between batches 1, 3 and 5 (green) and the high temperature treated batches

6, 7 and 8 (blue). The subplot of PC 1 and micro hardness demonstrates the strong
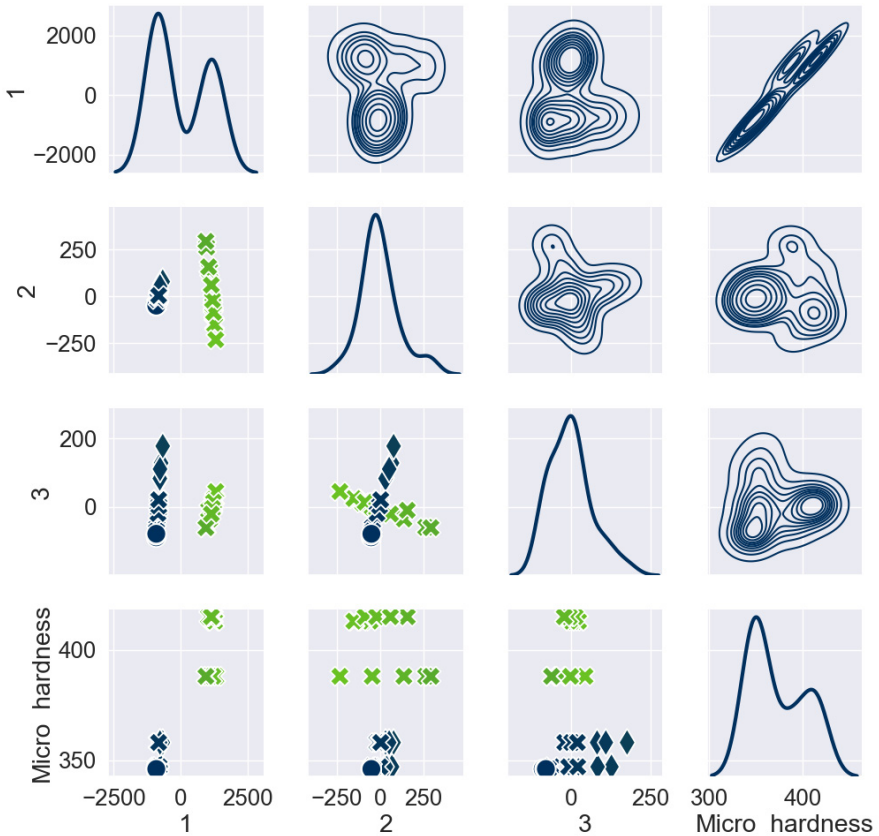
Fig. 7.9: Visualisation of principle components 1, 2 and 3, and micro hardness. The upper triangular shows contour lines of cross-plots, the main diagonal represents the density of the individual parameters. In the lower triangular, there is a scatter plot of the specimens. The colour represents the value of the first principal component, for the blue specimens, the marker differentiates the shape of the larger alpha sections in mainly compact, round inclusions (circular marker), mixed shapes (cross) and slim inclusions (diamond).

influence of the high temperature treatment process on the micro hardness. PC 2 has a small scattering range in the high temperature treated specimens but a large range in the low temperature stress relieved ones, so it can be assumed, that the value of this PC characterises a variation in the low temperature stress relieved specimens.

High temperature treated specimens can be sorted by the shape of the large α-phase sections to mainly compact, round inclusions (blue circular marker in **Fig. 7.9**), mixed shapes (cross), and slim inclusions (diamond). This shape variance is also represented in PC 3, where the low temperature stress relieved specimens all

are close to zero, while mainly round specimen have smaller values and slim ones larger value.

In order to simulate the prediction of the micro hardness based on grain microstructure images, the dataset is split in one test batch and five training batches. The spatial three-point auto-correlation of the training images is used to perform the PCA with $n_{PC} = 20$. Subsequently the LASSO regression is fitted to the PCs and the corresponding micro hardness values. Afterwards, the trained PCA and LASSO models are applied to the test set. In **Fig. 7.10** (a) this is demonstrated exemplarily for batch 1 as test batch and the remaining configurations as training data. Here, it can be seen, that the trained model fits the training data very well, while the model predicts values similar to the micro hardness of batch 3 and 5. This means, that the model could identify the similarity between low temperature stress relieved specimens, but since the correct result is unknown to the model, it obviously predicted those results already known.

In **Fig. 7.10** (b), the prediction results for all six runs, each fitted with the remaining five batches as training data, are combined. Here again, the model reliably differentiates between HIP and low temperature relieved specimens, but due to the limited training data set, the prediction results are scattered around the training data. The prediction results might be improved by extending the data set.

In many applications, it will not be necessary to predict a value for a complete new process configuration, but only for a new specimen of a known process. In this case, the model only has to compare the test specimen to very similar specimens in the training set and so the prediction would be significantly simplified.

A second challenge for the prediction can be found in the micro hardness results, which represent an average value of each batch, so all samples are assigned the same mean hardness. This complicates the identification of structure features that influence the specimens hardness, as individual variations of the micro hardness

(a) Model performance and prediction for batch 1 for PCA and metamodel fitted to results of batch 3, 5, 6 and 8.

(b) Prediction for each batch respectively trained with results of the remaining five batches.
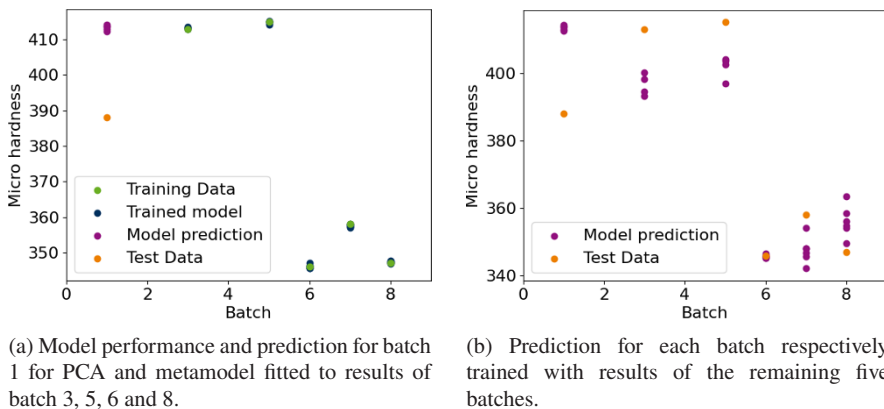
Fig. 7.10: Results of the prediction of micro hardness, based on SEM images of batches with different process parameters.

of a specimen cannot be recognized. Using a mean hardness limits the model to recognising only 'mean' features, that all specimens of one batch have in common. This means, ideally, the data set would contain results which can be directly assigned to the corresponding structure.

7.4 Conclusions

Two experimental-numerical analyses of microstructure-property relationships for AM materials were presented. At the example of the influence of pores on the fatigue behaviour, these relationships are derived by

(a) manufacturing specimen of Ti-6Al-4V,
(b) characterising their microstructure by LM and CT,
(c) computing meaningful structural descriptors based on statistical functions,
(d) conducting CP simulations to compute FIPs and
(e) post processing the results using extreme value distributions.

Although substantial computational and experimental effort is needed, the approach is promising for accessing PSP relationships. A first demonstrative study shows that local phenomena seem to significantly influence the fatigue behaviour. Even simple descriptors like the distribution of the pore ESDs and the shortest distance between pores are potentially influential. Experimental fatigue tests are planned and necessary to validate the findings.

Improving this first implementation of the workflow in terms of microstructure characterization and reconstruction, e.g. by employing the approach by Seibert et al. (2021a) and using a closed design of experiment loop will open up promising possibilities for deriving PSP relationships and accelerating materials innovation. Patterns yielding to fatigue failure could be identified by a more detailed analysis based on more sophisticated descriptors. Deliberately constructing microstructure constellations, like clusters of densely located large pores at triple grain boundaries, could yield an improved understanding of fatigue failure in AM materials. Combining the CP simulations with damage modelling seems another promising approach for improving the framework.

The presented approach for grain structure-property linkage characterisation of LPBF TI-6Al-4V shows a good prediction quality of the micro hardness based on SEM grain microstructure images, even for a limited data set. The presented data processing chain of three-point auto-correlation, PCA of the scaled values and finally LASSO regression can reliably identify significant characteristics and predict micro hardness values with an acceptable accuracy, which can be improved with an extension of the data set.

As Kühne et al. (2021) showed, the micro hardness indirectly correlates to the ductility and fatigue resistance, so this approach can easily be extended to further structure property relationships.

References

Bridier F, McDowell DL, Villechaise P, Mendez J (2009) Crystal plasticity modeling of slip activity in Ti–6Al–4V under high cycle fatigue loading. International Journal of Plasticity 25(6):1066–1082, DOI 10.1016/j.ijplas.2008.08.004

du Plessis A, Sperling P, Beerlink A, Tshabalala L, Hoosain S, Mathe N, le Roux SG (2018) Standard method for microCT-based additive manufacturing quality control 1: Porosity analysis. MethodsX 5:1102–1110, DOI 10.1016/j.mex.2018.09.005

Groeber MA, Jackson MA (2014) DREAM.3D: A Digital Representation Environment for the Analysis of Microstructure in 3D. Integrating Materials and Manufacturing Innovation 3(1):56–72, DOI 10.1186/2193-9772-3-5

Jiao Y, Stillinger FH, Torquato S (2007) Modeling heterogeneous materials via two-point correlation functions: Basic principles. Physical Review E 76:031,110, DOI 10.1103/PhysRevE.76.031110

Kim SJ, Koh K, Lustig M, Boyd S, Gorinevsky D (2007) An interior-point method for large-scale ℓ_1-regularized least squares. IEEE Journal of Selected Topics in Signal Processing 1(4):606–617, DOI 10.1109/JSTSP.2007.910971

Kühne R, Gruber S, Töppel T, Kästner M, Zimmermann M (2021) AMTwin – datengestützte Vorhersage des Ermüdungsverhaltens von additiv hergestelltem Ti-6Al-4V. Tagungsband Werkstoffprüfung 2021

Leuders S, Thöne M, Riemer A, Niendorf T, Tröster T, Richard HA, Maier HJ (2013) On the mechanical behaviour of titanium alloy TiAl6V4 manufactured by selective laser melting: Fatigue resistance and crack growth performance. International Journal of Fatigue 48:300–307, DOI 10.1016/j.ijfatigue.2012.11.011

Liu F, He C, Chen Y, Zhang H, Wang Q, Liu Y (2020) Effects of defects on tensile and fatigue behaviors of selective laser melted titanium alloy in very high cycle regime. International Journal of Fatigue 140:105,795, DOI 10.1016/j.ijfatigue.2020.105795

Maiti T, Eisenlohr P (2018) Fourier-based spectral method solution to finite strain crystal plasticity with free surfaces. Scripta Materialia 145:37–40, DOI 10.1016/j.scriptamat.2017.09.047

Mayeur JR, McDowell DL (2007) A three-dimensional crystal plasticity model for duplex Ti–6Al–4V. International Journal of Plasticity 23(9):1457–1485, DOI 10.1016/j.ijplas.2006.11.006

McDowell DL (2007) Simulation-based strategies for microstructure-sensitive fatigue modeling. Materials Science and Engineering: A 468–470:4–14, DOI 10.1016/j.msea.2006.08.129, The McEvily Symposium: Fatigue and Fracture of Traditional and Advanced Materials, TMS 2006

Murakami Y (1989) Effects of small defects and nonmetallic inclusions on the fatigue strength of metals. JSME international journal Ser 1, Solid mechanics, strength of materials 32(2):167–180, DOI 10.1299/jsmea1988.32.2_167

Muth A, John R, Pilchak A, Kalidindi SR, McDowell DL (2021) Analysis of Fatigue Indicator Parameters for Ti-6Al-4V microstructures using extreme value statistics in the HCF regime. International Journal of Fatigue 145:106,096, DOI 10.1016/j.ijfatigue.2020.106096

Pedregosa F, Varoquaux G, Gramfort A, Michel V, Thirion B, Grisel O, Blondel M, Prettenhofer P, Weiss R, Dubourg V, Vanderplas J, Passos A, Cournapeau D, Brucher M, Perrot M, Duchesnay E (2011) Scikit-learn: Machine learning in Python. Journal of Machine Learning Research 12:2825–2830

Roters F, Diehl M, Shanthraj P, Eisenlohr P, Reuber C, Wong S, Maiti T, Ebrahimi A, Hochrainer T, Fabritius HO, Nikolov S, Friák M, Fujita N, Grilli N, Janssens K, Jia N, Kok P, Ma D, Meier F, Werner E, Stricker M, Weygand D, Raabe D (2019) DAMASK – The Düsseldorf Advanced Material Simulation Kit for modeling multi-physics crystal plasticity, thermal, and damage phenomena from the single crystal up to the component scale. Computational Materials Science 158:420–478, DOI 10.1016/j.commatsci.2018.04.030

Seibert P, Ambati M, Raßloff A, Kästner M (2021a) Reconstructing random heterogeneous media through differentiable optimization. Computational Materials Science 196, DOI 10.1016/j.commatsci.2021.110455

Seibert P, Ambati M, Raßloff A, Kästner M (2021b) Reconstructing random heterogeneous media through differentiable optimization. Computational Materials Science 196:110,455, DOI 10.1016/j.commatsci.2021.110455

ter Haar GM, Becker TH (2021) Low temperature stress relief and martensitic decomposition in selective laser melting produced Ti6Al4V. Material Design & Processing Communications 3(1):e138, DOI 10.1002/mdp2.138

Zambaldi C, Yang Y, Bieler TR, Raabe D (2012) Orientation informed nanoindentation of α-titanium: Indentation pileup in hexagonal metals deforming by prismatic slip. Journal of Materials Research 27(1):356–367, DOI 10.1557/jmr.2011.334

Chapter 8
Multisurface Theory of Plasticity with one Active Surface: Basic Relations, Experimental Validation and Microstructural Motivation

Artem S. Semenov and Boris E. Melnikov

Abstract Constitutive equations, experimental foundation, and comparison with other inelastic models are considered for the multisurface theory of plasticity with one active surface. The proposed variant of multisurface theory is aimed to describe the inelastic deformation processes under the complex passive loading. The conditions of thermodynamic consistency of the theory are obtained. Generalization of the theory for the case of arbitrary shape of surfaces with equal compliances and the anisotropy of elastic properties was carried out. Surfaces of equal compliances for the multilink loading paths and for the complex cyclic loading with total and partial unloading are experimentally studied. Comparison of experimental data and the theory predictions was carried out on the polycrystalline nickel, steel and aluminium alloy specimens under complex non-proportional loading.

Key words: Plasticity, Multisurface theory, Passive loading, Constitutive modeling, Polycrystalline materials, Finite element homogenization, Experiment, Simulation

Artem S. Semenov
Peter the Great St. Petersburg Polytechnic University, Institute of Physics and Mechanics, Polytechnicheskaya, 29, 195251 St. Petersburg, Russian Federation &
Technische Universität Dresden, Institute of Solid Mechanics,
George-Bähr-Str. 3c, 01069 Dresden, Germany,
e-mail: semenov_as@spbstu.ru, asemenov@tu-dresden.de

Boris E. Melnikov
Peter the Great St. Petersburg Polytechnic University, Institute of Physics and Mechanics, Polytechnicheskaya, 29, 195251 St. Petersburg, Russian Federation,
e-mail: melnikovboris@mail.ru

8.1 Introduction

Concept of the multisurface plasticity has become widespread in theoretical and computational inelasticity. There are three different main directions of the multisurface formalism application:

- **Non-smooth yield surfaces.** Formulation of the plastic flow theory with non-smooth (singular) yield surfaces was proposed by Koiter (1953, 1960) and Mandel (1964, 1965). In metal plasticity, the classical Tresca yield criterion is characterized by several smooth yield surfaces (planes) intersecting in a non-smooth fashion. Furthermore, description of the single-crystal plasticity involves a number of yield conditions associated with the slip systems. Such systems might be activated simultaneously. In soil, rock, and concrete plasticity, the Mohr-Coulomb yield criterion, the Cap model, and the Cam-Clay models are examples of using the multisurface approach (Nemat-Nasser, 1983; Desai and Siriwardane, 1984; Chen, 1984).
- **Non-linear hardening under complex cyclic loading.** For description of the non-linear hardening, the multisurface theory was proposed by Mroz (1967); Mroz et al. (1978). There the set of nested yield surfaces were used to provide the piece-wise linear approximation of the stress-strain curve. The similar mathematical description was obtained by Iwan (1967) on the basis of the rheological (structural) model that consists of connection in series of blocks of parallel elastic and perfect plastic elements. The two-surface theories were developed by Krieg (1975); Dafalias and Popov (1976); Petersson and Popov (1977). An important feature of the multisurface approach is the significant dependence of the direction and value of hardening on the previous history and intensive hardening after changing the loading direction. The Mroz-type rule for the yield surface translations provides the correct multiaxial description of nonlinear hardening and preserves the Masing extended behavior (Masing, 1926) that is important for simulation of the cyclic response.
- **Passive loading processes.** For description of the passive loading paths (unloading, neutral loading, and loading inside the classical yield surface), the multisurface theory of plasticity with one active surface of equal plastic compliance was proposed by Izotov and Yagn (1961); Izotov (1963). The active surface translation and expansion rules were introduced empirically on the basis of numerous experimental results for various non-proportional loading paths. The model modifications are proposed in Melnikov et al. (1990); Melnikov and Semenov (1991, 1996b); Izotov et al. (2001). Analysis of the thermodynamic consistency of the multisurface theory of plasticity with one active surface is carried out in Semenov (2003a). The considered model describes the plastic strain accumulation under yield stress and applied to the high-cycle fatigue prediction.

This article deals with the detailed study within the framework of the third direction.

The classical theory of plastic flow with the combined isotropic-kinematic hardening is not sufficiently reliable (Lamba and Sidebottom, 1978) for the description of deformation processes under the loading including partial or complete unload-

ing after sharp breaks of the loading path. Typically, the models of plasticity are aimed to the improved description of the *active* loading. The detailed analysis of the *passive* loading is attempted only occasionally and, mostly, is limited by some assumption of the elastic behavior of material at the unloading.

In the theory of elastic-plastic processes of Ilyushin (1963), in the endochronic theory of plasticity Valanis (1980); Kadashevich and Mosolov (1989) and in the rheological (structural) models (e.g. Palmov, 1998), the plastic strain accumulation (under passive loading) is taken into account. But here, the governing equations and constants are set based on the only active loading mode without taking into account specifics of the processes under passive loading.

The multisurface theory of plasticity with one active surface (Izotov and Yagn, 1961; Melnikov et al., 1990; Melnikov and Semenov, 1996b) provides more precise formulation of the passive loading. Another specific feature of the theory version is the refusal of application of the *yield surface* to evaluation of the plastic deformation. The disadvantage of the yield surface is that its shape, size, and location depend on the off-set of the residual strain. This disadvantage is avoided when the *surfaces of the equal plastic compliance* are applied as it is done in the considered theory. The principle of building the surfaces of equal plastic compliance is shown in **Fig. 8.1**.

Mathematical formulation of the multisurface theory of plasticity (with one active surface under active loading) corresponds to the classical theory of plastic flow. Differences are observed only under passive loading. Under these conditions, special equations for evolution of the active surface are introduced. They are formulated based on the analysis of experimental data using the concept of reversing points of the deformation trajectory initiating appearance of the new active yield surface. Only the active surface changes location and size are considered. The rest of the surfaces remain frozen. However, they store information about the history of deformation in the form of many reversing points. This can affect the further behavior of the material when the active surface reaches the dimensions of the previous surface.
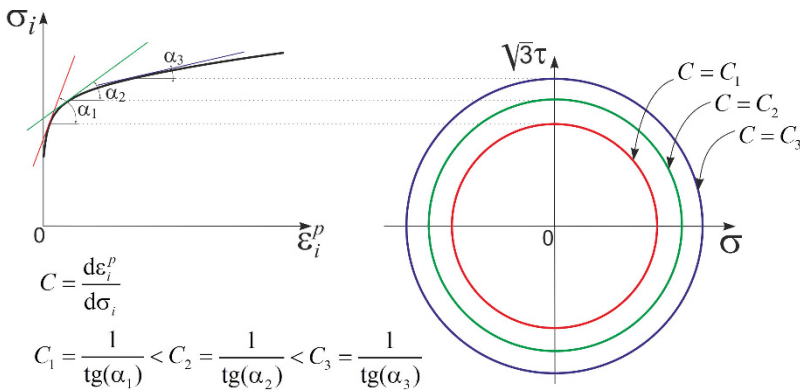
Fig. 8.1: Surfaces of equal plastic compliances.

Representative algorithmic treatments of the multisurface theory are in Sandler and Rubin (1979); Loret and Prevost (1986); Aravas (1987); Simo et al. (1988); Simo and Hughes (1998). Numerical integration of the constitutive equations of the multisurface theory of plasticity with one active surface is considered in Melnikov and Semenov (1996b); Semenov (1996).

Examples of the application of the multisurface theory of plasticity in practice cover a wide range of materials from wood (Mackenzie-Helnwein et al., 2003), paper (Bedzra et al., 2019), concrete (Fan and Yin, 2003), geomaterials (Whyte et al., 2020) to metals (Sawischlewski et al., 1996; Semenov et al., 2007; Shahrooi et al., 2010) and fibre reinforced composites (Bedzra et al., 2017) and allow describing the phenomena of instability (Sawischlewski et al., 1996), strain localization (Sawischlewski et al., 1996), fatigue (Garud, 1981; Shahrooi et al., 2010) and ductile fracture (Keralavarma, 2017).

The multisurface theory with one active surface plays the key role in the multi-model analysis (Melnikov and Semenov, 1995; Semenov and Melnikov, 1998; Melnikov and Semenov, 1996a; Melnikov et al., 2010) of the plastic deformation that is based on using the hierarchical sequence of models adequate to complexity of the problem.

8.2 Conditions of Reversing

Reversing is one of the basic concepts in the theory. The loading paths are assumed to be piece-wise smooth in the space of the stress tensor deviators. The subset of the loading path kinks, after which the following stress development is directed inside the surface of equal compliance, is defined as the reversing points of the loading path ($\boldsymbol{\sigma}_{R_1}$ and $\boldsymbol{\sigma}_{R_2}$ in **Fig. 8.2**).

Condition for initiation of the k-th new reversing point is defined as follows:

$$\frac{\partial f_k(\boldsymbol{\sigma} - \boldsymbol{\sigma}_{O_k})}{\partial \boldsymbol{\sigma}} \cdot \cdot \dot{\boldsymbol{\sigma}} < 0, \tag{8.1}$$

where $\boldsymbol{\sigma}$ is the stress tensor, $\boldsymbol{\sigma}_{O_k}$ is the center of the k-th surface of the equal plastic compliances that characterizes its translation as of a rigid body.
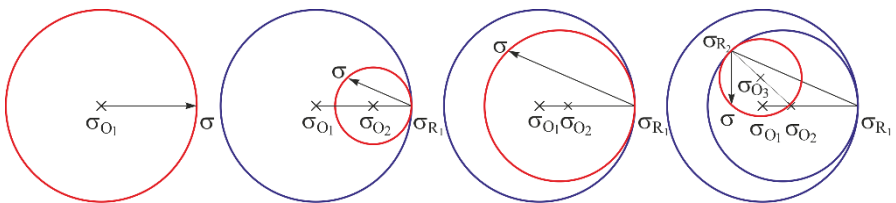
Fig. 8.2: Illustration of the reversing points birth and the evolution of the corresponding surfaces of the equal plastic compliances.

Occurrence of the new k-th reversing point $\boldsymbol{\sigma}_{R_k}$ causes developments of the new $k+1$-st surface

$$F_{k+1}(\boldsymbol{\sigma}_A, \boldsymbol{\sigma}_{R_j}, \boldsymbol{\varepsilon}^P) = f_{k+1}(\boldsymbol{\sigma}_A) - Y_{k+1}(\boldsymbol{\sigma}_{R_j}, \boldsymbol{\varepsilon}^P) = 0, \qquad j = \overline{1, k}, \qquad (8.2)$$

which determines the plastic deformation. The tensor of active stress is defined by the relation

$$\boldsymbol{\sigma}_A = \boldsymbol{\sigma} - \boldsymbol{\sigma}_{O_{k+1}}. \qquad (8.3)$$

In equation (8.2) the $\boldsymbol{\sigma}_{R_j}$ is the stress at the j-th reversing point, $\boldsymbol{\varepsilon}^P$ is the plastic strain tensor. Equation for the center of the k-th surface of the equal plastic compliances $\boldsymbol{\sigma}_{O_k}$ reflects the main feature of the theory under consideration and will be presented in the next section.

The birth condition of the first reversing point according to (8.1) at $k = 1$ coincides with condition for the elastic unloading postulated in the flow theory. However, in the multisurface theory, the reversing causes further plastic strain accumulation.

The family of $k+1$ surfaces occurs after appearance of k reversing points on the loading path. The initial surface F_1 has a non-reversing initiation and its evolution is defined by the stress-strain curve as it is similarly in the flow theory. The active surface (i.e., changing its dimensions and controlling plastic deformation) is the ultimate surface F_{k+1}. Parameters of all preceding surfaces remain unchanged. These surfaces are nested: every preceding surface completely envelops the successive one. So far, the active surface initially has the minimal dimensions, but under loading, it grows up and may become equal to the preceding surface. This issue is classified as the deletion of the conclusive k-th reversing point. The F_k-surface becomes the active one instead of the F_{k+1}-surface. This deletion is defined by coinciding of the $k+1$-th and k-th surfaces

$$f_{k+1}(\boldsymbol{\sigma} - \boldsymbol{\sigma}_{O_{k+1}}) = f_k(\boldsymbol{\sigma}_{R_k} - \boldsymbol{\sigma}_{O_k}). \qquad (8.4)$$

8.3 Constitutive Equations

In the infinitesimal case under the isothermal conditions, the constitutive equations (taking into account the elastic anisotropy and arbitrary shape of the surfaces) are given by the following expressions (Melnikov and Semenov, 1996b):

$$\dot{\boldsymbol{\sigma}} = {}^4\mathbf{D} \cdot\cdot (\dot{\boldsymbol{\varepsilon}} - \dot{\boldsymbol{\varepsilon}}^P) = {}^4\mathbf{D}^{ep} \cdot\cdot \dot{\boldsymbol{\varepsilon}}, \qquad (8.5)$$

$$\dot{\boldsymbol{\varepsilon}}^P = C \frac{\partial f(\boldsymbol{\sigma}_A)}{\partial \boldsymbol{\sigma}} \otimes \frac{\partial f(\boldsymbol{\sigma}_A)}{\partial \boldsymbol{\sigma}} \cdot\cdot \dot{\boldsymbol{\sigma}}, \qquad (8.6)$$

where $\boldsymbol{\varepsilon}$ and $\boldsymbol{\varepsilon}^P$ are the total and plastic strain tensors, the condition $f(\boldsymbol{\sigma}_A) = f_{k+1}(\boldsymbol{\sigma}_A)$ corresponds to the $k+1$-th active surface, C is the modulus of plastic compliance, ${}^4\mathbf{D}$ is the fourth-order tensor of the elastic moduli. This tensor (in the case of isotropic material) is defined by the Young's modulus E and Poisson's ratio ν

$$^4\mathbf{D} = \frac{E\nu}{(1+\nu)(1-2\nu)}\mathbf{1}\otimes\mathbf{1} + \frac{E}{2(1+\nu)}(\mathbf{1}\overline{\otimes}\mathbf{1} + \mathbf{1}\underline{\otimes}\mathbf{1}), \qquad (8.7)$$

where $\mathbf{1}$ is the unit tensor, $(\mathbf{A}\otimes\mathbf{B})_{ijkl} = A_{ij}B_{kl}$ is the direct dyadic product, and $(\mathbf{A}\overline{\otimes}\mathbf{B})_{ijkl} = A_{ik}B_{jl}$, $(\mathbf{A}\underline{\otimes}\mathbf{B})_{ijkl} = A_{il}B_{jk}$ are the indirect dyadic products. In Eqs. (8.5)-(8.6), the symbol $\cdot\cdot$ denotes the double contraction.

The tensor of the elastic-plastic tangent moduli is determined by the expression

$$^4\mathbf{D}^{ep} = {}^4\mathbf{D} - \frac{{}^4\mathbf{D}\cdot\cdot\frac{\partial f(\boldsymbol{\sigma}_A)}{\partial\boldsymbol{\sigma}}\otimes\frac{\partial f(\boldsymbol{\sigma}_A)}{\partial\boldsymbol{\sigma}}\cdot\cdot{}^4\mathbf{D}}{\frac{1}{C} + \frac{\partial f(\boldsymbol{\sigma}_A)}{\partial\boldsymbol{\sigma}}\cdot\cdot{}^4\mathbf{D}\cdot\cdot\frac{\partial f(\boldsymbol{\sigma}_A)}{\partial\boldsymbol{\sigma}}}. \qquad (8.8)$$

The simplest version of approximation of the plastic compliance $C = C_{k+1}$ was proposed in Melnikov et al. (1990) based on the analysis of experimental data:

$$C_{k+1} = C_0\, C_1\left(\frac{Y_{k+1}}{Y_1}\right)^n, \qquad (8.9)$$

where C_1 is the plastic compliance, corresponding to the first (outer) surface that is traditionally determined from the stress-strain curve (under the uniaxial monotonic loading) as $C_1 = \frac{d\varepsilon_i^p}{d\sigma_i}$, C_0 and n are the coefficients, which are determined from the experiment in presence of one reversing point (loading-unloading).

When the surface of equal compliance is assumed as the von-Mises hypersphere

$$f(\boldsymbol{\sigma}_A) = f(\mathbf{s}_A) = \sqrt{\frac{3}{2}\mathbf{s}_A\cdot\cdot\mathbf{s}_A}, \qquad (8.10)$$

where $\mathbf{s}_A = \boldsymbol{\sigma}_A - \frac{1}{3}\mathbf{1}\otimes\mathbf{1}\cdot\cdot\boldsymbol{\sigma}_A$ is the deviator of the active stress tensor $\boldsymbol{\sigma}_A$, then the flow rule (8.6) would become

$$\dot{\boldsymbol{\varepsilon}}^p = \frac{3}{2}C\frac{\mathbf{s}_A\cdot\cdot\dot{\mathbf{s}}}{\mathbf{s}_A\cdot\cdot\mathbf{s}_A}\mathbf{s}_A \qquad (8.11)$$

and the tensor of the tangent moduli (8.8) are simplified to the expression:

$$^4\mathbf{D}^{ep} = {}^4\mathbf{D} - \frac{{}^4\mathbf{D}\cdot\cdot\mathbf{s}_A\otimes\mathbf{s}_A\cdot\cdot{}^4\mathbf{D}}{\frac{\mathbf{s}_A\cdot\cdot\mathbf{s}_A}{3C} + \mathbf{s}_A\cdot\cdot{}^4\mathbf{D}\cdot\cdot\mathbf{s}_A}. \qquad (8.12)$$

If the hypothesis (8.11) is applied, then the process of plastic deformation is completely defined in the five-dimensional space of the stress deviators (**Fig. 8.3**). Therefore, the equations of evolution of the equal compliance surfaces and reversing conditions are defined in this case by the deviatoric components of the tensors $\boldsymbol{\sigma}, \boldsymbol{\sigma}_A, \boldsymbol{\sigma}_{R_k}, \boldsymbol{\sigma}_{O_k}$, denoted, respectively, as $\mathbf{s}, \mathbf{s}_A, \mathbf{s}_{R_k}, \mathbf{s}_{O_k}$.

To define the motion of the center of the active surface $\mathbf{s}_{O_{k+1}}$, the visual-geometric representations are used that are obtained as a result of generalization of experimental data (Melnikov et al., 1990). It is postulated that the active $k+1$-th surface passes through two characteristic points: the current stress state $\mathbf{s} = \mathbf{s}_{R_{k+1}}$

Fig. 8.3 Active ($F_{k+1} = 0$) and passive ($F_k = 0$) surfaces of the equal plastic compliances.
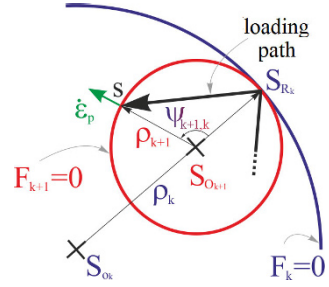
and the last reversing point $\mathbf{s}_{R_k}$ (see, also, **Fig. 8.3**), and the surface center $\mathbf{s}_{O_{k+1}}$ lies on the straight line connecting the center of the preceding k-th surface $\mathbf{s}_{O_k}$ and the reversing point $\mathbf{s}_{R_k}$

$$\mathbf{s}_{O_{k+1}} = \mathbf{s}_{O_k} + a_k(\mathbf{s}_{R_k} - \mathbf{s}_{O_k}), \tag{8.13}$$

where the scalar parameter $a_k \in [0,1]$ is defined by the relation:

$$a_k = \frac{(\mathbf{s}_{R_{k+1}} + \mathbf{s}_{R_k} - 2\mathbf{s}_{O_k}) \cdot \cdot (\mathbf{s}_{R_{k+1}} - \mathbf{s}_{R_k})}{2(\mathbf{s}_{R_k} - \mathbf{s}_{O_k}) \cdot \cdot (\mathbf{s}_{R_{k+1}} - \mathbf{s}_{R_k})}. \tag{8.14}$$

For the von Mises hypersphere surface equation (8.2) is simplified to

$$F_{k+1} = \sqrt{\frac{2}{3}\mathbf{s}_{A_{k+1}} \cdot \cdot \mathbf{s}_{A_{k+1}}} - Y_{k+1} = 0, \qquad Y_{k+1} = \sqrt{\frac{2}{3}}\rho_{k+1}. \tag{8.15}$$

The radius of the k-th passive surface is given by the formula

$$\rho_k = \sqrt{\mathbf{s}_{P_k} \cdot \cdot \mathbf{s}_{P_k}} = \sqrt{(\mathbf{s}_{R_k} - \mathbf{s}_{O_k}) \cdot \cdot (\mathbf{s}_{R_k} - \mathbf{s}_{O_k})}. \tag{8.16}$$

The radius of the k + 1-th active surface is defined by the similar expression

$$\rho_{k+1} = \sqrt{\mathbf{s}_{A_{k+1}} \cdot \cdot \mathbf{s}_{A_{k+1}}} = \sqrt{(\mathbf{s} - \mathbf{s}_{O_{k+1}}) \cdot \cdot (\mathbf{s} - \mathbf{s}_{O_{k+1}})}. \tag{8.17}$$

The nesting condition requires the fulfillment of the inequalities

$$0 < \rho_{k+1} < \rho_k < \ldots < \rho_2 < \rho_1. \tag{8.18}$$

Using the introduced notations, it can be shown that the parameter a_k (8.14) is linearly related with the radius of the active surface ρ_{k+1}

$$a_k = 1 - \frac{\rho_{k+1}}{\rho_k} \tag{8.19}$$

and, as a result of (8.13), we get the relation

$$\mathbf{s}_{O_{k+1}} = \sum_{j=1}^{k} \frac{\rho_{k+1}}{\rho_{j+1}} \left(1 - \frac{\rho_{j+1}}{\rho_j}\right) \mathbf{s}_{R_j}. \tag{8.20}$$

It was shown (Semenov, 2003a), that the multisurface theory with one active surface satisfies to the thermodynamic constraints in a form of the dissipative inequality

$$\boldsymbol{\sigma} \cdot \cdot \dot{\boldsymbol{\varepsilon}} - \rho \dot{\psi} \geqslant 0 \tag{8.21}$$

if the plastic compliance is approximated as

$$C_{k+1} = \begin{cases} C_1 \left(\dfrac{\rho_{k+1}}{\rho_1}\right)^n & \text{if } \rho_{k+1}^{**} \leqslant \rho_k \\[3mm] C_1 \dfrac{\rho_k - \rho_{k+1}}{\rho_1} \left(\dfrac{\rho_{k+1}}{\rho_1}\right)^n & \text{if } \rho_{k+1}^{**} > \rho_k \end{cases}, \tag{8.22}$$

where

$$\rho_{k+1}^{**} = -\frac{1}{1 - \cos(\psi_{k+1,k})}\left[\rho_k \cos(\psi_{k+1,k}) + \sum_{j=1}^{k-1}(\rho_j - \rho_{j+1})\cos(\psi_{k+1,j})\right].$$

8.4 Experimental Analysis

The program of experimental studies includes the complex loading tests of the thin wall tubular steel specimens (tension, internal, and external pressure) and the tubular pure nickel specimens (tension and torsion).

8.4.1 Test Results for Nickel Specimens

Specimen particulars are: the thin wall tubular of outer diameter 8.1 mm, the wall thickness 0.19 mm (not less than 6-7 grains), the gage length 150 mm. The material is a pure nickel (impurities: Si - 0.068%; Fe - 0.025%; Cu - 0.02%). The tolerance on the tube cylindricity does not prevail ± 0.01 mm ($\pm 0.1\%$); the maximum deviation of the cross-section area in the same specimen was achieved about ± 0.03 mm^2 ($\pm 0.7\%$). The specimens were annealed at $860°$C and cooled in the furnace.

Initially, the shape of surfaces of the equal plastic compliance was determined for various types of primary loading. Uniaxial tension, torsion, and combined loading: the tension together with torsion were applied. The maximum stress level achieved in the tests was characterized by σ_0 and τ_0. For all the cases of the primary loading, a nearly circular (the von Mises criterion) shape of the loading surface was observed (**Fig. 8.4**).

Fig. 8.4 Geometric locations of the equal plastic compliance surfaces for various primary loading programs (tension, torsion, and combined tension/torsion $\sigma = \sqrt{3}\tau$) of the tubular nickel specimens.
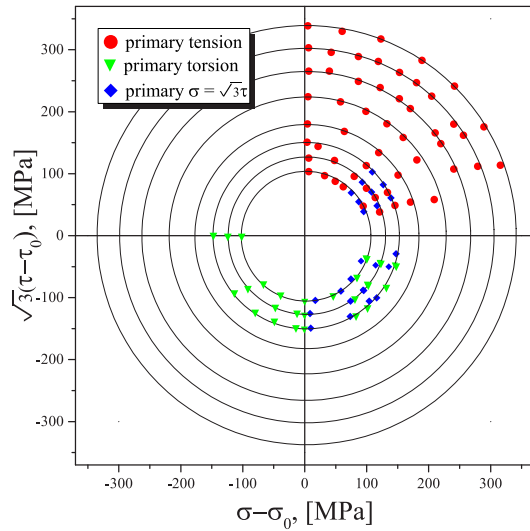
Geometric places of the equal $\delta\varepsilon_i^p$ (0.006%; 0.012%; 0.018%; 0.036%) and of the equal C (10^{-11}; $2\cdot10^{-11}$; $3\cdot10^{-11}$; $5\cdot10^{-10}$; 10^{-9} Pa^{-1}) deviate not more than 5% from the corresponding circles.

In **Fig. 8.5** the geometric places of the equal $\delta\varepsilon_i^p$ are shown (the curve 1 - 0.006%, 2 - 0.012%, 3 - 0.018%, 4 - 0.036%) under the primary loading by the tensile force up to $\sigma_0 = 148$ MPa.
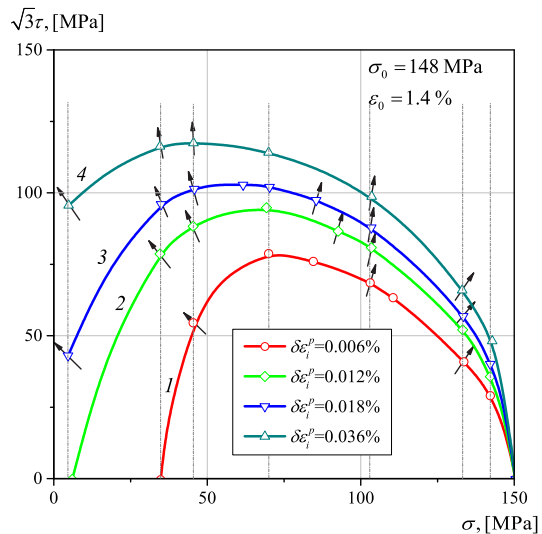
Fig. 8.5 Geometric locations of the equal plastic strain increment $\delta\varepsilon_i^p$ surfaces (the curve 1 - 0.006%, 2 - 0.012%, 3 - 0.018%, 4 - 0.036%) under the primary tension of the tubular nickel specimens. The secondary loading paths are shown with the thin dash-dot lines.

Directions of the secondary loading are shown by the dash-dotted lines. The arrows, for a number of the secondary loading paths, show the directions of the $\boldsymbol{\varepsilon}^{\mathrm{p}}$. Deviations of the $\boldsymbol{\varepsilon}^{\mathrm{p}}$ from the normals increase as the distance increases from the end point of the primary loading. In average, these deviations were $5°$. The practical use of the geometric places $\delta\varepsilon_i^{\mathrm{p}}$ (determining the direction of the vectors $\boldsymbol{\varepsilon}^{\mathrm{p}}$) is difficult, since the shapes of these surfaces change significantly depending on the value $\delta\varepsilon_i^{\mathrm{p}}$.

Next tests were carried out for five variants of the non-proportional primary loadings with maximal von Mises stress intensities of 100 MPa, 150 MPa, 250 MPa and 300 MPa, which were achieved in different ways as shown in **Fig. 8.6**. In tests, both with primary and secondary loading, the axial force and torque were simultaneously changed.

Geometric locations of the equal plastic compliance surfaces for various primary loading programs of the tubular nickel specimens are shown in **Fig. 8.7** for the primary tension and in **Fig. 8.8** for the primary torsion.

In all the cases studied, the deformation anisotropy manifested itself at the plastic strain of about 0.2% and did not disappear at the large values. Geometric places of the equal C were approximated by circles, the positions of the centers and radii of which were found by the method of the least squares. In this case, the deviation did not exceed 2–3% of the radius and was of the same order as the scatter due to the inhomogeneity of the samples.

In the case of the secondary loads that do not go beyond the the Mises circle (corresponding to the last point of the primary loading), the field equal C in the first approximation is uniquely determined only by the history of the primary loading. In the range of $10^{-11}\,\mathrm{Pa}^{-1} \leqslant C \leqslant 10^{-10}\,\mathrm{Pa}^{-1}$, the geometric places of the equal C are very close to the circles. Their centers are offset from the origin. The direction of the center displacement vector is approximately determined by the ratio of components of the primary plastic deformation, and the modulus of this vector depends only on the value of C for the given circle and does not depend on the loading history.
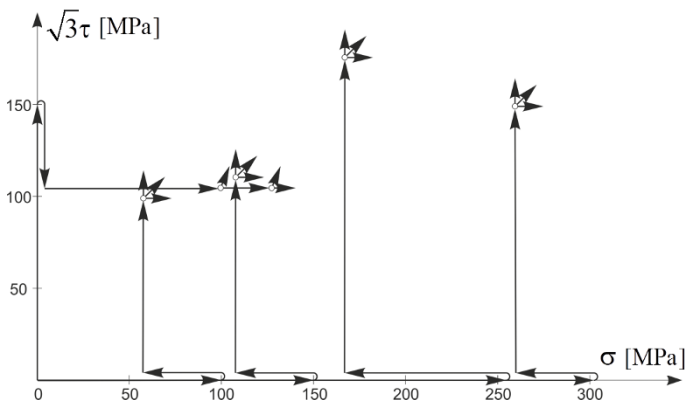
Fig. 8.6: Loading paths for the nickel specimens.
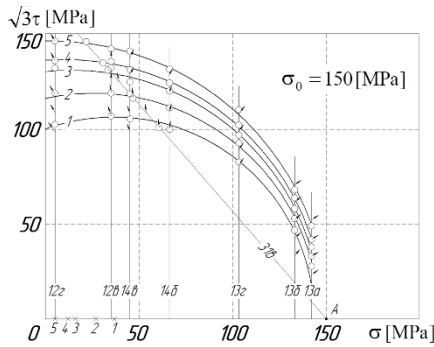
Fig. 8.7: Geometric locations of the equal plastic compliance surfaces for the primary tension.

$C_1 = 1 \cdot 10^{-11}\,\mathrm{Pa}^{-1}$
$C_2 = 2 \cdot 10^{-11}\,\mathrm{Pa}^{-1}$
$C_3 = 3 \cdot 10^{-11}\,\mathrm{Pa}^{-1}$
$C_4 = 5 \cdot 10^{-11}\,\mathrm{Pa}^{-1}$
$C_5 = 10 \cdot 10^{-11}\,\mathrm{Pa}^{-1}$
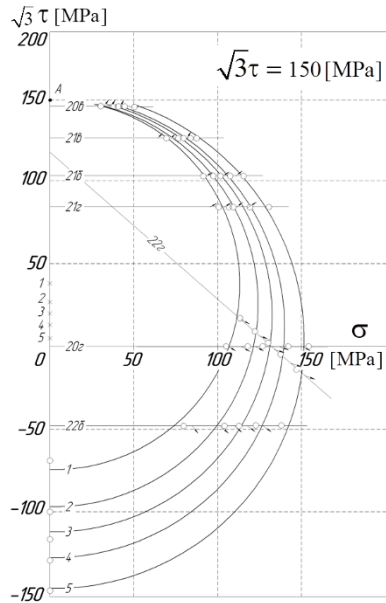
Fig. 8.8: Geometric locations of the equal plastic compliance surfaces for the primary torsion.

The radii of the circles do not depend on the primary loading path and are determined only by the corresponding value of C and the maximum stress intensity. For $C \leqslant 10^{-11}\ \mathrm{Pa}^{-1}$, the geometric places of the equal C can be approximately considered as the circles passing through the last point of the primary loading path. The centers of these circles are located on the same straight line as the centers of the circles corresponding to large values of the C.

The stress-strain curve for nickel (determined in experiments and used in further calculations) is shown in **Fig. 8.9**. The value of the Young's modulus is $E = 207$ GPa.
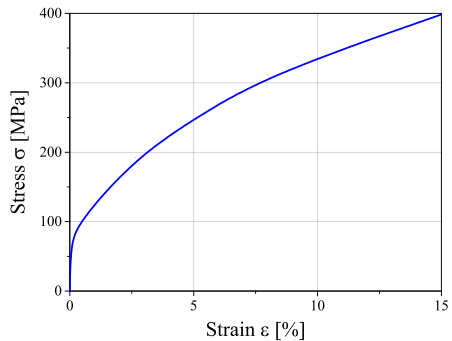
Fig. 8.9 Stress-strain curve for the nickel.

Comparison of various models predictions with the experimental data for nickel specimens (under the complex loading path) are discussed below for two variants of the loading program including the unloading and passive loading. Under the passive loading, the most intense accumulation of the plastic strains occurs near the outer surface on the paths making small angles with tangents to the loading surface. The "sawtooth" path of the non-proportional secondary loading (after the primary tension to $\sigma = 306$ MPa) are shown in **Fig. 8.10**. It passed near the von Mises circle corresponding to the end of the primary loading.

The material response to the "sawtooth" loading (**Fig. 8.10**) in the form of a strain path and measured in the experiment on the nickel specimen Izotov (1963), is shown in **Fig. 8.11** with the black solid line. The prediction of the multisurface theory with one active surface is shown by the red dashed line. The result of the plastic flow
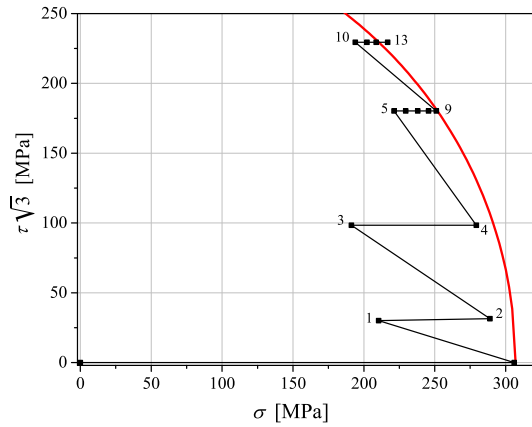
Fig. 8.10 "Sawtooth" loading path near to the yield surface given in the experiment on the nickel specimen.
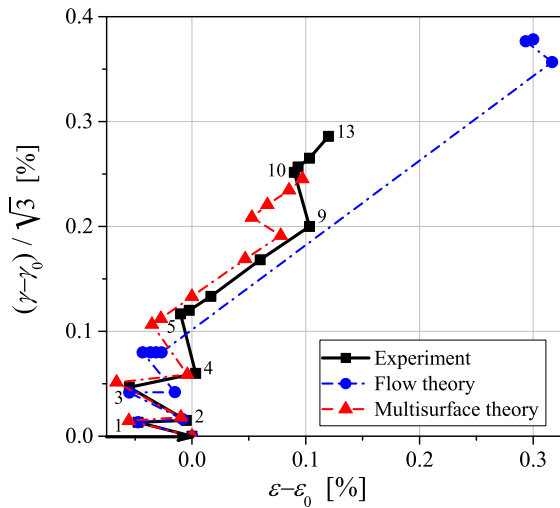
Fig. 8.11 Comparison of the simulation results (the plastic flow theory with the kinematic hardening and the multisurface theory with one active surface) with the experimental data (Izotov, 1963) for the "sawtooth" loading path performed in the experiment on the nickel specimen (see **Fig. 8.10**).

theory with the kinematic hardening and the von Mises yield criterion is shown by the blue dash-dotted line.

Experimental data illustrate the phenomenon of the plastic strain accumulation under the passive loading. The prediction of the multisurface theory demonstrates more accurate prediction in comparison with the plastic flow theory. It is since the latter does not take into account the plasticity under the passive loading.

The "five-link" loading path (including the passive loading sections) is shown in **Fig. 8.12** as the solid black line.

It includes the primary (proportional) loading and the secondary (the non-proportional) loading with an alternate change in the tensile force and torque. The loading path in the stress space $\sigma - \tau$ has the breaks of 90°.

Fig. 8.12 "Five-link" loading path including the passive loading sections given in the experiment on the nickel specimen.

Fig. 8.13 Comparison of simulation results (plastic flow theory with kinematic hardening and multisurface theory with one active surface) with experimental data (Izotov, 1963) for the "five-link" loading path (performed in the experiment on the nickel specimen) is shown in **Fig. 8.12**.

The material response to "five-link" loading (**Fig. 8.12**) in the form of the strain path measured in the experiment on the nickel specimen is shown in **Fig. 8.13** with the black solid line. The prediction of the multisurface theory with one active surface is shown by the red dashed line. The result of the plastic flow theory with the kinematic hardening and the von Mises yield criterion is shown by the blue dash-dotted line.

Comparative analysis of two theories predictions has shown the significant advantage of the multisurface theory over the theory of flow when describing the complex passive loading. The deviation from the experimental data for strains for the multisurface theory does not exceed 0.009% according to the plastic flow theory: 0.09% for ε and 0.22% for γ; that is they are by the order of magnitude about (see **Fig. 8.13**).

Also, in **Fig. 8.12**, the calculated loading paths for the flow theory (blue dash-dotted line) and the multisurface theory (red dashed line) are shown; they correspond to the experimentally observed secondary deformation path (see black solid line in **Fig. 8.13**). The largest deviation from the experimental loading path is 10.8 MPa for the multisurface theory and 33.3 MPa for the flow theory.

8.4.2 Test Results for Steel Specimens

The experiments were carried out for the Cr-Ni-Ti steel specimens under the complex multiaxial loading. The specimens sizes are: the length 170 mm; the nominal outer diameter 26.4 mm; the wall thickness of 0.3 mm; the ratio of the wall thickness of the sample to its average diameter is of 0.011. This ratio corresponds to the recommended values and provides a good uniformity in the distribution of the circumferential and radial stresses along the thickness of the wall. This makes it possible to calculate the stresses in the middle layer by the formulae for membrane shells. The chemical composition of the Cr-Ni-Ti steel (1H18N10T) is: C - 0.1%; Mn - 2%; Cr - 19%; Mo - 0.3% Ni - 11%; Cu - 0.4%.

Computation of the material response under the complex loading program has been performed using three theories:

- the plastic flow theory with kinematic hardening (stress-strain curve is shown in **Fig. 8.14** and approximated by the relation $\sigma_i = 325 + 1470\, \varepsilon_i^{0.678}$ [MPa]);
- the multisurface theory with one active surface ($C_0 = 1.6$, $n = 25.3$);
- the rheological (structural) model including 7 elements Izotov et al. (2001) (see **Fig. 8.15**) ($Y_2 = 325$ MPa, $Y_5 = 711$ MPa, $Y_7 = 770$ MPa).

The experiments were carried out in the high-pressure chamber with sample subjected to repetitive loading and unloading along the straight radial paths in the stress space. The typical non-proportional loading path is shown in **Fig. 8.16**. The experimental data (Kuznetsov, 2000; Kuznetsov et al., 2017) and results of the calculations by different theories are compared in **Fig. 8.17** for the loading path shown in
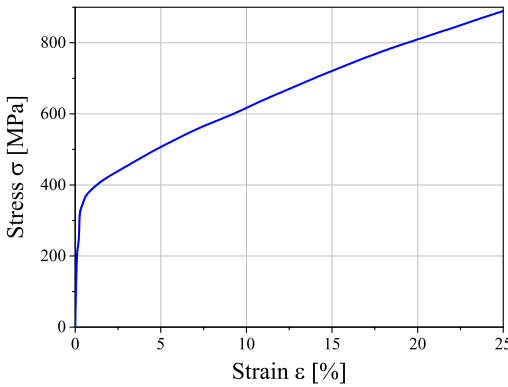
Fig. 8.14: Stress-strain curve for the Cr-Ni-Ti steel.
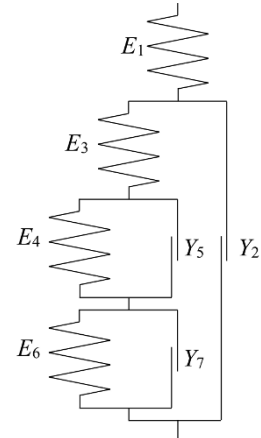
Fig. 8.15: Structural model used in computations.

Fig. 8.16. Comparison results indicate the best accuracy of the multisurface theory with one active surface.

The results of calculations by means of the plastic flow theory with the kinematic hardening indicate inadequate (unsatisfactory) describing the process of the complex non-proportional loading with the unloadings and passive loading paths. The multisurface plasticity theory with one active surface and the rheological (structural) model are in general better describe the process of the complex non-proportional loading. The predictive calculations for both models gave the satisfactory agreement with the experimental data.

No significant dependence of the parameters of the multisurface theory on the loading level has been discovered both in the reference test and for arbitrary loading paths. The theory adequately describes the complex cyclic loading with the stress intensities both above and below the stress intensity, at which the model parameters were determined. Additional adjustment of the parameters was not required.

The Odqvist's parameter has reached the following levels after loading:

- the experimental value 0.340;
- by the multisurface theory 0.345;
- by the rheological (structural) model (see **Fig. 8.15**) 0.551;
- by the plastic flow theory with the kinematic hardening < 0.020.

The comparison of simulation results with experimental data on the steel specimen for the "four-link" cyclic loading path including the passive loading sections is analyzed in details in Kuznetsov et al. (2017).

The results obtained confirm the advantage of the multisurface theory with one active surface in describing the material behavior under the complex non-proportional loading paths with the intermediate unloading.
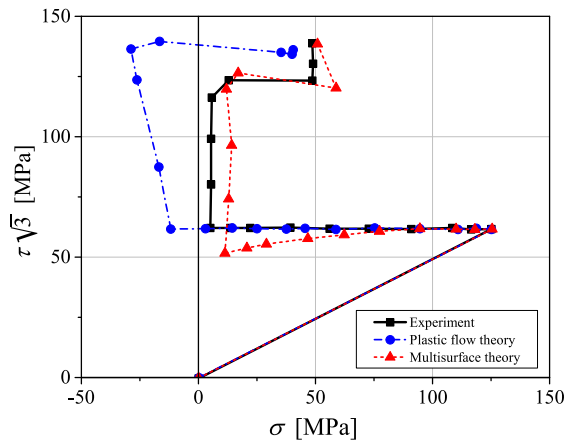
Fig. 8.16 "Five-link" cyclic
loading path including the
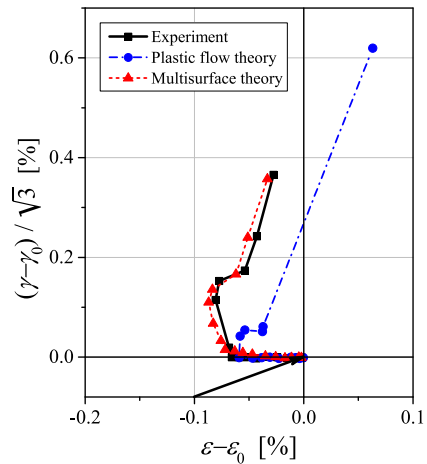passive loading sections given
in the experiment on the steel
specimen.
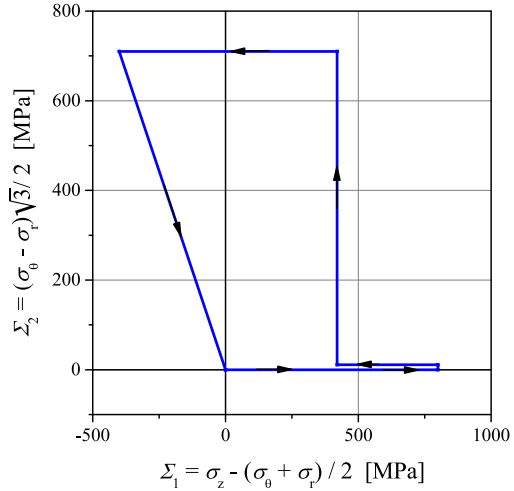
Fig. 8.17 Comparison of
simulation results (plastic
flow theory with the kine-
matic hardening, multisurface
theory with one active sur-
face, and rheological (struc-
tural) model (see **Fig. 8.15**)
with the experimental data
(Kuznetsov, 2000) for the
"five-link" loading path ob-
tained in the experiment
on the steel specimen (see
Fig. 8.16).
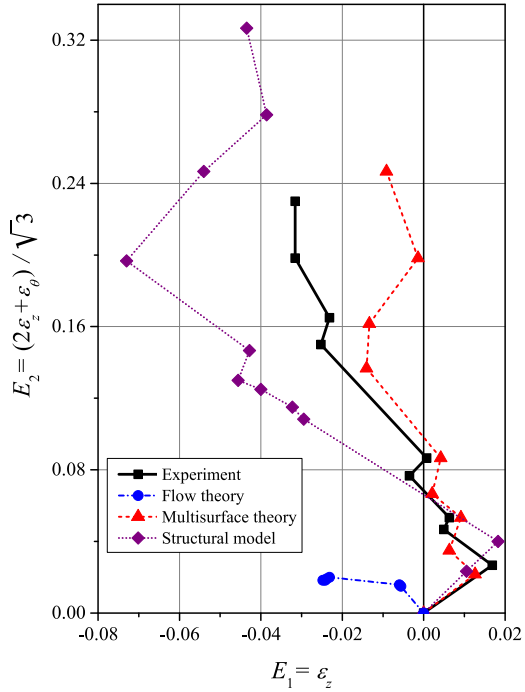
The check of the uniform curve hypothesis consistency (the invariance of the
stress-strain curve and the robustness of approximation of the modulus C) was car-
ried out for the multisurface theory and one possessing the specified properties.

Fig. 8.18 Experimental verification of the plastic compliance approximation (8.9) for the steel specimens.
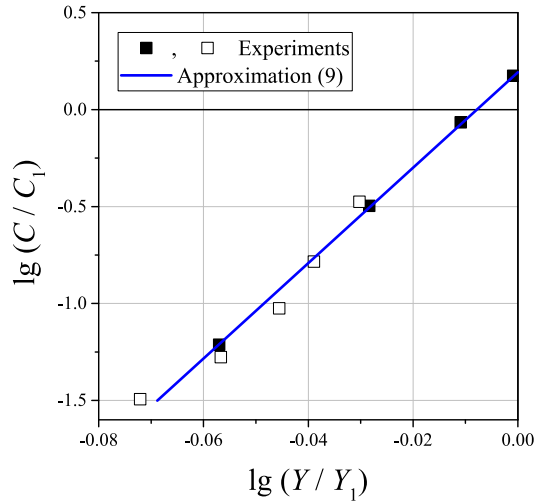
The results of experimental verification of the power-law approximation (8.9) for the plastic compliance C as a function of the radius of the active surface Y under non-proportional loading path for different levels of initial loading are shown in **Fig. 8.18**. There is a good agreement between the results of the approximation (8.9) with parameters $C_0 = 1.6$, $n = 25.3$ and the experimental data.

8.5 Comparison of the Multisurface Model and the Microstructural Model Predictions

The plastic strain accumulation under passive loading is a consequence of the microheterogeneity of the mechanical properties of the polycrystalline material, the presence of microstresses and microplastic strain in individual grains. Therefore, the comparison of the behavior of the multisurface theory with one active surface with the results of the micromechanical (microstructural, physical, crystallographic, multislip) model is of interest for a better understanding of the reasons for the origin of plastic deformations under passive loading and the possibility of describing it using the formalism of the multisurface theory.

Description of the passive loading processes of the polycrystal is carried out by direct mathematical modeling of the spatially inhomogeneous processes of the inelastic deformation of a *representative volume element* (RVE). The response of the polycrystalline material is obtained by means of the finite element *homogenization* of the representative volume, consisting of a set of randomly oriented individual single crystals. Behavior of each crystal is described by a micromechanical model taking in account the real deformation mechanisms on the micro- and meso-levels.

Within the framework of the micromechanical models of the material (Cailletaud, 1992; Asaro, 1983; Raabe et al., 2001; Besson et al., 2009; Trusov et al., 2013; Trusov and Shveikin, 2019; Staroselsky and Martin, 2015; Semenov, 2014), it is assumed that the plastic flow occurs as a result of the possible slip in the N slip systems characterized by the normal $\mathbf{n}^\alpha$ to the α slip plane; the slip direction $\mathbf{l}^\alpha$ ($\alpha = 1, ..., N$). For the considered case of single crystals with the face-centered cubic lattice, with taking into account only the octahedral slip systems (for example, $\{111\}\langle 011\rangle$ for the nickel) $N = 12$. In the case of joint activation of the octahedral and cubic slip systems (for example, $\{111\}\langle 011\rangle$ and $\{001\}\langle 011\rangle$ for nickel) $N = 18$.

The rate of plastic strain in the case of the isothermal infinitesimal approximation is determined by the equation:

$$\dot{\boldsymbol{\varepsilon}}^{\mathrm{P}} = \sum_{\alpha=1}^{N} \dot{\gamma}^\alpha \left(\mathbf{l}^\alpha \otimes \mathbf{n}^\alpha\right)^{\mathrm{S}}, \tag{8.23}$$

where the symmetrization operator is defined by

$$\left(\mathbf{l}^\alpha \otimes \mathbf{n}^\alpha\right)^{\mathrm{S}} = \frac{1}{2}\left(\mathbf{l}^\alpha \otimes \mathbf{n}^\alpha + \mathbf{n}^\alpha \otimes \mathbf{l}^\alpha\right).$$

For calculation of the rate of the shear strain $\dot{\gamma}^\alpha$ in the case of the rate independent material behavior, the following expression is used:

$$\dot{\gamma}^\alpha = \sum_{\beta=1}^{N} \left[\frac{\partial R^\beta}{\partial \gamma^\alpha} + \frac{\partial X^\beta}{\partial \gamma^\alpha}\, \mathrm{sign}\left(\tau^\beta - X^\beta\right)\right]^{-1} \mathrm{sign}\left(\tau^\beta - X^\beta\right)\dot{\tau}^\beta, \tag{8.24}$$

where $\tau^\beta = \boldsymbol{\sigma} \cdot\cdot \left(\mathbf{l}^\beta \otimes \mathbf{n}^\beta\right)^{\mathrm{S}}$ is the shear stresses in β slip system, R^β and X^β are the internal variables characterizing the isotropic and kinematic hardening. Only the active slip systems are taken into account when summing over β in (8.24); that is, satisfying the plasticity condition:

$$|\tau^\beta - X^\beta| - R^\beta - \tau_0 = 0. \tag{8.25}$$

The variables characterizing the nonlinear isotropic and kinematic hardening are determined by the equations:

$$R^\beta = bQ \sum_{\beta=1}^{N} h^{\beta\alpha} r^\alpha \quad \text{with} \quad \dot{r}^\alpha = (1 - br^\alpha)\dot{\gamma}^\alpha, \tag{8.26}$$

and
$$X^\beta = Cx^\beta \quad \text{with} \quad \dot{x}^\beta = \left[\mathrm{sign}\left(\tau^\beta - X^\beta\right) - Dx^\beta\right]\dot{\gamma}^\beta. \tag{8.27}$$

In Eqs. (8.25)-(8.27) τ_0, b, Q, C and D are material constants, the symmetric matrix $h^{\alpha\beta} = \left[q + (1-q)\delta_{\alpha\beta}\right]$ defines the latent hardening, $\delta_{\alpha\beta}$ is the Kronecker symbol, $\alpha \in [1, N]$, $\beta \in [1, N]$.

In computations of the stress-strain state of the polycrystalline nickel RVE, the following values of the parameters of the single-crystal material were used $\tau_0 = 50.2$ MPa, $Q = 36.9$ MPa, $b = 51.4$, $q = 0.7$, $C = 3921$ MPa, $D = 796$ (Murtazin et al., 2021). The RVE of the polycrystalline material has the cubic form with the regular subdivision into the finite elements. Each three dimensional finite element contains eight Gauss points of integration, each of which considered as a single crystal. The random orientation of each crystal (defined by 3 Euler's angles) is generated under assumption of the texture absence. The finite element mesh with $8 \times 8 \times 8$ subdivisions (4096 crystallites) is used in the computations. The homogenization procedure was carried out numerically using the finite element program PANTOCRATOR (Semenov, 2003b) where the microstructural model was implemented. Averaging the volume of the strain and stress tensors is performed as

$$\bar{\varepsilon} = \int_{V_{RVE}} \varepsilon \, dV, \qquad \bar{\sigma} = \int_{V_{RVE}} \sigma \, dV, \qquad \bar{\varepsilon}^P = \int_{V_{RVE}} \varepsilon^P \, dV \qquad (8.28)$$

and is used in the homogenization procedure.

The complex non-proportional "five-link" loading path (**Fig. 8.12**) including the passive loading sections is considered for RVE of the polycrystalline nickel. Examples of the axial and tangential stress field distributions at the last time point are shown in **Fig. 8.19**.

Comparison of predictions of the micromechanical model and the multisurface theory with one active surface (in the case of the "five-link" complex passive loading, **Fig. 8.12**) demonstrates closeness of the results of the material response in the strain space (**Fig. 8.20**). The microstructural model, as well as the multisurface theory, predicts intense accumulation of plastic deformations at the stage of the passive loading, while the theory of plastic flow demonstrates the significantly different result. Prediction of the flow theory in the last section of loading (see **Fig. 8.12**) shows the intensive growth of plastic strains due to the release of stresses beyond the limits of the primary loading yield surface that is not confirmed by the experimental data.
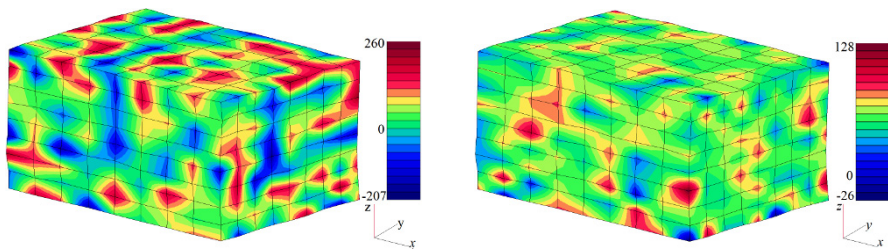
Fig. 8.19: The axial σ_x [MPa] (left) and tangential τ_{xy} [MPa] (right) stress field distribution in RVE of the polycrystalline nickel after the "five-link" loading (see **Fig. 8.12**). Displacements are scaled in 30 times for clarity.

Fig. 8.20 Comparison of
simulation results of the
microstructural model with
the plastic flow theory (with
the kinematic hardening)
and the multisurface theory
(with one active surface)
with the experimental data
(Izotov, 1963) for the "five-
link" loading path found in
the experiment on the nickel
specimen (see **Fig. 8.12**).
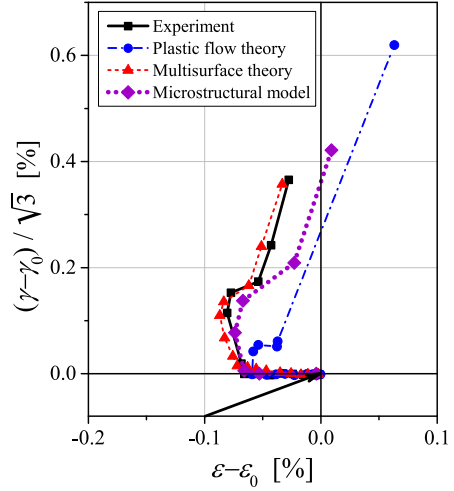
8.6 Numerical Implementation of the Constitutive Equations of the Multisurface Theory with one Active Surface

It is important to note that the equation for the center of the active surface (8.13)
is not differential, but algebraic one, and, therefore, does not require incremental
integration methods. In this model, influence of the loading history is taken into
account not continuously, but discretely, by storing the information only at the re-
versing points.

In presence of k reversing points on the loading path $2k+3$, the following situa-
tions are possible at the current loading step:

- there are no birth and deletion of reversing points;
- a birth of the new $k+1$-th reversing point can happen;
- there can appear k cases of simultaneous deletions from one to k reversing points;
- there can appear $k+1$ cases of the birth of the $k+1$-th reversing point after
  preceding deletion from one to $k+1$ reversing points.

The loading step is subdivided into the sub-steps with the aim to take into account
the mentioned peculiarities. The points of intersection of the stress path with the
deletable surfaces are defined by the equation

$$\mathbf{s}_{l+1}^{i} = \mathbf{s}_{l} + \alpha^{i}(\mathbf{s}_{l+1} - \mathbf{s}_{l}) \tag{8.29}$$

with

$$\alpha^{i} = -\frac{(\mathbf{s}_{l} - \mathbf{s}_{O_{k+1-i}}) \cdot \cdot \Delta\mathbf{s}}{\Delta\mathbf{s} \cdot \cdot \Delta\mathbf{s}} + \sqrt{\left[\frac{(\mathbf{s}_{l} - \mathbf{s}_{O_{k+1-i}}) \cdot \cdot \Delta\mathbf{s}}{\Delta\mathbf{s} \cdot \cdot \Delta\mathbf{s}}\right]^{2} + \frac{\rho_{R_{k+1-i}}^{2} - \rho_{l}^{2}}{\Delta\mathbf{s} \cdot \cdot \Delta\mathbf{s}}}, \tag{8.30}$$
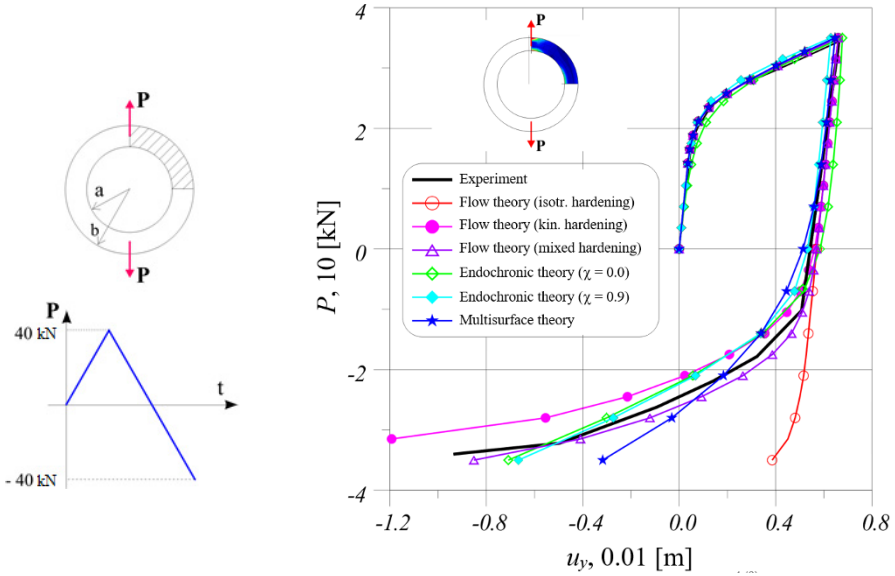
Fig. 8.21: Comparison of the FE analysis results for the aluminium ring under the uniaxial tension/compression with the experimental data (Axelsson and Samuelsson, 1979).

where

$$\rho_{R_{k+1-i}} = \sqrt{\left(\mathbf{s}_{R_{k+1-i}} - \mathbf{s}_{O_{k+1-i}}\right) \cdot \cdot \left(\mathbf{s}_{R_{k+1-i}} - \mathbf{s}_{O_{k+1-i}}\right)}, \qquad (8.31)$$

$$\rho_{l} = \sqrt{\left(\mathbf{s}_{l} - \mathbf{s}_{O_{k+1-i}}\right) \cdot \cdot \left(\mathbf{s}_{l} - \mathbf{s}_{O_{k+1-i}}\right)}. \qquad (8.32)$$

8.7 Finite-element Simulations

The constitutive equations (8.5)-(8.14) represent the quasilinear differential-algebraic equations and admit to obtain exactly the tangent moduli and the algorithmically consistent tangent moduli (Semenov, 2008). This allows one to use of the effective methods (e.g., the Newton-Raphson method) for the solution of nonlinear finite element (FE) equations (Semenov, 2008). The constitutive equations of the multisurface theory have been implemented in the FE program PANTOCRATOR (Semenov, 2003b), and solutions of the non-linear boundary value problems have been obtained (see **Figs. 8.21** and **8.22**).

The uniaxial tension-compression of the circular aluminium ring is considered. The problem formulation corresponds (Axelsson and Samuelsson, 1979). There the experimental data and results (of the finite element simulation with help of the flow theory) are presented. Geometric parameters of the model are $a = 0.635$ m and $b = 0.890$ m. Elastic-plastic characteristics of the aluminium alloy are $E = 87.6$ GPa,
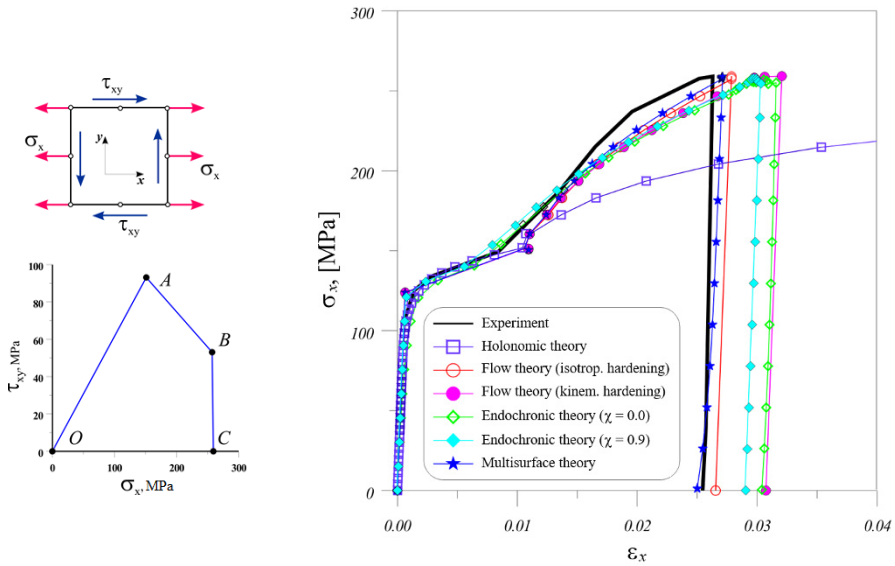
Fig. 8.22: Comparison of the FE analysis results for the steel tube (under the combined tension and torsion) with the experimental data (Szabo, 1984).

$\nu = 0.324$, $Y_0 = 192.5$ MPa, $H = 1/C = 3220$ MPa. The problem was solved under the assumption of the plane stress state.

Comparison of simulation results (obtained on the basis of various plasticity models) with the experimentally measured force-displacement curve is shown in **Fig. 8.21**. At the initial stage of the loading (tension), the predictions of all the practical theories under consideration coincide. Significant difference between the results is observed under the unloading and reverse loading (compression). The extreme estimates (upper and lower bounds) are observed for the kinematic and isotropic hardening of the flow theory. Simulation using the theory of plastic flow with the mixed hardening (the parameter of the mixed hardening is equal to 0.2) shows the most accurate approximation. The multisurface theory with one active surface demonstrates satisfactory results.

In the second test, the stress-strain state was investigated of the thin-walled pipe under the complex non-proportional loading induced by the combined action of the tensile force and torque. The finite element model and loading conditions are shown in **Fig. 8.22**. The four-link loading path $OABCO$ corresponding to the combined tension and torsion is shown in **Fig. 8.22**. In sections AB and BC, the loading is close to neutral.

In this simulation, the constitutive equations of four theories of plasticity were used:

- the theory of plastic flow with the mixed isotropic-kinematic hardening,
- the endochronic theory of plasticity,
- the multisurface theory of plasticity with one active surface,

- the holonomic (deformation) theory of plasticity.

The elastic-plastic characteristics of the steel 304 are: $E = 195$ GPa, $\nu = 0.3$, $Y_0 = 181$ MPa, $H = 1/C = 2700$ MPa. The bilinear approximation is used for the stress-strain curve.

Comparison of simulation results (obtained on the basis of the mentioned various plasticity models) with the experimentally measured curve is shown in **Fig. 8.22**. Under the proportional loading (OA section), there is coincidence of the results of all the considered theories and experimental data. Significant differences arise at the non-proportional loading stages AB and BC.

The holonomic theory of plasticity offers the prediction that is significantly different from the experimental results. The value of axial strain ε_x after the unloading based on the holonomic theory is 4.9 times higher than that observed in experiment. Solutions obtained by means of the flow theory with the mixed hardening are located between two extreme cases of the isotropic and kinematic hardening. The error in calculation of the residual strain ε_x for various versions of the flow theory varies from 3.9 % to 20.4 %.

Prediction by the multisurface theory of plasticity with one active surface is closest to the experiment in comparison with the all considered theories. In the simulation according to this theory, the power-law approximation of the plastic compliance (8.9) is used. The value of the exponent n was taken equal to 4, $C_0 = 1$. As n increases, the solution tends to the theory of flow with the isotropic hardening.

8.8 Conclusions

The proposed multisurface theory of plasticity with one active surface is aimed to describe the inelastic material behavior under the complex passive loading. The theory allows one to investigate the plastic strain accumulation under the unloading, neutral loading, and passive cyclic loading that is essential in the case of the high-cycle fatigue analysis. In this model, the loading history is taken into account discretely by storing the information only at the reversing points. Therefore the constitutive equations with the non-differential (recurrent) relations for the center of the active surface are used. The plastic strain rate tensor is determined by means of the associated plastic flow rule using only the one active surface as the plastic potential. Conditions of the thermodynamic consistency of the theory are considered. The peculiarities of numerical implementation within the framework of the finite-element analysis is discussed.

The results of computations based on the proposed theory reasonably good fit the results of the experimental studies for various polycrystalline materials: the nickel, steel, and aluminium alloy. The comparison of multisurface model with other plastic models (the plastic flow theory with isotropic and kinematic hardening, the endochronic theory, the holonomic theory and structural models) are performed and discussed. The multisurface model demonstrates fine proximity of predictions with ones by the microstructural model. This indicates the adequacy of the phenomeno-

logical physically consistent description of the passive loading paths using the multisurface theory with one active surface.

References

Aravas N (1987) On the numerical integration of a class of pressure-dependent plasticity models. International Journal for Numerical Methods in Engineering 24(7):1395–1416

Asaro RJ (1983) Crystal plasticity. Journal of Applied Mechanics 50:921–934

Axelsson K, Samuelsson A (1979) Finite element analysis of elastic-plastic materials displaying mixed hardening. International Journal for Numerical Methods in Engineering 14(2):211–225

Bedzra R, Reese S, Simon JW (2017) Meso-macro modelling of anisotropic metallic composites within the framework of multisurface plasticity. International Journal of Solids and Structures 120:186–198

Bedzra R, Li Y, Reese S, Simon JW (2019) A comparative study of a multi-surface and a non-quadratic plasticity model with application to the in-plane anisotropic elastoplastic modelling of paper and paperboard. Journal of Composite Materials 53(6):753–767

Besson J, Cailletaud G, Chaboche JL, Forest S, Bletry M (2009) Non-linear mechanics of materials. Solid Mechanics and Its Applications, Springer

Cailletaud G (1992) A micromechanical approach to inelastic behaviour of metals. International Journal of Plasticity 8(1):55–73

Chen WF (1984) Plasticity in reinforced concrete. McGraw-Hill, New York

Dafalias YF, Popov EP (1976) Plastic internal variables formalism of cyclic plasticity. Journal of Applied Mechanics 43:645–650

Desai CS, Siriwardane HJ (1984) Constitutive laws for engineering materials: with emphasis on geologic materials. Prentice-Hall, Englewood Cliffs

Fan S, Yin Z (2003) Multi-surface strength model for concrete beam-column joints subjected to cyclic loading. In: 7th Pacific Conferences on Earthquacke, NZSEE, New Zealand, paper number 44

Garud YS (1981) A New Approach to the Evaluation of Fatigue Under Multiaxial Loadings. Journal of Engineering Materials and Technology 103(2):118–125

Ilyushin AA (1963) Plasticity. Background of the general mathematical theory. Izd-vo AN SSSR, Moscow

Iwan WD (1967) On a class of models for the yielding behaviour of continuum and composite systems. Journal of Applied Mechanics 34:612–617

Izotov IN (1963) Study of metal anisotropy resulted by some types of plastic deformation. PhD thesis, Leningrad

Izotov IN, Yagn JI (1961) Analysis of plasticity preceded by imposed anisotropy. Reports of Academy of Sciences of USSR 139:575–579

Izotov IN, Kuznetsov NP, Melnikov BE, Mityukov AG, Musienko AY, Semenov AS (2001) Modification of the multisurface theory of plasticity with one surface. comparison with experimental data. In: Proc. of SPIE 4348. Fourth International Workshop on Nondestructive Testing and Computer Simulations in Science and Engineering, SPIE, pp 390–397

Kadashevich YI, Mosolov AB (1989) Endochronic plasticity theories: the main statements: future development. Reports of Academy of Sciences of USSR 1:161–168

Keralavarma SM (2017) A multi-surface plasticity model for ductile fracture simulations. Journal of the Mechanics and Physics of Solids 103:100–120

Koiter WT (1953) Stress-strain relations, uniqueness and variational theorems for elastic-plastic materials with singular yield surface. Quarterly Applied Mathematics 11(3):350–354

Koiter WT (1960) General theorems for elastic-plastic solids. In: Progress in Solid Mechanics, North-Holland, Amsterdam, pp 165–221

Krieg RD (1975) A practical two surface plasticity theory. Journal of Applied Mechanics 42:641–646

Kuznetsov NP (2000) Plastic deformation of metals along loading paths containing intermediate unloading. PhD thesis, Novgorod

Kuznetsov NP, Melnikov BE, Semenov AS (2017) Verification and adaptation of plasticity models under complex variable loading with intermediate complete and partial unloadings. St Petersburg Polytechnical University Journal: Physics and Mathematics 3(2):153–163

Lamba HS, Sidebottom OM (1978) Cyclic plasticity for nonproportional paths: Part 2 - comparison with predictions of three incremental plasticity models. Journal of Engineering Materials and Technology 100(4):104–111

Loret B, Prevost JH (1986) Accurate numerical solutions for drucker-prager elastic-plastic models. Computer Methods in Applied Mechanics and Engineering 54:259–277

Mackenzie-Helnwein P, Eberhardsteiner J, Mang H (2003) A multi-surface plasticity model for clear wood and its application to the finite element analysis of structural details. Computational Mechanics 31(1):204–218

Mandel J (1964) Contribution theorique a l'etude de l'ecrouissage et des lois de l'ecoulement plastique. In: Proc. of the 11th International Congress on Applied Mechanics, Springer, Berlin, Heidelberg, pp 502–509

Mandel J (1965) Generalisation de la theorie de la plasticite de W.T. Koiter. International Journal of Solids and Structures 1(3):273–295

Masing G (1926) Eigenspannungen und Verfestigung beim Messing. In: Proceedings of the 2nd International Congress of Applied Mechanics, Zürich

Melnikov BE, Semenov AS (1991) The multisurface theory of plasticity with one active surface of plastic compliance. Transactions of Leningrad state technical university Strength of Metals and Structures, Leningrad 441:26–31

Melnikov BE, Semenov AS (1995) Multimodel analysis as strategy of reliable description of elastic-plastic deformation processes. In: DRJ Owen EO (ed) Proc. IV Int. Conf. on Computational Plasticity. Fundamentals and Applications (COMPLAS IV), Pineridge Press, Swansea. UK, pp 181–189

Melnikov BE, Semenov AS (1996a) Creation and application of hierarchical sequence of material models for numerical analysis of elasto-plastic structures. Zeitschrift für angewandte Mathematik und Mechanik (ZAMM) 76(Sup. 2):615–616

Melnikov BE, Semenov AS (1996b) Evolution of equal compliance surfaces in the multisurface theory of plasticity. Transactions of St-Petersburg State Polytechnic University 456:52–61

Melnikov BE, Izotov IN, Kuznetsov NP (1990) Calculation and experimental examination of complex modes of elastoplastic deformation. Strength of Materials 22:1122–1127

Melnikov BE, Semenov AS, Semenov SG (2010) Multimodel analysis of elastic-plastic deformation of materials and structures. Proc of the AN Krylov Shipbuilding Research Institute 53:85–92

Mroz Z (1967) On the description of anisotropic hardening. Journal of the Mechanics and Physics of Solids 15(3):163–175

Mroz Z, Norries VA, Zienkiewicz OC (1978) An anisotropic hardening model for soils and its application to cyclic loading. International Journal for Numerical and Analytical Methods in Geomechanics 2(3):203–221

Murtazin IR, Melnikov BE, Semenov AS (2021) Simulation of inelastic response of polycrystalline nickel based on micromechanical model homogenization. In: Proc. APM-2021. Lecture Notes in Mechanical Engineering., Springer, St. Petersburg

Nemat-Nasser S (1983) On finite plastic flow of crystalline solids and geomaterials. Journal of Applied Mechanics 50:1114–1126

Palmov VA (1998) Vibrations of elastic-plastic bodies. Springer-Verlag, Berlin Heidelberg

Petersson H, Popov EP (1977) Constitutive equations for generalized loadings. Journal of the Engineering Mechanics Division 103(4):611

Raabe D, Sachtleber M, Zhao Z, Roters F, Zaefferer S (2001) Micromechanical and macro-mechanical effects in grain scale polycrystal plasticity experimentation and simulation. Acta materialia 49:3433–3441

Sandler IS, Rubin D (1979) An algorithm and a modular subroutine for the cap model. International Journal for Numerical and Analytical Methods in Geomechanics 3(2):173–186

Sawischlewski E, Steinmann P, Stein E (1996) Modelling and computation of instability phenomena in multisurface elasto-plasticity. Computational Mechanics 18(4):245–258

Semenov AS (1996) Improvement of the research methods of thermo-elasto-plastic deformation processes on the base on the multimodel analysis and exact integration of constitutive equations. PhD thesis, St. Petersburg State Polytechnical University

Semenov AS (2003a) Analysis of thermodynamic consistency of multisurface plastic theory with one active surface. Scientific and technical Bulletin of St-Petersburg State Polytechnic University 33:103–114

Semenov AS (2003b) Pantocrator - the finite element program specialized on the solution of non-linear problems of solid body mechanics. In: Proc. of the Vth Int. Conf. on scientific and engineering problems of predicting the reliability and service life of structures, St. Petersburg, pp 466–480

Semenov AS (2008) Computational methods in the theory of plasticity. Publishing house SPbSPU, St. Petersburg

Semenov AS (2014) The identification of anisotrophy parameters of phenomenological plasticity criterion for single crystals worked out on the micromechanical model basis. St Petersburg Polytechnical State University Journal Physics and Mathematics 194(2):15–29

Semenov AS, Melnikov BE (1998) Multimodel elasto-plastic and elasto-visco-plastic deformation processes in material and structures. In: Proc. of 4th Int. Conf. Low cycle Fatigue and Elasto-Plastic Behavior of Materials, Garmisch-Partenkirchen, pp 659–664

Semenov AS, Melnikov BE, Gorokhov MY, Ulbricht V (2007) Prevention of cyclic instability at the modeling of elasto-plastic deformation at large strains under proportional and non-proportional loading. In: Melker AI, Breczko T (eds) Nanodesign, Technology, and Computer Simulations, International Society for Optics and Photonics, SPIE, vol 6597, pp 235–252

Shahrooi S, Metselaar IH, Huda Z (2010) Evaluation of cyclic plasticity models of multi-surface and non-linear hardening by an energy-based fatigue criterion. Journal of Mechanical Science and Technology 24(6):1255–1260

Simo JC, Hughes TJR (1998) Computational Inelasticity. Springer-Verlag, New York

Simo JC, Kennedy JG, Govindjee S (1988) Non-smooth multisurface plasticity and viscoplasticity. loading/unloading conditions and numerical algorithms. International Journal for Numerical Methods in Engineering 26(10):2161–2185

Staroselsky A, Martin TJ (2015) Creep, plasticity and fatigue of single crystal superalloys: Physics-based life prediction for turbine components in severe operating environments. In: Altenbach H M Brünig (ed) Inelastic Behavior of Materials and Structures Under Monotonic and Cyclic Loading. Advanced Structured Materials., Springer, Cham, pp 207–241

Szabo L (1984) Comparison of some plasticity theories by means of the finite element method. Periodica Polytechnika Mech Eng 28(2-3):153–161

Trusov PV, Shveikin AI (2019) Multilevel models of mono and polycrystalline materials: theory, algorithms, application examples. SO RAN, Novosibirsk

Trusov PV, Volegov PS, Kondratyev NS (2013) The physical theory of plasticity. Perm Polytech. University, Perm

Valanis KC (1980) Fundamental consequences of a new intrinsic time measure: plasticity as a limit of the endochronic theory. Arch Mech Stasow 32:171–191

Whyte SA, Burd HJ, Martin CM, Rattley MJ (2020) Formulation and implementation of a practical multi-surface soil plasticity model. Computers and Geotechnics 117:103,092

Chapter 9
A Damage Model for Corrosion Fatigue due to Hydrogen Embrittlement

Yuhao Shi, Sven Harzheim, Martin Hofmann, and Thomas Wallmersperger

Abstract Predicting the durability of components subjected to mechanical load under environmental conditions leading to corrosion is one of the most challenging tasks in mechanical engineering. The demand for precise predictions increases with the desire of lightweight design in transportation due to environmental protection. Corrosion with its manifold of mechanisms often occurs together with the production of hydrogen by electrochemical reactions. Hydrogen embrittlement is one of the most feared damage mechanisms for metal constructions often leading to early and unexpected failure. Until now, predictions are mostly based on costly experiments. Hence, a rational predictive model based on the fundamentals of electrochemistry and damage mechanics has to be developed in order to reduce the costs.

In this work, a first model approach based on classical continuum damage mechanics is presented to couple both, the damage induced by the mechanical stress and the hydrogen embrittlement. An elaborated two-scale model based on the self-consistent theory is applied to describe the mechanical damage due to fatigue. The electrochemical kinetics are elucidated through the Langmuir adsorption isotherm and the diffusion equation to consider the impact of hydrogen embrittlement on the fatigue. The modeling of the mechanism of hydrogen embrittlement defines the progress of damage accumulation due to the electrochemistry. The durability results like the S-N diagram show the influence of hydrogen embrittlement by varying, e.g. the fatigue frequency or the stress ratio.

Key words: Hydrogen embrittlement, Fatigue, Continuum damage mechanics, Numerical simulation, Multi-field problem

Yuhao Shi · Sven Harzheim · Martin Hofmann · Thomas Wallmersperger
Institute of Solid Mechanics, Technische Universität Dresden, George-Bähr-Straße 3c, 01069 Dresden, Germany,
e-mail: yuhao.shi@tu-dresden.de,sven.harzheim@tu-dresden.de,martin.hofmann@tu-dresden.de, thomas.wallmersperger@tu-dresden.de

Nomenclature

a	Eshelby parameter		α	charge transfer coefficient
A	kinematic hardening		β	material parameter
b	model parameter		ε	tensor
c_H	hydrogen concentration		η	overpotential
c_{max}	maximal concentration		$d\Lambda$	indeterminate plastic multiplier
C	microscopic kinematic hardening parameter		μ	model parameter
D	damage variable		ν	Poisson's ratio
D_c	critical damage		$r_{1,2,3,4}$	reaction rate
D_H	diffusion coefficient of hydrogen		π	pi
E	Young's modulus		ρ	material density
f	frequency		σ_{el}	surface charge density
f^M	yield function		σ	stress
F	Faraday constant		σ_a	stress amplitude
$H(x)$	Heaviside function		σ_{EQ}	equivalent stress
J	flux		σ_F	fatigue limit
k	reaction rate constant		σ_{F0}	initial fatigue limit
L	length		σ_H	hydrostatic stress
M	molar mass		σ_{max}	maximal stress
N	fatigue cycles		σ_U	uniaxial tensile strength
p	accumulated plastic strain		Θ	hydrogen coverage
p_D	threshold value of accumulated plastic strain			
R	ideal gas constant			
R_ν	uniaxial function			
s	damage exponent			
S	damage strength			
t	time			
T	temperature			
Y	damage-associated variable			
X	dimensionless hydrogen concentration			
$\bar{X}$	uniform concentration			

9.1 Introduction

Corrosion is a detrimental and frequent phenomenon of metallic components in natural and artificial environments that occurs in many forms (Fontana, 2005). In general, corrosion degrades the metal's surface which often leads to loss of function of the metallic component. This surface degradation is caused by differences in the electric potential of the metal and its surroundings. Here, electrons are transferred from the metal (anode) to the cathode. The cathodic reaction strongly depends on the metal's environment. A general consequence, however, is the oxidation of the metal surface. Depending on the type of metal, an oxide layer may serve as a protective barrier against corrosion (e.g. aluminum oxide). In the case of iron, the occurring

hydroxide layer does not protect the surface from further corrosion, due to its relatively high molar volume.

In acidic regimes, hydrogen forms at the cathode during corrosion. This hydrogen is able to diffuse into the metal, posing an additional threat by degrading the metal's mechanical properties. Hydrogen embrittlement is subject to current research, and its most prominent degradation mechanisms are (i) hydrogen enhanced decohesion, (ii) hydrogen-assisted void nucleation, and (iii) hydrogen enhanced localised plasticity. An overview of the mechanisms is given, e.g., by Lynch (2012). Corrosion is not the only source of hydrogen in steels. Processes like electrolysis, using pickling solutions, or welding in moist atmospheres can also cause hydrogen embrittlement (Lynch, 2012; Ćwiek, 2010). Concluding, corrosion not only degrades the surface of metallic components, it also affects the fatigue life through hydrogen embrittlement (Gerard et al., 1998).

The aim of the present paper is to investigate the influence of hydrogen – created by corrosion – on the fatigue life of steel. We aim at extending the two-scale high-cycle fatigue damage model introduced by Lemaitre et al. (1999) with a reduction of the fatigue limit through hydrogen. Thus, we treat hydrogen damage as a generic category that is not representative of the hydrogen embrittlement damage types introduced above. The ultimate goal is to predict crack initiation in the metal sample, depending on different concentrations of hydrogen. In our modeling approach, the damage within a metal sample with no initial hydrogen is investigated. Furthermore, it is assumed that hydrogen serves as the unique source of damage resulting from corrosive effects, and the theoretical change in geometry of the metal sample is neglected. In the literature, this effect is known to also have a large influence on the fatigue life. However, we are only interested in investigating the effect of hydrogen on the fatigue life. Our approach is a phenomenological one and uses an ansatz function that describes the hydrogen concentration within the representative volume element of the two-scale model.

The source of hydrogen is assumed to stem from the hydrogen evolution reactions (HER), which result from the reaction rate models established in previous studies (Harrington and Conway, 1987; Lasia, 1993; Lasia and Grégoire, 1995; Lasia and Rami, 1990). Meanwhile, the fatigue damage caused by the cyclic stress will be approximated by a two-scale damage model concerning the plasticity of micro-inclusions to predict the cracking initiation at the metal surface.

The present paper is structured as follows. In Sect. 9.2, we introduce the mathematical model that is used to describe the damage accumulation due to hydrogen. In Sect. 9.3, we provide and discuss results of the numerical simulations. Finally, in Sect. 9.4, we give a conclusion of the obtained results.

9.2 Model Description

In the present section, we elucidate the setup of the predictive model based on the conclusion drawn from the relevant literature. The fundamental concept is to solve a

coupled multi-field problem, consisting of the mechanical field, i.e., the stress evaluation, and the chemical field, i.e., the hydrogen reaction and diffusion, by numerical methods. First, the fundamental equations for hydrogen formation, adsorption, and absorption are given in Subsect. 9.2.1. Then, the analysis of the damage is shown in Subsect. 9.2.2.

9.2.1 Hydrogen Formation, Adsorption, and Absorption

In this section, we consider the hydrogen accumulation kinetics based on a general model of hydrogen adsorption-desorption in the presence of hydrogen evolution reactions, see Harrington and Conway (1987); Lasia (1993); Lasia and Grégoire (1995); Lasia and Rami (1990). It is assumed that the reaction proceeds through the following characteristic steps:

$$H_2O + M + e^- \rightleftharpoons MH_{ads} + OH^- \qquad \text{(Volmer)} \qquad (9.1)$$

$$MH_{ads} + H_2O + e^- \rightleftharpoons H_2 + OH^- + M \qquad \text{(Heyrovsky)} \qquad (9.2)$$

$$2MH_{ads} \rightleftharpoons H_2 + 2M \qquad \text{(Tafel)} \qquad (9.3)$$
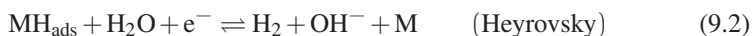
The transfer of the hydrogen adsorbed by the surface into the metal should be additionally taken into account:

$$MH_{ads} \rightleftharpoons MH_{abs} \qquad (9.4)$$

The kinetics equations of hydrogen reaction steps are given by the reaction rates

$$r_1 = \overrightarrow{k_1}(1 - \Theta) - \overleftarrow{k_{-1}}\Theta \qquad (9.5)$$

$$r_2 = \overrightarrow{k_2}\Theta - \overleftarrow{k_{-2}}(1 - \Theta) \qquad (9.6)$$

$$r_3 = k_3\Theta^2 - k_{-3}(1 - \Theta)^2 \qquad (9.7)$$

$$r_4 = k_4\Theta(1 - X_0) - k_{-4}(1 - \Theta)X_0 \qquad (9.8)$$

where the potential dependent rate constants $\overrightarrow{k_j}, \overleftarrow{k_{-j}} (j = 1, 2)$ are related to the reaction rate constants $k_j, k_{-j} (j = 1, 2)$ in the form of the equations

$$\overrightarrow{k_j} = k_j \exp(-f\eta) \qquad (9.9)$$

$$\overleftarrow{k_{-j}} = k_{-j} \exp[(1 -)f\eta]. \qquad (9.10)$$

The electrode equations are the Butler-Volmer equations for the anode reaction and the cathode reaction, respectively. The positive subscript $(\ )_j$ indicates the forward reaction, whereas the negative subscript $(\ )_{-j}$ presents the backward reaction, is the charge transfer coefficient and η is the overpotential. The symbol $\mathfrak{f}$ denotes $\mathfrak{f} = F/(RT)$, where F is the Faraday constant, R the ideal gas constant and T the temperature. Furthermore, Θ denotes the surface coverage by adsorbed hydrogen, and X is the dimensionless hydrogen concentration inside the metal. This concentration is obtained by the ratio of the hydrogen concentration to the maximal concentration, i.e., $c_H/c_{H,max}$. The index 0 designates the concentration at position $x = 0$ (surface), in the metal.

According to the former studies of HER, the Volmer-Heyrovsky mechanism is usually involved. Hence, we consider both, the kinetics of the Volmer-Heyrovsky reactions and the hydrogen absorption in our model. The time derivative of the hydrogen surface coverage Θ is obtained through the reaction rates:

$$\frac{d\Theta}{dt} = \frac{F}{\sigma_{el}}(r_1 - r_2 - r_4) \tag{9.11}$$

where σ_{el} is the total surface charge density. The reaction rates r_1, r_2 and r_4 can be obtained from Eqs. (9.5) to (9.8). Besides, the adsorption-absorption kinetics is obtained by the flux of hydrogen at the metal surface,

$$r_4 = J_H = -D_H \frac{\rho_{el}}{F} \left.\frac{\partial X}{\partial x}\right|_{x=0} \tag{9.12}$$

where ρ_{el} indicates the volume electric charge density due to the hydrogen concentration.

The hydrogen transfer within the metal corresponds to the general diffusion equation. The semi-infinite solution of the 1D diffusion equation is applied to describe the hydrogen absorption in the metal. If the surface concentration X_0 changes only slowly, one can assume that the concentration just beneath the surface of the metal is approximately equal to the concentration at the surface. Then, the boundary conditions at the surface and far away can be given by

$$X|_{x=0} = X_0, \qquad \left.\frac{dX}{dx}\right|_{x=\infty} = 0, \tag{9.13}$$

where x is the Cartesian coordinate. This approach aims at modeling the sample immersed in the inexhaustible source where the sample size is here not to be discussed. The concentration profile within the metal is expressed by the semi-infinite solution

$$X = X_0 \, \mathrm{erfc}\left(\frac{x}{2\sqrt{D_H t}}\right) \tag{9.14}$$

with the complimentary error function

$$\mathrm{erfc}\left(\frac{x}{2\sqrt{D_H t}}\right) = 1 - \frac{2}{\pi}\int_0^\infty \exp\left[-\left(\frac{x}{2\sqrt{D_H t}}\right)^2\right]\, dx \qquad (9.15)$$

The common solution with the error function is principally valid for a constant hydrogen concentration at the boundary and furthermore for an infinite half space. The constant hydrogen concentration requires the inexhaustible source in the environment. For this reason, the surface concentration is set as boundary condition. The characteristic length (penetration depth of the field) can be approximated by $\delta_{c_H} = 2\sqrt{D_H t}$. The half thickness of the sample should be much higher than the diffusion length when the representative volume element (RVE) is determined as failed, so that the error within the RVE is negligible. If the test duration exceeds the time of hydrogen species penetrating to the specimen center, the approximation with semi-infinite diffusion is not any longer reliable. With a thickness of $0.1\,\mathrm{cm}$ the maximum hydrogen diffusion time is $625000\,\mathrm{s}$ for a diffusion coefficient of $D_H = 10^{-9}$ cm^2/s. For this reason, the 1D-Fourier solution is appropriate for the diffusion in a small specimen in longitudinal direction. Since the aim of this paper is to show the principal efficiency of the model, we use the analytical solution here instead of the full solution that would require a large memory space to record the concentration profile for the long period test, e.g., for very high cycle fatigue. The analytical solution is beneficial for the forward method that the value of the hydrogen concentration of the last step can be overwritten. In future works the hydrogen concentration field inside the metal will be calculated numerically by applying the finite element method.

According to Eq. (9.14), the derivative of the dimensionless concentration X with respect to the position x is given by

$$\frac{\partial X}{\partial x} = -\frac{X_0}{\sqrt{\pi D_H t}}\exp\left[-\left(\frac{x}{2\sqrt{D_H t}}\right)^2\right] \qquad (9.16)$$

Hence, (i) the charge of the metal $\rho_{el} = F c_{H,max}$ corresponding to the saturation with hydrogen, and (ii) the diffusion coefficient of hydrogen within the metal D_H, are decisive for adsorption and absorption mechanisms. Associating Eq. (9.8) with Eq. (9.12) we obtain the explicit expression for hydrogen concentration at metal surface by

$$\left[\frac{D_H \rho_{el}}{F\sqrt{\pi D_H t}} + k_4\Theta + k_{-4}(1-\Theta)\right]X_0 = k_4\Theta \qquad (9.17)$$

$$\Leftrightarrow X_0 = \frac{k_4\Theta}{\left[\dfrac{D_H \rho_{el}}{F\sqrt{\pi D_H t}} + k_4\Theta + k_{-4}(1-\Theta)\right]} \qquad (9.18)$$

Even though Eq. (9.11) has the form of an ordinary differential equation, there still exists the obstacle to determine a solution since the term X_0 in Eq. (9.18) is also time-dependent. For this reason, Eq. (9.11) will be solved by using the Crank-

Nicolson Method, see Appendix. According to the discretisation of Eq. (9.11) with $d\Theta/dt = f(\Theta, X_0)$,

$$\Theta_{i+1} - \Theta_i = \tau\left[f(\Theta_{i+1}, X_{0,i+1}) + f(\Theta_i, X_{0,i})\right] \qquad (9.19)$$

is used, where $\tau = (F\Delta t)/(2\sigma_{el})$. Please note that the subscript $(\ )_i$ indicates the time step number. The initial conditions at $t = 0$ are given by

$$\Theta_1 = 0, \qquad X_{0,1} = 0. \qquad (9.20)$$

9.2.2 Damage Analysis

The elaborated two-scale damage model established by Lemaitre et al. (1999) serves as the framework for the damage analysis in the present work. It postulates a microscopic volume element M included in a RVE at the mesoscale, which has the same elastic properties as the RVE. However, it is subjected to elastic-plastic deformation with a microscopic yield stress σ_Y^M equal to the material fatigue limit σ_F. This process induces the damage within the RVE and leads to the failure of the RVE, i.e., the crack initiation occurs at the macroscale (Lemaitre et al., 1999). By means of the localization law of the self-consistent theory, the stress at the microscale σ_{ij}^M (please note that the superscript $(\ )^M$ denotes a variable at the microscale). The variables with the subscript $(\ )_{ij}$ are tensors with the index notation) is related to the mesoscopic stress σ_{ij} in the RVE (Berveiller and Zaoui, 1985; Kröner, 1961; Lemaitre and Sermage, 1997):

$$\sigma_{ij}^M = \sigma_{ij} - aE\varepsilon_{ij}^{Mp} \qquad (9.21)$$

where ε_{ij}^{Mp} is the microscopic plastic strain and a is the Eshelby solution for a spherical inclusion (Eshelby, 1957),

$$a = \frac{1-\beta}{1+\nu}, \qquad \text{where} \quad \beta = \frac{2(4-5\nu)}{15(1-\nu)}. \qquad (9.22)$$

The symbol ν denotes here the Poisson's ratio. The evolution law of the plastic strain at the microscale is obtained from the normality rule,

$$d\varepsilon_{ij}^{Mp} = \frac{\partial f^M}{\partial \sigma_{ij}^M} d\Lambda. \qquad (9.23)$$

Afterward, the yield function f^M concerning the linear kinematic hardening tensor $\mathbf{A}^M$ and the stress tensor $\boldsymbol{\sigma}^M$ at the microscale is obtained by elastic-plastic theory as follow:

$$f^M = \left(\frac{\sigma_{ij}^M}{1-D} - A_{ij}^M\right)_{EQ} - \sigma_F = 0 \qquad (9.24)$$

$$\mathrm{d}f^M = 0. \tag{9.25}$$

where the subscript $(\ )_{EQ}$ indicates the equivalent value of the tensor. The evolution law of the linear kinematic hardening is obtained by the elastic-plastic constitutive equations of isotropic damaged material

$$\mathrm{d}A_{ij}^{MD} = \frac{2}{3} C \,(1-D)\,\mathrm{d}\varepsilon_{ij}^{Mp} \tag{9.26}$$

where A_{ij}^{MD} denotes the deviatoric tensor of microscopic kinematic hardening and C is the microscopic kinematic hardening parameter (Lemaitre et al., 1999; Murakami et al., 2013). The indeterminate plastic multiplier $\mathrm{d}\Lambda$ can be determined in different ways (Malvern, 1969) whereas

$$\mathrm{d}\Lambda = 0, \quad \text{for } f^M < 0 \text{ or for } \mathrm{d}f^M < 0 \text{ and} \tag{9.27}$$

$$\mathrm{d}\Lambda \neq 0, \text{ for } f^M = 0 \text{ or for } \mathrm{d}f^M = 0. \tag{9.28}$$

The damage development in the element M is governed by the damage-associated variable Y^M which can be interpreted as the release rate of the strain energy density as a result of the damage evolution (Chaboche, 1988a,b). Then we obtain the damage evolution equation by

$$\mathrm{d}D = \left(\frac{Y^M}{S}\right)^s \mathrm{d}p^M H(p^M - p_D) \tag{9.29}$$

$$\mathrm{d}p^M = \left(\frac{2}{3}\mathrm{d}\varepsilon_{ij}^{Mp}\mathrm{d}\varepsilon_{ij}^{Mp}\right)^{1/2} \tag{9.30}$$

where the damage strength S and the damage exponent s are material dependent parameters. The Heaviside function $H(x)$ is applied here to indicate the fact that the damage can only increase when the accumulated plastic strain p^M exceeds the threshold value p_D. The variable Y^M is derived from the derivative of the Helmholtz free energy function with respect to the damage variable D (Lemaitre, 1996; Lemaitre and Desmorat, 2005; Murakami, 2011). The expression of Y^M is given by

$$Y^M = \frac{(\sigma_{EQ}^M)^2 R_v^M}{2E(1-D)^2} \tag{9.31}$$

where

$$R_v^M = \frac{2}{3}(1+v) + 3(1-2v)\left(\frac{\sigma_H^M}{\sigma_{EQ}^M}\right)^2. \tag{9.32}$$

The term R_v^M is designated as uniaxial function at the microscale. σ_H^M and σ_{EQ}^M denote the hydrostatic stress and the equivalent stress of the microelement, respectively.

The onset of the local fracture of the material on the mesoscale, i.e., the crack initiation is assumed to appear if the damage threshold D_C is attained. This variable is dependent on the material and the loading conditions (Lemaitre, 1996; Bonora et al., 2005). For the materials under uniaxial stress, the critical damage D_C is given as

$$D_C = 1 - \frac{\sigma_R^M}{\sigma_U} \tag{9.33}$$

where σ_R^M denotes the fracture stress on the microscale

$$\sigma_R^M = \sigma_{EQ}^M (R_v^M)^{1/2}. \tag{9.34}$$

σ_U is the uniaxial tensile strength, which can be related to the fatigue limit of materials.

Furthermore, we postulate that the hydrogen embrittlement affects the material durability by swaying the fatigue limit at the mesoscale. In this model, the relief of the fatigue limit is governed by the hydrogen diffusion beginning from the metal surface as

$$\sigma_F = \sigma_{F0} \left\{ \exp\left[-\mu\bar{X} + \ln(1-b) \right] + b \right\}, \tag{9.35}$$

where μ and b are the parameters for the purpose of investigating the effect of hydrogen. σ_{F0} indicates the initial fatigue limit of the material at $t = 0$. $\bar{X}$ denotes the uniform dimensionless hydrogen concentration within the RVE at the metal surface. This uniform concentration is governed by the integral of the local concentration within the RVE with a thickness L:

$$\bar{X} = \int_0^L \frac{X(x)}{L} dx \tag{9.36}$$

9.3 Numerical Results and Discussions

In this section, we provide results of the hydrogen adsorption and absorption, as well as the influence of hydrogen on the fatigue life. In order to approximate the fatigue life of a corroded material, the previously developed model is implemented and numerically solved for the simple loading case of uniaxial tension in a flat strip. **Figure 9.1** presents an illustration of the model to be solved. A metal specimen is immersed in water, the hydrogen species produced through HER diffuses into the metal and will be trapped by the microscopic inclusions. Meanwhile, the metal specimen undergoes a cyclic loading with the amplitude σ_a. The damage of an RVE on the metal surface will be determined to predict the crack initiation. The evolution equation of the hydrogen coverage Θ is given by Eq. (9.19), then the dimensionless concentration at the metal surface X_0 is obtained. The numerically obtained uniform hydrogen concentration $\bar{X}$ within the RVE is related to the reduced fatigue limit in Eq. (9.35). This effect has a large influence on the mechanical damage process, as the damage increment per cycle increases.

Fig. 9.1 Illustration of the 1D damage model.
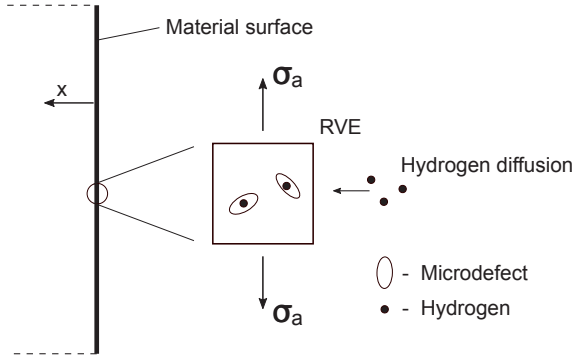
9.3.1 Hydrogen Adsorption and Absorption

In the present work, the production of hydrogen is only associated with HER due to the chosen model. The time-dependent hydrogen concentration at the metal surface results from the reaction kinetics and the adsorption capacity of the material. Since the Volmer-Heyrovsky reaction as a part of the entire HER is a potential-dependent electrochemical reaction, the overpotential η affects the rate of the hydrogen adsorption. **Figure 9.2** presents the dimensionless variables Θ and X_0 as functions of time – due to application of different overpotentials – assuming semi-infinite diffusion. The applied parameters are taken from Lasia and Grégoire (1995) and are listed in **Table 9.1**. The hydrogen coverage Θ as well as the dimensionless hydrogen concentration X_0 increase with increasing time. The curves for the overpotential $\eta = -0.5\,\text{V}$ show larger values of Θ and of X_0 than the curves for $\eta = -0.12\,\text{V}$. According to the
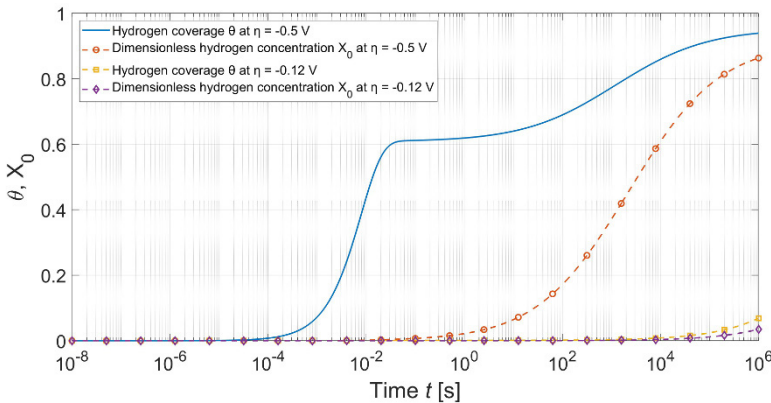
Fig. 9.2: Time dependence of the hydrogen concentration Θ and the dimensionless hydrogen concentration X_0 during the application of different overpotentials in the conditions of semi-infinite diffusion. The applied electrochemical parameters stem from **Table 9.2**.

Table 9.1: Material properties for the hydrogen capacity

Material	Density [g/cm^3]	Molar mass [g/mol]	Maximal concentration [mol/cm^3]
Aluminium	2.7	26.982	0.1001
Titanium	4.54	47.867	0.0948
Iron	7.87	55.845	0.1409
Nickel	8.9	58.6934	0.1516

Table 9.2: Electrochemical parameters for the numerical simulations (Lasia and Grégoire, 1995)

Parameter	Value
Maximal surface concentration $c_{H,max}$	0.1415 mol/cm^3
Diffusion coefficient within the metal D_H	$1 \cdot 10^{-9}$ cm^2/s
Faraday constant F	96485 C/mol
Volmer forward reaction rate constant $\overrightarrow{k_1}$	$1 \cdot 10^{-11}$ mol/cm^2/s
Volmer backward reaction rate constant $\overleftarrow{k_{-1}}$	$1 \cdot 10^{-10}$ mol/cm^2/s
Heyrovsky forward reaction rate constant $\overrightarrow{k_2}$	$1 \cdot 10^{-12}$ mol/cm^2/s
Heyrovsky backward reaction rate constant $\overleftarrow{k_{-2}}$	$1 \cdot 10^{-13}$ mol/cm^2/s
Diffusion forward reaction rate constant k_4	$1 \cdot 10^{-7}$ mol/cm^2/s
Diffusion backward reaction rate constant k_{-4}	$2 \cdot 10^{-7}$ mol/cm^2/s
Ideal gas constant R	8.314 J/K/mol
Temperature T	298 K
Charge transfer coefficient	0.5
Overpotential η	-0.5 V
Total surface charge density σ_{el}	$2.1 \cdot 10^{-4}$ C/cm^2

Butler-Volmer equations (9.9) and (9.10), at a certain metallic electrode, the more negative the overpotential is, the higher the reaction rate of HER gets (Hamann, 2007). The numerical results shown in **Fig. 9.2** match the results given in Lasia and Grégoire (1995) and therefore confirm the validity of the present model.

Besides the reaction kinetics, the saturation concentration of the metal with hydrogen also limits the rate to reach the threshold of the hydrogen coverage, as well as of the surface concentration. Lasia and Grégoire (1995) assumed that the maximal hydrogen concentration in metal equals one atom of hydrogen per metal atom. Hence, the maximal hydrogen concentration is equal to the quotient between the metal density and its molar mass $c_{H,max} = \rho/M$. This material dependent parameter $c_{H,max}$ limits the ability of hydrogen adsorption and absorption. Some typical applied metals together with their absorption properties are listed in **Table 9.1**. **Figure 9.3**, which shows the time dependence of the surface coverage by adsorbed hydrogen Θ and of the surface concentration X_0, indicates that the materials which

have the higher maximal absorption concentration, adsorb the hydrogen also faster. Nickel has the better ability of hydrogen absorption and its metal hydrides are thus applied for hydrogen storage technologies (Zhao and Ma, 2009).

9.3.2 Parameters of Damage Model

In this section, we present the material parameters used for the two-scale damage model, as well as the parameters used to describe the reduction of the fatigue limit.

9.3.2.1 Material Parameters and Size of RVE

After considering the electrochemical conditions, the material parameters have to be settled subsequently. The material parameters at the micro- and mesoscale will be determined through the results by former studies and are listed in **Table 9.3** (Lemaitre, 1996; Lemaitre et al., 1999). Some key parameters will be modified further to investigate the interactions between the mechanical model and the electrochemical model. The Lemaitre's two-scale damage model focuses on the micro-defect and its development within the representative volume element at the mesoscale. According to the statistical homogenization in the discontinuous structure, the RVE is supposed to represent the mechanical properties of the homogenized material. Hence, the failure of the RVE due to the propagation of microscopic voids and inclusions leads to the crack initiation at the macroscopic structure, even possibly leading to a complete fracture. Since the hydrogen embrittlement initiates the process at the metal surface while the metal adsorbs and absorbs the hydrogen,
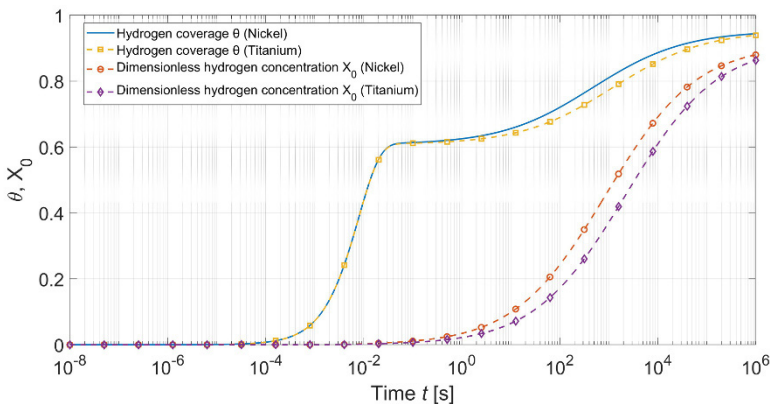
Fig. 9.3: Time dependence of Θ and X_0 for different metals with $\eta = -0.5\,\text{V}$; the applied electrochemical parameters are given in **Tables 9.1** and **9.2**.

Table 9.3: Material parameters for the damage model

Parameter	Value
Microscopic kinematic hardening parameter C	$2000\,\text{MPa}$
Young's modulus E	$2.1 \cdot 10^5\,\text{MPa}$
Threshold value of the accumulated plastic strain p_D	0
Damage strength S	$0.3\,\text{MPa}$
Damage exponent s	2
Poisson's ratio ν	0.3
Initial fatigue limit σ_{F0}	$200\,\text{MPa}$
Uniaxial tensile strength σ_u	$2\,\sigma_F$
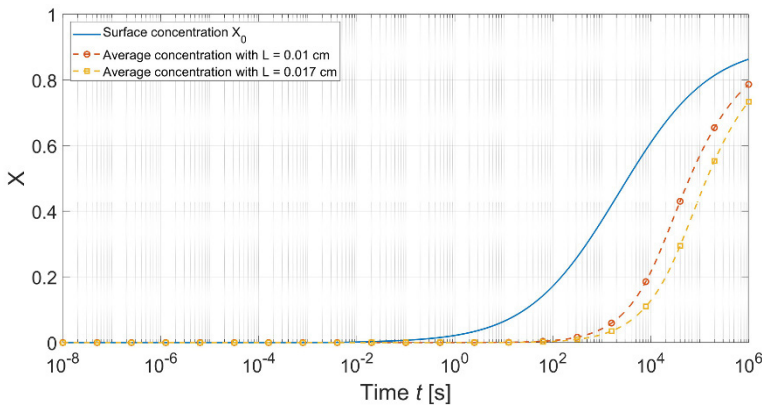
Fig. 9.4: Uniform concentration within an RVE in dependence of the RVE length L being the diffusion length; the applied electrochemical parameters are given in **Table 9.2**.

the crack initiation due to failure of the RVE at the metal surface occurs naturally before the complete fracture. The size of the RVE indicates the characteristic length for the hydrogen diffusion. In this work, we select the cubic-geometric RVE with a side length of 0.01 cm with respect to the literature (Lemaitre, 1996) for the model problems. It is further assumed that at least one RVE is in contact with the metal surface with at least one geometric point. By concerning the sample geometry, the maximal diffusion length can be considered as the space diagonal, which is about 0.017 cm. **Figure 9.4** illustrates the concentration-time profiles for different diffusion lengths L.
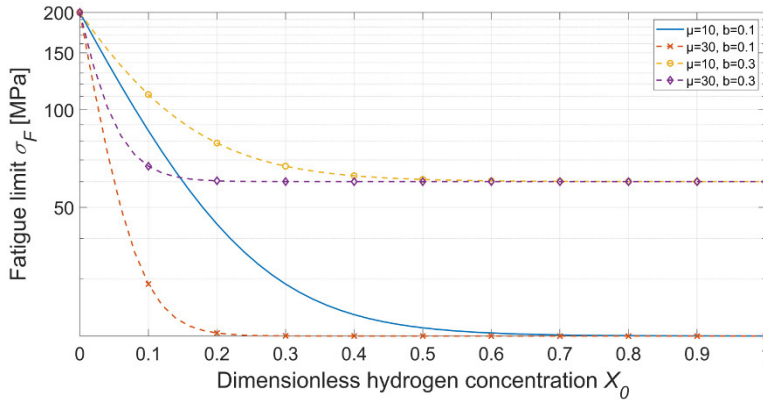
Fig. 9.5: Fatigue limit σ_F versus the dimensionless hydrogen concentration X_0.

9.3.2.2 Model Parameters for Reduction of Fatigue Limit

The deterioration of the investigated material is described by the exponential function, Eq. (9.35), in this work. As mentioned before, the corrosion fatigue can reduce the material thickness and the true fatigue limit can hardly be observed. Hence, it is reasonable to believe that hydrogen embrittlement can produce a similar effect as some experiments have proven (Johnson et al., 1958; Murakami et al., 2013; Ogata, 2010, 2012). In Eq. (9.35), the decrease of the value of the fatigue limit is governed by two material-dependent model parameters μ and b, which can be – in principle – determined by experiments. The parameter μ then serves as a factor to determine the hydrogen concentration according to the fatigue limit profile. The parameter b implies the ratio between the actual fatigue limit σ_F and its initial value σ_{F0}, since the lower limit of the exponential part approaches zero with increasing uniform concentration $\bar{X}$. Please note that $\bar{X}$ is restricted to be between 0 and 1. In **Fig. 9.5**, the fatigue limit is presented – for different model parameters – as a function of the dimensionless hydrogen concentration. It can be seen that for increasing hydrogen concentration, the fatigue limit is reduced. For $b = 0.3$, the fatigue limit converges to $\sigma_F = 60\,\text{MPa}$ while for $b = 0.1$ it converges to $\sigma_F = 20\,\text{MPa}$. An increase of μ results in a faster decrease of the fatigue limit versus the dimensionless hydrogen concentration.

Some perspectives confirm the assumption of a lower limit of the fatigue limit since the molecular hydrogen is trapped by the microscopic inclusions within the material to induce the hydrogen-assisted damage (Lynch, 2012; Murakami et al., 2013). Only a limited amount of inclusions are located within the material. It is thus assumed that the fatigue limit will not further be decreased when all inclusions are inhabited. The maximal concentration of absorption is not the prerequisite to obtain the lower limit since the hydrogen capacity of inclusions is undoubtedly lower than

of the entire matrix. A further developed model may include the information of the content within the matrix material, e.g. for alloys.

9.3.3 Influences of Frequency on the Fatigue Life

For illustrating the approximated fatigue life by the numerical damage models, we take advantage of the S-N diagram (stress versus number of cycles) to interpret our results. The applied single mechanical damage model implements the fatigue without hydrogen reaction to have a reference for a further comparison. Since the fatigue life is usually presented by the test cycles, the frequency of the workload is associated by describing the material endurance at the time scale $t = N/f$, where N is the number of cycles, and f is the frequency.

Based on the implemented model and its parameters, the results at the cycle scale in **Fig. 9.6** indicate that the frequency yields a significant influence on the fatigue life, except for the very low cycle fatigue, i.e., less than 10^3 cycles. It is comprehensible that the metal suffering high-frequency workload can achieve more loading cycles than for low-frequency since there is only little time for hydrogen embrittlement. On the other hand, the high cycle fatigue, i.e., more than 10^5 cycles, shows a weak dependence on the frequency. The starting point of the quasi-overlap of the curves in the high cycle range results from the exponential function (9.35) describing the reduction of the fatigue limit at the mesoscale. In **Figs. 9.4** and **9.5**, with the given model parameters ($\mu = 30, b = 0.1$), the fatigue limit does not vary considerably after $\bar{X} = 0.2$ where ca. 10^4 seconds elapse. Hence, we can observe the curve for a frequency of 1 Hz overlapping with the curve for 10 Hz at $N = 10^5$.
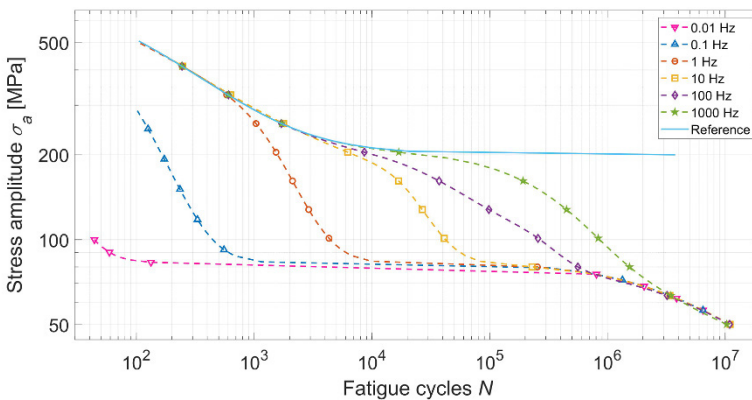
Fig. 9.6: Influence of frequency upon reduced fatigue life by hydrogen embrittlement at the cycle scale ($\eta = -0.5$ V, $\mu = 30$, $b = 0.1$, $L = 0.01$ cm. The other parameters can be found in **Table**s **9.2** and **9.3**).

Meanwhile, the curve for 100 Hz intersects at $N = 10^6$. However, it can be observed in **Fig. 9.7** that the curve for the lower frequency indicates a longer fatigue life at the time-scale, especially for the high cycle fatigue. This result stems from the fatigue life results depicted in **Fig. 9.6**. Moreover, the runs of the curves indicate that the material failure due to the fatigue corrosion is initiated by the mechanical loading. The sudden cracking of a corroded specimen often occurs (i) due to the long-time contact with the corrosive environment and (ii) due to the sufficiently large stress amplitude. It is the reason that the curves for frequencies of 0.1 Hz and 0.01 Hz end at a lower stress amplitude than the other curves. In **Figs. 9.6** and **9.7**, the influence of corrosion on the finite fatigue life can be seen. For high frequencies ($f \geqslant 10^3$ Hz), the corrosion has a weak effect, its endurance limit is not significantly aggrieved; for the medium frequencies (10 Hz $< f < 10^2$ Hz), the corrosion and the fatigue limit have a considerable interaction; for low frequencies ($f \leqslant 1$ Hz), the corrosion has a crucial effect owing to the long loading time. After the sufficient time of species diffusion, the residual fatigue limit dominates the further fatigue.

9.3.4 Influences of Stress Ratio

In cases concerning the fatigue due to the cyclical workload, the stress ratio $R = \sigma_{min}/\sigma_{max}$ also affects fatigue endurance. With the damage model applied in this work, only the stress amplitudes exceeding the material fatigue limit contribute to the damage. Since only the maximal and minimal stresses in the cycle sequence will be considered, if the magnitude of stress peak is below the fatigue limit, the yield condition is not satisfied. According to Eqs. (9.23) and (9.30), neither the accumulated plastic strain, nor the damage accumulation due to the plasticity at
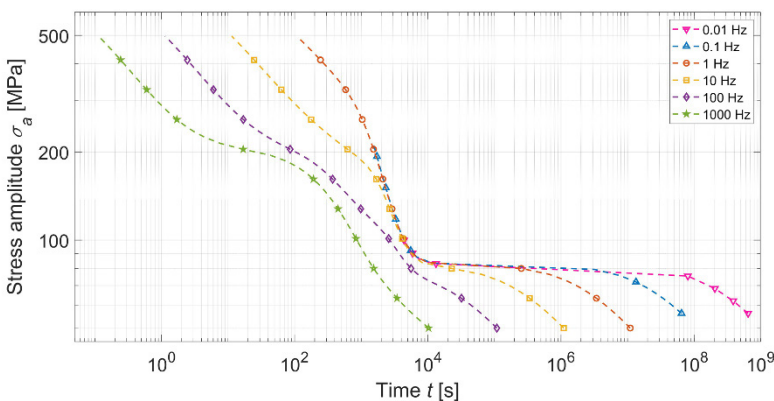
Fig. 9.7: Influence of frequency upon reduced fatigue life by hydrogen embrittlement at the time scale; the parameters are the same as in **Fig. 9.6**.

the microscale, will be considered. The solution of the elaborated two-scale model without hydrogen damage approximates the fatigue life with a fixed critical damage and fatigue limit. The results in dependence on the stress ratio are thus reliable in the coupled-field problem.

The discussions of the quantitative relationship between fatigue cycles N depending on the stress ratio R get benefit from the analytical formulation of the damage evolution in the two-scale damage model (Lemaitre et al., 1999; Murakami, 2011). Comparing the completely reverse stress ($R = -1$) and the stress ($R = 0$), the fatigue life of the latter one is the double of the former one with the equal maximal stress σ_{max}, since the minimal stress σ_{min} of repeated stress cycle does not count for the damage accumulation. As a result of the hydrogen embrittlement, the reduction of the fatigue limit, or to be precise, the reduction of the microscopic yield stress of the inclusions leads to the plastic deformation with the lower stress amplitude, which would not create damage. **Figures 9.8** and **9.9** present the maximal stress as function of the number of fatigue cycles N with different stress ratios R and with loading frequencies $f = 1\,\text{Hz}$ and $f = 1000\,\text{Hz}$, respectively. In these diagrams, the cases without chemical reactions are given as reference. It can be observed in both diagrams that the curves of the fluctuating stress ($0 < |R| < 1$) are located between the ones of stress ($R = 0$) and the ones of completely reverse stress ($R = -1$).
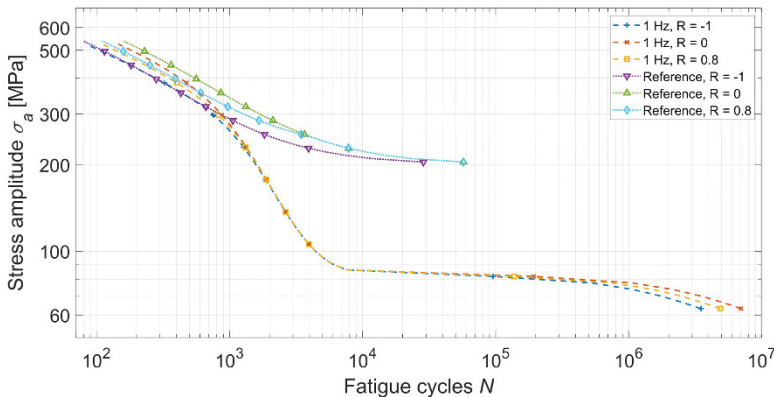
Fig. 9.8: S-N curves in dependence of the stress ratio R with a frequency of $f = 1\,\text{Hz}$.

The ratio between fatigue lives of various stress cycles with equal maximal stress is only dependent on their stress ratio in the cases, when only the mechanical stress generates damage. The chemical damage leads to a correlation between fatigue life and loading frequency, and it further results in a correlation between fatigue life and stress ratio. The significant chemical effect on low-frequency fatigue due to the long time diffusion causes the disparity in the ratio of the fatigue cycles. In the case of low cycle fatigue, the ratio of fatigue cycles under the same maximal stress between repeated stress and completely reverse stress $N(R = -1)/N(R = 0)$ is much less
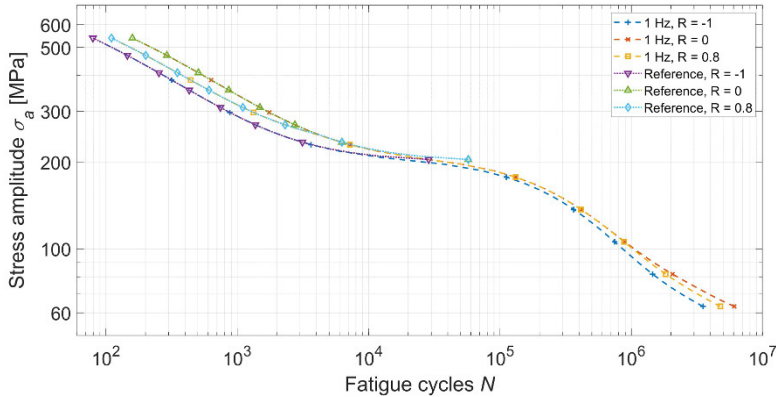
Fig. 9.9: S-N curves in dependence of the stress ratio R with a frequency of f $=$ 1000 Hz.

than the value of the issue without hydrogen embrittlement. In **Fig. 9.8**, the curves for the repeated stress approach the respective curves for the completely reverse stress in the region of low cycle fatigue, i.e., $10^3 < N < 10^5$. Please note that in this region, the reference curves for $R = 0$ and $R = -1$ show a different behaviour. This dissimilarity of the reference curves indicates the effect of hydrogen embrittlement by reducing the fatigue life. This issue results from the interaction between the damage increment dD and the critical damage D_c at the time scale. With the identical loading frequency, the workload sequence with the lower minimal stress profits from the slower damage accumulation throughout a fatigue cycle to obtain a longer fatigue life. In the meantime, the critical damage variable D_c decreases with the further elapsing time. It leads to the differentiation of $N(R = -1)/N(R = 0)$ from the principal value. The curves of fatigue with a frequency of f $= 1000$ Hz in **Fig. 9.9** show a similar behaviour as the reference points since the hydrogen embrittlement has a weak effect. Moreover, in both diagrams, **Figs. 9.8** and **9.9**, the curves of the fluctuating stress with the stress ratio $R = 0.8$ approach – for $N > 10^3$ – the curves for $R = 0$. Concluding, the obtained results are dependent on (i) the stress ratio, (ii) the initial fatigue limit, and also on (iii) the maximal stress. For the initial fatigue limit $\sigma_{F0} = 200$ MPa with the stress ratio $R = 0.8$, it can be seen that – if the maximal stress σ_{max} is equal or lower than 250 MPa – the minimum stress does not produce damage. Hence, the reference points for $R = 0.8$ and for $R = 0$ are coincident for $\sigma_{max} = 250$ MPa. The similar results can be obtained for the cases containing hydrogen embrittlement. However, these curves have different progression at a certain point of fatigue life for $N > 10^4$. It can be observed in **Figs. 9.8** and **9.9** that (i) for f $= 1$ Hz, the different run of the curves starts at $N \approx 10^5$, i.e., at t $\approx 10^5$ s and (ii) for f $= 1000$ Hz, it starts at $N \approx 10^6$, i.e., at t $\approx 10^3$ s. This difference in time results from the different maximal stresses, i.e., the different stress amplitudes. In further runs of the curves, the values of the ratios between fatigue lives $N(R = 0)/N(R = -1)$ and $N(R = 0.8)/N(R = -1)$ converge to the values

of the cases without the chemical damage. This is the case as the fatigue limit also converges to its lower limit. In our model, the fatigue strength of around 200 MPa is approached after around 10^4 cycles, which results from using parameters from the literature, see **Table 9.3**. The transition to the fatigue strength can be shifted by adjusting the damage strength S.

9.4 Conclusions

In this research, we postulated a coupled approach between the hydrogen evolution kinetics and the microscopic damage development, where the hydrogen diffusion and the microscopic plasticity are considered, respectively. The failure criterion results from the concept of continuum damage mechanics by defining the critical damage variable D_c as the threshold. The size of the representative volume element (RVE) serves as the critical crack length since the elements at the metal surface undergo the crucial chemical attack. The moment of failure is governed by both, the damage accumulation and the decrease of the critical damage variable. The damage evolution and the critical damage are affected by the hydrogen absorption kinetic since the reduced fatigue limit depends on the uniform hydrogen concentration within the RVE. Furthermore, the quantity of the dimensionless hydrogen concentration in the RVE is restrained by the material-dependent absorption capability and the diffusion length where they determine the maximal concentration and the concentration profile, respectively. The frequency of the workload has an influence on the fatigue comprising the simultaneous chemical attack. This leads to the difference of the S-N curves in the region of high cycle fatigue due to the hydrogen diffusion. The higher the loading frequency is, the weaker effect has the hydrogen embrittlement. Additionally to the stress frequency, also the stress ratio has a significant effect on the fatigue life. The longer fatigue life time promotes the hydrogen embrittlement to affect both, the damage accumulation and the damage threshold by reducing the fatigue limit.

Further work will concentrate on determining the parameters of the model by appropriate experiments, the extension to general geometries and loading situations by using the finite element method and including other corrosion mechanisms as for example contact corrosion. The latter is especially important for multi-material components.

9.5 Appendix

Let us discuss an analytical solution of hydrogen adsorption. According to Eqs. (9.5) to (9.19), the detailed expression of the Crank-Nicolson Method

$$
\begin{aligned}
\Theta_i + \tau \cdot \Big\{ \Big(\overrightarrow{k_1} + \overleftarrow{k_{-2}} + k_{-4} X_{0,i} \Big) - \Big[\overrightarrow{k_1} + \overleftarrow{k_{-1}} + \overrightarrow{k_2} \\
+ \overleftarrow{k_{-2}} + k_4 (1 - X_{0,i}) + k_{-4} X_{0,i+1} \Big] \Theta_i \Big\} \\
= \Theta_{i+1} - \tau \cdot \Big\{ \Big(\overrightarrow{k_1} + \overleftarrow{k_{-2}} + k_{-4} X_{0,i} \Big) - \Big[\overrightarrow{k_1} + \overleftarrow{k_{-1}} + \overrightarrow{k_2} \\
+ \overleftarrow{k_{-2}} + k_4 (1 - X_{0,i+1}) + k_{-4} X_{0,i+1} \Big] \Theta_{i+1} \Big\}
\end{aligned}
\tag{9.37}
$$

shows a progressing relationship of the hydrogen adsorption. By setting the initial condition $(\Theta_1 = 0, X_{0,1} = 0)$ into Eq. (9.37), the value at the next time step is then given. The explicit expression of the hydrogen adsorption rate at the new step Θ_{i+1} is then determined by Eqs. (9.18) and (9.37)

$$
\mathbb{F} = K_1 \cdot \Theta_{i+1} + \frac{k_4 (k_{-4} - k_4) \cdot \tau \cdot \Theta_{i+1} - k_4 k_{-4} \cdot \tau \cdot \Theta_{i+1}^2}{\dfrac{D_H \cdot \rho_{el}}{F \sqrt{\pi D_H t}} + k_4 \Theta_{i+1} + k_{-4} (1 - \Theta_{i+1})}
\tag{9.38}
$$

where

$$
\mathbb{F} = \Theta_i + \tau \cdot \Big\{ \Big(\overrightarrow{k_1} + \overleftarrow{k_{-2}} + k_{-4} X_{0,i} \Big) - \Big[\overrightarrow{k_1} + \overleftarrow{k_{-1}} + \overrightarrow{k_2} + \overleftarrow{k_{-2}} \\
+ k_4 (1 - X_{0,i}) + k_{-4} X_{0,i+1} \Big] \Theta_i \Big\} + \tau \cdot (\overrightarrow{k_1} + \overleftarrow{k_{-2}}).
\tag{9.39}
$$

Equation (9.38) is then expressed by the parabolic equation

$$
\mathbb{A} \cdot \Theta_{i+1}^2 + \mathbb{B} \cdot \Theta_{i+1} + \mathbb{C} = 0
\tag{9.40}
$$

where the explicit solution can be obtained by

$$
\Theta_{i+1} = \frac{-\mathbb{B} \pm \sqrt{\mathbb{B}^2 - 4 \mathbb{A} \mathbb{C}}}{2 \mathbb{A}}
\tag{9.41}
$$

where

$$\mathbb{A} = (K_1 - \tau \cdot k_4)(k_4 - k_{-4})$$

$$\mathbb{B} = \left[K_1 \left(\frac{D_H \rho_{el}}{F\sqrt{\pi D_H t}} + k_{-4} \right) - \tau \cdot k_4 k_{-4} - \mathbb{F}(k_4 - k_{-4}) \right] \qquad (9.42)$$

$$\mathbb{C} = \mathbb{F} \left(\frac{D_H \rho_{el}}{F\sqrt{\pi D_H t}} + k_{-4} \right).$$

Finally, the dimensionless concentration $X_{0,i+1}$ at the next time step can then be determined.

References

Berveiller M, Zaoui A (1985) Self-consistent schemes for heterogeneous solid mechanics. Journal of rheology 29(2):236–237

Bonora N, Gentile D, Pirondi A, Newaz G (2005) Ductile damage evolution under triaxial state of stress: theory and experiments. International Journal of Plasticity 21(5):981–1007

Chaboche JL (1988a) Continuum damage mechanics: Part i—general concepts. Journal of Applied Mechanics 55(1):59–64

Chaboche JL (1988b) Continuum damage mechanics: Part II—damage growth, crack initiation, and crack growth. Journal of Applied Mechanics 55(1):65–72

Ćwiek J (2010) Prevention methods against hydrogen degradation of steel. Journal of Achievements in Materials and Manufacturing Engineering 43(1):214–221

Eshelby J (1957) The determination of the elastic field of an ellipsoidal inclusion, and related problems. Proceedings of the Royal Society of London Series A Mathematical and Physical Sciences 241(1226):376–396

Fontana MG (2005) *Corrosion Engineering*. US: McGraw-Hill;

Gerard B, Pijaudier-Cabot G, Laborderie C (1998) Coupled diffusion-damage modelling and the implications on failure due to strain localisation. International Journal of Solids and Structures 35(31):4107 – 4120

Hamann C (2007) Electrochemistry. Wiley-VCH, Weinheim

Harrington D, Conway B (1987) ac impedance of faradaic reactions involving electrosorbed intermediates—i. kinetic theory. Electrochimica Acta 32(12):1703–1712

Johnson HH, Morlet JG, Troiano AR (1958) Hydrogen, crack initiation, and delayed failure in steel. Trans Met Soc AIME 212

Kröner E (1961) On the plastic deformation of polycrystals. Acta Metallurgica 9:155–161

Lasia A (1993) Study of electrode activities towards the hydrogen evolution reaction by a.c. impedance spectroscopy. International Journal of Hydrogen Energy 18(7):557–560

Lasia A, Grégoire D (1995) General model of electrochemical hydrogen absorption into metals. Journal of The Electrochemical Society 142(10):3393

Lasia A, Rami A (1990) Kinetics of hydrogen evolution on nickel electrodes. Journal of Electroanalytical Chemistry and Interfacial Electrochemistry 294(1-2):123–141

Lemaitre J (1996) A Course on Damage Mechanics. Springer Berlin Heidelberg

Lemaitre J, Desmorat R (2005) Engineering Damage Mechanics. Springer-Verlag

Lemaitre J, Sermage JP (1997) One damage law for different mechanisms. Computational Mechanics 20(1-2):84–88

Lemaitre J, Sermage J, Desmorat R (1999) A two scale damage concept applied to fatigue. International Journal of Fracture 97(1/4):67–81

Lynch S (2012) Hydrogen embrittlement phenomena and mechanisms. Corrosion Reviews 30(3-4)

Malvern LE (1969) Introduction to the Mechanics of a Continuous Medium. Englewood Cliffs, NJ: Prentice-Hall, c 1969

Murakami S (2011) Elastic-plastic damage. In: Continuum Damage Mechanics, Springer Netherlands, pp 141–200

Murakami Y, Yamabe J, Matsunaga H (2013) Microscopic mechanism of hydrogen embrittlement in fatigue and fracture. Key Engineering Materials 592-593:3–13

Ogata T (2010) Hydrogen environment embrittlement evaluation in fatigue properties of stainless steel sus304l at cryogenic temperatures. AIP Conference Proceedings 1219(1):25–32

Ogata T (2012) Influence of high pressure hydrogen environment on tensile and fatigue properties of stainless steels at low temperatures. AIP Conference Proceedings 1435(1):39–46

Zhao X, Ma L (2009) Recent progress in hydrogen storage alloys for nickel/metal hydride secondary batteries. International Journal of Hydrogen Energy 34(11):4788–4796

Chapter 10
A Thermodynamics-Based Wear Model and its Application with the Finite Element Analysis

Robert Tandler and Ulrich Gabbert

Abstract In the paper a generalized wear equation for sliding solid bodies at contact is derived from the fundamental law of thermodynamics. The wear model consists of a physical correlation between the wear, the binding potential of the materials in the contact area and the work done by friction in the tribological system. The wear model is based on the knowledge of material parameters of the bodies in sliding contact which can only be derived from measurements. The application of the wear model for analyzing industrial problems requires a powerful numerical solution approach. The finite element analysis (FEA) is a customary and widespread applied simulation approach in industry. Consequently, it is obvious to include the developed wear model into the frame of a commercial FEA software tool, where the FEA software Abaqus is used in the paper. Finally, as a complex industrial application problem the wear of automotive timing chains is presented. The simulated numerical wear results are compared with measurements at engines after mileage of about 50000 km.

10.1 Introduction

Friction and wear are important issues in technical systems influencing the quality of a product, such as the operation accuracy, the safety, the energy consumption as well as the life span of the product and its environmental compatibility. Wear is designated as a progressive loss of material at a solid body's surface caused from

Robert Tandler
BMW Group München, Germany,
e-mail: robert.tandler@bmw.de

Ulrich Gabbert
Lehrstuhl für Numerische Mechanik, Institut für Mechanik, Fakultät für Maschinenbau, Otto-von-Guericke-Universität Magdeburg, 39106 Magdeburg, Germany,
e-mail: ulrich.gabbert@ovgu.de

contact and relative movement with an opposing body. Such undesired change of the surface is very typical at bearings, clutches, gears and transmissions, chain drives, valve drives etc. The wear modifies the geometry of a component, influences its function and can lead to failures which affect the safety of a technical system. The reduction of wear is an important option to increase the life span of technical systems and to reduce costs. The wear is caused by several physical phenomena, such as adhesive and abrasive processes as well as a complete surface breakdown. An adhesive wear is mainly caused by an inadequate lubrication such that the surfaces in contact adhere. In a sliding motion the surface layers are sheared off such that material is being removed. An abrasive wear occurs if particles or roughness peaks of the material of one surface penetrate the boundary layer of the opposite surface which results in a micro scratching. For more details we refer to Ludema (1996); Sommer et al. (2018); Stolarski (1999). In the paper the focus is set on a numerical simulation of the wear process, which is based on an analytical wear model. Many wear models with respect to a generated wear volume are based on the equations of Holm-Archard (Archard, 1953; Holm, 1967) and Fleischer (Fleischer, 1973, 1990). There is a large variety of further wear equations available in the literature, which depend on numerous nonphysical parameters. For example, Beckmann et al. (1986) developed a conceptional approach to determine a wear equation. For applications with mainly stationary periodic sliding, Páczelt and Mróz (2010, 2015) have developed a wear model, where Coulombs friction law holds. Antusch (2008) investigated a correlation between wear and friction in his experiments. These measurements are done for fresh oil as well as for soot contaminated diesel oil. Popov (2017) stated an important influence of the surface roughness on the wear process in a system. For an overview about several other wear models we refer to the PhD thesis of Tandler (2020). For the numerical simulation of wear processes in engineering applications the finite element (FE) method is ideally suited. Põdra and Andersson (1999) as well as Mukras et al. (2009) describe FE-simulations with an underlying wear model. In these simulations the nodes of the finite element mesh are moved if wear occurs. Schmidt et al. (2018) describe a FE approach to simulate the wear of tilted shaft bearings.

In this paper the focus is set on the development of a stringent physically based wear model and its numerical realization with help of a FEA software tool. But, such a model can only be trustworthy applied if reliable input data from measurements are available. In Sect. 10.4 the required measurements are described briefly without going into the details. An overview of tribological measurements can be found in the textbooks Ludema (1996); Sommer et al. (2018); Stolarski (1999).

The paper is organized as follows. In Sect. 10.2 a generalized wear equation is derived from thermo-mechanical considerations. It is interesting that the result is in a general agreement with the early work of Fleischer (1973). In order to calculate the wear in industrial applications the wear equation has been embedded in a finite element analysis (FEA) software tool, where Abaqus CAE is used. This general approach is presented in Sect. 10.3. In Sect. 10.4 the developed approach is tested at timing chains of automotive engines. The simulation results are compared with

measured data of chains of automotive engines after different mileages up to 50000 km. A summary in Sect. 10.5 closes the paper.

10.2 Wear Equation Based on a Thermodynamics Approach

To determine a most general wear model an open system is assumed, where irreversible processes can occur. In this system a solid body is considered that slides on another solid body. This relative sliding process induces friction and wear. In the general case heat and work are transferred into the system. This leads to an increasing inner energy and kinetic energy in the system. The first law of thermodynamics in form of differentials is given as (Greiner et al., 1995)

$$dE_{kin} + dU = \delta W_{irrev} + \delta Q_{irrev}. \tag{10.1}$$

Here E_{kin} is the kinetic energy, U is the inner energy; the heat energy Q_{irrev} and the work W_{irrev} are irreversibly transferred into the system. The inner energy U for h components in a system is given by the Euler equation of thermodynamics as

$$U = TS - pV + \sum_{i=1}^{h} \mu_i N_i. \tag{10.2}$$

Here T is the temperature, S is the entropy, p is the pressure, V is the volume, μ_i describes the chemical potential and N_i is the particle count of the i-th component, respectively. It can be proven that the work and the heat energy in (10.1) are no total differentials and therefore written as δW_{irrev} and δQ_{irrev} because these physical quantities interfere with each other (Greiner et al., 1995). The difference $\delta W_{irrev} - dE_{kin}$ in Eq. (10.1) is equivalent to a dissipative work (of friction) δW_F, which cannot be converted into kinetic energy if work is applied into the system. Consequently, it remains the influence of the work of friction δW_F and the thermal energy δQ_{irrev} on the inner energy dU as

$$dU = \delta W_F + \delta Q_{irrev}. \tag{10.3}$$

Furthermore with respect to Greiner et al. (1995) for all stages of a system, including solid systems, the differential form of the Euler equation of thermodynamics holds as

$$dU = TdS - pdV + \sum_{i=1}^{h} \mu_i dN_i. \tag{10.4}$$

The pressure p is a scalar equivalent to the overlain stresses at infinite volume of the solid. An increase of the extensive state variables result in an increase of the inner energy as follows

$$U(aS, aV, a(N_i)_{i=1,...,h}) = aU(S, V, (N_i)_{i=1,...,h}), \tag{10.5}$$

where a is a scaling factor. This is verified by considering an infinitesimal change of $a = 1 + \varepsilon (\varepsilon \ll 1)$ and applying a Taylor series expansion, which is terminated after the first derivatives as follows

$$U((1+\varepsilon)S, (1+\varepsilon)V, (1+\varepsilon)(N_i)_{i=1,...,h})$$

$$= U + \frac{\partial U}{\partial S}\varepsilon S + \frac{\partial U}{\partial V}\varepsilon V + \frac{\partial U}{\partial N_1}\varepsilon N_1 + ... + \frac{\partial U}{\partial N_h}\varepsilon N_h. \tag{10.6}$$

From Eq. (10.2) it follows

$$\frac{\partial U}{\partial S} = T, \qquad \frac{\partial U}{\partial V} = -p, \qquad \frac{\partial U}{\partial N_i} = \mu_i. \tag{10.7}$$

Inserting Eq. (10.6) into Eq. (10.5) results in

$$U((1+\varepsilon)S, (1+\varepsilon)V, (1+\varepsilon)(N_i)_{i=1,...,h}) = U + \varepsilon(TS - pV + \sum_{i=1}^{h}\mu_i N_i)$$

$$= (1+\varepsilon)U = aU. \tag{10.8}$$

The total differential of Eq. (10.2) results in

$$dU = TdS - pdV + \sum_{i=1}^{h}\mu_i dN_i + SdT - Vdp + \sum_{i=1}^{h}N_i d\mu_i. \tag{10.9}$$

By coefficient comparison with Eq. (10.3) the well known Gibbs-Duhem relation follows as

$$0 = SdT - Vdp + \sum_{i=1}^{h}N_i d\mu_i. \tag{10.10}$$

The Gibbs-Duhem relation demonstrates that in a thermodynamical system the intensive state variables cannot be varied independently.

Hereafter we consider a solid body system with $h = 1$. From the Eqs. (10.3) and (10.4) it follows

$$dU = TdS - pdV + \sum_{i=1}^{h}\mu_i dN_i = \delta W_F + \delta Q_{\text{irrev}}. \tag{10.11}$$

For a macroscopic consideration of the wear the particle number N_i is expressed by a correlating volume V of a special material with the Avogadro constant $N_A = 6.02214076 \cdot 10^{-23}$ mol^{-1}, the molar mass M and a homogenous density ρ. This is used to derive a volumetric relation for the energetically relevant binding potential of the solid. If a constant material density is assumed we receive the relation

$$N_1 = \frac{\rho N_A}{M}V. \tag{10.12}$$

The infinitesimal form of Equation (10.12) is written as

$$dN_1 = \frac{\rho N_A}{M} dV. \tag{10.13}$$

Inserting Eq. (10.13) into Eq. (10.11) results in

$$TdS - pdV + \frac{\mu_1 \rho N_A}{M} dV = \delta W_F + \delta Q_{irrev}. \tag{10.14}$$

The second law of thermodynamics for an irreversible process reads as follows

$$\delta Q_{irrev} \leqslant TdS. \tag{10.15}$$

The entropy S in a system can rise without temperature change, e.g. by a wear process of a solid body. Consequently, from Eq. (10.14) it follows

$$TdS + \left(\frac{\mu_1 \rho N_A}{M} - p \right) dV - \delta W_F \leqslant TdS. \tag{10.16}$$

From Eq. (10.16) it follows

$$\left(\frac{\mu_1 \rho N_A}{M} - p \right) dV \leqslant \delta W_F. \tag{10.17}$$

Introducing a constant $\bar{k} \in R$ which is initially unknown, the Eq. (10.17) with an introduced wear volume V_W can be written as

$$\left(\frac{\mu_1 \rho N_A}{M} - p \right) dV_W = \bar{k} \delta W_F. \tag{10.18}$$

A certain part of the dissipative work of friction δW_F is equivalent to the binding potential of a solid body, represented by the chemical potential μ_1, reduced by an outlet pressure. The work of friction induces a shear stress in the contact area which leads to a local failure in the solids binding. This can be related to a produced wear volume V_W with the probability proportional to $\bar{k}$. The magnitude of p is limited by the binding potential

$$p < \frac{\mu_1 \rho N_A}{M},$$

which represents the stress limit of the material until a local breaking of the solid body occurs. Based on a different approach (Fleischer, 1973, 1990) received a similar result. In the following, Eq. (10.18) is used as a fundamental equation for modeling the wear in a solid body.

The binding potential of a material is represented by its hardness H. If the pressure p at outlet is sufficiently small in relation to the material binding potential from Eq. (10.18) we receive

$$\delta V_W = \frac{\bar{k}}{\frac{\mu_1 \rho N_A}{M} - p} \delta W_F := \frac{\bar{k}}{H} \delta W_F := k(H,\dots)\delta W_F. \qquad (10.19)$$

The physical quantity $k(H,\dots)$ has to be estimated experimentally. It is also important to determine a valid law of the work of friction in a specific system. This means an empirical adaptation of the wear model is necessary if a certain application is investigated. For a system of automotive bush chain drive systems the experimental investigations of Tandler et al. (2019) have shown that the work of friction can be approximated sufficiently accurate by Coulomb's law of friction $F_F = \mu F_N$, with the friction force F_F, the normal force F_N and the coefficient of friction μ. With the work of friction $\delta W_F = F_F ds$ from (10.19) the wear volume is received by integration as

$$V_W = \int_{s_0}^{s_1} k(H,\dots)\mu F_N ds, \qquad (10.20)$$

with the sliding path s from s_0 to s_1. Experimental investigations have shown (Tandler et al., 2019; Tandler, 2020) that the physical parameters in Eq. (10.20) are changing with time. Therefore, the integration over the sliding path is replaced by integration over time. It has also to be taken into account, that the coefficient of friction depends on the engine speed n, the kinematic viscosity η of the lubricating oil and its time dependent soot content ψ, the temperature T, the surface roughnesses R_A, R_B and the hardnesses H_A, H_B of the two surfaces A and B in contact, respectively. The wear volume of the contact partner j can be written as

$$V_{W_j} = \int_{t_0}^{t_1} k(H_j,\dots) \cdot \mu(n,\eta(T),\psi(t),R_A,R_B,H_A,H_B) \cdot F_N(n,t) \cdot \frac{ds}{dt} dt, \quad (10.21)$$

The soot is interacting with the material due to a chemical binding which could reduce the main binding potential of the material and may lead to a faster locally fatigue of the material, see Antusch (2008). This means that an increasing soot content in the oil causes more chemical bindings between the soot and the contacting surfaces of the material. This effect reduces the local binding potentials of the material and leads to a lower resistance against certain load cases, which increases the wear of the system.

10.3 Application with the Finite Element Analysis

10.3.1 Time Discretization

In order to solve Eq. (10.21) within the FE analysis the equation has to be discretized in time by introducing time increments Δt as $t \to i\Delta t$ and path increments $s \to$

$\Delta s(i\Delta t)$. Then from Eq. (10.21) it follows

$$V_{V_j} = \sum_{i=0}^{I-1} k(H_j,\ldots) \cdot \mu(n \cdot \eta(T),\ldots,\psi(i\Delta t)) \cdot F_N(n, i\Delta t) \cdot \Delta s(i\Delta t), \quad (10.22)$$

where $(I-1)$ is the total number of incremental time steps, and the i-th sliding path per time increment is defined as $\Delta s(i\Delta t) = s(((i+1)\Delta t) - s(i\Delta t))$, with $s(0) = 0$. In a FE analysis the contact surface j is normally subdivided in finite elements consisting of nodes (l). To each node (l) a contact area $A^{(l)}$ can be assigned. Then the wear depth $d^{(l)}$ can be calculated as

$$d^{(l)} = \frac{V_{V_j}}{A^{(l)}}. \quad (10.23)$$

Based on Eq. (10.23) the coordinate of the FE node (l) can be updated by shifting the node (l) in normal direction by $d^{(l)}$. In most cases of a wear analysis it can be assumed that the change of the FE coordinate $d^{(l)}$ is much smaller than the size of the assigned finite element. In this case no degeneration of the geometry of the finite element occurs. If this is not the case a remeshing of finite elements is required, which also requires a mapping of the meanwhile calculated data to the new mesh.

For solving the time discretized equation (10.22) the knowledge of all input data of the body under investigation are required at each time increment. Besides the material properties as function of time the simulation also requires the knowledge of the contact forces at each FE node in the contact area. The correct modeling of the contact conditions is a fundamental issue of the wear simulation. In the application example, presented in Sect. 10.4, it is shown how the contact forces are determined with help of a multibody simulation (MBS).

10.3.2 Contact Iteration

Independent from the specific application the modeling of the nonlinear contact conditions during the FE analysis is very decisive for receiving sufficient accurate wear results. The contact problem is nonlinear even in the frame of a linear elastic analysis and, consequently, requires another iterative solution procedure within each time increment. The contact problem is nonlinear because the regions of contact are not known in advance. If locally two surfaces are in contact, then a contact force is acting and the displacement difference of the surfaces is zero. If the displacement differences are larger than zero, then the two surfaces are separated. In this case the contact force is zero. But these situations can change with time, which makes the simulation complicated and time consuming. Only if contact forces are acting at the surfaces wear occurs. For the contact simulation in FE software tools, such as Ansys, Abaqus, Nastran etc., several well known and accepted iterative solution methods are available. The three standard methods which are available in each com-

mercial software tool are the method of Lagrange multipliers, the penalty method and the method of augmented Lagrange multipliers which can be applied to solve the contact problem (for details see Johnson, 1985; Wriggers, 2002).

10.4 The Wear Simulation of Timing Chains

As an application example in the following the wear analysis of automotive timing chains is presented. Modern combustion engines aim at high performances at low emission levels, which is especially present in the premium vehicle class. This results in high moments on the crankshaft and further in high forces in the chain links of the chain drive. The timing chain moves the camshafts as well as the balance shafts and pumps in a combustion engine. The chain wear results in an elongation of the chain, which can be as large as it cannot be compensated by the tensioning system. This can create loud noises, but in special situations the chain may jump off and causes fatale engine damages. Therefore it is important to calculate the wear of chain drive systems to receive information about the safety and the lifetime of the engine. A typical chain drive is shown in **Fig. 10.1**. In **Fig. 10.2** a detail of a chain link is illustrated. In the following we present an investigation on the wear of timing chains with coated pins and extruded hardened bushes. A detailed specification of such chains can be found in Bauer (2018).

10.4.1 Experimental Investigations

It is obvious that there are various influences on the intensity of internal chain friction during engine operation which is causing wear, such as the strand forces, the engine speed, the quality of the engine oil and its temperature as well as the viscosity of the oil and several other parameters as the surface roughness and hardness
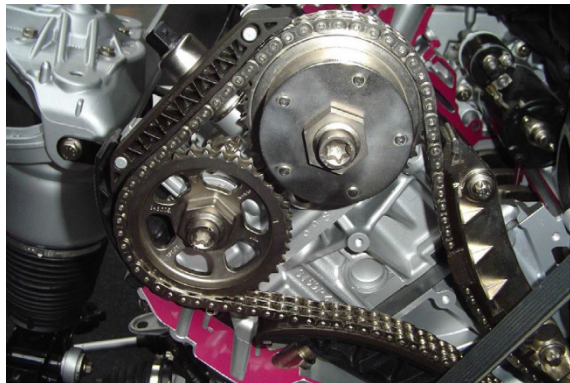
Fig. 10.1 A typical timing assembly (Ludema, 1996).
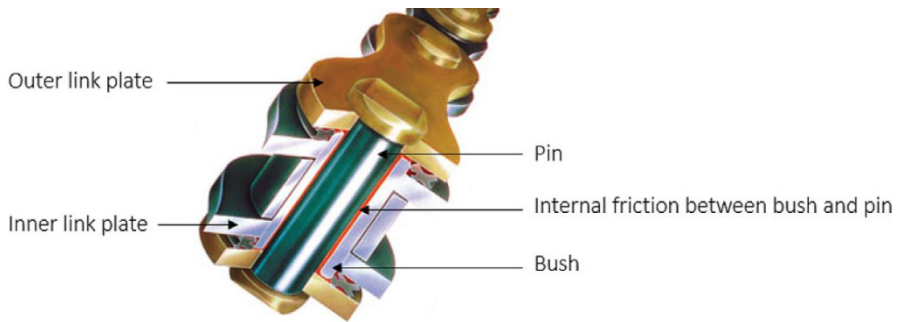
Fig. 10.2: Cross section of a chain link.

of the chain links. The strand force is defined as the specific chain tensile force in the area between two chain wheels. It is complicated to measure, but it can be received with great accuracy by multi-body simulations. The engine speed during operation is well defined, but the determination of the influences of the engine oil on the internal chain friction is not trivial, because the oil's properties change during the engine operation. The theory of Stribeck-curves is beneficial for the analysis of the measurements. It can be observed that the viscosity of the lubricating medium, the sliding speed in the contact area and the contact force in a system are important parameters. In case of the boundary lubrication the lubricating medium is displaced out of the contact area of a system. At full film lubrication the height of the lubricating medium is big enough, that there is no direct contact between the two solid bodies in the contact area. The state of mixed lubrication contains both conditions of full film lubrication and boundary lubrication.

In order to receive a reliable data basis for modelling and optimizing the wear of timing chains extensive experimental investigations are required. For this purpose a special experimental set up has been developed (see Tandler et al., 2019; Tandler, 2020, for details). It consists of the bush chain, the chain wheels, the bearings, the radial seal and the oil nozzle. An electric motor induces the torque to the chain assembly at a given engine speed, where the engine speed is verified by a measurement with a fork light barrier and slotted disc. On the driving shaft there is a torque gauge bar to detect the friction torque at each working point. Two different set-ups are used in the chain case. The first is necessary to measure the friction torque at some given working points. This torque contains all frictional effects, thus the internal friction of the bush chain, the bearings, the radial seal and the friction from the contact of the chain wheel to the bush chain. If another set-up can be found which contains all frictional effects except the internal chain friction, the internal chain friction can be determined from the difference of both measured values. Such a measurement can be done except for the friction of the contact of the chain wheel to the bush chain, which can be neglected (Tandler, 2020).

The experimental investigation provides the following essential findings and insights. The application of used oil in a bush chain drive system leads to an increased

internal chain friction and a faster onset of mixed or boundary lubrication for a corresponding engine speed. This can be seen in a comparison between the measured data of the internal chain friction versus the engine speed for the used oil and the fresh oil. This effect is aided at higher strand force and higher oil temperature. It is assumed that particles of the used engine oil get in the contact area of bush and pin, where the particles interact with the asperities of a certain contact surface. This induces additional friction in the contact area especially at higher oil temperatures. Furthermore, it is detrimental to operate such engine at elevated temperatures using used oil as opposed to fresh oil. Through a variation of the strand force with used oil at fixed temperature and engine speed the validity of Coulomb's friction law has been determined. These experimental investigations have been accompanied by a number of further special measurements such as the investigation of the surface roughness of bush and pin with help of the scanning electron microscopy (REM), the application of the laser scanning microscopy for component measurements, the determination of the surface hardness of pin and bush with help of nanoindentation methods. With the application of the radionuclide technology informations about the separate wear of pin and bush at different time steps are received. For details of the experimental investigation the interested reader is referred to Tandler (2020). These experimentally received data have been used as input data for the numerical investigations.

10.4.2 Description of the Finite Element Model

Due to the symmetry only one half of a bush chain link is required for the FE simulation. The developed finite element model is shown in **Fig. 10.3** (Tandler et al., 2020). The detailed mesh of the contact area can be observed in more detail in **Fig. 10.4**. The angle φ of the chain link to its axis is given by the geometrical design of the chain drive system. During one chain rotation the chain link passes various contours with different curvatures; where the position dependent angle changes permanently.

If a model as shown in **Fig. 10.3** is used for wear simulations for each position of the chain link during rotation the position of the chain link is required as well as the acting force. The force is changing during the chain rotation, but can be received from an elastic multi-body simulation (MBS) with a model as shown in **Fig. 10.5**. The parameters for the stiffness, the mass and the damping factor of the certain components can be received from the database of the respective vehicle manufacturer (Tandler, 2020). Only with this information the finite element model of the chain can be reduced to only one chain link as shown in **Fig. 10.3**.

For a specific position of the chain link the contact normal force at each node can be calculated during the finite element simulation with help of the given chain force. The corresponding coefficient of friction from the experimental investigations is also implemented in the model. The factor k is received from radionuclide wear measurements in a constant wear state with fresh oil. In the presented application a value of $k = 1 \cdot 10^{-10}$ mm^2/N was determined. For the simulation the ABAQUS
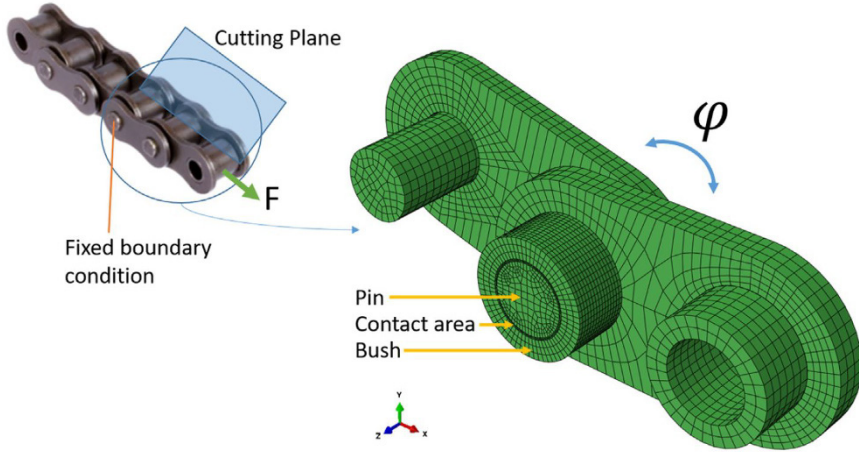
Fig. 10.3: Symmetric finite element model of a bush chain link.

Fig. 10.4 Mesh of the contact area.
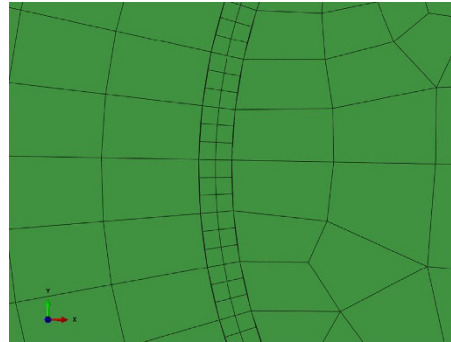
CAE software has been used. A linear element type of C3D8R and a fine mesh in the contact region (see **Fig. 10.4**) are applied to obtain sufficiently accurate values concerning the contact normal force and the contact sliding. This is required because the circular contour of the contact area has to be described numerically with a polygon, meaning that smaller edges of the elements lead to a better approximation of a circle. Another reason of the applied fine mesh with element edge size of $\approx 60\,\mu m$ in the contact area is that also topographically measured initial surface structures can be embedded into the model. But, a continuous overall mesh with such an element size would cause high computational times in the dynamic implicit simulation and consequently a TIE-contact has been used at the bush and the pin to couple a coarse meshed part outside the contact area with a fine meshed part in the contact region.

The proper mesh density and the contact approach have been developed with help of several test simulations in order to find a compromise between computa-
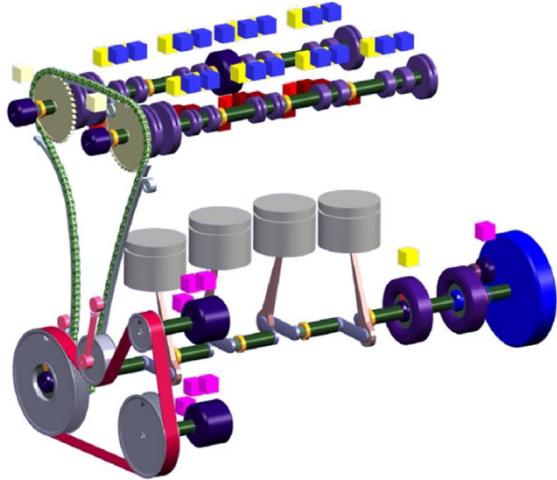
Fig. 10.5 MBS model of a
chain drive system.

tional time and sufficient solution accuracy. In **Fig. 10.6** two meshing variants are
compared. It can be seen that an overall very fine FE mesh in the contact area does
not provide much better results as the TIE coupling of the mesh in the contact area
with a coarser FE mesh.
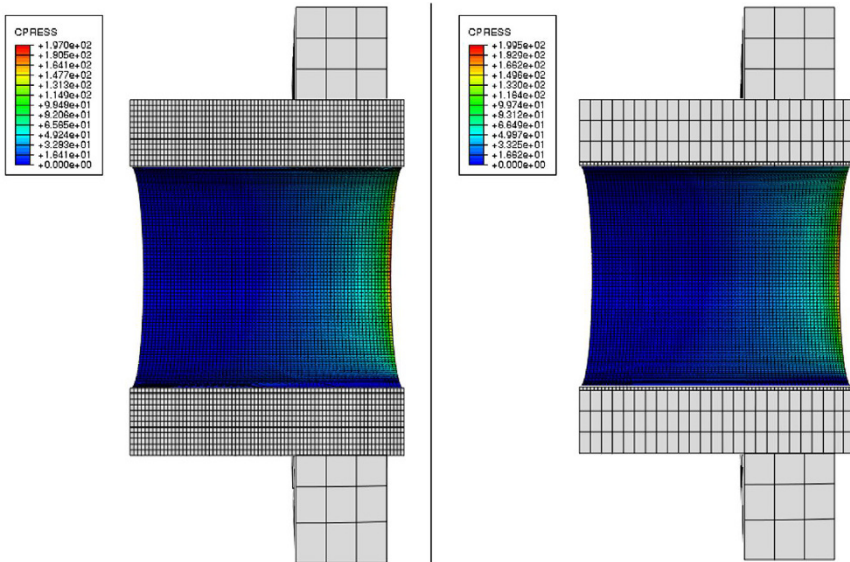
Fig. 10.6: Comparison of the pressure at the surface of the bush calculated with a uniform fine
mesh (left) and a coarse mesh coupled with TIE contact (right).

For the realization of the sliding contact between pin and bush the penalty method has been used. Other methods have been also tested. The method of Lagrange multipliers results in a large increase of the system of equations, since at each potential node of the very fine meshed contact area one additional degree of freedom – the unknown Lagrange multiplier – is introduced. This results in a huge increase of the computing time. The method of augmented Lagrange multipliers also increases the computing time because additional iterations are required to receive a converged solution. The penalty method is robust and has given sufficient accurate solutions without any additional computational time. But the application of the penalty method requires a proper selection of the penalty factor; if it is too small the constrained conditions are not sufficiently enough fulfilled. An increasing penalty factor results in an increasing loss of leading digits in the numerical calculation of the displacements, which is particularly critical if single precision real words are used during the calculation. A too large penalty number can finally result in an unsolvable singular system of equations. Several tests have demonstrated that in the given application a penalty number of only $2 \cdot 10^2 \, K_{ii,max}$ is a good compromise between stability of the solution process and the accuracy of the fulfilment of the constrained equations. Here K_{ii} are the elements of the main diagonal of the stiffness matrix.

10.4.3 Determining an Extrapolation Factor for the Wear Simulation

Since a common chain performs many millions of rotations during its lifetime it is important to determine an extrapolation factor for the simulation to get realistic computational times. To investigate this, convergence studies have been performed. The aim was to find a critical wear depth at the nodes of the contact area for each simulation step such that numerical stability holds and still physically reasonable results are received. Extrapolation means that at a given simulation step the wear depth after one complete chain rotation is calculated at each node. The wear depth is multiplied with an extrapolation factor (the number of chain rotations) and with this extrapolated wear depth the new geometry is determined. With this new generated mesh the next step – the simulation of a full chain rotation – is performed. This is done as often as the necessary number of total chain rotations is reached. As an example in **Fig. 10.7** the wear depth at the surface of the pin after 1.8 million chain rotations is presented which were calculated with different extrapolation factors. For the presented example it turns out that a sufficient accurate result can be calculated with acceptable computational times with extrapolation factors between 100000 and 200000. With an extrapolation factor of 200000 in the given example the error is limited to be smaller than 5% after 4000000 chain rotations in comparison to the most refined solution (a) in Fig **10.7**. If a completely different chain design with different tribological features has to be simulated, it would be necessary to recalculate the extrapolation factor.
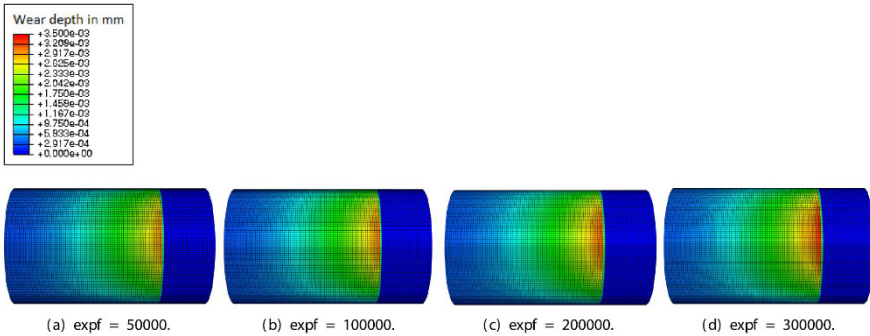
Fig. 10.7: Wear after 1.8 million chain rotations calculated with different extrapolation factors.

10.4.4 Comparison of the Numerical Results with Measurements

The presented simulation approach has been used to calculate the wear on timing chains of two test vehicles with a mileage of about 50000 km and a 75% partial-load range. The simulation results are compared with measurements of the real part chains. The wear factor k used in the simulation was estimated in advance for both applied timing chains with help of RNT measurements. The numerical results of the chain type with extruded bushes were generated with wear simulations of 90 chain rotations and extrapolations with a factor of 2000000. The total simulation time was 270 h on a computer system with a computational power of 8×3.6 GHz. The simulation confirms a contact opening on the unloaded surface of pin and bush. It can be observed that the maximum wear depth occurs at peak load in the simulation. The topographical profile of the pins worn area is measured with laser microscopy. **Figure 10.8** shows a comparison of the simulation results with measurements.

In the contact area of bush and pin, a smooth mirror-like area can be observed, which is characterised by an almost constant surface pressure during engine operation. The simulated and the measured wear depths show a good agreement. In **Fig. 10.8** a major difference between the simulated and the measured curve at the edge of the pins contact area is observed. The reason is that the ends of the bush in reality show an edge rounding which is not included in the FE model.

10.5 Summary

In the paper a theoretical wear model based on the fundamental principles of thermo-mechanics is developed. In this model the wear is calculated by taking into account the binding potential of the materials in the contact area and the work of friction. It depends on several physical data, such as the hardness, the roughness of the bodies, the contact forces, the friction coefficient, the velocity of the sliding
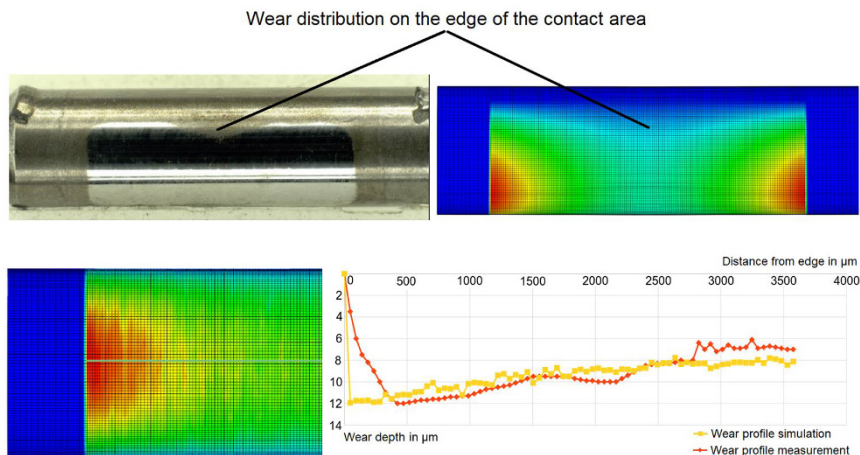
Fig. 10.8: Comparison of the measured and simulated wear for two different bush chains after a mileage of 50000 km.
Above: Comparison of the wear mirror at the pin of an extruded bush chain.
Below: Comparison of the wear depth along the pin surface for a wrapped bush chain.

bodies in contact, the quality of the lubricant, especially the soot content has shown to be an important factor, the temperature etc. Based on experimental investigations the required time depended input data of the model have to be estimated. For the application of the proposed wear model to real engineering problems it should be included into a FEA simulation process. In the paper the wear approach is implemented in the commercial FEA software tool ABAQUS CAE. For demonstrating the engineering application the wear of a timing chain of automotive engines is presented. It is shown that half of one chain link only is enough to receive the complete behaviour of the chain. But in this case it is required to know the time varying positions of the chain link in space and time as well as the chain forces at all positions during the chain rotation in the steady state. These data can be received from multibody simulations of the chain drive system including all relevant auxiliary units. The quality of the developed FE model has been ensured by numerous convergence studies with respect to the mesh density and the contact formulation. The calculated wear depth of a real engine chain drive has been examined by a comparison of the simulation results with measurements at test vehicles after different mileages. It is demonstrated that even after vehicle mileage of about 50000 km the simulation results are in a good agreement with measurements. In ongoing investigations the finite element model and the contact formulation are further improved to obtain lower computational costs with an increasing accuracy. Additionally the simulations will be applied to different fields of applications, such as bearings, clutches, gears, transmissions, valve drives etc.

References

Antusch S (2008) Untersuchungen zum Einfluss von Ruß im Öl auf den Motorenverschleiß. PhD thesis, Karlsruhe Institute of Technology, Karlsruhe

Archard JF (1953) Contact and rubbing of flat surfaces. Journal of Applied Physics 24(8):981–988

Bauer P (2018) Kettensteuertriebe - Stand der Technik, Anwendungen, Entwicklung und Herstellung, Die Bibliothek der Technik, vol 353, 2nd edn. Verlag Moderne Industrie, München

Beckmann G, Dierich P, Grau P, Petzold M, Fröhlich F (1986) A representation of the microhardness distribution and its consequences for wear prognoses. Wear 107(3):195–212

Fleischer G (1973) Energetische Methode der Bestimmung des Verschleißes. Schmierungstechnik 9(4):269–274

Fleischer G (1990) Zur Energetik der Reibung. Wissenschaftliche Zeitschrift der Technischen Universität Otto von Guericke Magdeburg 34(8):55–66

Greiner W, Neise L, Stöcker H (1995) Thermodynamics and Statistical Mechanics. Classical Theoretical Physics, Springer, New York

Holm R (1967) Electric Contacts - Theory and Application, 4th edn. Springer, Berlin-Heidelberg

Johnson KL (1985) Contact Mechanics. Cambridge University Press, Cambridge

Ludema KC (1996) Friction, Wear, Lubrication – A Textbook in Tribology. CRC Press LLC

Mukras S, Kim NH, Sawyer WG, Jackson DB, Bergquist LW (2009) Numerical integration schemes and parallel computation for wear prediction using finite element method. Wear 266(7):822–831

Põdra P, Andersson S (1999) Simulating sliding wear with finite element method. Tribology International 32(2):71–81

Páczelt I, Mróz Z (2010) Variational approach to the analysis of steady-state thermo-elastic wear regimes. International Journal for Numerical Methods in Engineering 81(6):728–760

Páczelt I, Mróz Z (2015) Analysis of thermo-mechanical wear problems for reciprocal punch sliding. Advances in Engineering Software 80:139–155

Popov VL (2017) Contact Mechanics and Friction - Physical Principles and Applications, 2nd edn. Springer, Berlin-Heidelberg

Schmidt AA, Schmidt T, Grabherr O, Bartel D (2018) Transient wear simulation based on three-dimensional finite element analysis for a dry running tilted shaft-bushing bearing. Wear 408-409:171–179

Sommer K, Heinz R, Schöfer J (2018) Verschleiß metallischer Werkstoffe, 3rd edn. Springer, Wiesbaden

Stolarski T (1999) Tribology in Machine Design. Butterworth-Heinemann

Tandler R (2020) Pysikalisch motiviertes Verschleißmodell für Kettentriebe in PKW-Motoren. PhD thesis, Otto von Guericke University, Magdeburg, Shaker Verlag

Tandler R, Bohn N, Gabbert U, Woschke E (2019) Experimental investigations of the internal friction in automotive bush chain drive systems. Tribology International 140:105,871

Tandler R, Bohn N, Gabbert U, Woschke E (2020) Analytical wear model and its application for the wear simulation in automotive bush chain drive systems. Wear 446-447:203,193

Wriggers P (2002) Computational Contact Mechanics. John Wiley & Sons Ltd.

Chapter 11

Discrete Description of Crack Kinematics in Regularized Free Discontinuities of Crack Faces

Bo Yin, Johannes Storm, and Michael Kaliske

Abstract The fracture mechanical free discontinuity problem can be associated with a generalized, variational approach of GRIFFITH's fracture theory. By introducing a regularization for the sharp displacement discontinuity at cracks and crack surfaces, stable computational fracture models are developed, e.g., the phase-field fracture formulation and the eigenfracture approach. The presented work summarizes recent findings regarding unrealistic deformation kinematics at cracks predicted by conventional formulations of both models and introduces the variational framework of *Representative Crack Element* to overcome these discrepancies. Illustrative examples for crack propagation and post-fracture behavior at small and finite deformations, brittle and cohesive failure as well as for rate-dependent materials frictional crack contact demonstrate the flexibility and the generality of of the introduced *Representative Crack Element*.

Key words: Free discontinuity, Eigenfracture, Phase-field fracture, Representative crack element

11.1 Introduction

The research on material failure, including strain softening, brittle rupture, cohesive delamination, and fatigue aging, is becoming an area of increasing interest in engineering application. A number of failure mechanisms is identified and a variety of criteria are postulated to effectively predict material strength within a safe and controllable application. To provide a reliable prediction, crack initiation, propagation, kinking, and branching studies are of importance and necessity. Meanwhile, crack deformation kinematics during fracture evolution plays an equivalent role as afore-

Bo Yin · Johannes Storm · Michael Kaliske
Institute for Structural Analysis, TU Dresden, 01062 Dresden, Germany,
e-mail: bo.yin@tu-dresden.de, johannes.storm@tu-dresden.de, michael.kaliske@tu-dresden.de

mentioned features during fracture evolution. Taking a closing crack deformation as one representative example, material integrity is preserved and loading normal to the crack surfaces can be fully transferred from one side to the other one through the crack surfaces. Furthermore, a relative motion of the two contacted crack faces may yield other mechanical phenomena, e.g., friction, abrasion and corrosion, which are realistically and physically featured in particular for complex and mixed load patterns. Originally inspired by experimental investigations, Griffith (1921) proposed a conceptual understanding of brittle crack formation, namely, the energetic balance between the stored strain potential and the crack forming dissipation. To depict the amount of strain energy consumed to generate a unit crack surface during fracture evolution, an important material parameter is defined, $\mathcal{G}_c$, known as the critical energy release rate or the fracture toughness. The triggering condition of fracture evolution is that the instantaneous energy $\mathcal{G}$ reaches or exceeds the critical value, i.e., $\mathcal{G} \geqslant \mathcal{G}_c$. This classical GRIFFITH fracture theory provides a physical understanding of crack nucleation and propagation criterion, but unfortunately, does not provide an explicit definition for the crack propagation path during fracture evolution.

In the past decades, a variety of numerical methods has been developed to model reliably fracture evolution. By categorizing the present models, crack approximation is numerically described by either a discrete or a continuous, smeared approach. Regarding the former one, a discrete crack methodology renders, e.g., the crack boundary as an explicit element edge within the finite element discretization. The crack-induced displacement discontinuity is, hence, naturally modeled based on the geometrical boundary. Material separation due to the existence of cracks is straightforwardly modeled for an opening or shearing crack deformation. Nevertheless, numerical complexity arises for a closing crack deformation with respect to crack surface interpenetration. To address crack contact, additional algorithmic efforts are required. The classical cohesive zone model (Barenblatt, 1962; Dugdale, 1960; Schellekens and de Borst, 1993; Alfano and Crisfield, 2001; Foulk et al., 2000; Ortiz and Pandolfi, 1999) is a representative approach of discrete crack approximation, which constitutes the traction-separation relationship based on the crack opening distance. It is intensively applied to pre-known crack path problems, unfortunately, the prediction of an unknown crack propagation largely increases computational efforts. Another concept, the configurational force method (Gurtin, 2000; Kienzler and Herrmann, 2000; Maugin, 1995; Braun, 1997; Maugin, 2010; Miehe and Gürses, 2007; Mueller and Maugin, 2002), is frequently applied to discrete crack approaches, which depicts a non-NEWTONIAN force acting on a crack tip within a homogeneous domain. The calculated material force allows for a prediction of crack growth direction and provides a crack evolving criterion. Thereafter, several approaches adopt a node splitting algorithm and an r-adaptivity re-meshing strategy to model crack propagation. Nevertheless, these methodologies are restricted by the fact that an initial notch is required to generate stress concentrations.

De Giorgi and Ambrosio (1988) have provided a general variational description through the formulation of free discontinuity problems. In general, unknown field variables are allowed to have jumps, meanwhile, the locations of the discontinuities are unknown. The existence of minimizers is successfully shown in the space of

special functions of bounded variation, see Ambrosio et al. (2000) for an overview. Although used in other contexts, free discontinuity problems can be interpreted as a generalization of GRIFFITH's criterion. However, computational solutions of free discontinuity problems are difficult and have lead to several regularized formulations, e.g., phase-field fracture and eigenfracture to name two representatives in the context of fracture mechanics. Closed form proofs exist for both methods, where the regularized models converge to the original free discontinuity problem for decreasing regularization lengths and discretization sizes, see e.g. Ambrosio and Tortorelli (1990) and Schmidt et al. (2009).

With respect to smeared crack approximation, the phase-field approach for fracture depicts a continuous and diffusive crack representation from the numerical point of view. Incorporating classical GRIFFITH's fracture theory, Francfort and Marigo (1998) formulates a brittle fracture model by thermodynamically minimizing the internal strain energy potential and the fracture energy, see also Bourdin et al. (2000, 2008); Hakim and Karma (2009); Miehe et al. (2010b); Pham et al. (2011) for detailed insights. Thereafter, several publications, e.g., Borden et al. (2014); Linse et al. (2017); Chambolle et al. (2018), study classical Γ-convergence for phase-field modeling in the field of fracture evolution. Furthermore, brittle phase-field modeling is subsequently extended to different features, e.g., rate-dependent fracture (Yin et al., 2020b; Yin and Kaliske, 2020c; Shen et al., 2019; Schänzel, 2015; Loew et al., 2019), ductile fracture (Ambati et al., 2015a; Miehe et al., 2015; Borden et al., 2016; Yin and Kaliske, 2020b), anisotropic fracture (Gültekin et al., 2018; Teichtmeister et al., 2017; Yin and Kaliske, 2020a), cohesive fracture (Verhoosel and de Borst, 2013; Vignollet et al., 2014; Nguyen and Wu, 2018; Geelen et al., 2019), and fatigue fracture (Alessi et al., 2018; Carrara et al., 2020; Seiler et al., 2020; Yin et al., 2020a), to name a few.

The much younger eigenfracture method is developed by Schmidt et al. (2009) and is applied to problems of linear elasticity and elasto-plasticity, see for instance Pandolfi and Ortiz (2012); Stochino et al. (2017); Qinami et al. (2020) for some early applications. Similar to phase-field fracture, a second field is introduced called eigenstrain in order to relax the sharp displacement jump at the crack. However, the second field is solved at the material level and equivalently the crack evolution in a post-processing step after each load step of the mechanical problem. Less degrees of freedom and a better convergence behavior yield relatively low computational costs compared to phase-field fracture. Pandolfi et al. (2021) have further demonstrated a larger Γ-convergence rate for eigenfracture versus phase-field fracture, which allows to obtain the same solution accuracy like for phase-field fracture on coarser meshes. On the other side, the eigenfracture method is still in an early development stage and further studies on the properties of the method are necessary.

The strength of the phase-field fracture and the eigenfracture method is the capability to capture crack initiation and propagation with complex patterns independent of any specific criterion. Nevertheless, one of the challenging tasks is prediction of the deformation kinematics of crack surfaces under complex loading states, e.g., opening, closing, shearing and mixed mode. A realistic determination of the material stiffness degradation considering complex crack deformation kinematics

is significantly important. In many publications, sophisticated approaches are proposed to approximate the correct crack kinematics by decompositions of the strain energy potential. A comprehensive review of existing split models can be found in Ambati et al. (2015b); Storm et al. (2020). As one common choice based upon a straightforward volumetric and deviatoric energetic decomposition, Amor et al. (2009) and Freddi and Royer-Carfagni (2009) propose the fracture driving force for volume shrinkage by excluding the volumetric energy contribution. Another commonly used split, postulated by Miehe et al. (2010a), is depending upon a spectral decomposition scheme. The strain tensor is decomposed into the eigenvalues and the elastic strain energy density is redefined by using the tensile and compressive strain components. For other representative split models, it is referred to e.g. Henry and Levine (2004); Lancioni and Royer-Carfagni (2009); Freddi and Royer-Carfagni (2010); Hesch and Weinberg (2014). Nevertheless, these models cannot yield physical crack deformations under complex loading conditions. Thereafter, several attempts are proposed to address this issue. A conceptual *Directional Decomposition* is considered by Strobl and Seelig (2016); Steinke and Kaliske (2019); Luo et al. (2021) to reformulate the strain or stress quantity by taking the local crack orientation into consideration. As a result, these models successfully address the issue of crack kinematics compared to the aforementioned V-D split and spectral split approaches. Nevertheless, the approaches are unfortunately restricted to an isotropic, linear elastic solid at small strain. The basis of the *Directional Decomposition* is formed by the local crack orientation. Applying the concept of maximum dissipation, the crack orientation can be formulated as a variational problem (Bryant and Sun, 2018). However, this minimization is non-convex and computationally hard to solve without further restrictions. Therefore, several approximation are proposed to capture crack orientation, e.g. the gradient of the phase-field (Strobl and Seelig, 2016) and the maximum principal stress direction (Steinke and Kaliske, 2019).

   With the intention to generalize the *Directional Decomposition* model and to overcome its limitations, the framework of *Representative Crack Elements (RCE)* is developed. On the basis of variational homogenization theory (Blanco et al., 2016), Storm et al. (2020) introduce the fundamental theory which allows to consistently derive realistic crack kinematics from representative discrete crack models and to transfer the overall behavior to the regularized crack models. The RCE concept is first applied to bulk materials considering anisotropic elasticity and thermoelasticity in the context of phase-field fracture. Subsequently, applications to viscoelasticity (Yin et al., 2021), crack face friction, inelastic materials and finite deformations, fully coupled thermo-mechanics (Storm et al., 2021b), cohesive fracture and eigenfracture (Storm et al., 2021a) are developed. Within the work at hand, a review of the RCE framework applied to phase-field fracture and to eigenfracture in the context of the regularized free discontinuity problem is presented. In particular, a fundamental theoretical background of the RCE framework is provided, which includes the strain kinematics for both the continuous and the RCE description. A virtual power principle is employed within the RCE to solve the unknown crack deformations within the RCE. In the sequel, the phase-field fracture and the eigenfracture modeling within an RCE framework are briefly summarized. Several

representative numerical examples have been presented to show the general applicability of the conceptual RCE modeling.

11.2 Representative Crack Elements

11.2.1 Structure and Notation

The classical *Representative Volume Element* concept bases upon the theory of homogenization. It is referred to Blanco et al. (2016) for a general summary. The principle of multi-scale virtual power, which is based on the first thermodynamical theorem, provides the theoretical foundation of homogenization theory. Meanwhile, this principle is a generalization of the HILL-MANDEL condition of stress work conservation (Hill, 1963). The work at hand adopts a similar methodology to formulate the so-called *Representative Crack Element (RCE)* framework, which on purpose incorporates a regularized approach to resolve the issues of accurate deformations kinematics in free discontinuity problems, see phase-field fracture modeling (Storm et al., 2020) and eigenfracture modeling (Storm et al., 2021a).

The fundamental derivation and illustration start from a definition of the basic notational description. Two classes of mathematical fonts, namely, a standard one and a fraktur one, are used to depict the quantities of the regularized fracture model and of the RCE model, respectively. Explicitly, the symbols

$$\mathfrak{G}\big|_{\mathfrak{x}} = \nabla_{\mathfrak{x}}\mathfrak{u} \qquad \text{and} \qquad \mathsf{G}\big|_{\mathbf{x}} = \nabla_{\mathbf{x}}\mathbf{u} \tag{11.1}$$

are the general spatial gradient terms of $\mathfrak{u}$ and $\mathbf{u}$ with respect to the RCE and the continuous descriptions, respectively. A schematic depiction of an RCE motion is shown in **Fig. 11.1** including the reference and deformed RCE blocks. The crack
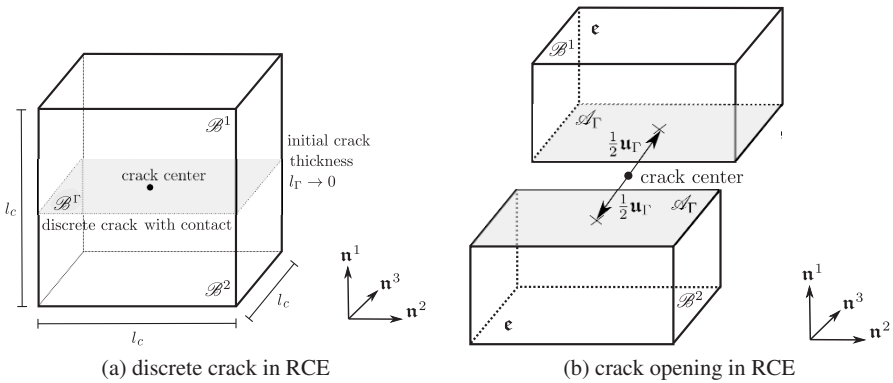

Fig. 11.1: Schematic description of crack kinematics of the RCE approach.

displacement in the RCE is denoted as

$$\mathbf{u}_\Gamma = \sum_{I=1}^{3} u_\Gamma^I \mathbf{n}^I, \tag{11.2}$$

where the normal and tangential unit vectors with respect to the crack surface are expressed by $\mathbf{n}^1$ and $\mathbf{n}^{2,3}$, respectively. Two important conditions

- linear boundary constraints of upper and lower block surfaces in respective $\mathcal{B}^1$ and $\mathcal{B}^2$,
- identical and homogeneous deformations of upper and lower blocks in respective $\mathcal{B}^1$ and $\mathcal{B}^2$, and also homogeneous crack deformation in $\mathcal{B}^\Gamma$

provide basic assumptions for the understanding and the derivation of the kinematics in an RCE. The dimensional length of the RCE is given as l_c and the two identical solid blocks ($\mathcal{B}^1$ for the upper one and $\mathcal{B}^2$ for the lower one) have the volumes $\mathcal{V}^1 = \mathcal{V}^2 = l_c^3/2$. In addition to the two solid subdomains $\mathcal{B}^1, \mathcal{B}^2$, another subdomain is characterized by the crack space $\mathcal{B}^\Gamma$, where the infinitesimal thickness of the crack space is assumed to be $l_\Gamma \to 0$. Hence, the cross-sectional area and the volume of the crack subdomain are approximated by $\mathcal{A}_\Gamma = l_c^2$ and $\mathcal{V}^\Gamma = \mathcal{A}_\Gamma l_\Gamma = l_c^2 l_\Gamma$, respectively. The total domain is expressed as $\mathcal{B} = \mathcal{B}^1 \cup \mathcal{B}^2 \cup \mathcal{B}^\Gamma$, and the entire volume of an RCE is $\mathcal{V} = \mathcal{V}^1 + \mathcal{V}^2 + \mathcal{V}^\Gamma$.

11.2.2 Kinematic Coupling

The fundamental coupling relation of the regularized fracture model and the RCE reads

$$\mathbf{u} = \mathbf{u} + \mathbf{G}\big|_\mathbf{x} \cdot \left(\boldsymbol{\mathfrak{X}} - \hat{\boldsymbol{\mathfrak{X}}}^{\text{ref}} \right) + \tilde{\mathbf{u}}. \tag{11.3}$$

Considering the homogeneous deformation fields at the RCE, the displacement fields at the three subdomains are given by

$$\mathbf{u} = \begin{cases} \hat{\mathbf{u}}^1 + \boldsymbol{\mathfrak{G}}_b\big|_{\boldsymbol{\mathfrak{X}}} \cdot \left(\boldsymbol{\mathfrak{X}} - \hat{\boldsymbol{\mathfrak{X}}}^{\text{ref}} \right) = \hat{\mathbf{u}}^1 + \left(\mathbf{G}\big|_\mathbf{x} + \tilde{\boldsymbol{\mathfrak{G}}}_b\big|_{\boldsymbol{\mathfrak{X}}} \right) \cdot \left(\boldsymbol{\mathfrak{X}} - \hat{\boldsymbol{\mathfrak{X}}}^{\text{ref}} \right), & \forall \boldsymbol{\mathfrak{X}} \in \mathcal{B}^1, \\ \hat{\mathbf{u}}^2 + \boldsymbol{\mathfrak{G}}_b\big|_{\boldsymbol{\mathfrak{X}}} \cdot \left(\boldsymbol{\mathfrak{X}} - \hat{\boldsymbol{\mathfrak{X}}}^{\text{ref}} \right) = \hat{\mathbf{u}}^2 + \left(\mathbf{G}\big|_\mathbf{x} + \tilde{\boldsymbol{\mathfrak{G}}}_b\big|_{\boldsymbol{\mathfrak{X}}} \right) \cdot \left(\boldsymbol{\mathfrak{X}} - \hat{\boldsymbol{\mathfrak{X}}}^{\text{ref}} \right), & \forall \boldsymbol{\mathfrak{X}} \in \mathcal{B}^2, \\ \hat{\mathbf{u}}_\Gamma + \boldsymbol{\mathfrak{G}}_\Gamma\big|_{\boldsymbol{\mathfrak{X}}} \cdot \left(\boldsymbol{\mathfrak{X}} - \hat{\boldsymbol{\mathfrak{X}}}^{\text{ref}} \right) = \hat{\mathbf{u}}_\Gamma + \left(\mathbf{G}\big|_\mathbf{x} + \tilde{\boldsymbol{\mathfrak{G}}}_\Gamma\big|_{\boldsymbol{\mathfrak{X}}} \right) \cdot \left(\boldsymbol{\mathfrak{X}} - \hat{\boldsymbol{\mathfrak{X}}}^{\text{ref}} \right), & \forall \boldsymbol{\mathfrak{X}} \in \mathcal{B}^\Gamma, \end{cases} \tag{11.4}$$

where the quantities $\hat{\mathbf{u}}^1$, $\hat{\mathbf{u}}^2$ and $\hat{\mathbf{u}}_\Gamma$ are the rigid body translations of the three subdomains. The reference coordinate is

$$\hat{\boldsymbol{\mathfrak{X}}}^{\text{ref}} = \frac{1}{\mathcal{V}} \int_{\mathcal{B}} \boldsymbol{\mathfrak{X}} \, d\mathcal{V}. \tag{11.5}$$

Thereafter, decomposing the RCE into three subdomains, the RCE displacements and gradients vary with respect to each other. The second assumption aforementioned characterizes the identical RCE displacement gradient $\mathbf{\mathfrak{G}}_b\big|_{\mathbf{\mathfrak{x}}}$ for the upper and lower block, reading

$$\mathbf{\mathfrak{G}}_b\big|_{\mathbf{\mathfrak{x}}} = \mathbf{G}\big|_{\mathbf{x}} + \tilde{\mathbf{\mathfrak{G}}}_b\big|_{\mathbf{\mathfrak{x}}} \qquad \forall \mathbf{\mathfrak{x}} \in \left(\mathcal{B}^1 \cup \mathcal{B}^2\right), \tag{11.6}$$

where the gradient fluctuation in the subdomains of solid blocks is described by $\tilde{\mathbf{\mathfrak{G}}}_b\big|_{\mathbf{\mathfrak{x}}}$. Similarly, the RCE gradient in the crack subdomain $\mathbf{\mathfrak{G}}_\Gamma\big|_{\mathbf{\mathfrak{x}}}$ reads

$$\mathbf{\mathfrak{G}}_\Gamma\big|_{\mathbf{\mathfrak{x}}} = \mathbf{G}\big|_{\mathbf{x}} + \tilde{\mathbf{\mathfrak{G}}}_\Gamma\big|_{\mathbf{\mathfrak{x}}} \qquad \forall \mathbf{\mathfrak{x}} \in \mathcal{B}^\Gamma, \tag{11.7}$$

where the gradient fluctuation in the crack subdomain is denoted by $\tilde{\mathbf{\mathfrak{G}}}_\Gamma\big|_{\mathbf{\mathfrak{x}}}$. Hence, a general relation in the RCE is defined as

$$\mathbf{\mathfrak{G}}\big|_{\mathbf{\mathfrak{x}}} = \mathbf{G}\big|_{\mathbf{x}} + \tilde{\mathbf{\mathfrak{G}}}\big|_{\mathbf{\mathfrak{x}}}, \qquad \text{where} \qquad \tilde{\mathbf{\mathfrak{G}}}\big|_{\mathbf{\mathfrak{x}}} = \begin{cases} \tilde{\mathbf{\mathfrak{G}}}_b\big|_{\mathbf{\mathfrak{x}}}, & \forall \mathbf{\mathfrak{x}} \in \left(\mathcal{B}^1 \cup \mathcal{B}^2\right), \\ \tilde{\mathbf{\mathfrak{G}}}_\Gamma\big|_{\mathbf{\mathfrak{x}}}, & \forall \mathbf{\mathfrak{x}} \in \mathcal{B}^\Gamma. \end{cases} \tag{11.8}$$

According to the evaluation of the compatibility condition for kinematically admissible displacement fluctuations, the relations

$$\mathbf{u} = \frac{1}{\mathcal{V}} \int_{\mathcal{B}} \mathbf{u}\,\mathrm{d}\mathcal{V} \qquad \text{and} \qquad \mathbf{0} = \frac{1}{\mathcal{V}} \int_{\mathcal{B}} \tilde{\mathbf{u}}\,\mathrm{d}\mathcal{V} \tag{11.9}$$

and

$$\mathbf{G}\big|_{\mathbf{x}} = \frac{1}{\mathcal{V}} \int_{\mathcal{B}} \mathbf{\mathfrak{G}}\big|_{\mathbf{\mathfrak{x}}}\,\mathrm{d}\mathcal{V} \qquad \text{and} \qquad \mathbf{0} = \frac{1}{\mathcal{V}} \int_{\mathcal{B}} \tilde{\mathbf{\mathfrak{G}}}\big|_{\mathbf{\mathfrak{x}}}\,\mathrm{d}\mathcal{V} \tag{11.10}$$

exist, where the terms $\tilde{\mathbf{u}}$ and $\tilde{\mathbf{\mathfrak{G}}}\big|_{\mathbf{\mathfrak{x}}}$ represent the displacement and the gradient fluctuations with respect to the RCE description in a general case. Furthermore, one obtains a symmetric rigid body translations of both, the upper and lower block, with respect to the crack center displacement at continuous level $\mathbf{u}$, reading

$$\hat{\mathbf{u}}^1 = \mathbf{u} + \frac{1}{2}\mathbf{u}_\Gamma, \qquad \hat{\mathbf{u}}^2 = \mathbf{u} - \frac{1}{2}\mathbf{u}_\Gamma, \qquad \hat{\mathbf{u}}_\Gamma = \mathbf{u}. \tag{11.11}$$

As a result, the displacement fluctuations eventually are obtained as

$$\tilde{\mathbf{u}} = \begin{cases} \frac{1}{2}\mathbf{u}_\Gamma + \left(\mathbf{G}\big|_{\mathbf{x}} + \tilde{\mathbf{\mathfrak{G}}}_b\big|_{\mathbf{\mathfrak{x}}}\right) \cdot \left(\mathbf{\mathfrak{x}} - \hat{\mathbf{\mathfrak{x}}}^{\text{ref}}\right), & \forall \mathbf{\mathfrak{x}} \in \mathcal{B}^1, \\ -\frac{1}{2}\mathbf{u}_\Gamma + \left(\mathbf{G}\big|_{\mathbf{x}} + \tilde{\mathbf{\mathfrak{G}}}_b\big|_{\mathbf{\mathfrak{x}}}\right) \cdot \left(\mathbf{\mathfrak{x}} - \hat{\mathbf{\mathfrak{x}}}^{\text{ref}}\right), & \forall \mathbf{\mathfrak{x}} \in \mathcal{B}^2, \\ \left(\mathbf{G}\big|_{\mathbf{x}} + \tilde{\mathbf{\mathfrak{G}}}_\Gamma\big|_{\mathbf{\mathfrak{x}}}\right) \cdot \left(\mathbf{\mathfrak{x}} - \hat{\mathbf{\mathfrak{x}}}^{\text{ref}}\right), & \forall \mathbf{\mathfrak{x}} \in \mathcal{B}^\Gamma. \end{cases} \tag{11.12}$$

The projection of the crack deformation normal to the crack surface in the RCE is

$$\tilde{\mathfrak{G}}_\Gamma\big|_{\boldsymbol{x}}\cdot\mathbf{n}^1 = \frac{\mathbf{u}_\Gamma}{l_\Gamma} = \sum_{I=1}^{3}\frac{u_\Gamma^I}{l_\Gamma}\mathbf{n}^I \qquad \forall\boldsymbol{\mathfrak{X}}\in\mathcal{B}^\Gamma, \tag{11.13}$$

which further leads to the crack deformation gradient as

$$\tilde{\mathfrak{G}}_\Gamma\big|_{\boldsymbol{x}} = \frac{\mathbf{u}_\Gamma}{l_\Gamma}\otimes\mathbf{n}^1 = \sum_{I=1}^{3}\frac{u_\Gamma^I}{l_\Gamma}\mathbf{n}^I\otimes\mathbf{n}^1 \qquad \forall\boldsymbol{\mathfrak{X}}\in\mathcal{B}^\Gamma. \tag{11.14}$$

Considering kinematic coupling of gradient terms in Eq. $(11.10)_1$, the relation

$$
\begin{aligned}
\mathbf{G}\big|_{\mathbf{x}} &= \frac{1}{\mathcal{V}}\left(\int_{\mathcal{B}^1\cup\mathcal{B}^2}\mathfrak{G}_b\big|_{\boldsymbol{x}}\,d\mathcal{V} + \int_{\mathcal{B}^\Gamma}\mathfrak{G}_\Gamma\big|_{\boldsymbol{x}}\,d\mathcal{V}\right)\\
&= \frac{1}{\mathcal{V}}\left(\int_{\mathcal{B}^1\cup\mathcal{B}^2}\left(\mathbf{G}\big|_{\mathbf{x}}+\tilde{\mathfrak{G}}_b\big|_{\boldsymbol{x}}\right)d\mathcal{V} + \int_{\mathcal{B}^\Gamma}\left(\mathbf{G}\big|_{\mathbf{x}}+\tilde{\mathfrak{G}}_\Gamma\big|_{\boldsymbol{x}}\right)d\mathcal{V}\right)\\
&= \frac{1}{\mathcal{V}}\left(\left(\mathbf{G}\big|_{\mathbf{x}}+\tilde{\mathfrak{G}}_b\big|_{\boldsymbol{x}}\right)\left(\mathcal{V}^1+\mathcal{V}^2\right) + \left(\mathbf{G}\big|_{\mathbf{x}}+\tilde{\mathfrak{G}}_\Gamma\big|_{\boldsymbol{x}}\right)\mathcal{V}^\Gamma\right)\\
&= \frac{1}{\mathcal{V}}\left(\mathbf{G}\big|_{\mathbf{x}}\mathcal{V}+\tilde{\mathfrak{G}}_b\big|_{\boldsymbol{x}}\left(\mathcal{V}^1+\mathcal{V}^2\right) + \tilde{\mathfrak{G}}_\Gamma\big|_{\boldsymbol{x}}\mathcal{V}^\Gamma\right)\\
&= \mathbf{G}\big|_{\mathbf{x}} + \frac{\tilde{\mathfrak{G}}_b\big|_{\boldsymbol{x}}\left(\mathcal{V}^1+\mathcal{V}^2\right) + \tilde{\mathfrak{G}}_\Gamma\big|_{\boldsymbol{x}}\mathcal{V}^\Gamma}{\mathcal{V}}
\end{aligned}
\tag{11.15}
$$

exists, which forces the condition

$$\frac{\tilde{\mathfrak{G}}_b\big|_{\boldsymbol{x}}\left(\mathcal{V}^1+\mathcal{V}^2\right) + \tilde{\mathfrak{G}}_\Gamma\big|_{\boldsymbol{x}}\mathcal{V}^\Gamma}{\mathcal{V}} = \mathbf{0}. \tag{11.16}$$

As a consequence, it subsequently leads to

$$\tilde{\mathfrak{G}}_b\big|_{\boldsymbol{x}} = -\frac{\mathcal{V}^\Gamma}{\mathcal{V}^1+\mathcal{V}^2}\tilde{\mathfrak{G}}_\Gamma\big|_{\boldsymbol{x}} = -\frac{l_c^2\,l_\Gamma}{l_c^3}\tilde{\mathfrak{G}}_\Gamma\big|_{\boldsymbol{x}} = -\frac{l_\Gamma}{l_c}\sum_{I=1}^{3}\frac{u^I}{l_\Gamma}\mathbf{n}^I\otimes\mathbf{n}^1 = -\sum_{I=1}^{3}\frac{u^I}{l_c}\mathbf{n}^I\otimes\mathbf{n}^1. \tag{11.17}$$

Meanwhile, the condition in Eq. (11.16) fulfills the second condition of the kinematically admissible displacement fluctuations in Eq. $(11.10)_2$, which can be interpreted as

$$
\begin{aligned}
\mathbf{0} &= \frac{1}{\mathcal{V}}\int_{\mathcal{B}}\tilde{\mathfrak{G}}\big|_{\boldsymbol{x}}\,d\mathcal{V} = \frac{1}{\mathcal{V}}\left(\int_{\mathcal{B}^1\cup\mathcal{B}^2}\tilde{\mathfrak{G}}_b\big|_{\boldsymbol{x}}\,d\mathcal{V} + \int_{\mathcal{B}^\Gamma}\tilde{\mathfrak{G}}_\Gamma\big|_{\boldsymbol{x}}\,d\mathcal{V}\right)\\
&= \frac{\tilde{\mathfrak{G}}_b\big|_{\boldsymbol{x}}\left(\mathcal{V}^1+\mathcal{V}^2\right) + \tilde{\mathfrak{G}}_\Gamma\big|_{\boldsymbol{x}}\mathcal{V}^\Gamma}{\mathcal{V}}.
\end{aligned}
\tag{11.18}
$$

Substituting the gradient fluctuation in Eq. (11.17) into Eq. (11.6), the RCE gradient of the block material of RCE reads

$$\mathfrak{G}_{b}\big|_{\mathfrak{X}} = \mathsf{G}\big|_{\mathbf{x}} - \sum_{I=1}^{3} \frac{u^{I}}{l} \mathbf{n}^{I} \otimes \mathbf{n}^{1} \qquad \forall \mathfrak{X} \in \left(\mathcal{B}^{1} \cup \mathcal{B}^{2}\right). \tag{11.19}$$

By further making use of the gradient terms, the second order strain tensors for both the continuous description and the RCE blocks are defined as

$$\boldsymbol{\varepsilon} = \frac{1}{2}\left(\mathsf{G}\big|_{\mathbf{x}} + \left(\mathsf{G}\big|_{\mathbf{x}}\right)^{\mathsf{T}}\right) \tag{11.20}$$

and

$$\mathfrak{e} = \frac{1}{2}\left(\mathfrak{G}_{b}\big|_{\mathfrak{X}} + \left(\mathfrak{G}_{b}\big|_{\mathfrak{X}}\right)^{\mathsf{T}}\right), \tag{11.21}$$

respectively. Substituting Eqs. (11.19) and (11.20) into Eq. (11.21), the relationship of the strain quantities between the continuous and the RCE description eventually yields

$$\mathfrak{e} = \boldsymbol{\varepsilon} - \sum_{I=1}^{3} \Gamma^{I} \mathfrak{P}^{I}, \tag{11.22}$$

where

$$\Gamma^{I} = \frac{u^{I}}{l_{c}} \qquad \text{and} \qquad \mathfrak{P}^{I} = \frac{1}{2}\left(\mathbf{n}^{I} \otimes \mathbf{n}^{1} + \mathbf{n}^{1} \otimes \mathbf{n}^{I}\right). \tag{11.23}$$

Therefore, two important aspects, namely, the unknown crack orientation $\mathbf{n}^{I}$ and the unknown crack deformation Γ^{I} with $I = 1, 2, 3$, need to be appropriately resolved to yield the consequent constitutive description of the RCE. The former one, the orientation of the orthogonal local RCE system $\mathcal{E}^{\Gamma} \sim \left\{\mathbf{n}^{1}, \mathbf{n}^{2}, \mathbf{n}^{3}\right\}$ with respect to the global coordinate system $\mathcal{E}^{e} \sim \left\{\mathbf{e}^{1}, \mathbf{e}^{2}, \mathbf{e}^{3}\right\}$ is determined by an accurate crack orientation criterion, which is, nevertheless, still challenging for a robust definition of crack orientation. Herein, several simplified criteria or a predefined crack orientation can be considered with regard to this issue. Therefore, the only remaining issue is the solution for the crack deformation in the RCE framework.

11.2.3 Solution for the Crack Deformation in the RCE

The RCE block material is assumed to be characterized by the same constitutive law as the intact bulk material, whereas the local strain fields $\mathfrak{e}$ and $\boldsymbol{\varepsilon}$ are different. To describe the constitutive laws of the RCE and the intact material by a straightforward understanding, the HELMHOLTZ free energy functional is adopted to derive the stress and the consistent material tangent, reading

$$\mathfrak{s} = \frac{\partial \, \varphi \, (\mathfrak{e})}{\partial \, \mathfrak{e}}, \qquad \mathfrak{C} = \frac{\partial^2 \, \varphi \, (\mathfrak{e})}{\partial \, \mathfrak{e}^2}, \qquad \text{and} \qquad \boldsymbol{\sigma}^0 = \frac{\partial \, \varphi \, (\boldsymbol{\varepsilon})}{\partial \, \boldsymbol{\varepsilon}}, \qquad \mathbb{C}^0 = \frac{\partial^2 \, \varphi \, (\boldsymbol{\varepsilon})}{\partial \, \boldsymbol{\varepsilon}^2},$$
$$(11.24)$$

respectively. The general form for the principle of total virtual power of the RCE reads

$$\delta\mathcal{P} = \underbrace{\int_{\mathcal{B}^1 \cup \mathcal{B}^2} \Big\{ \mathfrak{s} : \delta\dot{\mathfrak{e}} \Big\} d\mathcal{V}}_{\text{internal power}} -$$

$$\underbrace{\left(\int_{\mathcal{A}^\Gamma} \Big\{ \mathsf{t} \cdot \delta\dot{\mathsf{u}}_\Gamma \Big\} d\mathcal{A} + \int_{\partial\mathcal{V}_{\mathrm{RCE}}} \Big\{ \mathfrak{T} \cdot \delta\dot{\mathsf{u}} \Big\} d\mathcal{A} + \int_{\mathcal{V}_{\mathrm{RCE}}} \Big\{ (\mathfrak{f}^\mathrm{p} - \mathfrak{f}^a) \cdot \delta\dot{\mathsf{u}} \Big\} d\mathcal{V} \right)}_{\text{external power}} = 0.$$
$$(11.25)$$

It is noteworthy that the internal power is defined by the stress power in the block subdomains $\mathcal{B}^1 \cup \mathcal{B}^2$. The external power consists of the traction power $\mathfrak{T} \cdot \delta\dot{\mathsf{u}}$ at the external surface of the RCE domain $\partial\mathcal{V}_{\mathrm{RCE}}$. Besides, it may include some other constitutive characteristics, e.g. crack surface friction or cohesive traction. Hence, a virtual power term $\mathsf{t} \cdot \delta\dot{\mathsf{u}}_\Gamma$ within the crack surfaces $\mathcal{A}^\Gamma$ is necessarily included to depict the aforementioned considerations. Furthermore, the passive and active volume force power $(\mathfrak{f}^\mathrm{p} - \mathfrak{f}^a) \cdot \delta\dot{\mathsf{u}}$ within the RCE volume $\partial\mathcal{V}_{\mathrm{RCE}}$ is presented as well. For simplicities, the work at hand does not take the RCE surface traction power and the volume force power quantities into account, which simplifies Eq. (11.25) to

$$\delta\mathcal{P} = \int_{\mathcal{B}^1 \cup \mathcal{B}^2} \Big\{ \mathfrak{s} : \delta\dot{\mathfrak{e}} \Big\} d\mathcal{V} - \int_{\mathcal{A}^\Gamma} \Big\{ \mathsf{t} \cdot \delta\dot{\mathsf{u}}_\Gamma \Big\} d\mathcal{A} = 0. \qquad (11.26)$$

Another notable point is that the constitutive behavior of the RCE blocks and the intact bulk material is not restricted to simple linear elasticity. In contrast, it can also be associated with nonlinear elasticity as well as inelasticity, even at finite strains.

The virtual power principle of the RCE always exists for an arbitrary rate of virtual crack deformation, i.e. $\delta\dot{\Gamma}^\mathrm{I}$ with $\mathrm{I} = 1, 2, 3$. As a result, the relation

$$\delta_\Gamma\mathcal{P} = \int_{\mathcal{B}^1 \cup \mathcal{B}^2} \Big\{ -\mathfrak{s} : \sum_{\mathrm{I}=1}^{3} \delta\dot{\Gamma}^\mathrm{I} \, \mathfrak{P}^\mathrm{I} \Big\} d\mathcal{V} - \int_{\mathcal{A}^\Gamma} \Big\{ \mathsf{t} \cdot \sum_{\mathrm{I}=1}^{3} \delta\dot{\Gamma}^\mathrm{I} \, \mathsf{l}_\mathrm{c} \, \mathsf{n}^\mathrm{I} \Big\} d\mathcal{A} = 0 \quad (11.27)$$

exists, and the crack deformation Γ^I with $\mathrm{I} = 1, 2, 3$ can be consistently solved by a straightforward minimization method. Nevertheless, even a correct mathematical solution of Γ^I may possibly conflict with the physically correct crack deformation for a closing crack, i.e. a negative Γ^1 indicates crack surfaces penetrated instead of a stiff contact. In this regard, an additional constraint needs to be imposed to prevent penetrated crack surfaces, and to obtain a realistic crack deformation. The crack state is determined by a predictor-corrector procedure, which means prediction of an opening crack deformation and correction for a closing crack deformation.

11.2.3.1 Crack Opening

The initial guess is based on an opening crack deformation, the minimization problem leads to

$$\Gamma^{I} = \arg \left\{ \min_{\Gamma^{1,2,3} \in \mathcal{R}} \mathcal{P}\left(\boldsymbol{\varepsilon},\Gamma^{1},\Gamma^{2},\Gamma^{3}\right) \right\}. \tag{11.28}$$

Thereafter, the unique solution of Γ^{I} fulfills the equilibrium

$$\int_{\mathcal{B}^{1}\cup\mathcal{B}^{2}} \left\{ \mathfrak{s} : \mathfrak{P}^{I} \right\} d\mathcal{V} + \int_{\mathcal{A}^{\Gamma}} \left\{ l_{c}\, t \cdot n^{I} \right\} d\mathcal{A} = 0, \qquad \text{where} \qquad I = 1,2,3. \tag{11.29}$$

For a general nonlinear constitutive law with respect to the RCE blocks and bulk materials or a nonlinear definition of t with respect to u_{Γ}, this equilibrium is characterized as nonlinear as well. Therefore, analytical solutions of the unknown Γ^{I} are not straightforward, and even sometimes not possible to obtain. As a result, an internal NEWTON-RAPHSON algorithm is postulated to solve the equilibrium in Eq. (11.29). The local residual $\mathcal{R}_{\Gamma^{I}}$ is, thus, defined as

$$\begin{aligned}
\mathcal{R}_{\Gamma^{I}} &= \int_{\mathcal{B}^{1}\cup\mathcal{B}^{2}} \left\{ \mathfrak{s} : \mathfrak{P}^{I} \right\} d\mathcal{V} + \int_{\mathcal{A}^{\Gamma}} \left\{ l_{c}\, t \cdot n^{I} \right\} d\mathcal{A} \\
&= \left(\mathcal{V}^{1} + \mathcal{V}^{2} \right) \mathfrak{s} : \mathfrak{P}^{I} + \mathcal{A}^{\Gamma} l_{c}\, t \cdot n^{I} \\
&= l_{c}^{3} \left(\mathfrak{s} : \mathfrak{P}^{I} + t \cdot n^{I} \right)
\end{aligned} \tag{11.30}$$

and the internal consistent tangent is derived as

$$\begin{aligned}
\mathcal{K}_{\Gamma^{I}\Gamma^{J}} &= -\frac{\partial \mathcal{R}_{\Gamma^{I}}}{\partial \Gamma^{J}} = -l_{c}^{3} \left(\frac{\partial \mathfrak{s}}{\partial \Gamma^{J}} : \mathfrak{P}^{I} + \frac{\partial t}{\partial \Gamma^{J}} \cdot n^{I} \right) \\
&= -l_{c}^{3} \left(\mathfrak{P}^{I} : \frac{\partial \mathfrak{s}}{\partial \boldsymbol{\varepsilon}} : \frac{\partial \boldsymbol{\varepsilon}}{\partial \Gamma^{J}} + n^{I} \cdot \frac{\partial t}{\partial u_{\Gamma}} \cdot \frac{\partial u_{\Gamma}}{\partial \Gamma^{J}} \right) \\
&= l_{c}^{3} \left(\mathfrak{P}^{I} : \mathfrak{C} : \mathfrak{P}^{J} - l_{c}\, n^{I} \cdot \mathfrak{k} \cdot n^{J} \right),
\end{aligned} \tag{11.31}$$

where $\mathfrak{k} = \partial t / \partial u_{\Gamma}$ is defined. The internal iteration algorithm is illustratively shown in **Table 11.1**. It is noteworthy that the trial state of the crack deformation $\Gamma^{I,tr}_{k=0}$ in **Table 11.1** can be numerically implemented as a history variable, which consists of values of the previous loading step. This algorithmic treatment yields a relatively fast local convergence to a certain extent.

Table 11.1: Internal NEWTON-RAPHSON iteration to obtain the RCE crack deformation quantities Γ^{I}.

Initiation	$k = 0, \quad \Gamma_k^{\mathrm{I}} = \Gamma_k^{\mathrm{I,tr}}$
Do Loop	
Residual	$\mathcal{R}_{\Gamma^{\mathrm{I}}} = l_c^3 \left(\mathfrak{s} : \mathfrak{P}^{\mathrm{I}} + t \cdot \mathbf{n}^{\mathrm{I}} \right)$
Linearization	$\mathrm{Lin}\,\mathcal{R}_{\Gamma^{\mathrm{I}}} = \mathcal{R}_{\Gamma^{\mathrm{I}}}\Big|_{\Gamma_k^{\mathrm{I}}} + \dfrac{\partial \mathcal{R}_{\Gamma^{\mathrm{I}}}}{\partial \Gamma^{\mathrm{J}}}\Big|_{\Gamma_k^{\mathrm{I}}} \Delta\Gamma_k^{\mathrm{J}}$
Tangent	$\mathcal{K}_{\Gamma^{\mathrm{I}}\Gamma^{\mathrm{J}}} = -\dfrac{\partial \mathcal{R}_{\Gamma^{\mathrm{I}}}}{\partial \Gamma^{\mathrm{J}}}\Big|_{\Gamma_k^{\mathrm{I}}}$
Solving	$\Delta\Gamma_k^{\mathrm{J}} = (\mathcal{K})_{\Gamma^{\mathrm{J}}\Gamma^{\mathrm{I}}}^{-1} \mathcal{R}_{\Gamma^{\mathrm{I}}}$
Update	$\Gamma_{k+1}^{\mathrm{J}} = \Gamma_k^{\mathrm{J}} + \Delta\Gamma_k^{\mathrm{J}}, \quad k = k+1$
While	$\mathrm{Tol} \leqslant \|\mathcal{R}_{\Gamma^{\mathrm{I}}}\|$

11.2.3.2 Crack Closing

After the initial guess of crack opening prediction, the realistic crack deformation can be identified, i.e. opening or closing. Once the condition $\Gamma^1 < 0$ is fulfilled, the correction of a closing crack deformation is triggered. Thereafter, a mathematical constraint is artificially imposed to the new equilibrium and the relation in Eq. (11.27) is substituted by

$$\Gamma^{2,3} = \arg\left\{ \min_{\Gamma^{2,3} \in \mathcal{R}} \mathcal{P}\left(\boldsymbol{\varepsilon}, \Gamma^2, \Gamma^3\right)\Big|_{\Gamma^1=0}\right\} \quad \text{for} \quad \Gamma^1 < 0, \tag{11.32}$$
$$\Gamma^1 = 0.$$

From the numerical point of view, the implementation of such a constraint condition may potentially lead to oscillations between opening and closing cracks. That phenomenon is investigated when Γ^1 is within an interval around the contact point, where the interval size is in the order of the numerical precision for the calculation of Γ^1. To obtain a relatively stable contact condition, a numerical assumption by setting a contact tolerance Tol is employed in order to detect the change of a contact state. In this regard, the contact triggering condition is redefined as

$$\Gamma^1 \leqslant \mathrm{Tol}, \tag{11.33}$$

where the tolerance Tol can be a sufficiently small and positive number, e.g., $\mathrm{Tol} = 10^{-12}$. Introducing the constraint $\Gamma^1 = 0$, the block strain in Eq. (11.22) needs to be rewritten as

$$\mathfrak{e} = \boldsymbol{\varepsilon} - \Gamma^1 \mathfrak{P}^1 - \Gamma^2 \mathfrak{P}^2. \tag{11.34}$$

The RCE stress $\mathfrak{s}$ and tangent $\mathfrak{C}$ as well as the crack surface tractions $\mathfrak{t}$ and its tangent $\mathfrak{k} = \partial \mathfrak{t} / \partial u_\Gamma$ in Eq. (11.31) are necessarily rederived based on the constraint condition. Reperforming the NEWTON-RAPHSON iteration in **Table 11.1** using the updated quantities, the crack deformations Γ^I with $I = 2, 3$ for the closing state are eventually obtained. The solution procedure is given in **Fig. 11.2**.

11.3 Regularization of the Free Discontinuity Problem

11.3.1 Governing Equations

The free discontinuity problem for brittle fracture with conservative external forces reads

$$\mathcal{E}\left(\mathbf{u}, \mathcal{B}^\Gamma\right) = \int_{\mathcal{B} \setminus \mathcal{B}^\Gamma} \varphi\left(\nabla \mathbf{u}\right) \mathrm{d}V + \mathcal{G}_c \, \mathcal{H}^2\left(\mathcal{B}^\Gamma\right) \quad \longrightarrow \quad \min_{\mathbf{u}, \mathcal{B}^\Gamma} \mathcal{E}\left(\mathbf{u}, \mathcal{B}^\Gamma\right), \tag{11.35}$$

where the strain energy density φ is defined on the domain of the bulk material $\mathcal{B} \setminus \mathcal{B}^\Gamma$. The fracture energy is given by the fracture toughness $\mathcal{G}_c$ and the area of crack surfaces $\mathcal{H}^2\left(\mathcal{B}^\Gamma\right)$. Different regularization methodologies are proposed for this variational problem. The regularization in eigenfracture yields
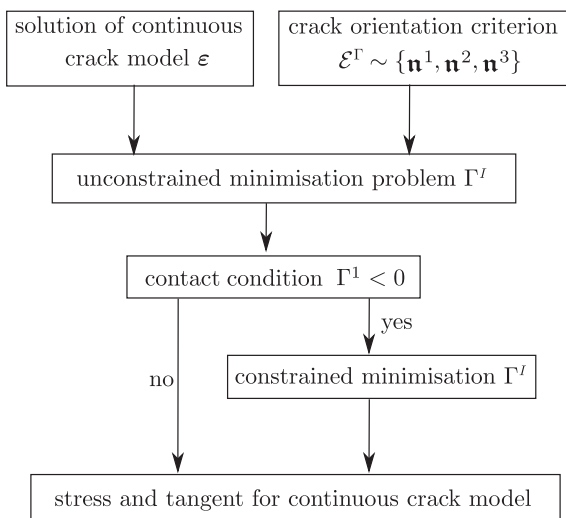
Fig. 11.2 Solution procedure for the RCE with homogeneous block deformations

$$\mathcal{E}\left(\mathbf{u}, \boldsymbol{\varepsilon}^*\right) = \int_{\mathcal{B}} \varphi(\boldsymbol{\varepsilon} - \boldsymbol{\varepsilon}^*) \, dV + \frac{\mathcal{G}_c}{2\epsilon} \left|\mathcal{B}^\epsilon\right| \quad \longrightarrow \quad \min_{\mathbf{u}, \boldsymbol{\varepsilon}^*} \mathcal{E}\left(\mathbf{u}, \boldsymbol{\varepsilon}^*\right) \tag{11.36}$$

with the approximated crack surfaces

$$\mathcal{B}^\epsilon := \left\{ \mathbf{X} \in \mathcal{B} \, \middle| \, \exists \, \mathbf{a} \in \mathrm{supp}\left(\boldsymbol{\varepsilon}^*\right); \epsilon \geqslant |\mathbf{a} - \mathbf{X}| \right\}, \tag{11.37}$$

and the regularization in phase-field fracture reads

$$\mathcal{E}\left(\mathbf{u}, d, \nabla d\right) = \int_{\mathcal{B}} \varphi(\boldsymbol{\varepsilon}) \, dV + \mathcal{G}_c \int_{\mathcal{B}} \gamma_l \left(d, \nabla d\right) dV \longrightarrow \min_{\mathbf{u}, d} \mathcal{E}\left(\mathbf{u}, d, \nabla d\right). \tag{11.38}$$

Herein, new variables are added to the energy formulation, namely the phase-field variable d and the eigenstrain $\boldsymbol{\varepsilon}^*$. For regularized eigenfracture, the ϵ-neighborhood $\mathcal{B}^\epsilon$ of the support of the eigenstrain can be determined a posteriori to the mechanical equilibrium, and allows to introduce the eigenstrain $\boldsymbol{\varepsilon}^*$ as an internal variable. Nevertheless, the phase-field regularization of the crack area by means of $\gamma_l(d, \nabla d)$ involves spacial gradients of the phase-field. Thus, it requires the phase-field variable d to be introduced as global state variable. A common crack surface density for the multi-dimensional problem is defined as

$$\gamma_l = \frac{1}{2l} \left(d^2 + l^2 |\nabla_{\mathbf{X}} d|^2\right), \tag{11.39}$$

where the internal length scale l is employed to govern the width of the transition zone between fractured ($d = 1$) and sound state ($d = 0$) of the material. For several intensive studies of the length scale l with respect to discretization, it is referred to Miehe et al. (2010b); Zhang et al. (2017); Mandal et al. (2019). The crack surface density function in Eq. (11.39) is also known as the AT2 model, which yields an exponentially shaped crack profile. Furthermore, another common alternative to approximate the crack surface density function is the classical AT1 model (Pham et al., 2011), which is not main scope of the discussion in this work.

The strain energy in the eigenfracture and the phase-field regularization can be related to the two material states φ^0 and φ^c, which are expressed by

$$\varphi\left(\boldsymbol{\varepsilon} - \boldsymbol{\varepsilon}^*\right) = \begin{cases} \varphi^c, & \text{for } \mathbf{X} \in \mathrm{supp}\left(\boldsymbol{\varepsilon}^*\right), \\ \varphi^0, & \text{else}, \end{cases} \tag{11.40}$$
$$\text{and} \quad \varphi = \varphi^c\left(\boldsymbol{\varepsilon}, \Gamma^I\right) + g\left(d\right)\left(\varphi^0\left(\boldsymbol{\varepsilon}\right) - \varphi^c\left(\boldsymbol{\varepsilon}, \Gamma^I\right)\right),$$

respectively. Thus, the regularizations of the strain energy in eigenfracture and phase-field fracture are based on the behavior of intact material φ^0, i.e. in absence of a crack, and of fully broken material φ^c, i.e. in presence of a crack. While the intact material is described by classical constitutive models, the material behavior in the presence of a crack can be derived from an RCE.

Neglecting the derivation process based on a straightforward variational principle, the governing equations for the RCE problem read

$$\rho\,\ddot{\mathbf{u}} - \nabla_{\mathbf{X}} \cdot \boldsymbol{\sigma} - \mathbf{b} = \mathbf{0} \quad \text{in} \quad \mathcal{B} \quad \text{and} \quad \boldsymbol{\sigma}\cdot\mathbf{n} = \mathbf{t} \quad \text{at} \quad \partial\mathcal{B} \qquad (11.41)$$

and

$$\int_{\mathcal{B}^1\cup\mathcal{B}^2} \left\{ \boldsymbol{\mathfrak{s}} : \boldsymbol{\mathfrak{P}}^I \right\} d\mathcal{V} + \int_{\mathcal{A}^\Gamma} \left\{ l_c \mathbf{t}\cdot\mathbf{n}^I \right\} d\mathcal{A} = 0 \quad \text{in} \quad \mathcal{V}_{RCE} \quad \text{with} \quad I = 1,2,3$$

$$(11.42)$$

for the continuous deformation equilibrium and the RCE response, respectively. The notation $\nabla_{\mathbf{X}} \cdot (*)$ represents a divergence operator. The evolution equilibrium in Eq. (11.42) exactly coincides with the virtual power principle of Eq. (11.26) and the solution of crack deformation is according to the minimization problem Eq. (11.27). For eigenfracture modeling, the eigenstrain $\boldsymbol{\varepsilon}^*$ is regarded as an internal quantity, and the fracture evolution process is mainly based on a post-processing technique according to an ϵ-neighborhood algorithm. Nevertheless, in particular for phase-field fracture modeling, a degree of freedom is necessary to model fracture evolution, and the governing equation eventually reads

$$\partial_d\, g(d)\left(\varphi^0 - \varphi^c\right) + \frac{\mathcal{G}_c}{l}\left(d - l^2\,\nabla_{\mathbf{X}}\cdot d\right) = 0 \quad \text{in} \quad \mathcal{B} \quad \text{and} \quad \nabla_{\mathbf{X}} d\cdot\mathbf{n} = 0 \quad \text{at} \quad \partial\mathcal{B}.$$

$$(11.43)$$

The phase-field driving force term $\left(\varphi^0 - \varphi^c\right)$ is based on two types of definitions, i.e. a damage-like approximation (Miehe et al., 2010a) or a fracture-like approximation (Kuhn and Müller, 2010).

11.3.2 Stress and Consistent Tangent

According to a straightforward derivation, the stress response and the consistent material tangent can be derived from the total effective HELMHOLTZ energy density function for both eigenfracture and phase-field fracture. In the intact material, the stress $\boldsymbol{\sigma}^0$ and the consistent tangent $\mathbb{C}^0$ can be straightforwardly derived based on the constitutive law, see Eqs. (11.24)$_1$ and (11.24)$_3$, respectively. However, with respect to the RCE description, the stress and material tangent tensors are obtained indirectly. Basically, the stress for the fully cracked state is characterized to be the RCE stress, i.e., $\boldsymbol{\sigma}^c = \boldsymbol{\mathfrak{s}}$. The consistent tangent $\mathbb{C}^c$ yields

$$
\begin{aligned}
\mathbb{C}^{c} = \frac{d\boldsymbol{\sigma}^{c}}{d\boldsymbol{\varepsilon}} &= \frac{d\mathbf{s}}{d\boldsymbol{\varepsilon}} \\
&= \frac{\partial \mathbf{s}}{\partial \boldsymbol{\varepsilon}} + \sum_{J=1}^{3} \frac{\partial \mathbf{s}}{\partial \Gamma^{J}} \otimes \frac{\partial \Gamma^{J}}{\partial \boldsymbol{\varepsilon}} \\
&= \frac{\partial \mathbf{s}}{\partial \boldsymbol{\varepsilon}} + \sum_{J=1}^{3} \left(\frac{\partial \mathbf{s}}{\partial \boldsymbol{\epsilon}} : \frac{\partial \boldsymbol{\epsilon}}{\partial \Gamma^{J}} \right) \otimes \frac{\partial \Gamma^{J}}{\partial \boldsymbol{\varepsilon}} \\
&= \mathfrak{C} + \sum_{J=1}^{3} \left(-\mathfrak{C} : \mathfrak{P}^{J} \right) \otimes \frac{\partial \Gamma^{J}}{\partial \boldsymbol{\varepsilon}},
\end{aligned}
\tag{11.44}
$$

where the partial derivative $\partial \Gamma^{J}/\partial \boldsymbol{\varepsilon}$ cannot be derived in a straightforward manner. Therefore, by making use of the unconditional equilibrium of the minimization, one obtains the term $\partial \Gamma^{J}/\partial \boldsymbol{\varepsilon}$ indirectly, reading

$$
\begin{aligned}
\mathcal{R}_{\Gamma^{I}} = 0 \quad &\Rightarrow \quad \frac{d\mathcal{R}_{\Gamma^{I}}}{d\boldsymbol{\varepsilon}} = \mathbf{0} \\
&\Rightarrow \quad \frac{\partial \mathcal{R}_{\Gamma^{I}}}{\partial \boldsymbol{\varepsilon}} + \sum_{J=1}^{3} \left(\frac{\partial \mathcal{R}_{\Gamma^{I}}}{\partial \Gamma^{J}} \frac{\partial \Gamma^{J}}{\partial \boldsymbol{\varepsilon}} \right) = \mathbf{0} \\
&\Rightarrow \quad \frac{\partial \mathcal{R}_{\Gamma^{I}}}{\partial \mathbf{s}} : \frac{\partial \mathbf{s}}{\partial \boldsymbol{\epsilon}} : \frac{\partial \boldsymbol{\epsilon}}{\partial \boldsymbol{\varepsilon}} = \sum_{J=1}^{3} \left(-\frac{\partial \mathcal{R}_{\Gamma^{I}}}{\partial \Gamma^{J}} \frac{\partial \Gamma^{J}}{\partial \boldsymbol{\varepsilon}} \right) \\
&\Rightarrow \quad -\mathfrak{P}^{I} : \mathfrak{C} : \mathbb{I} = \sum_{J=1}^{3} \left(\mathcal{K}_{\Gamma^{I}\Gamma^{J}} \frac{\partial \Gamma^{J}}{\partial \boldsymbol{\varepsilon}} \right) \\
&\Rightarrow \quad \frac{\partial \Gamma^{J}}{\partial \boldsymbol{\varepsilon}} = -\sum_{I=1}^{3} \left((\mathcal{K}^{-1})_{\Gamma^{J}\Gamma^{I}} \mathfrak{C} : \mathfrak{P}^{I} \right).
\end{aligned}
\tag{11.45}
$$

As a result, substituting Eq. (11.45) into Eq. (11.44), the consistent tangent tensor for the fully cracked material yields

$$
\begin{aligned}
\mathbb{C}^{c} &= \mathfrak{C} + \sum_{J=1}^{3} \sum_{I=1}^{3} \left(-\mathfrak{C} : \mathfrak{P}^{J} \right) \otimes \left(-(\mathcal{K}^{-1})_{\Gamma^{J}\Gamma^{I}} \mathfrak{C} : \mathfrak{P}^{I} \right) \\
&= \mathfrak{C} + \sum_{J=1}^{3} \sum_{I=1}^{3} (\mathcal{K}^{-1})_{\Gamma^{J}\Gamma^{I}} \left(\mathfrak{C} : \mathfrak{P}^{J} \right) \otimes \left(\mathfrak{C} : \mathfrak{P}^{I} \right),
\end{aligned}
\tag{11.46}
$$

Thus, based on Eq. (11.40)$_1$, the deformation response can be straightforwardly formulated within an eigenfracture framework, since

$$\boldsymbol{\sigma} = \begin{cases} \boldsymbol{\sigma}^c, & \text{for } \mathbf{X} \in \text{supp}(\boldsymbol{\varepsilon}^*), \\ \boldsymbol{\sigma}^0, & \text{else}, \end{cases} \quad \text{and} \quad \mathbb{C} = \begin{cases} \mathbb{C}^c, & \text{for } \mathbf{X} \in \text{supp}(\boldsymbol{\varepsilon}^*), \\ \mathbb{C}^0, & \text{else}. \end{cases}$$

(11.47)

Nonetheless, for a variational phase-field fracture modeling, a further manipulation needs to be accounted for according to the similar relationship in Eq. $(11.40)_2$, namely

$$\boldsymbol{\sigma} = \boldsymbol{\sigma}^c + g(d)\left(\boldsymbol{\sigma}^0 - \boldsymbol{\sigma}^c\right) \quad \text{and} \quad \mathbb{C} = \mathbb{C}^c + g(d)\left(\mathbb{C}^0 - \mathbb{C}^c\right). \quad (11.48)$$

11.4 Numerical Applications

This section introduces a comprehensive application of eigenfracture and phase-field fracture modeling within an RCE framework with respect to different model problems. Each constitutive approach is consistently derived and implemented into an in-house simulation platform.

11.4.1 Self-consistent Test

Phenomenologically, without considering cohesive traction and friction at crack surfaces, an open-crack leads to a stress-free boundary. A closed and friction-free crack at a compressive state is supposed to fully transfer the normal compressive stress, which is characterized as an equivalent contact mechanism. Furthermore, a pure shear deformation along the friction-free crack surface should not transfer any force neither. The aforementioned characteristics have been studied in Steinke and Kaliske (2019); Strobl and Seelig (2016); Storm et al. (2020) to evaluate the correct phase-field crack kinematics for realistic applications. The first numerical example, herein, attempts to examine the crack kinematics to demonstrate the advantages of the presented eigenfracture and phase-field modeling in an RCE description compared to the classical spectral split and the V-D split approaches with respect to tension, compression and shearing deformation.

The two-dimensional boundary value problem is depicted in **Fig. 11.3**, which consists of a contact model, an eigenfracture model, and a phase-field model with the same dimensions. The contact model consists of two blocks and a contact pair. The eigenfracture model depicts the crack using a row of fully eroded elements, and the phase-field model describes the straight crack by prescribing the phase-field value $d = 1$ at the nodes attached to the middle row of elements. All models are discretized by 2500 four-node elements uniformly with the element size $h_e = 2\,\text{mm}$. The upper and lower edges are fully bounded and a displacement load is subjected to the upper edge with a loading function given in **Fig. 11.4** for tension, compression and shear deformation in a linear elastic body as well as compressive relaxation for linear viscoelasticity.
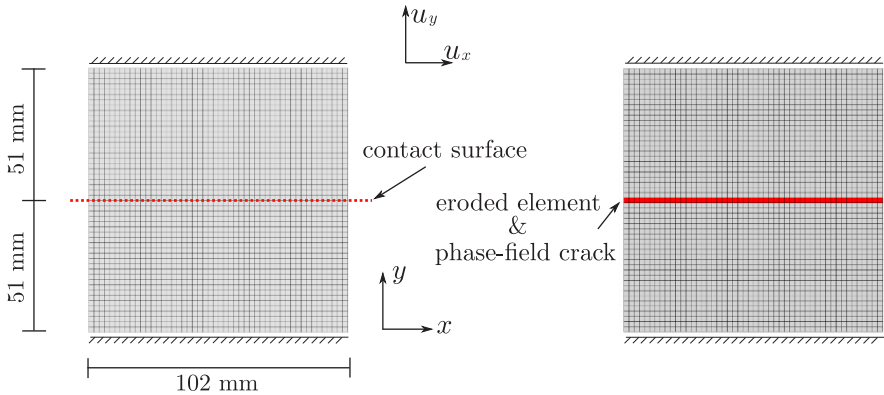
Fig. 11.3: Geometric setup for contact surface and phase-field crack.

11.4.1.1 Linear Elasticity

The simulations are based on the spectral split, V-D split as well as the RCE description of both eigenfracture and RCE phase-field modeling. The material parameters are given as $\lambda = 19.6\,\text{MPa}$, $\mu = 2.06\,\text{MPa}$ for linear elasticity. Based on the loading in **Fig. 11.4** (a), the RCE eigenfracture results are shown in **Fig. 11.5** (with $\epsilon = 14\,\text{mm}$), and the RCE phase-field solutions are shown in **Fig. 11.6** (with $l = 4\,\text{mm}$). Apparently, the three simulations, the spectral split, the V-D split and the RCE approach, have obtained realistic crack opening deformations compared to the reference discrete crack simulation, i.e. non residual material deformations exist in the upper and lower block at the maximum separation $t = 1$ s. In the sequel, the material is compressed and both the spectral and the V-D split simulations are not capable to
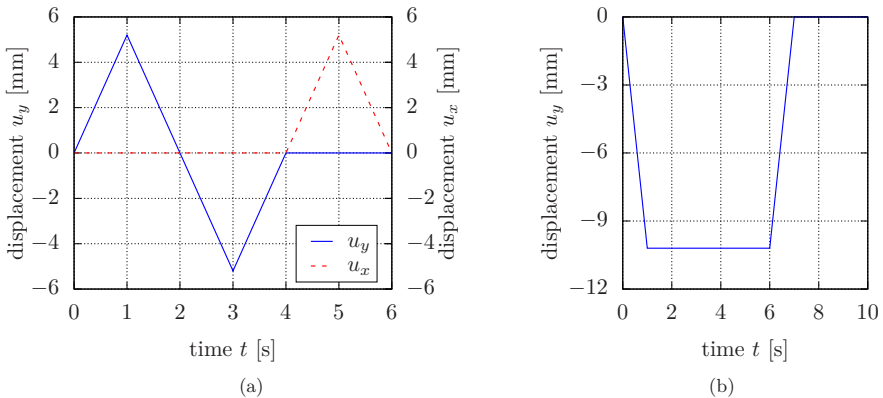
Fig. 11.4: Displacement loading function at (a) tension, compression and shear deformation for linear elasticity and only at (b) compression and relaxation for linear viscoelasticity.

capture the realistic crack closing deformations at t = 3 s. A slight unphysical lateral expansion by the spectral split is obtained. Unfortunately, this lateral expansion is significantly increased by the V-D split result. Nevertheless, this unphysical behavior does not appear at all for the proposed RCE modeling. Furthermore, the spectral split result fails to capture a realistic shear deformation at the crack, see **Figs. 11.5** (b) and **11.6** (a).

11.4.1.2 Linear Viscoelasticity

It is noteworthy that the constitutive laws in Steinke and Kaliske (2019); Strobl and Seelig (2016); Storm et al. (2020) are restricted to linear elasticity. Nevertheless, the RCE phase-field approach provides a general framework, which may be applied to any constitutive material model. For the total derivation, it is particularly referred to Yin et al. (2021). Furthermore, the RCE eigenfracture does not restrict the constitutive law as well. This work does not present the linear viscoelasticity model for an RCE eigenfracture description, but it is one of the next priorities for future publications. Due to linearity of the material, the RCE phase-field formulation aforementioned eventually returns to a relatively simple problem. The material tangent tensors for both bulk material and RCE blocks, i.e. $\mathbb{C}^0$ and $\mathfrak{C}$ are always constant. Meanwhile, $\mathbf{t}$ and $\mathfrak{t}$ vanish due to traction-free and friction-free considerations. As a result, the crack deformations $\Gamma^{1,2,3}$ (opening) or $\Gamma^{2,3}$ (closing) can be resolved by a closed form solution, which largely simplify the model problems.

It is necessary to point out that the standard spectral split (Miehe et al., 2010a) is not included for linear viscoelasticity due to some difficulties. The coupled constitutive equations of the spectral split model in Miehe et al. (2010a) are straightforwardly and consistently derived out of a predefined strain energy density functional involving the spectral decomposition of the strain tensor. However, the present linear viscoelastic model is governed by internal stress-type quantities, which cannot be obtained by a straightforward variational algorithm of strain based energy density function. Furthermore, the elastic energy for the non-equilibrium branches is obtained based on the non-equilibrium stress and the conjugate elastic tensor due to the constitutive linear characteristics. Therefore, the spectral split of the internal stress governed viscoelastic model has shown significant complexities. As a result, several existing phase-field models regarding fracture of viscoelastic material, see e.g. Shen et al. (2019); Schänzel (2015); Loew et al. (2019); Yin and Kaliske (2020c), are developed depending on the framework of the V-D split. Instead of the spectral split, a classical contact model is additionally considered for a representative reference for the crack kinematics demonstration in viscoelastic materials.

Another loading function in **Fig. 11.4** (b) describes pure compression and subsequent relaxation for the viscoelastic solid. The spectral split simulation is considered. Instead, classical contact modeling is performed. In a detailed description, the viscoelastic response of the material is supposed to relax from t = 1 s to t = 6 s at compressive state and from t = 7 s to t = 10 s at a non-external load state. Regarding viscoelasticity, only one PRONY term is considered and the parameters are given as
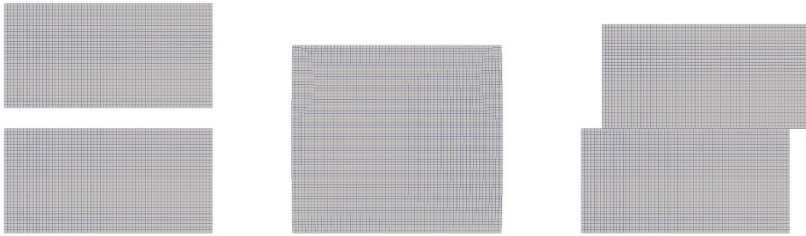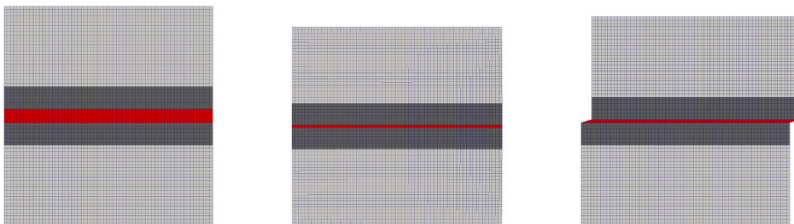
(a) deformation by discrete crack
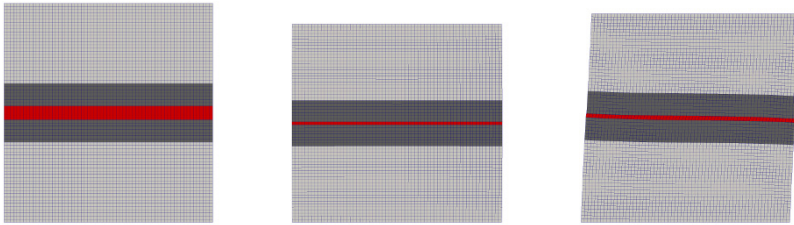
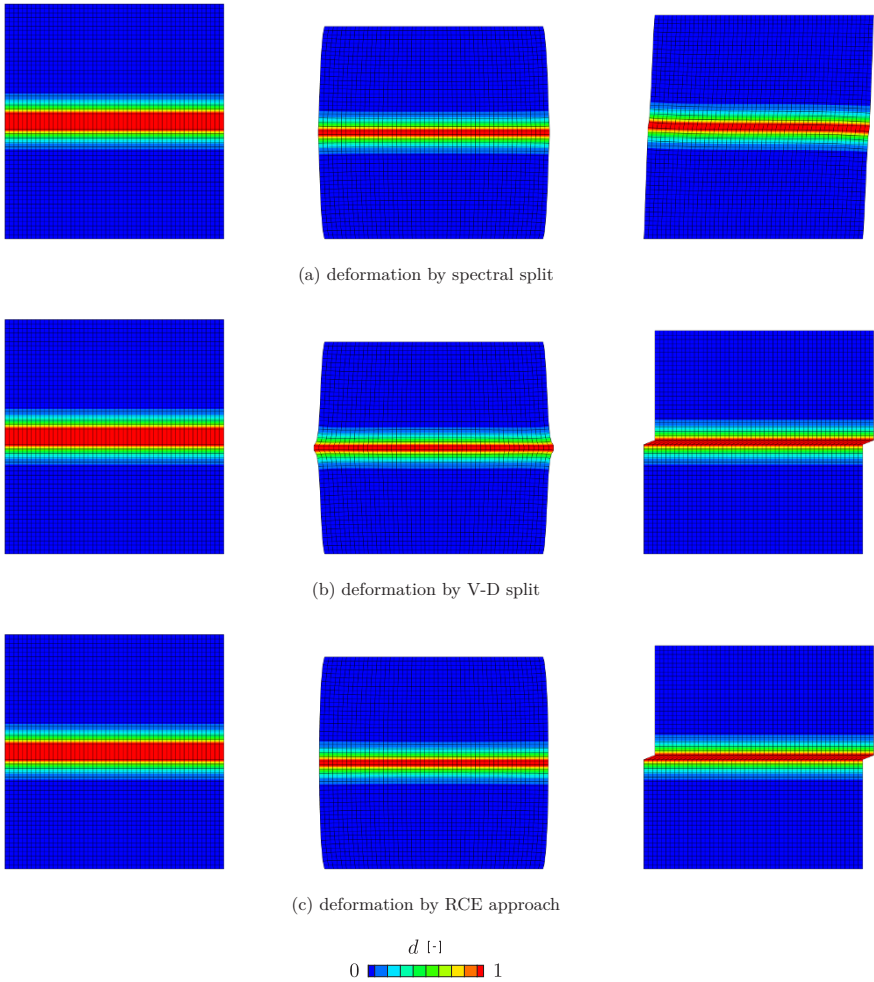

(b) deformation by spectral split
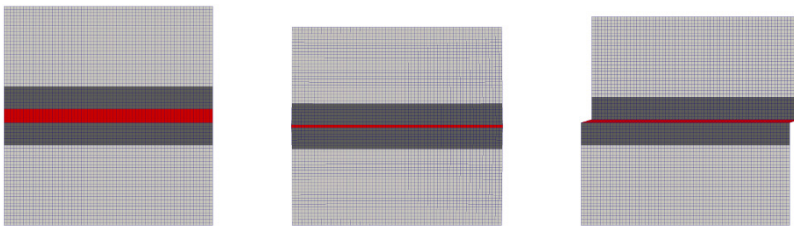
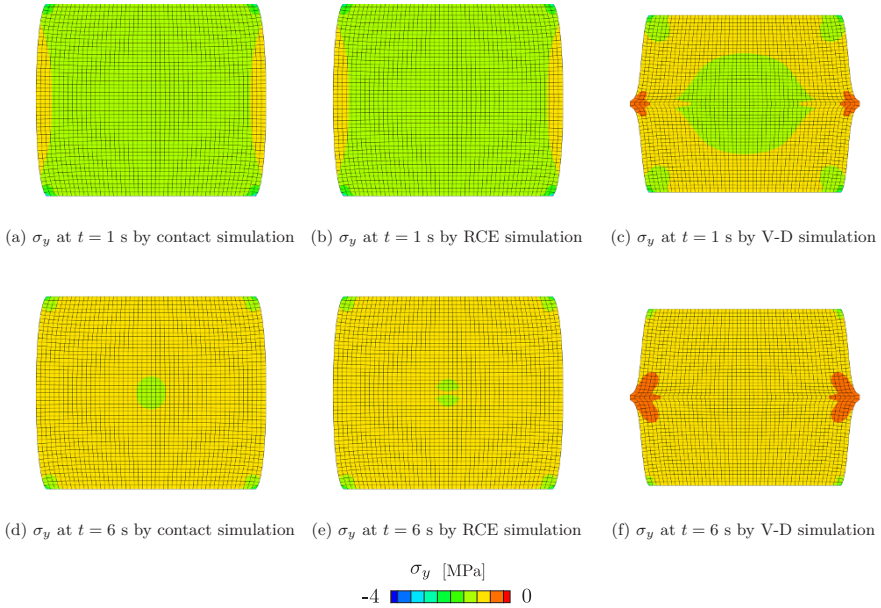(c) deformation by V-D split

(d) deformation by RCE

Fig. 11.5: Crack deformation at $t = 1\,$s, $t = 3\,$s and $t = 5\,$s regarding the loading function in **Fig. 11.4** (a) for spectral split, V-D split and RCE approach using the eigenfracture approach.

(a) deformation by spectral split

(b) deformation by V-D split

(c) deformation by RCE approach

d [-]

0 ▮▮▮▮▮▮▮▮▮▮ 1

Fig. 11.6: Crack deformation at $t = 1\,\mathrm{s}$, $t = 3\,\mathrm{s}$ and $t = 5\,\mathrm{s}$ regarding the loading function in **Fig. 11.4** (a) for spectral split, V-D split and RCE approach using phase-field modeling.

$\tau = 0.98\,\mathrm{s}$ and $\chi = 0.6$. As aforementioned, the V-D split model is not capable of capturing an appropriate compressive deformation in a viscoelastic body neither due to an unrealistic lateral stretch. Nevertheless, the RCE simulation properly addresses this issue and shows similar behavior compared to the contact model. Meanwhile, the contour distributions of the vertical stress σ_y for three approaches are compared at $t = 1\,\mathrm{s}$ and $t = 6\,\mathrm{s}$ in **Fig. 11.7**, where the RCE modeling successfully predicts the results that the contact model shows.

Furthermore, the effective strain energy φ^{mech}, the viscous dissipation $\mathcal{W}^{\mathrm{vis}}$ as well as their summation $\hat{\varphi} = \varphi^{\mathrm{mech}} + \mathcal{W}^{\mathrm{vis}}$ for the three models are evaluated. The V-D split model uses the standard form of $\varphi^{\mathrm{mech}} = \varphi^- + g\,(d)\,\varphi^+$, where for the de-

(a) σ_y at $t = 1$ s by contact simulation   (b) σ_y at $t = 1$ s by RCE simulation   (c) σ_y at $t = 1$ s by V-D simulation

(d) σ_y at $t = 6$ s by contact simulation   (e) σ_y at $t = 6$ s by RCE simulation   (f) σ_y at $t = 6$ s by V-D simulation

σ_y [MPa]

-4 ▮▮▮▮▮▮▮▮ 0

Fig. 11.7: Comparison of the distribution of the vertical stress σ_y for contact modeling, RCE simulation and V-D split simulation at $t = 1$ s (a)-(c) and $t = 6$ s (d)-(f), respectively.

tailed algorithmic setup, it is referred to Schänzel (2015); Yin and Kaliske (2020c). In the sequel, by a post-processing technique of volume integration of these two quantities, the total elastic strain energy and dissipation energy are obtained. Then, the quantity $\hat{\varphi} = \varphi^{\mathrm{mech}} + \mathcal{W}^{\mathrm{vis}}$ is also evaluated, since it straightforward indicates the external work induced into the closed system. Observing the energy components evolution in **Figs. 11.8** (a)-(c), φ^{mech} and $\mathcal{W}^{\mathrm{vis}}$ increase initially along with the external load application. Subsequently, the constant load leads to a slight decrease of φ^{mech} and a gradual increase of $\mathcal{W}^{\mathrm{vis}}$ up to the situation that the specimen is fully relaxed. The summation $\hat{\varphi}$ stays almost constant during the relaxation. It is explained that the external work does not change as long as the external load is kept constant. After the displacement returns to $u = 0$ mm and the material is fully relaxed, e.g. $t = 10$ s, φ^{mech} returns to 0 kJ and the total external work is fully dissipated due to viscous effects. Comparing these three approaches, the RCE formulation sufficiently agrees to the results of the contact modeling. However, the V-D split always underestimates the results, also see the reaction forces given in **Fig. 11.8** (d). Based on the aforementioned comments, the RCE approach is demonstrated to capture realistic crack kinematics for a closing crack within linear elastic and viscoelastic materials.
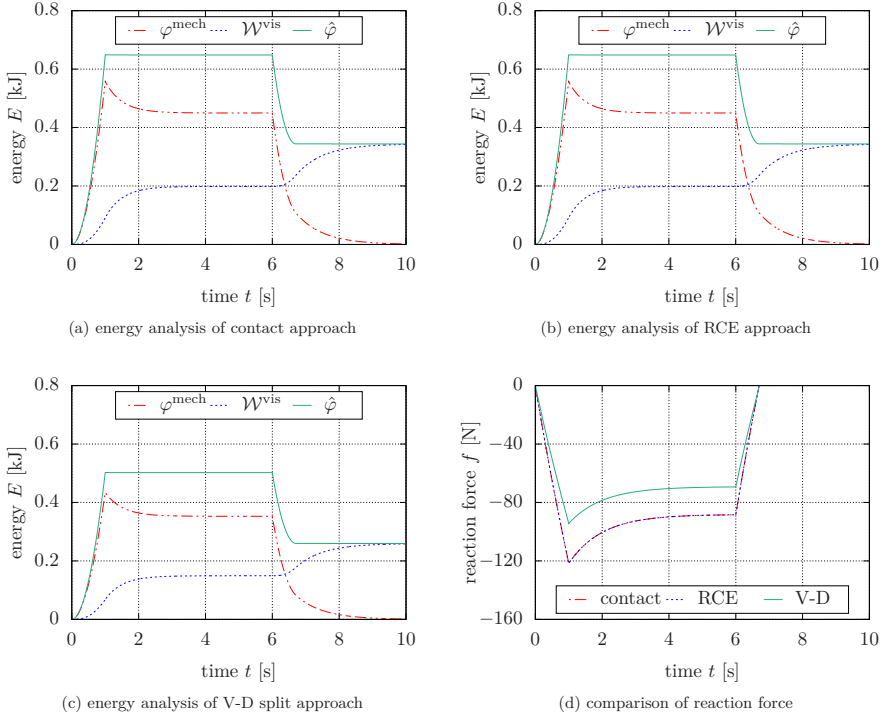
Fig. 11.8: Investigation of energy components: elastic strain energy φ^{mech}, viscous dissipation energy $\mathcal{W}^{\mathrm{vis}}$ and their summation $\hat{\varphi} = \varphi^{\mathrm{mech}} + \mathcal{W}^{\mathrm{vis}}$ for (a) contact modeling, (b) RCE simulation and (c) V-D split simulation, (d) reaction force f for the three approaches.

11.4.2 A Single Edge Notch Plate (SENP) at Shear Load

Using the similar geometric setup as in Miehe et al. (2010a), an elastic plate of length 100 mm, which is cracked half by an initial notch, is studied in this example. The plate edges parallel to the crack are clamped, and one edge is displaced parallel to the crack, leading to shear failure. The elastic parameters are $\lambda = 121.15$ GPa, $\mu = 80.77$ GPa, the fracture toughness is $\mathcal{G}_c = 2.7$ N/mm^2 and the length scale for phase-field is $l = 0.2$ mm. The displacement application is linearly increasing with time. For the numerical discretization of the two-dimensional boundary value problem, a total of 27225 uniform quadrilateral elements for plane strain with linear shape functions are used. In particular, in the used eigenfracture implementation, a new mechanical equilibrium state is determined before the next most critical element may fracture. The simulations are performed using the eigenfracture approach based on well known spectral split (Miehe et al., 2010a) and the V-D split (Amor et al., 2009), as well as for the eigenfracture model based on the RCE framework. A noteworthy point for the RCE framework is that the crack orientation for each element is calculated at the GAUSS point applying a reduced integration scheme.

Regarding the simulation results of the *SENP* test, the crack evolution and the crack neighborhood ($\varepsilon = 30.1\,h_e$) are shown in **Figs. 11.9** (a) and (b). In particular, the crack paths of the models with the spectral split, V-D split, and based on the RCE framework are compared. In principle, considering frictionless features, the crack surfaces along the initial crack should slide on each other without force transfer through the crack. Using the spectral split, the result based on a discrete crack description significantly differs from the model with pre-eroded elements. Therefore, the spectral split approach cannot be equivalently used for a discrete and a numerical crack due to the unphysical force transfer through a sliding crack surface. The crack paths predicted by the V-D and the RCE model differ in the propagation angle. Furthermore, both models yield a crack broadening in the region of the initial crack tip. The broadening is possibly caused by the regularized formulation of the increment of the crack surface area. As a consequence, crack surface increments for crack propagation perpendicular to the crack ligament are systematically smaller than in the direction of the crack ligament. Moreover, crack surface increments behind the crack tip are systematically smaller than at the crack tip. Thus, the elastic energy required to propagate a crack is largest at the crack tip for cracks propagating towards the crack ligament.

In addition to the eigenfracture simulation, the phase-field approach is also employed to simulate the *SENP* cracking as a comparison, see **Figs. 11.9** (c) and (d). Based on the same reason, the spectral split crack is not capable of predicting the realistic crack evolution by prescribing a phase-field crack as the initial notch. Since the whole process of *SENP* shear does not introduce any compressive deformation, the V-D split and the RCE framework yield good agreement to each other regarding the crack path prediction. Nevertheless, as long as compressive deformation exists, the V-D split immediately fails to predict the correct crack path as aforementioned in Sect. 11.4.1.

Furthermore, the influence of the ε-neighborhood size is studied in **Fig. 11.10**. The simulation is performed for different values of ε on the same mesh. The load at which the crack begins to propagate in the simulation is evaluated for different value of ε. Apparently, **Fig. 11.10** shows that the maximum force converges asymptotically with increasing neighborhood size. Convergence of the results can be accepted for the presented study when the neighborhood size parameter ε is about 15 times the element size h_e. However, crack propagation is disturbed when the ε-neighborhood reaches the geometry boundary of the model, e.g., crack kinking.

11.4.3 Structural Fracture at Finite Strain

The presented example is performed to demonstrate the capability of the phase-field model applied to hyper-elastic material by studying a promising benchmark of polymer fracture. The experimental tests are conducted by Hocine et al. (2002) to estimate the critical fracture energy. In the sequel, this example is studied by several different numerical approaches, e.g. the material force method Özenç and Kaliske
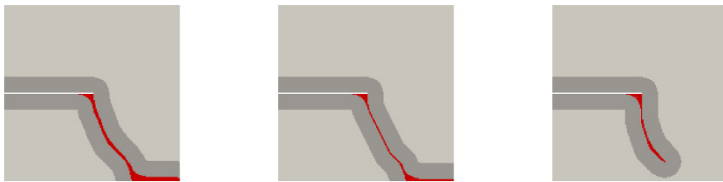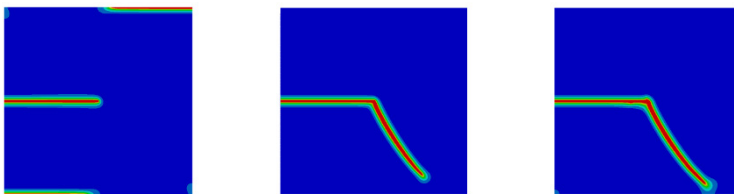
(a) eigenfracture with discrete crack for spectral split, V-D split and RCE, respectively
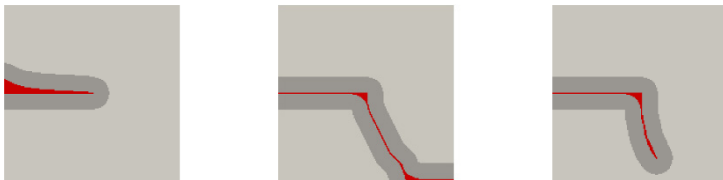
(b) eigenfracture with element erosion crack for spectral split, V-D split and RCE, respectively
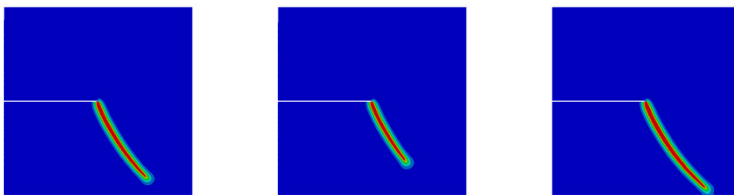
(c) phase-field with discrete crack for spectral split, V-D split and RCE, respectively

(d) phase-field with smeared phase-field crack for spectral split, V-D split and RCE, respectively

Fig. 11.9: Eigenfracture and phase-field simulation of crack evolution for both discrete crack and numerical crack (pre-eroded elements or phase-field crack) with respect to spectral split, V-D split and the RCE framework, respectively.

Fig. 11.10 Dependency of the maximum reaction force norm on the neighborhood size parameter ε.
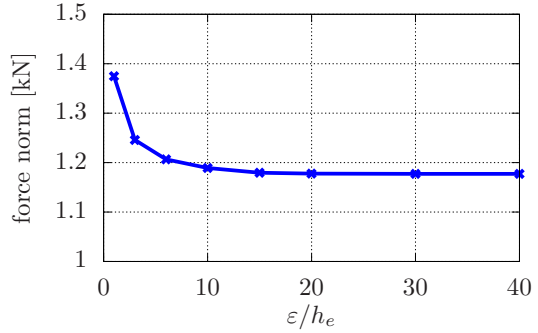
(2014) and the phase-field model (Miehe and Schänzel, 2014), which show good agreement compared to the evaluations of Hocine et al. (2002).

Regarding the constitutive law, Özenç and Kaliske (2014) simulates polymer fracture using the ARRUDA-BOYCE model, whose HELMHOLTZ energy density function generally reads

$$\varphi^0 = \kappa \left(J - \ln J - 1 \right) + \mu N \left(\lambda_r \mathcal{L}^{-1} \left(\lambda_r \right) + \ln \frac{\mathcal{L}^{-1} \left(\lambda_r \right)}{\sinh \mathcal{L}^{-1} \left(\lambda_r \right)} \right). \tag{11.49}$$

The segmentation N is a material parameter in addition to the bulk and shear moduli κ and μ. The stretch quantity λ_r is obtained by $\lambda_r = \sqrt{\operatorname{tr}\left(\bar{\mathbf{C}} \right) / 3N}$, where $\bar{\mathbf{C}}$ is the isochoric part of the right CAUCHY-GREEN tensor, and the inverse LANGEVIN function is defined by $\mathcal{L}^{-1}$. By applying the phase-field approach, Miehe and Schänzel (2014) describes the polymer based on the compressible NEO-HOOKEAN formulation, whose energy density function is defined as

$$\varphi^0 = \frac{\mu}{\beta} \left(J^{-\beta} - 1 \right) + \frac{\mu}{2} \left(\operatorname{tr} \left(\mathbf{C} \right) - 3 \right), \tag{11.50}$$

where β and μ are two governing parameters. For the purpose of simplicity and generality, this work chooses a nearly incompressible NEO-HOOKEAN model, which depends on the energy density function

$$\varphi^0 = \kappa \left(J - \ln \left(J \right) - 1 \right) + \frac{\mu}{2} \left(\operatorname{tr} \left(\bar{\mathbf{C}} \right) - 3 \right). \tag{11.51}$$

As a result of a consistent and straightforward derivation, the intact KIRCHHOFF stress and the corresponding material tangent tensors yield

$$\boldsymbol{\tau}_0 = p\, \mathbf{1} + \underbrace{\mu \left(\bar{\mathbf{b}} - \frac{1}{3} \operatorname{tr} \left(\bar{\mathbf{C}} \right) \mathbf{1} \right)}_{\boldsymbol{\tau}_{\mathrm{iso}}} \tag{11.52}$$

and

$$\mathbb{C}_0 = \left(p+s\right)\mathbf{1}\otimes\mathbf{1} - 2p\,\mathbb{I} + \frac{2}{3}\left(\mu\,\mathrm{tr}\left(\bar{\mathbf{C}}\right)\mathbb{P} - \boldsymbol{\tau}_{\mathrm{iso}}\otimes\mathbf{1} - \mathbf{1}\otimes\boldsymbol{\tau}_{\mathrm{iso}}\right), \qquad (11.53)$$

respectively. The definition of the isochoric right and left CAUCHY-GREEN tensors are $\bar{\mathbf{C}} = J^{\frac{2}{3}}\mathbf{C}$ and $\bar{\mathbf{b}} = J^{\frac{2}{3}}\mathbf{b}$. The hydrostatic scalar p and its corresponding modulus are obtained based on the first and the second order partial derivative of the volumetric energy density with respect to J, i.e. $p = J\,\partial_J\,U\,(J)$ and $s = J^2\,\partial^2_{JJ}\,U\,(J)$.

According to the material description aforementioned, a two-dimensional boundary value problem is taken into account. The geometry and boundary condition setup are depicted in **Fig. 11.11**. The bottom edge is fully fixed and the top one is fixed by a vertical upward displacement, which leads to monotonic tensile failure. Three symmetrical notch widths $a_0 = [12, 20, 28]$ mm are evaluated. Due to the symmetric geometry, loading as well as boundary conditions, a simplification can be employed by only considering half of the original specimen with appropriate symmetry conditions. The finite element discretizations consist of approximately 1200 4-node quadratic elements, where the potential damage paths are meshed by the uniform element size $h_e = 1$ mm. The model parameters are given as $\kappa = 5.49$ MPa, $\mu = 0.57$ MPa, $\mathcal{G}^0_c = 6.16$ J/mm^2 and the length-scale parameter for the phase-field evolution is $l = 2$ mm. The initial crack normal coincides with the loading direction.

The visualization of the phase-field crack evolution of the specimen with $a_0 = 20$ mm is shown in **Fig. 11.12**. With the help of a post-processing blanking technique, i.e. the phase-field value $d \geqslant 0.95$ is not visible, a vivid crack initiation and propagation before the complete separation can be effectively investigated. Furthermore, the load-displacement relations obtained by the present phase-field modeling are compared to the experimental results in **Fig. 11.13** for all the three specimen geometries. The fact of a smaller initial notch leading to larger overall strength is validated. Meanwhile, both the peak and the fracture displacements for the three cases can be approximately predicted. The force-displacement characteristics and the structural deformations are in good agreement with the experimental findings. Before structural rupture, a sudden drop of the reaction force along with unstable
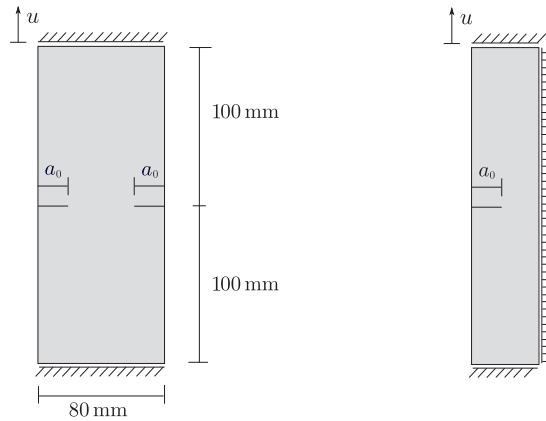

Fig. 11.11 (a) Geometrical setup of two-dimensional notched specimen and (b) its simplified half model due to symmetry.
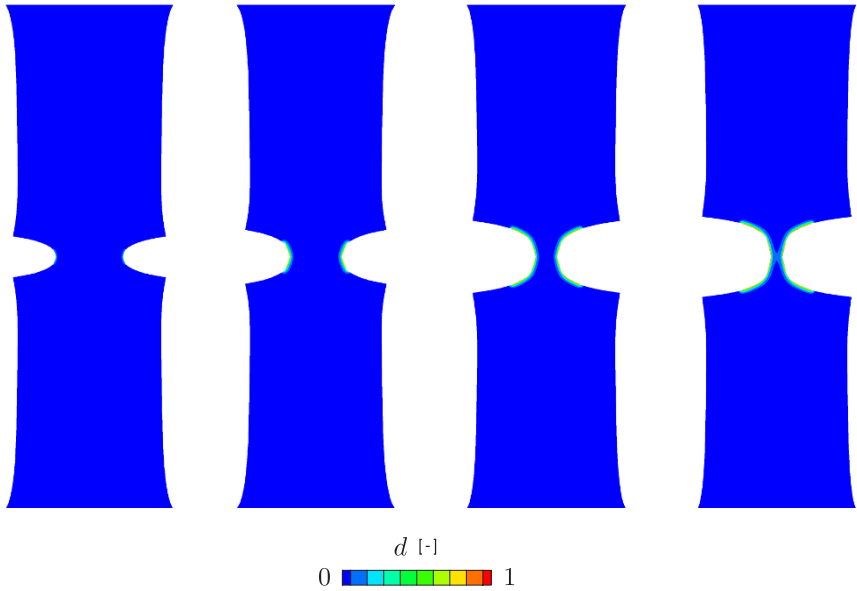
Fig. 11.12: Fracture evolution of the two-dimensional model by blanking the phase-field $\mathrm{d} \geqslant 0.95$.

Fig. 11.13 Comparison of the load-displacement relations of styrene butadiene rubber obtained by experimental results (Hocine et al., 2002) to the present phase-field model.
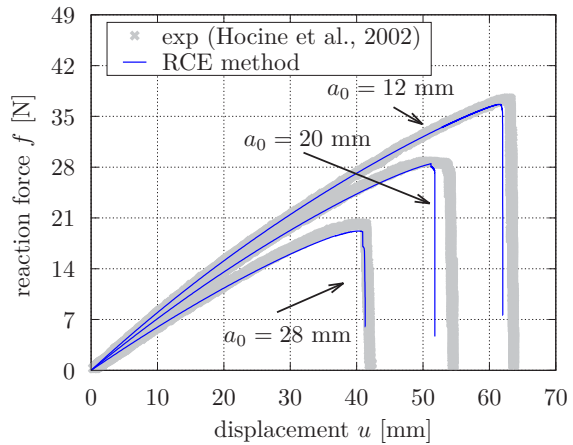
crack growth is obtained. The numerical convergence of the model in this final part of the simulation is hard to achieve due to large distortions of the elements at the crack tip. Therefore, full rupture is not reached.

11.4.4 Cohesive Failure Modeling

The example at hand studies cohesive failure within an RCE phase-field framework. The mechanism is mainly governed by the classical traction-separation law, which is commonly taken into consideration by the interface element approach.

The cohesive traction at the crack surface denoted by $\mathbf{t}$ in Eq. (11.25) usually cannot be neglected. This term is defined to be oriented outwards at the crack surface and the direction opposite the crack surface deformation $\mathbf{u}_\Gamma$. Herein, a classical traction-separation law (van den Bosch et al., 2008) is considered, and the pseudo potential functional is defined as

$$\varphi_{TS} = \phi - \frac{(\|\mathbf{u}_\Gamma\| + \Delta)\,\phi}{\Delta} \exp\left(-\frac{\|\mathbf{u}_\Gamma\|}{\Delta}\right), \tag{11.54}$$

where ϕ is a model parameter to represent the work or energy of separation and Δ is another parameter for the characteristic opening length. The maximum tractions T_{max} can be indirectly calculated by means of $T_{max} = \phi/(\exp(1)\,\Delta)$. According to variational derivation, the surface traction is derived as

$$\mathbf{t} = -\frac{\partial\,\varphi_{TS}}{\partial\mathbf{u}_\Gamma} = -\frac{\phi}{\Delta^2}\exp\left(-\frac{\|\mathbf{u}_\Gamma\|}{\Delta}\right)\mathbf{u}_\Gamma, \qquad \text{where} \qquad \mathbf{u}_\Gamma = \sum_{I=1}^{3} l_c\,\Gamma^I \mathbf{n}^I \tag{11.55}$$

and the consistent tangent reads

$$\mathbf{\hat{t}} = \frac{\partial^2\,\varphi_{TS}}{\partial\mathbf{u}_\Gamma^2} = -\frac{\partial\mathbf{t}}{\partial\mathbf{u}_\Gamma} = \frac{\phi}{\Delta^2}\exp\left(-\frac{\|\mathbf{u}_\Gamma\|}{\Delta}\right)\left(\mathbf{1} - \frac{\mathbf{u}_\Gamma \otimes \mathbf{u}_\Gamma}{\Delta\,\|\mathbf{u}_\Gamma\|}\right). \tag{11.56}$$

The aforementioned traction and tangent quantities characterize the path independent traction-separation formulation, which describe crack healing phenomena of the unloading and reloading processes. In order to achieve a general damage-like formulation, an algorithmic manipulation is proposed that distinguishes between loading and unloading paths. A representative approach is based on the comparison between the current separation and the maximum history separation (during the whole loading history from first load step till current one). The loading case is assumed when the current separation is the maximum one. In contrast, an unloading or reloading procedure is identified as long as the current separation is smaller than the maximum one, where the linear traction law is substituted. The maximum separation needs to be updated and saved as an internal variable at each loading step. Thereafter, the surface traction and the tangent quantities are rewritten as

$$\mathbf{t} = -\frac{\phi}{\Delta^2}\exp\left(-\frac{u_\Gamma^{max}}{\Delta}\right)\mathbf{u}_\Gamma \tag{11.57}$$

and

$$\mathfrak{k} = \begin{cases} \dfrac{\phi}{\Delta^2}\exp\left(-\dfrac{u_\Gamma^{\max}}{\Delta}\right)\mathbf{1} & \text{if } u_\Gamma^{\max} > \|\mathbf{u}_\Gamma\|, \\[2ex] \dfrac{\phi}{\Delta^2}\exp\left(-\dfrac{u_\Gamma^{\max}}{\Delta}\right)\left(\mathbf{1} - \dfrac{\mathbf{u}_\Gamma \otimes \mathbf{u}_\Gamma}{\Delta u_\Gamma^{\max}}\right) & \text{if } u_\Gamma^{\max} = \|\mathbf{u}_\Gamma\|, \end{cases} \tag{11.58}$$

respectively, by introducing the maximum separation

$$u_\Gamma^{\max} = \underset{\tau \leqslant t_{n+1}}{\text{Max}}\ \|\mathbf{u}_\Gamma(\tau)\| = \underset{\tau \leqslant t_{n+1}}{\text{Max}}\ \sqrt{\sum_{I=1}^{3}\left(l_c\,\Gamma^I\right)^2}. \tag{11.59}$$
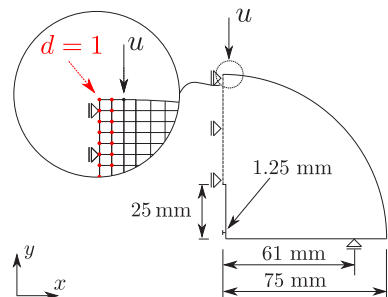
Returning the quantities $\mathbf{t}$ and $\mathfrak{k}$ to the RCE description, a consistent cohesive RCE phase-field modeling is obtained.

It is noteworthy that, in this example, the cohesive adhesion failure mechanism is formulated within a predefined phase-field crack path by setting the DIRICHLET boundary condition, which indicates that the crack orientation is also predefined in advance. As a result, the cohesive failure only occurs with respect to the existing phase-field crack path. Simultaneous evolution of crack propagation and cohesive adhesion failure at the evolved crack surfaces is not the scope of this work.

Inspired by Kim and Aragao (2013); Aragao (2011), which study a three-point bending test of a semi-circular specimen, the presented cohesive RCE phase-field approach is adopted for a numerical investigation. The experiment is shown in **Fig. 11.14** (a) and it is referred to Kim and Aragao (2013) for detailed insights. The specimen is a pre-notched semi-circular structure and it is characterized as bituminous mixture material. Two symmetrical points at the bottom edge are constrained along with the vertical direction and a downward displacement is applied at the top center of the curved boundary. Due to the symmetric properties of the geometry, the constraint and the loading condition, only half of the structure is taken into account for the numerical simulation, see **Fig. 11.14** (b). Since the cohesive crack path is known
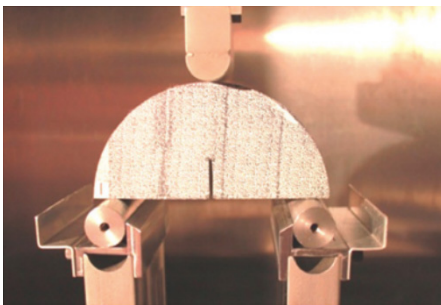
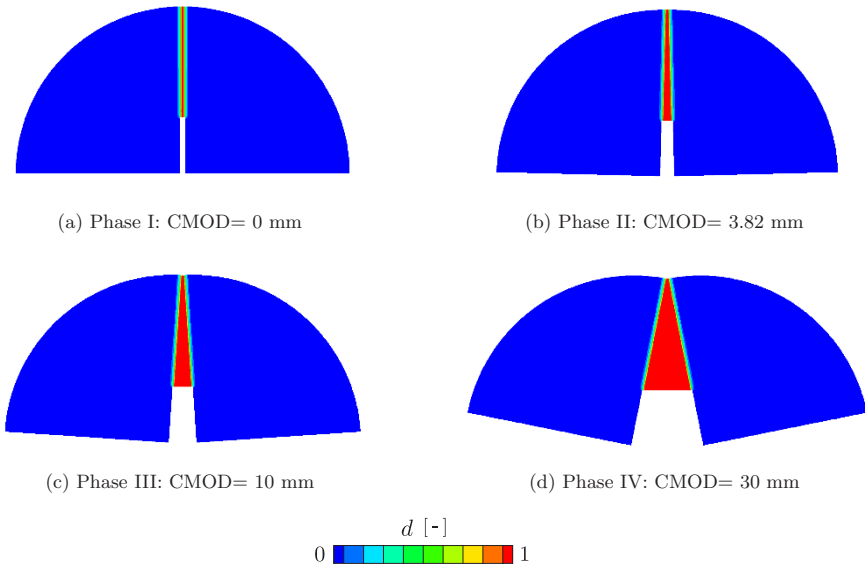(a) experimental setup in Kim and Aragao (2013)   (b) simplified numerical model

Fig. 11.14: (a) Experimental setup according to Kim and Aragao (2013) and (b) corresponding geometrical setup for cohesive failure simulation for the SCB test.

as a fact according to the experimental validations in Kim and Aragao (2013); Aragao (2011), the present model is applied to study the cohesive behavior during the crack opening. The loading governed by displacement control is applied to a single node next to the crack path, see **Fig. 11.14** (b) for the numerical setup in detail.

According to a parametric calibration study, the material parameters are identified as λ=11.3 GPa, μ=26.5 GPa, T_{max}=19.2 kPa, ϕ=110 kN/m^2, l_c=1 mm and l=0.85 mm based on the experimental result in Aragao (2011). The relationship of the resultant load with respect to the crack mouth opening displacement (CMOD) shows good agreement with the data in Aragao (2011). As can be observed, the simulation successfully captures the gradual increase of reaction force at the initial loading phase (Phase I). After reaching the peak load (Phase II), the traction starts to decrease and the expected softening behavior (Phase III) is investigated. A slight difference exists for the final failure status (Phase IV), where the experimental result completely reduces the reaction force but the simulation does not yet.

Furthermore, **Fig. 11.15** shows the deformed shapes of the specimen at four representative phases, which are in accordance with **Fig. 11.16**. It is noteworthy that the rotation of the symmetric specimen results in a combination of a stiff contact in the vicinity top region of the cohesive zone and a tensile separation in the rest part. The aforementioned constrained minimization algorithm can appropriately address the issue and guarantee numerical robustness in such loading conditions. Another interesting investigation is the norm of the cohesive traction $\|\mathbf{t}\|$ in the cracked region, see **Figs. 11.17** (a)-(d) for Phase I-IV, respectively. For a straightforward un-

(a) Phase I: CMOD= 0 mm

(b) Phase II: CMOD= 3.82 mm

(c) Phase III: CMOD= 10 mm

(d) Phase IV: CMOD= 30 mm

d [-]

0   1

Fig. 11.15: Deformation of SCB specimen with a prescribed phase-field crack path using a mirroring post-processing technique.

Fig. 11.16 Comparion of the
load-CMOD relationships for
the present simulation and
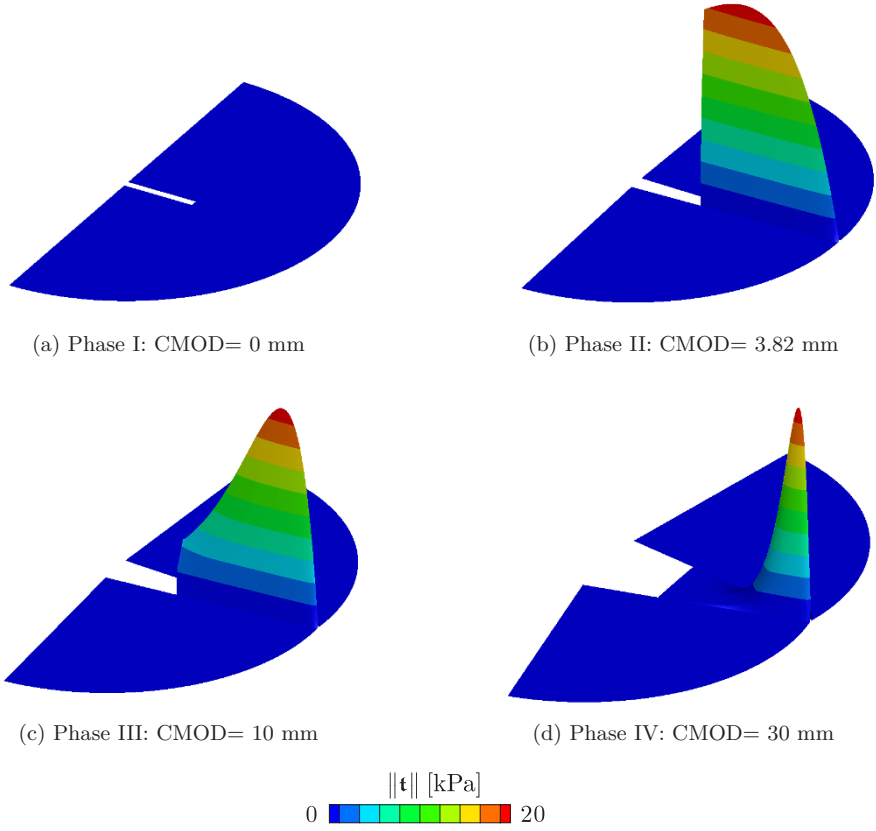the experimental prediction in
Aragao (2011).
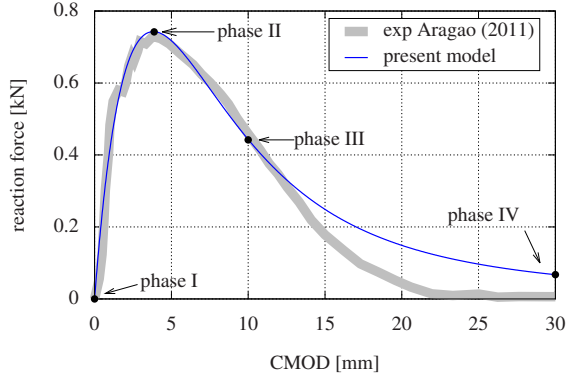
derstanding, the traction norm is plotted as outwards norm to the geometry plane
and the height represents the magnitude of the traction norm. It can be easily seen
that the traction norm evolves initially at the notch tip and 'propagates like a wave'
from the notch tip towards the top of the specimen along the prescribed phase-field
crack path. Eventually, **Fig. 11.17** (d) still shows a portion of cohesive tractions at
the top region, which explains the reason why the reaction force in **Fig. 11.16** does
not decrease to 0 at Phase IV. Using the same setup for the SCB test and model
parameters, a further investigation with respect to different initial notch lengths is
also included in this example. Three different initial lengths, i.e. $a = [20, 25, 30]$
mm, are simulated, where the loading-CMOD relations are shown in **Fig. 11.18**. It
can be found that the peak loads and the subsequent softening behavior are strongly
affected by the initial notch length.

11.4.5 Contact Friction Modeling

Friction between crack faces is a well known property which influences crack prop-
agation and the deformation of a fully evolved crack. However, friction is frequently
neglected in models of phase-field fracture even in investigations on Mode II, Mode
III and mixed mode deformations at the crack front. The influence of friction on
brittle fracture is demonstrated in the following examples. Results are compared to
the frictional phase-field approaches of Fei and Choo (2020a,b) and to discrete crack
models considering friction.

Considering the present RCE framework, the traction term **t** is reformulated
based on a classical COULOMB friction law. The friction force components for
$I = 2, 3$ are written as

(a) Phase I: CMOD= 0 mm

(b) Phase II: CMOD= 3.82 mm

(c) Phase III: CMOD= 10 mm

(d) Phase IV: CMOD= 30 mm

$$\|\mathbf{t}\|\ [\mathrm{kPa}]$$

0 ▮▮▮▮▮▮▮▮▮ 20

Fig. 11.17: Visualization of the cohesive traction norm $\|\mathbf{t}\|$ along with the prescribed phase-field crack path by an out-plane description.

$$
\begin{aligned}
\mathbf{t}^{\mathrm{I}} &= -\frac{1}{\mathcal{A}^{\Gamma}}
\begin{cases}
\mathbf{f}^{\mathrm{I}}_{\mathrm{stat}}, & \text{for} \quad \|\mathbf{f}^{\mathrm{I}}_{\mathrm{stat}}\| \leqslant \|\mathbf{f}^{\mathrm{I}}_{\mathrm{dyna}}\|, \\
\mathbf{f}^{\mathrm{I}}_{\mathrm{dyna}}, & \text{else},
\end{cases} \\
\mathbf{t}^{\mathrm{IJ}} &= \frac{1}{\mathcal{A}^{\Gamma}}
\begin{cases}
\mathsf{E}^{\Gamma}\delta_{\mathrm{IJ}}, & \text{for} \quad \|\mathbf{f}^{\mathrm{I}}_{\mathrm{stat}}\| \leqslant \|\mathbf{f}^{\mathrm{I}}_{\mathrm{dyna}}\|, \\
0, & \text{else},
\end{cases}
\end{aligned}
\tag{11.60}
$$

where

$$
\begin{cases}
f^{\mathrm{I}}_{\mathrm{stat}} = -\mathsf{E}^{\Gamma}\left(\Gamma^{\mathrm{I}} - \Gamma^{\mathrm{I}}_{\mathrm{pl}}\right), \\
f^{\mathrm{I}}_{\mathrm{dyna}} = \mu\mathcal{A}^{\Gamma}\mathbf{s} : \mathfrak{P}_{\mathrm{I}} \dfrac{f^{\mathrm{I}}_{\mathrm{stat}}}{\|\mathbf{f}^{\mathrm{I}}_{\mathrm{stat}}\|}.
\end{cases}
$$

The parameters μ and $\mathcal{A}^{\Gamma}$ are the friction coefficient and the crack surface area. Static friction (without surface sliding) is modeled via the penalty parameter E^{Γ}. The dynamic friction force $\mathbf{f}^{\mathrm{I}}_{\mathrm{dyna}}$ is proportional to the normal compression force, obtained from current stresses and the crack normal. Dynamic friction causes per-

Fig. 11.18 Load-CMOD relationships evaluated at different lengths of the initial notch.
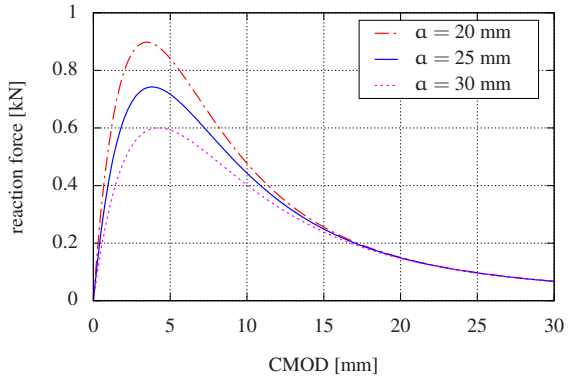

manent sliding deformation Γ_{pl}^I between the crack surfaces. The crack state is considered for the evolution equation as

- opened crack, $\Gamma_{pl,t_{n+1}}^I = \Gamma_{t_n}^I$,
- closed crack and static friction, $\Gamma_{pl,t_{n+1}}^I = \Gamma_{pl,t_n}^I$,
- closed crack and dynamic friction, $\Gamma_{pl,t_{n+1}}^I = \Gamma_{t_n}^I + \dfrac{f_{dyna}^I}{E^\Gamma}$.

It is notable that COULOMB's assumption of area independent friction forces is preserved in this model.

A long strip at compressive and shear loading is presented by Palmer et al. (1973), compare **Fig. 11.19**. The experiment is applied to over-consolidated clay observing significant cohesive fracture and crack surface friction. However, the experimental setup is adopted for the subsequent example and applied to brittle material behavior ($\mathcal{G}_c = 30$ J/mm) with COULOMB friction at the crack surfaces. The bulk material is considered as linear elastic (E = 1 GPa, $\nu = 0.3$) at small deformations. A fully constrained support is applied at the lower edge of the strip. The upper edge first undergoes a compressive displacement of $u_y = -0.01$ mm, followed by a tangential displacement of $u_x = 0.25$ mm applied in increments of $\Delta u_x = 0.25e-2$ mm. The model is uniformly discretized by 48400 linear elements.

The evolution of the phase-field is given in **Fig. 11.20** for different time steps and a friction coefficient of $\mu = 0.3$. The relations of the normal and tangential reaction
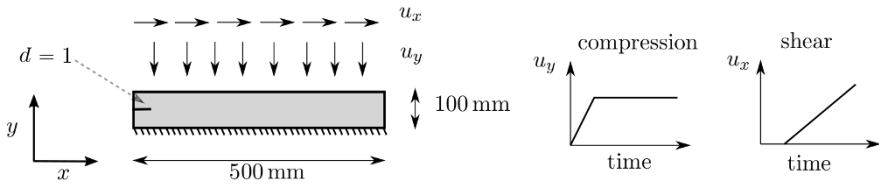

Fig. 11.19: Sketch of the long shear apparatus with initial phase-field crack and load history of normal and tangential displacement boundary conditions.
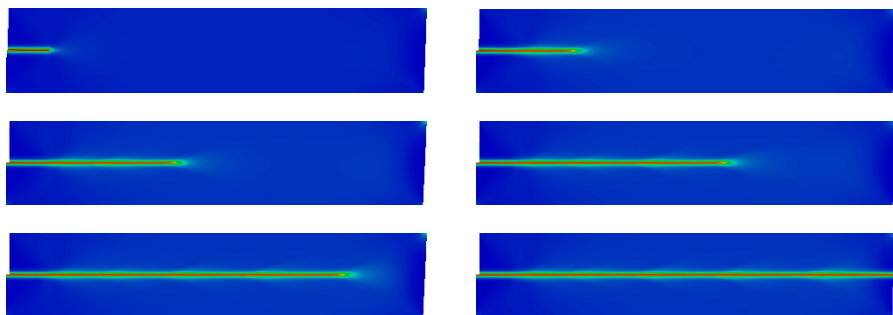
Fig. 11.20: Deformed shear strip with scaling factor 25 for different loading states, phase-field crack distribution during crack propagation.

forces versus tangential displacements are presented in **Fig. 11.21** for friction coefficients between $\mu = 0$ and $\mu = 1$. The comparison of the normal to the tangential reaction forces shows that the COULOMB law, which is applied at material level to the RCE model, is fulfilled at the component level, too. Furthermore, the initiation of crack propagation is significantly influenced by the frictional reaction force at the crack surface. The realistic relation between compression and friction force is also obtained by the cohesive phase-field model of Fei and Choo (2020b) considering crack friction. However, the approach presented there uses a directional decomposition of the stress based on the crack orientation but without considering lateral
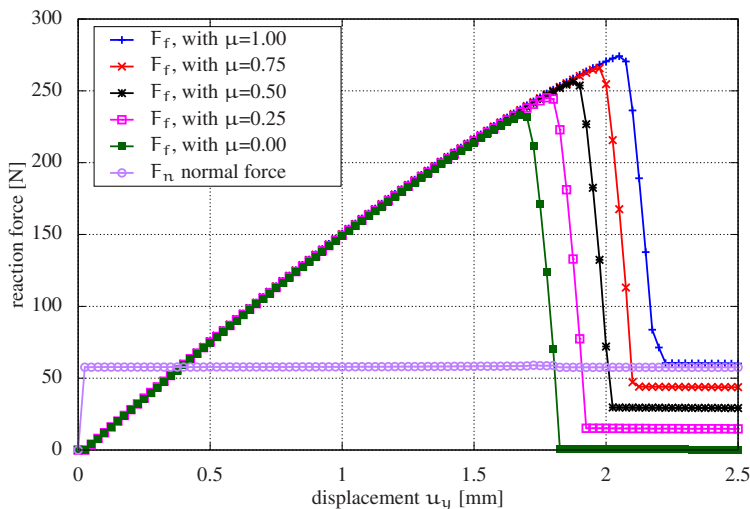
Fig. 11.21: Characteristics of normal force F_n versus tangential displacement and tangential frictional forces F_f for coefficients varied between $\mu = 0$ and $\mu = 1$.

contractions caused by POISSON's ratio ν. Additional criteria are introduced in order to distinguish frictional sticking and sliding. Crack surface contact is identified based on the sign of the normal strain which also misses lateral contractions at the crack surface. In contrast, the RCE framework allows for a realistic frictional crack model without the introduction of additional assumptions in order to approximate crack contact and frictional sticking.

11.5 Conclusions

Regularized formulations of the free discontinuity problem have been successfully applied to many classical and advanced problems of fracture mechanics in the past decade. A rapid development of phase-field fracture models could be observed, for instance, towards inelastic and anisotropic materials, fatigue behavior, multiphysical, multi-scale problems, frictional contact, and pore pressure models etc. Moreover, some fundamental challenges of classical fracture mechanical models, e.g., crack nucleation, crack branching, and proper discretizations, are solved by phase-field fracture and eigenfracture models. However, those models are recently shown to lack of reliable predictions for the crack contact state and the deformation kinematics at cracks. These intrinsic features of a fracture mechanical model are further related to the prediction of crack nucleation, propagation and branching. The recently introduced concept of representative crack elements provides a variational framework to couple physical crack models to regularized fracture formulations.

In this contribution, the fundamentals of representative crack elements are derived and the framework is presented in the context of phase-field fracture and eigenfracture. Discrepancies in previous models are demonstrated by consistency tests through a comparison to contact mechanical simulations. Same examples are further studied to verify deformation kinematics for cracks predicted by the models based on representative crack elements. The flexibility of the approach is finally proven by some applications to rate-dependent material, finite deformations, cohesive failure and crack surface friction.

References

Alessi R, Vidoli S, De Lorenzis L (2018) A phenomenological approach to fatigue with a variational phase-field model: The one-dimensional case. Engineering Fracture Mechanics 190:53–73, DOI 10.1016/j.engfracmech.2017.11.036

Alfano G, Crisfield MA (2001) Finite element interface models for the delamination analysis of laminated composites: mechanical and computational issues. International Journal for Numerical Methods in Engineering 50:1701–1736, DOI 10.1002/nme.93

Ambati M, Gerasimov T, De Lorenzis L (2015a) Phase-field modeling of ductile fracture. Computational Mechanics 55:1017–1040, DOI 10.1007/s00466-015-1151-4

Ambati M, Gerasimov T, De Lorenzis L (2015b) A review on phase-field models of brittle fracture and a new fast hybrid formulation. Computational Mechanics 55:383–405, DOI 10.1007/s00466-014-1109-y

Ambrosio L, Tortorelli VM (1990) Approximation of functional depending on jumps by elliptic functional via Γ-convergence. Communications on Pure and Applied Mathematics 43:999–1036, DOI 10.1002/cpa.3160430805

Ambrosio L, Fusco N, Pallara D (2000) Functions of Bounded Variation and Free Discontinuity Problems. Clarendon Press, Oxford

Amor H, Marigo JJ, Maurini C (2009) Regularized formulation of the variational brittle fracture with unilateral contact: Numerical experiments. Journal of the Mechanics and Physics of Solids 57:1209–1229, DOI 10.1016/j.jmps.2009.04.011

Aragao FTS (2011) Computational microstructure modeling of asphalt mixtures subjected to rate-dependent fracture. Ph.d. thesis, University of Nebraska-Lincoln

Barenblatt GI (1962) The mathematical theory of equilibrium cracks in brittle fracture. Advances in Applied Mechanics 7:55–129, DOI 10.1016/S0065-2156(08)70121-2

Blanco PJ, Sánchez PJ, Souza Neto EA, Feijóo RA (2016) Variational foundations and generalized unified theory of RVE-based multiscale models. Archives of Computational Methods in Engineering 23:191–253, DOI 10.1007/s11831-014-9137-5

Borden MJ, Hughes TJR, Landis CM, Verhoosel CV (2014) A higher-order phase-field model for brittle fracture: Formulation and analysis within the isogeometric analysis framework. Computer Methods in Applied Mechanics and Engineering 273:100–118, DOI 10.1016/j.cma.2014.01.016

Borden MJ, Hughes TJR, Landis CM, Anvari A, Lee IJ (2016) A phase-field formulation for fracture in ductile materials: Finite deformation balance law derivation, plastic degradation, and stress triaxiality effects. Computer Methods in Applied Mechanics and Engineering 312:130–166, DOI 10.1016/j.cma.2016.09.005

Bourdin B, Francfort GA, Marigo JJ (2000) Numerical experiments in revisited brittle fracture. Journal of the Mechanics and Physics of Solids 48:797–826, DOI 10.1016/S0022-5096(99)00028-9

Bourdin B, Francfort GA, Marigo JJ (2008) The variational approach to fracture. Journal of Elasticity 91:5–148

Braun M (1997) Configurational forces induced by finite-element discretization. Proceedings of the Estonian Academy of Sciences Physics - Mathematics 46:24–31

Bryant EC, Sun W (2018) A mixed-mode phase field fracture model in anisotropic rocks with consistent kinematics. Computer Methods in Applied Mechanics and Engineering 342:561–584, DOI 10.1016/j.cma.2018.08.008

Carrara P, Ambati M, Alessi R, De Lorenzis L (2020) A framework to model the fatigue behavior of brittle materials based on a variational phase-field approach. Computer Methods in Applied Mechanics and Engineering 361:112,731, DOI 10.1016/j.cma.2019.112731

Chambolle A, Conti S, Francfort GA (2018) Approximation of a brittle fracture energy with a constraint of non-interpenetration. Archive for Rational Mechanics and Analysis 228:867–889, DOI 10.1007/s00205-017-1207-z

De Giorgi E, Ambrosio L (1988) Un nuovo tipo di funzionale del calcolo delle variazioni. Atti della Accademia Nazionale dei Lincei Classe di Scienze Fisiche, Matematiche e Naturali Rendiconti Lincei Matematica e Applicazioni 82:199–210

Dugdale DS (1960) Yielding of steel sheets containing slits. Journal of the Mechanics and Physics of Solids 8:100–104, DOI 10.1016/0022-5096(60)90013-2

Fei F, Choo J (2020a) A phase-field method for modeling cracks with frictional contact. International Journal for Numerical Methods in Engineering 121:740–762, DOI 10.1002/nme.6242

Fei F, Choo J (2020b) A phase-field model of frictional shear fracture in geologic materials. Computer Methods in Applied Mechanics and Engineering 369:113,265, DOI 10.1016/j.cma.2020.113265

Foulk JW, Allen DH, Helms KLE (2000) Formulation of a three-dimensional cohesive zone model for application to a finite element algorithm. Computer Methods in Applied Mechanics and Engineering 183:51–66, DOI 10.1016/S0045-7825(99)00211-X

Francfort GA, Marigo JJ (1998) Revisiting brittle fracture as an energy minimization problem. Journal of the Mechanics and Physics of Solids 46:1319–1342, DOI 10.1016/S0022-5096(98)00034-9

Freddi F, Royer-Carfagni G (2009) Variational models for cleavage and shear fractures. Proceedings of the XIX AIMETA Symposium pp 715–716

Freddi F, Royer-Carfagni G (2010) Regularized variational theories of fracture: A unified approach. Journal of the Mechanics and Physics of Solids 58:1154–1174, DOI 10.1016/j.jmps.2010.02.010

Geelen RJM, Liu Y, Hu T, Tupek MR, Dolbow JE (2019) A phase-field formulation for dynamic cohesive fracture. Computer Methods in Applied Mechanics and Engineering 348:680–711, DOI 10.1016/j.cma.2019.01.026

Griffith AA (1921) The phenomena of rupture and flow in solids. Philosophical Transactions of the Royal Society of London Series A 221:163–198, DOI 10.1098/rsta.1921.0006

Gültekin O, Dal H, Holzapfel GA (2018) Numerical aspects of anisotropic failure in soft biological tissues favor energy-based criteria: A rate-dependent anisotropic crack phase-field model. Computer Methods in Applied Mechanics and Engineering 331:23–52, DOI 10.1016/j.cma.2017.11.008

Gurtin ME (2000) Configurational Forces as Basic Concepts of Continuum Physics. Applied Mathematical Sciences, Springer, New York, DOI 10.1007/978-0-387-22656-9_5

Hakim V, Karma A (2009) Laws of crack motion and phase-field models of fracture. Journal of the Mechanics and Physics of Solids 57:342–368, DOI 10.1016/j.jmps.2008.10.012

Henry H, Levine H (2004) Dynamic instabilities of fracture under biaxial strain using a phase field model. Physical Review Letters 93:105,504, DOI 10.1103/PhysRevLett.93.105504

Hesch C, Weinberg K (2014) Thermodynamically consistent algorithms for a finite-deformation phase-field approach to fracture. International Journal for Numerical Methods in Engineering 99:906–924, DOI 10.1002/nme.4709

Hill R (1963) Elastic properties of reinforced solids: Some theoretical principles. Journal of the Mechanics and Physics of Solids 11:357–372, DOI 10.1016/0022-5096(63)90036-X

Hocine N, Abdelaziz M, Imad A (2002) Fracture problems of rubbers : J integral estimation based upon η factors and investigation on the strain energy density distribution as a local criterion. International Journal of Fracture 117:1–23, DOI 10.1023/A:1020967429222

Kienzler R, Herrmann G (2000) Mechanics in Material Space: with Applications to Defect and Fracture Mechanics. Springer, Berlin, Heidelberg, DOI 10.1007/978-3-642-57010-0_4

Kim YR, Aragao FTS (2013) Microstructure modeling of rate-dependent fracture behavior in bituminous paving mixtures. Finite Elements in Analysis and Design 63:23–32, DOI 10.1016/j.finel.2012.08.004

Kuhn C, Müller R (2010) A continuum phase field model for fracture. Engineering Fracture Mechanics 77:3625–3634, DOI 10.1016/j.engfracmech.2010.08.009

Lancioni G, Royer-Carfagni G (2009) The variational approach to fracture mechanics. A practical application to the French Panthéon in Paris. Journal of Elasticity 95:1–30, DOI 10.1007/s10659-009-9189-1

Linse T, Hennig P, Kästner M, de Borst R (2017) A convergence study of phase-field models for brittle fracture. Engineering Fracture Mechanics 184:307–318, DOI 10.1016/j.engfracmech.2017.09.013

Loew PJ, Peters B, Beex LAA (2019) Rate-dependent phase-field damage modeling of rubber and its experimental parameter identification. Journal of the Mechanics and Physics of Solids 127:266–294, DOI 10.1016/j.jmps.2019.03.022

Luo C, Chen L, Huang Y (2021) A phase-field crack model based on a directional strain decomposition and a stress-driven Crack-Opening Indicator. Computer Methods in Applied Mechanics and Engineering 384:113,928, DOI 10.1016/j.cma.2021.113928

Mandal TK, Nguyen VP, Wu JY (2019) Length scale and mesh bias sensitivity of phase-field models for brittle and cohesive fracture. Engineering Fracture Mechanics 217:106,532, DOI 10.1016/j.engfracmech.2019.106532

Maugin GA (1995) Material forces: Concepts and applications. Applied Mechanics Reviews 48:213, DOI 10.1115/1.3005101

Maugin GA (2010) Configurational Forces: Thermomechanics, Physics, Mathematics, and Numerics. Routledge & CRC Press, Boca Raton

Miehe C, Gürses E (2007) A robust algorithm for configurational-force-driven brittle crack propagation with r-adaptive mesh alignment. International Journal for Numerical Methods in Engineering 72:127–155, DOI 10.1002/nme.1999

Miehe C, Schänzel LM (2014) Phase field modeling of fracture in rubbery polymers. Part I: Finite elasticity coupled with brittle failure. Journal of the Mechanics and Physics of Solids 65:93–113, DOI 10.1016/j.jmps.2013.06.007

Miehe C, Hofacker M, Welschinger F (2010a) A phase field model for rate-independent crack propagation: Robust algorithmic implementation based on operator splits. Computer Methods in Applied Mechanics and Engineering 199:2765–2778, DOI 10.1016/j.cma.2010.04.011

Miehe C, Welschinger F, Hofacker M (2010b) Thermodynamically consistent phase-field models of fracture: Variational principles and multi-field FE implementations. International Journal for Numerical Methods in Engineering 83:1273–1311, DOI 10.1002/nme.2861

Miehe C, Hofacker M, Schänzel LM, Aldakheel F (2015) Phase field modeling of fracture in multi-physics problems. Part II. Coupled brittle-to-ductile failure criteria and crack propagation in thermo-elastic-plastic solids. Computer Methods in Applied Mechanics and Engineering 294:486–522, DOI 10.1016/j.cma.2014.11.017

Mueller R, Maugin GA (2002) On material forces and finite element discretizations. Computational Mechanics 29:52–60, DOI 10.1007/s00466-002-0322-2

Nguyen VP, Wu JY (2018) Modeling dynamic fracture of solids with a phase-field regularized cohesive zone model. Computer Methods in Applied Mechanics and Engineering 340:1000–1022, DOI 10.1016/j.cma.2018.06.015

Ortiz M, Pandolfi A (1999) Finite-deformation irreversible cohesive elements for three-dimensional crack-propagation analysis. International Journal for Numerical Methods in Engineering 44:1267–1282

Özenç K, Kaliske M (2014) An implicit adaptive node-splitting algorithm to assess the failure mechanism of inelastic elastomeric continua. International Journal for Numerical Methods in Engineering 100:669–688, DOI 10.1002/nme.4774

Palmer AC, Rice JR, Hill R (1973) The growth of slip surfaces in the progressive failure of over-consolidated clay. Proceedings of the Royal Society of London A Mathematical and Physical Sciences 332:527–548, DOI 10.1098/rspa.1973.0040

Pandolfi A, Ortiz M (2012) An eigenerosion approach to brittle fracture. International Journal for Numerical Methods in Engineering 92:694–714, DOI 10.1002/nme.4352

Pandolfi A, Weinberg K, Ortiz M (2021) A comparative accuracy and convergence study of eigenerosion and phase-field models of fracture. Computer Methods in Applied Mechanics and Engineering 386:114,078, DOI 10.1016/j.cma.2021.114078

Pham K, Amor H, Marigo JJ, Maurini C (2011) Gradient damage models and their use to approximate brittle fracture. International Journal of Damage Mechanics 20:618–652, DOI 10.1177/1056789510386852

Qinami A, Pandolfi A, Kaliske M (2020) Variational eigenerosion for rate-dependent plasticity in concrete modeling at small strain. International Journal for Numerical Methods in Engineering 121:1388–1409, DOI 10.1002/nme.6271

Schänzel LM (2015) Phase field modeling of fracture in rubbery and glassy polymers at finite thermo-viscoelastic deformations. Phd thesis, Universität Stuttgart, Stuttgart

Schellekens JCJ, de Borst R (1993) On the numerical integration of interface elements. International Journal for Numerical Methods in Engineering 36:43–66, DOI 10.1002/nme.1620360104

Schmidt B, Fraternali F, Ortiz M (2009) An eigendeformation approach to variational fracture. Multiscale Modeling & Simulation 7(3):1237–1266, DOI 10.1137/080712568

Seiler M, Linse T, Hantschke P, Kästner M (2020) An efficient phase-field model for fatigue fracture in ductile materials. Engineering Fracture Mechanics 224:106,807, DOI 10.1016/j.engfracmech.2019.106807

Shen R, Waisman H, Guo L (2019) Fracture of viscoelastic solids modeled with a modified phase field method. Computer Methods in Applied Mechanics and Engineering 346:862–890, DOI 10.1016/j.cma.2018.09.018

Steinke C, Kaliske M (2019) A phase-field crack model based on directional stress decomposition. Computational Mechanics 63:1019–1046, DOI 10.1007/s00466-018-1635-0

Stochino F, Qinami A, Kaliske M (2017) Eigenerosion for static and dynamic brittle fracture. Engineering Fracture Mechanics 182:537–551, DOI 10.1016/j.engfracmech.2017.05.025

Storm J, Supriatna D, Kaliske M (2020) The concept of representative crack elements for phase-field fracture: Anisotropic elasticity and thermo-elasticity. International Journal for Numerical Methods in Engineering 121:779–805, DOI 10.1002/nme.6244

Storm J, Qinami A, Kaliske M (2021a) The concept of representative crack elements applied to eigenfracture. Mechanics Research Communications 116:103,747, DOI 10.1016/j.mechrescom.2021.103747

Storm J, Yin B, Kaliske M (2021b) The concept of representative crack elements (rce) for phase-field fracture - transient thermo-mechanics. submitted

Strobl M, Seelig T (2016) On constitutive assumptions in phase field approaches to brittle fracture. Procedia Structural Integrity 2:3705–3712, DOI 10.1016/j.prostr.2016.06.460

Teichtmeister S, Kienle D, Aldakheel F, Keip MA (2017) Phase field modeling of fracture in anisotropic brittle solids. International Journal of Non-Linear Mechanics 97:1–21, DOI 10.1016/j.ijnonlinmec.2017.06.018

van den Bosch MJ, Schreurs PJG, Geers MGD (2008) On the development of a 3D cohesive zone element in the presence of large deformations. Computational Mechanics 42:171–180, DOI 10.1007/s00466-007-0184-8

Verhoosel CV, de Borst R (2013) A phase-field model for cohesive fracture. International Journal for Numerical Methods in Engineering 96:43–62, DOI 10.1002/nme.4553

Vignollet J, May S, de Borst R, Verhoosel CV (2014) Phase-field models for brittle and cohesive fracture. Meccanica 49:2587–2601, DOI 10.1007/s11012-013-9862-0

Yin B, Kaliske M (2020a) An anisotropic phase-field model based on the equivalent crack surface energy density at finite strain. Computer Methods in Applied Mechanics and Engineering 369:113,202, DOI 10.1016/j.cma.2020.113202

Yin B, Kaliske M (2020b) A ductile phase-field model based on degrading the fracture toughness: Theory and implementation at small strain. Computer Methods in Applied Mechanics and Engineering 366:113,068, DOI 10.1016/j.cma.2020.113068

Yin B, Kaliske M (2020c) Fracture simulation of viscoelastic polymers by the phase-field method. Computational Mechanics 65:293–309, DOI 10.1007/s00466-019-01769-1

Yin B, Khodor J, Kaliske M (2020a) Fracture and fatigue failure simulation of polymeric material at finite deformation by the phase-field method and the material force approach. Advances in Polymer Science 286:347–376, DOI 10.1007/12_2020_63

Yin B, Steinke C, Kaliske M (2020b) Formulation and implementation of strain rate dependent fracture toughness in context of the phase-field method. International Journal for Numerical Methods in Engineering 121:233–255, DOI 10.1002/nme.6207

Yin B, Storm J, Kaliske M (2021) Viscoelastic phase-field fracture using the framework of representative crack elements. International Journal of Fracture DOI 10.1007/s10704-021-00522-1

Zhang X, Vignes C, Sloan SW, Sheng D (2017) Numerical evaluation of the phase-field model for brittle fracture with emphasis on the length scale. Computational Mechanics 59:737–752, DOI 10.1007/s00466-017-1373-8

Chapter 12
Applications of Viscoplasticity and Damage Models, the Thermomechanical Consistency and the Prospect of a Microstructural Representation

Matthias Ziegenhorn, Rainer Adelung, Rainer Franke, Robert Roszak, Ilja Sagradov, Daniela Schob, Holger Sparr, and Tomasz Kurzynowski

Abstract Material models in the framework of continuum mechanics cover the experimentally observed phenomena with a mathematical representation and a corresponding set of material parameters, which need to be established and validated. The theory of viscoplasticity plays an important role to describe the material behaviour of polymers and metals for a conventional as well as an additive manufacturing process. Naturally, the manufacturing process influences the microstructure and is to be reflected in the analysis and the characterisation of the material. The geometry reconstruction of microscopic images supports the extension of well-known material models and motivates the investigation of the interaction in bicontinuous composites. A universal measurement method as the contactfree thermography can be applied to validate the analytical assumption by an extended set of characteristics.

Key words: Viscoplasticity, Continuum damage mechanics, Porosity, Additive manufacturing, Thermomechanical consistency, Thermography, μComputed tomography, Image geometry reconstruction

Matthias Ziegenhorn · Rainer Franke · Robert Roszak · Ilja Sagradov · Daniela Schob · Holger Sparr
BTU Cottbus-Senftenberg, Universitätsplatz 1, 01968 Senftenberg, Germany,
e-mail: matthias.ziegenhorn@b-tu.de, rainer.franke@b-tu.de, robert.roszak@b-tu.de, ilja.sagradov@b-tu.de, daniela.schob@b-tu.de, holger.sparr@b-tu.de

Rainer Adelung
CAU Kiel, Kaiserstraße 2, 24143 Kiel, Germany,
e-mail: ra@tf.uni-kiel.de

Tomasz Kurzynowski
Politechnika Wrocławska, Wydział Mechaniczny, ul. Ignacego Łukasiewicza 5, 50-371 Wrocław, Poland,
e-mail: tomasz.kurzynowski@pwr.edu.pl

12.1 Introduction

The interest in describing complex material behaviour is ongoing and is fed by the development of new materials and their application in medical technology or automotive and aerospace engineering. These design materials should work safely and predictably until the defined end-of-life of the corresponding component or part. Material and damage models are developed at differentiated levels of abstraction and verified with adequate test procedures.

The fundamental model comparisons analysed by Krempl (1987) consider models applying a yield surface, e.g. Perzyna (1963) and Chaboche (1989), and models without using a yield surface, like in Bodner and Partom (1975). The application of these models is documented for metals in Olschewski (1996). The research on strain rate dependent models for elastic as well as plastic behaviour carried out by Reese (1998) justifies the attempt to capture the material behaviour of metals and polymers with the Chaboche or Bodner-Partom model.

Currently, the number of testing standards for additively manufactured polymers is limited. According to Forster (2015), only 20 of 47 available testing standards are conditionally applicable. This challenge adds up onto the constantly improved and modified manufacturing processes and an increased set of variable process parameters. The manufacturing process itself generates inhomogeneities on the microscale predominantly in form of voids. Under mechanical loading, a stress concentration in the vicinity of the voids occurs and, thus, a localized damage evolution is initiated. With the assumption of a statistically uniform void distribution and restrictions on the void properties, the original material models can be enhanced by ideas from the continuum damage mechanics, where ductile damage, referencing void initiation, growth and coalescence, can be represented by the models of Gurson (1977) or Lemaître and Desmorat (2005).

The generalised classification of material behaviour according to Haupt (2002) is used. The tensorial formulations of backstress, overstress and equilibrium stress developed by Haupt are applied and reference is made to the presentation of these variables in connection with the arguments related to dislocation movement and velocity in Krempl (1987).

To substantiate the material classification and to assess the suitability of the chosen modelling approach, a temperature evolution is very sensitive to certain deformation mechanisms. The required accuracy in the temperature measurement is given by modern infrared cameras. The pioneering works of Taylor and Quinney (1934); Oldyrev and Tamuzh (1969); Chrysochoos (2012) concerning a temperature evolution due to mechanical loading and the accompanying experimental methods for metallic and polymer materials have been initiating new thermomechanical modelling approached over the last decades. The fundamental KELVIN effect can be used to determine the yield point, while the dissipative phenomena for inelastic deformation or the microstructural evolution in cyclic loading becomes clearly evident for self-heating. The principles of continuum thermomechanics generate a universal framework for the formulation of thermodynamically consistent material models not limited to certain material classes and also provided the functionality for incor-

porating scale effects. The here considered models (Bodner and Lindenfeld, 1995; Bröcker and Matzenmiller, 2013; Kamlah and Haupt, 1998) are applied to casted and additively manufactured metal alloys with respect to plastic and viscoplastic deformation processes, where microstructural effects in terms of a material phase interaction are not in focus.

Complex material configurations due to strengthening, weakening or functional integration by particles require the representation of inhomogeneity. The analysis of models using representative volume elements (RVE) at the appropriate scale are very successful in this respect. Following the Eshelby approach for elastic material, Yanase et al. (2020) investigate the influence of the particle shape on the overall stiffness properties of a two-phase composite. A multi-step method proposed by El Ghezal and Doghri (2018) combines of the Eshelby-based Mori-Tanaka method, the generalized self-consistent scheme and the Gurson model to account for plastic deformations and a concurrent porosity evolution. A random dispersion of elastic spheres in an elastic-plastic polymer matrix is the subject of the FE-based numerical homogenisation by Khdir et al. (2013), where the statistical deviation was quantified with respect to the number of particles per control volume. Examples for bicontinuous material configuration (two interpenetrating phases) and a corresponding homogenised representation are given in Carolan et al. (2015); Soyarslan et al. (2019) and address three-dimensional networks within a matrix as in Arndt et al. (2021).

In this contribution, the addressed topics are reflected in the three main sections. Sect. 12.2 focuses on classical, viscoplastic material models in conjunction with continuum damage mechanics. An external temperature load is incorporated. The self-heating phenomenon is the core of Sect. 12.3. Especially, the extended evaluation of the thermomechanical process is pointed out, and the significance of the applied models is emphasized. In Sect. 12.4, the beginning of the analysis of bicontinuous or multiphase materials is shown by a model generation technique through microscopic image data processing, where the aforementioned procedures can be applied to.

12.2 Experimental and Numerical Investigation of Temperature-dependent Mechanical Behaviour of 3D Printed Polyamide 12

The engineering requirements for additively manufactured polymer components are growing as well as their applications are becoming more complex. Therefore, the additively manufactured polymers are increasingly used in mechanically stressed components. To ensure that additively manufactured polymers can withstand the new conditions, it is essential to subject them to a testing procedure.

It cannot be assumed that a homogeneous material structure is achieved in additive manufacturing in contrast to conventionally manufactured injection-molded components. The thermoplastic polyamide 12 (PA12) is one of the materials used and the subject of the described analysis. The damage behaviour under quasi-static

tensile stress and the relaxation properties are of special interest in the characterisation procedure.

## 12.2.1 Experimental Analysis

12.2.1.1 Sample Preparation

The samples have been prepared by selective laser sintering (SLS). The SLS PA2200 material has been used. A sPro 230 printer from 3D Systems with a power of 70 W was used. It was operated with a laser scanning speed of 10 m/s for the infill and 5 m/s for contours. The nominal layer thickness was $0.08 - 0.15$ mm. The temperature of the pressure chamber and the process were 170 °C and 200 °C. The spherical powder particles had a size in the range of $20 - 80$ μm. Due to the fact that no test standards exist for additive manufactured (AM) polymers, the geometry of the test specimens was chosen according to DIN EN ISO 527-2 Type 1A (DIN Deutsches Institut für Normung e.V., 2012), **Fig. 12.1**a. In previous investigations, it was found that the material properties only slightly depend on the printing direction (Franke et al., 2017). Therefore, all samples were printed in x-direction, according to the definition in **Fig. 12.1**b.

12.2.1.2 Test Conditions

Exhibiting PA12 at a temperature from 10 to 40 °C shows a significant influence on the mechanical properties. Therefore, three different types of tests were performed - (I) isothermal and (II) non-isothermal tensile tests and (III) isothermal multirelaxation tests. A servo-hydraulic test machine from ZwickRoell with a 25 kN load cell and temperature chamber were used. (I) For the isothermal tensile tests four levels of chamber temperature, 10 °C, 20 °C, 30 °C and 40 °C were selected. Five tests were carried out for each temperature level with a displacement rate of 0.5 mm/min, **Fig. 12.2** (*a*). (II) Five non-isothermal tests were performed with the temperature
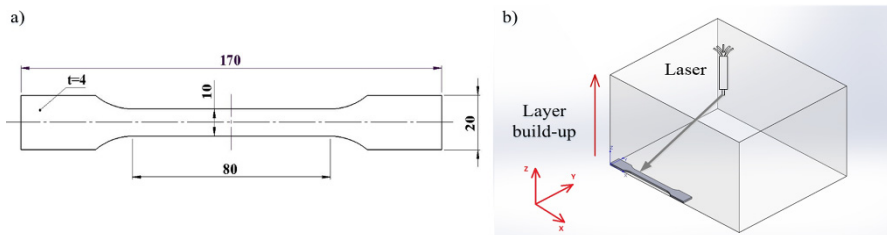
Fig. 12.1: (*a*) Dimensions of the specimen, (*b*) Sketch of the printing job: individual layers printed in xy-plane; the build-up (stacking direction) in z-direction.

(a)

(b)

(c)
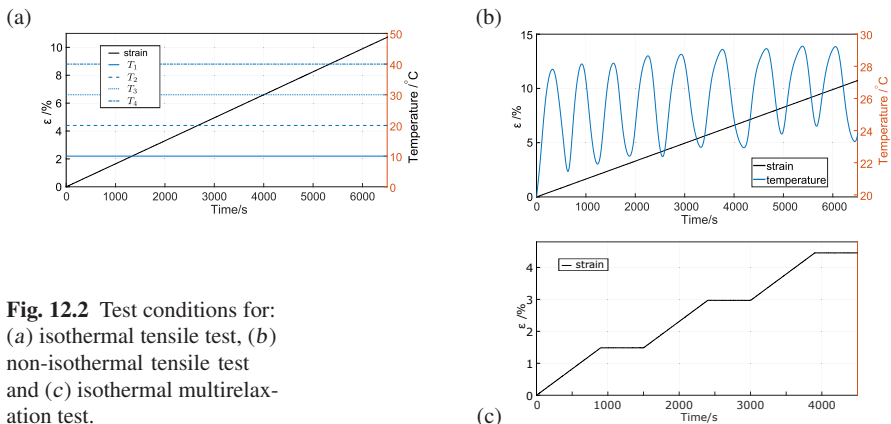
Fig. 12.2 Test conditions for: (*a*) isothermal tensile test, (*b*) non-isothermal tensile test and (*c*) isothermal multirelaxation test.

cyclically changing between $10 - 40\,°C$ at a rate of $0.2\,°C/s$ during tensile loading, **Fig. 12.2** (*b*). (III) Multirelaxation tests were built up stepwise and divided into three holding times and three tensile load steps. The holding times were 4 min and the displacement rate of the tensile load was kept constant during the test at 5 mm/min, **Fig. 12.2** (*c*).

12.2.2 Microanalysis

12.2.2.1 Scanning Electron Microscopy

To describe the damage behaviour, the microstructure of the fracture surfaces of the specimens was examined by means of a scanning electron microscopy (SEM) after the tensile tests, **Fig. 12.3**. The images show an inhomogeneous microstructure containing pores. In the fringe area, it was found that the printing process does not produce a smooth surface and that small notches are formed on the surface.
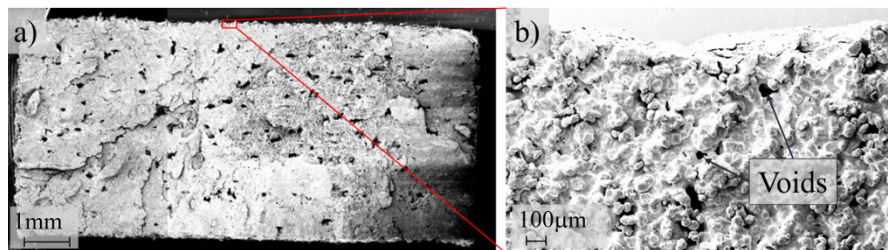
Fig. 12.3: Scanning electron micrographs, (*a*) fracture surface 40× magnification, (*b*) Section of the upper edge area, 150× magnification.

12.2.2.2 X-ray Computed Tomography

Figure 12.4 shows the reconstructed computed tomography (CT) images of a specimen at a virgin state and after tensile loading. A porosity of 3.7% for the virgin state resp. 3.6% for the loaded sample was measured. The distribution of the cavities over the specimen is very uniform, which means that an intensified melting on the surfaces and edges during the printing process did not take place.

A statistical uniform void distribution together with the average void size suggests that the assumption of material homogeneity and the validity of the phenomenological approach are justified.

12.2.3 Numerical Analysis

Previous investigations (Schob et al., 2019) have shown that additively manufactured PA12 behaves viscoplastically. The viscoplastic models established in recent years can essentially be divided into two groups. One group introduces a specific yield limit, while the other renounces an explicit yield limit and, consequently, a pure elastic domain altogether. The first group includes the material model of Chaboche (1989) and the material model of Bodner and Partom (1975); Bodner (2000) belongs to the second group.

A separated temperature dependency for each material parameter can be established for a temperature range of interest. A complete map involving a interdependence of all relevant parameters is usually experimentally out of scope. Instead, the Johnson-Cook approach allows a generalised covering of the temperature dependency in a material model and is mathematically applicable to the models of Bodner-Partom and Chaboche (Bodner, 2000; Cook and Cook, 1983).

Furthermore, the microstructure analysis in Schob et al. (2019) showed a porosity of 4.7% in the virgin samples. The pores have a spherical shape and change the shape during loading. To model the damage behaviour of PA12, the Gurson-Tvergaard-Needleman (GTN) model was successfully applied in Schob et al. (2019, 2020) for static and cyclic loading at room temperature.
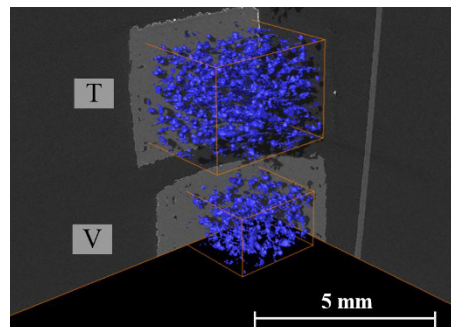
Fig. 12.4 CT rendering of pores for a virgin (V, bottom) and a loaded (T, top) specimen.

The Gurson (1977) and Lemaître and Desmorat (2005) damage models are the most commonly used approaches for simulating processes with ductile fracture. The approach of Lemaitre is based on the model of effective stresses by Kachanov (1980). In the initially two-dimensional formulation, Lemaitre derives the damage value from the ratio of the pore area fraction to the total area. The Gurson model was developed on the studies of void growth by Rice and Tracey (1969) and takes the void volume fraction of the total volume for the damage evolution into account.

In the following paragraphs, the Chaboche and the Bodner-Partom material models as well as the Johnson-Cook extension and the damage models of Gurson-Tvergaard-Needleman and Lemaitre are described. Furthermore, they are applied to the additively manufactured PA12 samples with the previously outlined loading schemes.

12.2.3.1 The CHABOCHE Model

The CHABOCHE model is composed as a system of differential equations. Considering the theory of infinitesimal deformation, the total strain rate $\dot{\boldsymbol{\varepsilon}}^{\text{tot}}$ follows the additive split into an elastic $\dot{\boldsymbol{\varepsilon}}^{\text{el}}$ and a viscoplastic $\dot{\boldsymbol{\varepsilon}}^{\text{vp}}$ rate fraction,

$$\dot{\boldsymbol{\sigma}} = \mathbb{C} \cdot \left(\dot{\boldsymbol{\varepsilon}}^{\text{tot}} - \dot{\boldsymbol{\varepsilon}}^{\text{vp}} \right) \tag{12.1}$$

with the CAUCHY stress $\boldsymbol{\sigma}$ and the linear elastic stiffness tensor $\mathbb{C}$. Here, the definition of the viscoplastic strain rate $\dot{\boldsymbol{\varepsilon}}^{\text{vp}}$ is decisive:

$$\dot{\boldsymbol{\varepsilon}}^{\text{vp}} = \dot{\lambda} \frac{\partial \phi}{\partial \boldsymbol{\sigma}} \quad \text{with} \quad \lambda = \left\langle \frac{\phi}{K} \right\rangle^{n} \tag{12.2}$$

with the viscosity factor K and n. The viscoplastic multiplier λ describes the evolution of the viscoplastic deformation increment. The flow function ϕ enables the determination whether the material undergoes a pure elastic or an elastic-viscoplastic deformation (in the elastic domain $\phi < 0$; in the elastic-viscoplastic domain $\phi = 0$). The following equation defines the flow function, where σ^{y} is the yield stress and q_1, q_2 are the damage parameters according to Tvergaard and Needleman (1984).

$$\phi = \left(\frac{\sigma_{\text{eq}}^{\text{eff}}}{\sigma^{y}} \right)^{2} + 2q_1 f^{*} \cosh \left(\frac{3q_2}{2} \frac{\sigma_{\text{m}}^{\text{eff}}}{\sigma^{y}} \right) - 1 - (q_1 f^{*})^{2} \geqslant 0 \tag{12.3}$$

Furthermore, the flow function is defined by the effective stress $\sigma_{\text{m}}^{\text{eff}}$ and the VON MISES equivalent stress $\sigma_{\text{eq}}^{\text{eff}}$,

$$\sigma_{eq}^{eff} = \sqrt{\frac{1}{2}\left[(\sigma_1^r - \sigma_2^r)^2 + (\sigma_2^r - \sigma_3^r)^2 + (\sigma_3^r - \sigma_1^r)^2\right]} \qquad (12.4)$$

$$\sigma_m^{eff} = \left(\frac{\sigma_{kk}^r}{3}\right) \qquad (12.5)$$

$$\boldsymbol{\sigma}^r = \boldsymbol{\sigma} - \boldsymbol{\alpha}^* \qquad (12.6)$$

$$\boldsymbol{\alpha}^* = (1 - f^*) \sum_{k=1}^{2} \boldsymbol{\alpha}^{(k)} \qquad (12.7)$$

where $\boldsymbol{\sigma}^r$ is the relative stress and f^* the damage evolution. Compared to the previous investigation (Schob et al., 2019), the kinematic hardening $\boldsymbol{\alpha}^*$

$$\boldsymbol{\alpha}^* = T^h(1 - f^*) \sum_{k=1}^{2} \boldsymbol{\alpha}^{(k)} \quad \text{with} \quad k = 1,2 \qquad (12.8)$$

was extended by the Johnson-Cook equation T^h, Cook and Cook (1983); Bodner (2000). This approach takes into account the displacement of the flow surface due to the influence of temperature change. The Johnson-Cook equation is defined as,

$$T^h = \left(1 - \frac{T - T^0}{T^m - T^0}\right)^d \qquad (12.9)$$

by the empirical value d and the melting temperature T^m, with $(T \geqslant T^0)$. For the isothermal experiments T^h equals to one. In Eq. (12.8), the kinematic hardening $\boldsymbol{\alpha}^{(k)}$ is defined by the following equation,

$$\dot{\boldsymbol{\alpha}}^{(k)} = \frac{2}{3}C^{(k)}\dot{\boldsymbol{\varepsilon}}^{vp} - \gamma^{(k)}\boldsymbol{\alpha}^{(k)}\dot{\varepsilon}_M^{vp} \quad \text{with} \quad k = 1,2 \quad \text{and} \quad \dot{\varepsilon}_M^{vp} = \frac{\boldsymbol{\sigma}^r\dot{\boldsymbol{\varepsilon}}^{vp}}{(1 - f^*)\sigma^y} \qquad (12.10)$$

where C and γ are hardening parameters and $\dot{\varepsilon}_M^{vp}$ is the rate of the equivalent viscoplastic strain.

12.2.3.2 The BODNER-PARTOM Model

The BODNER-PARTOM model has been used for modelling the mechanical behaviour of metals (Olschewski, 1996) and polymers (Zaïri et al., 2005). In contrast to the CHABOCHE model, it contains no formulation of an established yield criterion (Bodner, 2000). Thus, plastic deformation occurs at any time on the load-path, no matter whether loading or unloading takes place. The BODNER-PARTOM model is a system of ordinary first order differential equations and can be decomposed into an equation for the viscoplastic strain rate $\dot{\varepsilon}^{vp}$, the multiplier $\dot{p}$ connecting the strain rate with the stress deviator, the scalar variable Z_I representing isotropic hardening,

the tensorial variable $\mathbf{Z}_D$ representing kinematic hardening as well as the evolution equation for the inelastic work W^{vp}.

Here, the isotropic hardening variable Z_I consists of the coefficient for isotropic hardening m_1, the initial value for isotropic hardening K_0, the limiting (maximum) value for isotropic hardening K_1, the fully recovered (minimum) value for isotropic hardening K_2, the recovery rate coefficient for isotropic hardening A_1 and the recovery exponent for isotropic hardening r_1. The tensorial variable $\mathbf{Z}_D$ combines the coefficient for kinematic hardening m_2, the limiting (maximum) value for kinematic hardening K_3, the recovery rate coefficient for kinematic hardening A_2 and the recovery exponent for kinematic hardening r_2. The BODNER-PARTOM model is summarized in Eqs. (12.11) - (12.15).

$$\dot{\boldsymbol{\varepsilon}}^{vp} = \frac{3}{2}\dot{p}\frac{\boldsymbol{\sigma}'}{J(\boldsymbol{\sigma}')} \quad \text{with} \quad \boldsymbol{\sigma}' = \boldsymbol{\sigma} - \sigma_{ii}\mathbf{I} \tag{12.11}$$

$$\dot{p} = \frac{2}{\sqrt{3}}D_0\exp\left[-\frac{1}{2}\left(\frac{Z_I + \mathbf{Z}_D \cdot \dfrac{\boldsymbol{\sigma}}{J(\boldsymbol{\sigma})}}{J(\boldsymbol{\sigma}')}\right)^{2n}\right] \tag{12.12}$$

Isotropic hardening

$$\dot{Z}_I = m_1(K_1 - Z_I)\dot{W}^{vp} - A_1\left(\frac{Z_I - K_2}{K_1}\right)^{r_1} \tag{12.13}$$

Kinematic hardening

$$\dot{\mathbf{Z}}_D = m_2\left(K_3\frac{\boldsymbol{\sigma}}{J(\boldsymbol{\sigma})} - \mathbf{Z}_D\right)\dot{W}^{vp} - A_2\left(\frac{\frac{2}{3}J(\mathbf{Z}_D)}{K_1}\right)^{r_2}\frac{\mathbf{Z}_D}{J(\mathbf{Z}_D)} \tag{12.14}$$

Specific viscoplastic work rate

$$\dot{W}^{vp} = \boldsymbol{\sigma} \cdot \dot{\boldsymbol{\varepsilon}}^{vp} \tag{12.15}$$

12.2.3.3 The GURSON-TVERGAARD-NEEDLEMAN model

Since the CT results (Schob et al., 2019) suggest assuming spherical pores, the GTN model (Tvergaard and Needleman, 1984) was applied. The original Gurson model from 1977 is based on the assumption of spherical pores (Gurson, 1977). Whereby a rigid-perfect plastic material behaviour is accepted and the flow criterion of VON MISES is applied. A constant strain rate is applied. The flow function ϕ (Eq. (12.3)) is defined as a function of the macroscopic stress and the randomly distributed void

volume. Tvergaard and Needleman (1984) extended the Gurson model. The extended model considers growth, nucleation and coalescence.

With the modified void volume fraction f*, it is now possible to model the load capacity loss above a critical void volume fraction f_c. When a critical void volume fraction f_c is reached, coalescence occurs. This process continues until a failure value f_F is reached and the specimen fails. The initial porosity f_0 is determined at time $t = 0$.

$$f^* = \begin{cases} f_0 & \text{if} \quad t = 0 \\ f & \text{if} \quad f \leqslant f_c \\ f_c + \dfrac{\dfrac{1}{q_1} - f_c}{f_F - f_c}(f - f_c) & \text{if} \quad f_c < f \leqslant f_F \end{cases} \tag{12.16}$$

The void volume fraction considers the growth f_g and nucleation f_n of voids, Eqs. (12.17) - (12.20).

$$\dot{f} = \dot{f}_g + \dot{f}_n \tag{12.17}$$

$$\dot{f}_g = (1 - f)\dot{\varepsilon}_{kk}^{vp} \tag{12.18}$$

$$\dot{f}_n = \frac{f_N \dot{\bar{\varepsilon}}^{vp}}{S_N \sqrt{2\pi}} \exp\left(-\frac{1}{2} \left(\frac{\bar{\varepsilon}^{vp} - \varepsilon_N}{S_N} \right)^2 \right) \tag{12.19}$$

$$f_0 = f(t = 0) \tag{12.20}$$

Nucleation is controlled by the nucleation porosity f_N, the effective viscoplastic strain $\bar{\varepsilon}^{vp}$, the viscoplastic strain rate $\dot{\bar{\varepsilon}}^{vp}$, the mean strain ε_N and the standard deviation of the stress S_N. The GTN model contains 8 damage parameters. The initial damage parameter f_0 was determined by computed tomography in Schob et al. (2020) and is 4.7%.

12.2.3.4 The LEMAITRE Damage Model

Layered building of components in AM results in anisotropy and material defects, e.g. microcracks. Recent research (Stichel et al., 2017) revealed the correlation between microcracks in AM materials and anisotropy. Therefore, the focus of this work is the mathematical description of the microcracks.

The anisotropic mechanical response could be the direct result of distinct pore shapes or arrangements since pores are analogous to small pre-existing cracks (Stichel et al., 2017). 3D printed PA12 shows distinct brittle material behaviour in contrast to PA12 manufactured by injection moulding (Franke et al., 2017). The issue of brittleness should be addressed considering two features: first, the nucleation of a crack, which is favoured by the residual voids due to incomplete sintering; secondly the crack propagation (Dupin et al., 2012). If the material does not fully consolidate, crack initiation and failure can occur. (van Hooreweder et al., 2010) performed fatigue tests on laser sintered PA12 and found that the crack initiation

resulted from inclusions in the material caused by unfused powder particles. As a result, lower density parts had a higher chance of crack initiation and undergoing fatigue damage (Goodridge et al., 2012). The material density is a crucial influence factor for the fatigue life of the components. The lower the density, the more unfused powder particles appear and the higher the chance for crack initiation to start will be.

To predict rupture of structures with good accuracy, it is necessary to use coupled constitutive equations. Therefore, the viscoplastic model of BODNER-PARTOM is coupled with the LEMAITRE damage model (Lemaître and Desmorat, 2005). It is based on the concept of effective stress due to material damage and fatigue. The damage is caused by micro-cracks and only determined by the state in one single material point. So, the impact of damage nearby is not considered. A macro-crack is then considered as the set of points for which the local damage has reached its critical value at failure. The Lemaitre model has the form of a system of ordinary first order differential equations and can be decomposed into the effective stress rate $\dot{\sigma}_{\text{eff}}$, the damage rate $\dot{D}$ and energy release rate Y. The damage rate consists of the elastic modulus E, the damage parameters s and S, as well as of the rupture time t_r. The LEMAITRE damage model for the one-dimensional case is given in Eqs. (12.21) - (12.24).

Effective stress

$$\dot{\sigma}_{\text{eff}} = (1-D)E(\dot{\varepsilon} - \dot{\varepsilon}^{\text{vp}}) \tag{12.21}$$

Damage rate

$$\dot{D} = \left(\frac{Y}{S}\right)^s \dot{p} \tag{12.22}$$

$$S = \frac{(2s+1)^{\frac{1}{s}}}{2E} \left(\int_0^{t_r} \sigma_{\text{eff}}^{2s} \dot{p}\, dt\right)^{\frac{1}{s}} \tag{12.23}$$

Energy release rate

$$Y = \frac{\sigma_{\text{eff}}^2}{2(1-D)^2 E} \tag{12.24}$$

Further explanations on the LEMAITRE damage model can be found in Lemaître and Desmorat (2005). For simplicity reasons, only isotropic material damage was considered.

12.2.4 Results

The material model parameters were optimized by the nonlinear least square method. This method is commonly used for obtaining material parameters of the CHABOCHE viscoplastic material model (Gong et al., 2010). The solution of the equations of the material models with optimal material parameters is then compared with experimental results. In **Fig. 12.5** the results of the isothermal tensile test are presented and validated with the CHABOCHE-GTN model. Throughout all temperature stages an excellent agreement between experiment and simulation could be achieved. A direct dependency between temperature and the elastic modulus could be observed. The higher the temperature, the lower the elastic modulus. Furthermore, a decrease of the maximum stress with increasing temperature could be noticed.

In **Fig. 12.6** the results of the non-isothermal tensile test are presented and validated with the CHABOCHE-GTN-JC model. An excellent agreement between ex-
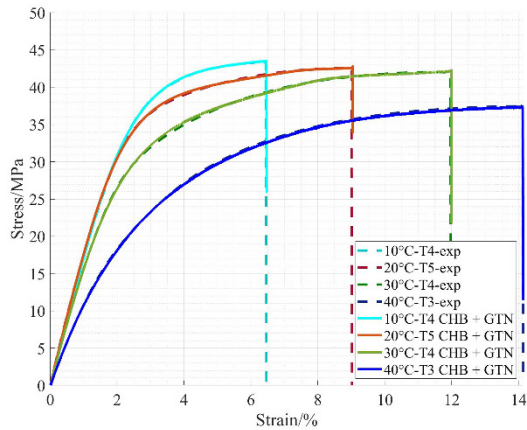

Fig. 12.5 Results of the isothermal tensile test, validation with the CHABOCHE-GTN model.
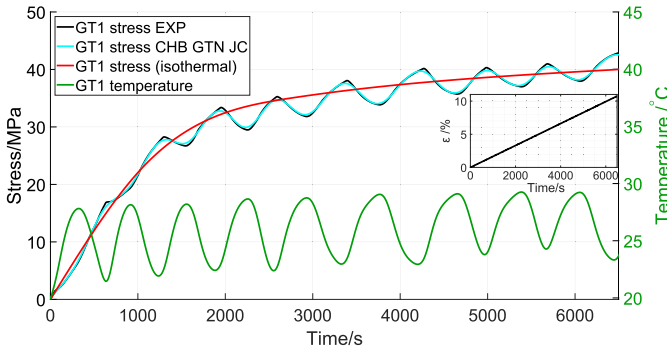

**Fig. 12.6**: Results of the non-isothermal tensile test, validation with the CHABOCHE-GTN-JC model.

periment and simulation could be achieved. The JOHNSON-COOK extension of the Chaboche-GTN model causes a stress increase with falling temperature and a stress decrease with growing temperature. So, the JOHNSON-COOK extension allows to precisely depict stress hardening and softening.

In **Fig. 12.7** the results of the multirelaxation test are presented and validated with the BODNER-PARTOM model as well as with the LEMAITRE micromechanical damage extension. The solution of the equations of the material models with optimal material parameters is compared with experimental results using the absolute deviation (Agius et al., 2017). It reproduces the discrepancy between measured and calculated stress of the material model at each time step of the experiment. An excellent agreement between experiment and simulation could be achieved with both approaches, but the extended model reached a slightly lower absolute deviation and thus a more realistic depiction of the material behaviour. This is due to consideration of the effective stress due to damage of the LEMAITRE micromechanical damage extension.

12.3 Thermomechanical Approach

In contrast to the described phenomenological description in the framework of continuum mechanics with the assumption of decoupling the mechanical and the thermal process, this section provides the full set of equations in terms of continuum thermomechanics towards a thermomechanical consistent material model. In this scheme, the second law of thermodynamics leads to the well-known COLEMAN-NOLL procedure motivating constitutive assumptions and the equation of heat conduction, as a major result of the energy balance, which is integrated in the set of equations to solve. Therefore, the applied load and the corresponding deformation path is understood as a thermodynamic process, which is expressed in a fully coupled thermomechanical problem and implies a temperature evolution in the specimen.

In this respect, the thermomechanical approach opens up the observation methods in the experimental analysis to the evolving temperature field of the samples and extents the classical characterisation procedure.
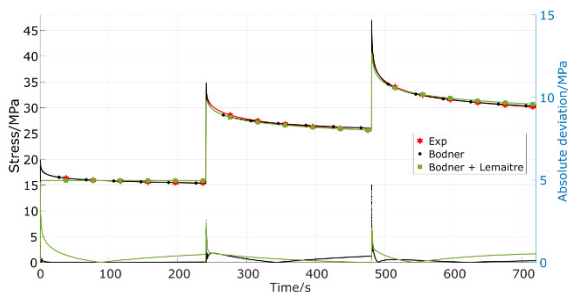
Fig. 12.7 Results of the multirelaxation test, validation with the BODNER-LEMAITRE model.

The central stress-strain characteristics are accompanied by the temperature evolution and the evolution of derived quantities such as the energy resp. energy-rate transformation ratio (ETR). These three characteristics combined can improve the assessment of the investigated deformation load path qualitatively as well as quantitatively.

The initial boundary value problem of the coupled displacement and temperature fields is experimentally well supported by a high-resolution infrared camera. A reduced thermal boundary value control simplifies the experimental measures to be realised. It is shown in the analysis that the attained surface temperature accuracy is well-suited for the identification of model parameters related to dissipative deformation phenomena.

12.3.1 Analytical Formulation in the Framework of Continuum Thermomechanics

As the analytical foundation for the description of deformation processes of fluids and solids in the framework of thermodynamics was initiated among others by the contributions of Truesdell and Noll (1992) in the 1960ies. Numerous valuable books and articles followed. A more recent book by Haupt (2002) collects the earlier findings in a clear systematisation and notation and addresses the theory of materials and its applicability to generalized material classes with a large set of various deformation phenomena comprehensively.

Thermodynamic consistency is proven by the fulfillment of the second law of thermodynamics, which can be rewritten by the reduced dissipation inequality of eq. (12.25).

$$\delta = \frac{1}{\rho}\boldsymbol{\sigma}\cdot\dot{\boldsymbol{\varepsilon}}^{\,i} - \frac{\partial\hat{\psi}}{\partial\mathbf{a}}\cdot\dot{\mathbf{a}} - \frac{1}{\rho\theta}\mathbf{q}\cdot\mathbf{g} \geqslant 0 \quad \text{with} \quad \psi = \hat{\psi}\big(\boldsymbol{\varepsilon}^{e},\theta,\mathbf{a}\big), \qquad (12.25)$$

$$\mathbf{g} = \nabla\theta \quad \text{and} \quad \mathbf{q} = -k\mathbf{g}\,.$$

The reduced dissipation inequality is the result of the COLEMAN-NOLL procedure, which connects the HELMHOLTZ free energy with the CAUCHY stress tensor $\boldsymbol{\sigma}$ as well as with the entropy designated by η in the next equation. Here, the thermodynamic potential of the HELMHOLTZ free energy ψ depends on the elastic fraction of the total strain, the temperature θ and a set of internal variables of tensorial and/or scalar type represented by $\mathbf{a}$. The notation above incorporates the theory of infinitesimal deformation ($\boldsymbol{\varepsilon} = \boldsymbol{\varepsilon}^{e} + \boldsymbol{\varepsilon}^{i}$ – additive decomposition of the strain tensor into an elastic resp. inelastic strain fraction) as well as the concept of internal variables $\mathbf{a}$ to formulate the inelastic deformation phenomena. The temperature gradient is defined by $\mathbf{g}$ and forms by being multiplied with the thermal conductivity k the heat flux $\mathbf{q}$ – the isotropic case of FOURIER's law.

Then, the mechanical fraction, the first and second term in (12.25), of the internal dissipation δ consists of the plastic stress power and the rate of stored energy dominated by the evolution of the internal variables assembled in $\mathbf{a}$.

The thermodynamic restrictions lead to the GIBBS equation and furthermore, with the balance of energy, to the equation of heat conduction (12.26), which forms a coupled initial boundary value problem with the balance of momentum and the appropriate set of boundary conditions.

$$c_\varepsilon\left(\boldsymbol{\varepsilon}^e,\theta,\mathbf{a}\right)\dot{\theta} = \theta\,\frac{\partial^2\psi}{\partial\theta\partial\boldsymbol{\varepsilon}^e}\cdot\dot{\boldsymbol{\varepsilon}}^e + \frac{1}{\rho}\boldsymbol{\sigma}\cdot\boldsymbol{\varepsilon}^i - \frac{\partial}{\partial\mathbf{a}}\left(\psi+\theta\eta\right)\cdot\dot{\mathbf{a}} - \frac{1}{\rho_R}\operatorname{div}\mathbf{q} + r \quad (12.26)$$

In (12.26), the heat capacity c_ε belongs to the thermodynamic potential ψ and refers to fixed state of deformation. The volumetric heat supply r is negligible for the observed materials.

Work ratios dating back to the pioneering findings of TAYLOR/QUINNEY, 1934, are used to give insight into the material behaviour. Additionally, the ratio φ (resp. "ETR" in **Fig. 12.8**) of the corresponding rates assesses the kinetics on the energetic level along the load path and provides, therefore, even more information with respect to the chosen material model.

$$e_i = \frac{1}{\rho}\boldsymbol{\sigma}\cdot\dot{\boldsymbol{\varepsilon}}^i \quad \text{and} \quad e_s = \frac{\partial\hat{\Psi}}{\partial\mathbf{a}}\dot{\mathbf{a}} \quad \text{combined to} \quad \varphi := e_s/e_i \quad (12.27)$$

The generalised understanding of mechanical deformation as a thermomechanical process can be connected to all sorts of possible deformation mechanisms and their analytical representation. In the last decades, numerous contributions investigated the mechanical deformation behaviour, with reference to plastictity or viscoplasticity (replacing the index "i" by either "p" or "vp" in the equations above).

The presented results of the thermomechanical analyses focus on metal alloys, where the experimental findings for a copper alloy suggest a viscoplastic behaviour (Sparr et al., 2020). In this case, the thermomechanical analysis adopts two significantly different material models for viscoplastic deformation phenomena. The first viscoplasticity model by Bodner and Lindenfeld (1995) is slightly extended in the description of the hardening behaviour, which has been outlined in 12.2.3.2, but maintains it overall structure. It is again emphasised that it does not apply a yield limit. The plastic strain rate is proportional to the stress deviator and its kinetics is
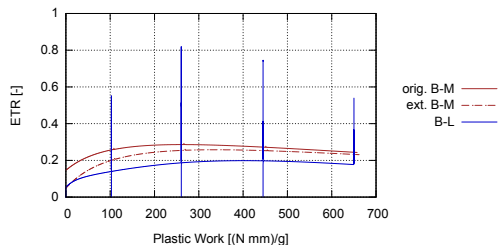
Fig. 12.8 Tensile test with stepwise increased strain rate – ETR–Plastic Work curve.

represented in the proportionality factor by an exponential function. The negative exponent itself contains the hardening parameters and is limited by the stress deviator. The saturation behaviour in the hardening range is accounted for through the plastic stress power in the evolutionary equations, which is also the regulatory entity for the consistent thermomechanical coupling.

The second model proposed by Bröcker and Matzenmiller (2013) is based on rheological model principles and returns to the strict separation of pure elastic and elastic-viscoplastic deformation with a classical yield function, which is the core of the PERZYNA rule of viscoplasticity. The hardening variables obey simple evolution equations and account for the typical saturation behaviour. The original model was extended to account for viscous deformation below the yield limit. For both cases, the reader is referred to the original articles and the given sources therein.

In the context of finite deformation, a more generalized approach was given by Shutov and Ihlemann (2011). The presented framework is a more detailed additive split of the HELMHOLTZ free energy by adding an energy fraction, which "... stands for the remaining part of the energy storage on the microstructural level ... [and] is not directly connected to any hardening effects".

A second investigation was directed at an additive manufactured stainless steel. The Ultrafuse 316L filament from BASF is well suited for 3D printing on typical FDM 3D printers. After printing, the tensile testing samples are subjected to a standard MIM (Metal Injection Molding) rinsing and a sintering processes to obtain the final shape (Form $E2 \times 6 \times 25$ according to DIN 50 125). In this case, a classical elasto-plastic material model is applied. Its motivation, mathematical formulation and the thermomechanical consistency are thoroughly discussed in Kamlah and Haupt (1998).

The basic ingredients for the stress-strain characteristic are the VON MISES type yield function:

$$f = \sqrt{\frac{2}{3}(\boldsymbol{\sigma}-\boldsymbol{\xi})' \cdot (\boldsymbol{\sigma}-\boldsymbol{\xi})'} - \sigma^y \tag{12.28}$$

and an associated flow rule. The symbol $()'$ expresses the deviatoric part of the tensorial entity, where the back stress and the yield limit are identified by $\boldsymbol{\xi}$ and by σ^y, respectively. Here, the analysis for this material model is restricted to kinematic hardening, where the evolutionary equation for the back stress follows the FREDERICK-ARMSTRONG type:

$$\dot{\boldsymbol{\xi}} = c\dot{\boldsymbol{\varepsilon}}^p - \frac{\dot{s}b}{1+ap}\boldsymbol{\xi}. \tag{12.29}$$

The material parameters a, b and c are non-negative and the accumulated plastic strain s is calculated from the consistency condition $\dot{f} = 0$. The first order differential equation in Eq. (12.29) is non-linearly coupled with the evolution of the second internal variable p:

$$\dot{p} = \frac{\dot{s}}{s_0}\big(\|\boldsymbol{\xi}\| - p\big) \quad . \tag{12.30}$$

The positive material parameter s_0 reflects the range of cycles, which is necessary to adapt to a new plastic strain amplitude in a cyclic loading regime with the amplitudes being stepwise constant. The proposed model accounts for cyclic hardening as well as cyclic softening. In consequence to the applied stress-like internal variables ξ, and p, Kamlah and Haupt (1998) develop the equation of heat conduction by means of the free enthalpy as the corresponding thermodynamic potential. All related equations can be transferred to the potential of the free HELMHOLTZ energy by the LEGENDRE transform.

All models are implemented in the finite element software suite Abaqus FEA as a user subroutine in the one-dimensional representation and are numerically analysed accordingly.

12.3.2 Experimental Approach

Fundamental contributions to the experimental setup were made by Chrysochoos et al. (1989); Rosakis et al. (2000). The technical progress in accuracy (≈ 0.01 K) and resolution (≈ 1 Megapixel) of current infrared (IR) cameras extended the applicability and simplified the experimental setup. By own experiences (Sparr et al., 2020), no extra measures have to be applied to control the thermal boundary conditions. Standardized, blackened, flat copper samples were investigated by using the ImageIR$^\circledR$ 8300 camera (InfraTec GmbH, Germany).

Additionally, the IR camera was used as an extensometer. In this regime, a random, high emissive pattern was applied on the surface of the sample. A well-designed correlation algorithm of the IR image sequence combined with an emissivity correction scheme allows an accurate displacement compensation in the temperature measurement as well as a surface strain field evaluation, which meets the accuracy of other contact-free methods.

The temperature evolution of the full specimen surface as well as the temperature of the clamps were established. The machine and the camera were synchronized by a trigger signal.

12.3.3 Results and Discussion

The model parameters were identified by tensile tests at various strain rates. The model was validated by a more complex loading scheme. **Figure 12.9** (*left*) shows the calculated stress-strain curve of four load-unload loops, while the strain rate is increased stepwise. Especially, the unloading slopes are best met by the BODNER-LINDENFELD model (B-L). The temperature evolution is illustrated by **Fig. 12.9** (*right*) and is in good accordance with the measured temperature field.

The graphs in **Fig. 12.8** of the applied models gives a third characteristic - the ratio φ over the plastic work. The final plastic work value after four steps is almost
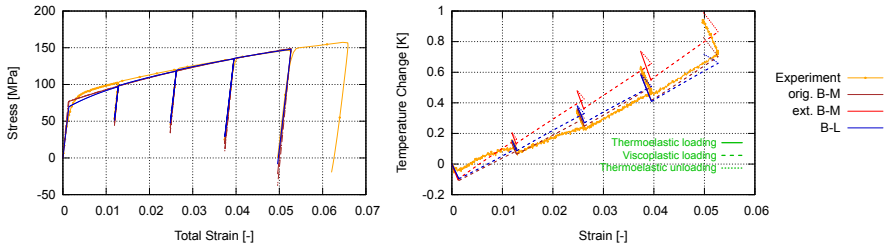
Fig. 12.9: Tensile test with stepwise increased strain rate – (*left*) σ−ε curve and (*right*) ΔT−ε curve.

identical for all three curves, while the values of the ETR ratio for the BRÖCKER-MATZENMILLER models (original resp. extended B-M) are slightly higher than for the B-L model. The starting ETR ratios at the beginning of the elastic-viscoplastic deformation match for the extended B-M and the B-L model only. In contrast to the B-M models, the BODNER-LINDENFELD model shows a very pronounced dynamics in the turning points of the load parameter (transition for loading to unloading and vice versa) .

In the pure tensile test, the elastic-plastic material model by Kamlah and Haupt (1998) is limited to kinematic hardening. The graphs in **Figs. 12.10** and **12.11** compare two parameter sets for the additive manufactured stainless steel. The main differences occur quali- and quantitatively at the beginning of plastic deformation. While the σ-ε curve of set 2 agrees very well with the experimental data (blue),
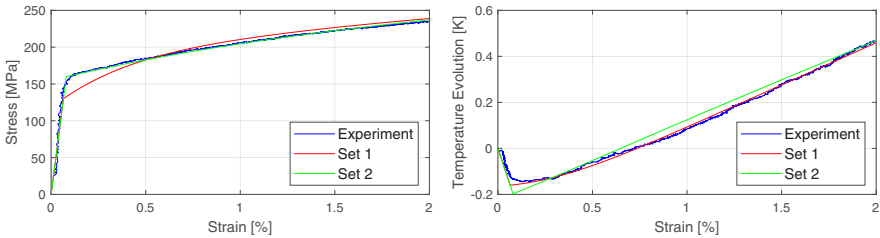
Fig. 12.10: Tensile test stainless steel (AM) with the application of the KAMLAH-HAUPT model – (*left*) σ−ε curve and (*right*) ΔT−ε curve.

Fig. 12.11 Tensile test stainless steel (AM) with the application of the KAMLAH-HAUPT model – ETR–Plastic Work curve.
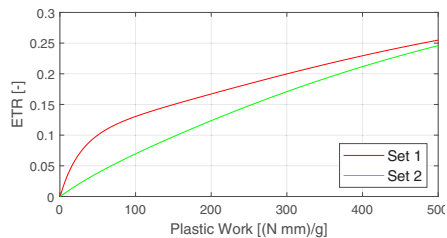
the set 1 is better suited to describe the smooth transition at the yield limit in the temperature characteristics.

This becomes even more obvious in the ETR characteristics. The larger slope of the parameter set 1 at the beginning of plastic deformation accommodates better the behaviour observed of other metals or metal alloys, which poses questions on the applied material model. The microstructure of the printed material has significant differences to its casted counterparts in terms of grain size and voids. Therefore, it is sensible to look for theoretical enhancements in the thermomechanical formulation, which reflect the described effects of continuum damage mechanics in Sect. 12.2 for polymers, or to investigate the microstructure of materials with a complex manufacturing procedure in more detail and apply suitable homogenisation strategies. Both approaches rely on the numerical and experimental methods and tools in the macroscopic scale.

12.4 Numerical Models Based on CT Data

While materials with moderate void volume fraction can be modeled with an ansatz from continuum damage mechanics (cf. Sect. 12.2), other microstructures need to be investigated at their corresponding scale. In the case of complex deformation mechanisms of network structures or an unknown multiphase material interaction, **Fig. 12.12**, it is necessary to take the actual microstructure of the material into account. It is important in the description of the material behaviour for numerical analyses. One of the methods of analysing such materials is the preparation of a geometry model and its discretization based on computed tomography (CT) (Richert and Huber, 2018).
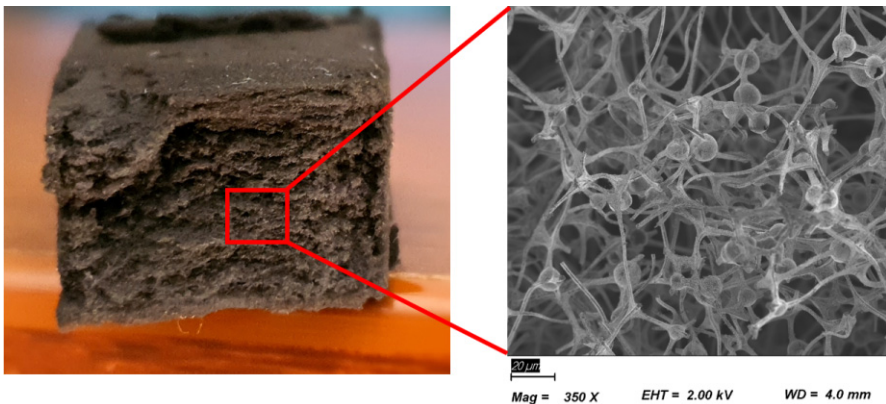

Fig. 12.12: An example of a material with a non-homogeneous microstructure and a microscopic image made with the SEM technique.

Various modelling approaches simplify and parametrise the complex microstructure of porous materials for studying the structure–property relationship based on artificially generated structures. This chapter presents an approach to generate computational efficient and versatile finite element (FE) beam models which are based on skeletonization and diameter information derived from CT data. The geometrical skeleton network is thoroughly examined for a better understanding of the microstructural material behaviour and to define an effective representative volume element (RVE). A skeleton FE beam model is derived that can predict the macroscopic mechanical behaviour of the material (**Fig. 12.13**). Comparisons of the mechanical response between a beam model and a model based on a volumetric discretisation for the skeleton structure are conducted. The skeletonization algorithm was implemented in the open-source software FIJI (Schindelin et al., 2012), among other things commonly used for the geometry analysis and reconstruction of image data.

Based on the imaging process (DICOM), the skeleton is obtained using the FIJI software package. The sequence of grayscale images are thresholded first to obtain binary data. For this purpose, Otsu method (Otsu, 2018) was used. Next, using medial surface axis thinning algorithms (Lee et al., 1994) images of this sequence were skeletonized (**Fig. 12.14**) resulting in a new sequence of images, with white pixels on the estimated axes of beams only. In-house tools, based on the OpenCV library and the Python environment, were then used to create a finite element mesh.

First, the data from Fiji, in the form of a series of monochrome bitmaps, are read. Then, the whole volume is scanned, pixel by pixel, for all x, y and z coordinates, using a frame of the size $3 \times 3 \times 3$ pixels. The further actions will be applied if the central pixel is white, depending on the number of neighbouring white pixels within the frame.

If there is only one neighbouring white pixel, the current pixel is considered as an endpoint. If there are exactly two neighbours, the current pixel lies on the beam. If there are three or more neighbours, the current pixel represents a beam junction (**Fig. 12.15**). Between neighbouring points the linear elements are created, forming an initial mesh. After the scanning of the bitmap series, the initial mesh is being simplified. The endpoint and junction nodes are preserved, while the most of the
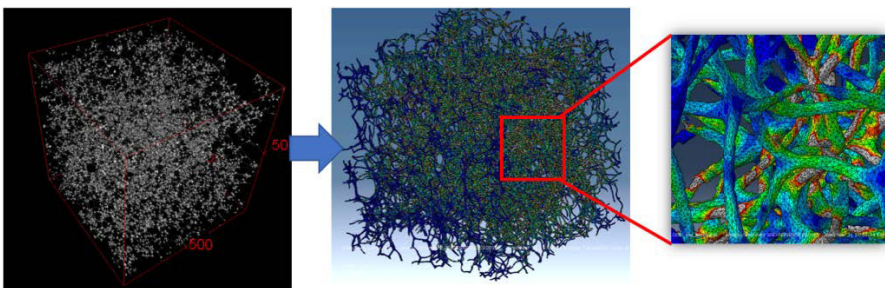
Fig. 12.13: CT model and its representative FE model based on a full geometry volume.
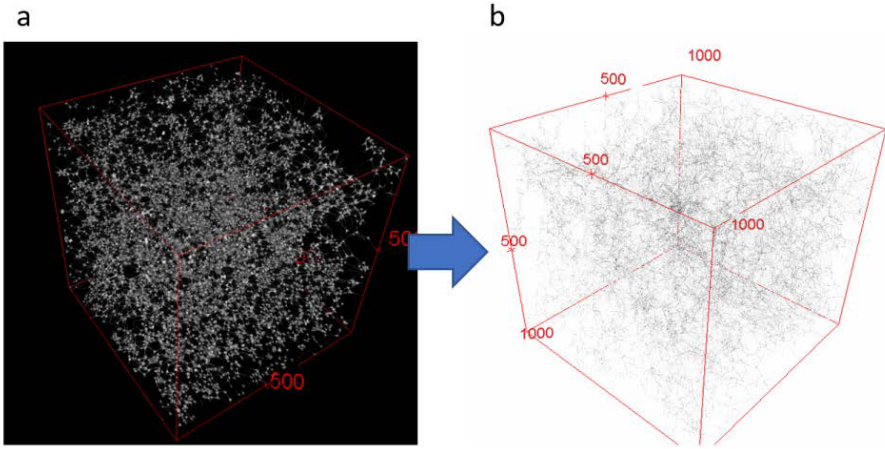
Fig. 12.14: The process of skeletonization from CT data in FIJI software.
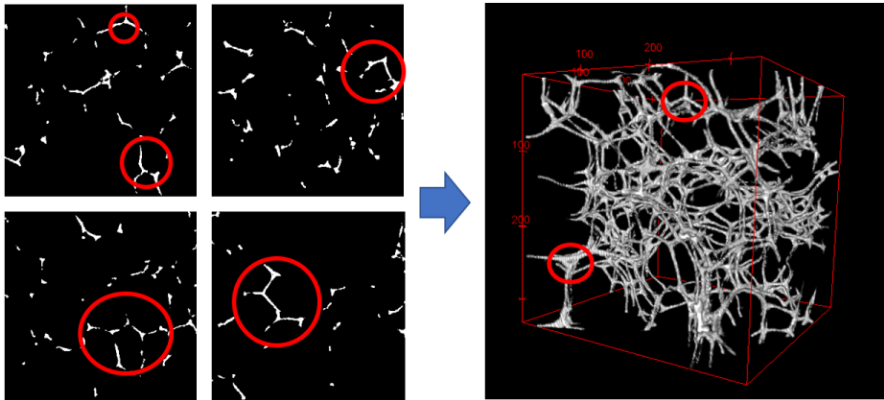
Fig. 12.15: Selected CT imaging sequences and a view of the nodes identifying the connections of individual branches.

rest of the nodes (lying along the beams) are removed. The only exception are nodes lying in the middle of longer beams, which are preserved as well. The same applies to the elements of the initial mesh that connect removed nodes. The next step is the process of filling in the obtained FE model. The Gmsh software will be used for this process. Based on the existing nodes of the skeleton, a mesh is added where matrix properties are assigned to.

The generated FE model incorporates the geometry of the real microstructure and allows for a high computational efficiency (**Fig. 12.16**). To this end, the discretisation of the structure has made use of beam elements available in Abaqus FEA (Abaqus, 2014). As proposed by Huber *et al.*, the cylindrical B31 beam element is used, which account for transverse shear strain in the Timoshenko beam
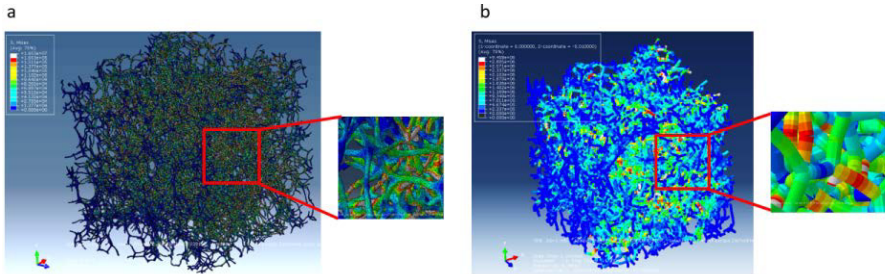
Fig. 12.16: Model comparison: a) FE model based on volumetric elements; b) reduced FE model based on beam elements.

theory (Huber et al., 2014; Roschning and Huber, 2016). In comparison to the artificially generated beam model of Huber *et al.*, the novelty is that the skeleton FE beam model emulates the actual ligament path and shape of the sample, which is based on the skeleton and diameter information, respectively, and extracted from the computed tomography. As for the translation of the tomography data into the beam model, each ligament is divided into several beam elements along the skeleton line. The number of beam elements per ligament depends on the chosen discretisation. Each cylindrical beam element receives the average diameter of the associated voxels. Preliminary numerical validation (**Fig. 12.16**) was performed on the basis of the obtained beam models. The obtained result and the stress concentration in the same computational node were evaluated. The resulting numerical model is useful for creating an effective RVE.

12.5 Summary

Each of the three main sections of this contribution can be considered separately. However, in our understanding, essential points of overlaps exist in the three examined sub-areas of mechanics, so that in the overall view, the combination of the different aspects makes a significant contribution to the analysis of new materials. This concerns both the experimental investigations as well as the numerical simulations.

The temperature dependency of the respective material parameters in Sect. 12.2 is based on the classical decoupling of purely mechanical and purely thermal processes in the context of a continuum mechanical description for the numerical analysis. With the help of experimental observations, a microstructural evolution by nucleation and/or pore growth is proven. This development could be successfully depicted with the integration of continuum mechanical damage models. Slow temperature changes by external heating in a climatic chamber can be adequately represented by the model variants as well, whereby the self-heating due to loading is not accounted for in the material models.

The analytical extension to the full thermomechanical coupling with regard to an evolving temperature field considered in Sect. 12.3 gives additional information about the physicality of the applied material models. The self-heating is driven by the elastic and inelastic deformation and determined by the thermal parameters in the general equation of heat conduction. The temperature evolution is dominated by the internal dissipation and, therefore, strongly related to plastic resp. viscoplastic deformation mechanisms covered in the material models in different ways. The models need to obey to second law of thermodynamics. In addition to the classical stress-strain characteristic, the temperature evolution as well as derived parameters by evaluating of the energy balance are available and complement the physical understanding. The quantification of the dissipation due to damage is currently not taken into account. With respect to damage modeling, additional energy terms according to nucleation and/or pore growth have to be integrated, and the corresponding material parameters have to be quantified.

A similar approach is also conceivable for multiphase materials from complex manufacturing processes. However, the basis for this is an analysis of the components and a microstructural analysis of the interaction of these components. The described image processing and the associated reconstruction algorithms of Sect. 12.4 provide access to a deeper understanding. With the general assumptions of continuum mechanics, the aforementioned methods can be applied on different scales.

References

Abaqus (2014) Documentation 6.14. Dassault Systèmes, Providence Road, Rhode Island, USA

Agius D, Kajtaz M, Kourousis KI, Wallbrink C, Wang CH, Hu W, Silva J (2017) Sensitivity and optimisation of the chaboche plasticity model parameters in strain-life fatigue predictions. Materials & Design 118:107–121, DOI 10.1016/j.matdes.2017.01.027

Arndt C, Hauck M, Wacker I, Zeller-Plumhoff B, Rasch F, Taale M, Nia AS, Feng X, Adelung R, Schröder RR, Schütt F, Selhuber-Unkel C (2021) Microengineered hollow graphene tube systems generate conductive hydrogels with extremely low filler concentration. Nano Letters 21(8):3690–3697, DOI 10.1021/acs.nanolett.0c04375, pMID: 33724848

Bodner SR (2000) Unified plasticity - an engineering approach. Final Report for Period 01 AFRL-ML-WP-TR-2001-4019, Technion-Israel Institute of Technology, Haifa 32000, Israel

Bodner SR, Lindenfeld A (1995) Constitutive modelling of the stored energy of cold work under cyclic loading. European Journal of Mechanics - A/Solids 14(3):333–348

Bodner SR, Partom Y (1975) Constitutive equations for elastic-viscoplastic strain-hardening materials. Transaction ASME Journal of Applied Mechanics 42(2):385–389, DOI 10.1115/1.3423586, https://asmedigitalcollection.asme.org/appliedmechanics/article-pdf/42/2/385/5118618/385_1.pdf

Bröcker C, Matzenmiller A (2013) An enhanced concept of rheological models to represent nonlinear thermoviscoplasticity and its energy storage behavior. Continuum Mechanics and Thermodynamics 25(6):749–778, DOI 10.1007/s00161-012-0268-3

Carolan D, Chong H, Ivankovic A, Kinloch A, Taylor A (2015) Co-continuous polymer systems: A numerical investigation. Computational Materials Science 98:24–33, DOI 10.1016/j.commatsci.2014.10.039

Chaboche JL (1989) Constitutive equations for cyclic plasticity and cyclic viscoplasticity. International Journal of Plasticity 5(3):247–302, DOI 10.1016/0749-6419(89)90015-6

Chrysochoos A (2012) Infrared thermography applied to the analysis of material behavior: a brief overview. Quantitative InfraRed Thermography Journal 9(2):193–208, DOI 10.1080/17686733.2012.746069

Chrysochoos A, Maisonneuve O, Martin G, Caumon H, Chezeaux J (1989) Plastic and dissipated work and stored energy. Nuclear Engineering and Design 114(3):323–333, DOI 10.1016/0029-5493(89)90110-6

Cook G, Cook W (1983) A constitutive model and data for metals subjected to large strains, high strain rates and high temperatures. Proceedings of the Seventh International Symposium on Ballistics, The Hague pp 541–547

DIN Deutsches Institut für Normung eV (2012) DIN EN ISO 527-2: Kunststoffe - Bestimmung der Zugeigenschaften: Teil 2: Prüfbedingungen für Form- und Extrusionsmassen

Dupin S, Lame O, Barrès C, Charmeau JY (2012) Microstructural origin of physical and mechanical properties of polyamide 12 processed by laser sintering. European Polymer Journal 48(9):1611–1621, DOI 10.1016/j.eurpolymj.2012.06.007

El Ghezal M, Doghri I (2018) Porous plasticity: Predictive second moment homogenization models coupled with Gurson's single cavity stress-strain solution. International Journal of Plasticity 108:201–221, DOI 10.1016/j.ijplas.2018.05.006

Forster AM (2015) Materials testing standards for additive manufacturing of polymer materials: State of the art and standards applicability. Nist interagency/internal report (nistir), National Institute of Standards and Technology, Gaithersburg, MD, DOI 10.6028/NIST.IR.8059

Franke R, Schob D, Ziegenhorn M (2017) Prüfverfahren und numerische Simulation von mechanischen Eigenschaften 3D-gedruckter thermoplastischer Kunststoffe, Springer Fachmedien Wiesbaden, pp 137–158. DOI 10.1007/978-3-658-17780-5_9

Gong YP, Hyde CJ, Sun W, Hyde TH (2010) Determination of material properties in the chaboche unified viscoplasticity model. Proceedings of the Institution of Mechanical Engineers, Part L: Journal of Materials: Design and Applications 224(1):19–29, DOI 10.1243/14644207JMDA273

Goodridge RD, Tuck CJ, Hague RJM (2012) Laser sintering of polyamides and other polymers. Progress in Materials Science 57(2):229–267, DOI 10.1016/j.pmatsci.2011.04.001

Gurson AL (1977) Continuum theory of ductile rupture by void nucleation and growth - Part I. Yield criteria and flow rules for porous ductile media. Journal of Engineering Materials and Technology 99(1):2–15

Haupt P (2002) Continuum Mechanics and Theory of Materials, 2nd edn. Springer-Verlag, DOI 10.1007/978-3-662-04775-0

Huber N, Viswanath R, Mameka N, Markmann J, Weißmüller J (2014) Scaling laws of nanoporous metals under uniaxial compression. Acta Materialia 67:252–265, DOI 10.1016/j.actamat.2013.12.003

Kachanov M (1980) Continuum model of medium with cracks. Journal of the Engineering Mechanics Division 106(5):1039–1051, DOI 10.1061/JMCEA3.0002642

Kamlah M, Haupt P (1998) On the macroscopic description of stored energy and self heating during plastic deformation. International Journal of Plasticity 13(10):893–911, DOI 10.1016/S0749-6419(97)00063-6

Khdir Y, Kanit T, Zaïri F, Naït-Abdelaziz M (2013) Computational homogenization of elastic–plastic composites. International Journal of Solids and Structures 50(18):2829–2835, DOI 10.1016/j.ijsolstr.2013.03.019

Krempl E (1987) Models of viscoplasticity some comments on equilibrium (back) stress and drag stress. Acta Mechanica 69(1):25–42, DOI 10.1007/BF01175712

Lee T, Kashyap R, Chu C (1994) Building skeleton models via 3-d medial surface axis thinning algorithms. Graphical Models and Image Processing 56(6):462 – 478, DOI 10.1006/cgip.1994.1042

Lemaître J, Desmorat R (2005) Engineering Damage Mechanics: Ductile, Creep, Fatigue and Brittle Failures. Springer, Berlin and New York

Oldyrev PP, Tamuzh VP (1969) Energy dissipation in a glass-reinforced plastic during prolonged cyclic deformation. Strength of Materials 1(3):244–248, DOI 10.1007/BF01543209

Olschewski J (1996) Viskoplastische Materialmodellierung und Anwendung im Gasturbinenbau. Technische Mechanik 16(1):39–50

Otsu N (2018) A threshold selection method from gray-level histograms. IEEE Transactions on Systems, Man, and Cybernetics 9(1):62 – 66, DOI 10.1109/TSMC.1979.4310076

Perzyna P (1963) The constitutive equations for rate sensitive plastic materials. Quarterly of Applied Mathematics 20:321–332, DOI 10.1090/qam/144536

Reese S (1998) Multiplicative thermo-viscoplasticity: A thermodynamic model and its finite element implementation. Technische Mechanik 18(3):209–216

Rice J, Tracey D (1969) On the ductile enlargement of voids in triaxial stress fields. Journal of the Mechanics and Physics of Solids 17(3):201–217, DOI 10.1016/0022-5096(69)90033-7

Richert C, Huber N (2018) Skeletonization, geometrical analysis, and finite element modeling of nanoporous gold based on 3d tomography data. Metals 8(282):1 – 20, DOI 10.3390/met8040282

Rosakis P, Rosakis A, Ravichandran G, Hodowany J (2000) A thermodynamic internal variable model for the partition of plastic work into heat and stored energy in metals. Journal of the Mechanics and Physics of Solids 48(3):581–607, DOI 10.1016/S0022-5096(99)00048-4

Roschning B, Huber N (2016) Scaling laws of nanoporous gold under uniaxial compression: Effects of structural disorder on the solid fraction, elastic poisson's ratio, young's modulus and yield strength. Journal of the Mechanics and Physics of Solids 92:55–71, DOI 10.1016/j.jmps.2016.02.018

Schindelin J, Argenda-Carreras I, Frise E (2012) Fiji: an open-source platform for biological-image analysis. Nature Methods 9:676 – 682, DOI 10.1038/nmeth.2019

Schob D, Roszak R, Sagradov I, Sparr H, Ziegenhorn M, Kupsch A, Léonard F, Müller BR, Bruno G (2019) Experimental and numerical simulation of material and damage behaviour of 3D printed polyamide 12 under quasi-static loading. Archives of Mechanics 71(4-5):507–526, DOI 10.24423/aom.3162

Schob D, Sagradov I, Roszak R, Sparr H, Ziegenhorn M, Kupsch A, Léonard F, Müller B, Bruno G (2020) Experimental determination and numerical simulation of material and damage behaviour of 3D printed polyamide 12 under cyclic loading. Engineering Fracture Mechanics 229(106841), DOI 10.1016/j.engfracmech.2019.106841

Shutov AV, Ihlemann J (2011) On the simulation of plastic forming under consideration of thermal effects. Materialwissenschaft und Werkstofftechnik 42(7):632–638, DOI 10.1002/mawe.201100821

Soyarslan C, Pradas M, Bargmann S (2019) Effective elastic properties of 3d stochastic bicontinuous composites. Mechanics of Materials 137:103,098, DOI 10.1016/j.mechmat.2019.103098

Sparr H, Roszak R, Sagradov I, Schob D, Ziegenhorn M (2020) Thermo-viscoplastic material modelling for self-heating loads and its experimental verification. Technische Mechanik 40(1):66–76, DOI 10.24352/UB.OVGU-2020-015

Stichel T, Frick T, Laumer T, Tenner F, Hausotte T, Merklein M, Schmidt M (2017) A round robin study for selective laser sintering of polyamide 12: Microstructural origin of the mechanical properties. Optics & Laser Technology 89:31–40, DOI 10.1016/j.optlastec.2016.09.042

Taylor G, Quinney H (1934) The latent energy remaining in a metal after cold working. Proceedings of the Royal Society of London Series A, Containing Papers of a Mathematical and Physical Character 143(849):307–326

Truesdell C, Noll W (1992) The Non-Linear Field Theories of Mechanics, 3rd edn. Springer-Verlag, Berlin, DOI 10.1007/978-3-662-10388-3

Tvergaard V, Needleman A (1984) Analysis of the cup cone fracture in a round tensile bar. Acta Metallurgia 32(1):157–169, DOI 10.1016/0001-6160(84)90213-X

van Hooreweder B, de Coninck F, Moens, Boonen R, Sas P (2010) Microstructural characterization of SLS-PA12 specimens under dynamic tension/compression excitation. Polymer Testing 29(3):319–326, DOI 10.1016/j.polymertesting.2009.12.006

Yanase K, Chatterjee H, Ghosh SK (2020) On numerical evaluation of eshelby tensor for superspherical and superellipsoidal inclusions in isotropic elastic material. Composites, Part B 192:107,964, DOI 10.1016/j.compositesb.2020.107964

Zaïri F, Naït-Abdelaziz M, Woznica K, Gloaguen JM (2005) Constitutive equations for the viscoplastic-damage behaviour of a rubber-modified polymer. European Journal of Mechanics - A/Solids 24(1):169–182, DOI 10.1016/j.euromechsol.2004.11.003